# A 151.5 MHz Southern Sky Survey covering the RA range $0^h < \mathbf{RA} < 6^h$ and the Declination range $-70° \leq DEC \leq -10°$
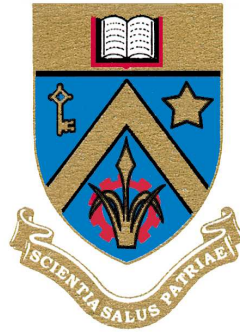
Soobash Daiboo

Physics Department

University of Mauritius, Mauritius
Supervisors:
N. Udaya Shankar (RRI), G.K. Beeharry (UoM)

PhD Thesis
30$^{\text{th}}$ August 2011

Raman Research Institute, Bangalore, India

I would like to dedicate this thesis to my loving parents ...

Acknowledgements

It is a pleasure to thank all those who made this thesis possible.

Declaration

I hereby declare that the work presented in this thesis has been done by me. No part of this work has been submitted for another degree or qualification.

Date:

(Soobash Daiboo)

Abstract

The Mauritius Radio Telescope has been built with the main objective of carrying out an equivalent of 6C survey in the southern hemisphere. The present work is a step in this direction. MRT data processing is both complex and challenging due to the non-coplanarity of the array and the heterogeneous nature of its database containing 20,000 hours of observations carried out over a span of five years. This thesis summarizes the important out comes of the present work, challenges faced and methodologies developed to meet those challenges.

The main outcome of the present work is a set of images of the sky at 151.5 MHz with a resolution of $4' \times 4'.6 \sec(DEC + 20°.14)$ and a sensitivity of $\sim$ 300 mJy covering DEC range $-75° \leq DEC \leq -10°$ and RA range $0^h <$ RA $< 6^h$ (Set II images), a source catalog containing 3000 sources, a subset of this catalog giving the flux density at 151.5 MHz of $\approx 100 MS4 sources and a compendium of several extended sources seen in Set II images.$

The present work began with the investigation of systematics in the positional errors of sources seen in the MRT source catalog extracted from set I images covering DEC range $-75° \leq DEC \leq -10°$ and RA range $18^h <$ RA $< 24^h$the RA range (Pandey & Udaya Shankar, 2006). Systematics in positional errors were found when the positions of sources common to MRT and MRC catalogues were compared. The positional errors in declination were found to be significant (up to about 50% of the MRT beamwidth in declination). We applied two-dimensional homography to correct for systematic positional errors in the image domain and thereby avoid re-processing the visibility data. Positions of bright point sources, common to MRT catalogue and MRC, were used to set up an over determined system to solve for the homography matrix. After correction the errors were found to be within 10% of the beamwidth for these bright sources and the systematics are eliminated from the images. We are of the view that this technique will be of relevance to the new generation radio telescopes where, owing to huge data rates, only images after certain integration would be recorded as opposed to raw visibilities.

Our investigations cued to possible errors in the array geometry. We re-estimated the array geometry using the astrometry principle. The estimates show an error of 1 mm/m, which results in an error of about half a wavelength at 150 MHz for a 1 km north-south baseline. The estimates also indicate that the east-west arm is inclined by an angle of

$4''$ to the true east-west direction. We re-imaged regions of sky common to set I images using the re estimated array geometry and proved that the systematic positional errors disappear by incorporating the new array geometry.

To provide the right hardware and software environments to meet the challenges of processing MRT data, we assembled a set of 8 computers inter-connected using a 100 Mbps Ethernet link to store the intermediate products of analysis and developed a set of software pipelines to run MARMOSAT (The Mauritius Minimum Operating System for Array Telescopes) effectively on this MRT cluster. The main focus of the new development was inter-process communication and homogenization of the database, which had kept changing in structure along with system development and commissioning. We also paid attention to the fact that one required the final products in FITS image format to be able to distribute the images to the astronomical community.

Armed with good hardware and software environments, we examined the quality of data for the RA range 0 to 18 hours. We found that the data quality decreased as one moved away from the calibrators used for phase/amplitude calibration of the array. In view of this we designed and developed a field of view based calibration procedure to facilitate calibration. This helped us to get calibration very close to the proximity of the sky area being analyzed and helped us include several files which were earlier excluded for imaging due to lack of calibrators.

With feed back from data quality assessment we analyzed the MRT data for the RA range 0 to 6 hr (Set II images), covering approximately one steradian of the sky. We have been able to detect 3837 sources in Set II images. 1500 of these sources have matching MRC sources. By carrying out a statistical analysis of positional errors and flux densities of sources common to MRC and MRT, we have carefully corrected for positional errors in our images and have revised our flux density scale. This shows that the median spectral index of sources between 150 and 408 MHz to be 0.87. This is along the expected lines. From the catalog we have made a list of sources, which have steep spectral indices ($\alpha < 1.3$) for further studies.

The MRT has a very good uv coverage with baselines going down to 2m both along EW and S directions. With this we were indeed expecting to detect extended sources in the images. We were able to detect all the 71 SUMSS extended sources listed in the ?? paper in the RA range 0 to 6 hr. 33 of these sources show extended emission at 151.5 MHz. In addition we find 16 extended sources in MRT not listed by them. The median spectral index of the 33 extended sources common to MRT and SUMSS is -0.74. We have prepared a source list including the integrated flux densities and spectral indices of these sources. We envisage a follow-up study of these sources in our future work.

Contents

Chapter 1

Introduction

1.1 Low frequency surveys

Surveying the sky is a major part of astronomy. Large surveys of the sky give a broad view of the Universe. They point out where sources are in the sky and generate large samples of sources for statistical studies of their properties and their evolution. In some cases astronomers interested in a particular object will find that the survey images are sufficient to entirely obviate the need for telescope time. Surveys also help astronomers get observing time on larger and more powerful telescopes.

Enormous data-sets covering thousands of square degrees of sky at different wavelengths and entirely new approaches are required to answer outstanding unsolved questions in astronomy (CAASTRO, http://www.caastro.org/).

Three interlinked scientific programmes, each of which can be addressed only with the all-sky perspective provided by wide-field telescopes are:

1. The Evolving Universe: When did the first galaxies form, and how have they then evolved ? A study of EoR being one of its main components.

2. The Dynamic Universe : What is the high-energy physics that drives change in the Universe ?

3. The Dark Universe: What are the Dark Energy and Dark Matter that dominate the cosmos ?

In the jigsaw puzzle of the Universe requiring assembly of numerous tiles, the present work, a low frequency (151.5 MHz) survey of the southern sky, is an attempt to provide a small interlocking tile.

It is important to briefly review the surveys conducted in the past and the ones planned in the future to gain an insight into the importance of the present work. The next sections in this chapter briefly describe surveys connected with the work presented in this thesis.

There have been many surveys conducted in the past and there are many more planned in the future. Though all surveys have the common objective to quickly sample the population of sources, the design of specific surveys make them probe different parameter spaces. The low frequency surveys (f $\leq$ 1 GHz) conducted in the past have been a source of new discoveries of astronomical phenomena as well as the starting point for detailed study of individual objects in the sky.

Even though radio astronomy started at low frequencies, the quest for higher angular resolution and the difficulties in handling ionospheric effects shifted most radio observations towards higher frequencies. Only a few low frequency surveys have been carried out so far. This has left the low frequency (below 150 MHz) spectrum poorly explored. This is despite many unique astrophysical questions that can be better addressed at low frequencies as well as those problems requiring accurate source spectra at both high and low frequency ends. Fortunately, there is a renewed interest in exploring the Universe at low frequencies due to its scientific potential. Lessons learnt in wide-field imaging, self-calibration, interference mitigation, development of multi-channel digital correlators and advances in computing have helped to overcome the problems plaguing low frequency observations. This has re-kindled interest in surveying both the northern and southern hemispheres. Existing telescopes like Giant Metrewave Radio Telescope (GMRT) and Westerbok Synthesis Radio Telescope (WSRT) are getting low frequency feeds (refs). Low Frequency Array (LOFAR) (Kassim *et al.*, 2004) and Murchison Widefield Array (MWA) (Morales *et al.*, 2006) are at an advanced state of development, building and commissioning .

Table 1.1 lists the major low frequency surveys in both the hemispheres. The table clearly indicates that the southern sky is poorly explored at low frequencies. On the other hand the 6C survey in the northern sky provides a moderately deep radio catalog reaching source densities of about 2×10^4 sources per steradian.

Past and on-going major low frequency surveys are briefly reviewed and planned low frequency telescopes are briefly discussed in the next section.

1.1.1 Ongoing and past low frequency surveys

NVSS

The NRAO VLA Sky Survey (NVSS) (Condon *et al.*, 1998) covers the sky north of $\delta \geq -40°$ (82% of the celestial sphere) at 1.4 GHz. The principal data products are (1) a set of 2326 $4° \times 4°$ continuum "cubes" with three planes containing Stokes I, Q, and U images plus (2) a catalog of almost 2×10^6 discrete sources stronger than S$\approx$2.5 mJy. The images all have $\theta = 45"$ FWHM resolution and nearly uniform sensitivity. Their rms brightness fluctuations are $\sigma \sim 0.45$ mJy beam^{-1} ~ 0.14 K for Stokes I and $\sigma \sim 0.29$ mJy beam^{-1} ~ 0.09 K for Stokes Q and U. The rms uncertainties in right ascension and

Northern declination surveys					
Frequency (MHz)	Observatory	Resolution	Declination Coverage	Sensitivity	Number of Sources
34.5	GEETEE	26×42	-30 to +60	15 Jy	≈3000
38	Cambr. WKB	45× 45	-45 to +35	14 Jy	1000
74	VLSS	80×80	-30 to +90	500 mJy	ongoing
151	Cambr. 6C	4× 4	+30 to +90	120 mJy	≈35,000
178	Cambr. 3CR	2×2	-5 to +90	9 Jy	328
178	Cambr. 4C	75× 75	-7 to +80	2 Jy	4843
232	MSRT	38× 38	30 to +90	150 mJy	≈34,000
325	Westerbork	$54'' \times 54''$	29to 90	18 mJy	229,576
365	Texas	$10'' \times 10''$	-357 to 715	150 mJy	67,551
408	Effelsberg	085 × 085	-10 to +50	0.2 Jy	–
150	TGSS	$20'' \times 20''$	$> -30°$	9 mJy	ongoing
Southern declination surveys					
34.5	GEETEE	26×42	-30 to +60	15 Jy	≈3000
38	Cambr. WKB	45× 45	-45 to +35	14 Jy	1000
74	VLSS	80×80	-30 to +90	500 mJy	70000
352	Westerbork	$54'' \times 54''$	-26 to 9	18 mJy	73,570
365	Texas	$10'' \times 10''$	-357 to 715	150 mJy	67,551
408	Parkes	085×085	-60 to +10	1 Jy	–
408	Molonglo	2× 2	-60 to +18	0.6 Jy	>12000
843	SUMSS	$45'' \times 45''$	$< -30°$	6 mJy	>210412
150	TGSS	$20'' \times 20''$	$> -30°$	9 mJy	ongoing

Table 1.1: Surveys below 0.5 GHz (Also see Pandey (2006), Golap (1998). This is only a representative sample of the surveys available.

declination vary from $<\sim 1''$ for the $N \sim 4 \times 10^5$ sources stronger than 15 mJy to about $7''$ at the survey limit.

SUMSS

The Sydney University Molonglo Sky Survey (SUMSS) (Mauch *et al.*, 2008) is being carried out at 843 MHz with the Molonglo Observatory Synthesis Telescope (MOST) with its upgraded wide-field capability. The survey consists of $4°.3 \times 4°.3$ mosaic images with $45'' \times 45'' \operatorname{cosec}(\delta)$ resolution, covering 2.4 steradians of the sky from $-30°$ declination southwards with galatic latitude $|b| > 10°$. The resolution and sensitivity of SUMSS (1-σ limit ~ 1 mJy) are well-matched to the NRAO VLA Sky Survey (NVSS). Together NVSS and SUMSS cover the whole sky. A comparison of sources in NVSS and SUMSS

catalogues show that the median spectral indices of sources in the frequency range 408 MHz to 1.4 GHz is -0.83 (Mauch *et al.*, 2003).

The version 2.0 of the SUMSS catalogue consists of 210,412 radio sources made by fitting elliptical Gaussians in 633 SUMSS mosaics to a limiting peak brightness of 6 mJy beam^{-1} at declinations $< -50°$, and 10 mJy beam^{-1} at declination $> -50°$. Positional accuracies are $1''$ to $2''$ for sources with $S_p \geq 20$ mJy beam^{-1}, and are always better than $10''$. The internal flux density scale is accurate to 3%. Image artefacts have been classified using a decision tree, which correctly identifies and rejects spurious sources in over 96% of cases.

MRC

The Molonglo Reference Catalog (MRC) (Large *et al.*, 1991) lists 12,141 discrete sources with flux density ≥ 0.7 Jy. The survey covers 7.85 steradians of the sky defined by $-85° \leq \delta(1950) \leq +18°.5$, $|b| \geq 3°$. A few sources beyond the declination limits mentioned above are also included. The catalogue gives the celestial coordinates along with standard errors which are typically between 3 and 10 arcsec. 408-MHz flux densities have errors typically lying between 4 and 10 per cent of the flux density. The overall source density is 1,500 sources per steradian, corresponding to 0.001 per beam area. There are 7,347 sources listed with flux density ≥ 1.00 Jy, at which level the catalogue is 99% complete.

TEXAS

The TEXAS survey (Douglas *et al.*, 1996) was carried out at 365 MHz with the Texas Interferometer during 1974-1983. It lists 67,551 radio sources between $-35.5° \leq \delta \leq 71.5°$. The positional uncertainty is between 1% to 5% of the beam, the rms noise ≈ 20 mJy and the limiting flux density 150 mJy. The Texas Interferometer is a 5-element meridian transit synthesis system. The *uv* coverage is poor and the survey suffers from irregular beam shapes and lobe shifts. The completeness of the survey is a function of declination.

WENSS

The Westerbork Northern Sky Survey (WENSS) (Rengelink *et al.*, 1997) is a low-frequency radio survey that cover the whole sky north of $\delta = 30°$, covering $\approx \pi$ steradians, at a frequency of 326 MHz to a limiting flux density of approximately 18 mJy (5-σ rms). This survey has a resolution of $54'' \times 54''$ cosec(δ) and a positional accuracy for strong sources of $1.5''$. A source catalogue comprising 229,576 sources has been made. This survey has detected many giant radio galaxies and double-double radio galaxies (Schoenmakers *et al.*, 2000).

6C

The 6th Cambridge Survey (6C survey) (Baldwin *et al.*, 1985) covers most of the sky north of $\delta + 30°$ ($\approx \pi$ steradians) with an angular resolution of 4.2×4.2 cosec(δ) arcmin^2 with a point source sensitivity of 200 mJy. Approximately 35,000 sources were detected. The source catalogue from this survey has been used for many astronomical investigations, e.g an investigation of the variation of the sizes of radio sources with cosmic epoch (Eales, 1985), detection of high red-shift galaxies (Blundell *et al.*, 1998), (Jarvis *et al.*, 2001), and detection of giant radio sources and clusters (Saunders *et al.*, 1987).

VLSS

The VLA Low-frequency Sky Survey (VLSS)(Lane *et al.*, 2005) has imaged 95% of the 3π steradians of the sky north of $\delta = -30°$ at a frequency of 74 MHz (4 m wavelength). The resolution is $80''$ (FWHM) throughout, and the typical rms noise level is $(1\text{-}\sigma) \approx 0.1$ Jy beam^{-1}. The typical point-source detection limit is 0.7 Jy beam^{-1}, and so far nearly 70,000 sources have been catalogued. This survey used the 74 MHz system added to the VLA in 1998. It required new imaging algorithms to remove the large ionospheric distortions at this very low frequency throughout the entire 11.9° field of view, which is the primary beam of a VLA dish at 74 MHz.

TGSS

The TIFR GMRT Sky Survey (http://tgss.ncra.tifr.res.in/) is an ongoing extragalactic radio continuum survey at 150 MHz, using the Giant Metrewave Radio Telescope (GMRT), covering about 32,000 sq. deg of the sky north of declination of -30 degrees and reaching an rms noise of 7-9 mJy/beam at an angular resolution of about 20 arcsec. When complete, the survey is expected to detect more than 2 million sources.

1.1.2 Future surveys at low frequencies

This section describes three planned widefield telescopes LOFAR, MWA and ASKAP and their science goals.

LOFAR

The Low Frequency Array (LOFAR) radio telescope (de Bruyn, 2009) plans to explore the low frequency radio spectrum with unprecedented resolution and sensitivity. LOFAR will have long baselines up to 400 km covering the frequency 10-240 MHz with a collecting area of $\approx 10^6$ m^2 (at 15 MHz). LOFAR will provide sub-mJy sensitivity across much of its operating frequency range. LOFAR will be a powerful instrument for solar system and planetary science. Key astrophysical science drivers include acceleration, turbulence,

and propagation in the galactic interstellar medium, exploring the high red-shift universe and transient phenomena, as well as searching for the red-shifted signature of neutral hydrogen from the cosmologically important epoch of re-ionization.

MWA

The goal of the Murchison Widefield Array (MWA) (Morales *et al.*, 2006), formerly known as the Mileura Widefield Array, is to develop powerful new capabilities for radio astronomy and heliospheric science in the frequency range 80 to 300 MHz, optimized for extremely wide fields of view and unprecedented sensitivity at these frequencies. The MWA will consist of 8000 dipole antennas optimised for the 80-300 MHz frequency range, arranged as 512 "tiles", each a 4×4 array of dipoles. Each tile responds to both the orthogonal linear polarisations.

The MWA is designed to detect and characterise red-shifted 21 cm emission from the Epoch of Reionisation (EOR). Such a result would be of profound cosmological significance and broad interest. The MWA will also allow high-precision remote sensing the heliosphere via measurement of radio propagation effects such as Faraday rotation and interplanetary scintillations, and it offers the prospect of constraining the magnetic field properties of coronal mass ejections, with associated benefits for space weather prediction.

Additionally the MWA will conduct a search for transient radio emission that is 6 orders of magnitude more sensitive than any previous work, yielding a variety of scientific opportunities. The MWA will be able to make observations that contribute to pulsar research, measurement of interstellar medium properties, and the study of radio recombination lines. Moreover, by virtue of the need to calibrate the array for ionospheric effects, the MWA is expected to yield interesting and useful information about the Earths ionosphere on short time scales and small spatial scales.

Even though due to the constraints imposed by budget, MWA is now downsized to a 128 T system there is a constant ongoing effort to get funds for 512 T system. In view of this the above paragraphs describes the scientific objectives of a 512 T MWA.

ASKAP

The Australian Square Kilometre Array Pathfinder (ASKAP) (http://www.atnf.csiro.au/SKA/) is a next generation radio telescope being built on a radio-quiet site in Western Australia and expected to be operational in 2013. The ATNF has set in motion an open process to determine the key science questions that will be addressed over the first 5 years of ASKAPs operational life. As part of the process, the ATNF received proposals for ASKAP Survey Science Projects (SSPs) from the international community. SSPs are defined as large and coherent projects that utilize ASKAPs wide field-of-view and fast survey speed to enable major science outcomes.

Two of the many surveys highly recommended by a committee set up to evaluate the proposals received are:

- Evolutionary Map of the Universe (EMU) is a deep (10 μ Jy/beam rms) radio continuum survey of 75% of the entire sky. EMU will probe typical star forming galaxies to redshift 1, powerful starbursts to even greater redshifts, Active Galactic Nuclei to the edge of the Universe, as well as undoubtedly discovering new classes of rare objects. The key science goals for EMU are to trace the evolution of star forming galaxies and massive black holes throughout the history of the Universe and to explore large-scale structure. EMU will create the most sensitive wide-field atlas yet made, and provide a long-lasting legacy survey.

- Widefield ASKAP L-Band Legacy All-Sky Blind Survey (WALLABY) is an extra-galactic neutral hydrogen survey over 75% of the entire sky and will detect up to 500,000 galaxies to a redshift of 0.26. The fundamental aims of WALLABY are to examine the HI properties and large-scale distribution of these galaxies in order to study galaxy formation and the missing satellite problem in the Local Group, evolution and star formation of galaxies, the role of mergers and galaxy interactions, the HI mass function and its variation with galaxy density, the physical processes governing the distribution and evolution of cool gas at low redshift, cosmological parameters relating to gas-rich galaxies and the nature of the cosmicweb. WALLABY will provide the largest, most homogeneous HI sample of galaxies yet made, and will be an important pathfinder for key SKA science.

1.2   MRT Survey

As already mentioned the table 1.1 clearly indicates that the southern sky is poorly explored at low frequencies. On the other hand the 6C survey in the northern sky provides a moderately deep radio catalog reaching source densities of about 2×10^4 sources per steradian. With this background the Mauritius Radio Telescope (MRT) (Golap *et al.*, 1998; Udaya Shankar *et al.*, 2002) was built with the main objective of carrying out an equivalent of 6C survey in the southern hemisphere. The principal products of the survey will include deconvolved wide field images covering ~ 5 steradians of the sky (in the dec range -75 to -10) with a sensitivity of ~ 200 mJy (1 σ) with a four arc minute x four arc minute resolution. A catalogue of around 10,000 unresolved and extended sources along with their flux densities estimated from the images would be made. This will help to extend the spectra of the radio source population to 151.5 MHz.

Burgess & Hunstead (2006) defined a complete sample of southern radio sources closely equivalent to the well studied northern 3CRR sample. MRT survey will aid the study of these sources down to 151.5 MHz.

We expect MRT survey to yield a good sample of steep spectrum sources. The MRT has a large overlap with the MRC catalogue and is close in frequency. A large number of sources from the MRC catalog already have optical identifications and redshift information (Burgess & Hunstead, 2006) The MRT survey will be a good database for studies of z-α correlation in the low frequency range.

Being a T-shaped array, MRT has a fully filled UV coverage. This makes it sensitive to extended features in the sky and will allow us to explore low surface brightness parameter space in the study of sources at low frequency. The surface brightness sensitivity of the MRT is $\approx 2.1 \times 10^{-21}\mathrm{Wm}^{-2}\ \mathrm{Hz}^{-1}\ \mathrm{Sr}^{-1}$ (1-σ) (Pandey, 2006). This will enable studies of extended galactic and extra-galactic radio sources. Jones & McAdam (1992) studied the structure of southern extragalactic radio sources at a frequency of 843 MHz. The MRT survey will be an important addition to this study.

In the study of the southern part of the galactic plane MRT survey will be useful to investigate extended features of SNRs which have a typical surface brightness sensitivity of $\approx 1.5 \times 10^{-21}\mathrm{Wm}^{-2}\ \mathrm{Hz}^{-1}\ \mathrm{Sr}^{-1}$ (Green, 2009)

Thus will enable studies of SNRs with a brightness temperature sensitivity an order of magnitude better than the completeness limit currently available in the literature.

An all sky 150 MHZ survey using the GMRT, the TIFR GMRT Sky Survey(TGSS) is currently being conducted with a point source sensitivity of 8 mJy (1 σ) and angular resolution of 20 arc secs. This is far more sensitive and has a higher angular resolution than the MRT survey. In spite of this, the MRT data base is important since GMRT cannot reach declinations south of $-40°$.

The MRT survey will be an important input to the MWA since they have a large overlap in sky coverage and frequency.

1.3   Motivation for the present work

Approximately 20,000 hours of observations have been carried out for the MRT survey. Using these observations, deconvolved images covering one steradian of the sky ($18^h \leq RA \leq 24^h 30^m$, $-75° \leq \delta \leq -10°$) and a source catalog containing approximately 2,800 sources have already been made in a previous work (Pandey, 2006).

The present work began with an aim to complete 24 hours of imaging of the sky in the declination range $-75° \leq \delta \leq -10°$ and generate a catalog consisting of approximately 10,000 sources at 5-σ detection level. A detailed analysis of these images which include

estimation of rms noise, positional and flux calibration errors will have also be carried out.

However due to the poor quality of data for the RA range 6 to 18 hours, the thesis describes the MRT survey for the RA range 0 to 6 hours.

1.4   Thesis outline

Chapter 2 of this thesis gives a brief introduction to the MRT survey, the observations carried out, the data collected for the survey, the software system for processing, work carried out earlier and a few sample images from that work. Chapter 3 describes the systematics in the positional errors of sources detected in the earlier work. This chapter describes the application of 2-D homography, a technique ubiquitous in the computer vision and graphics community to correct the systematics in the positional errors in the image domain. In our view this technique will be of relevance to the new generation radio telescopes only images after a certain integration are recorded. The chapter also describes investigations tracing the positional errors to errors in the array geometry and re-estimation of array geometry using the principles of astrometry. A brief discussion of imaging with the new array geometry is included in this chapter. Chapter 4 describes the present work and describes problems with the existing software pipelines,the streamlining of the software pipelines, development of new software pipelines for MRT data processing and conversion of MRT images to FITS format. One of the important aspect of the present work is related to the development of a new calibration strategy for imaging MRT data. Why did such a need arise, the limitations of the present calibration scheme, development of field of view calibration and its demonstration are described in this chapter. This is folowed by a description of the MRT data base in the RA range $00^h \leq RA \leq 06^h$ data the problems of imaging the entire 24 hr RA range. Eventhough various stages of MRT data processing have evolved over a period of time and several members are involved in its development for completeness this chapter describes briefly various stages of MRT data processing emphasising wherever possible the challenges faced while imaging the RA range 0 to 6 Hr. Chapter 5 presents and discusses the main outcome of the present work namely the deconvolved images covering $\sim$ one steradian of the sky with a four arc minute resolution and a sensitivity of $\sim$ 200-600 mJy. the sensitivity depends upon the RA and the Dec of the sky being imaged due to the changing sky brightness, primary beam of the helix, grating responses, bandwidth decorrelation effects and effect of sidelobes of strong sources both within and outside the primary beam. The unresolved point sources seen ($\sim$ 3000), a comparison of their positions and flux densities with sources in the MRC catalog are also discussed. This chapter also presents a number of extended sources seen in this part of the survey overlaid on SUMMS images convolved to the resolution of the MRT

beam. Finally, Chapter 6 gives a summary of the work done, describes the future course of work and touches upon the main conclusions of this thesis.

Chapter 2

Background to the present work

2.1   Introduction

This chapter gives the background to the present work. A brief introduction to the Mauritius Radio Telescope (MRT) is given and the array is described. The software system developed in-house for imaging with MRT is described. Earlier phases of MRT survey work are also described.

2.2   Introduction to the MRT

The Mauritius Radio Telescope is a non-tracking Fourier synthesis radio telescope, operating at 151.5 MHz (Golap *et al.*, 1998; Udaya Shankar *et al.*, 2002), constructed and operated collaboratively since the early 1990's by the Raman Research Institute, Indian Institute of Astrophysics and the University of Mauritius. It is situated in the North-East of Mauritius (Latitude 20.14° degrees South, Longitude 57.74° East), an island in the Indian ocean. It is a T-shaped array with a 2 Km long east-west (EW) arm and a 880 m long south arm. There are 1024 helical antennas placed 2 m apart in the EW arm and are configured into 32 groups each containing 32 antennas. 64 antennas in the north-south (NS) arm are mounted on 16 trolleys and move on a rail track for carrying out the synthesis along the NS direction.

Table 2.1 gives a summary of the specifications of the MRT.

2.2.1   Primary element

The primary element is a peripherally fed monofilar[1] axial-mode helix of 3 turns with a diameter of 0.75 m and a height of 1.75 m (Golap *et al.*, 1998). This is mounted above a stainless steel reflector mesh. The axial mode provides maximum radiation along the

---

[1]Monofilar: A term used to distinguish single conductor helix from helices with two or more conductors.
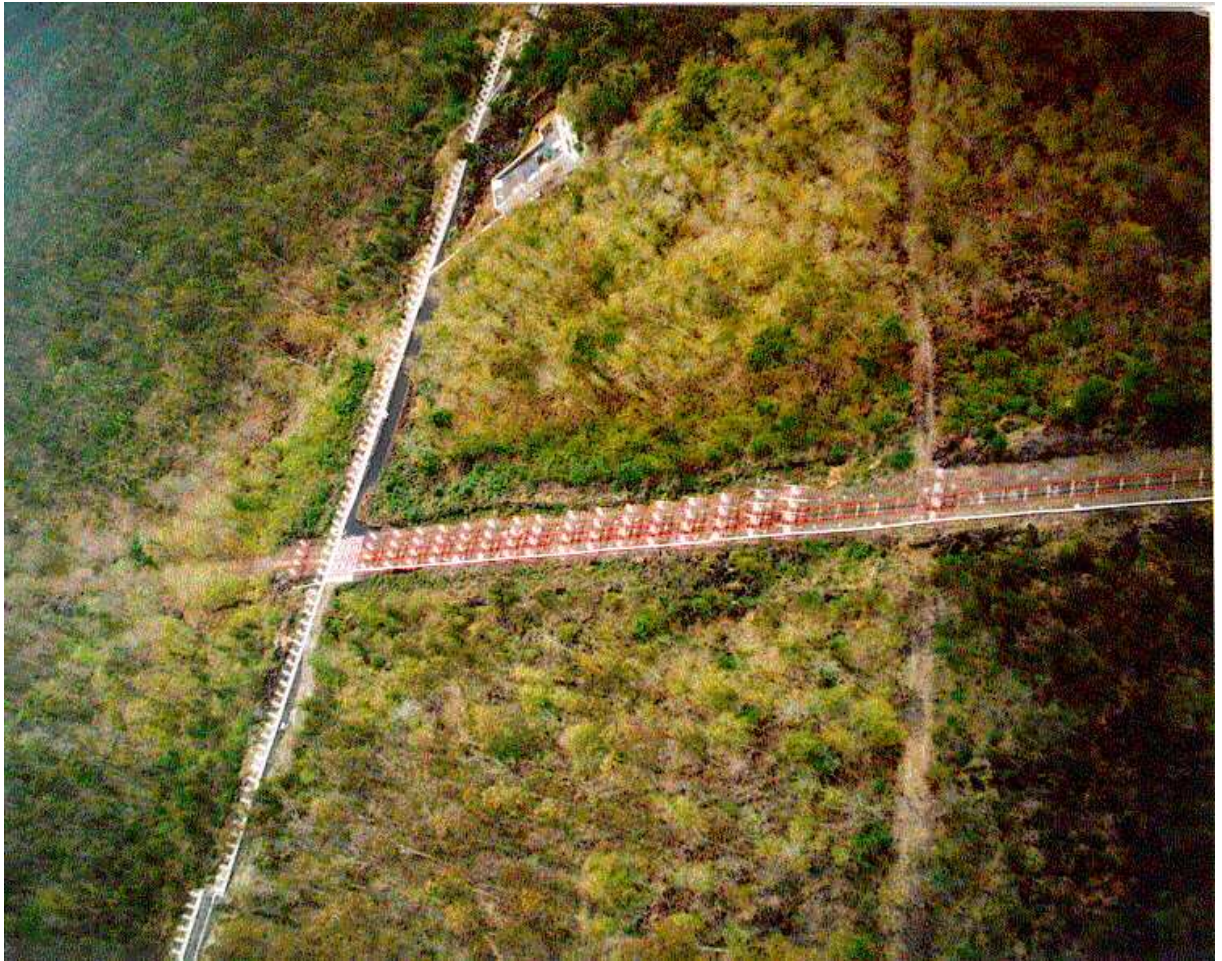
Figure 2.1: Aerial view of the central part of the T-shaped MRT array. The observatory building is to the right of the centre of the array.

helix axis. The helix responds to frequencies between 100 and 200 MHz with right circular polarisation (IEEE definition). The circularly polarised radiation antenna was used as it does not suffer from loss of amplitude due to the Faraday rotation of the radio waves. The helical antenna, with its reflector, has a canonical collecting area of λ^2 (4 m² at 150 MHz) with a HPBW of about $60° × 60°$. The helices are mounted with a tilt of $20°$ towards the South to get a better coverage of the southern sky. the primary beam has maximum pointing towards $-40°$ giving a coverage of $-70°$,which includes the southern-most part of the galactic plane, a region largely unexplored at metre wavelengths.

2.2.2 MRT array

The EW arm consist of 1024 helices mounted on a 2 m wide ground plane with an inter-element spacing of 2 m (this is equal to one wavelength at 150 MHz) and is divided into 32 groups of 32 helices each. Due to the local terrain the EW groups are at different heights making MRT a non-coplanar array. The maximum height difference in the E-W arm is 35m. Due to this the PSF of MRT is declination dependent. The tangent plane

Frequency	151.5 MHz
Bandwidth	1 MHz
Sky coverage	00h $<$RA$\leq$24h, -70$\leq DEC \leq$-10
Synthesized beam width	4×46 sec(+2014)
Point source sensitivity* (1σ)	$\approx$110 mJy
Surface brightness sensitivity* (1σ)	$\approx$7×10^{-22} Wm^{-2}Hz^{-1}Sr^{-1}
Typical image size	15×15
Polarization	Right circular (IEEE)
uv coverage	uniform and complete
Aperture synthesis	sidereal hour wise, meridian transit

Table 2.1: Characteristics of MRT images. * refers to expected values.

approximation is not a viable method for inverting the measured visibilities at MRT. At a zenith angle of around 40° the tangent plane approximation for a zone of 5° leads to a shift in the source away from the meridian by almost 4.5'. Thus the Direct Fourier Transform technique which compensate for height at each ZA on the meridian is more appropriate for inverting the measured visibilities at MRT. The Half Power Beam Width of the primary beam of each EW group is 2° × 60° and allows observation of a source for approximately $8 \times$ sec(DEC) minutes. In each group, four helices are combined using power combiners and the combined output is pre-amplified in a low noise amplifier having noise temperature of $\approx$ 300 K. Eight such amplified outputs are further combined and amplified to form a group output in the EW arm. A group in the NS arm consists of 4 helices with a 4 m wide ground plane. Each NS group has a primary beam of HPBW of 15° × 60° and are mounted on a trolley which moves along a 880 m rail track.

2.2.3 RF front end

The RF front end of MRT (Golap *et al.*, 1998) consists of single-side band superheterodyne receivers. The output from a sub-group consisting of 4 helices is passed through a 127 MHz high-pass filter to filter out the communications band below 127 MHz. It is then amplified in a low noise amplifier. 8 such sub-group outputs are combined to give one group output. The first conversion from the observing frequency of 151.5 MHz to the first intermediate frequency of 30 MHz with a bandwidth of 3 MHz is done in the field using an LO signal at 121.5 MHz from the observatory and then transmitted to the observatory building using co-axial cables. The transmission loss at 30 MHz $\approx$ 40 dB Km^{-1} . The first IF is transmitted to the observatory building via equal length of coaxial cables irrespective of their distance from the observatory building to ensure that the interferometer outputs are not affected by change in the ambient temperature. At the observatory the first IF is further amplified to compensate for the transmission loss and then down-converted to

the second IF of 10 MHz with a bandwidth of 1 MHz. This IF is kept at a constant level by an automatic gain control (AGC) circuitry.

2.2.4   The digital back end

Each of the 16 group outputs of the NS arm and the 16 group outputs of the east arm are split in a quadrature hybrid to obtain the in-phase and quadrature components. Together with the in-phase output of the 16 west group outputs they are then digitised to 2-bit 3-level, sampled at a rate of 12 MHz and fed into a 32×16 complex correlators to obtain the EW $\times$ NS products. The 16 quadrature outputs from the west arm are used for getting the EW $\times$ E products. Higher than the Nyquist rate is used to reduce the loss in sensitivity due to coarse quantisation, (Bowers & Klingler, 1974). MRT used the Clark Lake correlator. More details of the digital backend and its reconfiguration are described in Erickson *et al.* (1982). and its reconfiguration is described in Golap *et al.* (1998). The last group of the east arm (E16) is fed to the correlator instead of the 16th trolley of the south arm. This forms a set of baselines between E16 and the EW arm on all observing days. Since these baselines have non-moving antenna positions, they can be used to check the repeatability of the data. They also give 31 independent closure information which can be used in the calibration.

It is worthwhile noting that only 15x32 correlations are used for imaging. However to keep the confusion in reading this report to a minimum, in most of the places we talk about 16x32 correlations.

2.2.5   Total power measurements

The AGC maintains the total power fed to 2-bit 3-level samplers at a constant value and ensures an optimum signal to noise ratio in a correlator with coarse quantisation. In doing so amplitude information of the signal is lost and results in similar correlations for a strong source in a strong background and a weak source in a weak background. The variations of the sky brightness as seen by one of the EW and NS groups is measured separately by switching off the AGCs and using the self-correlators to measure the total power output of these groups. This information is used to estimate flux density of sources.

2.2.6   Recirculator for wide field imaging

The correlator used at the MRT is an XF correlator. Although the use of larger bandwidths results in better sensitivity of a telescope in an XF correlator, it restricts the angular range over which an image can be made if the relative delays between the signals being correlated are not compensated. When the uncompensated delay between the signals becomes comparable to the inverse of the bandwidth used, the signals will be

decorrelated. Moreover in a low frequency telescope the usable bandwidth is severely restricted by the Radio Frequency Interference (RFI) environment. In view of this the bandwidth used at MRT is only 1 MHz. Since the EW group has a narrow primary beam of $2°$ in RA, this bandwidth does not pose a problem for synthesising the primary beam in this direction. However, both the EW and the NS groups have wide primary beams in declination extending from $-70° \leq DEC \leq -10°$ (HPBW). For signals arriving from zenith angles greater than $10°$ on NS baselines longer than 175 m, the uncompensated delay results in bandwidth decorrelations of the order of 20%. To overcome this loss of signal one has to measure the visibilities with appropriate delay settings, while imaging different declination regions. To keep the loss of signal for a bandwidth of 1 MHz to less than 15% in the entire declination range $-70° \leq DEC \leq -10°$, the longer baselines have to be measured with four delay settings. At MRT a recirculator is used to measure visibilities with different delay settings using the available correlators in a time multiplexed mode. the recirculator system is described in detail in Sachdev & Udaya Shankar (2001b). Each declination strip imaged with a certain delay settings is referred to as an imaging zone. Each imaging zone covers roughly the same angular extent and have an overlap of a few degrees. This overlap helps to cross-check imaging algorithms as there are sources in the overlap region which will appear in two zones. Table 2.2 shows the declination zones imaged.

Table 2.2: Declination zones imaged at the MRT

ZONE 1	ZONE 2	ZONE 3	ZONE 4
$-10° \leq DEC \leq -25°$	$-25° \leq DEC \leq -37°$	$-37° \leq DEC \leq -52°$	$-52° \leq DEC \leq -70°$

2.3 Observations for the MRT survey

Observations for the survey (Golap *et al.*, 1998) are carried out in the T-configuration which correlates NS antennas with EW antennas. The NS baselines are sampled at 1 m interval to ensure that the grating response falls well outside the primary beam response. To sample the full 880 m of the NS arm with a 1 m sampling, 60 days of observations are required with 15 trolleys. Each day the trolleys are spread over 84 m with an inter-trolley spacing of 6 m. 512 visibilities with an integration period of ≈ 1 s are recorded. After obtaining good data for 24 sidereal hours the trolleys are moved by 1 m. After 6 days of successful observations visibilities over 90 m are obtained. The trolleys are then

Cycle No.	Allocations covered	Observation period Start - End		Sampling frequency (MHz)	Mode	Data collected (hours)
1	1-12	July 94	Sep 94	12	EW×NS	835
2	13-24	Sep 95	Dec 95	2.65625	EW×NS	1469
3	1-25; 1-63	Jan 96	Mar 99	2.65625	EW×NS E×EW, NS×(NS+W)	17320
Total	1-63	July 94	Mar 99			19624

Table 2.3: The various cycles during which the observations were carried out for the survey. Only the data files which are complete for one sidereal hour range have been considered. For observations with allocations 1 to 12, each visibility value is stored as **int** (occupies four bytes) while for observations with allocations 13-63, each visibility value is stored as **short** (occupies two bytes). (Pandey, 2006)

moved as a whole to the next unsampled position to measure the next set of visibilities. Each placement of the 15 trolleys along NS arm is called an allocation. There are 63 such allocations along the NS arm over which observations have been carried out. 63 allocations were arrived at to take care of exigency that arose due to the local terrain. Observations for the survey were carried out from May 1994 to March 1999. This covers a period of approximately 5 years. Table 2.3 (Pandey, 2006) gives the chronology of the observations carried out with the MRT.

2.4   MRT survey data archive

Approximately 20,000 hours of observations were carried out for the MRT survey. MRT uv data occupies approximately 1 Terabyte of computer disk space. The data was recorded in files containing one hour of data for ease of handling and transferred to magnetic tapes for storage. The data is in binary format and contains records of the cross-correlation and self-correlation values and a time-stamp for each integration ($T_{int} \approx 1s$). There is no header to record other information about the observations. Most of the log has been coded in the data file name. The observers' logs have to be referred to deduce further information about the data. Antenna positions and delay settings are recorded in separate files.

2.5   Work carried out earlier

In the 1st phase, observations for the MRT survey were carried out up to 175 m south baselines, with only one delay setting. Golap *et al.* (1998) made low resolution images for the RA range $17^h30^m \leq RA \leq 05^h00^m, -70° \leq DEC \leq -10°$ using this data. The

images had a resolution of $13' \times 17' \sec(DEC + 20°.14)$ and a sensitivity of ≈ 1 Jy beam^{-1} (1-σ). A catalogue of 895 sources was also made. A deconvolution technique for the array taking into account its non-coplanarity was also developed by Golap & Udaya Shankar (2001).

Dodson (1997) imaged a few known supernova remnants with MRT and studied a subset of them associated with pulsars.

Sachdev & Udaya Shankar (2001b) made nearly full resolution wide field dirty images for the RA range $19^h20^m \leq RA \leq 19^h52^m, -70° \leq DEC \leq -10°$ with a resolution of $4' \times 9'.2 \sec(DEC + 20°.14)$ and a sensitivity of ≈ 550 mJy beam^{-1} (1-σ) to demonstrate the functionioning of correlator in the mode in which it measures visibilities with four delay settings and the procedure developed in-house to image 4 delay zones. A technique based on Fourier analysis for Radio Frequency Interference (RFI) detection and mitigation and Clean algorithm for spectral lines was also developed (Sachdev & Udaya Shankar, 2001a).

Pandey (2006); Udaya Shankar & Pandey (2006) made deconvolved images covering $\sim$ 1 steradian of the sky for the RA range $18^h00^m \leq RA \leq 24^h00^m, -75° \leq DEC \leq -10°$), with a resolution of $4' \times 4'.6 \sec(DEC + 20°.14)$ and an rms noise of 260 mJy beam^{-1}. A catalogue of $\sim 2,800$ sources was prepared and its initial analysis was carried out. Techniques for automatic data quality classification, hierarchical RFI detection and mitigation and deconvolution of widefield images with a declination-dependent point spread function were developed. Some of these aspects are briefly described in later sections of this paper.

Somanah (2007) made dirty images covering the range $05^h00^m \leq RA \leq 18^h00^m, -70° \leq DEC \leq -10°$) and a resolution of $13' \times 19' \sec(DEC + 20°.14)$ and having an rms noise of ≈ 1 Jy beam^{-1}. A complete sample of bright southern sources was made.

2.6   MRT data reduction

MRT data processing is carried out along similar lines to that of general radio interferometric arrays to connect hourly files and NS synthesis and having one day images concept.

The data processing steps can be broadly divided as follows:

- Data editing:

    RFI detection

    Automated data quality estimation.

- Calibration

- Data selection (one hour with a one hour guard band on either side)

- Fourier inversion of the calibrated visibilities (taking into account the non-coplanarity of the array) to get one-day images.

- Regridding one day images to a common epoch

- RFI detection and mitigation in one day images

- Estimation of relative gains of one day images

- Co-addition of images

- Estimation and removal of artifacts in the co-added images.

- Deconvolution

- Source extraction

- Flux calibration

Figure 2.2 shows the steps in the MRT data processing. The constraints of wide field imaging with a non-coplanar array and aperture synthesis using movable antennas along the NS arm of the MRT array makes the data processing for the survey complicated.

The visibilities needed to synthesise the MRT images were recorded over five years of observation. Precession is significant during this length of time and this makes combining different sets of observations difficult. One simple solution is to make images with each set of observations and precess these images to a common epoch before co-adding them to give images with the full uv coverage of the array.

These one-day images are similar to snapshot images in earth-rotation synthesis imaging, except that in the case of MRT the v coverage on a given day is sparse and under-sampled and results in images which are heavily aliased along the declination direction. Figure 2.3 shows the aliasing due to the strong source (MRC0915-118: RA $09^h18^m05.8^s$ and DEC $-12°05'44''$) having flux of 253.4 Jy at 151.5 MHz.

The method of producing one-day images and the co-addition to obtain the final image has been implemented in the the MARMOSAT suite of programs (Dodson, 1997). This approach has been maintained in the X-Marmosat suite which is an extended version of of MARMOSAT developed by Pandey (2006) and is continued in the present work.

2.6.0.1 Decision based data selection

For making images using the MRT data archive, the first step in the data imaging process is to choose data for the region of the sky of interest. The best data from the MRT data archive is selected to give the best possible images for the survey. The concept of data quality is subjective and is most often based on the science goal the data is used for. Since the MRT data archive consisting of 20,000 hours of observations, classifying data by
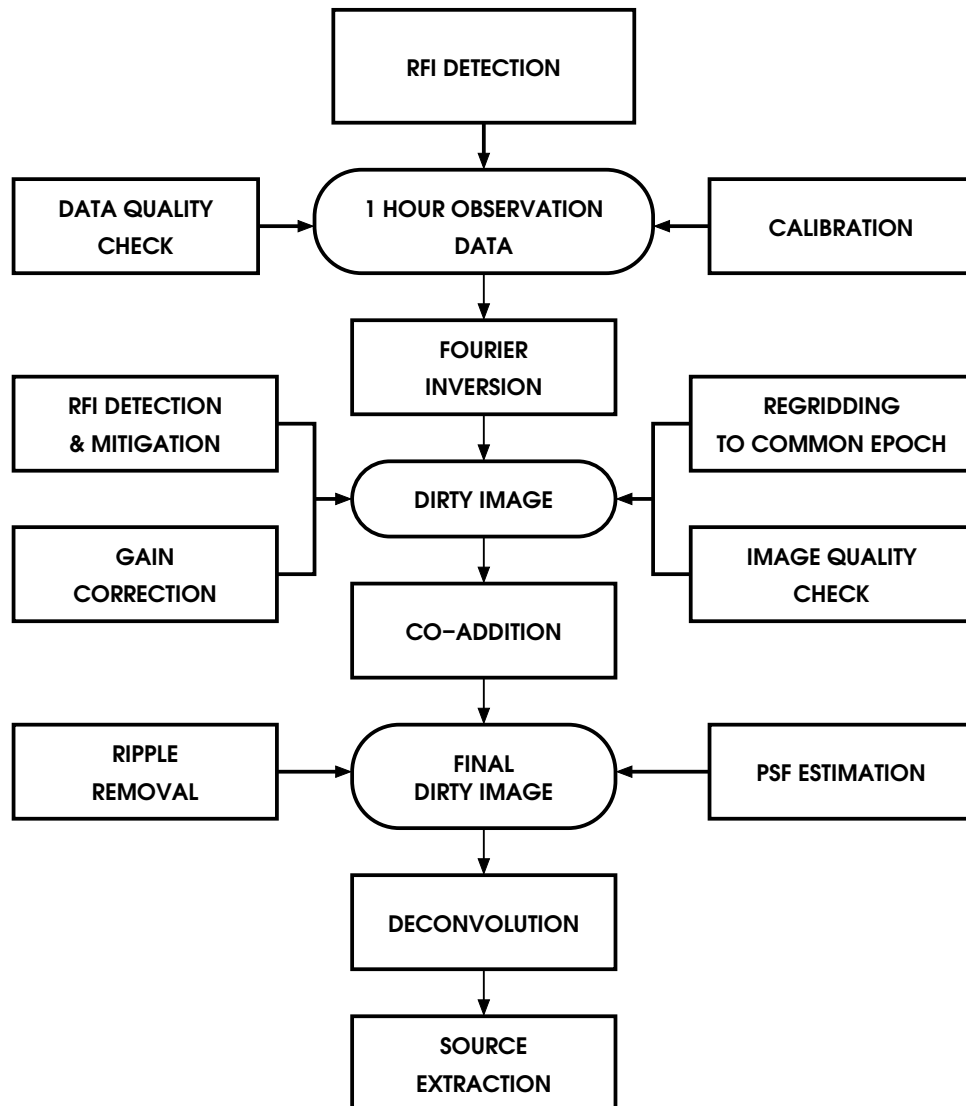
Figure 2.2: Steps in the MRT data processing.

hand is a slow process. A decision based algorithm has been developed (Pandey & Udaya Shankar, 2006) to automatically classify the MRT data according to their suitability for imaging. The algorithm is based on giving a quality factor to a data file based on the following parameters:

- Completeness of the visibility data.

- RFI in the visibility data.

- RMS noise in the visibility file.

- Strength and position of the Sun, which is the main interfering celestial source, during the observation of the visibility data.

- Quality factor of the calibrator visibility data.
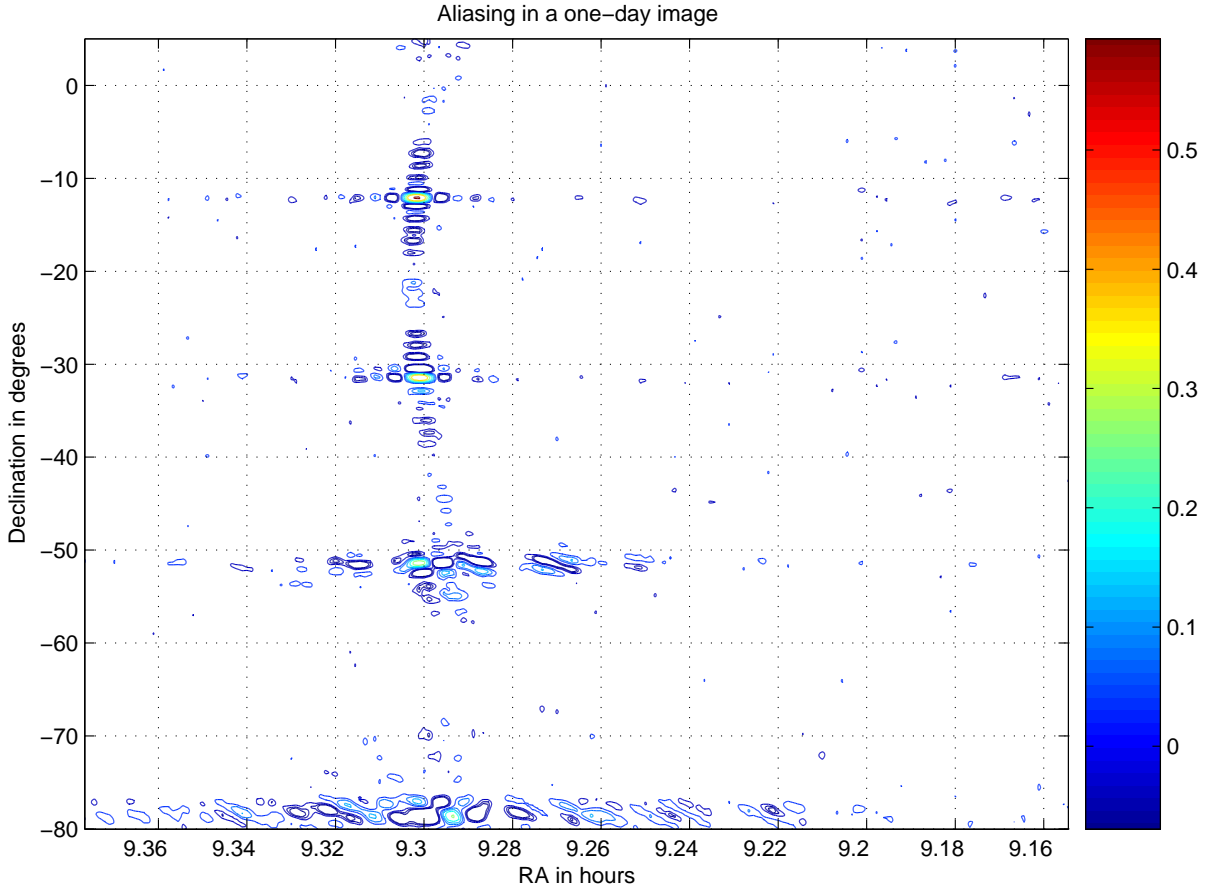
Figure 2.3: Aliasing of strong sources in the one-day MRT images. MRC0915-118 (RA $09^h18^m05.8^s$ and DEC $-12°05'44''$) having flux of 253.4 Jy at 151.5 MHz and its aliases images along the declination. The twisting of the beam along the declination, due to the non-coplanarity of the MRT array, can clearly be seen. The contour levels are (-5, -2.5, 2.5, 5, 8, 12, 18, 24, 40, 70)$\times\sigma$, where σ is the rms noise in the image. The intensity levels are in arbitrary units.

In the practical implementation of this data selection scheme, the RFI detection is carried out en mass in the sum of magnitude of the visibility data and the calibrator visibility, which gives a one-dimensional representation of the visibilities. The calibration files are also produced in a similar fashion. All the statistics generated are fed as an input to the decision-based algorithm. A quality factor for the file under consideration is automatically generated. Data for the present work was chosen based on the gradings given by the automated data selection program.

2.6.0.2 Hierarchical RFI detection and mitigation

A hierarchical RFI detection and mitigation (Udaya Shankar & Pandey, 2006) is used for editing the data. The RFI is detected and mitigated along the data reduction path both in the visibilities domain and the image domain. In the visibilities RFI is detected in the sum of magnitudes of the 16x32 measured visibilities. A Fourier filtering algorithm is used based on the *a priori* information that the rate of change of signal for RFI much is

faster than the signal from the sky (Sachdev & Udaya Shankar, 2001b). A hampel filter is subsequently used (Pandey, 2006) to detect remaining low-level RFI. The RA points affected by RFI are stored in a flag file. The RFI detection and mitigation process is continued after the Fourier inversion of the visibilities by the application of a hampel filter to detect and remove suspected RFI in the images. Visual inspection of the images is carried out to further detect and remove images suspected of being contaminated by RFI.

2.6.0.3 Calibration of the MRT images

The visibilities observed for the calibrators MRC0915-119, MRC1932-464 and MRC2211-173 are used (Golap *et al.*, 1995) for calibration. The visibility phase is estimated by fringe fitting, where the sky is assumed to be dominated by the calibrator. The instrumental phase is taken as the difference between the phases of the observed visibilities and the expected geometric phases due to the calibrator. The instrumental gain is estimated by measuring the relative amplitudes of fringes on different baselines. The instrumental phase is insensitive to short term interference and to fringes due to other sources in the sky, provided their fringe rate is significantly different from that of the calibrator on a given baseline. This filtering of offsets and effects of other sources at other declinations works better for those declinations and baselines where the number of fringes are greater than 3. At short baselines where there are less than 2 fringes, the calibration is not satisfactory. The complex baseline gains are re-estimated by calculating 47 antenna gains from the 512 visibilities measured. This baseline to antenna conversion is done using Singular Value Decomposition (SVD). The day to day rms phase variation of MRT array measured by using the same calibrator is of the order of 6°.

2.6.0.4 Meridian transit imaging

MRT array is a non-coplanar array with height differences in the EW arm upto 35 m. For imaging a 60° field of view of MRT primary beam, the approximate coplanar assumption that the phase term due to the heights of the groups is assumed to be constant over the synthesised field of view is invalid. In this case a 3-dimensional imaging is required (Golap *et al.*, 1998). A Direct Fourier Transform (DFT) is used to invert the calibrated visibilities into images. The calibrated visibilities are re-phased at each point along the meridian and combined to give the dirty image at that point. The sampling along RA is 1 s while in along sine of zenith angle it is of the order of 4.910^{-4} The heights of the EW groups and the distance along the NS from the array centre are used. The sampling along the meridian is linear in sine of zenith angle as this keeps the resolution constant along declination.

Along the EW arm of the MRT array the sampling is equal to the size of an EW group. While synthesised beam on the meridian gives a grating response which falls on

the nulls of the primary beam, for synthesis away from the meridian, the grating lobe starts moving into the primary beam. This makes the synthesised beam a function of hour angle. To keep the imaging simple, imaging is carried out only on the meridian. Scanning along the RA is provided by the rotation of the Earth. MRT maps are thus stacks of these 1-dimensional images made along the meridian.

To keep the loss of signal due to bandwidth for a bandwidth of 1 MHz to less than 15% in the entire declination range $-70° \leq DEC \leq -10°$, the longer baselines have to be measured with four delay settings. Each range of declination imaged with one delay is refered to as a declination zone.

MRT data archive is arranged in hourly observations file to facilitate handling. Imaging is thus carried out in one hour RA patches. But for the purpose of regridding the images to a common epoch J2000, co-addition of images and deconvolution data for 3 continuous hours of RA range are analysed in each stage.

2.6.0.5 Co-addition of one-day images

The one-day images are concatenated with adjacent hours of observations and regridded to the common epoch J2000 to correct for the effect of precession on the observations. Post-integration for 4s is carried out on the images to increase the signal to noise ratio of the image. Hampel filtering is used to detect RFI. While post-integrating RFI is mitigated on the image by giving zero weightage to the points affected by interference.

The concatenated image gives guard zone on both sides of the hour of observation for deconvolving strong sources which are outside the central one hour but their sidelobes extend into the region being imaged. Similar guard zones are used along the declination edges to take care of sidelobes of strong sources which are away from the declination range imaged.

The selection of measured visibilities for imaging was done using the sum of magnitudes of the visibilities data. While this one dimensional representation of the data is good enough for detecting RFI, very strong transients like the Sun, there are still RFI and transients which escape detection at this level.

To detect these low level RFI and weak transients, the quality of the regridded images is assessed by visual inspection, fitting the expected beam to strong point sources and measuring the background variation in the images. Images with poor signal to noise for sources expected to be in the image, transient sources which appear on only a few baselines and RFI which appear as strips along DEC are rejected.

A fairly large number of the images are co-added after each image has been scaled to a common gain level. The gain level is derived from fitting the expected beam to a strong point source in the image. This ensures that the PSF in the final image is close to a sinc function (Pandey, 2006).

2.6.0.6 Generation of PSF

The Point Spread Function (PSF) of MRT array for imaging is declination dependent due to the non-coplanarity of the array. To deconvolve the images by the conventional Clean algorithm, PSFs have to be generated for the sources at different zenith angles. For a given dynamic range, the size of the PSF is dependent on the strength of the source. Strong sources need larger PSFs for cleaning than weaker sources. Also instead of generating PSFs for each and every source in the sky, PSFs are generated for a short range of zenith angles within which the PSF is assumed to be constant for a given dynamic range. All the PSFs required for cleaning the whole declination range of MRT are pre-generated and stored on computer hard-disks ($\approx$ 400 for a dynamic range of 500 for each RA range) (Pandey, 2006). During deconvolution the PSFs are retrieved as and when needed. This procedure avoids the computationally expensive operations of PSFs generation and interpolation during the deconvolution. This significantly speeds up the deconvolution. The PSFs are generated taking into account the uv coverage and the decorrelation in the images across the allocations.

2.6.0.7 Deconvolution

Deconvolution of MRT images (Pandey, 2006) is done using the Clean algorithm. To take care of the declination dependence of the PSF, pre-generated PSF for a given dynamic range are used. Care is taken to identify and flag regions containing spurious emissions due to aliases and sources in the grating lobes. Aliases appear as sources which repeat themselves along the declination. The real source is identified and the declination strip where the source is located is visually inspected to detect aliases. Strong interfering sources in the grating lobes look like a source which changes its declination from day to day. Such sources can be detected by the sudden appearance of a source and its movement across the declination when the images are displayed in sequence over the observations period. The most common strong source in the grating lobes is the Sun.

In case the deconvolution routine tries to clean such regions of spurious emissions, the Clean program diverges. It was found practical to Clean the images down to 5-σ. The inability to clean down to this level is indicative of spurious emissions in the images which have not been flagged.

2.6.0.8 Source extraction

The source extraction program (Pandey, 2006) is based on the AIPS task HAPPY. The program looks for islands of emissions in MRT images and fits the expected 2-dimensional Gaussians to the detected peaks. Sources down to 5 σ level were extracted. Sources which do not appear genuine were rejected after visual inspection.

2.6.0.9 Primary beam correction

Pandey (2006) made an empirical estimation of the MRT primary beam by measuring the ratios of 560 unresolved sources common to the MRT and MRC catalogue in the $(20^h21^m \leq RA \leq 24^h39^m, -75° \leq DEC \leq -10°)$. The estimated MRT beam shape along the declination was found to be $\approx 8°$ wider than the theoretical MRT helix beam of $\approx 60°$ and it peaks at $\approx -44°$ instead of the expected -40°.14. This estimated beam is used to apply the primary beam correction on the images along the declination since we image only along the meridian.

2.6.0.10 Total power corrections

The use of the automatic gain control in the MRT receiver results in the loss of the amplitude information about the variation of the sky background. To put back this amplitude information in the MRT maps, the total power measurements by the self-correlators of those groups where the AGC had been switched off are used.

The self correlators of the MRT are wired in such a way that they measure the probability (P) that the input signal amplitude V, is in between the thresholds levels used for digitisation. This probability for a zero mean noise Gaussian signal with an rms fluctuation of σ and a symmetric 2-level digitizer with voltage threshold levels $\pm V_{th}$ is given by,

$$P = \frac{1}{\sigma\sqrt{2\pi}} \int_{-V_{th}}^{+V_{th}} e^{-(\frac{V}{\sqrt{2}\sigma})^2} dV = erf(\frac{V_{th}}{\sqrt{2}\sigma}) \tag{2.1}$$

Knowing P, the $\frac{v_{th}}{\sigma}$ of the signal can be obtained. The equivalent analog correlation, ρ_a, can be obtained using the relation,

$$\rho_a = \rho \times \sigma_1 \times \sigma_2 \tag{2.2}$$

where ρ is the normalized correlation coefficient, σ_1 and σ_2 are the rms of the signals being correlated and can be obtained from the channels where the AGCs have been switched off.

Since the self-correlations values are heavily corrupted by RFI, it is not possible to correct for the images on a day to day basis. The best self-correlation files are chosen from the observations and the average of these values is taken as the best estimate of the total power of the sky.

This measured total power is modeled as the scaled version of the true power by a gain factor and shifted by a DC term and some unexplained varying dc off sets (Pandey, 2006). To estimate the scale factor and the DC term values, the images are first scaled to a common level. A reference image is picked and the the deflection due to sources found in the guard band which are common to the images are found. The ratios of the deflection

of the common sources gives the scaling factor to be applied to the image to bring it to the same level of the reference image. After scaling the primary beam correction is applied on the images to remove the declination dependence. The deflections in the images due to the MRC 4 Jy sample (MS4 sample) (Burgess & Hunstead, 2006) sources are measured in the images. The ratio of the deflections to the estimated flux at 150 MHz of the sources are calculated. These ratios are expected to follow the total power corrections which need to be applied to the MRT images. The measured total power is scaled to fit the ratios and the gain factor and DC term for the total power measurement estimated. This corrected total power is then applied to the images.

2.6.0.11   Flux calibration

After the total power and primary beam correction, MRT images are calibrated to the Jansky level by scaling the MRT images to the level of a primary flux calibrator source which is found in the MRT images. The criteria for choosing such a calibrator are:

- The source should be non-variable according to the list of Slee & Siegman (1988).

- The source should be unresolved at the resolution of the MRT ($4'$) and the SUMSS survey ($43''$).

- The source should be detectable at MRT at or above 50-σ level.

- The flux density of the calibrator shoudl have been measured at a large number of frequencies around 151.5 MHz and its fitted spectrum should be in good agreement with the measured flux densities.

- the source should in an empty region away from the Galactic plane.

Pandey (2006) chose the source MRC2354-350, having a flux density of 26.65 at 151.5 MHz, as the primary flux calibrator based on all these criteria.

2.7   Data reduction software

2.7.1   The MARMOSAT suite of programs

MRT visibilities are processed offline using the MARMOSAT[1] (Dodson, 1997), the MAu-Ritius Minimum Operating System for Array, suite of programs. This has been designed in-house to transfer the visibilities to images which can be ported to better supported astronomical software suites like AIPS.

---

[1]A marmosat is a small monkey, distantly related to the ape.

The programs in MARMOSAT are used for detection of bad data, radio frequency interference (RFI) detection and mitigation, calibration of the visibilities, transforming the visibilities to images and combination of different sets of images.

The MARMOSAT consist of programs written in C and are modular in nature and communicate with each other via standard files. Specific programs are written to perform a specific task instead of having a monolithic program which performs all the tasks. Since there were many hardware and recording format changes during different periods of observations there are different versions of the programs to deal with these changes. This aspect made adoption of MARMOSAT in as it is condition very difficult to be adapted for the survey.

2.7.2   The X-MARMOSAT suite of programs

The X-MARMOSAT (Pandey, 2006) is an extended version of the MARMOSAT with several new functionalities like assessment of data quality, RFI mitigation in the self-correlation values, analysis of dirty images, image addition, generation of point spread function, deconvolution and source extraction. The X-MARMOSAT is written mostly in C, Matlab and Perl and follows the same structure as the MARMOSAT. This made MARMOSAT usable for the MRT survey and 1 steradian of the sky was imaged using this.

2.8   Images of 1 steradian of the sky by Pandey and Udaya Shankar (2006)

In the previous work (Pandey & Udaya Shankar, 2006) a set of deconvolved images for the range $18^h \leq RA \leq 24^h 30^m$, $-75° \leq DEC \leq -10°$ and a resolution of $4' \times 4'.6$ $\sec(DEC + 20°.14)$ and having an rms noise of ≈ 260 mJy beam^{-1} were produced. These images are referred to as 'Set I' images whiles the images produced for the present work are called 'Set II' images.

Figure 2.4 shows a contour plot from the earlier work. The contour levels are -5, -3.6, -2.5, -1.8, 1, 1.4, 2, 2.8, 3.6, 5, 7, 10, 14, 20, 29, 40, 54, 72, 90, 100, 136, 180, 216, 252, 288 Jy beam^{-1}. The rms noise in the image is $\approx$425 mJy beam^{-1}. This is a region away from the Galatic plane and most of the sources seen in this image are point sources.

Deconvolved images with a resolution $4' \times 4'.6 \sec(DEC + 20°.14$ in J2000 coordinates covering more than one steradian of the sky ($18^h \leq RA \leq 24^h 30^m$, $-75° \leq DEC \leq -10°$) was made. The full resolution dirty images with the same resolution covering an additional, about half a steradian of the sky (15h06m $\leq$RA$\leq$18h, -75$\leq DEC \leq$-10) which includes a large part of the southern Galactic plane including the Galactic center were also presented.

Unavoidably certain regions of the map have been affected due to a variety of features which can be broadly divided into sources appearing in grating lobes/aliased images, sidelobes of strong sources which could not be deconvolved properly and regions affected by residual DC along RA which could not be effectively removed from the images. The reliability in such affected areas is best judged by the examination of the contour maps itself.

The rms noise is not uniform throghout all the RA ranges. It varies from 250 mJy to 400 mJy dependingon the region imaged.. The measured noise in the images is higher compared to the expected noise on an average by a factor of 1.7.

Taking the worst case for rms noise as $\approx$390 mJy the surface brightness sensitivity is $\approx 2.1 \times 10^{-21} \mathrm{W\,m^{-2}\,Hz\,Sr}$ (1σ at 151.5 MHz). Due to this good surface brightness sensitivity at low frequency, the images are suitable for the study of extended features.

A source catalogue of nearly 2,800 (5σ) unresolved and extended radio sources derived from the images was presented. Initial analysis of the catalogue and its cross comparison with the MRC Catalogue at 408 MHz and Culgoora Catalogue at 160 MHz were carried out and is on the expected lines.

Figure 2.4: Contour map covering the range $00^h00^m \leq RA \leq 00^h30^m$, $-75° \leq DEC \leq -70°$. The contour levels are -5, -3.6, -2.5, -1.8, 1, 1.4, 2, 2.8, 3.6, 5, 7, 10, 14, 20, 29, 40, 54, 72, 90, 100, 136, 180, 216, 252, 288 Jy beam^{-1}. The rms noise in the image is $\approx$425 mJy beam^{-1}.
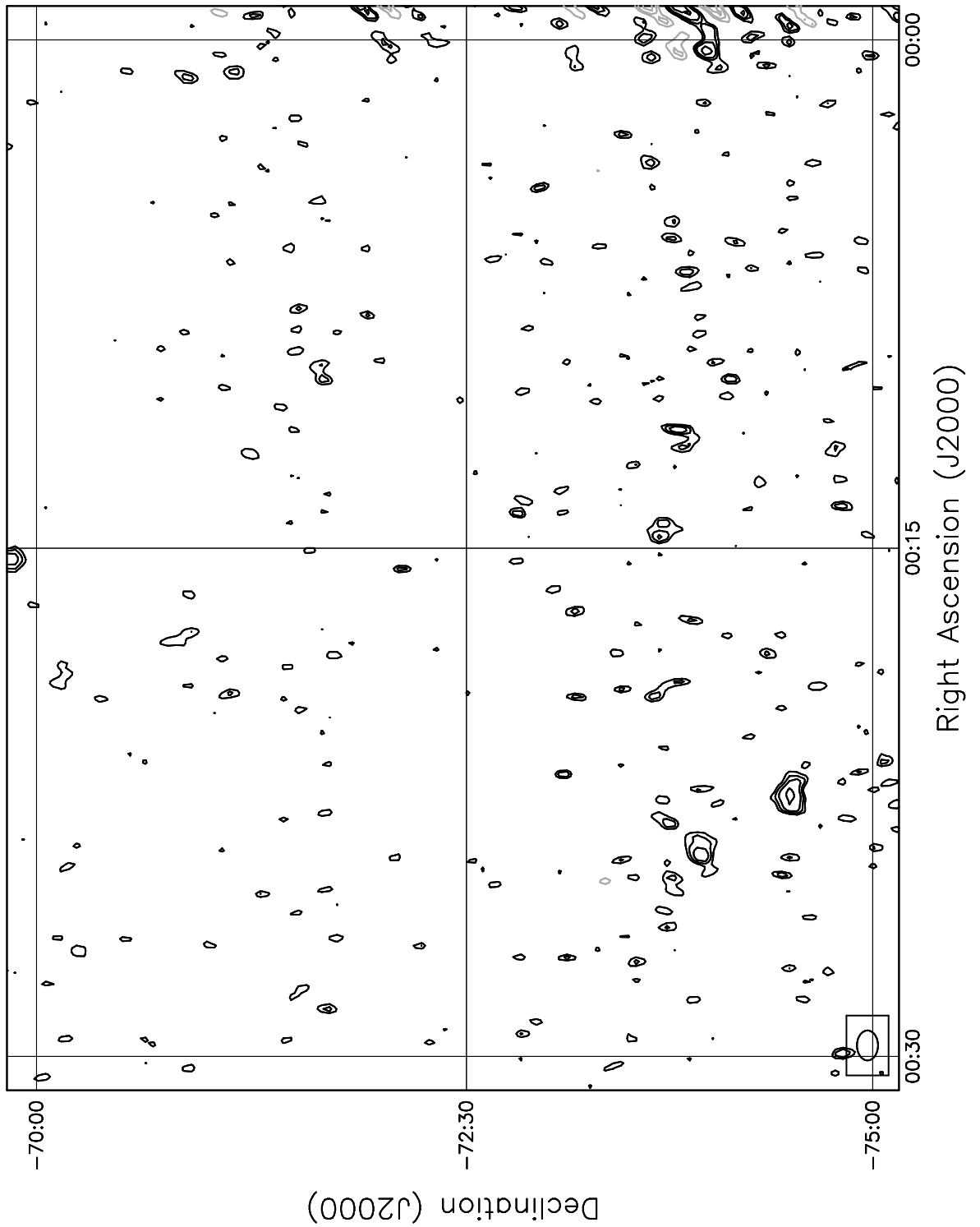
Chapter 3

2-D Homography for correction of images

3.1   Introduction

In the previous chapter we described the imaging of a steradian of the southern sky has been using the Mauritius Radio Telescope (MRT). Investigations revealed that these images show systematics in positional errors of sources when compared to source positions in the Molonglo Reference Catalogue (MRC).This chapter describes application of two-dimensional homography to correct for systematic positional errors in the image domain and thereby avoid re-processing the visibility data. Positions of bright (above 15 σ) point sources, common to MRT catalogue and MRC, are used to set up an over-determined system to solve for the homography matrix. After correction the errors are found to be within 10% of the beamwidth for these bright sources and the systematics are eliminated from the images. We are of the view that this technique will be of relevance to the new generation radio telescopes where, owing to huge data rates, only images after a certain integration would be recorded as opposed to raw visibilities. This chapter also describes how our investigations cued to possible errors in the array geometry and re-estimation of array geometry using the astrometry principle. The estimates show an error of 1 mm/m, which results in an error of about half a wavelength at 150 MHz for a 1 km north-south baseline. The estimates also indicate that the east-west arm is inclined by an angle of $\sim 40''$ to the true east-west direction. Our work has been reported in the publication Nayak, Daiboo & Udaya Shankar (2010).

3.2   Systematic positional errors in MRT images

We compared positions of sources common to MRT and MRC catalogues in the one steradian MRT images previously imaged by Pandey (2006). As mentioned several times in this thesis, MRC catalogue was used because it overlaps with MRT survey, its proximity

in frequency compared to other reliable catalogues available and, comparable resolution ($2'.62 \times 2'.86 \sec(DEC + 35°.5)$). the MRC catalogue is reported to be substantially complete for sources of listed flux density ≥ 1.00 Jy (at 408 MHz) and, the reliability is reported to be 99.9% (Large *et al.*, 1991). For further discussions errors in MRC source positions are considered random and without any systematics.

About 400 bright (above 15-σ at MRT) sources, common to the two catalogues, in the steradian were identified and their positions compared. The sources were labelled as common if they lie within $4'$ of each other. Since MRC catalogue has source density of about 0.5 source $\deg^{-2}$, the chances of considering two unrelated sources as common are extremely low. A lower flux threshold of 15-σ ensures a source population abundant to reliably estimate homography (explained in next section).

Our analysis showed systematics in the positional errors of sources. The positional errors in RA and DEC show no systematics as a function of RA. However, errors show a linear gradient as a function of DEC. The errors are plotted in figure 3.4. The gradient in RA error, plotted against DEC, is very small (refer *second row* of Fig. 3.2a) whereas, DEC errors, plotted against DEC, are significant and reach about 50% of the MRT beamwidth in DEC (refer *second row* of Fig. 3.2b). Histograms in Fig. 3.2c and Fig. 3.2d show the distribution of errors in RA and DEC, respectively. The histogram of DEC errors show a larger spread compared to RA errors.

While preparing a source catalog from images Pandey (2006) used 1-D least squares-fit and separately corrected RA and DEC errors in the source catalogue. However, the errors remained in the images, which impede usefulness of MRT images for multi-wavelength analysis of sources.

Re-imaging, to correct for the errors in the images, would involve reducing $\sim$5,000 hours (about a quarter of the total $\sim$20,000 hours observed during the survey) of visibilities that were recorded over a span of $\sim$5 years (Udaya Shankar *et al.*, 2002). Owing to the complexity involved, it was decided to correct for the positional errors in the images thus avoiding re-processing. The 2-D homography estimation technique, ubiquitously used in the computer vision and graphics community, was employed for correcting positional errors in images and is discussed in detail in the following section.

3.3 2-D Homography for correction of images and re-estimation of Array Geometry

We describe the application of 2-D homography, a technique ubiquitous in the computer vision and graphics community, to correct the errors in the image domain. Homography is used to estimate a transformation matrix (which includes rotation, translation and non-isotropic scaling) that accounts for positional errors in the linearly gridded 2-D images. In our view, this technique will be of relevance to the new generation radio telescopes where,
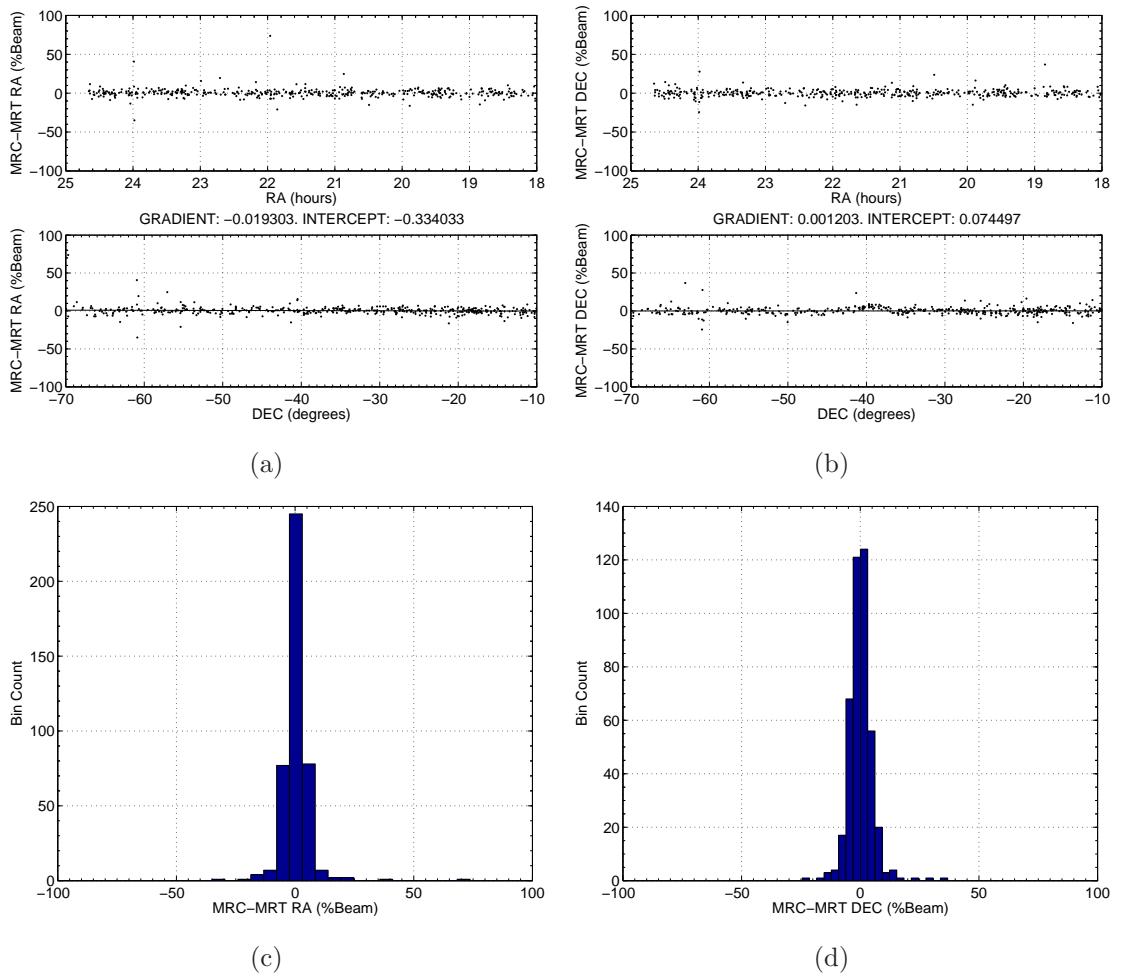
Figure 3.1: Positional error analysis after homography-based correction. **(a)** *First* and *second row* subplots show RA errors against RA and DEC, respectively. **(b)** The *first* and *second row* subplots show DEC errors against RA and DEC, respectively. **(c)** and **(d)** show histograms of RA and DEC positional errors, respectively.
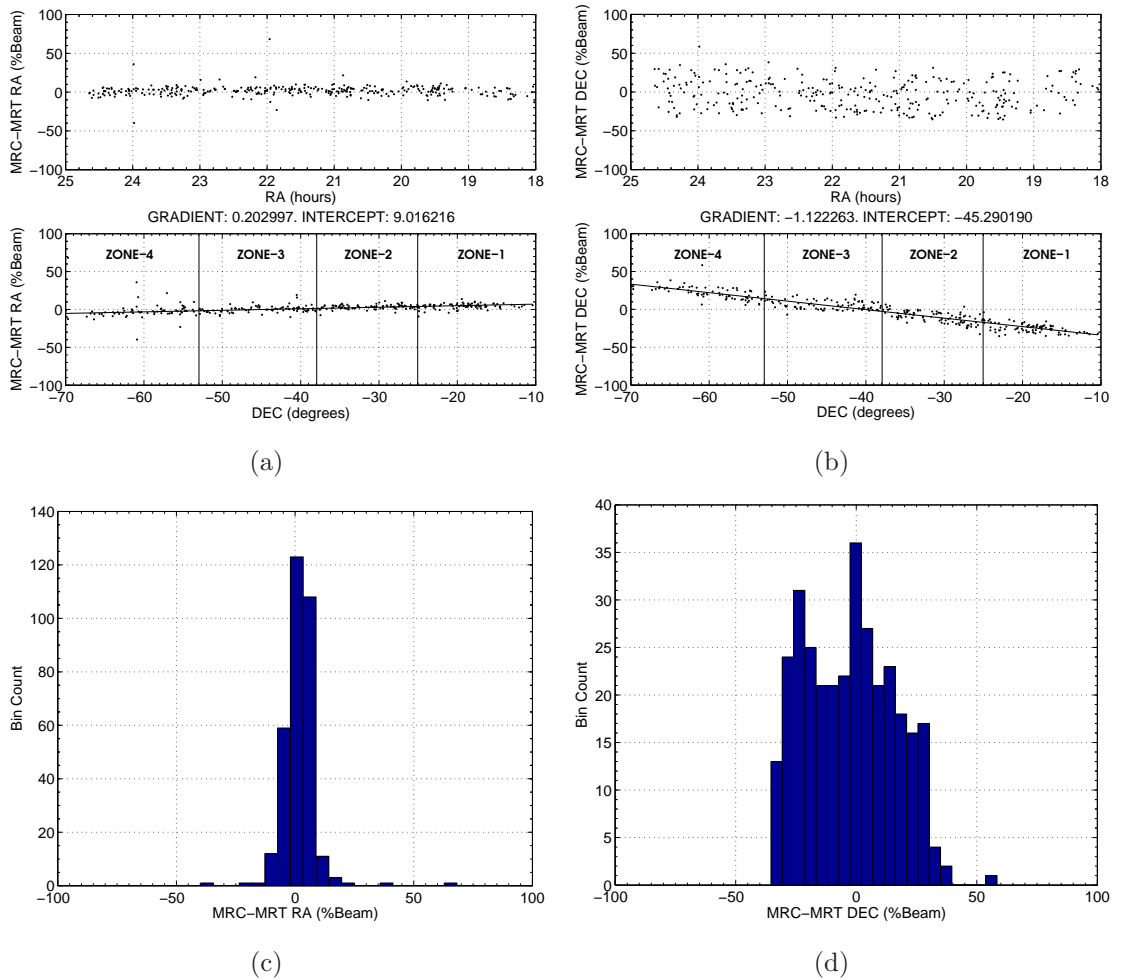
Figure 3.2:   Positional error analysis of ~400 sources (above 15-σ) common to MRT and MRC catalogues in one steradian images. **(a)** The *first row* subplot shows RA errors against RA; no systematics are observed. The *Second row* subplot shows RA errors against DEC; errors show a small linear gradient as a function of DEC. **(b)** The *first row* subplot shows DEC errors against RA; no systematics are observed. The *Second row* subplot shows DEC errors against DEC; errors show a linear gradient as a function of DEC. Note, the *second row* subplots in (a) and (b) indicate the DEC ranges of four *zones* imaged with different delay settings. **(c)** and **(d)** show histograms of positional errors in RA and DEC, respectively.
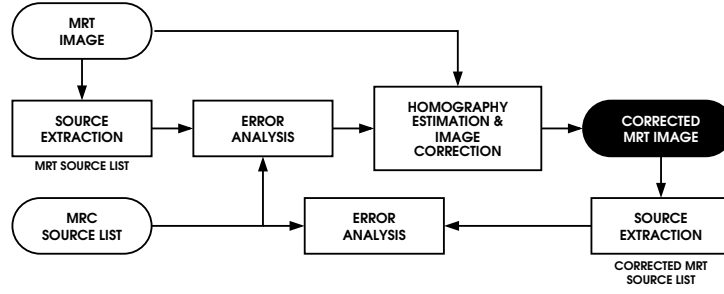
Figure 3.3: Block schematic of the correction scheme. Rectangular boxes represent processes; rounded boxes, data or results.

owing to huge data rates, only images after a certain integration cycle would be recorded as opposed to raw visibilities. This section also describes our investigations tracing the positional errors to the errors in the array geometry used for imaging. Our hypothesis and the subsequent confirmation endorsed by the re-estimation of the array geometry and its effect on the images are also described in the next sections.

3.3.1 Positional errors

3.3.2 2-D homography

2-D planar homography is a non-singular linear relationship between points on planes. Given two sets of corresponding image points in projective coordinates, $\mathbf{p}, \mathbf{p}' \in \mathbb{P}^2$, homography maps each $\mathbf{p}$ to the corresponding $\mathbf{p}'$ (Hartley & Zisserman, 2004). The homography sought here is a non-singular 3×3 matrix H such that:

$$\begin{bmatrix} x' \\ y' \\ 1 \end{bmatrix} = \begin{bmatrix} h_{11} & h_{12} & h_{13} \\ h_{21} & h_{22} & h_{23} \\ h_{31} & h_{32} & h_{33} \end{bmatrix} \begin{bmatrix} x \\ y \\ 1 \end{bmatrix}. \tag{3.1}$$

Where, (x, y) and (x', y') represent $(RA, \sin(ZA))$ of MRT and MRC sources, respectively. At MRT imaging is done in RA and $\sin(ZA)$ coordinate system. Therefore, we convert DEC of MRC sources to equivalent $\sin(ZA)$ at MRT. Note, for visualisation, all plots of positional errors (for example in *second rows* of Fig. 3.2a and 3.2b) are represented in DEC as opposed to $\sin(ZA)$.

In Equation 3.1, $(x, y, 1)$ and $(x', y', 1)$ are referred to as *homogeneous coordinates* and are always represented one dimension higher than the dimension of the problem space. This is a commonly used representation in computer graphics. The simple reason is, with a 2×2 matrix one can only rotate a set of 2-D points around the origin and *scale* them towards or away from the origin. A 2×2 matrix is incapable of *translation* of 2-D coordinates. Homogeneous coordinates allow one to express a translation as a multiplication. A single 3×3 matrix, with homogeneous coordinates, can account for rotation, scaling and translation of 2-D coordinates. For example, from Equation 3.1,
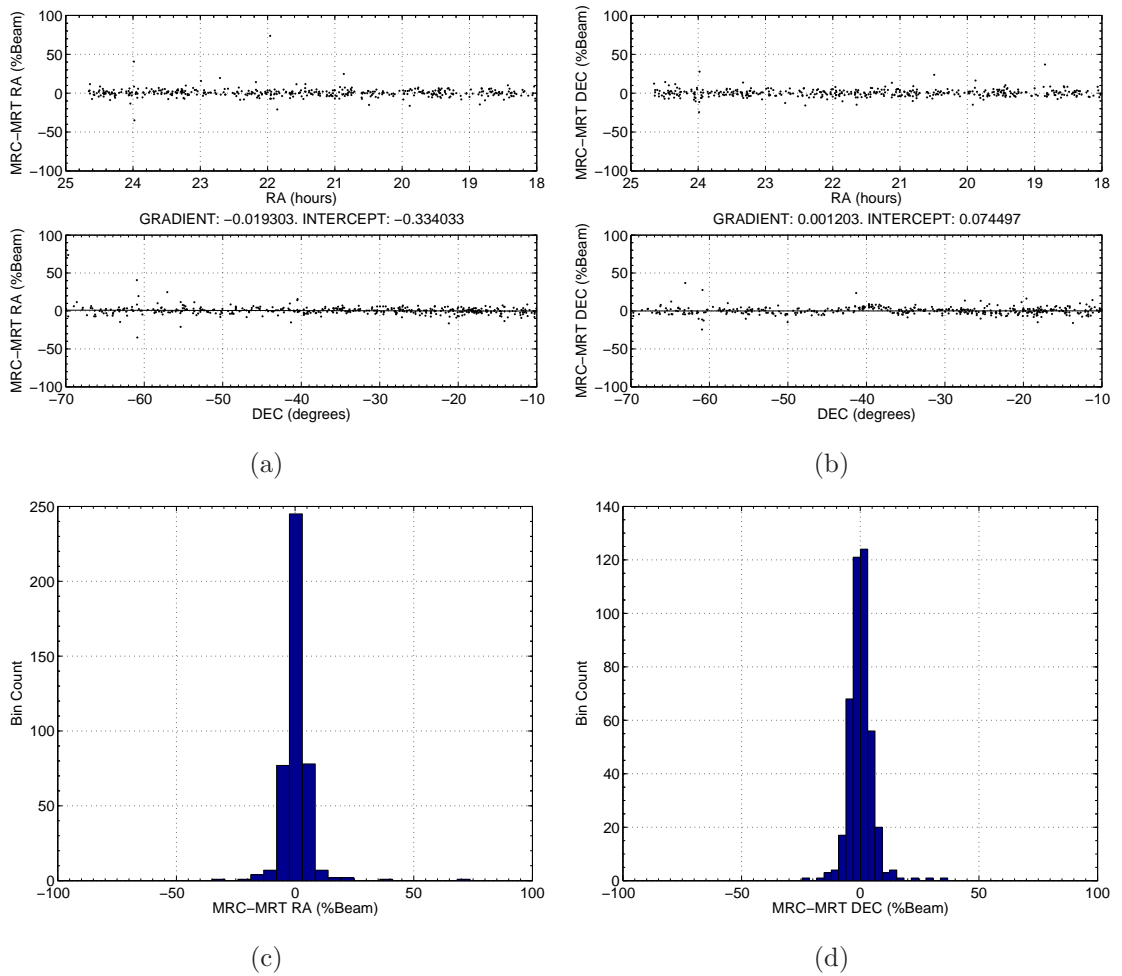
Figure 3.4: Positional error analysis after homography-based correction. **(a)** *First* and *second row* subplots show RA errors against RA and DEC, respectively. **(b)** The *first* and *second row* subplots show DEC errors against RA and DEC, respectively. **(c)** and **(d)** show histograms of RA and DEC positional errors, respectively.

$x' = h_{11}x + h_{12}y + h_{13}$. Notice, h_{13} (representing translation in RA-dimension) is simply being added to the normal dot product $(h_{11}x + h_{12}y)$ that together represents rotation and scaling. Another way of visualising this is, the 2-D problem space is a plane hovering in the third (homogeneous) dimension of unity value.

A general homography matrix, for projective transformation, has 8 degrees-of-freedom (DOF). For our system, both RA and DEC errors have only $\sin(ZA)$-dependency. Therefore, a less general, 2-D affine transformation is sufficient. A 2-D affine transformation (two rotations, two translations and two scalings) requires 6-DOF (Hartley & Zisserman, 2004), therefore in H, h_{31} and h_{32} are zero. Since each 2-D point provides two independent equations, a minimum of 3 point correspondences are necessary to constrain H in the affine space. The equation contributed by each corresponding pair can be re-arranged to obtain:

$$x'_n (h_{31}x_n + h_{32}y_n + h_{33}) = h_{11}x_n + h_{12}y_n + h_{13}$$
$$y'_n (h_{31}x_n + h_{32}y_n + h_{33}) = h_{21}x_n + h_{22}y_n + h_{23}. \tag{3.2}$$

Where, $n = 1, \ldots, N$. A set of N such equation pairs, contributed by N point correspondences, form an over-determined linear system $\mathbf{Ah} = \mathbf{b}$, as shown in Eq. 3.5, where,

$$\mathbf{A} = \begin{bmatrix} x_1 & y_1 & 1 & 0 & 0 & 0 & -x_1x'_1 & -x'_1y_1 \\ 0 & 0 & 0 & x_1 & y_1 & 1 & -x_1y'_1 & -y_1y'_1 \\ \vdots & & & \vdots & & & & \vdots \\ x_N & y_N & 1 & 0 & 0 & 0 & -x_Nx'_N & -x'_Ny_N \\ 0 & 0 & 0 & x_N & y_N & 1 & -x_Ny'_N & -y_Ny'_N \end{bmatrix}, \tag{3.3}$$

$$\mathbf{h} = \begin{bmatrix} h_{11}, h_{12}, h_{13}, h_{21}, h_{22}, h_{23}, h_{31}, h_{32} \end{bmatrix}^T \text{ and,} \tag{3.4}$$

$$\mathbf{b} = \begin{bmatrix} x'_1, y'_1, \ldots, x'_N, y'_N \end{bmatrix}^T. \tag{3.5}$$

In Equation 3.5, T represents a matrix transpose. This system can be solved by least squares-based estimators.

As mentioned earlier, $\mathbf{p}$ and $\mathbf{p}'$ are represented in $(RA, \sin(ZA))$. The RA, represented in hours, ranges from 00 hours to 24 hours. Whereas, the $\sin(ZA)$ ranges from -1 to 1. Moreover, in matrix $\mathbf{A}$ (refer Equation 3.5), for example, there are entries of 1's & 0's and also product entries like xx', xy', $x'y$ & yy'. Such a matrix is ill-conditioned and in the presence of noise in the source positions, the solution for an over-determined system may diverge from the correct estimate (Hartley & Zisserman, 2004). The effect of an ill-conditioned matrix is that it amplifies the divergence. A normalisation (or pre-conditioning) is therefore required.

3.3.2.1   Data normalisation

To obtain a good estimate of the transformation matrix we adopted the normalisation scheme proposed by Hartley (1997). The scheme is briefly described below. The normalisation ensures freedom on arbitrary choices of scale and coordinate origin, leading to
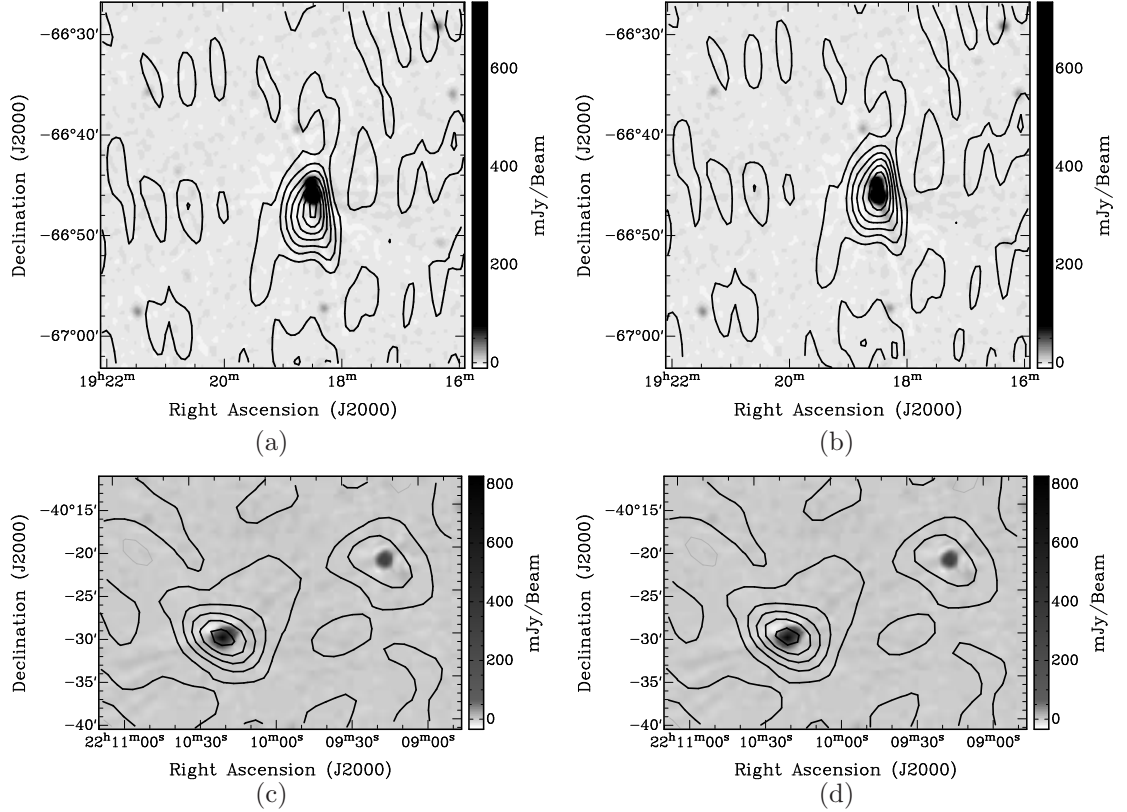
Figure 3.5:   MRT contours overlaid on SUMSS image. **(a)** and **(c)** MRT contours before correction for sources at about -66° and -40° DEC, respectively. **(b)** and **(d)** Corresponding MRT contours after homography-based correction clearly show that 2-D homography corrected the positional errors.

algebraic minimisation in a fixed canonical frame. The canonical frame is obtained by translating and scaling the source coordinates as follows:

1. First, the coordinates in each image are translated so as to bring the centroid of the set of all points to the origin.

2. Then, coordinates are scaled with an isotropic scaling factor such that the average distance from the origin is equal to $\sqrt{2}$.

The homography matrix H is estimated from normalised coordinates by the least-squares method using singular value decomposition (SVD). The matrix is then denormalised, thus bringing it to its original coordinate frame.

3.3.3   The Correction scheme

Fig. 3.3 shows the block schematic of the correction scheme. At MRT, the full DEC range for each sidereal hour range is divided into 4 *zones* (refer *second row* in Fig. 3.2a or 3.2b). Each zone is imaged with different delay settings to keep the bandwidth decorrelation at

acceptable levels. Therefore, the 6 sidereal hours of the steradian under consideration, have 24 images.

Using the population of common sources, there are four possible alternatives to correct MRT images by independently computing:

1. 24 homography matrices - one for each image.

2. 6 matrices for each sidereal hour (combining all 4 zones).

3. 4 matrices for each DEC zone (combining 6 sidereal hours).

4. A single global homography matrix for the entire steradian.

The plots of both RA and DEC errors plotted against RA and DEC (refer to Fig. 3.2a and 3.2b) clearly indicate that the errors are independent of the four delay zones and the RA range. In addition, there are no discontinuities at the zone and hour boundaries. This implies, estimating a single homography matrix from the entire source population should suffice in representing the errors. Using Equation 3.1, the matrix is used to project each pixel from the images to a new position, effectively correcting for positional errors in images. The homography matrix estimated using $\sim$400 common sources (described in Section 3.3.1) is:

$$
\mathtt{H} = \begin{bmatrix} 1.0000 & 0.0006 & 0.0001 \\ 0.0000 & 0.9990 & -0.0009 \\ 0.0000 & 0.0000 & 1.0000 \end{bmatrix}. \tag{3.6}
$$

The value of $h_{11} = 1.0000$ indicates there is no correction required in RA, as a function of RA. $h_{12} = 0.0006$ indicates MRT images should be corrected in RA with a $\sin(ZA)$ dependence. The estimated correction is up to $\sim 5\%$ of the beam in RA, at the extreme ends of the MRT $\sin(ZA)$ range. Similarly, h_{21} indicates that there is no correction required in $\sin(ZA)$, as a function of RA. However, $h_{22} = 0.9990$ indicates MRT images should be scaled in $\sin(ZA)$ by a factor of 0.9990 (which is $\sim$1 part in 1000). h_{13} and h_{23} indicate, $\sin(ZA)$ is not equal to zero at the local zenith but near to the position of the calibrator (MRC 1932-464) used for imaging the steradian.

3.3.3.1 Corrected images and discussion

Fig. 3.4 shows positional errors in DEC after homography-based correction. A comparison of these plots with Fig. 3.2 clearly demonstrate that homography has removed the systematics and the residual errors are well within 10% of the beamwidth for sources above 15-σ, as expected.

Fig. 3.5a and 3.5b show MRT contours before and after correction, respectively, overlaid on SUMSS (Sydney University Molonglo Sky Survey) image (Mauch *et al.*, 2003), for a source around -67° DEC. The corrected MRT image contours in Fig. 3.5b overlap well with the source in SUMSS image. Figs. 3.5c and 3.5d show similar comparison for

(a)
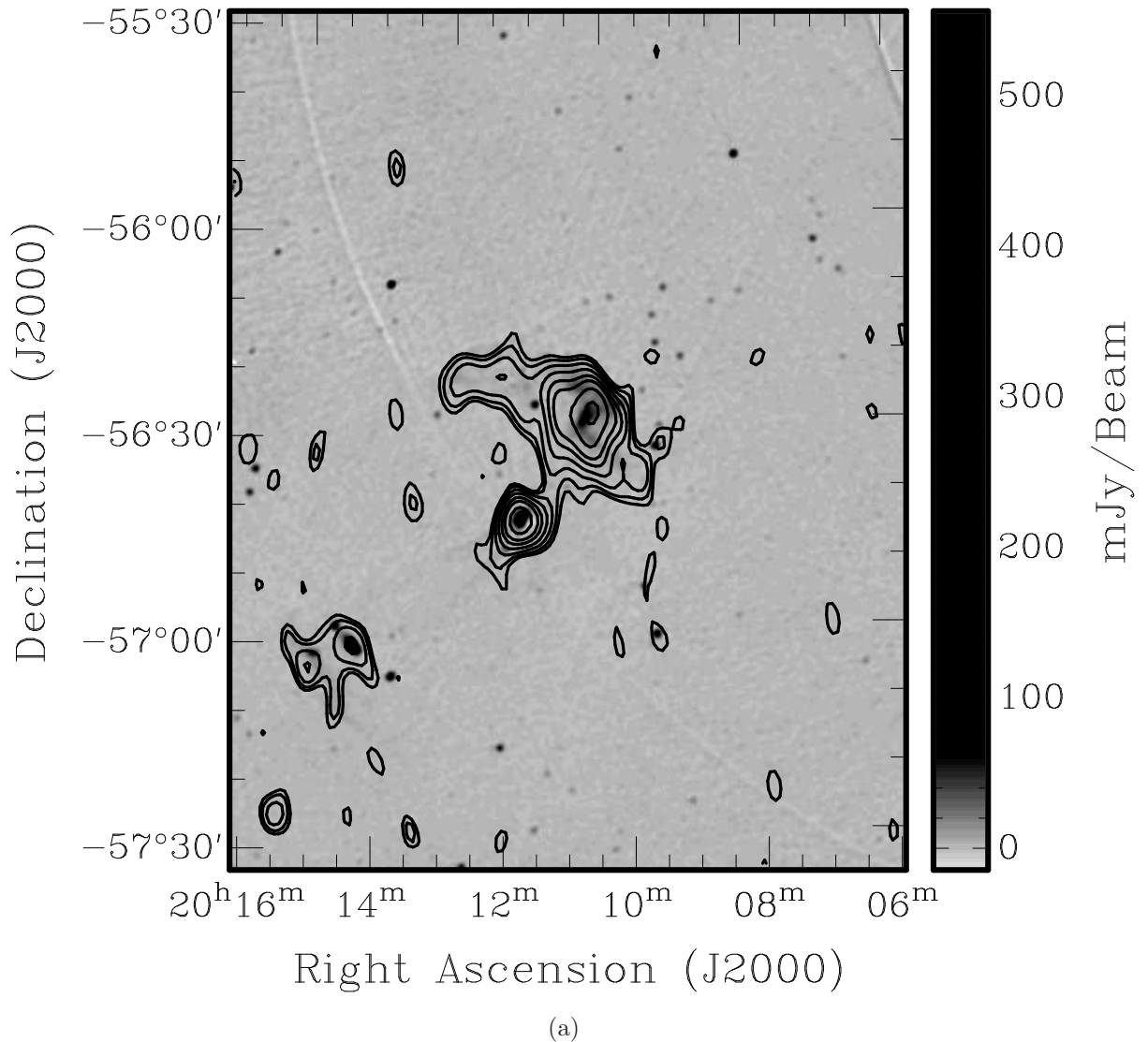
Figure 3.6:   MRT contours overlaid on SUMSS image of a region around Abell 3667.

a source around -40° DEC. Notice Fig. 3.2d, since the errors around -40° DEC are well within 10% of the beamwidth, the contours in both Figs. 3.5c and 3.5d show a good overlap as expected and homography has not applied perceivable correction to images at this DEC. We have overlaid MRT contours on a number of extended sources at 843 MHz, reported by Jones & McAdam (1992). Fig. 3.6 shows a typical overlay of MRT contours on the SUMSS image of a region around the cluster Abell 3667. The overlay is perceivably satisfactory.

The 2-D homography corrected the positional errors in the image domain. For imaging the remaining ∼3.5 steradians of the MRT survey, ∼15000 hours of data has to be reduced. Ideally, for imaging the new regions, one would like to trace the source of these errors and correct them in the visibilities. In the following section we discuss how we traced the source of errors and corrected them in visibility domain.

3.4   Array Geometry: Hypothesis and Re-estimation

This section describes our *expansion-compression* hypothesis to account for the source of errors in our images and, the subsequent corrections we estimated and applied to eliminate the errors.

For meridian transit imaging, $m = \sin(ZA)$. The brightness distribution in the sky as a function of $\sin(ZA)$ and the complex visibilities measured for different values of the north-south (NS) baseline vector component v form a Fourier pair (Christiansen & Hogbom, 1969). A scaling error of κ in m will result in a scaling factor of κ^{-1} in the v-component of the baseline vector. By positional error analysis it is clear that MRT images were stretched (*expanded*) in DEC, i.e.,

$$m_{\text{imaged}} = \kappa \, m_{\text{true}} \tag{3.7}$$

$$\therefore v_{\text{measured}} = \kappa^{-1} \, v_{\text{true}}. \tag{3.8}$$

Note, for images the 2-D homography rightly estimated a correction (*compression*) factor, κ^{-1}, of 0.9990. This easily cued to the hypothesis that the north-south baseline vectors were compressed. Equation 3.4b means, a baseline distance of $\sim$1000 m in the NS arm was wrongly measured as $\sim$999 m. Similarly, a $\sin(ZA)$-dependent correction in RA cued to possible v-component in the east-west (EW) baseline vectors. Next, we describe the re-estimation of array geometry.

As menstioned in section 2.2 MRT has 32 fixed antennas in the EW arm and 15 movable antenna trolleys in the NS arm. For measuring visibilities, the 15 NS trolleys are configured by spreading them over 84 m with an inter-trolley spacing of 6 m (to avoid shadowing of one trolley by another). MRT measures different Fourier components of the brightness distribution of the sky in 63 different configurations (referred to as *allocations*) in order to sample NS baselines every 1 m. Therefore, effectively, there are 945 antenna positions (63 allocations * 15 antennas/allocation) in the NS arm and a total of 30,240 (945 * 32) visibilities are used for imaging.

A small error in a measuring scale of relatively shorter length is likely to build up systematically while establishing the geometry of longer baselines. This effect would be observed in the instrumental phases estimated using different calibrators. In principle, the instrumental phases estimated using two calibrators at different declinations, for a given baseline, should be the same, allowing for temporal variations in the instrumental gains. A non-zero difference in these estimates may be due to positional errors of the baseline or positions of calibrators. As mentioned earlier, our analysis of positional error in sources and the homography matrix cued to positional errors in baseline (or antenna) positions. The simple principle of astrometry (Thompson *et al.*, 2001) was used to estimate errors in antenna positions and is discussed below.

(a)
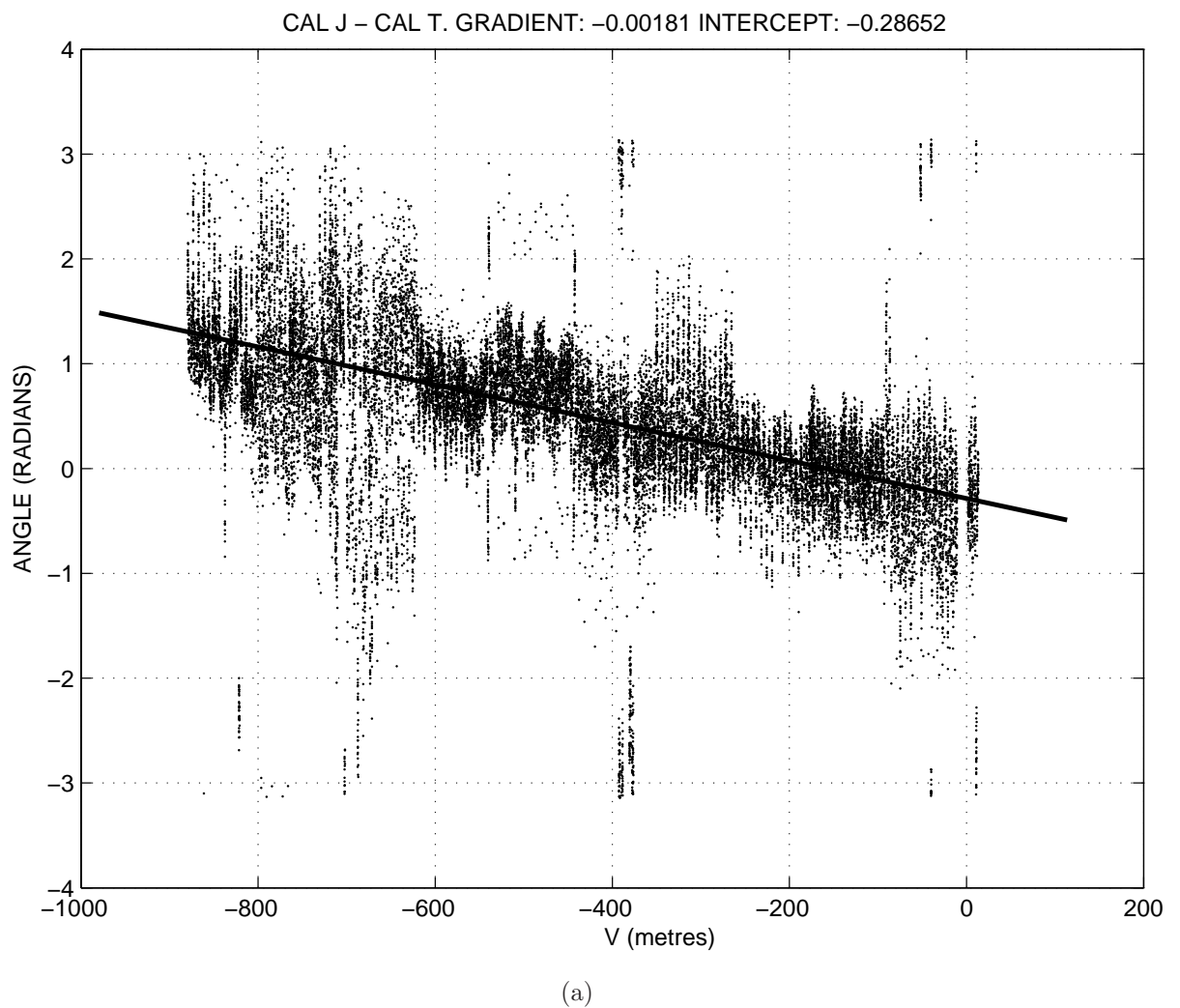
Figure 3.7: Typical calibrator phase differences (in radians) of MRC 0915-118 & MRC 1932-464, plotted against v (metres). The straight line shown is a linear robust fit obtained for the data.
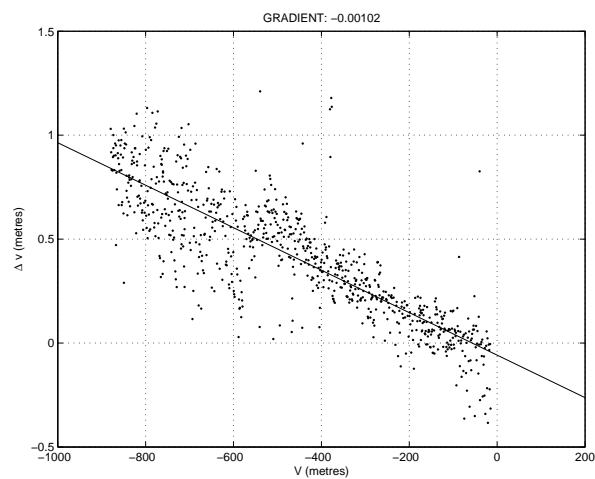
(a)
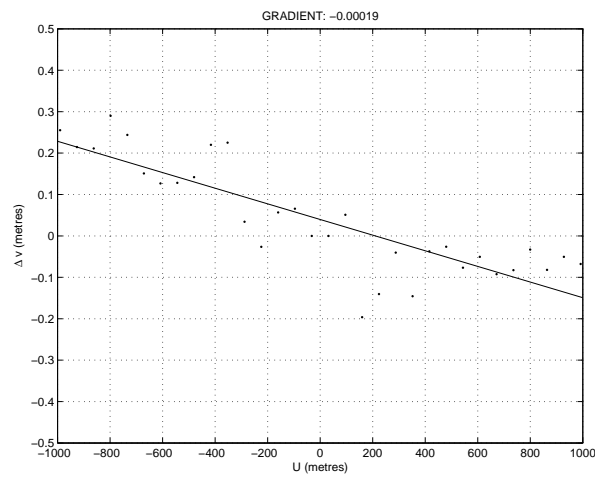
(b)

Figure 3.8: **(a)** Estimate of the antenna position along the North-South arm of MRT array. The fit to the estimates shows a gradient of 1 part in 1000, along the north-south. **(b)** Estimate of the error in v coordinate of MRT east-west arm. The fit to the estimate shows a gradient of 2 part in 10,000, along the east-west.

The observed visibility phase, $\psi_{ij}^{S_1}$, in a baseline with components (u_{ij}, v_{ij}, w_{ij}), due to calibrator S_1 with direction cosines $(l^{S_1}, m^{S_1}, n^{S_1})$, is given by:

$$\psi_{ij}^{S_1} = l^{S_1} u_{ij} + m^{S_1} v_{ij} + n^{S_1} w_{ij} + \phi_{ij}^{ins}. \tag{3.9}$$

Where, ϕ_{ij}^{ins} represents true instrumental phases, $i = 1, 2, \ldots, 32$ represents EW antennas and $j = 1, 2, \ldots, 945$ represents NS antennas. Substituting $H = 0$ (for meridian transit) for $(l^{S_1}, m^{S_1}, n^{S_1})$, Equation 3.9 becomes:

$$\psi_{ij}^{S_1} = -v_{ij} \sin\left(ZA^{S_1}\right) + w_{ij} \cos\left(ZA^{S_1}\right) + \phi_{ij}^{ins}. \tag{3.10}$$

By astrometry (Thompson *et al.*, 2001), the instrumental phases for calibrator S_1, estimated using the measured geometry, are given by:

$$\phi_{ij}^{S_1} = -\Delta v_{ij} \sin\left(ZA^{S_1}\right) + \Delta w_{ij} \cos\left(ZA^{S_1}\right) + \phi_{ij}^{ins}. \tag{3.11}$$

Here, Δv_{ij} and Δw_{ij} are the errors in the assumed baseline vectors. $\phi_{ij}^{S_1}$ are phases of complex baseline gains obtained in the process of calibration. Equation 3.11 has three unknowns. To reduce the number of unknowns, one can eliminate the true instrumental phases by taking a difference $\left(\Delta\phi_{ij}^{S_{12}} = \phi_{ij}^{S_1} - \phi_{ij}^{S_2}\right)$ between measured instrumental phases of two calibrators, estimated using the measured geometry.

$$\Delta\phi_{ij}^{S_{12}} = -\Delta v_{ij} \left[\sin\left(ZA^{S_1}\right) - \sin\left(ZA^{S_2}\right)\right]$$
$$+\Delta w_{ij} \left[\cos\left(ZA^{S_1}\right) - \cos\left(ZA^{S_2}\right)\right]. \tag{3.12}$$

Note, the w-components of the baseline vectors are short and local measurements. Therefore, in principle, one can consider Δw_{ij} as zero-mean random errors with no systematics. Equation 3.12 in that case can be written as:

$$\Delta\phi_{ij}^{S_{12}} = -\Delta v_{ij} \left[\sin\left(ZA^{S_1}\right) - \sin\left(ZA^{S_2}\right)\right]. \tag{3.13}$$

Describing the system in terms of errors in antenna positions, as opposed to errors in baseline positions, Equation 3.13 becomes:

$$\Delta\phi_{ij}^{S_{12}} = -\left(\Delta v_i - \Delta v_j\right) \left[\sin\left(ZA^{S_1}\right) - \sin\left(ZA^{S_2}\right)\right]. \tag{3.14}$$

This equation is also not sufficient to solve for the errors in antenna positions as we have two unknowns and one equation. We set up another equation using a third calibrator source, S_3, spaced away in declination from S_1 and S_2:

$$\Delta\phi_{ij}^{S_{23}} = -\left(\Delta v_i - \Delta v_j\right) \left[\sin\left(ZA^{S_2}\right) - \sin\left(ZA^{S_3}\right)\right]. \tag{3.15}$$

The Equations 3.14 and 3.15 are a linear set of equations for one baseline. For the measurements in 63 allocations, the set of equations can be formulated in a matrix form and solved by SVD-based least-squares estimator:

$$\mathcal{A}\mathbf{x} = \mathbf{b}. \tag{3.16}$$

Where, the *measurement vector* $\mathbf{x} \in \mathbb{R}^c$ is to be determined. Here, $c = 977$. The measurement vector gives Δv_i and Δv_j estimates for 32 EW and 945 NS antenna locations, respectively. The *observation vector* $\mathbf{b}$ consists of two sub-matrices, $\mathbf{b}_1 \in \mathbb{R}^{r_1}$ and $\mathbf{b}_2 \in \mathbb{R}^{r_2}$, formed using the left-hand-side of Equations 3.14 and 3.15, respectively. Here, $r_1 = r_2 = 30240$, i.e., the total number of visibilities measured for imaging. Therefore, $\mathbf{b} \in \mathbb{R}^{60480}$. The *data matrix* $\mathcal{A} \in \mathbb{R}^{60480 \times 977}$. Each row in the data matrix has only two non-zero elements, corresponding to a baseline formed by one EW and one NS antenna, making it very sparse.

The observation vector is constructed from the gain tables of the array, obtained using MRC 0407-658 ($\mathcal{S}_1$), MRC 0915-118 ($\mathcal{S}_2$) and MRC 1932-464 ($\mathcal{S}_3$). A plot of typical phase differences obtained using the pair of calibrators $\mathcal{S}_2$ and $\mathcal{S}_3$ is shown in Fig. 3.7. Fig. 3.8a shows the estimated errors in 945 NS antenna positions. The errors show a gradient of 1 part in 1000 along the NS arm. This matches with the linear gradients in the phase differences estimated from the calibrators. The estimates in Fig. 3.8b show alignment errors of the 32 antennas in the EW arm along the NS-direction. The fit shows a gradient of about 2 part in 10,000. This indicates that the EW arm is mis-aligned from the true EW-direction. At one extreme end (1 km from the centre of the array) of the EW arm the error is ~ 0.2 m, equivalent to an angular distance of $\sim 40''$ from the centre of the array. This is the source of a small $\sin(ZA)$-dependent error in RA that was observed in both positional error analysis and the homography matrix.

3.5 Conclusions

The homography-based correction was able to correct for systematics in positional errors in the image domain and the errors are now well within 10% of the beamwidth for sources above 15-σ. The corrected images of one steradian are available for download at *http://www.rri.res.in/surveys/MRT*.

Positional error analysis clearly showed that uncorrected MRT images are stretched in declination (about 1 part in 1000). This translates to a compression of the NS baseline vector, in the visibility domain. It also showed a $\sin(ZA)$-dependent error in RA. This cued towards possible errors in our estimation of the array geometry. By formulating a linear system, using instrumental phases estimated from three well separated calibrators whose positions are well known, the array geometry was re-estimated. The estimated error in the v-component of the NS baseline vectors is about 1 mm/m. In other words, the error is about half a wavelength at 150 MHz (1 m) for a 1 km baseline. The estimates also show a small (2 part in 10,000) v-component in the purely EW baseline vectors. This indicates that the EW arm is mis-aligned and inclined at an angle of $\sim 40''$, to the true EW direction and curves towards the NS-direction. These estimates match with the

observed stretching of MRT images shown by both the positional error analysis and the homography matrix.

Development of 2-D homography-based correction enabled us to correct for the positional errors in the image domain, both in catalogue and images. In our view, this new technique will be of relevance to the new generation radio telescopes where, owing to huge data rates, only images after a certain integration cycle would be recorded as opposed to raw visibilities.

―――――――

3.6   Imaging with new antenna positions

The previous section discussed re-estimation of the MRT antenna positions. An error of 1 mm per metre was found for the NS antenna position. This tallies well with the observed stretching of the images in declination. The systematic errors of source positions in RA and the related errors in the position of EW antennas were small. The results vindicated our understanding. However the loop is incomplete without demonstrating imaging with the new antenna estimates.

Imaging with new antenna positions were carried out for the range $22^h30^m \leq RA \leq 00^h30^m$. However new antenna positions lead to a series of new estimations of:

1. Antenna calibration tables
2. New PSFs for deconvolution.

Both involved going back into the imaging process and were quite time-consuming. The entire set of calibration tables for the MRT images were regenerated with the re-calibrated antenna positions.

Figure 3.9 shows a sample contour plot of the image for the RA range $23^h00^m \leq RA \leq 23^h30^m$, $-45° \leq DEC \leq -40°$. The contour levels are $(-10, -7, -5, -3, 3, 4, 5, 7, 10, 14, 20, 28, 35, 40, 50, 60, 70, 80, 100) \times \sigma$. σ is 286 mJy beam^{-1}.

The noise level in the images for the RA range 2230 to 0030 is on average 286 mJy. This is close to the average of 291 mJy obtained by Pandey (2006) for the same region of the sky.

1141 MRT sources were detected in this region. There are 620 MRC source in this region. 523 matches between MRT and MRC were found. The numbers tally with the expected source counts.

Figure 3.10a shows the error in RA between the matching MRC-MRT sources as a ratio of the fitted beam against RA for the earlier work. The upper plot is errors against RA and the lower plot is against declination. The errors are within 10% of the RA beam. There is no visible systematics in the errors in RA.

Figure 3.10b shows the error in DEC between the matching sources as a ratio of the DEC beam against RA (upper plot) and against sin(ZA) (lower plot) for the earlier work. The error against RA shows a scatter with most of the errors lying within 10% of the RA beam. There is no systematics in the error as a function of RA.

Figure 3.9: Contour plot for the range $23^h00^m \leq RA \leq 23^h30^m, -45° \leq DEC \leq -40°$. Contour levels are $(-10, -7, -5, -3, 3, 4, 5, 7, 10, 14, 20, 28, 35, 40, 50, 60, 70, 80, 100) \times \sigma$. σ is 286 mJy beam^{-1}.
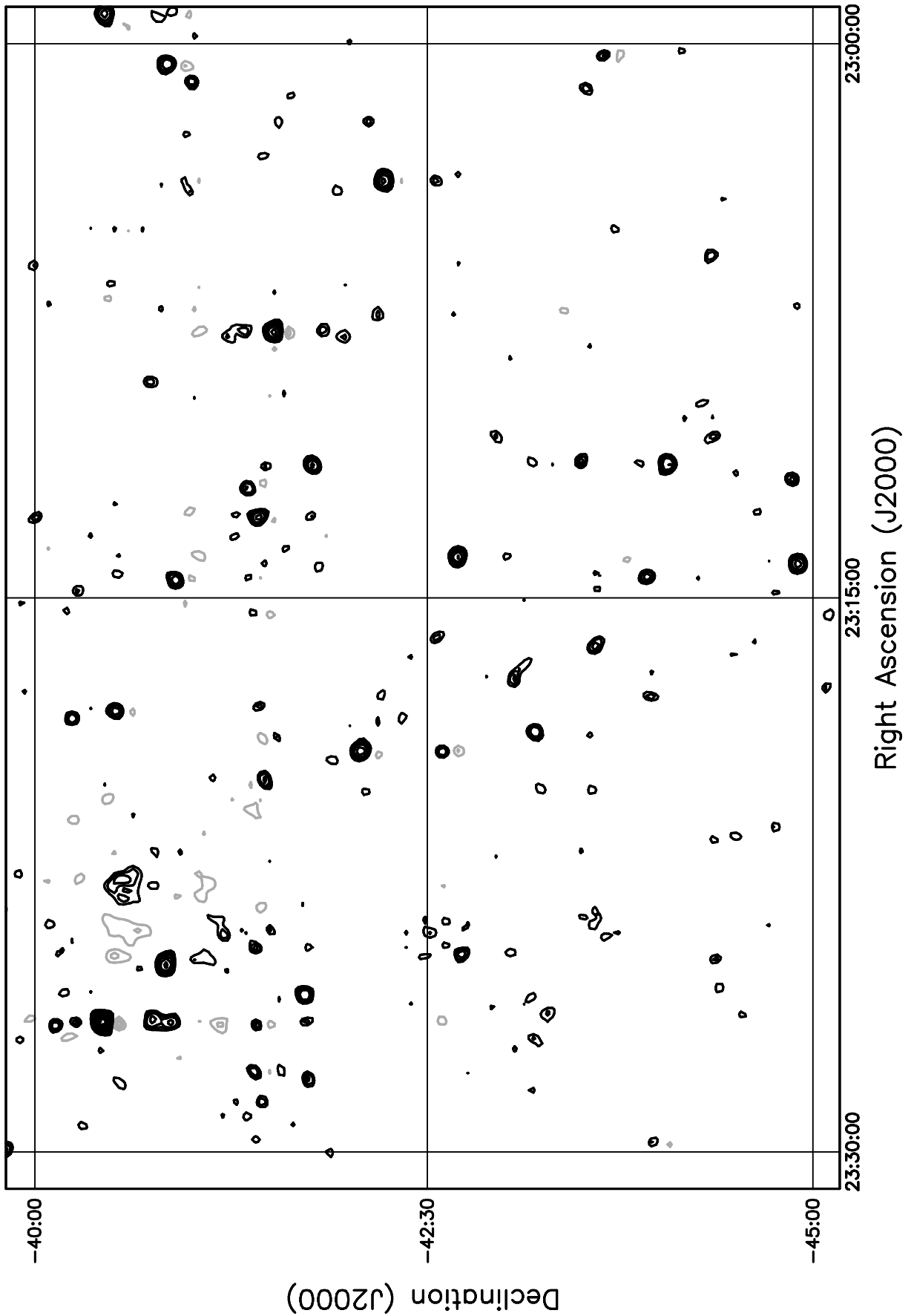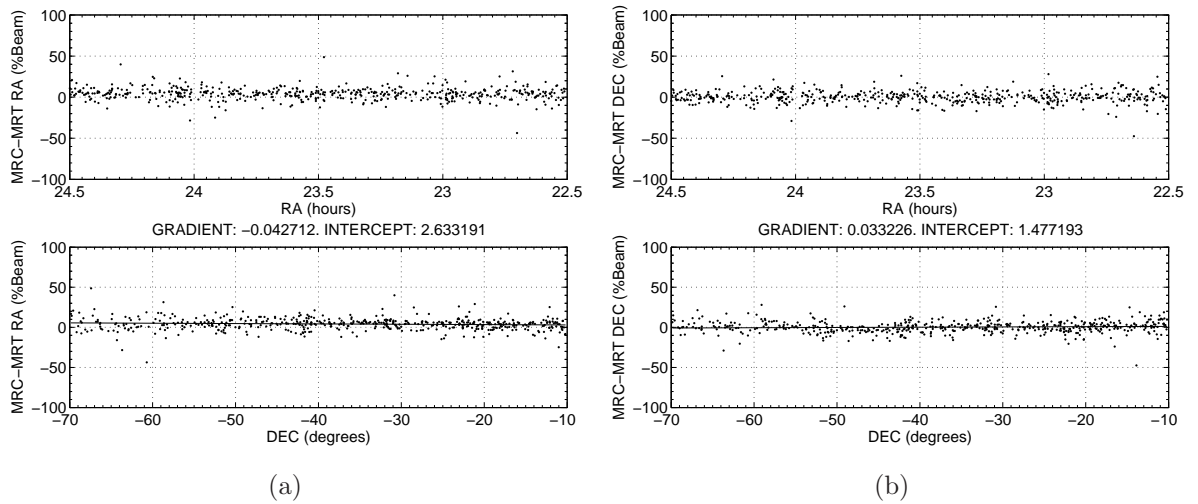
Figure 3.10: (a) Plot of error in RA as a ratio of the fitted beam against RA (upper plot) and against declination (lower plot) between MRC and MRT sources in the range $22^h30^m \leq RA \leq 00^h30^m$, $-70° \leq DEC \leq -10°$. (b) Plot of error in DEC as a ratio of the fitted beam against RA (upper plot) and against declination (lower plot) between MRC and MRT sources for the same RA and DEC range as (a)

Chapter 4

Imaging for the survey

4.1 Introduction

The aim of the MRT data reduction is to image the declination range $-75° \leq DEC \leq -10°$ and RA range $0^h < \text{RA} < 6^h$ with a resolution of $4' \times 4'.6 \sec(DEC + 20°.14)$. The expected rms noise is ≈ 110 mJy beam^{-1} at 151.5 MHz for a system temperature of 600 K. We describe here the procedure we have used for making the images using data from the Mauritius Radio Telescope (MRT) Survey data archive.

The MRT data archive consists of 20,000 hours of observations occupying approximately 1 Terabyte of computer disk space. Handling this large amount of data is a non-trivial task. Estimate for the manual method of processing the data archive (see section 2.6) shows that it would take approximately 2 years to process the whole data archive. This includes all stages of data processing from data editing to deconvolved images.

The experience gained from reducing part of the data archive by manual method was used to write software pipelines in Perl to speed up the data reduction and make the process easily repeatable. This has reduced the data reduction time for the MRT data archive from 2 years to approximately 6 months.

The range $22^h 30^m \leq RA \leq 02^h 30^m$, $-75° \leq DEC \leq -10°$ was imaged to test the software pipelines and check and understand the previously developed methodology for data processing. The next few sections describe the data reduction process in some detail.

4.1.1 Data processing environment

The observations for the MRT survey were carried out over a period of 5 years from May 1994 to March 1999. The telescope hardware and software were constantly under development during this extended observation time. This resulted in hardware and software changes and modifications in the observing modes. For example a recirculator was

built to image the sky with different delay settings to take care of bandwidth decorrelation over wide field of views (Sachdev & Udaya Shankar, 2001b).

The MARMOSAT suite of programs (Dodson, 1997) to reduce the MRT data was written while the observations were being carried out. It was not designed in a way to absorb these changes and present a uniform processing environment. As data reduction progressed beyond the observation phase of the survey, new software development had to be incorporated in MARMOSAT and resulted the X-MARMOSAT (Pandey, 2006) which is an extended version of the MARMOSAT. The data processing environment is still not uniform with the X-MARMOSAT as there are several processing programs, file-naming nomenclatures, and separate information files which have to be manually linked together to perform data reduction. This results in the data reduction by the present method being laborious and time consuming.

To address these issues, streamlining of the data reduction procedure was carried out to decrease the complexity of the data reduction and complete the data reduction within a reasonable time. An added benefit of streamlining is that the data reduction can become repeatable with the possibility to rapidly cycle back and forth data reduction process and easily incorporate improvements in methodology.

The mode of reducing the MRT data is as follows:

1. Identification of the file name from the 4 filenaming nomenclatures, used to identify files during different stages of the observations. The file name encodes information about the data collected.

2. The file name contains information coded in order to contain as much information as possible in the limited set of characters which constitute the filename. For example the last 3 or 4 digits of the Julian date was used to record the Julian date. This varied from nomenclature to nomenclature. Two nomenclatures did not contain any information except being a unique identifier to the file. For these nomenclatures only the observers' log contain the information needed to process the data file. For example the file name 30b177r1.ab3 for the visibility data can be broken down into 30 b 177 r1.a b 3 where 30 is the allocation number , (here it is the 30th allocation number for the NS antennas), b is the session number, it starts from a and is manually incremented each time observation is re-started, 177 is the last 3 digits of the Julian date, r1 is the recirculator mode, b is the number of 24 hours of observations completed from start of observations on that particular session, b is the RA 0100 to RA 0200 observation hour, 3 is the correlation mode, here it is EW×NS observed with the delay setting for imaging the third declination zone. This last correlation mode is dependent of the Julian date observed, so that the Julian date has to be correctly identified before interpreting the correlation mode.

3. Identification of the correct version of the X-Marmosat program, since different version of the Marmosat programs were written to handle different hardware setting in the MRT receivers.

4. Identification of the input files like antenna positions files, delay setting files and pre-processed files like RFI statistics and calibration values. These files are stored in addition to the raw data file as independent database. The raw data has to be linked to these files.

5. Quality check on the data based parameters like RFI statistics, position of the Sun and completeness of data are also stored in the database. An automated grading programs (Pandey, 2006) grades the data's suitability for imaging. Data is selected based on these gradings.

6. Identification of the output files of the processing program.

7. Hand assembly of a shell file for processing the data.

8. Checking of the shell file to verify if all the processing parameters are correct.

9. Execution of the processing by running the shell file.

10. Checking the output files to see if the processing was successful.

11. Repetition of the whole procedure for processing the next hour along the processing chain.

This is a slow and error-prone method and is not convenient for repetition. It takes approximately 1 month to process 1 hour in right ascension of observations and it would take approximately 2 years to reduce the entire data set for the MRT survey.

Figure 4.1 shows a diagram of the information required for processing the MRT data. This information is inferred from the data file name and by looking up the observers' logs recorded during the observations.

It was realised that the MRT data processing had become more complicated with the inclusion of new algorithms for editing of interference, evaluation of data quality, checking quality of each day's image, co-addition of images, deconvolution, source extraction and resulted in the X-Marmosat. The data processing steps were more numerous and the present method of data reduction was out of step with the need to process large amount of data quickly and repeat the process if required and to incorporate improvements.

In the present method information needed to process the data is inferred from the data file name and this information is linked to observers' logs, pre-processed files, antenna position files, delay settings and processing programs.
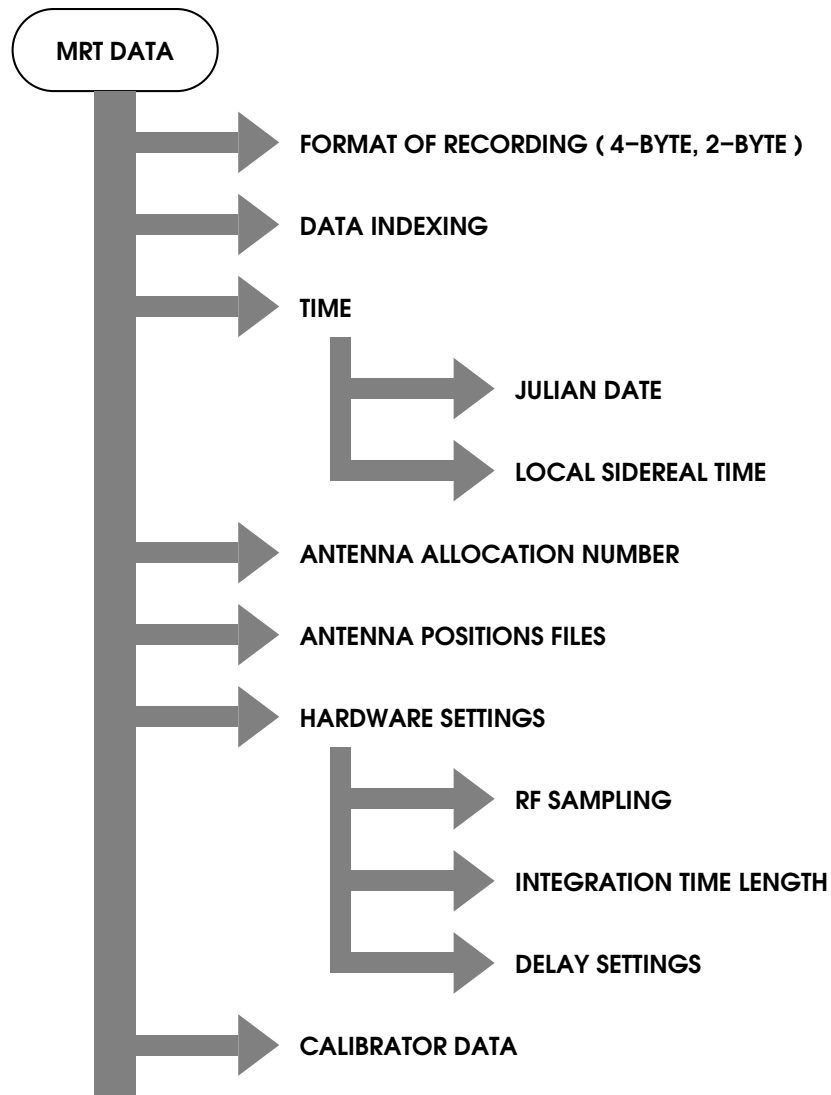
Figure 4.1: The information needed for processing MRT data.

It was also realised that most of the tasks being done manually in the data reduction, e.g reading the data file name, judging the file naming nomenclature used and decoding the information contained in the filename, could be handled by a computer program. The program could also store the location of input files like raw data, antenna positions files, delay setting files and the output files.

With this background it was decided to develop new software pipelines to streamline the data reduction procedure.

4.1.2   New software pipelines for MRT data processing

New software pipelines have been developed which are made up of processing programs 'glued' together by programs written in Perl. The Perl programming language (Wall *et al.*, 2000) was chosen for its character processing capability and its ease of coding and debugging.

A pipeline consists of an interpreter which decodes the filename and infers the information needed for processing based on a reduced version of the observers' logs stored in the program. This is analogous to creating a header file on the fly while processing. The interpreter also uses *a priori* information like the observations were sequential and there cannot be two different hardware settings for the same data file. The interpreter also determines the processing parameters to be used, the programs to be used, the input and output files to be created. Based on the processing sequence needed it automatically generates the shell files for processing the data and sequentially runs them, checks the outputs files till it reaches the end of the processing chain.

Development of the software pipeline started by the automation of a single data processing step which usually consists of running one program. The shell files generated were checked against all possible type of data which would be fed to the program. This exercise was repeated with all the programs in the data reduction suite. Once this step was completed different software pipelines were integrated under one software pipeline program.

The integrated software pipeline was tested against a training set of data representative of the whole MRT data archive, that is data spread over the whole observation period of MRT survey.

4.1.3 Stages of the data processing pipelines

It is possible to run such a software pipeline for processing data from the raw data stage till the sources are extracted (see Section 5.5) by integrating the individual software pipelines under one main software pipeline. However human intervention is required for quality checks in between the stages of the data processing. Therefore it has been found to be more useful to break the pipeline into 3 stages and have human intervention in between the stages for quality checks and introduce new parameters like regions in the map for ripple removal and flag windows for deconvolution.

There are extensive logging facilities in the pipelining software so that it is possible to replay the data reduction post processing.

The stages in the software pipelines are:

1. From observations data files to the 3 hours of one-day dirty images regridded to the common epoch J2000.

2. From the 3 hours one day images to the co-added images.

3. From deconvolution to source extraction.

For regridding the images to the common epoch J2000, 3 continuous hours of images are concatenated together and regridded to provide guard zones on both sides of 1 hour

image for regridding and deconvolution. The criteria for choosing adjacent hour images is that they should have been observed preferably on the same day or in the worse case the day before or the day after the central hour image. In other words, this means observation carried out on any allocation in the same schedule before moving the trolleys in the NS arm to a different position.

There are images for which no adjacent images can be found. In such a case so the reduction pipelines abort imaging with this set of files and jumps to the next file in the queue. All these aborts on the processing are logged by the software pipeline program. Inspection of the logs showed that the errors are few and far in between to seriously affect the data processing.

It should be noted that these failures to give output files have nothing to do with the software pipelines but with the underlying data reduction methodology which requires 3 continuous hours of images to be present for deconvolution. In the data selection stage attention had been focused only on individual hours and their calibration files. One more parameter that can be included in the data selection is the availability of adjacent hour data files (see Section 2.6.0.1).

The software pipeline took approximately 6 months to develop and debug and demonstrate its utility by imaging the RA range $22^h30^m \leq 02^h30^m$. This development time, it is hoped, is more than offset by the increase in the speed of the processing, the aility to repeat the data processing and the reduction in the manpower needed to process the data.

4.2   Computing environment

This setup was a dedicated computing system to store and process the MRT data. Each computer is used for data storage as well as for data processing. Storage hard-disk are made visible to all the processing computers using the Network File System (NFS) over the 100 Mbps ethernet link. Each computer acts as a processing node. The software pipelines are run simultaneously on all the computers mimicking a parallel processing system. This set-up increased the speed of the data reduction considerably.

Figure 4.2 shows the layout of the computer network used for data processing. This configuration grew out of the need to have large data storage and high computing power. Personal computers are used as they are low-cost and readily available. Also the cost of maintenance of such a computing environment is relatively low compared to custom-made computing systems.
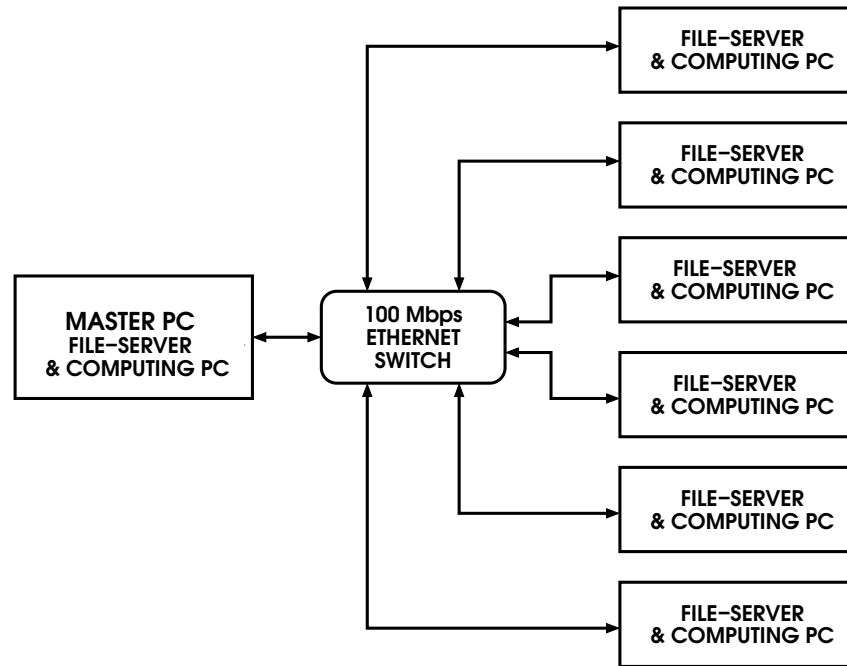
Figure 4.2: MRT data processing computing environment consist of 7 general purpose PCs operating in a linux environment in a 100 Mbps local area network. Each PC hold high capacity hard disks and have approximately 1 Terabyte of disk space each. The whole setup has 7 Terabyte of disk space.

4.3 Conversion of images to FITS format

4.3.1 The need for standardisation

The MARMOSAT and its extension the X-MARMOSAT suite of programs have the limited ambition of being the link between MRT correlator and better supported astronomical software packages. The X-MARMOSAT writes output images which are not in a standard format. MRT images were written in a standard format to make them portable to other astronomical packages and to increase their user base.

4.3.2 Conversion of MRT images to the FITS format

The most widely used digital file format in astronomy is the Flexible Image Transport System (FITS) (Calabretta & Greisen, 2002). For images the FITS format provides a human and machine readable header.

MRT images as produced by the X-Marmosat suite of programs are in sin(ZA) and RA coordinates. This is a natural choice of projection for a non-tracking telescope like MRT where the imaging has been done in the meridian transit mode. The sin(ZA) projection ensures the HPBW to be constant along zenith angle.

MRT images were first converted to a linear projection in declination. In this projection the right ascension is linear in hours and the declination is linear in degrees. MRT

image was interpolated to this new grid by using a spline interpolation in order to reduce the smoothing due to different sampling rates across the original MRT images. The header for this projection was written and the FITS image loaded in AIPS. The task HGEOM in AIPS was used to regrid the linear projection to the SIN projection. This projection was chosen as it is the most widely used projection in radio astronomy.

The conversion of the image was checked by doing a source extraction in AIPS using the task SAD for the RA range $22^h30^m \leq 00^h30^m$. and comparing the source positions against the source positions extracted by the X-MARMOSAT source extraction program for sources having a flux density of $\approx$7 Jy (20-σ). The source positions agree to within the fitting errors. Most of the errors are within 10% of the beam. Images made by Pandey (2006) have been converted to FITS and are made available at http://www.rri.res.in/SURVEYS for download.

4.4   MRT data re-organisation for data reduction

The MRT data has been re-organised to make it easier to reduce the data and to archive it. To remove the hardware-dependent corrections needed for handling the data, the data archive have been re-written to files after all the hardware-dependent corrections have been applied. This results in a uniform format for the MRT data archive. For each data file written out a human and a machine readable header file is created. This header file gives the name and path on the processing computer to the original MRT data file, the written out data files, the time stamp file, the u, v and w coordinates file, the RFI statistics files and the decorrelation curve calculated for that particular data file. The field of view calibration procedure described in section 4.5.2 was developed using this uniform format of the data archive. The benefits accruing from uniformisation are manifold. It allows an abstraction of the data from the local telescope collective knowledge to the level of common astronomical packages for handling the data. This decreases the time to build new applications for processing the data and also increases the user base for the data.

4.5   An Improved calibration scheme for MRT

4.5.1   Description of present calibration scheme

The present calibration scheme at MRT (Golap *et al.*, 1998) depends on observations of strong unresolved sources to derive the calibration values. MRC0915-119 and MRC1932-464 are used as calibrators at MRT. The complex gains of the 47 antennas are estimated using the measured visibilities for the calibrators MRC0915-119 and MRC1932-464. the sensitivity per baseline is 30 Jy for an integration time of one second. In the 2° beam of E-W group the above sources are observable in each baseline with a minimum SNR of about

35. The complex gain of the telescope is estimated by fringe fitting , where it is assumed that the sky in the primary beam is dominated by the calibrator. The instrumental phase estimated is the difference between the phase of the observed visibilities and the expected geometric phase due to the point source calibrator. The instrumental gain is estimated by measuring the relative amplitudes of the fringes on different baselines. the instrumental phase is insensitive to short term interference and also to fringes due to other sources in the sky, provided their fringe rate is significantly different from that of the calibrator for a given baseline. Therefore at short baselines where there are less than two fringes in the E-W group due to the calibrator, satisfactory calibration cannot be obtained. this is tackled at MRT by calculating complex gains of 47 antenna from the measured 512 complex visibilities. At this stage the baselines with short E-W components (essentially the first four east and west group outputs with the south array) are rejected. The closure information obtained from multiplying the E16 group with the E-W and south array group outputs are benificially used in moving from the baseline to antenna calibration.

4.5.2 Limitations of the present calibration scheme

The present calibration scheme has the following limitations:

- MRT is a non-tracking telescope. It is not possible to alternate between pointing to a calibrator source and the region of sky under observation. The calibration values derived when a calibrator source transits the meridian are used to calibrate the antenna. There is a paucity of strong point sources in the southern sky required for reliable calibration. There are only 2 calibrators separated by 10 hours in RA used at MRT. Thus the array can be calibrated at most 2 times per day. The time interval between calibrations is 10 hours in LST. Such a calibration scheme is critically dependent on the system stability. Also there may be ionospheric scintillations in between calibrations which can cause the gain of the instrument to be different from what had been determined from the calibrators in a different part of the sky and also far in time. This results in a poor dynamic range in the images.

- A minimum separation of 10 hours in LST between calibrations also means a high probability that one of the calibrators may have been observed during the day. At MRT the data quality of observations taken during the day is rated as poor due to the presence of the Sun which is a strong interfering source. Thus the calibrators observed during the day are not very useful for calibrating the array. This in effect reduces the rate of calibration to once per 24 hours. This rate of calibration is not a satisfactory state to be in.

- The case of the calibration rate of once every 24 hours can be worsened by non-observation of the only reliable calibrator, poor calibration due to RFI or instrument
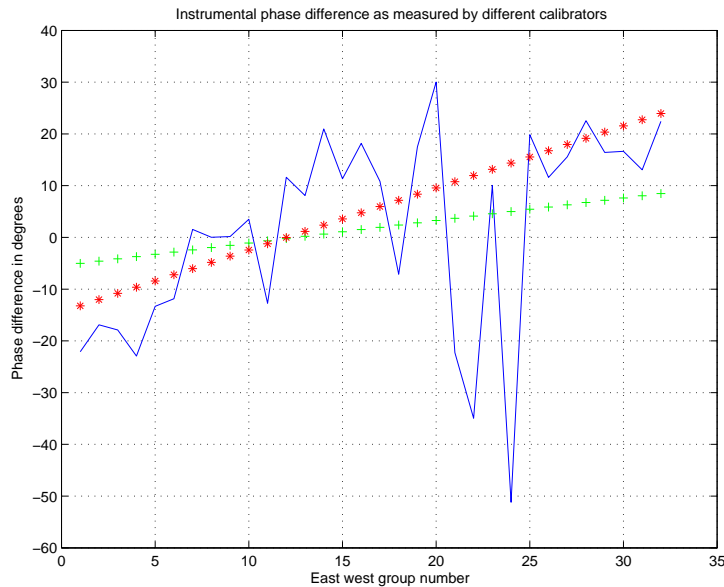
Figure 4.3: Phase difference between MRC0915-119 and MRC1932-464, showing a phase gradient

mal-function. This results in loss of data as the observed data cannot be calibrated and imaged.

We checked the phase stability of the array by comparing the estimated instrumental phases derived form the two calibrators MRC0915-119 and MRC1932-464 which are spaced approximately 10 hours in RA. Figure 4.3 shows the calculated phase difference. most often a phase gradient is observed along the EW arm of the array. A phase gradient across the EW arm could be due to ionospheric perturbations, inacuracy of source positions and partly due to system variation from one calibrator to another.

An improved calibration scheme for MRT: Field of view calibration

As mentioned earlier in the section on automatic data quality assesment, the total quality of a data file becomes poorer when the calibrator data is of poor quality. As we started imaging away from the bright sources used for calibration, the quality of images deteriorated.

It became imminent to develop a calibration scheme to go beyond the bright sources used for calibration.

We investigated a field of view calibration whereby sources in the field of view are used to obtain the calibration table.

MRC catalogue lists $\sim$ 12,000 sources for the 24 hours in RA range. This translates to 500 sources per sidereal hour. With 4 delay zones for MRT, this reduces to an average of 100 sources per delay zone in one sidereal hour, Taking into account non-overlapping

declination ranges of MRC and MRT. Comparison with the MRT source catatlog of 2,800 sources of Pandey (2006) gives similar figures.

The MRC catalgue is 99.99 % complete at the level of 1 Jy. Using a median spectral index of 0.94 (Pandey, 2006) there will be $\sim$ 100 observable sources per sideral hour with a flux density of 2.4 Jansky at 151.5 MHz.

The sensitivity per baseline for MRT is 30 Jy for 1 second of integration. A source is observable for 8 minutes in the 2° wide beam of an EW of group. So a source of 2.4 Jy will be observable with a SNR of $\sim$ 2. The sensitivity per baseline for 100 such sources in the field of view will give a calibration equivalent of one bright source observable with a SNR of 20. Encouraged by this estimation we derived the calibration in one sidereal hour using model visibilities of all the sources in the field of view. We compared it with a calibration table derived from our calibrator MRC1932-464. This showed a phase similar to the day to day rms variation per baseline in amplitude (6 %) and phase (6°).

Figure 4.5.2 shows the phase difference along the NS and EW arm of the array between calibration table derived using calibrator MRC1932-464 and the multi-source calibration scheme. A straight line fit shows that there is a phase gradient along the EW arm of the array from West end to East end. The gradient is probably due to an error in the position of the single bright sources used as calibrators. After removal of the gradient, the rms phase variation is of the order of 6° along the arms of the array, which is not far from the day to day variation observed earlier. Encouraged by this, we imaged a region of sky which overlapped with Set I images. The noise performance was superior with multi-source calibration. In view of this we adopted this improvised calibration scheme for imaging.

4.6   Flux calibration

4.6.1   Correction for Automatic Gain Control used in MRT receiver

The deconvolved images are in arbitrary units and have to be calibrated in units of Jy/beam. At lower frequencies, the calibration is based on observations of a small set of compact galactic and extragalactic sources whose absolute flux densities are known through observations with antennas of known gain (Baars *et al.*, 1977). The flux density scale of Baars is most suitable for northern sky surveys. The RBC scale is another widely used flux density scale (Roger *et al.*, 1973). Cambridge 6C survey used this flux scale to establish the flux densities of sources in their survey. Since all the sources in the RBC scale definition are in the northern hemisphere, it cannot be used for establishing a flux scale for the MRT survey. Unfortunately there have been not much information available on flux density calibrators for the southern sky. In our view the Molonglo 4 Jy
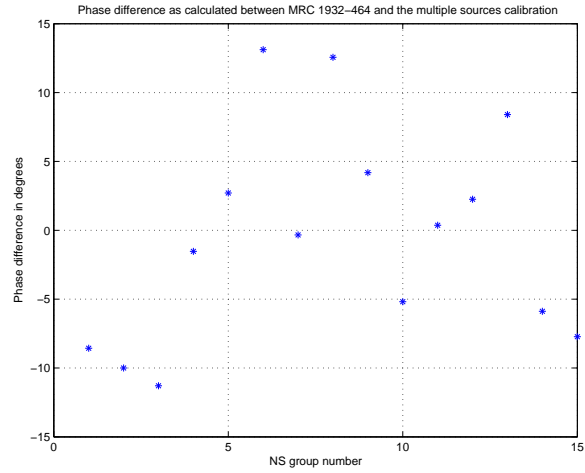
(a)
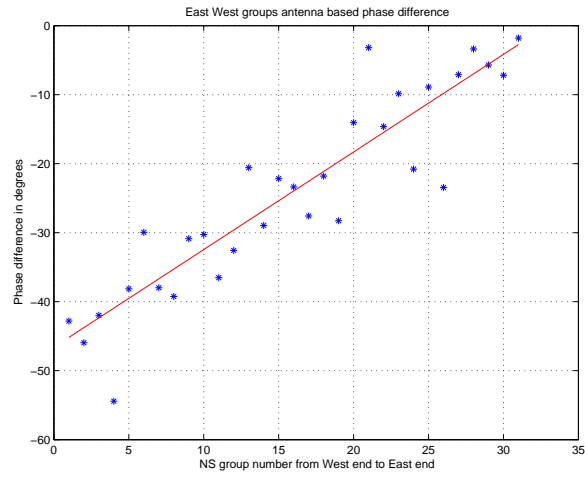
(b)
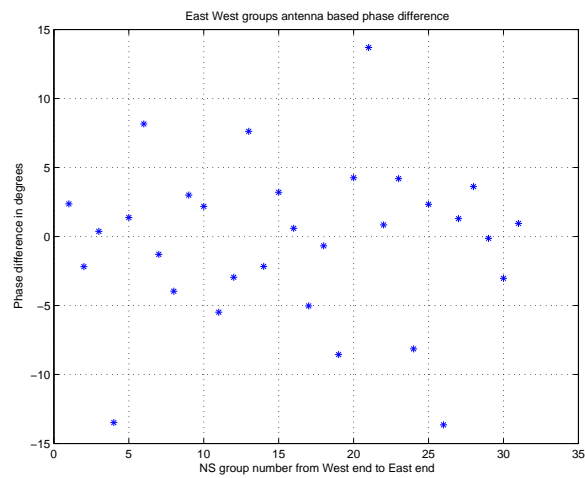
(c)

Figure 4.4: Difference in phase between calibration table derived using calibrator MRC1932-464 and multi-source scheme,

(a) Along the NS arm

(b) Along the EW arm

(c) Along the EW arm with gradient removed

Frequency (MHz)	Flux density (Jy)	error (Jy)	Reference
80	52	2.4	CUL2354-350
160	25.3	1.0	CUL2354-350
408	8.70	0.35	MRC2354-350
843	3.00	0.18	VOL2354-350
1425	1.30	0.06	MOF2354-350
2700	0.35	0.02	PKS2354-350
4850	0.117	0.014	PMNZ2354-350

Table 4.1: Flux densities of the MRT primary flux calibrator MRC2354-350 at different frequencies (Burgess & Hunstead, 2006),(Pandey, 2006).

Survey (MS4) (Burgess & Hunstead, 2006) giving a detailed account of the measurements of at 228 southern radio sources at 408 MHz with integrated flux densities $S_{408} > 4.0$ Jy, Galactic latitude ($b > 10$), is best suited for flux calibration of MRT survey. Radio spectra for the MS4 have been compiled from the literature and used to estimate their flux densities at 178 MHz. The MS4 flux densities recalculated at 151.5 MHz (Private communication Burgess and Hunstead) have been used to calibrate our images. The first set of images made using MRT in the RA range $18^h \leq RA \leq 24^h 30^m$, were also calibrated using the estimated flux densities of 55 MS4 sources lying in the region surveyed. Finally the scale was tied to the flux density of MRC2354-350 being 26.30 Jy at 151.5 MHz. The existing literature shows that it is not a variable source (Slee & Siegman, 1988), its extent is only $17''$ as measured at 4.8 GHz and can be considered a point source for MRT and has sufficient SNR in our images ($\sim$50). Fortunately the region imaged for this work had this source appearing in the guard band for the image covering the RA range 00 to 01 hour. In view of this the flux densities of sources in this work are also tied to the flux density of MRC2354-350. The flux densities of MRC 2354-350 at various frequencies are given in the table 4.1 ((Pandey, 2006) and references there in).

However before proceeding to calibrating the images in Jy/beam scale, one has to correct for the loss of amplitude information in images made using a 2-bit 3-level correlator system using an automatic gain controller in the analog signal path. This is described in the next section.

99106

4.6.1.1   Total power curve for 24 hours in RA

The use of the automatic gain control (AGC) in the MRT receiver results in the loss of information about the variation of the sky background. In view of this a strong source in a bright sky and a weak source in a cold sky give similar deflections. To put back amplitude information in the MRT images, total power measurements of one group in the EW (16 helices phased to meridian) and another in NS (4 helices phased to meridian) are measured

using the self-correlators of those groups where the AGC had been switched off The self correlators of the MRT are wired in such a way that they measure the probability (P) that the input signal amplitude V, is in between the thresholds levels used for digitisation. This probability for a zero mean noise Gaussian signal with an rms fluctuation of σ and a symmetric 2-level digitizer with voltage threshold levels $\pm V_{th}$ is given by,

$$P = \frac{1}{\sigma\sqrt{2\pi}} \int_{-V_{th}}^{+V_{th}} e^{-(\frac{V}{\sqrt{2}\sigma})^2} dV = erf(\frac{V_{th}}{\sqrt{2}\sigma}) \tag{4.1}$$

Knowing P, the $\frac{v_{th}}{\sigma}$ of the signal can be obtained. The equivalent analog correlation, ρ_a, without an AGC, can be obtained using the relation,

$$\rho_a = \rho \times \sigma_1 \times \sigma_2 \tag{4.2}$$

where ρ is the normalized correlation coefficient, σ_1 and σ_2 are the rms of the signals being correlated (EW X NS group) and can be obtained from the channels where the AGCs have been switched off.

Since the self-correlation values are heavily corrupted by RFI, affected by the drifts in the value of V_{th} used and dc off-sets (jumps) unexplained, it is not realistic to apply the total power correction to the images on a day to day basis. So it was decided to correct for the total power variation after obtaining the deconvolved images. However a careful examination of the total power measurements carried out over many days revealed that it is not possible to find a single reliable measurement for EW and NS total powers in one days observation. After carefully editing bad total power scans, we could get data for streches which are about six hours long , covering in four sections the 24 hour total power curve required.

Many good stretches were selected and plotted (See figure 4.5). As expected data on different days, for different streches of RA had different gains and varying DC offsets. We carried out linear regression of different streches in RA separately, taking into account that the curve should fold back after 24 Hr and the total power curve for the RA range 18-24 hr (used for Set I images), defines a reference. This is so because 55 MS4 sources distributed over 6 Hr in RA , were used to calibrate the flux scale of the Set I images using this curve. This resulted in two plots one for EW and another for a NS group (see figure 4.6(a)). To calibrate these two scans in terms of temperatures, we convoled the all sky map of the sky at 408 MHz (Haslam *et al.*, 1981) with the primary beams of EW and NS groups and derived the total power curves at 151.5 MHz using a spectral index of -2.7 for the background sky. The model so obtained was fitted to the total power curves using linear regression. This resulted in a $\sqrt{(T_{EW}T_{NS})}$ shown in the figure 4.6(b). The section of the scan between 0 and 6 hr is used for calibrating the Set II images. this part of the scan is discussed in the chapter on images. .
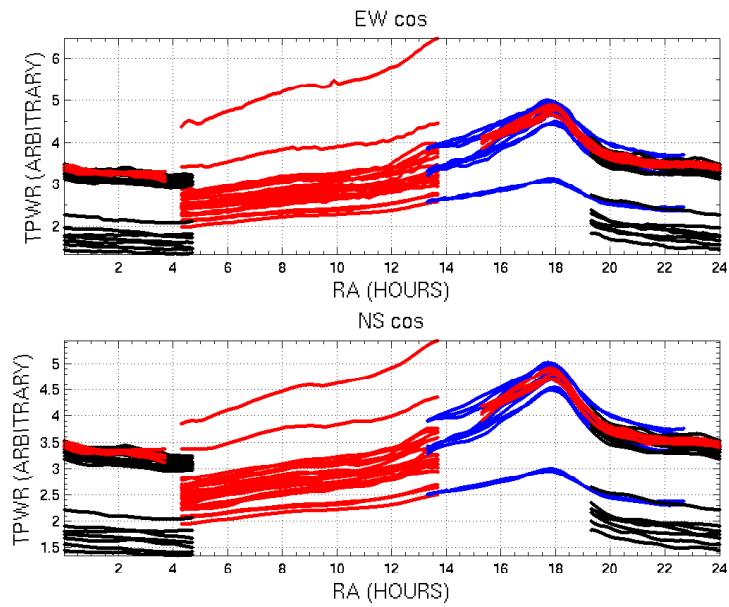
(a)
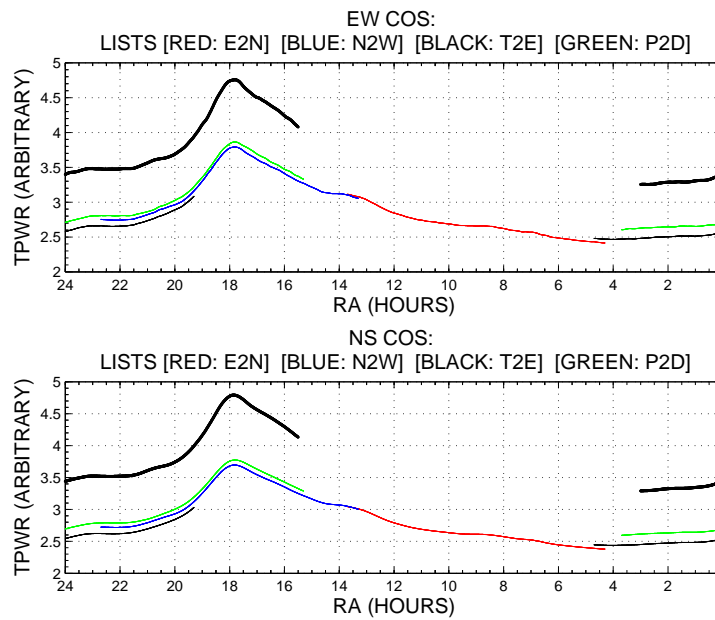
(b)

Figure 4.5: Scans of self-correlation values for 24 hrs in RA
(a) Starting with good scans of self-correlation values for 24 hrs in RA
(b) Connecting the scans using linear regression
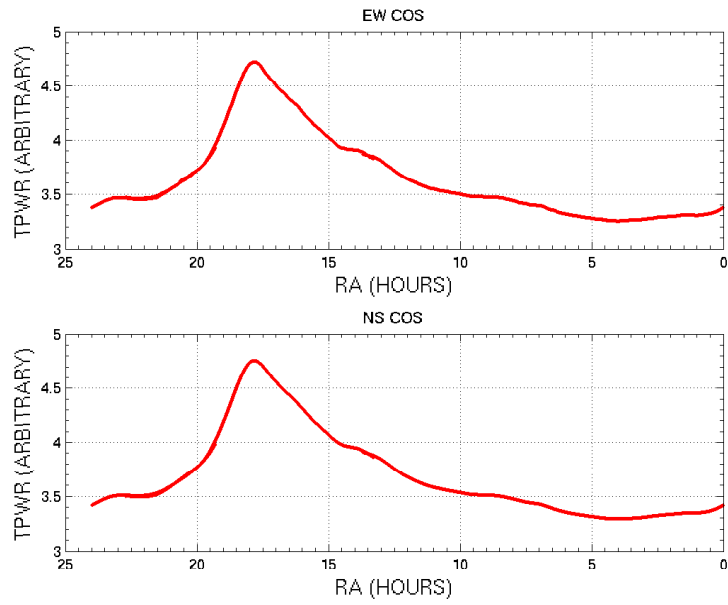
(a)
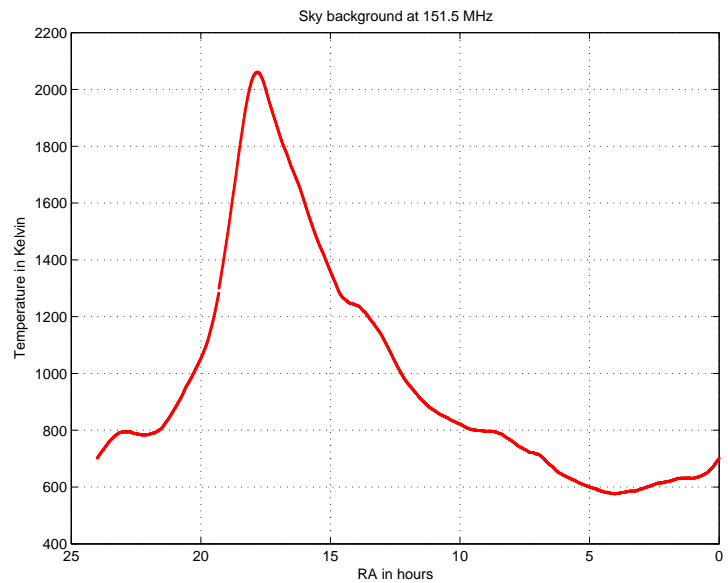
(b)

Figure 4.6:

(a) Continuous total power curve for 24 hrs in RA

(b) Receiver temperature ($sqrt(EW cocx NScos)$), obtained after fitting to the total power curve at 408 MHz convolved to the MRT groups resolution and modified using a spectral index of -2.7. A $T_{receiver} = 400°K$ was added to this.

4.6.2 Flux scale

After using the total power curve to compensate for the loss of amplitude information the images are brought to the Jansky level by scaling the MRT images to the level of a flux calibrator source which is found in the MRT images. The deflection due to the calibrator is measured and the ratio of the flux density in Jansky to the measured deflection calculated. This ratio is used to scale all the images to the Jansky level as referenced by the flux calibrator. The calibrator chosen is MRC2354-350 due to its non-variability at frequency near 150 MHz according to the list of Slee & Siegman (1988) and is unresolved at the resolution of the MRT and SUMSS and can be detected at a level of $\geq$ 50-σ at the MRT (see Section 4.6). This is the same primary flux calibrator used for the earlier work (Pandey, 2006) at MRT.

4.7 Imaging the RA range $0^h < \mathbf{RA} < 6^h$ and the Declination range $-70° \leq DEC \leq -10°$

4.7.1 Description of the sky

The region of the sky imaged in the present work is away from the galactic plane. At the resolution of MRT this region is dominated by point sources. In this RA range MRC lists 1789 sources down to a flux limit of 0.7 Jy.

Jones & McAdam (1992) list 71 sources in this range as extended when imaged with the Molonglo Observatory Synthesis Telescope (MOST) with a resolution of $44''$.

Prominent sources in this region are: Fornax A (NGC1316) which is a powerful radio galaxy at RA: 03:22:41.50, Dec: -37:12:33.00 (J2000) and a flux density of 259 Jy at 408 MHz . Pictor A (MRC0518-458) with a flux density of 45 Jy at 408 MHz is also in the range.

One of the out of field of view strong sources likely to affect our images is the galactic centre appearing in the grating lobe (Sachdev, 1999). Details are discussed in the chapter on "Images and their preliminary analysis".

4.7.2 Description of the database

For the sidereal hour range 0 to 6 hr, the MRT data archive have $\sim$ 5000 hours of observations. Approximately 200 files were selected per sidereal hour imaged per delay zone. The selection is based on data quality assessment. The quality assigned to different data files are stored as a subset of MRT data base. For the 6 hours imaged $\sim$ 20,000 files were selected for imaging the four delay zones.

To image any hour we need a guard band of 30 minutes on either side. Due to the format of database, which stores one hour data files, it is more convinient to analyse 3 hour data files in one stretch.

With this choise of three hours it did upset the earlier methodology of chosing good data from the data quality assignment of each hour. One had to modify the X-Marmosat and choose data for three hours, only if the quality of all these files are of acceptable quality.

At first sight this looks as though for imaging 6 hours, one has to create a data base of 18 hours. This is not so. For example, for imaging the RA range 0 to 1 hrs we image the RA range 23 to 2 hr. For the next RA 1 to 2 hr to be imaged we should have imaged RA 0 to 3 hr. Instead we image RA 1 to 4 hr. The RA 1 to 2 hr is found in the overlap region between these two regions and need not be re-imaged. using this methodology for imaging the 6 hr in RA, we carefully avoided extra processing by $\sim 33\%$

4.8   Making dirty images

As mentioned in the previous section, selection of good data from the data archive was done by selecting data within a given threshold of total quality factor given by the automatic data evaluation algorithm referred to in section 2.6.0.1.

To speed up the selection of good data based on the quality gradings, we developed a program in Perl to read the grading files and produce lists of selected data which could be readily used as an input to the automated software pipelines. This program was fine-tuned to take in all the complexities of reading the grading files. Furhermore the program gave matching calibrator filenames for each good quality data. In case of the new calibration scheme developed (as done in the present work) a different version of the program was developed to output the name of the observation data file which was to be used for generating the calibration table.

To satisfy the constraints of imaging 3 hours in one go, we first select the central sidereal hour we want to image. Next we select the adjacent sidereal hour. In many cases we found that it was not possible to have adjacent hours data to conform to the qualifty factor of the central hour. In these cases we fail to get 3 hours of good data for imaging. This reduces the number of good data file available for imaging.

The quality of data was found to be non-uniform across the sidereal hours. It was generally found that as we moved from 0 hour to 6 hour in sidereal time, the quality of data tended to deteriorate. This meant that there is a decrease in the number of good data files. Further investigation into the data quality showed in many cases the quality of data was poor during specific periods of time during the observation phase of the survey. In many cases one 'block' of observations, which corresponds to 6 allocations observed continuously over a few days were not of good qulaity. This hinted towards particularly

bad external RFI and/or generated within the lab situations during the observation of 'blocks'.

This situation left many gaps in the deisred *uv* coverage of the T-array. As a first remedy to this situation we gradually lowered the quality threshold of the data selection till we could fill these gaps with data of slighly poorer quality. This was possible in the hr 3 to 4, but was not easy for the hr 4 to 6 hr.This effect is seen in the poor quality of images leading to detection of lower number of sources.

Figure 4.7 shows the *uv* coverage achieved for imaging the RA range 0 to 6 hr. The x-axis shows the central RA of a band of 3 hours of images made. The y-axis shows the south antenna positions used. We can see more gaps in the *uv* coverage as we move from RA 0 to 6 hours. Especially short spacings are missing in the RA range 4 to 6 hr.

Figure 4.8 shows a histogram of data having a total quality factor of better than 2 (considered good for imaging). The best data have been found to be in the RA range 18 to 24 hr (imaged by Pandey (2006)). For the RA range 0 to 6 hr corresponding to regions imaged for the present work, the number of available good data files drops steadily till it reaches a minima at RA 8 hr. This decrease of data quality was one of the main stumbling block to complete 24 hr imaging.
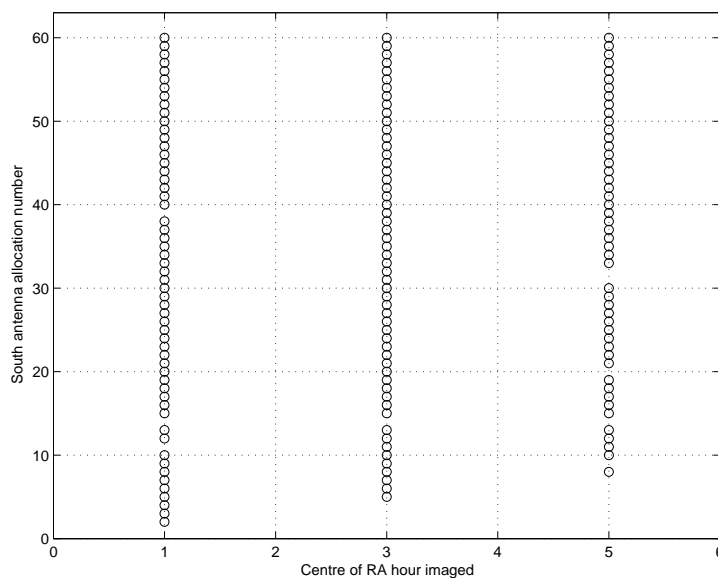
Figure 4.7: *UV* coverage achieved for the RA 0 to 6 hours.

4.8.1 Dirty images

As described in section 2.6 the Fourier inversion for MRT to get the final dirty images is done in several steps. The RFI statistics of the data files were generated en mass by the software pipelines developed. For the 6 sideral hours imaged, this involved generating the intermediate products like filtered self-correlations values and sum of magnitude of the visibilities for approximately 5000 data. For each sidereal hour 800 files are processed.
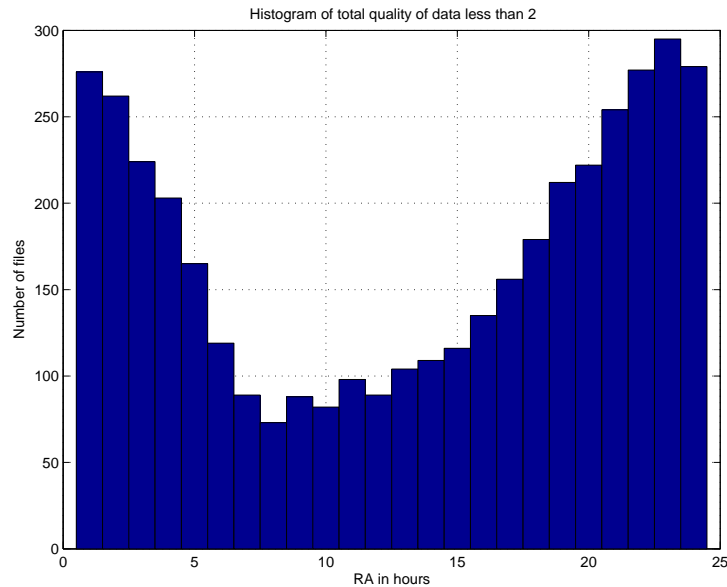
Figure 4.8: histogram of data files having total quality factor less than 2 per hour

Running on 8 computers, it took about 6 hours to generate the RFI statistics for 1 sidereal hour of data. This creates the database of RFI statistics which is used as input to the subsequent programs in the data reduction chain.

We apply all the hardware dependent correction required to the data and write out the data in a uniform format. A header file is also generated. This data is fed to the field of view calibration program written in Matlab.

Using the field of view calibration we generate the calibration tables required for calibrating the data. In the 3 hr we want to image one hr has overlap with the RA range imaged previously. The source list generated from this overlapping hour is used to build up model visibilities and generate the calibration table. The header file has a reference to the files required to carry out the calibration. This file includes the time stamp, antenna position file and decorrelation curves for each data. The calibration program is embedded within the software pipelines developed and the calibration table is generated en mass on 8 computers. The software pipelines incorporate an interprocess communication via lock files which regulates which processes work on a specific data file at a given time. This avoids duplication of processing among the processes running on several computers simultaneously. It takes approxmately 12 hours to generate calibration tables required to image 1 sidereal hour (on all sixty allocations).

4.8.1.1 Calibration tables

The calibration tables are converted from baselines based calibration (16 x 32 baseline) (48 antennas) to antenna based calibration. This is also carried out in a single batch. It takes approximately 1 hour to generate the antenna based calibration. This creates the database of calibration tables.

4.8.2   Fourier inversion of the visibilities

Each day's data is Fourier inverted to give one day dirty images. The new software pipeline developed carries out this step automatically. The databases of RFI and calibration tables together with database of files containing the antenna position files are used. The RFI is mitigated during the step of post integrating one second data to 4 seconds of integration by setting to zero in the dirty map those sidereal times affected by RFI. It takes approximately 36 hours on 8 computers to carry out the Fourier inversion. of three hours of visibility data on all allocations This creates the database of one day dirty images.

In the next step 3 dirty images representing the 3 hours being imaged are concatenated and regridded to the common epoch J2000. A hampel filter is used to detect and mitigate RFI points in the image. From the database of dirty images, the software pipeline automatically selects the appropriate 3 image files and runs regridding and hampel filtering on the images. This forms the database of regridded images stored on disk.

4.8.2.1   Assessing the quality of images for co-addition

The quality of the one-day images are assessed before they are co-added to give the final images. This is done in 2 steps.

In the first step the images are displayed in pseudo colors based on intensity range of the pixels in the image. This allows fast display of the images and gives a global picture of the image.

RFI not detected in the first round appears as strips along the declination at constant RA. This is due to the meridian transit mode of imaging where the image is made as a stack of meridian strips at constant RA. Data points which are affected by RFI show a strip along DEC which is different from the other areas of the map. If there are large gaps in the RA range of the images caused by long duration RFI mitigatation such images are flagged. However the rate of occurence of such gaps are rare.

Isolated interference which are very strong sources which appear in only a few maps and can be identified against the background of normal strong radio sources. An example of a source is the Sun appearing in the grating lobe of the array. Our data assessment program takes this scenario into account and assigns a low data quality tag to such files. But in the present scenario of imaging 3 continuous data files, occassionly such data files had sneaked in the data reduction process and they were flagged in the one day image. Gross calibration errors can also be identified by the absence of strong sources expected in the map.

In the second round of image quality assessment the deflections due to known strong point sources were estimated by fitting the expected beam to the positions of strong point sources. The noise and ripples in the images are estimated. One dimensional profiles of the image along the RA and DEC are also computed. All these measurements give a

quantitative estimate of the quality of the images. Images with signal to noise which are approximately 2 times lower than the signal to noise of images of nearby allocations are rejected. Images showing uneven noise background are also rejected.

The one-day images are affected by ripples which are ridge like structures along the RA. These may be due to DC terms in the correlation values resulting due to constant offsets in the MRT correlators. Though these ripples do not affect the estimation of the signal to noise of well known bright sources which are used to gauge the quality of the images, these ripples hamper visual inspection of the images and also the quality of final images.

DC removal is carried out in the one-day images for the purpose of visual inspection of the map. The DC removal helped visual inspection. This resulted in identification of a few cases of interference which would have otherwise be missed.

Figure 4.9 shows the quality checks performed on the one-day images before they are used for co-addition into the final dirty images.

Figure 4.10 shows the fitting of the expected beam to determine the the peak of a strong point source in the dirty map. The upper plot is a one-dimensional representation of the two-dimensional fit, while the lower plot shows the fit of the expected beam along RA.

On an average we start with sets of around 200 data files for imaging. Around 40 files get flagged in this phase of imaging. We found that the quality of the final image was crucially dependent on this step. In cases where we found the final images to be of poor quality or showing any of the problems listed above, we repeated the visual inspection step to identify problems in the one day images and reject them.

4.8.3   Co-addition of 1 day images

The amplitude of the one day images are recalibrated to ensure that the PSF in the final image is nearly a sinc function.

to a strong MRC point source used as calibrators.

Even the true PSF deviates from a sinc function due to the non-coplanarity of the array and also the effects of the bandwidth decorrelation. The weightage used for co-addition is the inverse of the gain measured in the image. This ensures that the contribution of each observed allocation in the final image is same.

The gains are derived by fitting the expected beam to a strong point source found in the images. The sensitivity of MRT one day's images is 1.25 Jy. Taking this into account, sources were selected from the MRC catalog by selecting those which are within the RA and DEC range of the MRT, and would show a flux density at MRT which can be detected with a minimum signal to noise ratio of 10 in each day's images. The morphology flags in the MRC catalog were used to filter out those sources which are extended. A further filtering criteria is that the sources should be non-variable at frequencies close to 150 MHz according to the list by Slee & Siegman (1988).

Approximately 8 such sources were found per hour RA range. Only one source is used per hour of RA range, usually the one showing the highest signal to noise ratio in the images from the list of sources selected, to calculate the weights. This is preferred to taking the average deflection for several sources, since it is easier to estimate the PSF affected by bandwidth decorrelation. The gains from several sources will have their gains affected by bandwidth decorrelation in a more complicated way.

Table 4.2 shows the list of MRC sources used to estimate the relative gains in each day's image for images co-addition. These sources can be detected at more than 10-σ detection level in the one day's images.

Table 4.2: MRC sources used to estimate the relative gains in each day's image for images co-addition

	SOURCE NAME	RA (J2000)	DEC (J2000)	FLUX (408 MHz)	FLUX (150 MHz)
1	MRC0023-263	00 25 49.3	-26 02 14	17	22.57
2	MRC0237-197	02 37 43.8	-19 32 34	13.27	24.79
3	MRC0453-206	04 55 23.7	-20 34 15	11.25	15.82

A software pipeline was written to provide the interface between the images co-addition program, database of regridded images and the database of decorrelation files. The decorrelation files Pandey (2006) are pre-generated and stored on disk.

The images co-addition program was run in several cycles. In the first cycle the fit of the strong point souce to the expected beam was visualised to acertain the range of SNR of good fits. In the second cycle the co-additon program was re-run and maps showing poor SNR and higher than expected sidelobes were flagged.The flagged files were removed from the list of good regridded files and the software pipeline was run to carry out the image addition. Approximately 5 to 10 files were rejected at this stage of the processing. Higher rejection rates than this generally meant the images were of poor quality and the calibration of the data was poor.

4.8.4   Ripple removal in the co-added images

The co-added images are affected by ripples which are ridge like structures along the RA. The dirty image is first convolved along the RA with the beam expected at $DEC = 0$ to increase the signal to noise ratio of the dirty image. To estimate and remove the DC, regions devoid of emission are identified and the DC estimated in those regions. The mean of the points along RA below twice the noise level is calculated. When no DC is present along the RA , this mean should be zero. A value above the mean is treated as the DC term as no astronomical signal is assumed to be present in that region. The mean is subtracted from the image along the RA. this operation is repeated for each RA strip. In case an RA strip does not have enough points devoid of emission, the DC estimated from the neighbouring RA strip is used for the DC removal. Figure 4.11 shows the contour plots of part of dirty co-added images (a) with ripples (b) ripples removed.

4.8.5   Generation of the PSF of MRT array

The Point Spread Function (PSF) of the MRT array for imaging is declination dependent due to the non-coplanarity of the array. To deconvolve the images by the conventional Clean algorithm, PSFs have to be generated for sources at different zenith angles. For

a given dynamic range, the size of the PSF is dependent on the strength of the source. Strong sources need larger PSFs for cleaning than weaker sources (Pandey, 2006).

Also instead of generating PSFs for each and every source in the sky, PSFs are generated for a short range in zenith angles within which the PSF is assumed to be constant without affecting the dynamic range.

Since we had re-estimated the array geometry of the array as decribed in section 3.4 we regenerated the PSFs required for cleaning the whole declination range of MRT and stored them on computer hard disks. This constitutes our database of PSFs. During deconvolution the PSFs are retrieved as and when needed. This procedure avoids the computationally expensive operations of PSFs generation and interpolation during the deconvolution. This significantly speeds up the deconvolution. The PSFs are generated taking into account the uv coverage of the different images co-added to get the final image as well as the decorrelation in the images across the allocations (Pandey, 2006).

The default size of the pre-generated PSF is $\approx 9° \times 15°$ at zenith. In case there are sources in the dirty image which are bright enough for their sidelobes in the default PSF to be above the expected rms noise, PSFs having a larger extent of $\approx 18° \times 15°$ are generated and stored. 400 PSF's for a dynamic range of 500 are required for one sidereal hr and the declination range of MRT.

A software pipeline was written to interface between the database of PSFs, the decorrelation files and the uv coverage file.

4.8.6   Deconvolution

The dirty images for the range covered were deconvolved using the PSFs generated. Spurious sources were identified by visual inspection of the images and flagged so that these features do not get deconvolved and generate noise in the image and cause the deconvolution algorithm to diverge. Regions devoid of emissions were identified for estimation of the DC and the noise in the image so that these estimates are not biased by astronomical sources.

For the purpose of deconvolution guard zones of 00 : 54 hours on both sides of the hour in RA under consideration has been used. Along declination guard zones $\approx 5°$ wide have been used on both sides of the image.

Deconvolution was carried out down to the level of 5-σ to check if the deconvolution algorithm converges. Failure to deconvolve down to this level is indicative of spurious sources in the image causing the deconvolution algorithm to diverge. In this case the images are checked again to identify spurious sources and flag them. A loop gain of 0.05 was used for the deconvolution.

The CLEAN components were convolved with the expected two-dimensional elliptical gaussians. Bandwidth decorrelation causes the dirty beam to broaden the declination

axis. This reduces the amplitude of the dirty beam. To ensure that the flux is appropriately restored, the area of the normalised dirty beam and the normalised restoring beam at each declination is estimated and the convolving gaussian is appropriately scaled while convolving the CLEAN component. The residues were added to the map resulting from the convolution of the CLEAN components with the restoring beam to obtain the deconvolved map.

4.8.7 Quality check on the deconvolution

at of

The deconvolution of a few strong sources were checked to gauge how well the deconvolution has been performed. It is found that some strong sources still have residual sidelobes. As an example, in Figure 4.12 the strong source MRC0235-19 , whose flux density is 13.27 Jy at 408 MHz and 24.79 Jy at 151.5 MHz, is shown. Some residual sidelobes can be seen both above and below the source in the image. (The dynamic range is ~ 65).

figure=figures$_c hap4/source_l ist_p gwinw6_{cnt_s rc_1 0.cps, height=angle=270} MHz$

Sources which are approximately below 30-σ, where σ is the rms noise measured in the images have been Cleaned properly. Figure 4.13 shows the source MRC0305-226 which has a flux of 4.95 Jy at 408 MHz. The measured flux density in our map is 9.77 Jy/beam . The residual sidelobes are buried in the noise.
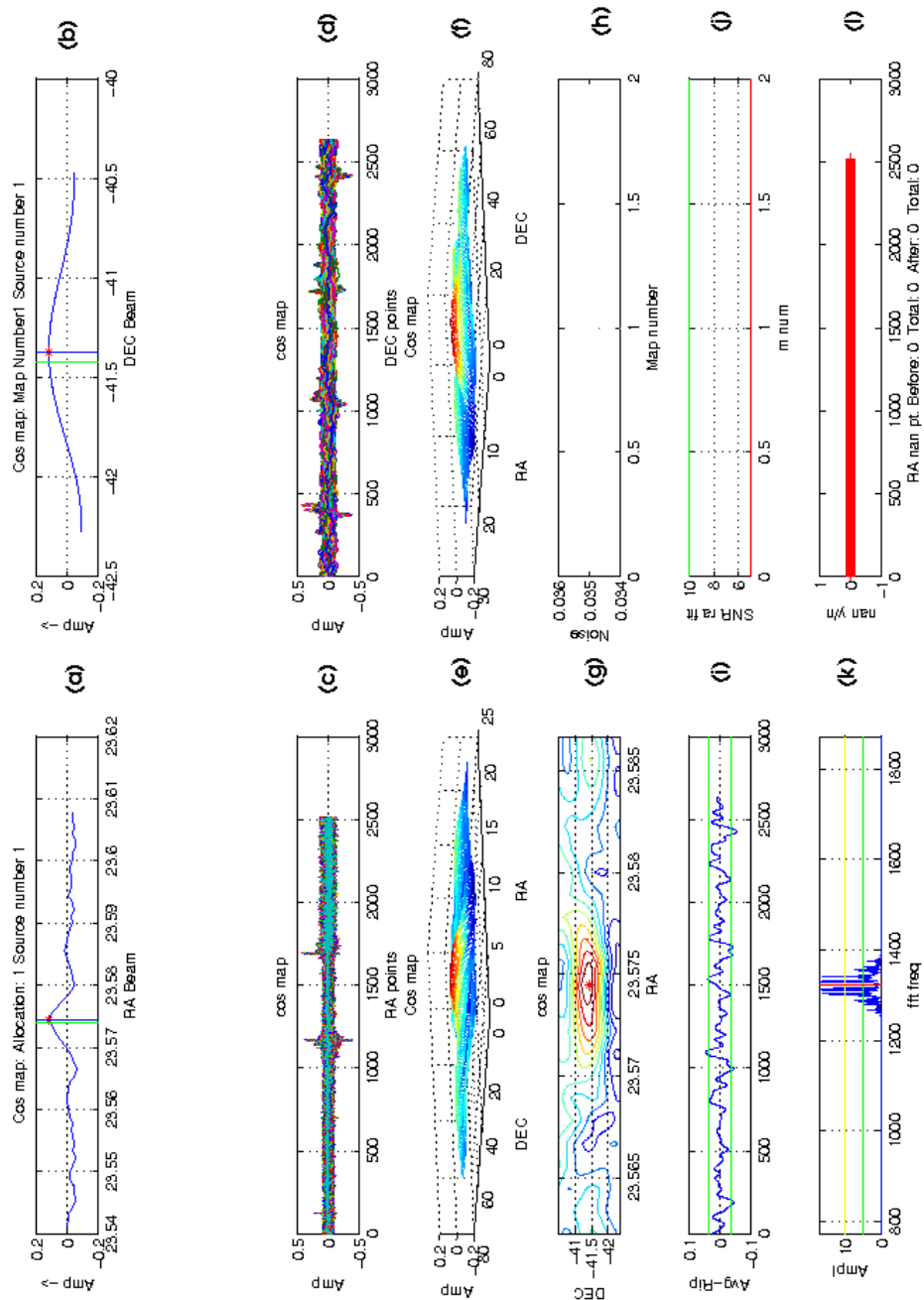
Figure 4.9: Quality check on the one-day regridded images. (a) The fitted RA beam (b) the fitted DEC beam (c) 1-dimensional plot along RA (d) 1-dimensional plot along DEC (e) 3-dimesional mesh plot (g) Contour plot (i) estimate of the DC (j) plot of signal to noise of the maps (k) FFT plot (l) number of bad pixels in the map.
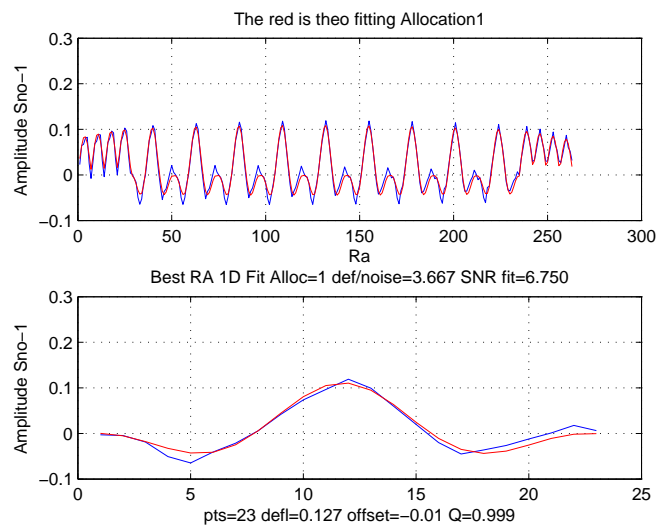
Figure 4.10: Fit of the expected beam to determine the the peak of a strong point source in the dirty map. The upper plot is a one-dimensional representation of the two-dimensional fit, while the lower plot shows the fit of the expected beam along RA.
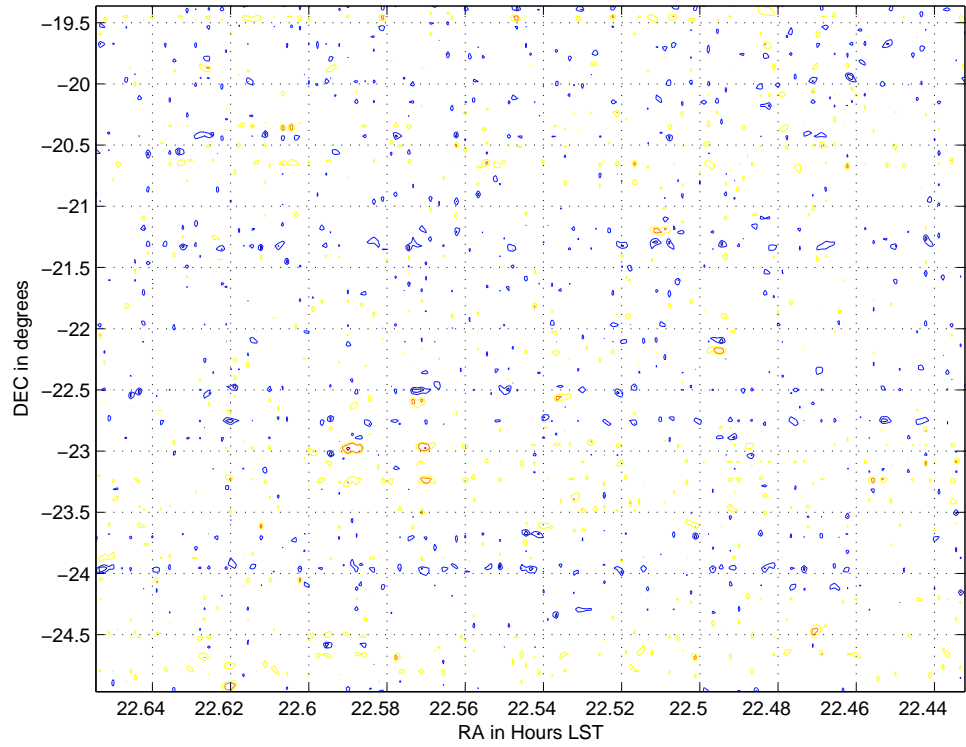
(a)
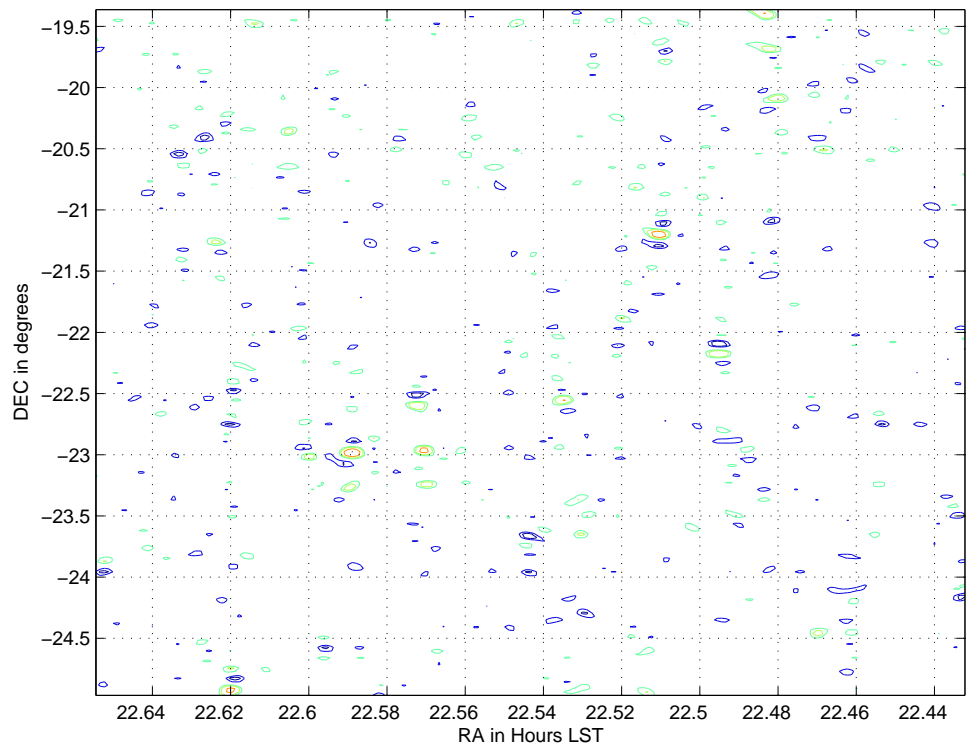
(b)

Figure 4.11: Contour plots of dirty co-added images (a) with ripples (b) ripples removed. The contour levels are (-5, -3, -2, 2, 3, 5, 8, 12, 17, 25, 35, 50, 70, 100, 200)$\times \sigma$, where σ is the rms noise measure in the dirty image in arbitrary units.
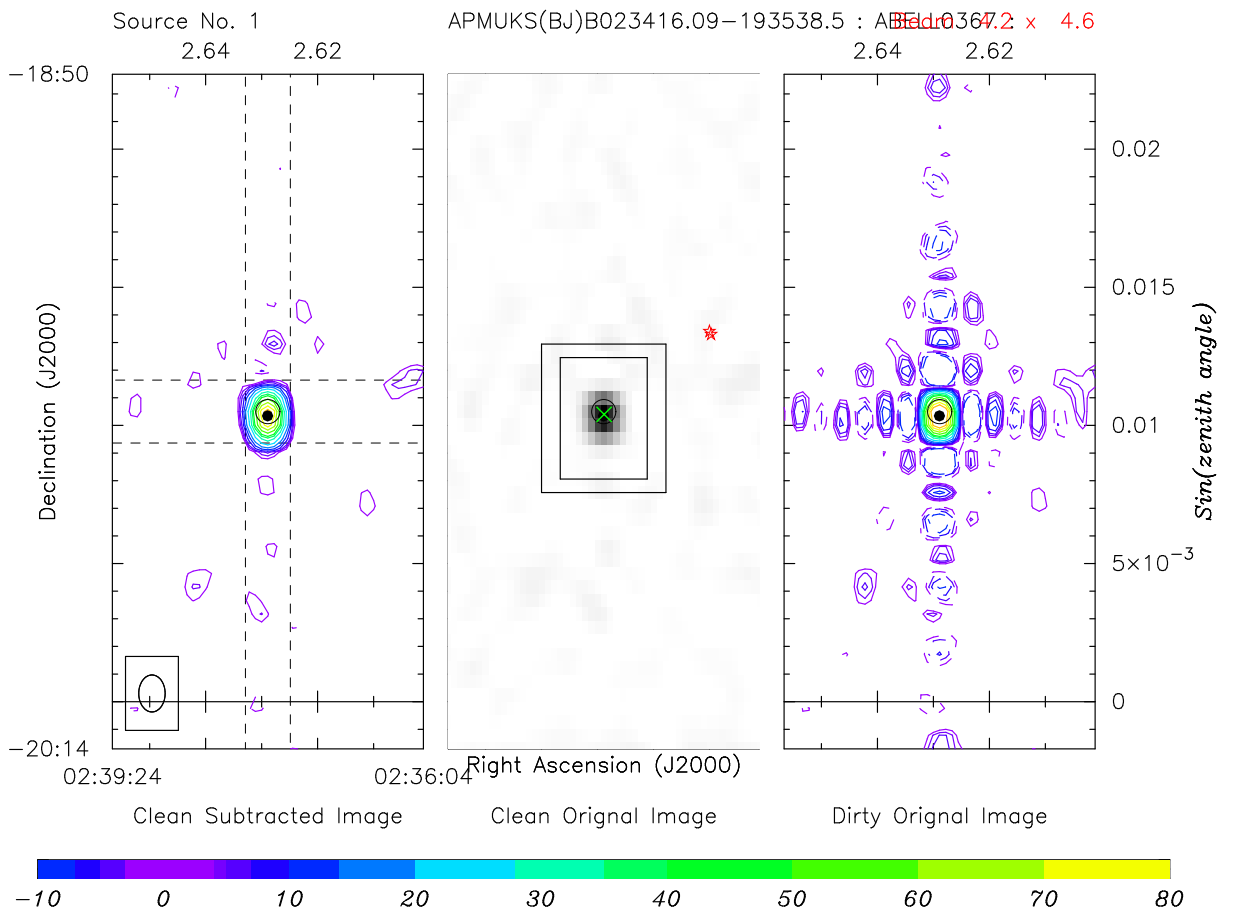
Figure 4.12: Deconvolution of the strong source MRC0235-197. Flux density at 408 MHz is 13.27 Jy. In this image the flux is 24.79 Jy at 151.5 MHz after the primary beam correction. Residual sidelobes are visible to the top and bottom of the image on the left.

Figure 4.13: Deconvolution of the source MRC0305-226. Flux density at 408 MHz is 4.95 Jy. In this image the flux density is 9.77 Jy/beam at 151.5 MHz. The sidelobes do not show up in the deconvolved image.

Chapter 5

Images and their preliminary analysis

5.1 Introduction

In this chapter we describe the principal products of the present work: Images at 151.5 MHz covering the range $00^h \leq RA \leq 06^h$, and the DEC range $-75° \leq DEC \leq -10°$ with a resolution of $4' \times 4'.6 \sec(\delta + 20°.14)$. The rms noise in the images vary from 200 to 600 mJy depending on RA and DEC. We describe our source extraction program briefly and the outcome of comparing ~ 3000 sources extracted with sources in MRC. We focus on positional errors, flux densities of sources detected and their statistical analysis. We describe how our analysis lead us to a better flux calibration of our images. We also discuss the noise in the images, give a source catalog, list out flux densities of ~ 100 MS4 sources and display some extended sources in this region.

5.2 Set II Images

We present deconvolved images covering $\sim$ a steradian of the sky in the range $00^h \leq RA \leq 06^h$ [1], and the declination range $-75° \leq DEC \leq -10°$ with a resolution of $4' \times 4'.6$ $\sec(DEC + 20°.14)$ in J2000 equatorial coordinates. The contour plots are given at the end of this chapter. These form a part of the southern sky survey using MRT at 151.5 MHz and will be referred to as Set II images.

Set I images are those made by Pandey & Udaya Shankar (2006) in the range $18^h \leq RA \leq 00^h$, $-75° \leq DEC \leq -10°$.

The Set I images have the same format as Set II . The Set I images are available on the web at **http://www.rri.res.in/surveys/MRT/**. Shortly Set II images will also be

---

[1] due to the problems associated with regridding, the RA range stops at 5:54 hrs. However, we have chosen the option of saying that the Set II images cover the RA range 00:00 to 06:00 hr for ease of communication

made available at the same location.

All these images have been corrected for the primary beam of the helix. The Half Power Beamwidth (HPBW) of the helix permits us to image the declination range $-75° \leq DEC \leq -10°$. More details are in section 5.4. At lower declinations a source spends much larger time in the RA beam, one can indeed gain some signal to noise lost due to the primary beam attenuation by increasing the integration time at lower declinations.

The deconvolved images presented are split into 156 sub-images for display. Each sub-image spans 00:30 hours in RA and 5° in DEC. Along the RA, the images are split in 12 bands and along DEC in 13 bands. This gives a total of 156 images. The RA and DEC coverage of each sub-image are summarised and a reference to the figure numbers are given in tables 5.1 and 5.2

The contour images were drawn using the contour routine **contour-region-map** in the X-Marmosat suite of programs. The same program was used by Pandey & Udaya Shankar (2006) in their earlier work. Negative contours are represented in gray while positive contours are black in colour.

The RA range 23 to 24 hr and 00 to 02 hr were imaged in the same batch. Due to a bug in the X-marmosat, the RA ranges are marked 23 to 26 hr.

Table 5.1 and 5.2 are keys to the set-II. There are 156 images in all. The images are displayed in the order of increasing declination for the range $-75° \leq DEC \leq -5°$. Each image shows a region of the sky having a span of 5° in DEC and a span of 30 minutes in RA.

Table 5.1: Key to MRT images. The RA ranges are a=$[24^h00^m \le RA \le 24^h30^m]$, b=$[24^h30^m \le RA \le 25^h00^m]$, c=$[25^h00^m \le RA \le 25^h30^m]$, d=$[01^h30^m \le RA \le 02^h00^m]$, e=$[02^h00^m \le RA \le 02^h30^m]$, f=$[02^h30^m \le RA \le 03^h00^m]$, g=$[03^h00^m \le RA \le 03^h30^m]$

	a	b	c	d	e	f	g
$-75° \le DEC \le -70°$	Fig.5.48	Fig.5.61	Fig.5.74	Fig.5.87	Fig.5.100	Fig.5.113	Fig.5.126
$-70° \le DEC \le -65°$	Fig.5.49	Fig.5.62	Fig.5.75	Fig.5.88	Fig.5.101	Fig.5.114	Fig.5.127
$-65° \le DEC \le -60°$	Fig.5.50	Fig.5.63	Fig.5.76	Fig.5.89	Fig.5.102	Fig.5.115	Fig.5.128
$-60° \le DEC \le -55°$	Fig.5.51	Fig.5.64	Fig.5.77	Fig.5.90	Fig.5.103	Fig.5.116	Fig.5.129
$-55° \le DEC \le -50°$	Fig.5.52	Fig.5.65	Fig.5.78	Fig.5.91	Fig.5.104	Fig.5.117	Fig.5.130
$-50° \le DEC \le -45°$	Fig.5.53	Fig.5.66	Fig.5.79	Fig.5.92	Fig.5.105	Fig.5.118	Fig.5.131
$-45° \le DEC \le -40°$	Fig.5.54	Fig.5.67	Fig.5.80	Fig.5.93	Fig.5.106	Fig.5.119	Fig.5.132
$-40° \le DEC \le -35°$	Fig.5.55	Fig.5.68	Fig.5.81	Fig.5.94	Fig.5.107	Fig.5.120	Fig.5.133
$-35° \le DEC \le -30°$	Fig.5.56	Fig.5.69	Fig.5.82	Fig.5.95	Fig.5.108	Fig.5.121	Fig.5.134
$-30° \le DEC \le -25°$	Fig.5.57	Fig.5.70	Fig.5.83	Fig.5.96	Fig.5.109	Fig.5.122	Fig.5.135
$-25° \le DEC \le -20°$	Fig.5.58	Fig.5.71	Fig.5.84	Fig.5.97	Fig.5.110	Fig.5.123	Fig.5.136
$-20° \le DEC \le -15°$	Fig.5.59	Fig.5.72	Fig.5.85	Fig.5.98	Fig.5.111	Fig.5.124	Fig.5.137
$-15° \le DEC \le -10°$	Fig.5.60	Fig.5.73	Fig.5.86	Fig.5.99	Fig.5.112	Fig.5.125	Fig.5.138

Table 5.2: Key to MRT images. The RA ranges are i=$[03^h30^m \le RA \le 04^h00^m]$, j=$[04^h00^m \le RA \le 04^h30^m]$, k=$[04^h30^m \le RA \le 05^h00^m]$, l=$[05^h00^m \le RA \le 05^h30^m]$, m=$[05^h30^m \le RA \le 05^h54^m]$

	i	j	k	l	m
$-75° \le DEC \le -70°$	Fig.5.139	Fig.5.152	Fig.5.165	Fig.5.178	Fig.5.191
$-70° \le DEC \le -65°$	Fig.5.140	Fig.5.153	Fig.5.166	Fig.5.179	Fig.5.192
$-65° \le DEC \le -60°$	Fig.5.141	Fig.5.154	Fig.5.167	Fig.5.180	Fig.5.193
$-60° \le DEC \le -55°$	Fig.5.142	Fig.5.155	Fig.5.168	Fig.5.181	Fig.5.194
$-55° \le DEC \le -50°$	Fig.5.143	Fig.5.156	Fig.5.169	Fig.5.182	Fig.5.195
$-50° \le DEC \le -45°$	Fig.5.144	Fig.5.157	Fig.5.170	Fig.5.183	Fig.5.196
$-45° \le DEC \le -40°$	Fig.5.145	Fig.5.158	Fig.5.171	Fig.5.184	Fig.5.197
$-40° \le DEC \le -35°$	Fig.5.146	Fig.5.159	Fig.5.172	Fig.5.185	Fig.5.198
$-35° \le DEC \le -30°$	Fig.5.147	Fig.5.160	Fig.5.173	Fig.5.186	Fig.5.199
$-30° \le DEC \le -25°$	Fig.5.148	Fig.5.161	Fig.5.174	Fig.5.187	Fig.5.200
$-25° \le DEC \le -20°$	Fig.5.149	Fig.5.162	Fig.5.175	Fig.5.188	Fig.5.201
$-20° \le DEC \le -15°$	Fig.5.150	Fig.5.163	Fig.5.176	Fig.5.189	Fig.5.202
$-15° \le DEC \le -10°$	Fig.5.151	Fig.5.164	Fig.5.177	Fig.5.190	Fig.5.203

5.3 Noise in the images

The expected minimum rms noise in the images is given by

$$\Delta S'_{min} = \sqrt{\left(S^2_{thermal} + S^2_{conf}\right)}. \tag{5.1}$$

Where $S_{thermal}$ is the thermal noise and S_{conf} is the confusion noise. S_{conf} is ≈ 18 mJy beam^{-1} for MRT survey (Pandey, 2006). This is a low value compared to the expected thermal noise and so, the noise in MRT images is predominately thermal.

The expected thermal noise in the images when using a correlation receiver, without taking bandwidth decorrelation into account (Thompson $et\ al.$, 2001) is given by

$$\Delta S'_{min} = \sqrt{\left(\frac{\sqrt{2}\, 2K_B(\sqrt{T_{sys_{ew}} T_{sys_{ns}}})}{\eta_{eff}\sqrt{N_b} A_e \sqrt{\Delta vt}} \right)^2}, \tag{5.2}$$

so the expected minimum rms noise can be written as

$$\Delta S'_{min} = \sqrt{\left(\frac{\sqrt{2}\, 2K_B(\sqrt{T_{sys_{ew}} T_{sys_{ns}}})}{\eta_{eff}\sqrt{N_b} A_e \sqrt{\Delta vt}} \right)^2 + S^2_{conf}}. \tag{5.3}$$

Where,

$\mathbf{\Delta} S'_{min}$ is the rms noise in Watts Hz^{-1} m^{-2},

$\mathbf{K}_B$ is the Boltzmann constant,

$\mathbf{T}_{sys_{ew}}$ is the system temperature of an EW group in K

$\mathbf{T}_{sys_{ns}}$ is the system temperature of a NS group in K

η_{eff} is the efficiency of a digital correlator (0.81 for a 2-bit 3-level correlator operating at Nyquist rate (Bowers & Klingler, 1974)),

$\mathbf{N_b}$ is the number of baselines used in the images (number of groups in the EW times the number of antenna positions used in the NS arm),

$\mathbf{A}_e$ is the effective area of an interferometer pair in m^2.

For MRT

$$A_e = 2\sqrt{A_{ew} A_{ns}}, \text{ where } A_{ew} = 128 \text{ m}^2 \text{ and } A_{ns} = 16 \text{ m}^2 \tag{5.4}$$

for MRT, 4 m^2 is the effective collecting area of each helix,

$\mathbf{\Delta} v$ is the bandwidth in Hz ($\approx 1 \times 10^6$ Hz for MRT)

$\mathbf{t}$ is the integration time in seconds. (4 s for both set-I and set-II images).

Figure 5.1 shows the variation of the system temperature over the RA range 0 to 6 hrs. It has a value of $\sim$ 700 K at 0 hours and reaches a minimum value of $\sim$ 600 K at RA 4 hrs. It raises to about 650 K at an RA of 6 hrs. For a 600 K system temperature the expected system noise is $\sim$ 110 mJy.

The estimated beam for the helix used as the primary element of MRT array is wider than the expected beam (see section 5.7). This effectively brings down the effective collecting area. The MRT primary beam along declination was found to be $\approx 8°$ wider than the theoretical MRT helix beam of $\approx 60°$ (Half Power Beam Width). This would translate to an actual effective collecting area for the helix to be $60^2/68^2$ which is ≈ 0.7785 times the collecting area assumed of the helix. This results in an increase of $\approx 28\%$ in the expected noise. With these arguments the expected rms noise is ≈ 140 mJy beam^{-1} for a system temperature of 600 K.

The noise in the images was estimated by considering regions devoid of strong emissions. The regions in the guard zones were not considered for the estimation. The rms
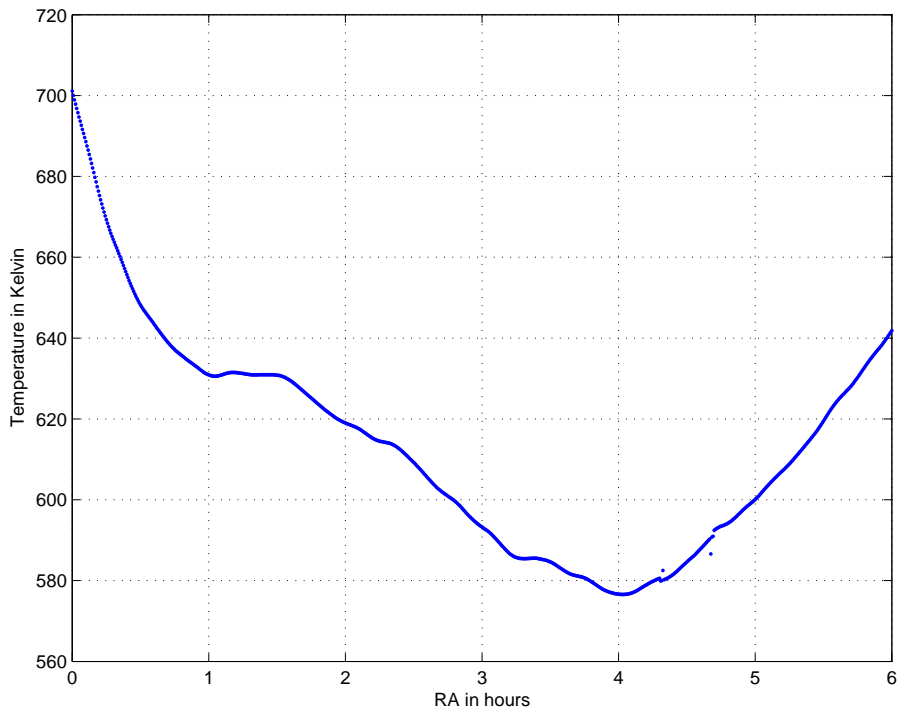
Figure 5.1: System temperature variation in the RA range 0 to 6 hr. This is a section of the curve shown in figure 4.6(b). The receiver temperature is taken to be 400 K.

noise was measured in each selected region and then averaged in quadrature to get the overall noise in the image. Each region was weighted by the number of pixels in each region.

To calculate the expected noise, ideally the number of days of observations actually used for making should be employed rather than using the total number of allocations (60). One should also use the information about how much of data is used for each allocation. The number of days of observations used for each allocation is highly uneven and observations at any given allocations are averaged before co-adding images at different allocations and uniformly weighted. In view of this the number of allocations used for imaging was used to give an estimate of the noise. Figure 4.7 showing the UV coverage for different RA ranges indicate that the number of allocations used for making different images shown in this thesis is $\sim$ 60.

Figure 5.2 shows the measured and expected noise in the images for the range $00^h \leq RA \leq 06^h00^m$, It is found that the measured noise is consistently twice the expected noise in the set-II images. The four different curves are for four different zones imaged using visibilities measured with different delay settings.

Between RA 0 to 4 hrs the worst case scenario is one in which the noise in the image is twice the noise expected. The plot also shows a consistently higher noise in the RA range 4 to 6 hours. This is due to the poor quality of data for this RA range and also due to the presence of strong extended sources like Pictor A, leaving behind high levels of

residual sidelobes after deconvolution. It is also possible that the system noise is higher than expected due to the loss in the cables and beamformers used for combining the primary elements. This behaviour of the measured noise in relation to the expected noise is similar in the Set I images covering the RA range 18 to 24 hours (Pandey, 2006).

5.4 Description of spurious features in the images

Before getting into the details of noise analysis, sources extracted from images and their statistics, it is useful to understand the non-astronomical (spurious) features in the images. Most of large-scale surveys do end up with some spurious sources in the images due to a variety of reasons. MRT survey is not an exception.

Sidelobes of strong sources are the main cause of spurious features seen in the six-hour images. In the EW array of MRT the helices are spaced 2m apart ($\sim$ one wavelength) and this causes grating responses close to the horizon when imaging on the meridian (Described in more detail below). Sources in grating lobes cause undesirable responses in images. Images corrected for primary beam responses show increased noise at the beam edges and the source picks up spurious sources.

In this section dividing the survey into three parts (RA ranges 0-2, 2-4 and 4-6 hr) we have summarised the spurious sources seen in the SET II images.
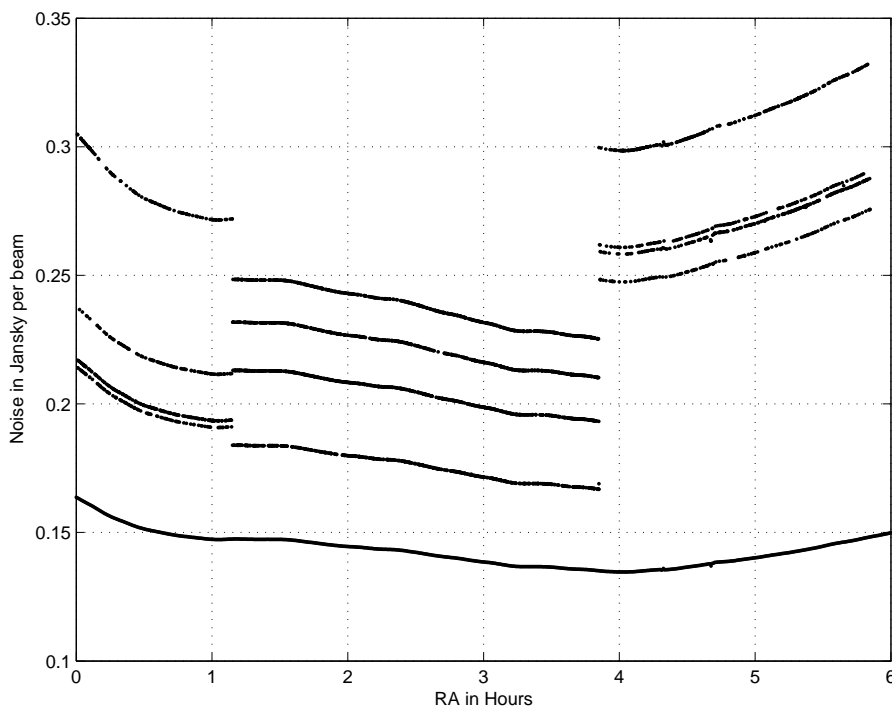
Figure 5.2: Noise in the images in the RA range $00^h \leq RA \leq 06^h$. Four lines in each RA range represents four different zones imaged using visibilities measured with different delay settings. The unbroken lower line is the expected noise in the images

The correlation beam of a T array is a product of the resultant beams of the EW and NS arrays. This results in a beam looking like a cross with point source response decreasing faster along the diagonals. So the residual sidelobes of a strong source after deconvolution contaminate the images along strips in RA and DEC centered around the source itself.

It is worth noting an interesting aspect of these sidelobes. The sidelobe at a DEC δ_2 due to a source at a declination δ_1 has a width proportional to $sec\ \delta_1$ along RA. In other words while the HPBW of the array along RA changes from 16 s to 61.85 s, the sidelobe of a source at DEC=0° seen at DEC =−75° remains 16 s wide in RA.

These effects are seen in the residual sidelobes of MRC2356-612 in the images (images A3, B3). This a strong source sitting very close to one edge of the field imaged in the present survey. It has a flux density of 60 Jy at 408 MHz and about 108 Jy (not well determined due to the crowding of the field) at 151.5 MHz.

A very interesting spurious feature is seen in the image (images A11 and A12)) covering the RA range 24:00 to 24:30 and the DEC range −27.5° to −22.5°.

As mentioned earlier there are grating responses along the east-west direction due to the helices being spaced 2 m apart in the east-west and in north-south trolleys. These grating responses are at intervals of

$$\delta_{psi} = \lambda \div d_{ew} \tag{5.5}$$

At 151.5 MHz, 2m is 1.01λ. This results in grating responses at hour angles ±82°.

Although the grating responses are in the direction where a theoretical beam response of the helix is expected to have an attenuation of about 30 dB, we still see the Sun coming through these grating beams when it is in the declination range $-10° \leq \delta_{sun} \leq 10°$ (Sachdev, 1999). These declinations represents the region in which a two dimensional grating response peaks of the EW array at 151.5 MHz..

It is well known that helices have a response along the horizon. Many high frequency helices are built with a ground plane folded upwards at the edges to suppress this response. One simple way to understand this response is to consider it as an end-fire on response of an array constituted by different turns of helices.

On longer baselines, the signal from a source present in the grating lobe directions gets bandwidth decorrelated and does not pose a serious problem. Strong sources in this declination range will contribute to the visibility measurements on short baselines. Since we do not have many strong sources in this declination range, this may not be a serious problem. However, sources like the Sun and the Galatic plane in this declination range will pose a problem and must be accounted for. In the RA range (1950 coordinates) from 6^h28^m to 7^h10^m and from 18^h28^m to 19^h10^m, the galactic plane ($b = 0$) is in this declination range. This would therefore cause the images to be corrupted at RAs which are about ±5.47 hours ($HA_{grating} \pm 82°$) away.

It is interesting to note that a source in the grating response does not appear at its true declination when imaging on the meridian (Golap, 1998). There was indeed a large structure seen in the low resolution images made with visibility measurements of the first two blocks (first 12 allocation, baselines 2m to 178m along NS) and the central eight groups in the east-west arm. This structure spanned RA from 23h55m to 00h30m and the declination range $-32°$ to $-23°$ (images A10, A11, A12). Presently our understanding is that this structure is due to the galactic plane in the grating response. Simulations by Sachdev (1999) of the effect of the grating response using the 408 MHz all sky image confirms our understanding. The structure in the low resolution image appears displaced in declination from the position seen in the simulation. This can arise because of wrong phasing of the short baselines.

With this we conclude that the spurious features seen (images A10, A11, A12) covering the RA range 00:00 to 00:30 and the DEC range $-27.5°$ to $-22.5°$ is due to the Galactic plane in the grating lobe. The image displayed here has very low spatial frequencies filtered and hence the extended nature is not seen in the deconvolved images.

An effect seen at all RA ranges is the increased noise along the edges of the primary beam. A sky noise dominated signal to the input of the correlators results in a signal to noise which is similar at all declinations in the field of view after applying the primary beam correction. If an image is confusion limited, after applying the primary beam correction the rms of the noise remains the same at all declinations.

In general system noise is a linear combination of the receiver noise temperature and contributions from the sky. In cases where the receiver noise starts playing an equal or a major role in determining the system noise temperature, the effect of primary beam correction causes an enhancement of noise at the field edges. This effect is seen clearly seen in our images at declinations close to $-10°$. However the enhancement of noise near DEC $-70°$ is not so noticeable. This is due to the fact that the helices at MRT are tilted towards the south by $20°$ to get a better view of the southern sky. However our measurements and also by Pandey (2006) have shown that the primary beam peaks around $-45°$ and is also asymmetrical, falling off slower at southern declinations. In view of this, the primary beam attenuation is higher around DEC $= -10°$. When corrected for higher attenuationnoise gets emphasised more.

In the section describing the addition of one day images, we have described the effect of day to day gain variations in the image. Observations are carried out keeping the NS trolleys 6 meters apart from each other, $(d \sim 3\lambda)$. This results in grating response separated by

$$\theta = sin(1/3) \tag{5.6}$$

of a radian, in images made using visibilities of any one day's observations only. When observations are completed over six allocations and the measured visibilities are phased with proper amplitude and phase, the resulting grating response should coherently cancel

out (except for the noise - both receiver noise and also source noise does not get coherently cancelled). However when different days of data are co-added, day to day gain variations results in leaving behind these grating responses in the final image. We use the phrase "aliases" to describe the residual grating response.

The aliases of Fornax A (MRC0320-313) are seen in the figures (images H12 and H14). Fornax A has a peak flux density of around 23 Jy at 151.5 MHz (image H8).

We had also discussed in the section on co-addition of images about DC in one day images and about lines parallel to RA arising after co-adding them. Offsets in correlators are known to be one possible source of these parallel lines. We have indeed developed routines to remove these lines parallel to RA in the images. While the (method described in section 4.8.4) is indeed effective, there are instances when this did not succeed in certain regions. One such region is in the RA range 4 to 6 hours where the ripples are clearly seen at $-20°$ to $-24°$. There is an enhancement of noise images from DEC $-27°30^m$ to $-30°$ (images I J K L 11). the origin of this is not clear.

In addition to these parallel lines in the same RA range we also notice enhancement of the sky in the declination range 30° to 27°, which are also related to the residual DC. The sources MRC0521-365 (image K8) , with a flux density of 36 Jy at 408 MHz, and MRC 0442-282 (image J10), which has a flux density of 18.85 Jy at 408 (50 Jy at MRT), MRC0407-658 (image J2), which has a flux density of 51 Jy at 408 (seems to have a reduced flux density of 48 Jy at 150 MHz) corrupts strips along RA and Dec centered around the sources. . The images also show the aliases of the source MRC0521-365 around DEC $-58°$ (image K4) and $-17°$ (image K12).

The residual side lobes of Pictor A (image K6) dominate the RA range 04 to 06 hours. This is an extended and a bright source (MRC0518-458, Flux density 45 Jy at 408 MHz). The strips along RA and declination centred around the Pictor A are rather bright and masks rather a large region of sky being explored (images JKL 6 and J4 to J8). The sidelobes along declination shows the expected curvature due to the changing value of the zenith angle as the source moves away from the meridian (or approaches the meridian). The residual sidelobes along RA shows the effect of non-coplanar baselines on the PSF. Pictor A being a very strong source also shows its aliases at DEC $-70°$ (image K2) and at $-25°$ (image K10). Being an extended source, its aliases smear out substantial regions of the sky.

5.5   Sources detected in the Set II images

We extracted sources from our images using the source extraction program which is a part of the X-Marmosat (Pandey, 2006).

The approach of the source extraction program is similar to the task HAPPY in AIPS for catalogue construction. HAPPY was written primarily for catalogue construction

from the FIRST survey and was publicly not available in the AIPS distribution. Salient features of the algorithm are described by White *et al.* (1997), some of which were also adopted in design of the source detection algorithm.

The end product of the source extraction program is a list of elliptically fitted Gaussians. For each island the source extraction program gives RA and DEC of the fitted position of the source, the peak and integrated flux density, position angle of the fitted Gaussian and input DC estimated from the background. In addition the error estimate on each parameter is provided by the fit. The island number, fitted parameters and the initial guess parameters are saved as these quantities are often helpful in doubtful cases and identifying complex islands. Although some of this information is not included in the catalogue it has not been discarded and would be used for rechecking in case any discrepancies are found later.

The images are processed on sidereal hour basis. In order to have minimum change of detection threshold (ratio of detected peak to noise), the source detection is carried out before any background correction is applied to incorporate the variation in the brightness temperature of the sky. As explained earlier the rms noise was estimated by selecting regions which seemed to be devoid of strong sources. A weighted average of the rms noise in each individual regions are combined in quadrature (weights equal to the number of pixels in each selected region) to estimate the overall rms noise (global rms). The source detection program uses this single global rms noise for determining the detection threshold for the image. In addition we find that due to the difference between global rms and the true local rms often sources with a signal slightly lesser than 5 sigma also gets detected in the process of source extraction.

In our present work 3837 sources were detected. Figure 5.3 shows a plot of RA against DEC for sources detected in the range $00^h \leq RA \leq 06^h$, $-70° \leq DEC \leq -10°$. MRT sources are marked by a dot in this diagram. In the same region MRC lists 1789 sources down to a flux limit of 0.7 Jy. 1543 of them have a matching MRT source. MRC sources are shown by a circle in this diagram. A detailed analysis on the outcome of the comparison of sources in MRT images will follow.

Out of 1543 sources common to MRT and MRC only 3 sources have a detection poorer than a 5 sigma detection at MRT. Out of the 2302 MRT source which do not have a matching MRC source 349 have a detection limit below 5 sigma. A histogram showing the distribution of their detection limit is shown in figure 5.4. The histogram shows a rapidly decreasing source count below a detection limit of 4.5. Approximately 215 of these sources lie between detection limits of 4.5 and 5 σ. Of the 1789 MRC sources in this region, 1543 had a matching MRT source, while 255 sources did not have matching MRT sources. Figure 5.5 shows a histogram of those non-matching MRC sources. Approximately 200 of these sources lie below or close to 1 Jy which is the completeness limit of of the MRC catalogue.

MRC0320-373 having a flux density of 259 Jy per beam do not appear in our source list as it was flagged during the deconvolution process.

In the previous section 5.4 we have already described several spurious features in our survey. A few regions with spurious features were flagged during the deconvolution process itself. The information about search region is preserved and passed on to the source extraction program. Even after deconvolution some regions are flagged and are not used for source extraction, In spite of this we do not rule out the possibility of spurious sources picked up in some regions. One intends to carry out several rounds of rechecking to weed out spurious sources.

Figure 5.6 shows the number of sources detected as a function of RA. There are on an average 850 sources detected per hour in the RA range $01^h \leq RA \leq 04^h00^m$, while the number of sources detected per hour in the RA range $00^h \leq RA \leq 01^h00^m$ and $04^h \leq RA \leq 06^h00^m$ is about half of this number. In the RA range 4 to 6 as mentioned earlier the noise is higher, the detection limits are also therefore higher and the decrease in the number of sources per hour is expected. However in the RA range 00 to 01 hours the noise is not high but the number of sources detected is still lower. This is due to flagging of a few regions around MRC 2356-612 and the Galactic plane appearing in the grating lobe of the array in this RA range. (See section 5.4).

5.6 Analysis of positional errors

We have carried out an analysis of positional errors of sources detected in our survey by comparing it with the MRC sources. The Molonglo Reference Catalogue (MRC) at 408 MHz has a resolution of $(2'.62 \times 2'.86 \sec(\delta + 35°.5))$. MRC is believed to be 99.9% complete above the flux density limit of 1 Jy. To this limit it contains 7301 sources, corresponding to an average surface density of 930 sources per steradian. In total there are 12,143 sources down to a flux density limit of 0.6 Jy.

We used MRC because of its overlap in sky coverage, its proximity in frequency compared to other reliable catalogues available. In our comparison the sources were labeled as
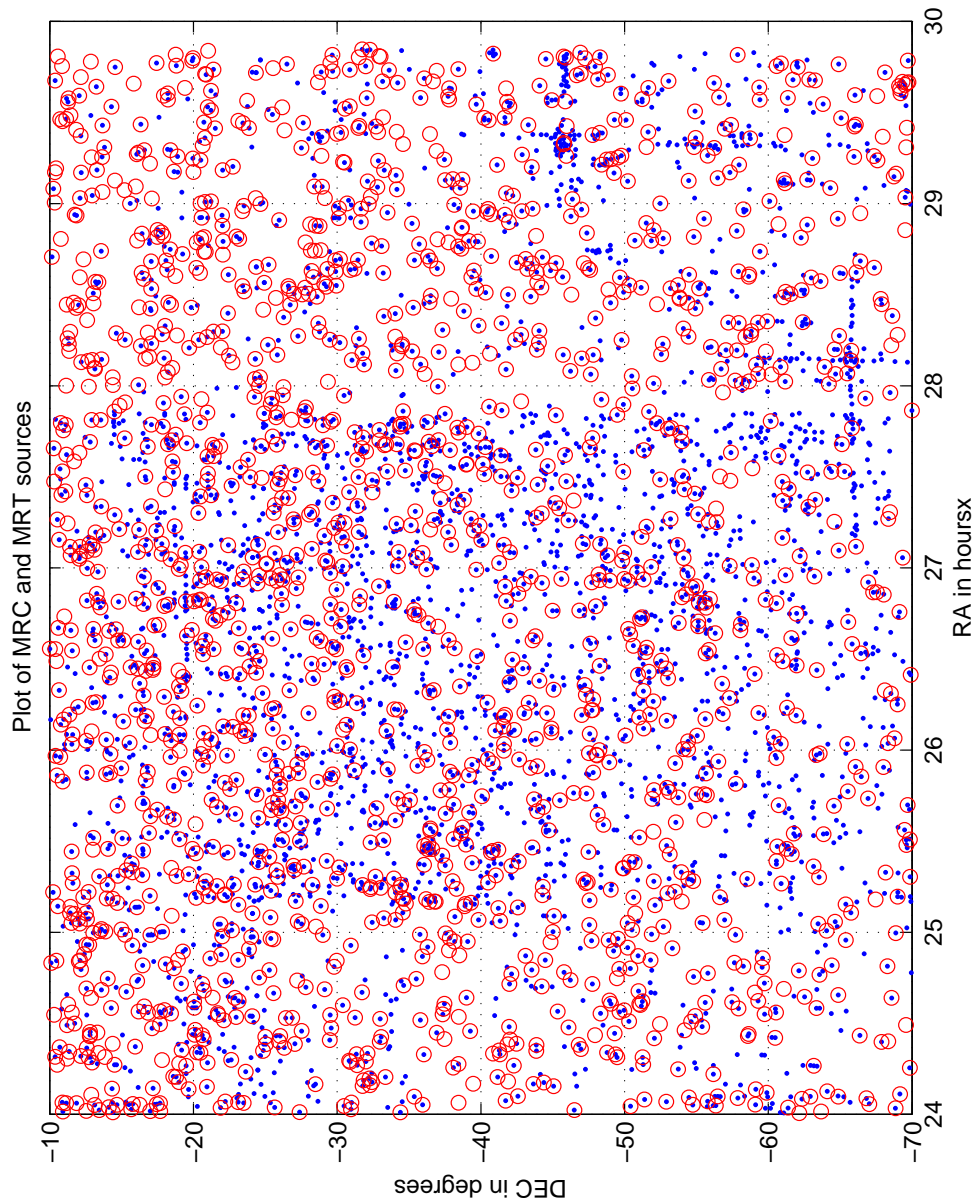
Figure 5.3: Plot of RA against DEC for sources detected in the range $(00^h \leq RA \leq 05^h 54^m, -70° \leq DEC \leq -10°)$. MRT sources are shown as dots. MRC sources are shown as circles.

common if they lie within 4′ of each other. Since the MRC catalogue has a source density of about 0.5 source deg^{-2}, the chances of considering two unrelated sources as common
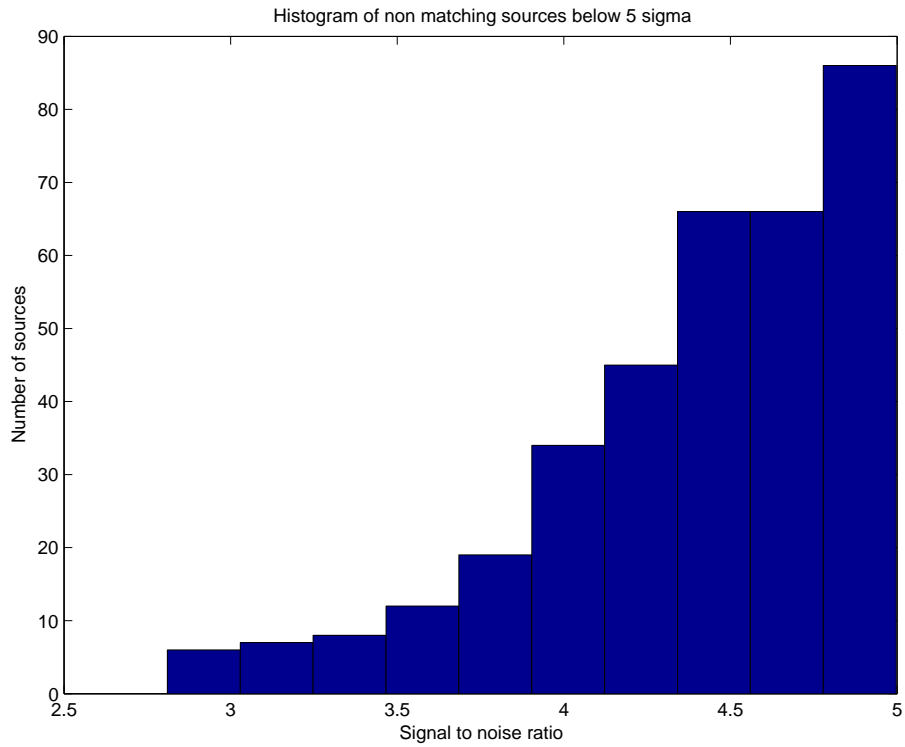
Figure 5.4:   Histogram of non-matching MRT sources having a signal to noise ratio of less than 5 in their detection.
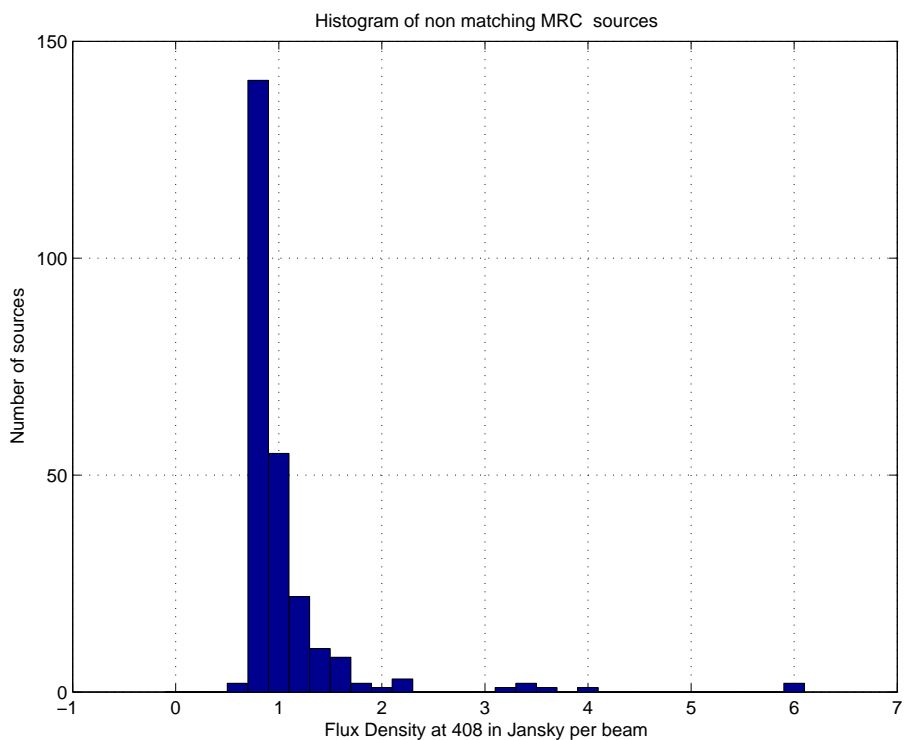
Figure 5.5:   Histogram of the flux density of non-matching non-matching MRC sources.

are negligible.

The positional errors in RA and DEC as functions of RA and DEC are shown in figure 5.7 and figure 5.8. With FWHM of beams changing both in RA and DEC as a function of DEC the errors are shown in fractional beamwidths for easy visualisation, .

Figure 5.7(a) and 5.7(b) show the error in RA as a fraction of the RA beam against RA and DEC respectively.A least squares straight line fit was made to the both plots. Both fits show small gradients. Referring to figure 5.7(a) one notices a systematic error in RA with a gradient of $\sim 1\%$ of the RA beam (0.06% per degree) . However the error in RA along the DEC (see figure 5.7(b)) has a gradient of only $\sim 0.01\%$ per degree which is negligible. The RA error against RA grows to about $\sim 4\%$ at RA = 6 hrs. This translates to a linear phase gradient of $16°$ along the EW arm of the MRT array.

One possible reason for such a systematic increase in the RA error could be due to our calibration scheme. We used for array calibration at any given sidereal hour, sources detected in the previous sidereal hour. This could have led to propagation of errors in a systematic way. Since all the sources above a certain flux threshold are used for calibration, systematics should have shown discrete steps rather than a smooth variation as a function of RA. A further investigation is under progress.

Figures 5.8(a) and 5.8(b) show errors in DEC against RA and DEC respectively. Least square straight line fits were made to both the plots. Along RA the gradient is of the the order of $\sim$-1% of the DEC beam per hr. The error starts at $\sim$1% at the begining
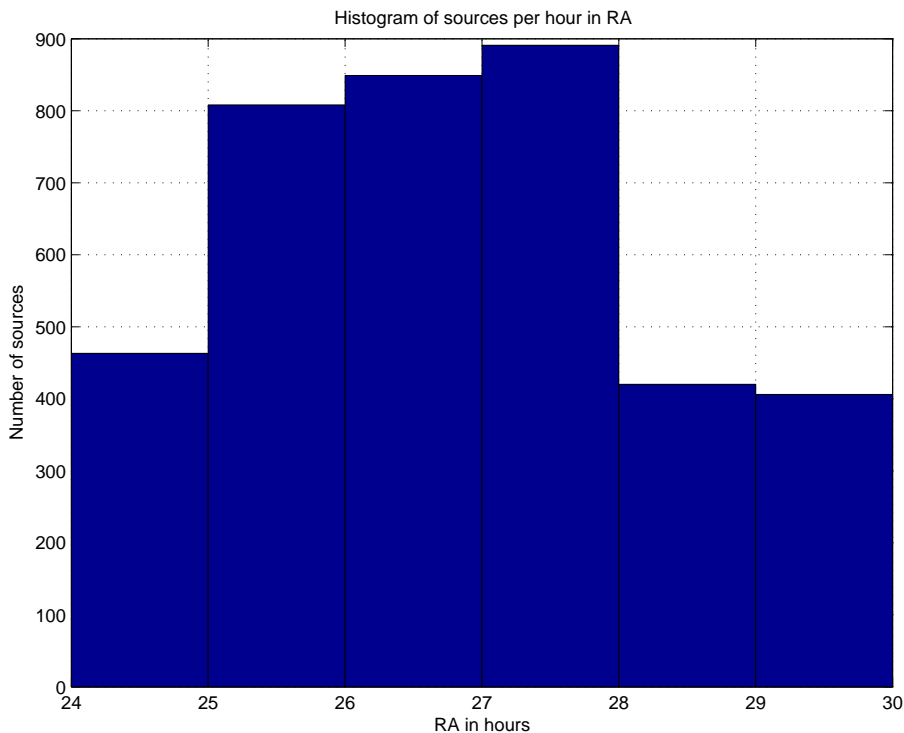
Figure 5.6:   Histogram of sources detected per hour in RA in the range ($00^h \leq RA \leq 05^h 54^m$, $-70° \leq DEC \leq -10°$).

of the RA range imaged and grows to ∼7%. The error in dec as a function of RA has a behaviour similar to the error in RA. Along the declination the gradient is ∼0.1% and is negligible.

In figure 5.9(a) we plotted errors in DEC against errors in RA. This strictly should be a scatter plot with zero mean (removing the outliers). A '+' denoted the centre of the plot if there were no systematics. The mean error calculated is shown as a '*' on the same plot. thus the centroid of the plot lies at ∼3% of RA beam and ∼4% of the DEC beam along RA and DEC respectively. A 3% error in RA means a clock setting error of ∼ 0.5 seconds of time. A 4% error in DEC means pointing error of the order of $(4 * 4)/100 = 0.16' = 10''$. We have chosen to correct for these errors which are basically small offsets to sources in our catalog.

Figure 5.9(b) shows errors after correction. The errors are now centred around the origin as shown by the '+' on the plot. The errors now lie within a cirle with a radii ∼6% of the RA and DEC beams.

5.7   Bootstrapping of MRT flux calibration

The flux ratio between sources common to MRT to MRC were analysed. Figure 5.10 shows a plot of ratio of the flux densities of sources measured at MRT and MRC as a function of RA. The flux ratios are separated in two distinct bands. One band is from RA 0 to 4 hours and a second band is from RA 4 to 6 hours.

A straight line fit was made to each band. For the first band the fitted line shows a gradient of -0.07 per hour while for the second band the gradient is 0.149 per hour.

This implies a systematic error in flux as a function RA. The most probable source of this is in the estimation of our total power used to get the unnormalised correlation coefficient. As a first corrective measure for this error, we removed the gradients from both bands, while fixing the y-intercept of the flux ratios to the value at 0 hours which is close to the RA of the primary flux calibrator MRC2354-350. We have chosen this source for fixing the MRT flux scale in the images (see section 4.6 for more details).

After removal of the gradients the flux ratios along RA show a slope of -0.003 as shown in figure 5.11. The value can be considered to be insignificant ($\sim \sigma/\sqrt{n}$, where σ is the rms of the distribution of the flux ratios of n sources).

After correcting for the flux error along RA, the flux ratios along DEC were investigated. Figure 5.12 shows a plot of the flux ratios against DEC. A straight line fit was made to the flux ratios. The fitted line goes from 2.6 at DEC $-70°$ to 2.1 at DEC $-10°$. The median value is 2.3 and the gradient of the line is 0.009 units/degree. The gradient seems to suggest that the primary beam correction applied to the MRT images has over-compensated towards lower declinations and under-compensated at higher declinations.
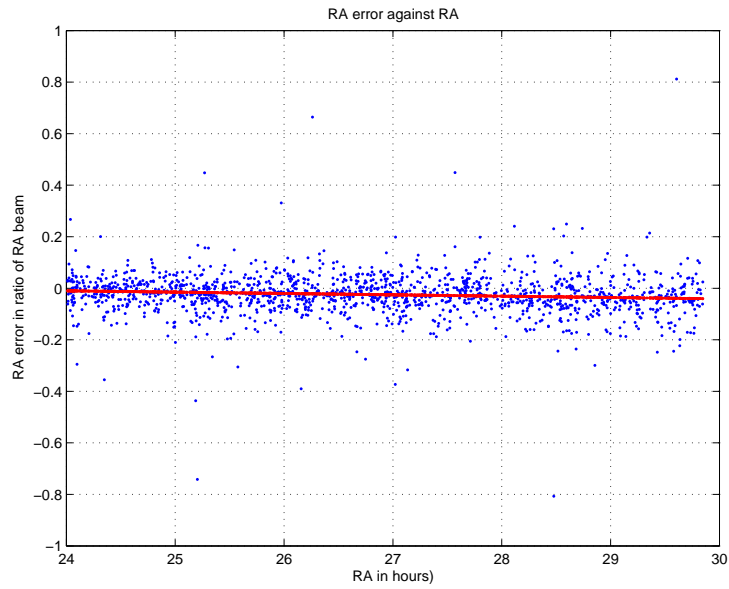
(a)
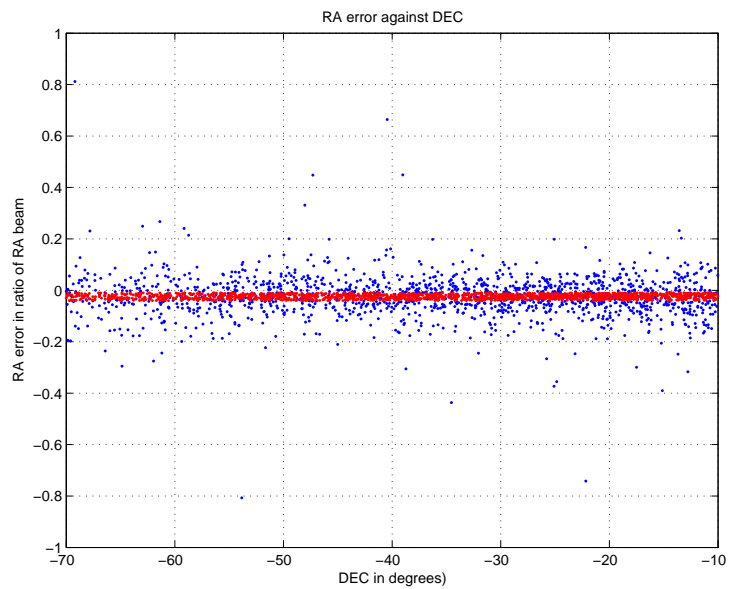
(b)

Figure 5.7:   Plot of positional errors between matching MRT to MRC sources as a ratio of their respective beams

(a) Error in RA as a ratio of the RA beam against RA

(b) Error in RA as a ratio of the RA beam against DEC

(a)

(b)
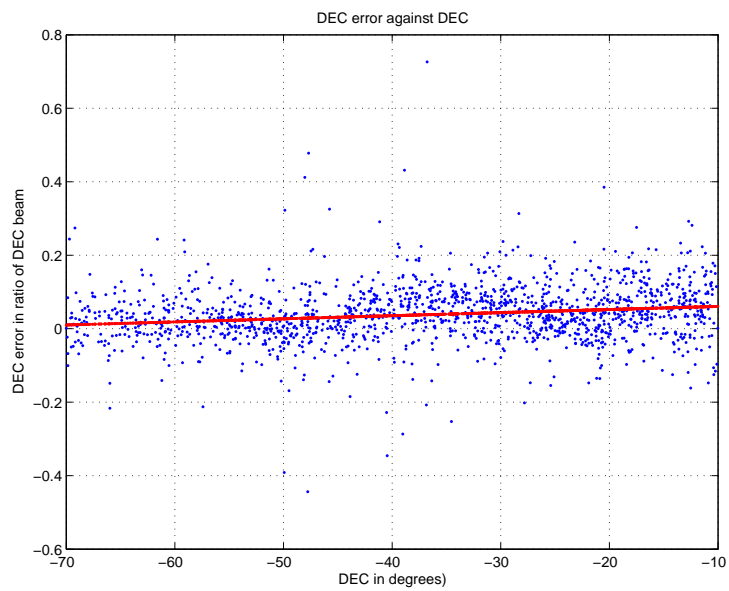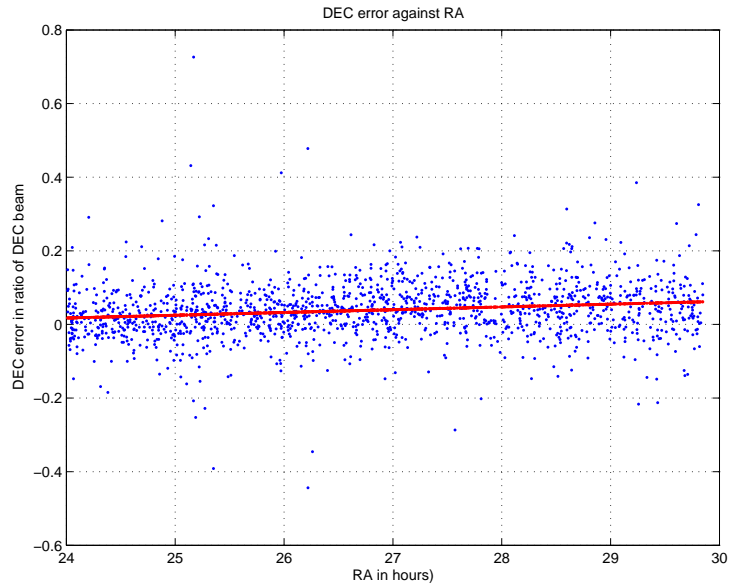
Figure 5.8:   Plot of positional errors between matching MRT to MRC sources as a ratio of their respective beams

(a) Error in DEC as a ratio of the DEC beam against RA

(b) Error in DEC as a ratio of the DEC beam against DEC
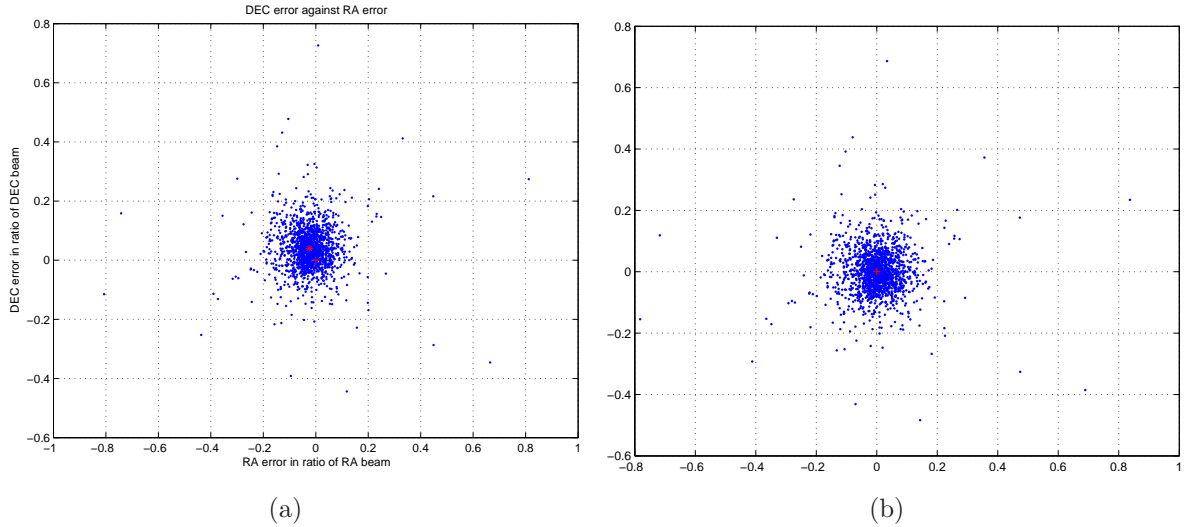
Figure 5.9:   Plot of RA error against DEC error as a ratio their respective beams
(a) Before correction for the errors
(b) After correction for the errors

To investigate this systematic error, the primary beam correction applied to the MRT flux densities was removed. A second order polynomial was fitted to the flux ratios against declination. A second order polynomial is the best approximation to the primary beam of the helix used at MRT (Pandey, 2006).

Figure 5.13 shows the flux ratios with the primary beam removed and a second order polynomial fitted. A normalised version of the fitted curve was applied as primary beam correction to the flux ratios.

Figure 5.14 shows the flux ratios after application of the new primary beam correction. The median value of the flux ratios is 2.34. The systematic in flux ratio along the DEC is now insignificant.

Figure 5.15 shows the new derived primary beam (thick red curve) plotted together with the previously estimated primary beam (thin blue curve) (Pandey, 2006). The new primary beam shows a peak response at DEC $\sim -47°$ while the previous beam shows a peak response at DEC $\sim -44°$. The half power beamwidth of the new derived primary beam is $\sim 66°$, slightly wider than the half power beamwidth of $\sim 64°$ of the previous estimation.

Figure 5.16 shows the ratio of the new derived primary beam to the previously estimated primary beam. In the DEC range considered, the ratio varies by $\pm \sim 15\%$ towards the ends of the DEC range.

Figure 5.17 shows the flux density ratio (MRT to MRC) against MRC flux density. The flux ratio has a slightly decreasing trend with the flux densities. This may be due to the increased accuracy of estimation of the flux densities of bright sources apart from any

genuine behaviour of spectral index distribution of strong sources and this dependence on
the flux density of sources.
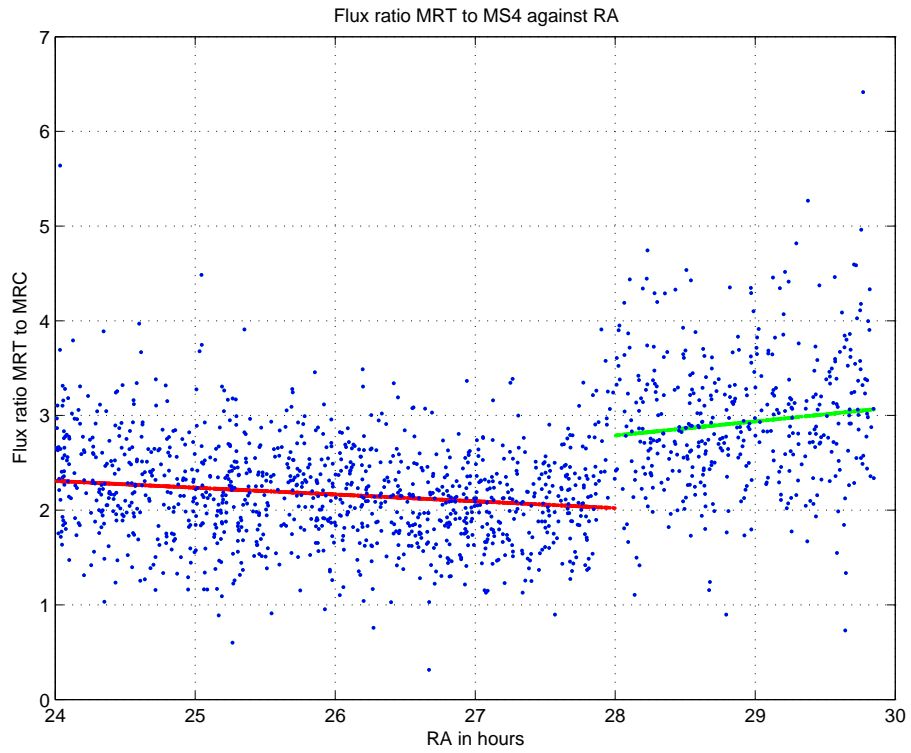
Figure 5.10:   Ratio of MRT to MRC flux densities against RA.
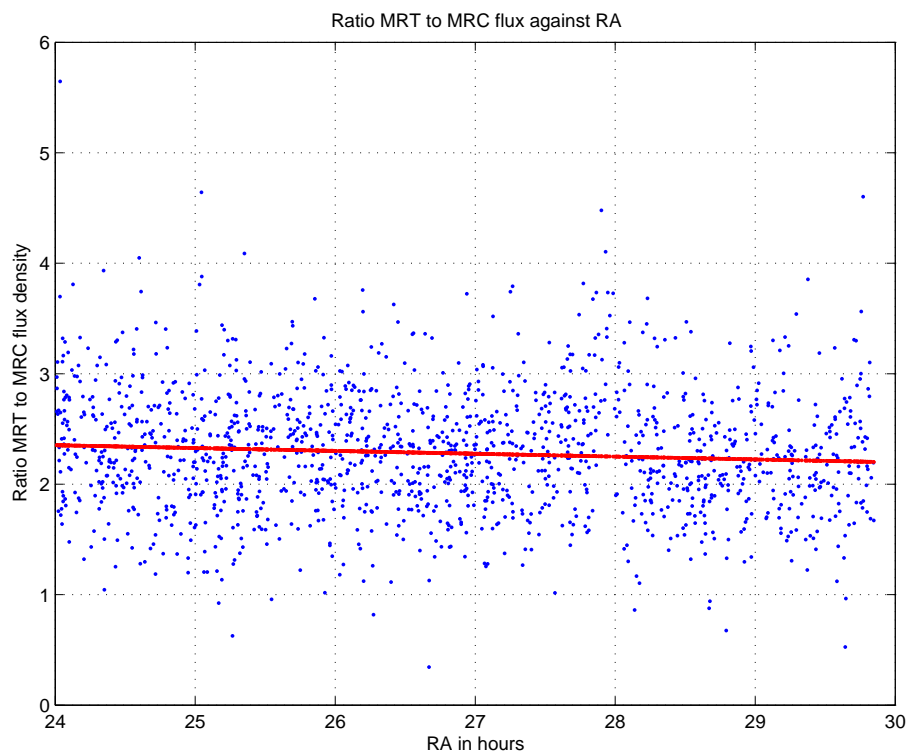
Figure 5.11:   Ratio of MRT to MRC flux densities against RA after correction.
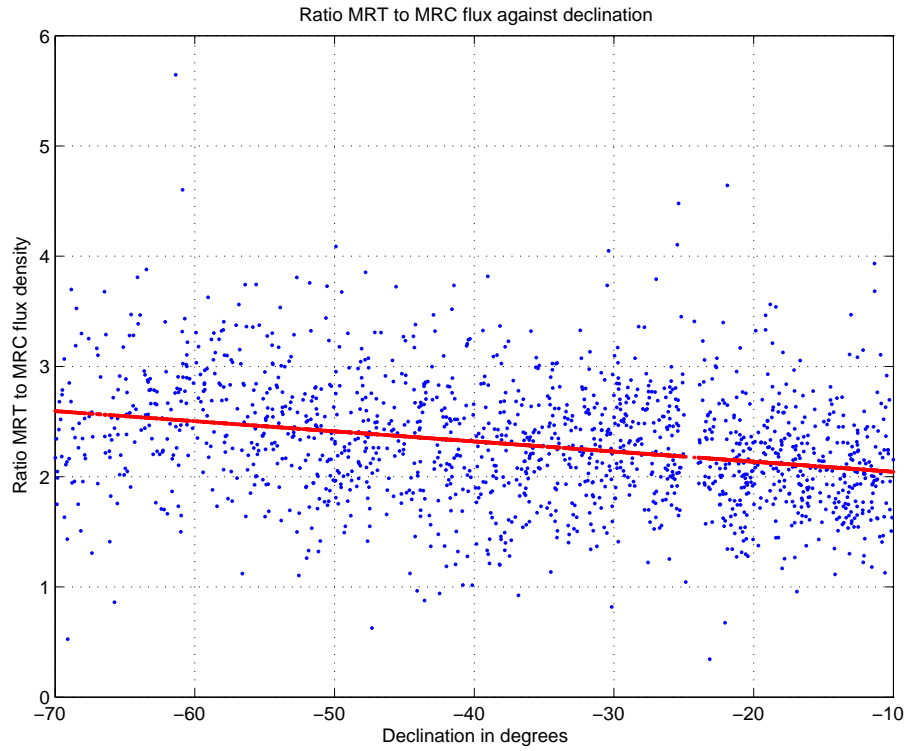
Figure 5.12: Ratio of MRT to MRC flux densities against DEC.
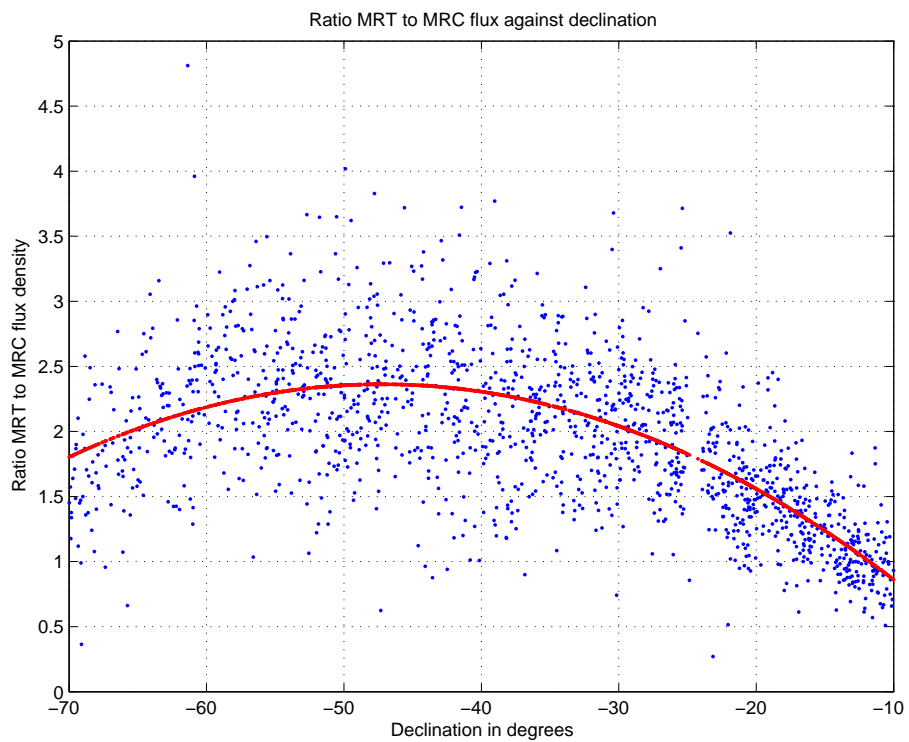
Figure 5.13: Ratio of MRT to MRC flux densities against DEC. A second order polynomial is fitted to the ratios to estimate the primary beam of the helix.

5.8   MRT source catalog

We present a source list of 52 MS4 detected in the Set I MRT images and 62 MS4 sources detected in the Set I MRT images.
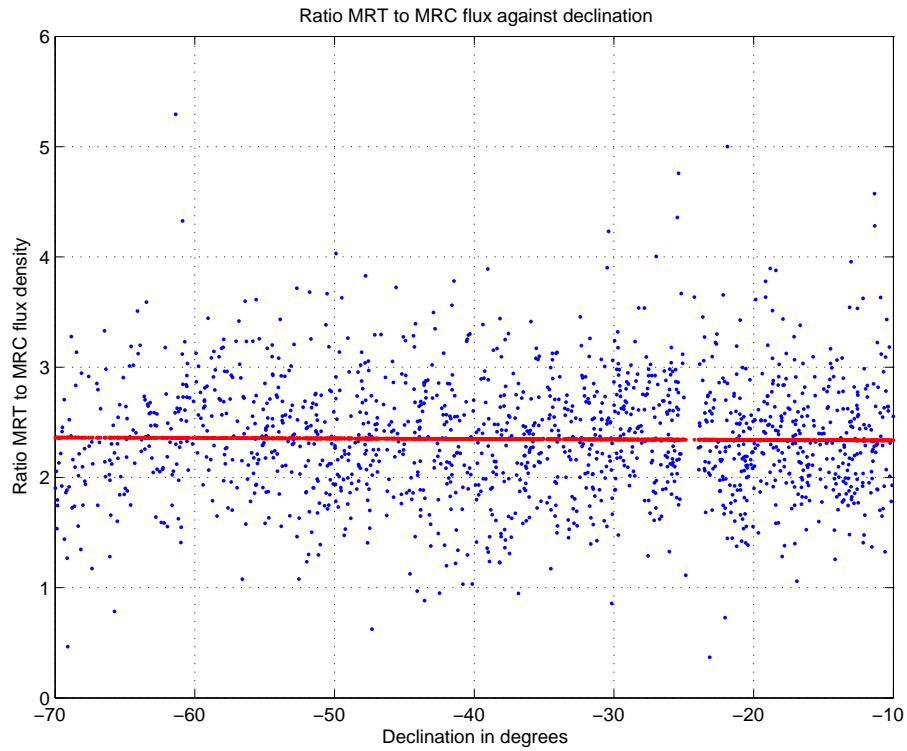
Figure 5.14:   Ratio of MRT to MRC flux densities against DEC after correction.
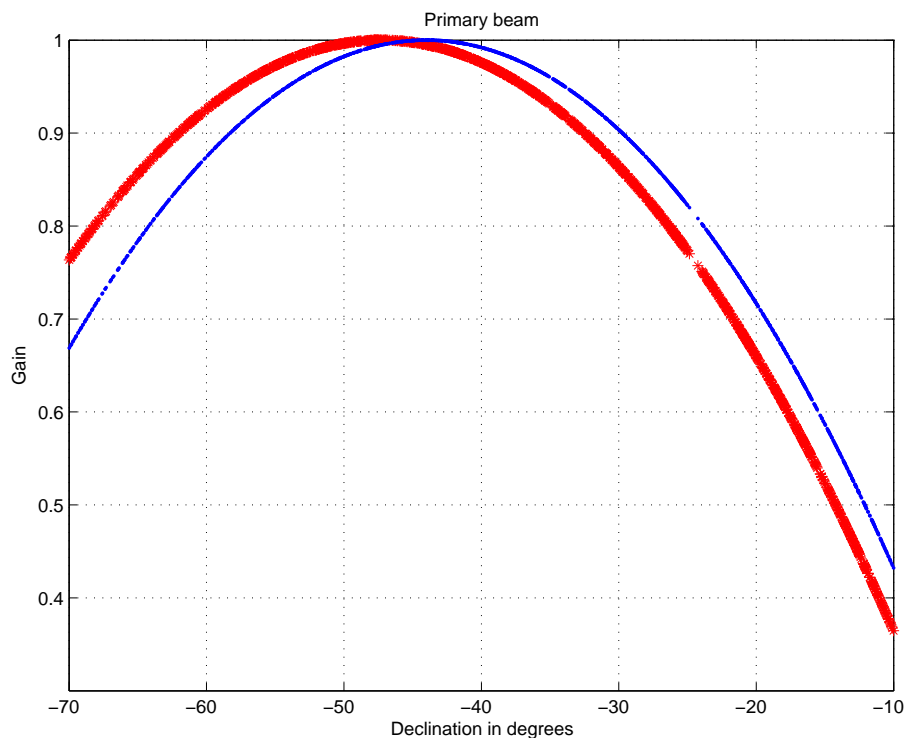
Figure 5.15:   New derived primary beam (thick red curve) and previous derived beams (thin

Table 5.4 gives the source list for sources from the Set 2 images , with MRC name (B1950), RA (J2000), DEC (J2000) and $S_{151.5}$ listed.
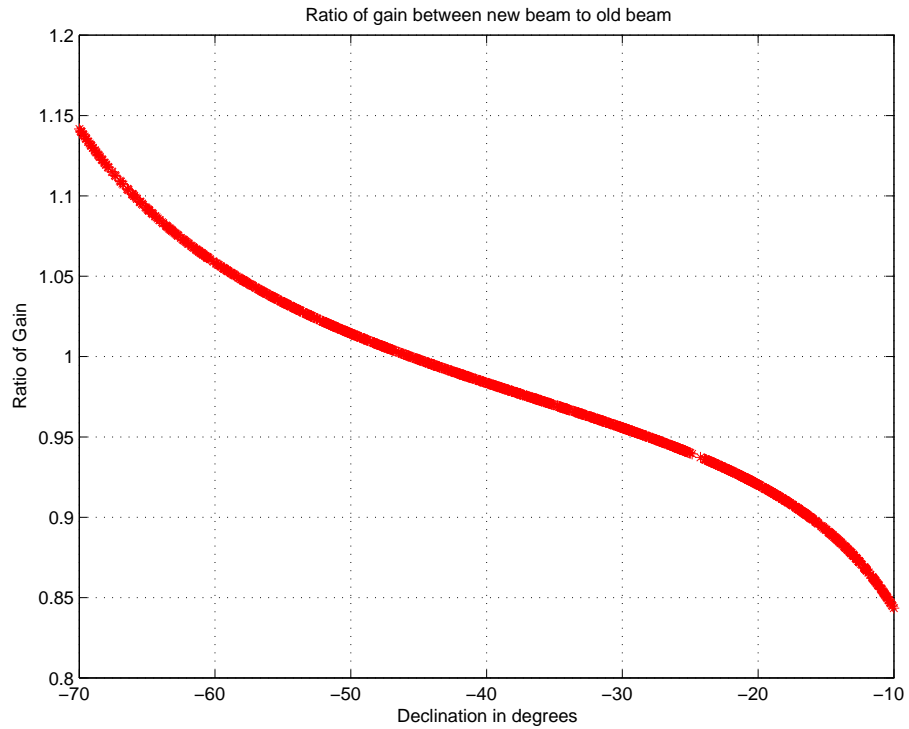
Figure 5.16: Ratio new derived primary beam to previous derived beams.
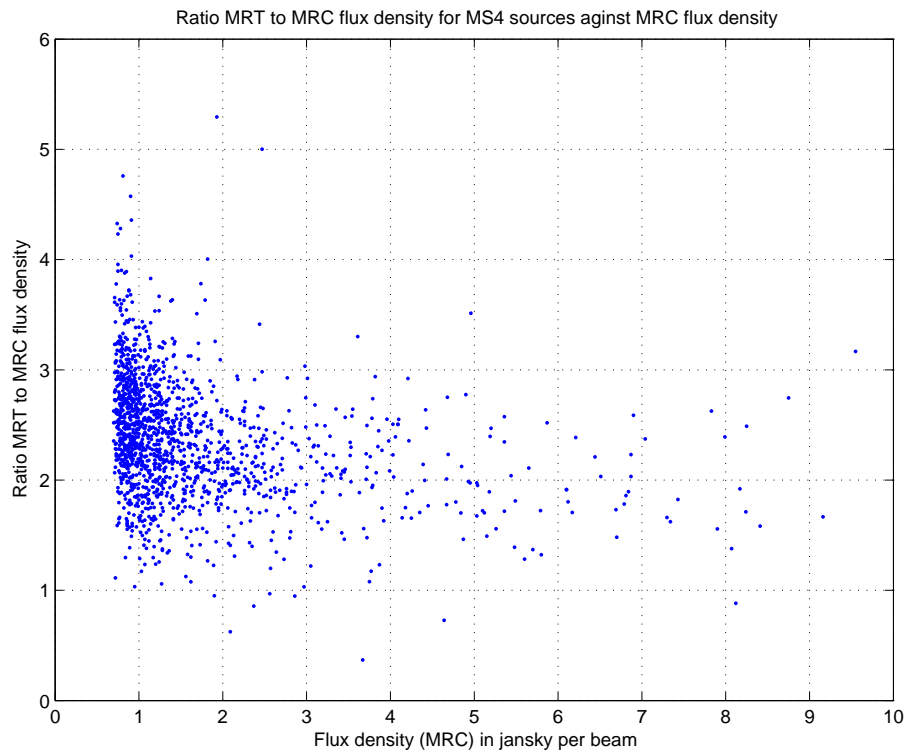
Figure 5.17: Ratio of MRT to MRC flux densities against MRC flux density in Jansky per beam.

Table 5.5 gives the source list or sources from the Set 2 images, with MRC name (B1950), RA (J2000), DEC (J2000) and $S_{151.5}$ listed.

The internal consistency between the flux densities measured in Set I and Set II images with reference to the common flux calibrator is of the order of the flux densities in the Set II images being 3% higher than the Set I images.

A sample source list of sources detected in the survey is given in the table 5.7. The list gives the MRT name of the source its RA and DEC, the detected flux density in Jy per beam and the signal to noise of detection.

5.9 Steep spectrum sources in the survey

Steep spectrum radio sources have been a starting point for different kinds of studies. For example, Ultra Steep Spectrum (USS) sources have been efficient tracers of high redshift radio galaxies. Although new optical selection techniques such as colordropouts, deep spectroscopy of blank fields, and narrowband Ly-alpha imaging have now found galaxies at high redshifts , radio sources are still the only objects that can be selected uniformly over all redshift ranges, and in a way that does not suffer from optical biases such as dust extinction, which is known to be important at these high redshifts (De Breuck *et al.*, 2000). van Weeren *et al.* (2011) in their study of diffuse steep-spectrum sources from the 74 MHz VLSS survey found that diffuse steep-spectrum radio sources are not only found in massive X-ray luminous galaxy clusters but also in smaller systems. Future low-frequency surveys will uncover large numbers of steep-spectrum radio relics related to previous episodes of AGN activity.

Zhang *et al.* (2003) in their study of the spectral index-flux density relation for large samples of radio sources found that the spectral indices calculated for about 200 000 sources from the WENSS (327 MHz) and NVSS (1.4 GHz) catalogs, gave:

1. The median spectral index increases from $RA_{med} \sim -0.9$ to 0.8 while 337 MHz flux densities decrease from from 0.1 Jy down to 25 mJy. The median spectral indices nearly show no variation within the error bars when the flux density is larger than 0.1 Jy.

2. A dependence of the fraction of ultra-steep spectrum sources (USS; $-1.5 < RA < -1$), steep spectrum sources (SSS; $-1.0 < RA < -0.5$) and flat spectrum sources (FSS; $-0.5 < RA < 0.0$) is partly responsible for the spectral flattening. Another contribution to the spectral flattening comes from the variation of RA_{med} of steep spectrum sources ($RA < -0.5$) themselves which increases with decreasing flux densities

Klamer *et al.* (2006) in their paper 'A search for distant radio galaxies from SUMSS and NVSS: III. radio spectral energy distributions & the z-alpha correlation' put forth, a new physical mechanism to explain the redshift spectral index correlation: extremely steep spectrum radio galaxies in the local universe usually reside at the centres of rich galaxy clusters. They argue that if a higher fraction of radio galaxies, as a function of redshift, are located in environments with densities similar to nearby rich clusters, then this could be a natural interpretation for the correlation.

With this background we estimated the spectral index distribution of sources in our source list and found the following :

Figure 5.18 shows a histogram of the spectral indices between MRT and MRC. The median spectral index is -0.86. The spectral indices are symmetrically distibuted about the median spectral index. The rms variation is ~ 0.19

Approximately 93% of the MRC sources above a flux density of 1 Jy at 408 MHz are also detected in the MRT images. These sources form a complete sample at 408 MHZ. Figure 5.19 shows a histogram of spectral index of the 701 MRC sources matching with MRT and with a flux density above 1 Jy at 408 MHz. The median spectral index is 0.81 with an rms of 0.19. This implies that below 1 Jy at 408 MHz, steeper spectrum sources are preferentially detected. Figure 5.20 shows the histogram of plotted against the MRC flux density. The fitted straight line has a gradient of 0.048 and shows the variation of spectral indices with flux densities. Pandey (2006) found a similar trend. the median spectral index of 1648 sources common to MRT and MRC for the range $18^h00^m \leq RA \leq 24^h30^m$, $-75° \leq DEC \leq -10°$ is 0.98. The median spectral index came down to 0.9 by including brighter sources only, which define the completeness limit of MRC. Pandey (2006) concluded that this downwards trend in spectral index is obviously expected as we would have favourably detected sources with steeper spectral indices near the detection threshold of our survey. in view of this we cannot conclude that our trend contradicts the trend observed by Zhang *et al.* (2003).

In our sample , 29 sources were found to have to have $\alpha_{151.5}^{408} < -1.3$. In the sample of extended sources detected in the present work, 3 sources show a spectral index < -1.3. A detailed study of these sources along with a sample of steep spectrum sources detected from Set I images will be pursued.

5.10   The EoR field

Several synthesis telescopes such as MWA (http://www.mwatelescope.org), LOFAR (http://www.lofar.org) , and PAPER (http://astro.berkeley.edu/ dbacker/eor) are currently being built to study the Epoch of Reionization (EoR) by observing the redshifted 21 cm line transition from neutral hydrogen. While future instruments may map the 21

cm brightness in three dimensions (frequency corresponds to line of sight), current experiments lack the required sensitivity and instead hope to estimate the power spectrum of
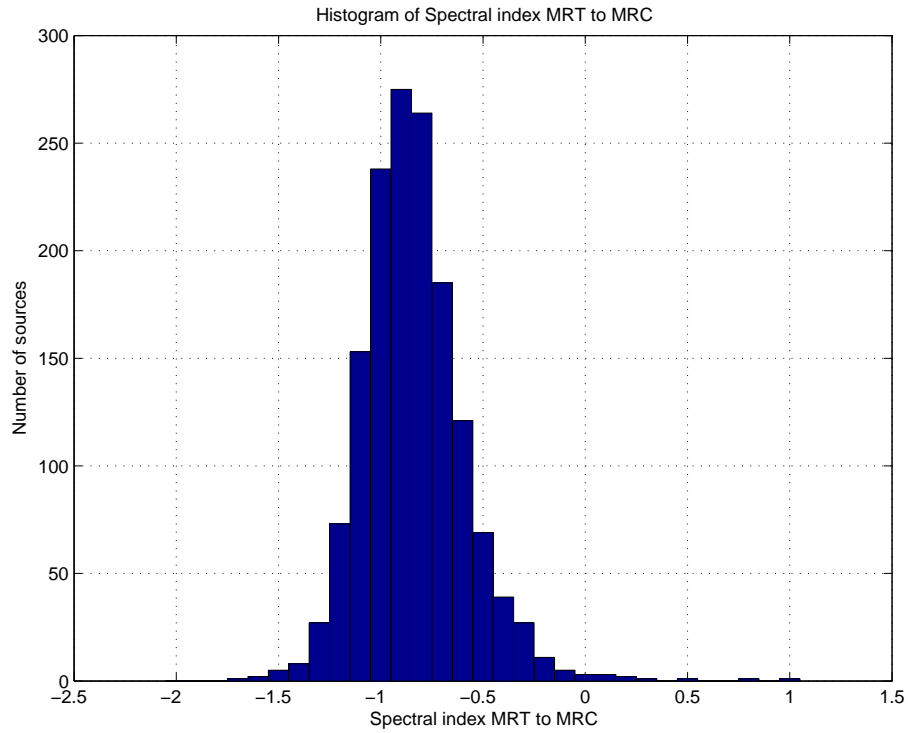
Figure 5.18: Histogram of spectral indices MRT to MRC.
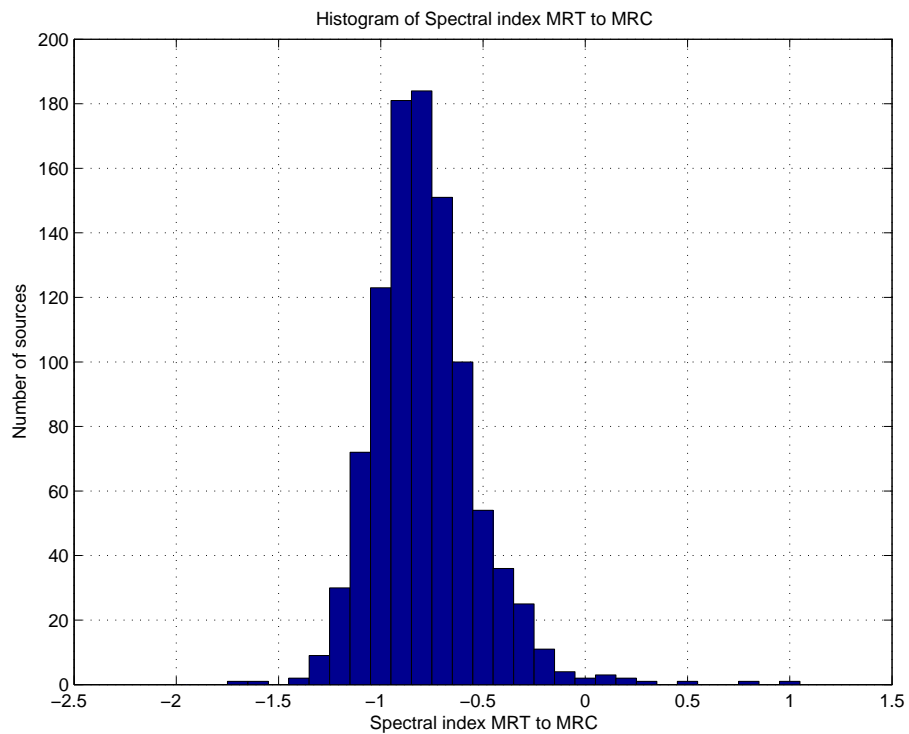
Figure 5.19: Histogram of spectral index MRT to MRC for sources having MRC flux density greater than 1 Jy per beam.

21 cm brightness fluctuations. The brightness of these fluctuations is about 5 orders of magnitude smaller than the Galactic and Extragalactic foregrounds. Moreover, removing the effects of the telescope point spread function (PSF) from the synthesis images may not be possible to the level of sensitivity demanded by EoR power spectrum measurements. Consequently, foreground contamination and instrumental effects present a major hurdle to 21 cm tomography. It is important to estimate the foreground by the same telescope used for EoR detection at exactly the same frequencies of operation. It may not be feasible to apply the information obtained by some other telescopes for removing the foreground contamination to the level required for EoR detection. However a priori information about the foreground obtained by other telescopes help in bootstrapping the calibration of the EoR telescope and also help in establishing reliable flux scale. In this connection it is important to point out that the MRT survey is a blind survey covering the southern sky at 151.5 MHz, which is near the centre of the observing frequency band of MWA. So we believe that the results of the MRT survey will provide useful information and check points for carrying out surveys with MWA and a reliable flux scale. Three target fields have been proposed at MWA, to carry out EoR observations. These are cold patches of the sky which minimizes noise contributions from the sky to the system temperature. The coordinates of the fields being discussed are :

1. Target 1: RA=135d, Dec=0d

2. Target 2: RA=60d, Dec=-30d
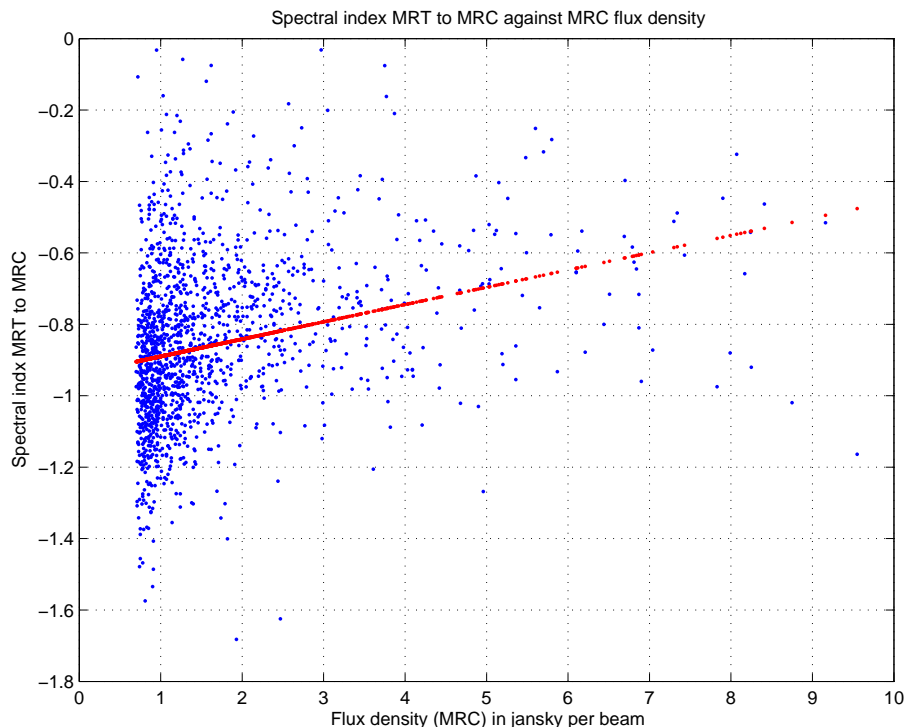
Figure 5.20: Spectral index MRT to MRC against MRC flux. Straight line fit is in red.

3. Target 3: RA=40d, Dec=-60d

The present work, surveying the southern sky at 151.5 MHz in the RA range ($00^h \leq RA \leq 05^h54^m$, $-70° \leq DEC \leq -10°$) covers target2 proposed for EoR observations with MWA. In view of this we examined statistics of the sources detected in this field of view.

Each tile of MWA consists of 16 bow-tie antennas spaced 1.07m apart. At 150 MHz, the FWHM of the primary beam of the tile is $\sim 30°$. This FWHM is for the tile phased to look at zenith. This does change while looking away from zenith. For our present discussion we have assumed the same FWHM while observing the target field. This is not going to affect the present discussion.

With this knowledge we examined the number count and flux density of sources detected by MRT in a region centered around target 2 field (RA=04 Hrs, Dec= $-30°$). Taking a guard band of 5° around the FWHM, we examined the source count and flux density of sources in the RA ranges 2:40 to 05:20 hours and the DEC range 50° to $-10°$.

Figure 5.21 shows the histogram of the flux density of sources detected at MRT. We have 1083 detections above a detection limit of 5 sigma. In the same field of view MRC has listed 620 sources. We find 507 matching sources. Adding up sources detected only at MRT, sources common to MRC and MRT and those listed only in MRC leads to a source count of 0.75 sources per deg^2 with a detection limit of around 1 Jansky at 150 MHz. With this database it is possible to examine the spectral behaviour of several sources at low frequencies. Especially creating such a model for the MS4 sources detected can give an insight into the spectral behaviour of a well understood sample of sources at low frequencies.

We have detected 16 sources with diffused emission exceeding the MRT beamwidth of 4. Fornax A and Pictor A being the two bright extended sources to be imaged with caution for foreground removal. The figures show the contour plots of these extended sources (Pictor A is flagged for deconvolution and we do not have a contour plot for the same).

5.11 Extended sources in the survey

Being a T-shaped array, MRT has a fully filled uv coverage. This makes it sensitive to extended features in the sky and will allow us to explore low surface brightness parameter space in the study of sources at low frequency. This is a parameter space which have been poorly explored in understanding the radio sky.

The surface brightness sensitivity of the MRT is $\approx 2.1 \times 10^{-21}$Wm^{-2} Hz^{-1} Sr^{-1} (1-σ) (Pandey, 2006). This will enable studies of extended galactic and extra-galactic radio sources. Extended features of SNRs (Green, 2009) have a typical surface brightness sensitivity of $1.510^{-21}Wm^{-2}Hz^{-1}Sr^{-1}$. MRT will enable studies of SNRs with a brightness

temperature sensitivity an order of magnitude better than the completeness limit currently available in the literature.

Jones & McAdam (1992) studied the structure of southern extragalactic radio sources lying south of DEC $-30°$. The sources have been imaged with the Molonglo Synthesis Telescope (MOST) at 843 MHz with a resolution of $44''$. The sample includes those sources noted in the MRC as extended (larger than $\sim 1'$) as well as those noted as multiple, that is, within $8'$ of a neighbor and possibly related. The sample is representative of the strong extended extragalactic radio sources of the southern sky, but is not statistically complete. Images of 383 sources as well their flux densities, positions and sizes were given.

We started with this set of images from SUMSS survey. In the RA range 0 to 6 hours imaged at MRT, ~ 71 sources are listed. All the sources are detected at MRT. The SUMSS images of $4° x 4°$ extent were convolved with the MRT beam. Contour plots of the MRT images were overlayed on the grayscale image of the convolved SUMSS images. This allowed us to compare the structure of the MRT sources to check if they showed extended emission. 33 sources do show extended emission.

Figures 5.11 to 5.11 shows the overlays, together with the peak flux measured at MRT and the lowest flux density level used for contouring..

During our search for the extended sources in the selected SUMSS images, we also found 16 MRT sources which show extended emission and which are not listed by Jones & McAdam (1992).These sources are also shown in figures 5.11 to 5.11
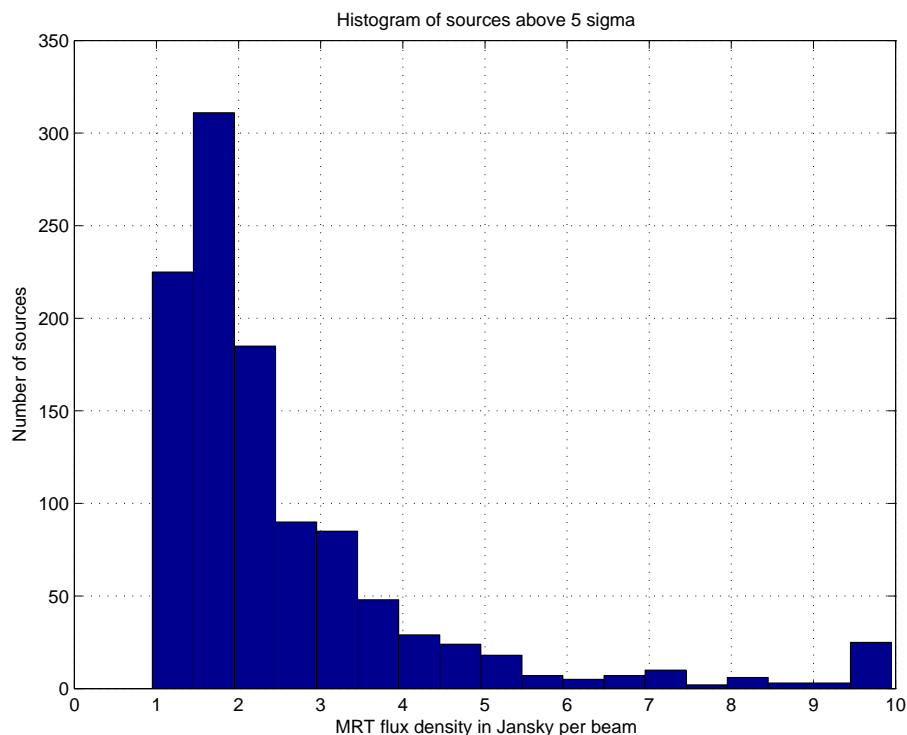
Figure 5.21:   Histogram of flux densities of MRT sources detected in EoR target 2 field

Table 5.3 gives the positions, flux densities and spectral index MRT to SUMSS, $S_{151.5}$ and S_{843} of the 33 extended sources listed by Jones & McAdam (1992). In the table given, we have quoted a value of the integrated flux densities seen at MRT, restricting the area of calculation to regions which show up both in SUMSS and MRT surveys.

The median spectral index of the sources is 0.74 . The rms is 0.23 .

3 sources, J0231-666,J0507-6242 and J0540-6142 have a spectral index -1.3 and can be classified as steep spectrum sources.

Table 5.3: Extended sources detected in the MRT images

MRC name (J2000)	RA (J2000)	DEC	Spectral index	$S_{151.5}$	S_{843}
J0017-3054	00 17 18.2	-30 54 36	-0.74	2.955	0.83
J0025-5834	00 25 50.7	-58 34 16	-0.75	4.00	1.10
J0030-5018	00 30 39.2	-50 18 41	-0.85	5.98	1.4
J0036-5105	00 36 04.4	-51 05 46	-0.64	2.11	0.70
J0046-4207	00 46 16.4	-42 07 38	-0.74	42.09	11.8
J0105-4505	01 05 20.5	-45 05 32	-0.89	18.5	4.04
J0110-3437	01 10 59.9	-34 37 34	-0.64	3.97	1.38
J0111-6859	01 11 43.3	-68 59 59	-0.50	7.39	3.10
J0016-4725	01 16 30.0	-47 25 46	-0.815	16.84	3.79
J0121-4956	01 21 04.8	-49 56 00	-0.77	4.6	1.22
J0133-3633	01 33 30.2	-36 28 49	-0.701	34.02	10.3
J0213-4741	02 13 06.1	-47 41 29	-0.89	6.97	1.51
J0216-4748	02 16 45.2	-47 48 58	-0.93	15.29	3.12
J0231-666	02 31 50.8	-66 26 40	-1.31	22.12	2.058
J0252-6733	02 52 02.5	-67 33 16	-0.95	6.52	1.28
J0256-4815	02 56 01.2	-48 15 36	-0.51	3.73	1.15
J0321-4540	03 21 24.5	-45 10 14	-0.722	16.51	4.82
J0322-3712	03 22 42.5	-37 12 31	-0.68	545.19	169
J0334-3859	03 34 02.8	-38 59 02	-0.707	8.04	2.41
J0338-3527	03 38 46.6	-35 22 47	-0.789	14.73	3.84
J0424-728	04 23 57.8	-72 45 52	-0.68	10.63	3.336
J0428-5350	04 28 42.6	-53 50 07	-0.82	34.2	8.41
J0435-5835	04 35 57.6	-58 38 00	-0.50	2.25	0.97
J0437-6607	04 37 21.8	-66 07 57	-1.2	6.54	0.769
J0451-3839	04 52 13.4	-38 41 06	-0.66	4.75	1.53
J0507-6242	05 07 51.5	-62 42 35	-1.31	10.09	1.07
J0512-482	05 12 51.3	-48 23 59	-0.72	19.41	5.616
J0513-3026	05 13 29.5	-30 30 44	-0.46	10.01	4.57
J0548-3255	05 48 35.4	-32 55 03	-0.53	3.93	1.85
J0520-454	05 20 00.6	-45 47 39	-0.68	275.9	85.7
J0534-6121	05 34 48.5	-61 21 55	-1.06	12.29	2.01
J0540-6142	05 40 49.7	-61 42 33	-1.31	10.95	1.09
J0545-4756	05 45 11.0	-47 56 29	-0.84	4.65	1.117

(a)   (b)
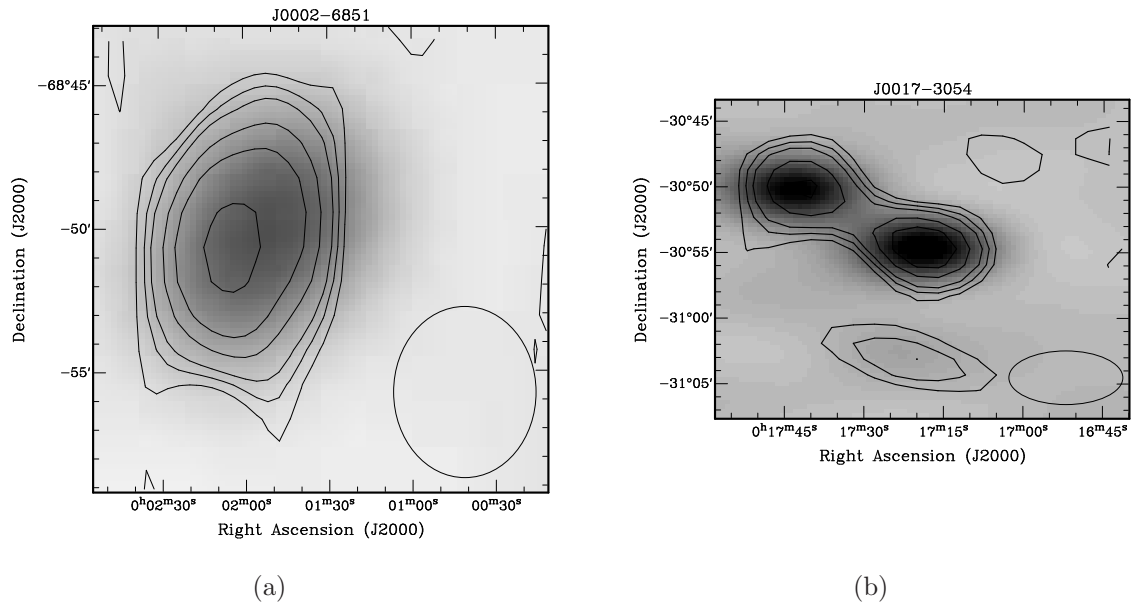
Figure 5.22:   Maximum flux density in each map and lowest contour level (Jy)
(a) J0002-6851 4.11 Jy 0.60 Jy
(b) J0017-3054 2.72 Jy 0.46 Jy
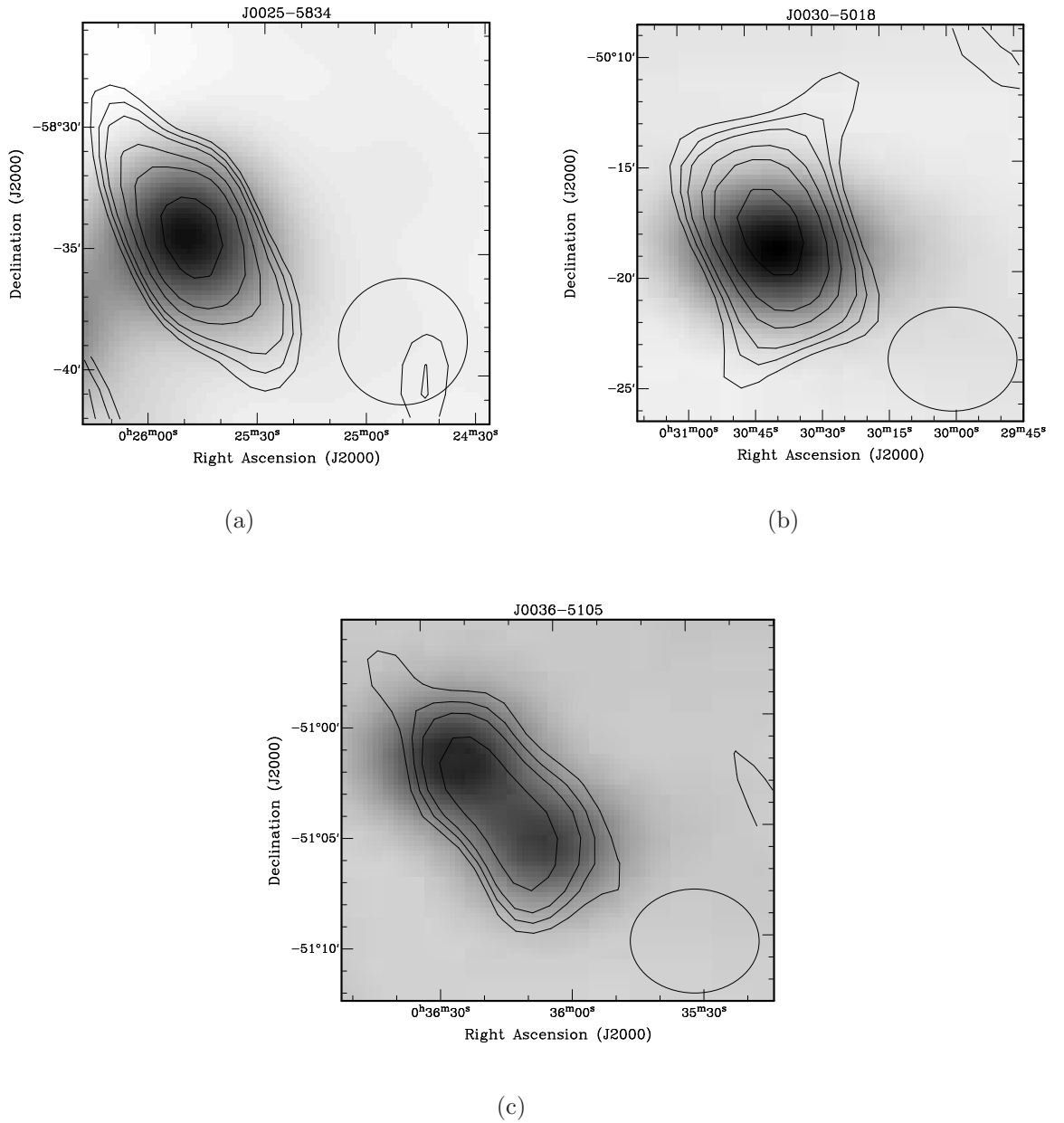
Figure 5
(a) J013

Figure 5.23:   Maximum flux density in each map and lowest contour level (Jy)
(a) J0025-5834 3.02 Jy 0.46 Jy
(b) J0030-5018 4.90 Jy 0.42 Jy
(c) J0036-5105 2.23 Jy 0.42 Jy
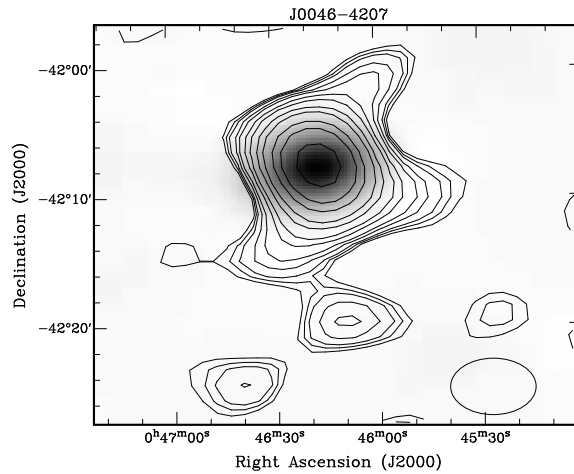
(a)

Figure 5.24:   Maximum flux density in each map and lowest contour level (Jy)
(a) J0046-4207 33.36 Jy 0.41 Jy
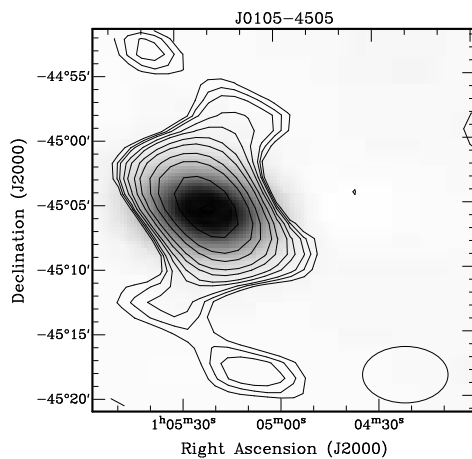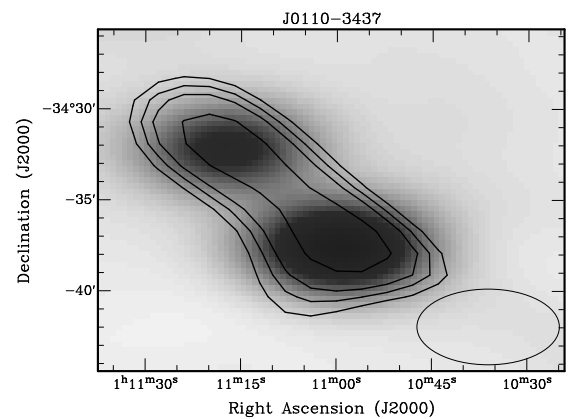
(a)   (b)

Figure 5.25:   Maximum flux density in each map and lowest contour level (Jy)
(a) J0105-4505 19.57 Jy 0.41 Jy
(b) J0110-3437 2.88 Jy 0.69 Jy

(a)

(b)

(c)
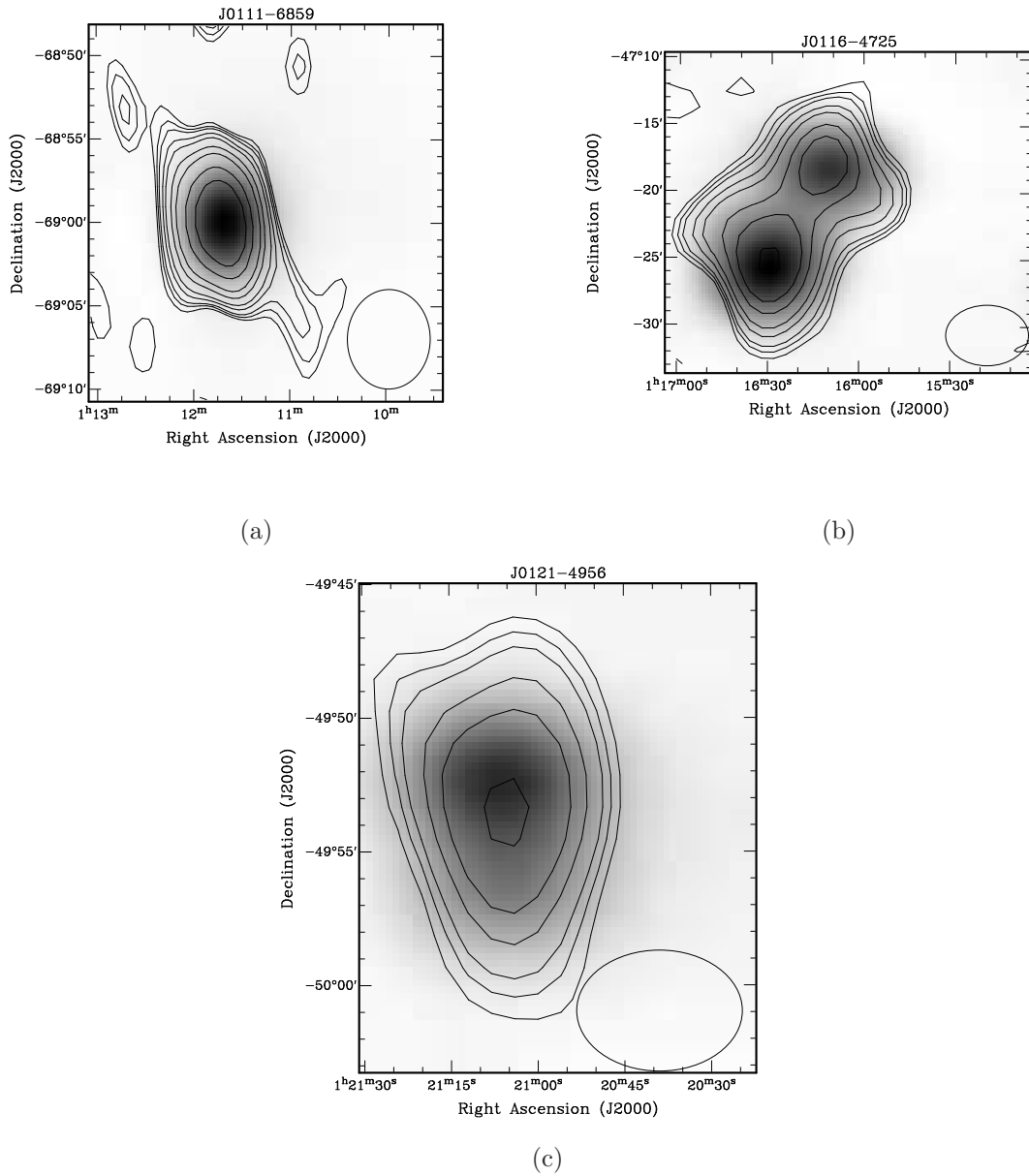
Figure 5.26:   Maximum flux density in each map and lowest contour level (Jy)
(a) J0111-6859 13.68 Jy 0.69 Jy
(b) J0116-4725 7.54 Jy 0.41 Jy
(c) J0121-4956 3.73 Jy 0.41 Jy

(a)

(b)

(c)
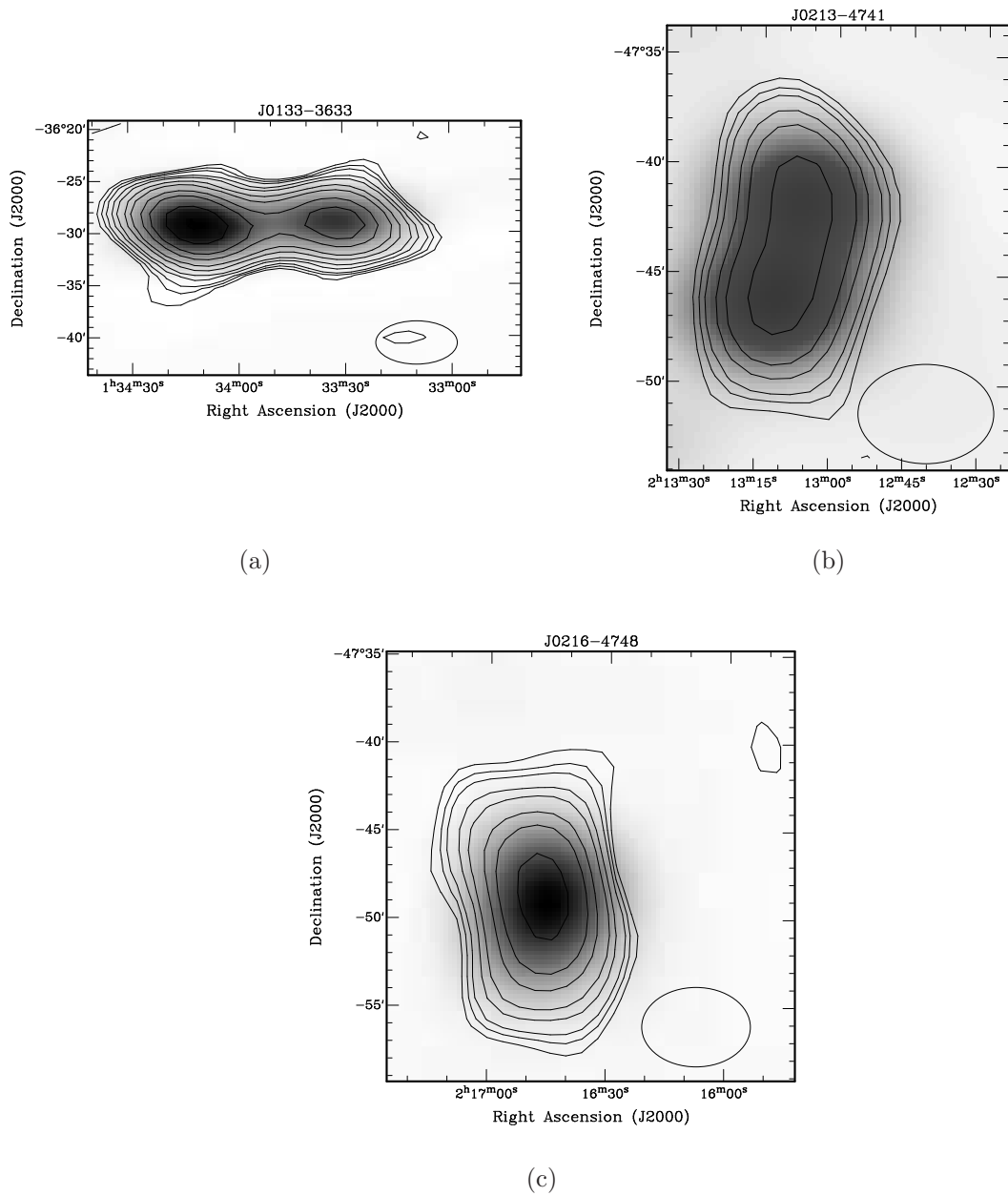
Figure 5.27:   Maximum flux density in each map and lowest contour level (Jy)
(a) J0133-3633 14.63 Jy 0.41 Jy
(b) J0213-4741 2.96 Jy 0.408 Jy
(c) J0216-4748 5.62 Jy 0.408 Jy

(a)

(b)

(c)
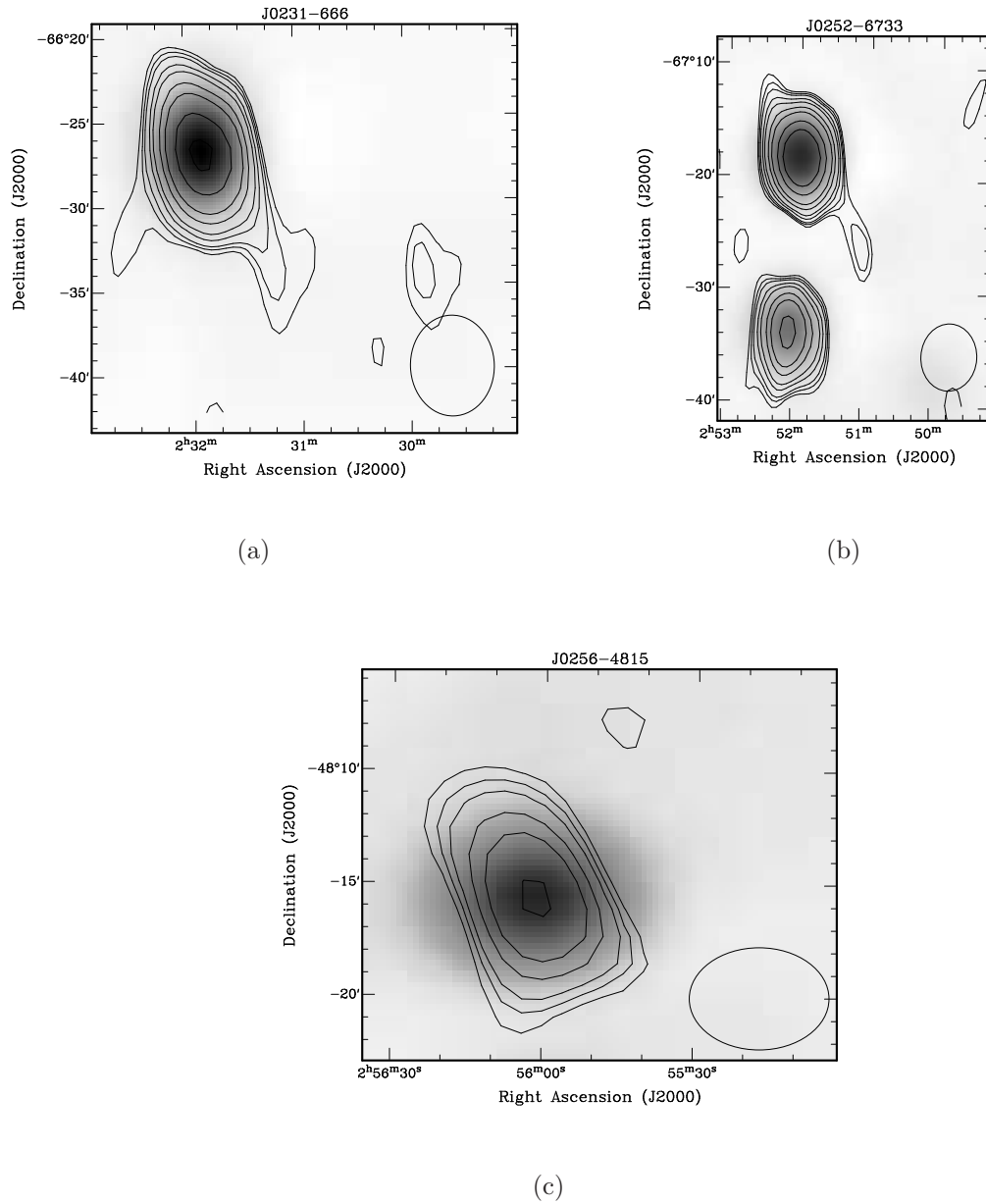
Figure 5.28:   Maximum flux density in each map and lowest contour level (Jy)
(a) J0231-666 10.19 Jy 0.46 Jy
(b) J0252-6733 11.24 Jy 0.46 Jy
(c) J0256-4815 2.54 Jy 0.46 Jy
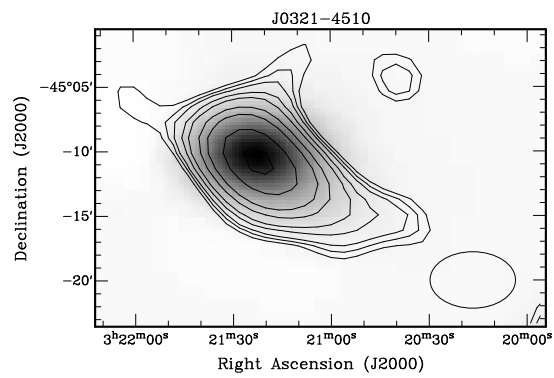
(a)

Figure 5.29:   Maximum flux density in each map and lowest contour level (Jy)
(a) J0321-4510 6.86 Jy 0.408 Jy
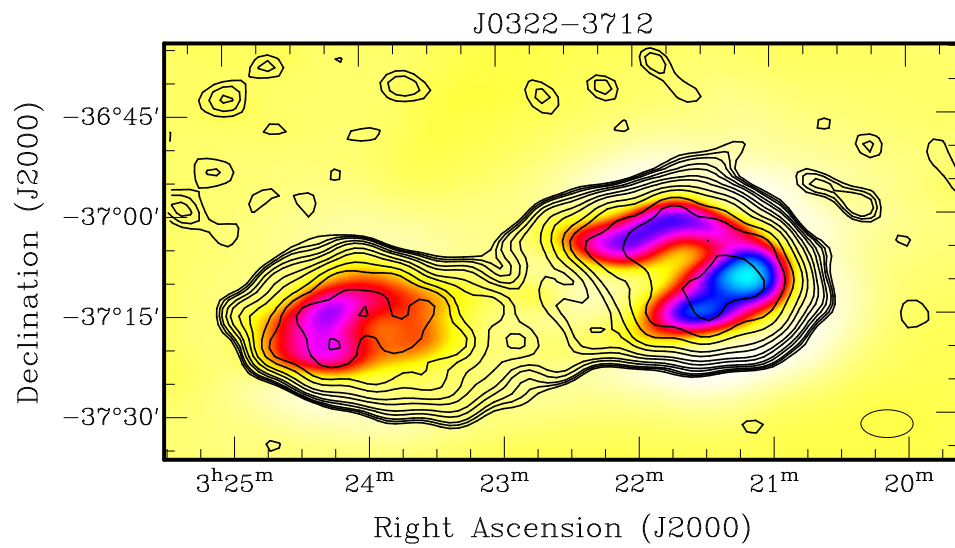
(a)

Figure 5.30:   Maximum flux density in each map and lowest contour level (Jy)
(a) J0322-3712 23.58 Jy 0.408 Jy

(a)

(b)
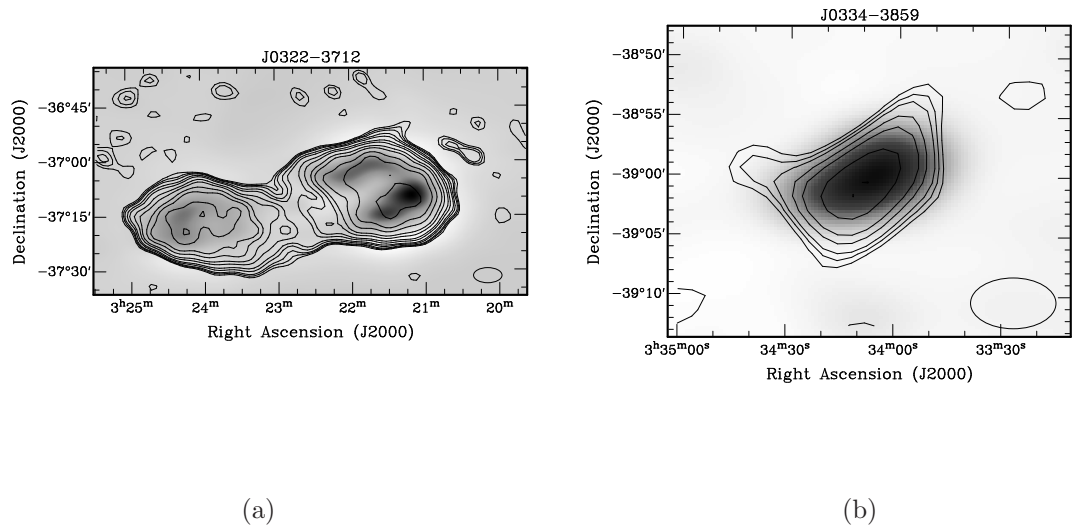
Figure 5.31:   Maximum flux density in each map and lowest contour level (Jy)
(a) J0322-3712 23.58 Jy 0.408 Jy
(b) J0334-3859 3.27 Jy 0.408 Jy
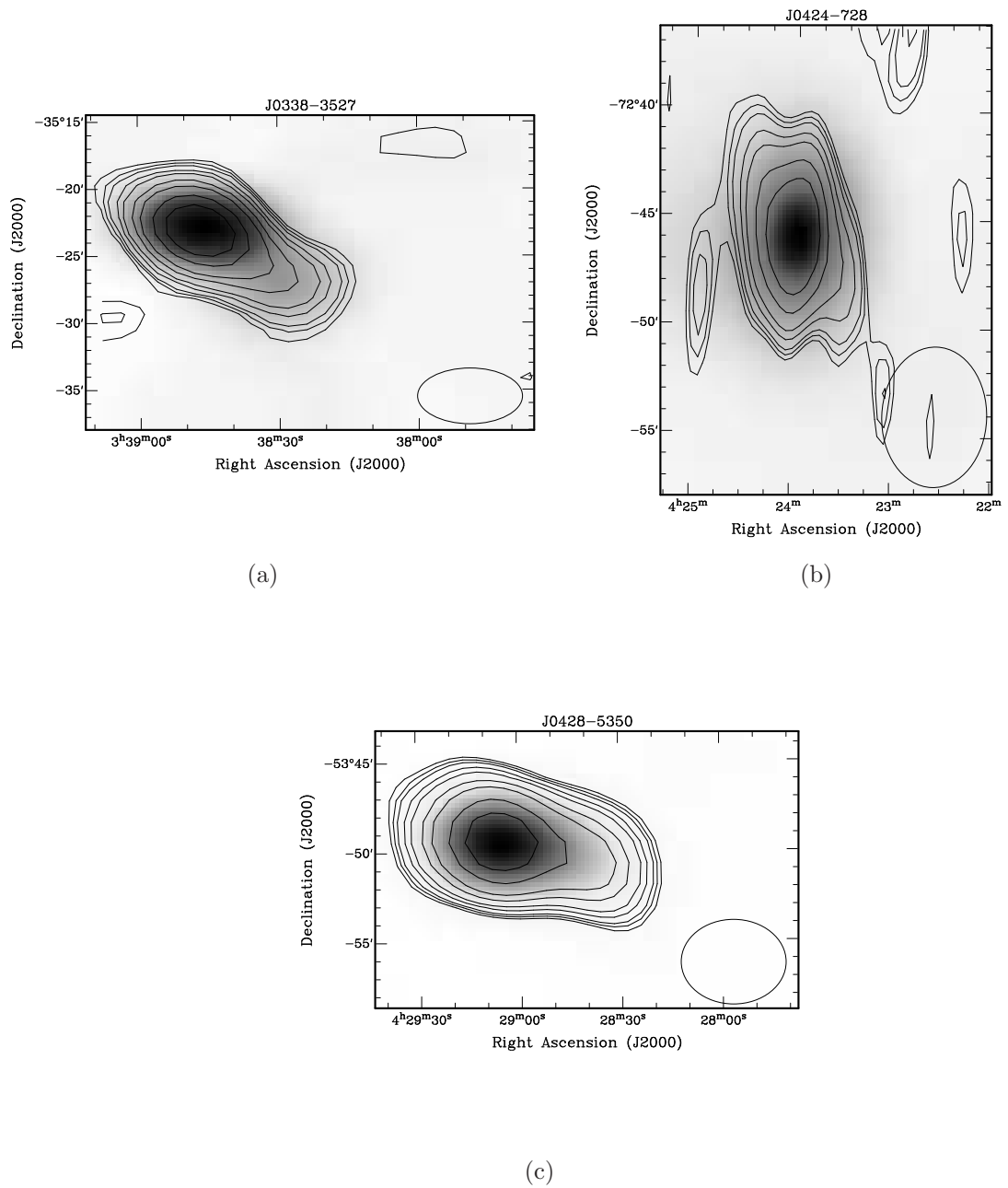
Figure 5.32:   Maximum flux density in each map and lowest contour level (Jy)
(a) J0338-3527 9.29 Jy 0.408 Jy
(b) J0424-728 9.37 Jy 0.822 Jy
(c) J0428-5350 14.58 Jy 0.822 Jy

(a)

(b)

(c)
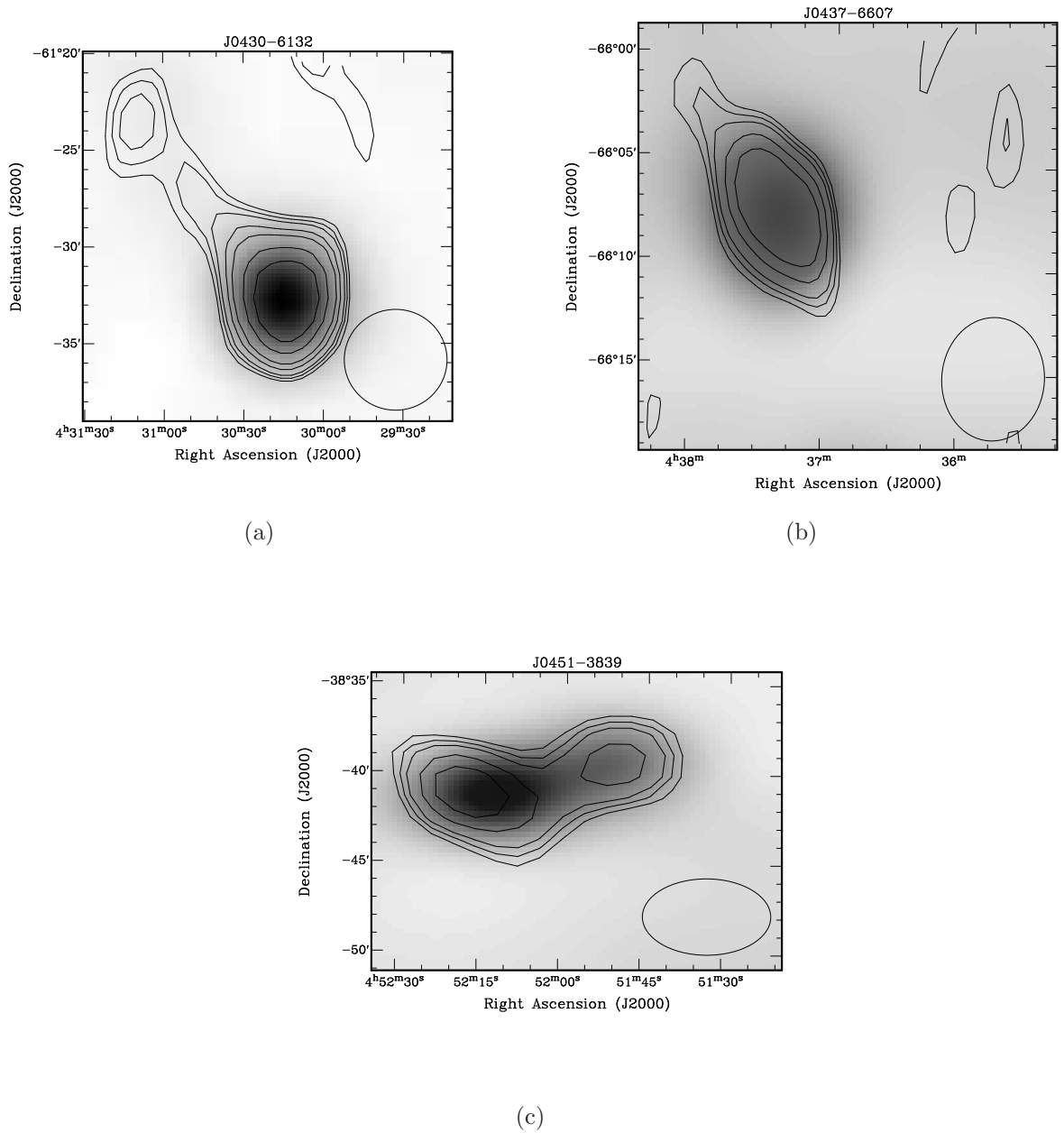
Figure 5.33:   Maximum flux density in each map and lowest contour level (Jy)

(a) J0430-6132 7.27 Jy 0.822 Jy

(b) J0437-6607 3.10 Jy 0.822 Jy

(c) J0451-3839 4.86 Jy 0.684 Jy
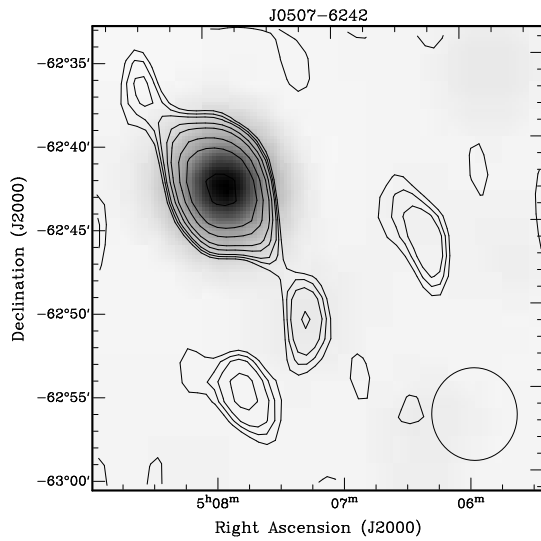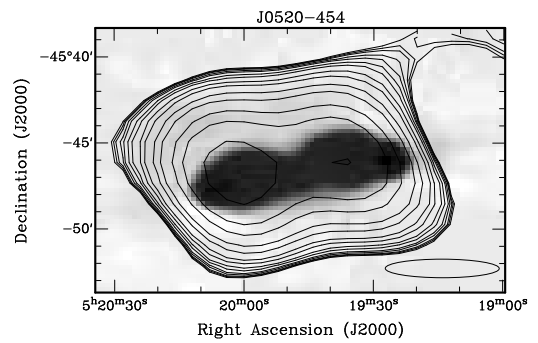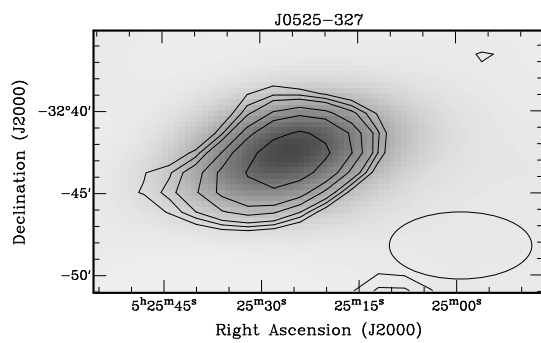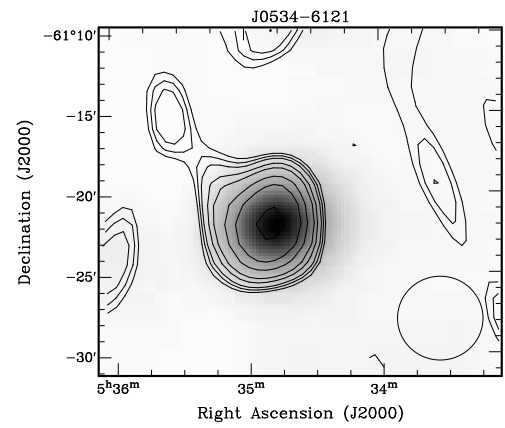
Figure 5.34:   Maximum flux density in each map and lowest contour level (Jy)
(a) J0507-6242 7.12 Jy 0.822 Jy
(b) J0520-454 121.92 Jy 0.684 Jy
(c) J0525-327 5.71 Jy 0.684 Jy
(d) J0534-6121 7.75 Jy 0.822 Jy
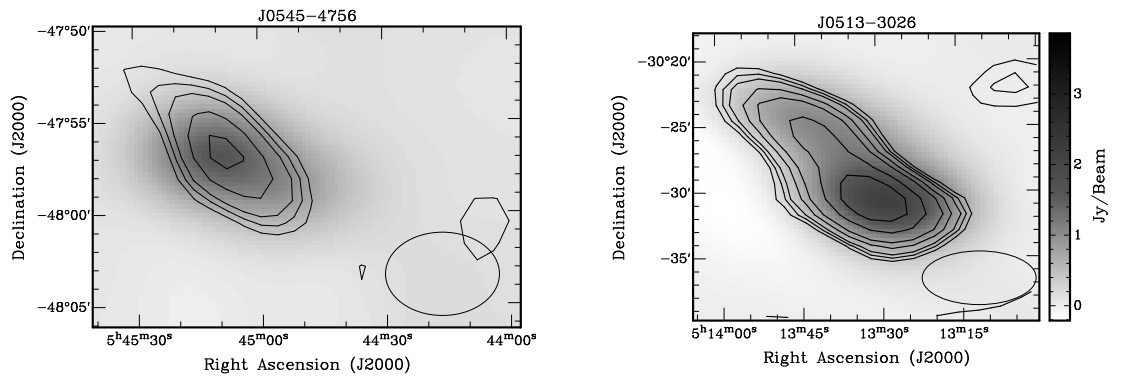
(a)

(b)
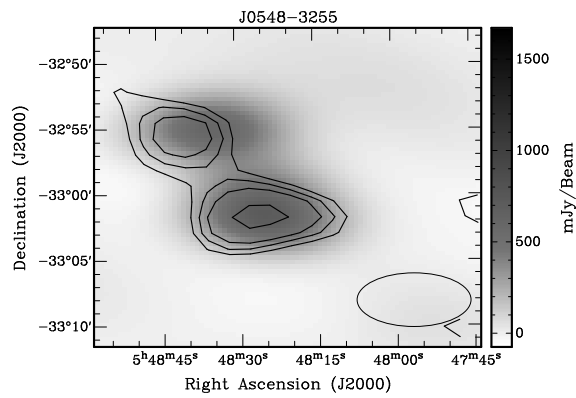
(c)

Figure 5.35:   Maximum flux density in each map and lowest contour level (Jy)
(a) J0545-4756 4.96 Jy 0.684 Jy
(b) J0513-3026 7.04 Jy 0.684 Jy
(c) J0548-3255 2.00 Jy 0.684 Jy

(a)   (b)
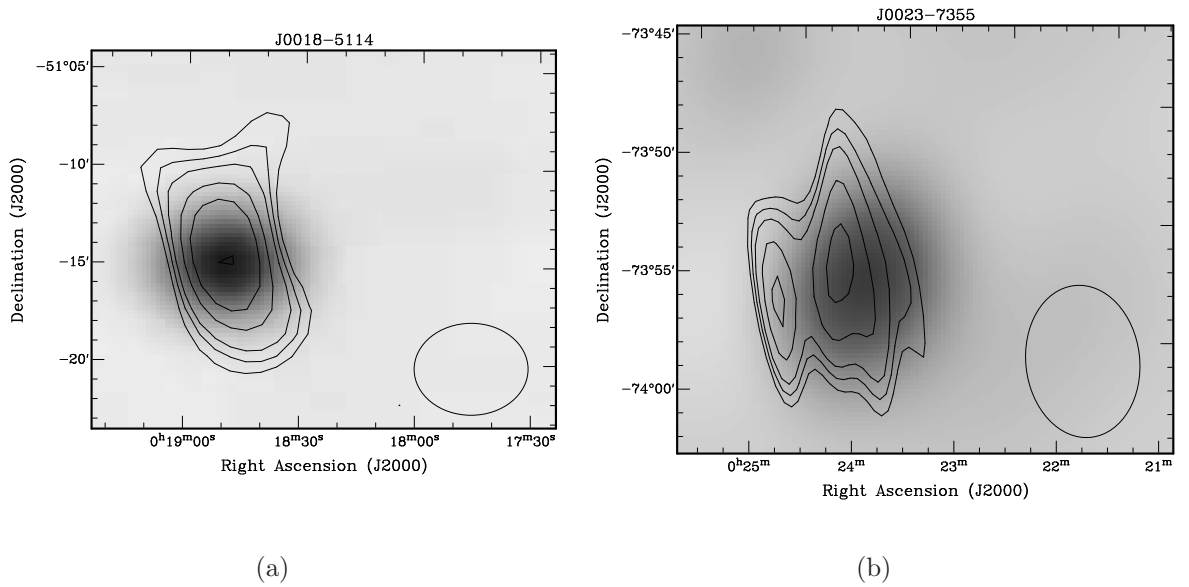
Figure 5.36:   Maximum flux density in each map and lowest contour level (Jy)
(a) J0018-5114 4.41 Jy 0.42 Jy
(b) J0023-7355 2.62 Jy 0.54 Jy
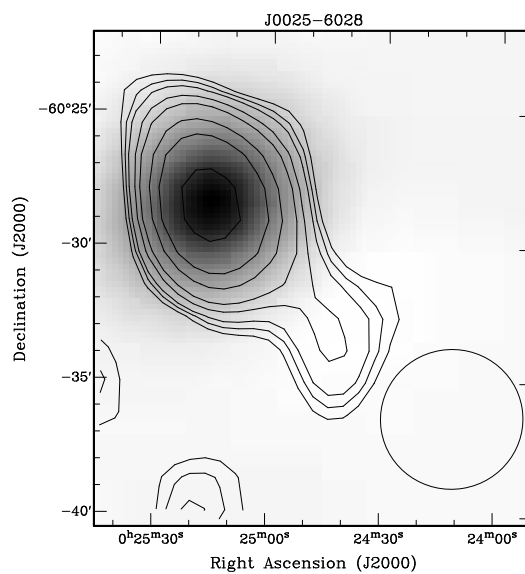
(a)

Figure 5.37:   Maximum flux density in each map and lowest contour level (Jy)
(a) J0025-6028 7.27 Jy 0.46 Jy

(a)

(b)

(c)
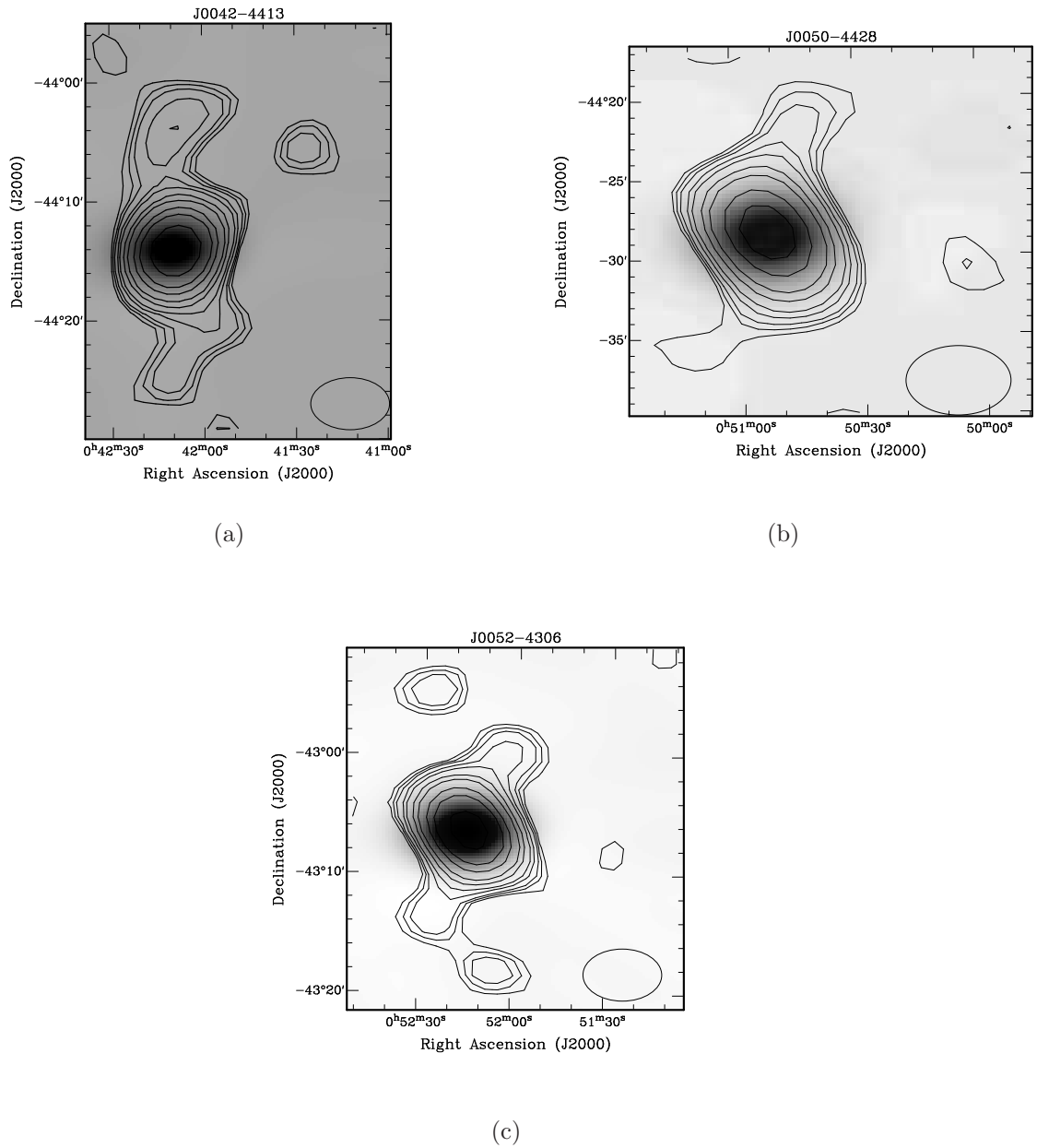
Figure 5.38:   Maximum flux density in each map and lowest contour level (Jy)
(a) J0042-4413 21.48 Jy 0.41 Jy
(b) J0050-4428 12.39 Jy 0.41 Jy
(c) J0052-4306 16.28 Jy 0.41 Jy

(a)

(b)
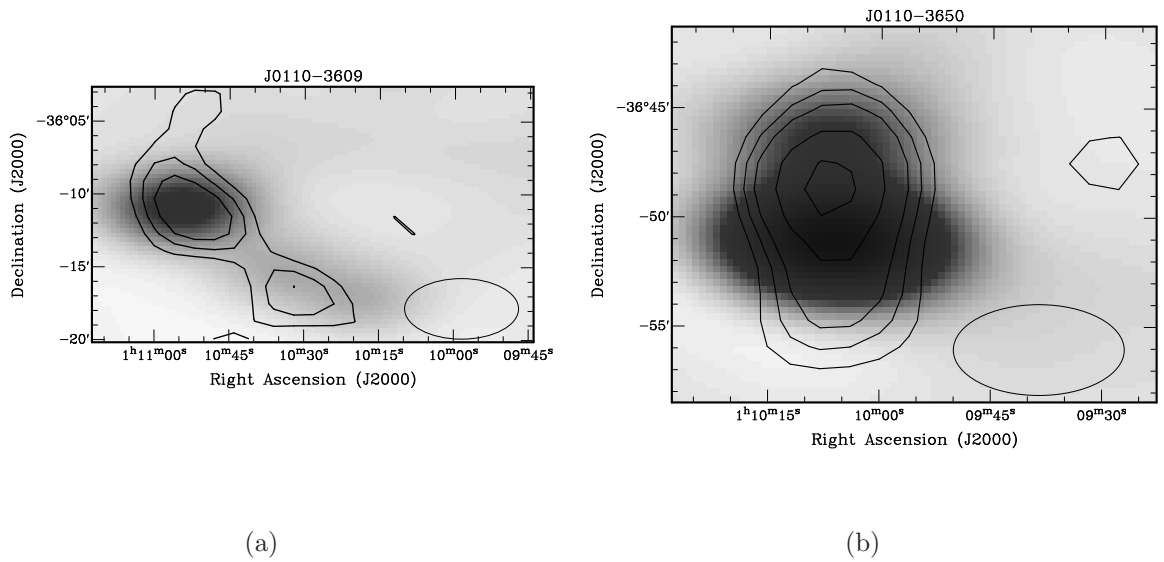
Figure 5.39:   Maximum flux density in each map and lowest contour level (Jy)
(a) J0110-3609 2.20 Jy 0.69 Jy
(b) J0110-3650 3.18 Jy 0.69 Jy
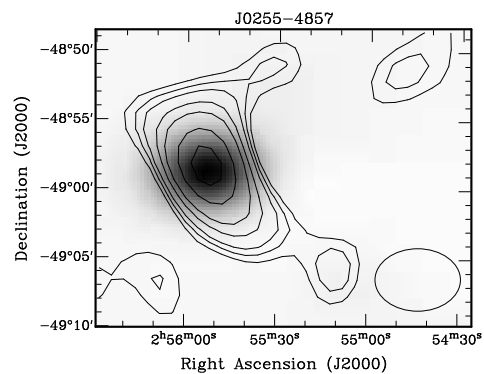
(a)

Figure 5.42:   Maximum flux density in each map and lowest contour level (Jy)
(a) J0255-4857 3.69 Jy 0.408 Jy

(a)

(b)
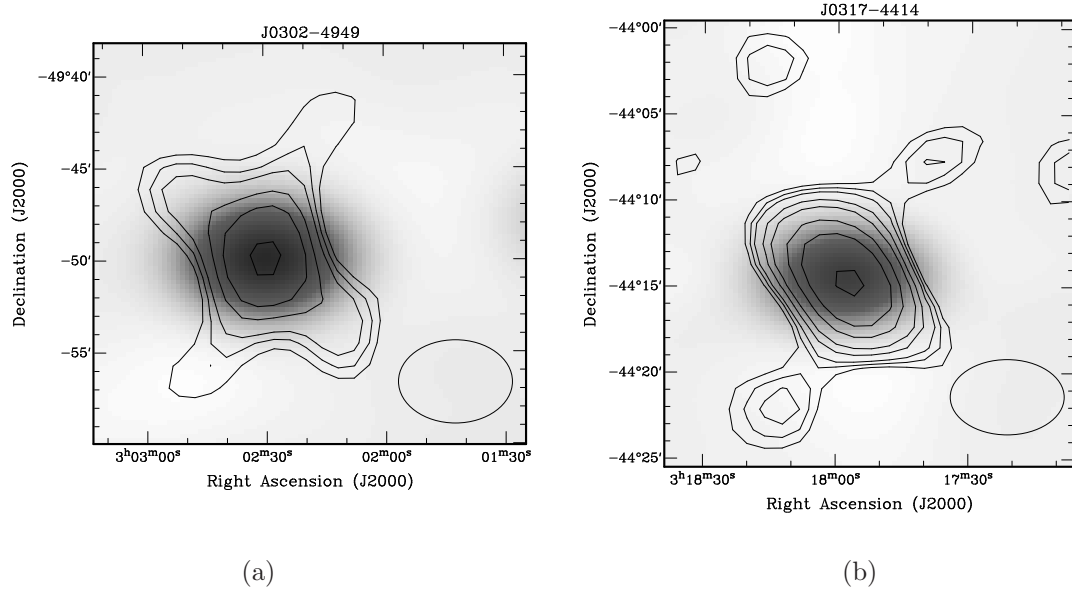
Figure 5.43:   Maximum flux density in each map and lowest contour level (Jy)
(a) J0302-4949 2.61 Jy 0.408 Jy
(b) J0317-4414 5.22 Jy 0.408 Jy

Figure 5.44:   Maximum flux density in each map and lowest contour level (Jy)
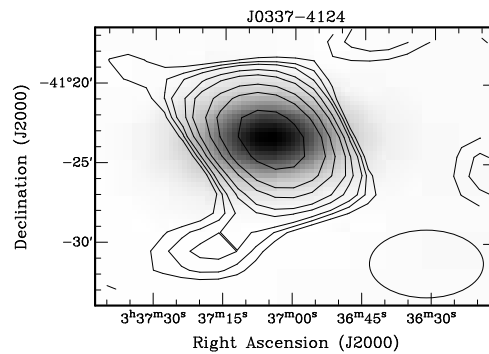
(a)

Figure 5.45:   Maximum flux density in each map and lowest contour level (Jy)
(a) J0337-4124 6.43 Jy 0.408 Jy
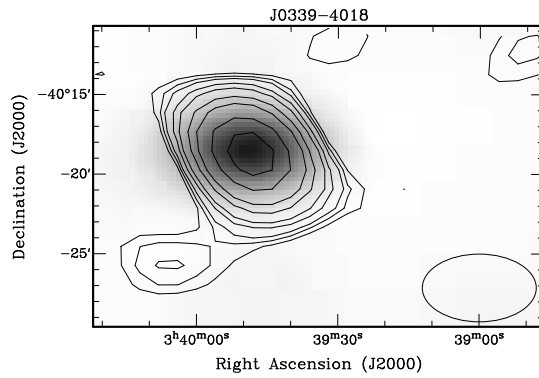
(a)

Figure 5.46:   Maximum flux density in each map and lowest contour level (Jy)
(a) J0339-4018 7.69 Jy 0.408 Jy
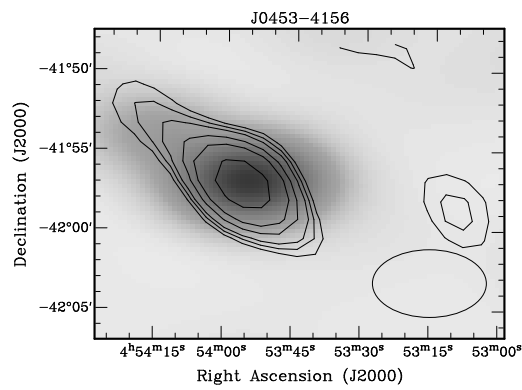
(a)

Figure 5.47:   Maximum flux density in each map and lowest contour level (Jy)
(a) J0453-4156 7.45 Jy 0.684 Jy

Figure 5.48: Contour plot for the range $24^h00^m \leq RA \leq 24^h30^m$, $-75° \leq \delta \leq -70°$. Contour levels are -5.04, -3.6, -2.52, -1.8, -1.08, 1.08, 1.8, 2.52, 3.6, 5.04, 7.2, 10.08, 14.4, 20.16, 28.8, 39.6, 54, 72, 100.8, 136.8, 180, 216, 252, 288 Jy beam^{-1}.
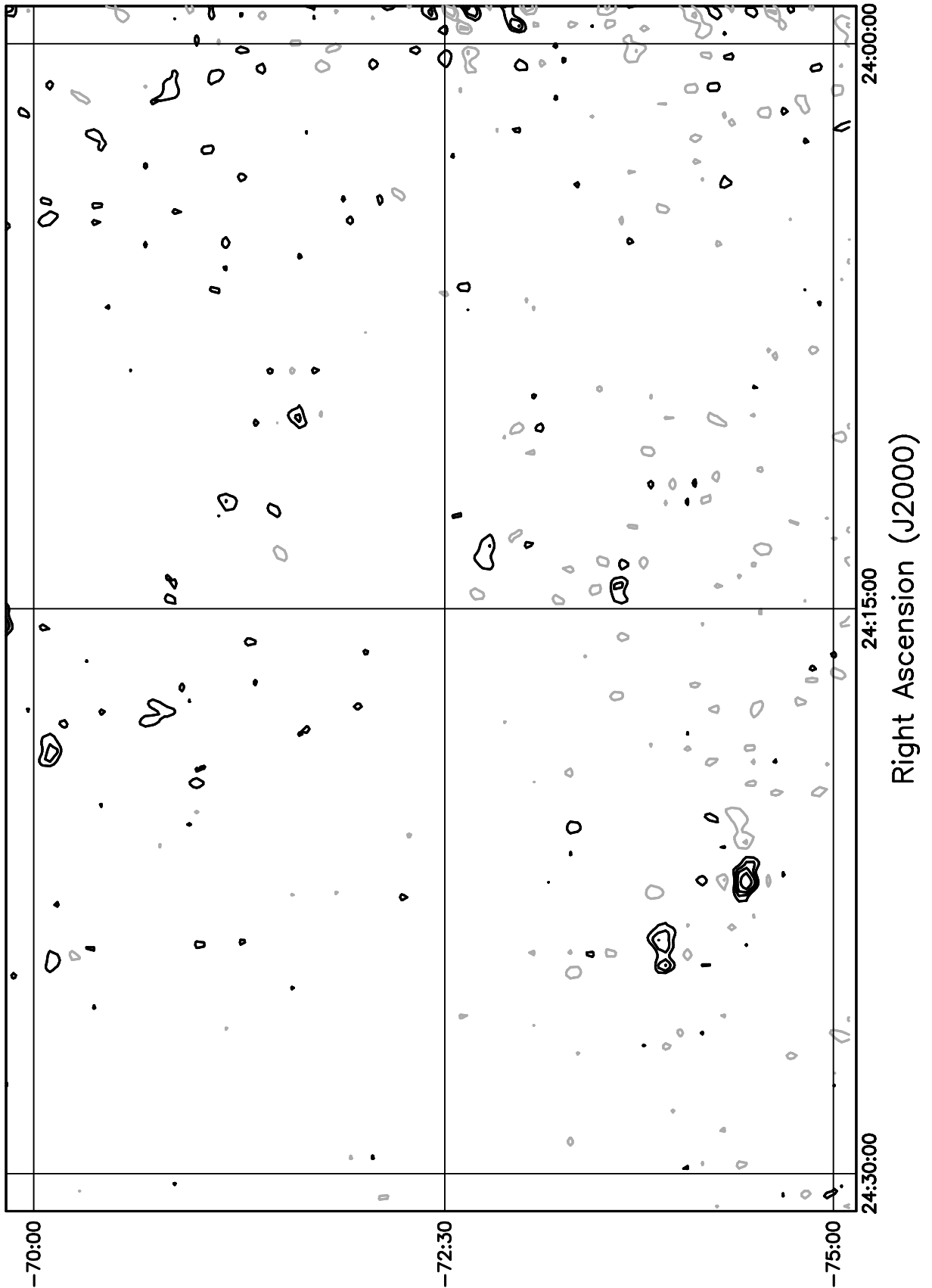
Figure 5.49: Contour plot for the range $24^h00^m \leq RA \leq 24^h30^m$, $-70° \leq \delta \leq -65°$. Contour levels are -5.04, -3.6, -2.52, -1.8, -1.08, 1.08, 1.8, 2.52, 3.6, 5.04, 7.2, 10.08, 14.4, 20.16, 28.8, 39.6, 54, 72, 100.8, 136.8, 180, 216, 252, 288 Jy beam^{-1}.
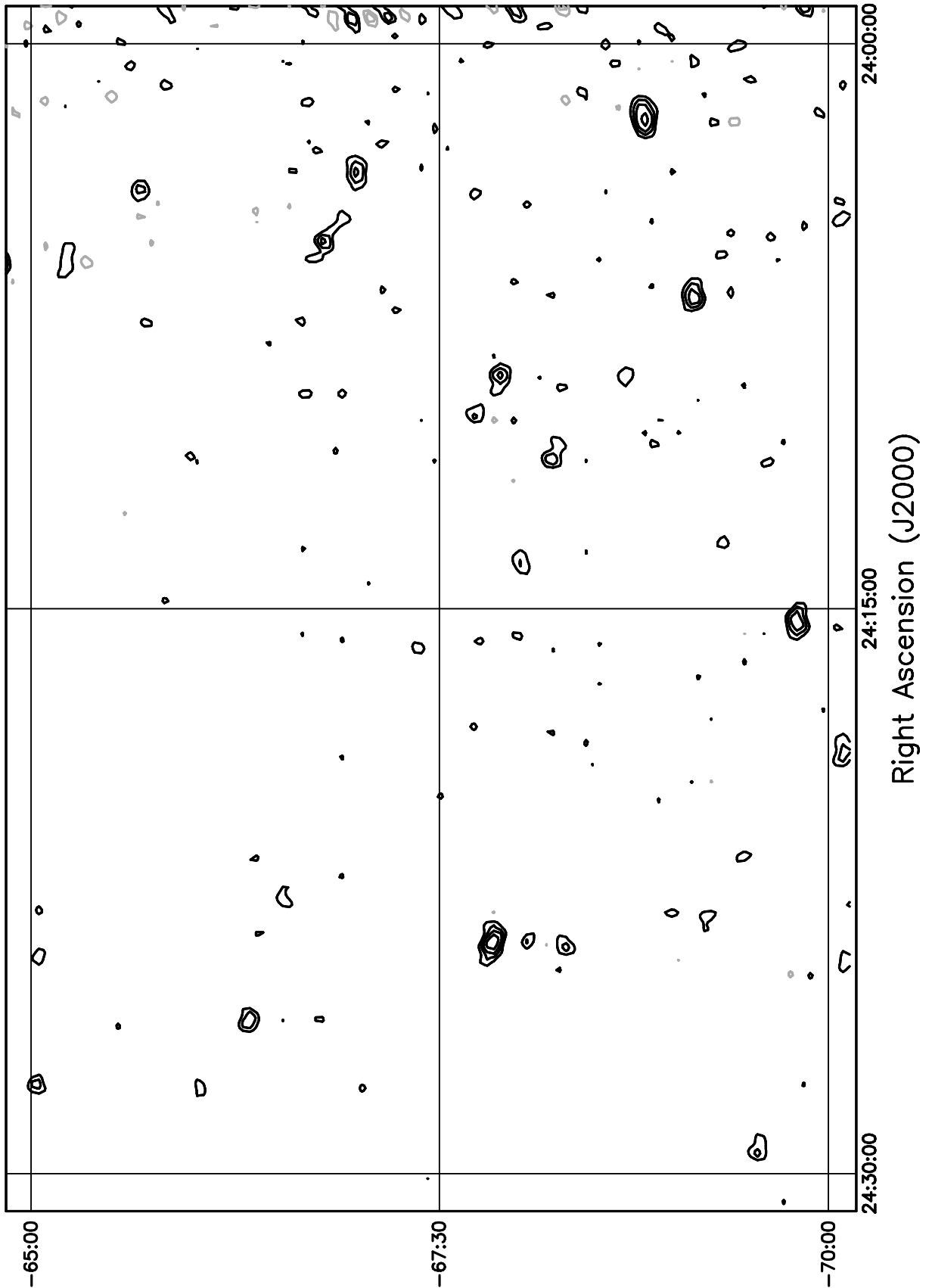
Figure 5.50: Contour plot for the range $24^h00^m \leq RA \leq 24^h30^m$, $-65° \leq \delta \leq -60°$. Contour levels are -5.04, -3.6, -2.52, -1.8, -1.08, 1.08, 1.8, 2.52, 3.6, 5.04, 7.2, 10.08, 14.4, 20.16, 28.8, 39.6, 54, 72, 100.8, 136.8, 180, 216, 252, 288 Jy beam^{-1}.
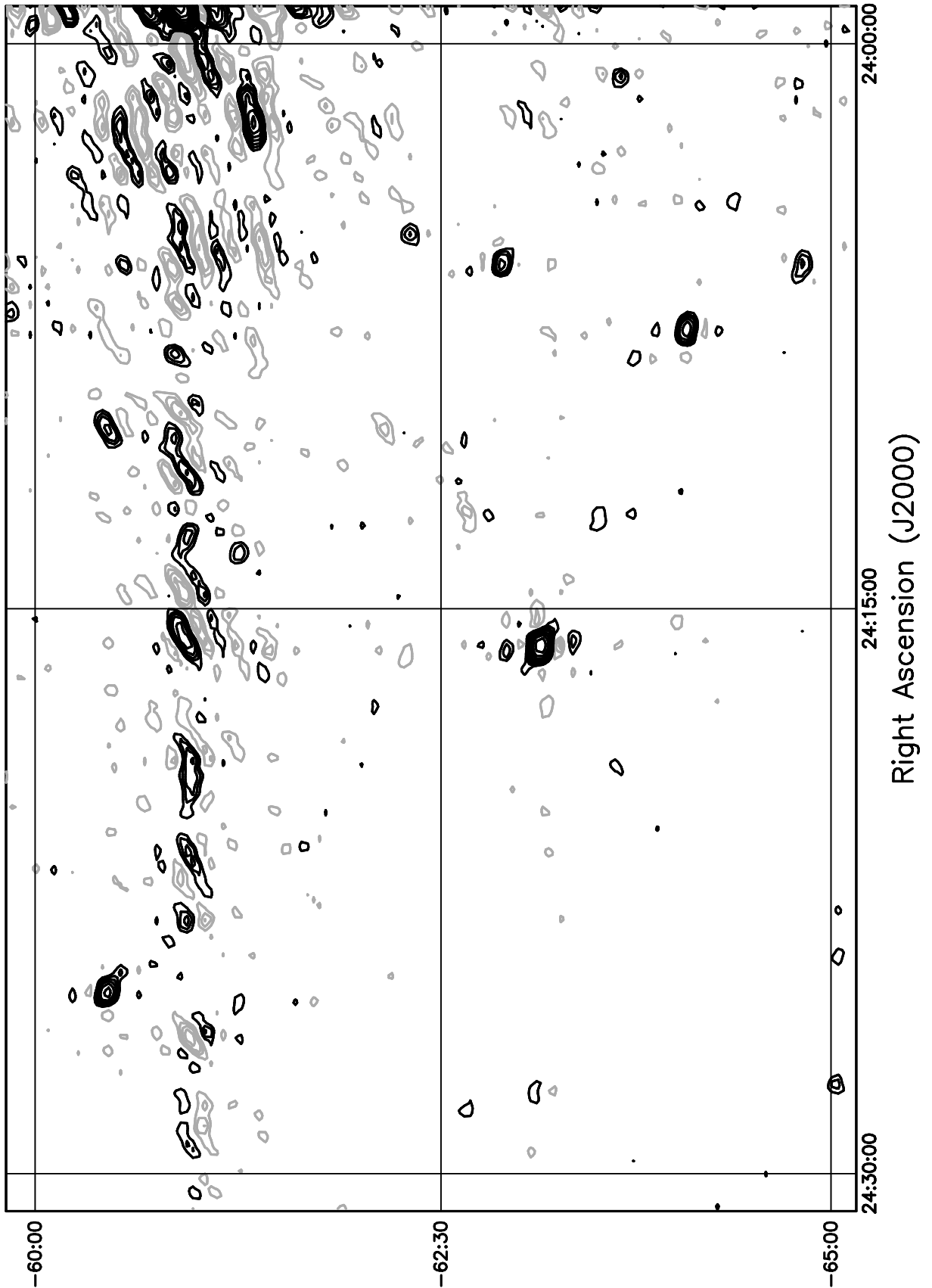
Figure 5.51: Contour plot for the range $24^h00^m \leq RA \leq 24^h30^m$, $-60° \leq \delta \leq -55°$. Contour levels are -5.04, -3.6, -2.52, -1.8, -1.08, 1.08, 1.8, 2.52, 3.6, 5.04, 7.2, 10.08, 14.4, 20.16, 28.8, 39.6, 54, 72, 100.8, 136.8, 180, 216, 252, 288 Jy beam^{-1}.
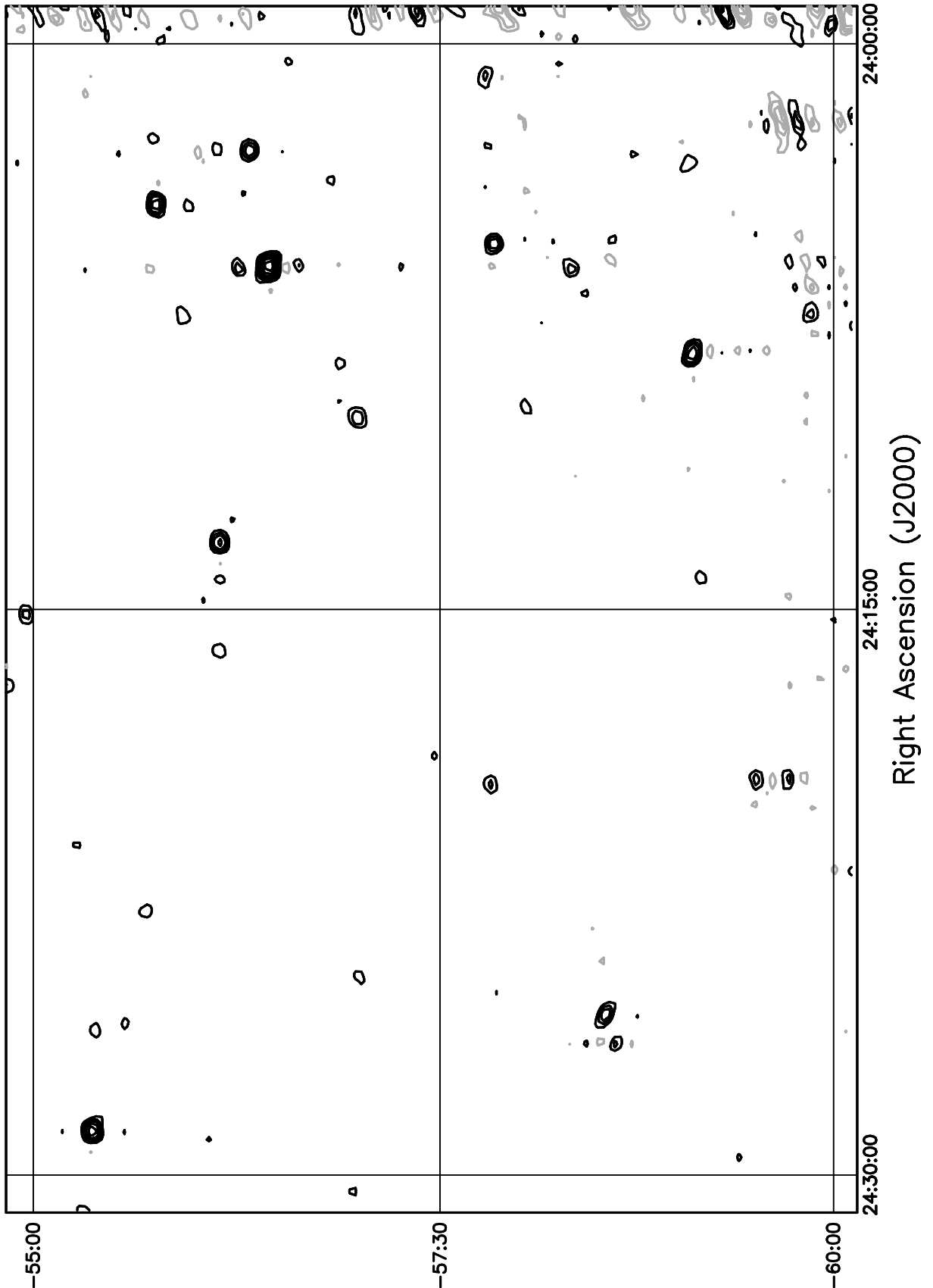
Figure 5.52: Contour plot for the range $24^h00^m \leq RA \leq 24^h30^m$, $-55° \leq \delta \leq -50°$. Contour levels are -5.04, -3.6, -2.52, -1.8, -1.08, 1.08, 1.8, 2.52, 3.6, 5.04, 7.2, 10.08, 14.4, 20.16, 28.8, 39.6, 54, 72, 100.8, 136.8, 180, 216, 252, 288 Jy beam^{-1}.
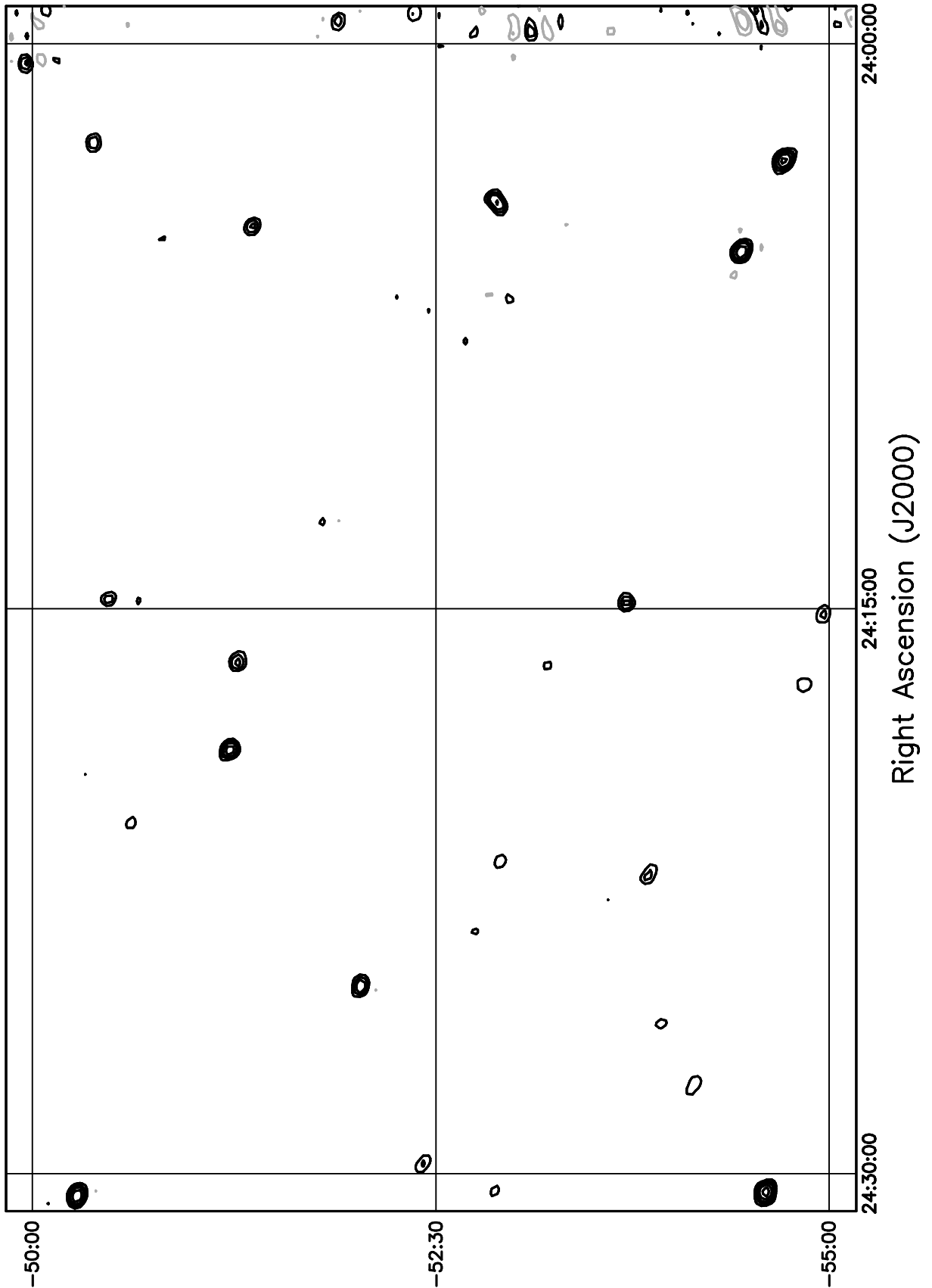
Figure 5.53: Contour plot for the range $24^h00^m \leq RA \leq 24^h30^m$, $-50° \leq \delta \leq -45°$. Contour levels are -5.04, -3.6, -2.52, -1.8, -1.08, 1.08, 1.8, 2.52, 3.6, 5.04, 7.2, 10.08, 14.4, 20.16, 28.8, 39.6, 54, 72, 100.8, 136.8, 180, 216, 252, 288 Jy beam^{-1}.
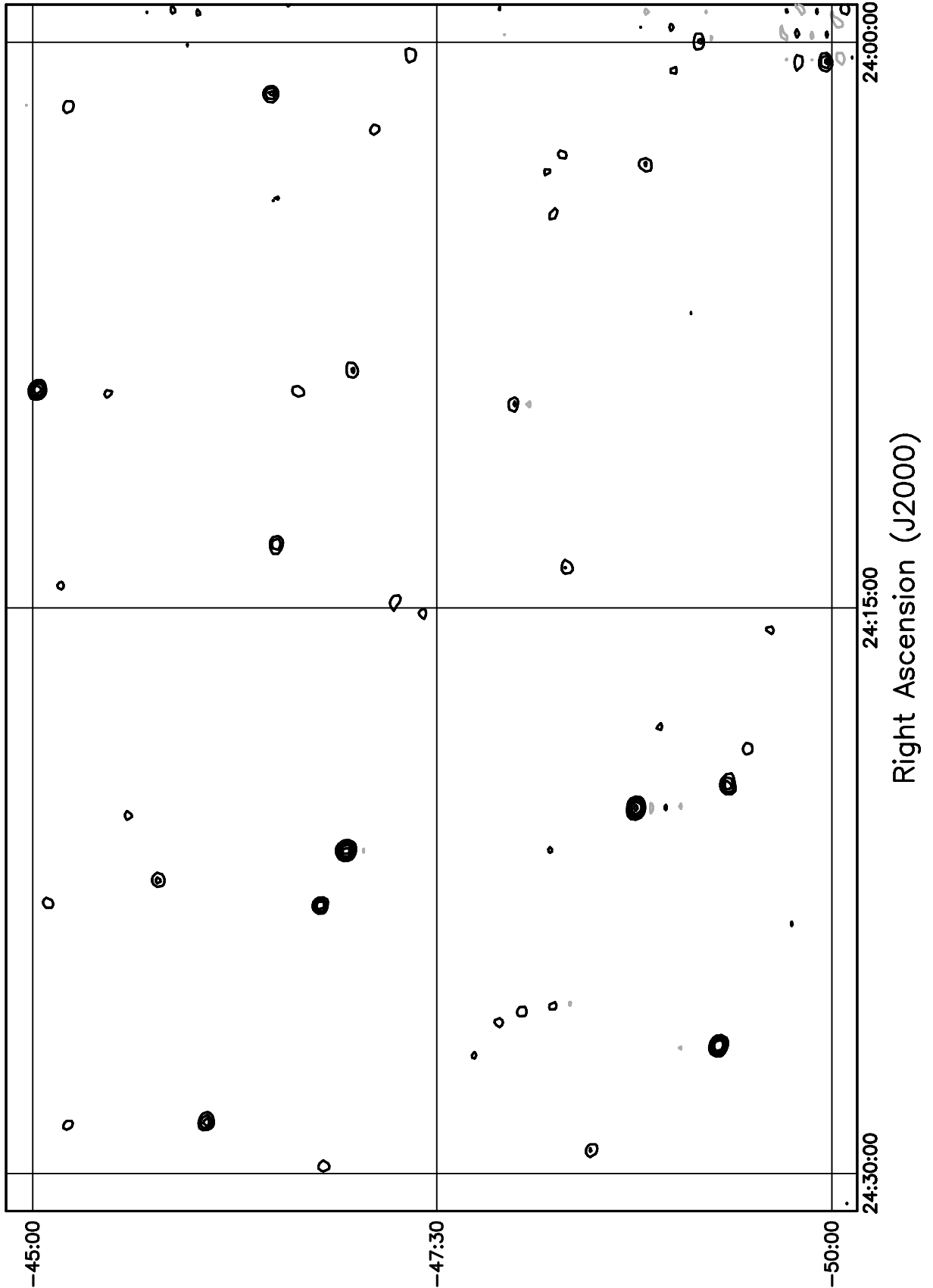
Figure 5.54: Contour plot for the range $24^h00^m \leq RA \leq 24^h30^m$, $-45° \leq \delta \leq -40°$. Contour levels are -5.04, -3.6, -2.52, -1.8, -1.08, 1.08, 1.8, 2.52, 3.6, 5.04, 7.2, 10.08, 14.4, 20.16, 28.8, 39.6, 54, 72, 100.8, 136.8, 180, 216, 252, 288 Jy beam^{-1}.
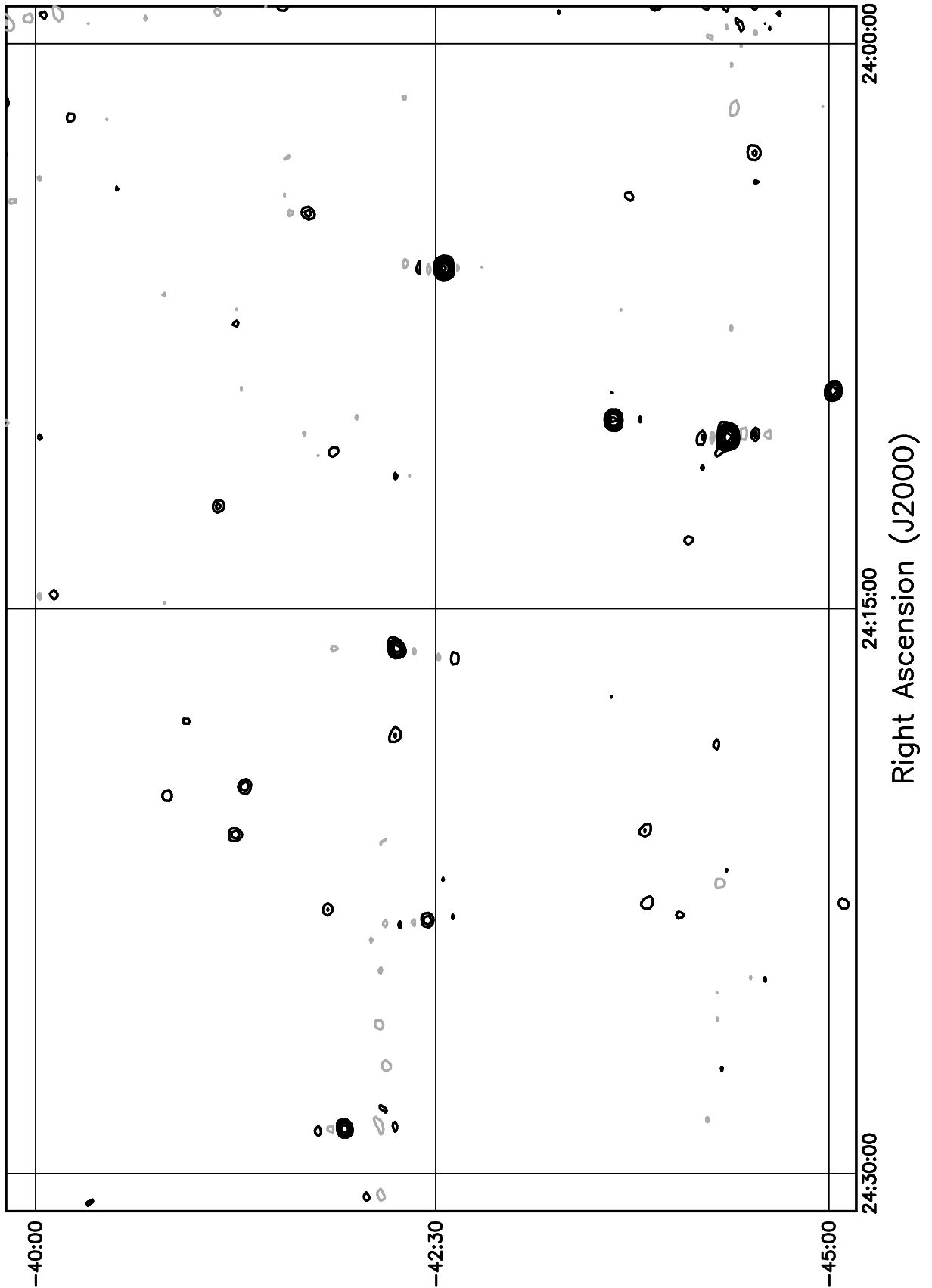
Figure 5.55: Contour plot for the range $24^h00^m \leq RA \leq 24^h30^m$, $-40° \leq \delta \leq -35°$. Contour levels are -5.04, -3.6, -2.52, -1.8, -1.08, 1.08, 1.8, 2.52, 3.6, 5.04, 7.2, 10.08, 14.4, 20.16, 28.8, 39.6, 54, 72, 100.8, 136.8, 180, 216, 252, 288 Jy beam^{-1}.

Right Ascension (J2000)
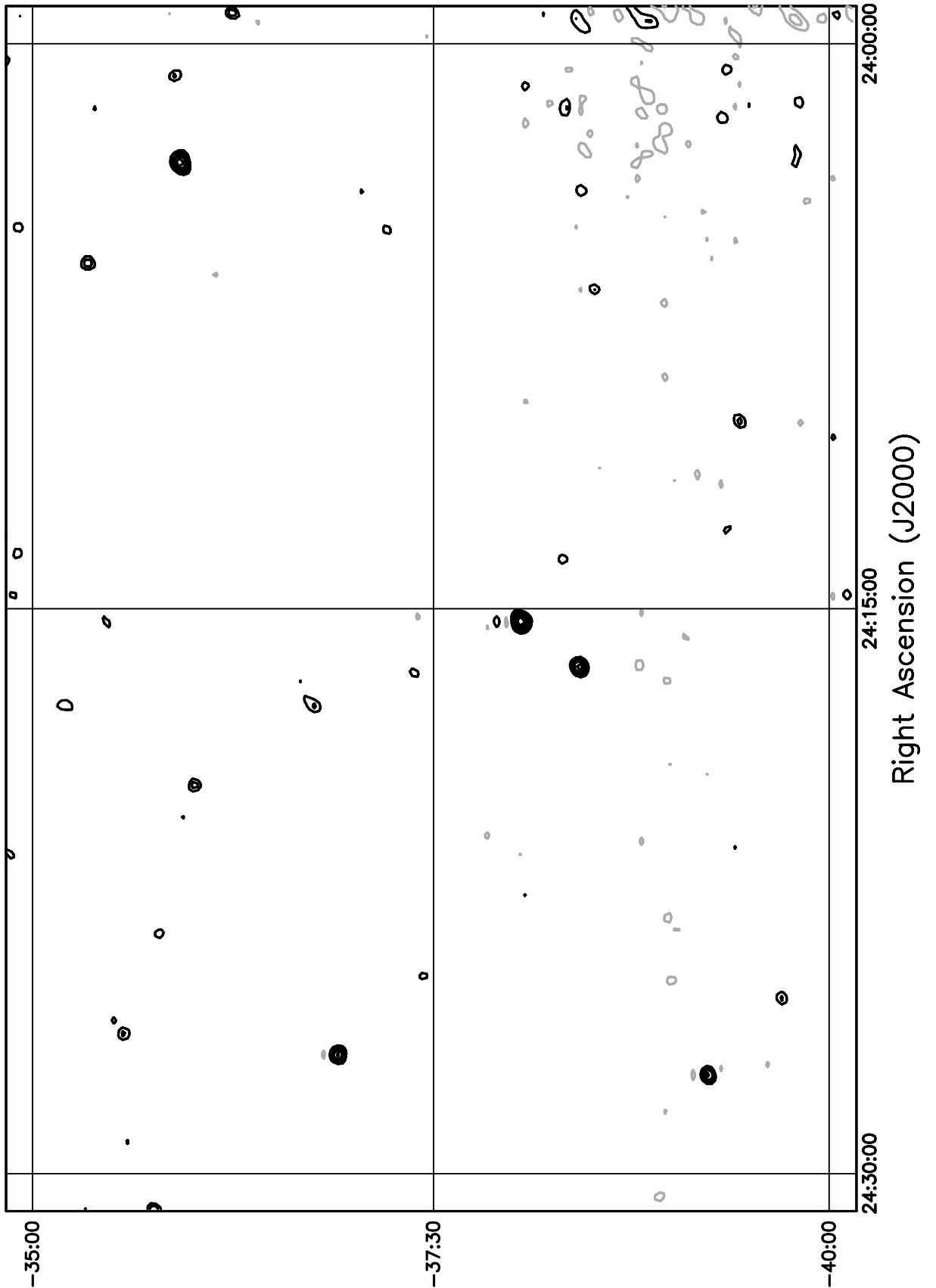
Figure 5.56: Contour plot for the range $24^h00^m \leq RA \leq 24^h30^m$, $-35° \leq \delta \leq -30°$. Contour levels are -5.04, -3.6, -2.52, -1.8, -1.08, 1.08, 1.8, 2.52, 3.6, 5.04, 7.2, 10.08, 14.4, 20.16, 28.8, 39.6, 54, 72, 100.8, 136.8, 180, 216, 252, 288 Jy beam^{-1}.
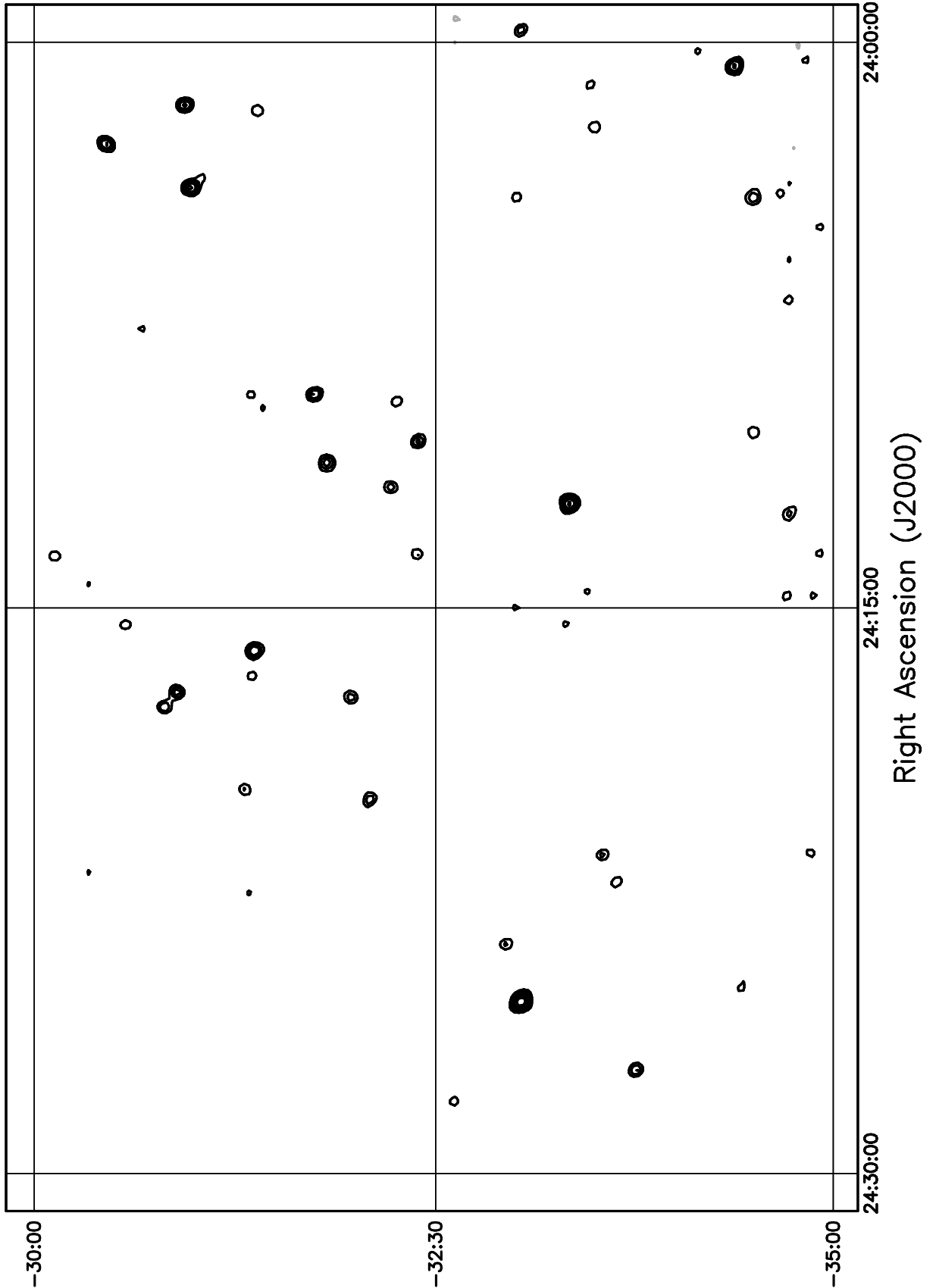
Figure 5.57: Contour plot for the range $24^h00^m \leq RA \leq 24^h30^m$, $-30° \leq \delta \leq -25°$. Contour levels are -5.04, -3.6, -2.52, -1.8, -1.08, 1.08, 1.8, 2.52, 3.6, 5.04, 7.2, 10.08, 14.4, 20.16, 28.8, 39.6, 54, 72, 100.8, 136.8, 180, 216, 252, 288 Jy beam^{-1}.
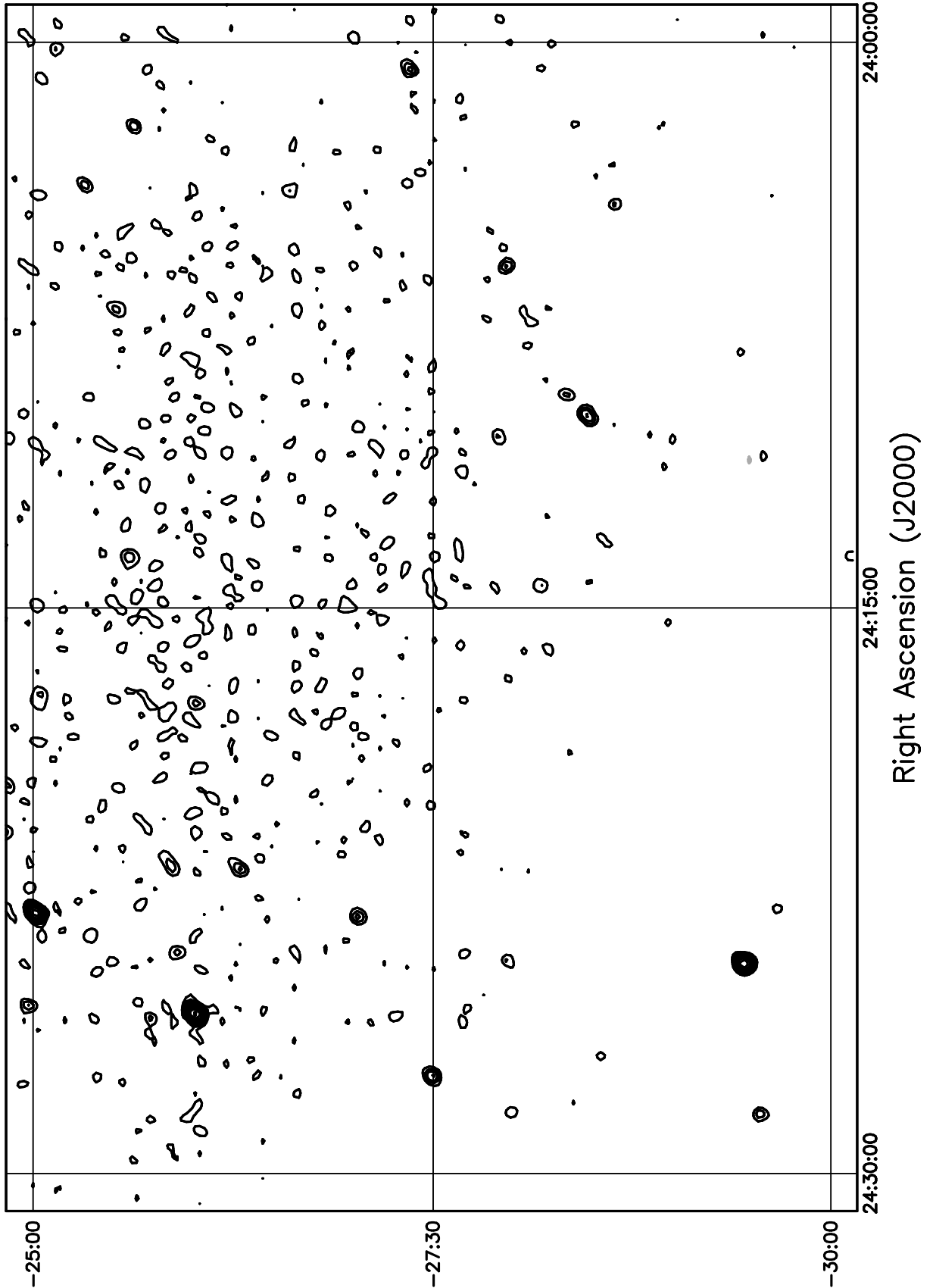
Figure 5.58: Contour plot for the range $24^h00^m \leq RA \leq 24^h30^m$, $-25° \leq \delta \leq -20°$. Contour levels are -5.04, -3.6, -2.52, -1.8, -1.08, 1.08, 1.8, 2.52, 3.6, 5.04, 7.2, 10.08, 14.4, 20.16, 28.8, 39.6, 54, 72, 100.8, 136.8, 180, 216, 252, 288 Jy beam^{-1}.
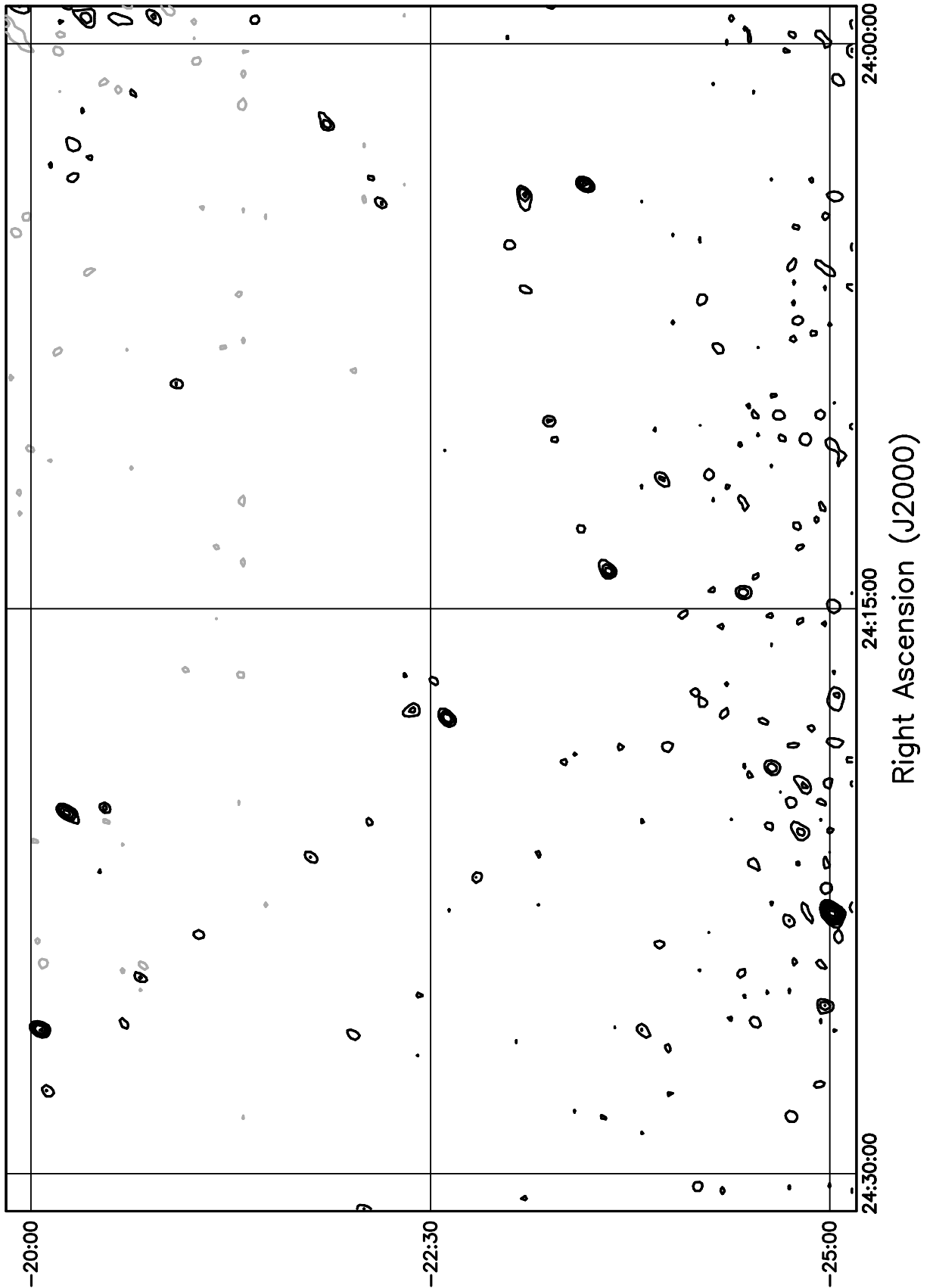
Figure 5.59: Contour plot for the range $24^h00^m \leq RA \leq 24^h30^m$, $-20° \leq \delta \leq -15°$. Contour levels are -5.04, -3.6, -2.52, -1.8, -1.08, 1.08, 1.8, 2.52, 3.6, 5.04, 7.2, 10.08, 14.4, 20.16, 28.8, 39.6, 54, 72, 100.8, 136.8, 180, 216, 252, 288 Jy beam^{-1}.
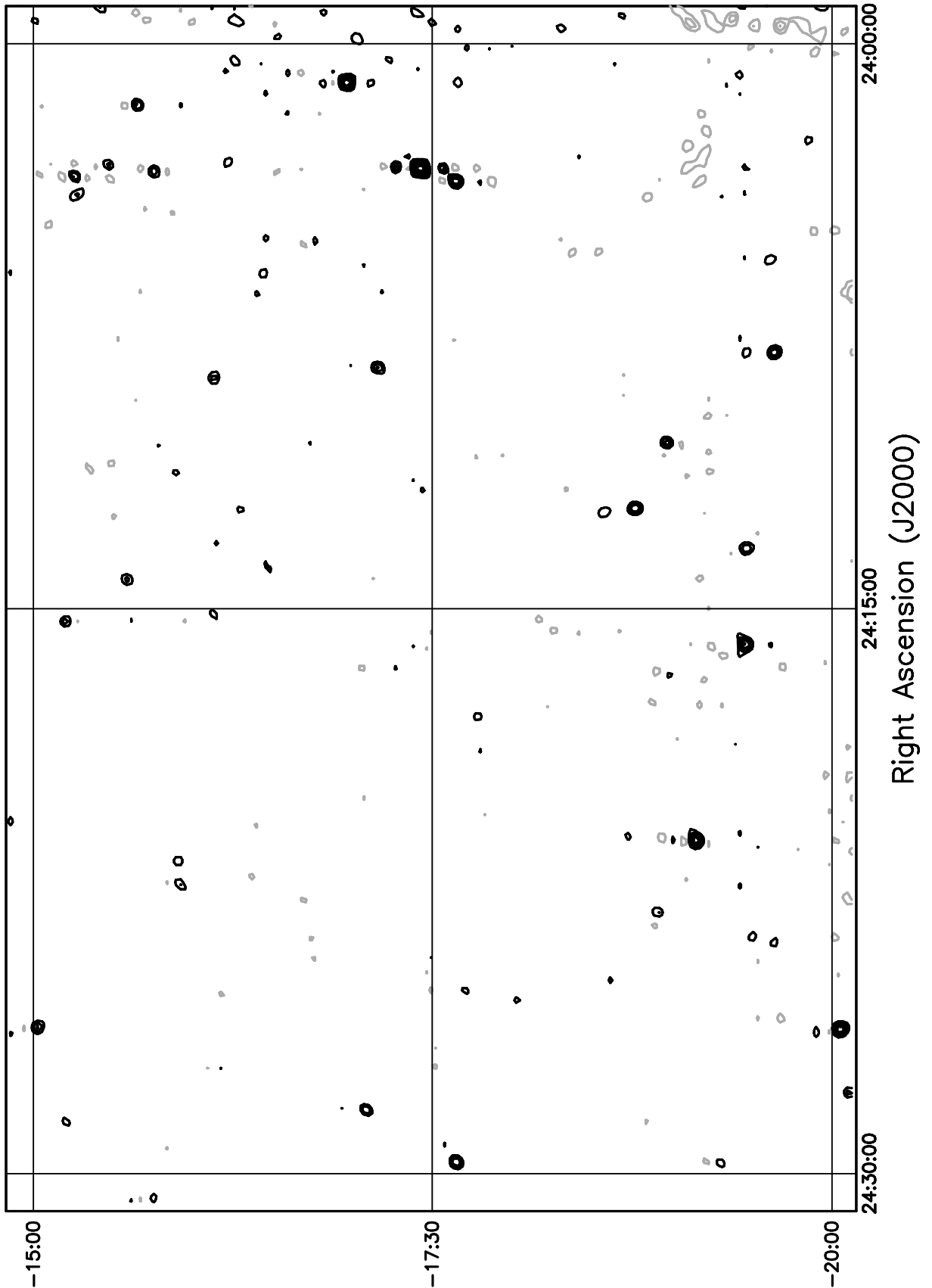
Figure 5.60: Contour plot for the range $24^h00^m \leq RA \leq 24^h30^m$, $-15° \leq \delta \leq -10°$. Contour levels are -5.04, -3.6, -2.52, -1.8, -1.08, 1.08, 1.8, 2.52, 3.6, 5.04, 7.2, 10.08, 14.4, 20.16, 28.8, 39.6, 54, 72, 100.8, 136.8, 180, 216, 252, 288 Jy beam^{-1}.
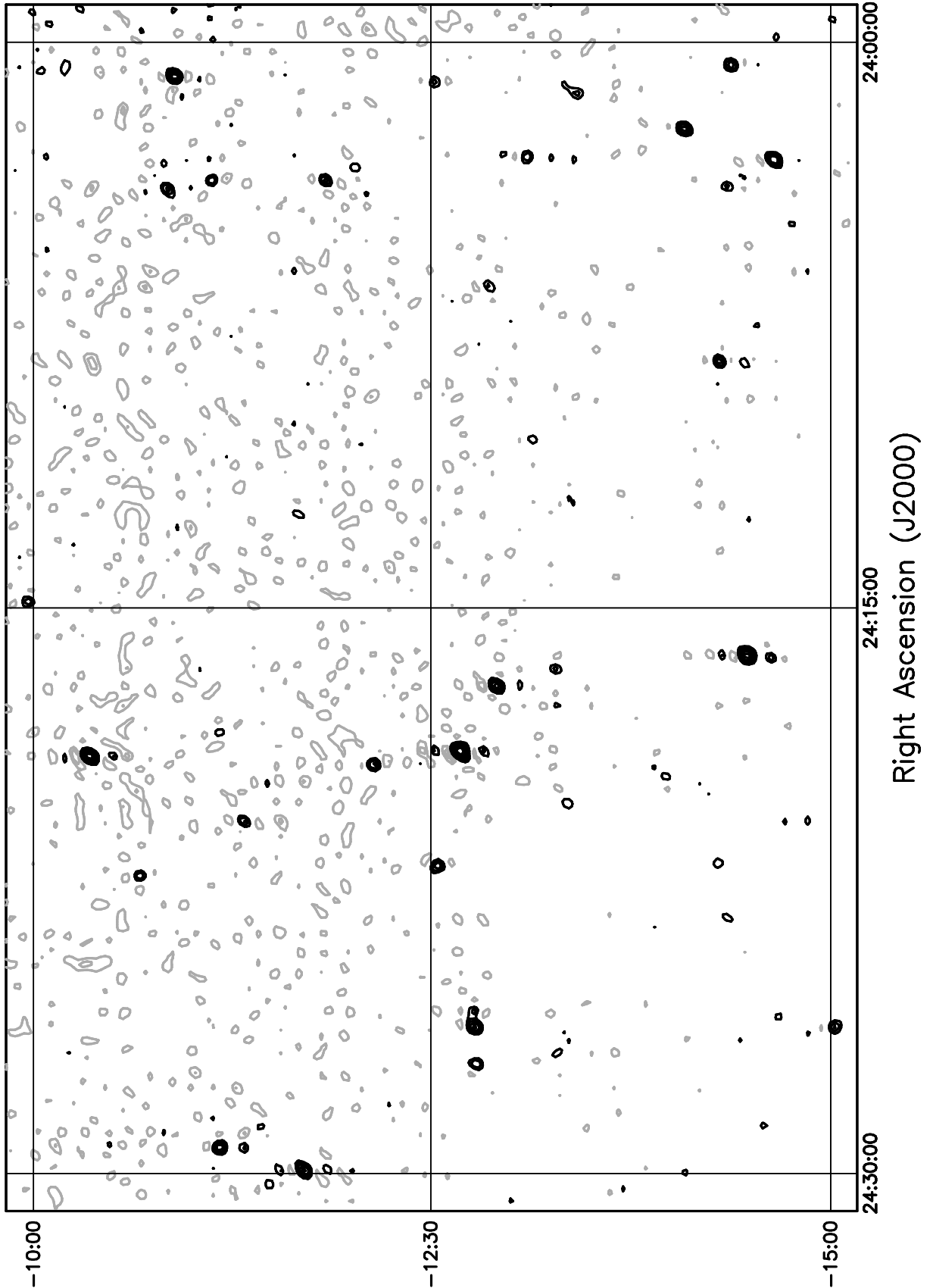
Figure 5.61: Contour plot for the range $24^h30^m \leq RA \leq 25^h00^m$, $-75° \leq \delta \leq -70°$. Contour levels are -5.04, -3.6, -2.52, -1.8, -1.08, 1.08, 1.8, 2.52, 3.6, 5.04, 7.2, 10.08, 14.4, 20.16, 28.8, 39.6, 54, 72, 100.8, 136.8, 180, 216, 252, 288 Jy beam^{-1}.
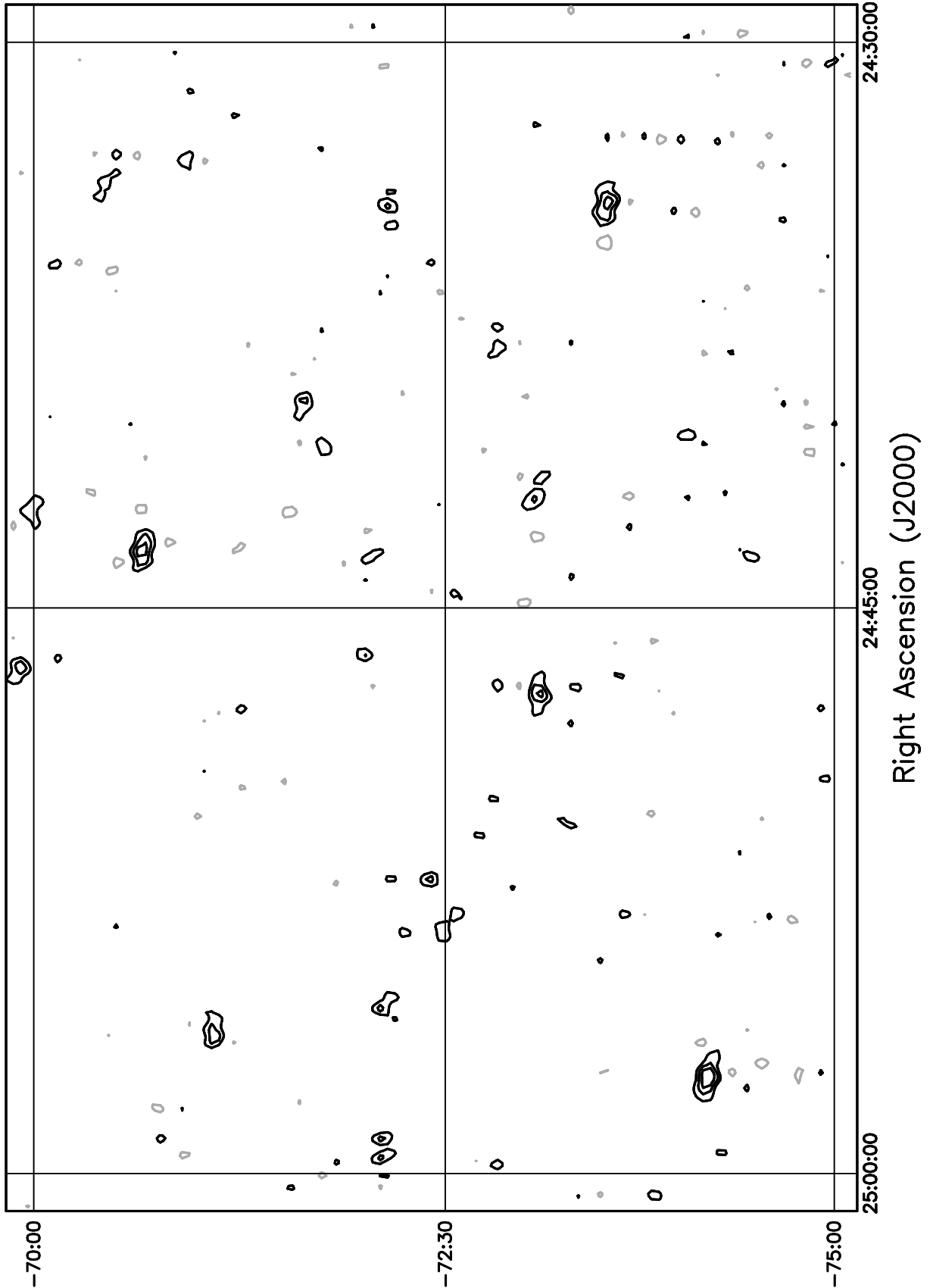
Figure 5.62: Contour plot for the range $24^h30^m \leq RA \leq 25^h00^m$, $-70° \leq \delta \leq -65°$. Contour levels are -5.04, -3.6, -2.52, -1.8, -1.08, 1.08, 1.8, 2.52, 3.6, 5.04, 7.2, 10.08, 14.4, 20.16, 28.8, 39.6, 54, 72, 100.8, 136.8, 180, 216, 252, 288 Jy beam^{-1}.
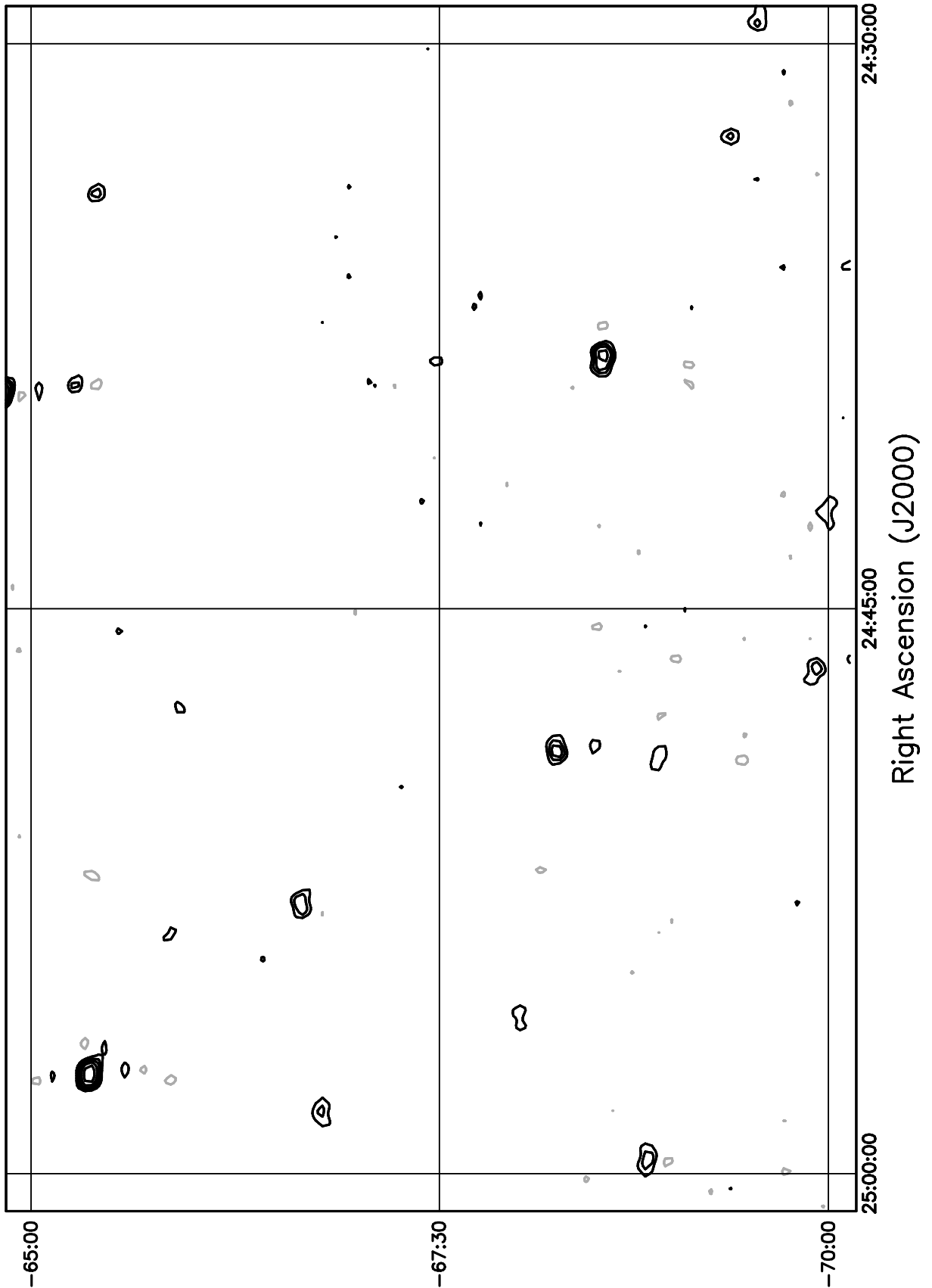
Figure 5.63: Contour plot for the range $24^h30^m \leq RA \leq 25^h00^m$, $-65° \leq \delta \leq -60°$. Contour levels are -5.04, -3.6, -2.52, -1.8, -1.08, 1.08, 1.8, 2.52, 3.6, 5.04, 7.2, 10.08, 14.4, 20.16, 28.8, 39.6, 54, 72, 100.8, 136.8, 180, 216, 252, 288 Jy beam^{-1}.


Right Ascension (J2000)
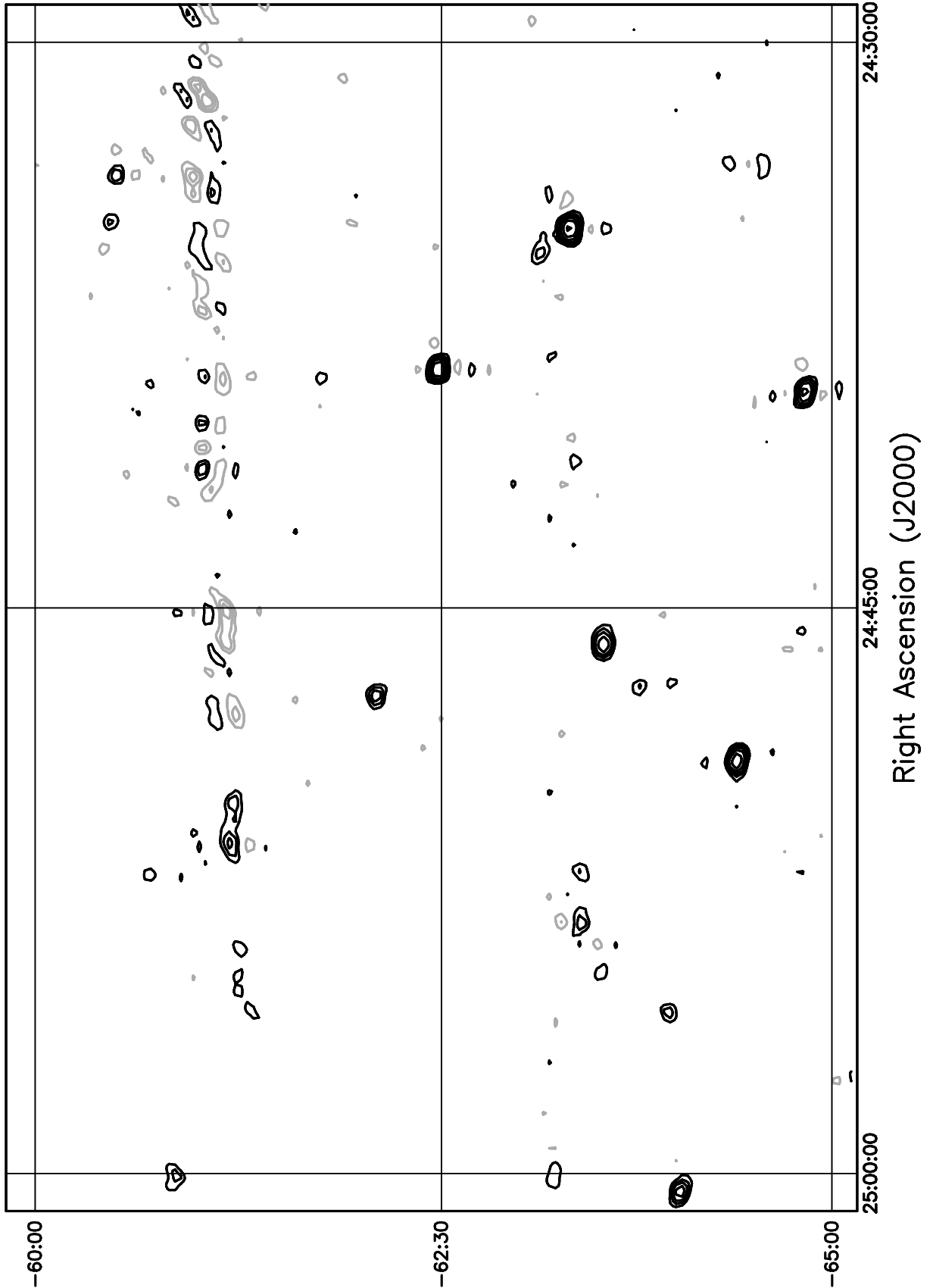
Figure 5.64: Contour plot for the range $24^h30^m \leq RA \leq 25^h00^m$, $-60° \leq \delta \leq -55°$. Contour levels are -5.04, -3.6, -2.52, -1.8, -1.08, 1.08, 1.8, 2.52, 3.6, 5.04, 7.2, 10.08, 14.4, 20.16, 28.8, 39.6, 54, 72, 100.8, 136.8, 180, 216, 252, 288 Jy beam^{-1}.
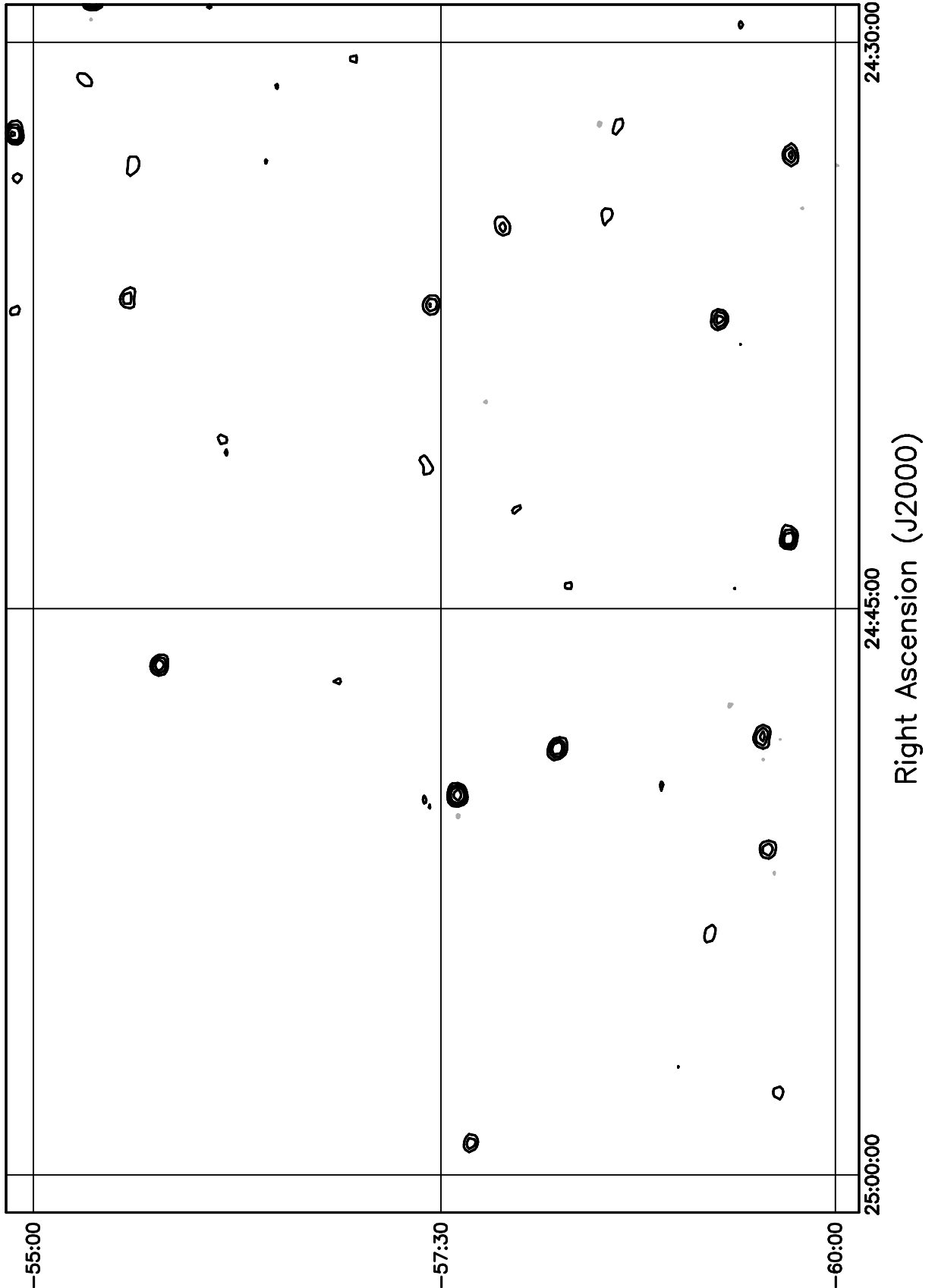
Figure 5.65: Contour plot for the range $24^h30^m \leq RA \leq 25^h00^m$, $-55° \leq \delta \leq -50°$. Contour levels are -5.04, -3.6, -2.52, -1.8, -1.08, 1.08, 1.8, 2.52, 3.6, 5.04, 7.2, 10.08, 14.4, 20.16, 28.8, 39.6, 54, 72, 100.8, 136.8, 180, 216, 252, 288 Jy beam^{-1}.


Right Ascension (J2000)
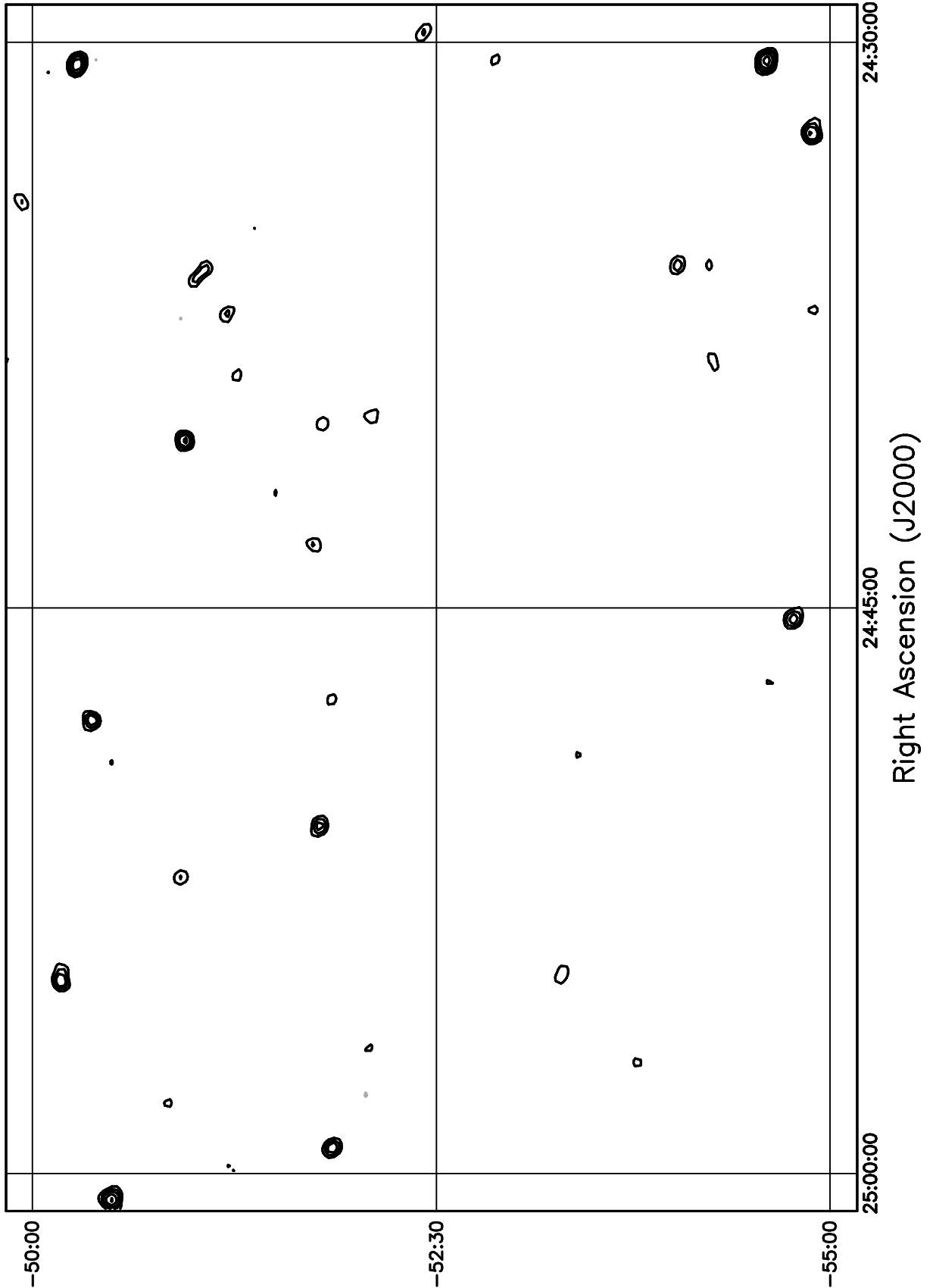
Figure 5.66: Contour plot for the range $24^h 30^m \leq RA \leq 25^h 00^m$, $-50° \leq \delta \leq -45°$. Contour levels are -5.04, -3.6, -2.52, -1.8, -1.08, 1.08, 1.8, 2.52, 3.6, 5.04, 7.2, 10.08, 14.4, 20.16, 28.8, 39.6, 54, 72, 100.8, 136.8, 180, 216, 252, 288 Jy beam^{-1}.
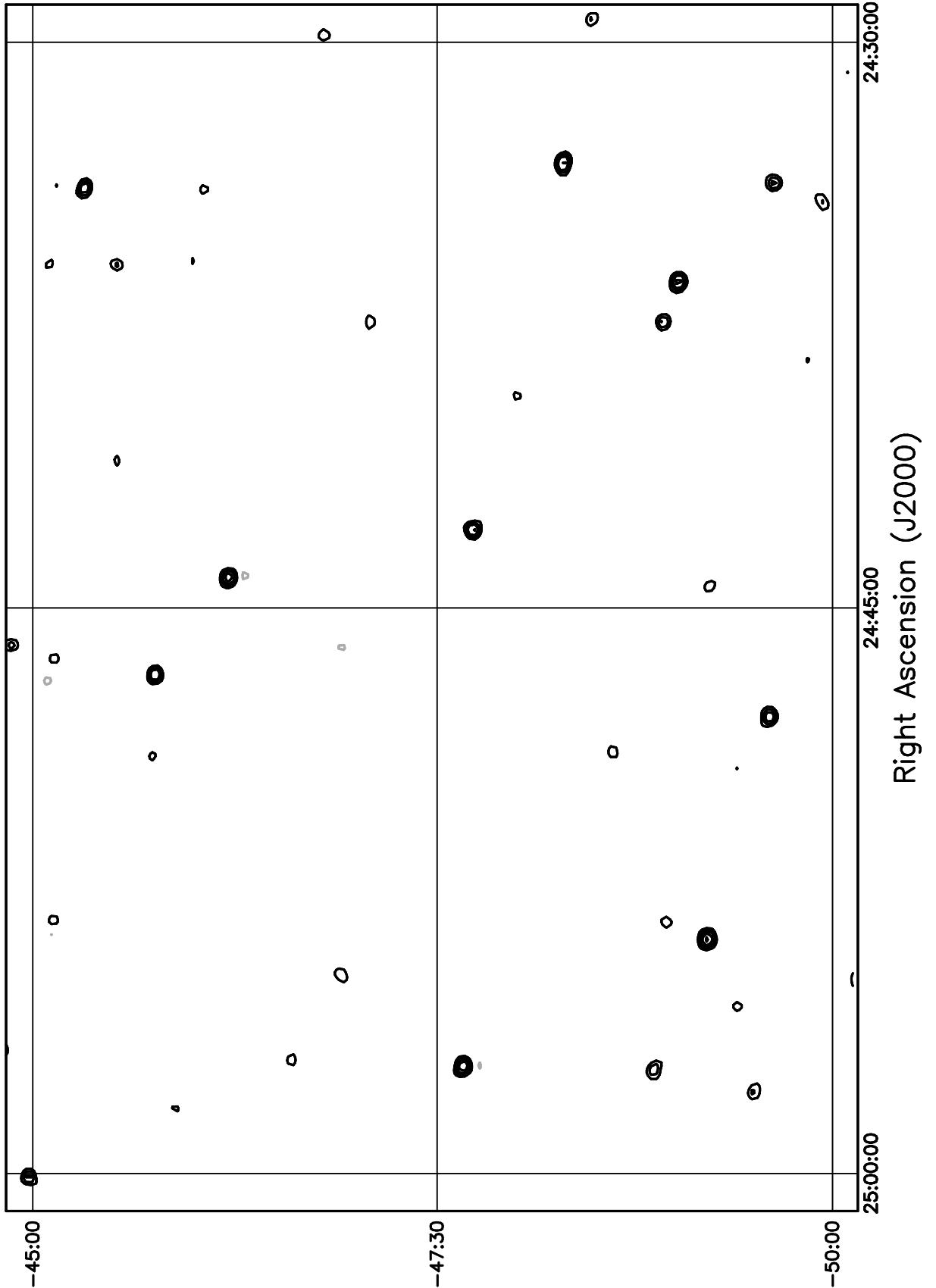
Figure 5.67: Contour plot for the range $24^h30^m \leq RA \leq 25^h00^m$, $-45° \leq \delta \leq -40°$. Contour levels are -5.04, -3.6, -2.52, -1.8, -1.08, 1.08, 1.8, 2.52, 3.6, 5.04, 7.2, 10.08, 14.4, 20.16, 28.8, 39.6, 54, 72, 100.8, 136.8, 180, 216, 252, 288 Jy beam^{-1}.
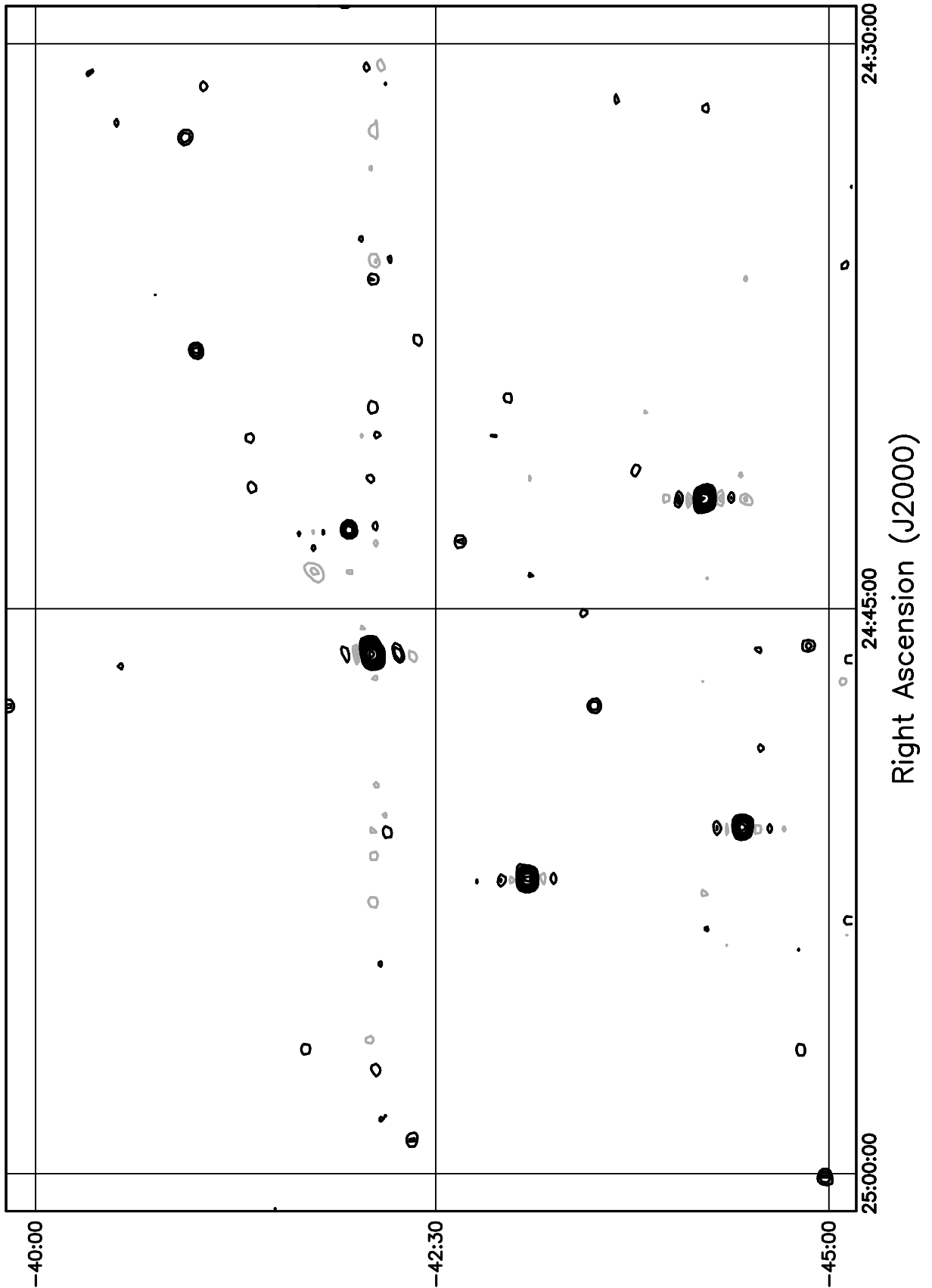
Figure 5.68: Contour plot for the range $24^h30^m \leq RA \leq 25^h00^m$, $-40° \leq \delta \leq -35°$. Contour levels are -5.04, -3.6, -2.52, -1.8, -1.08, 1.08, 1.8, 2.52, 3.6, 5.04, 7.2, 10.08, 14.4, 20.16, 28.8, 39.6, 54, 72, 100.8, 136.8, 180, 216, 252, 288 Jy beam^{-1}.
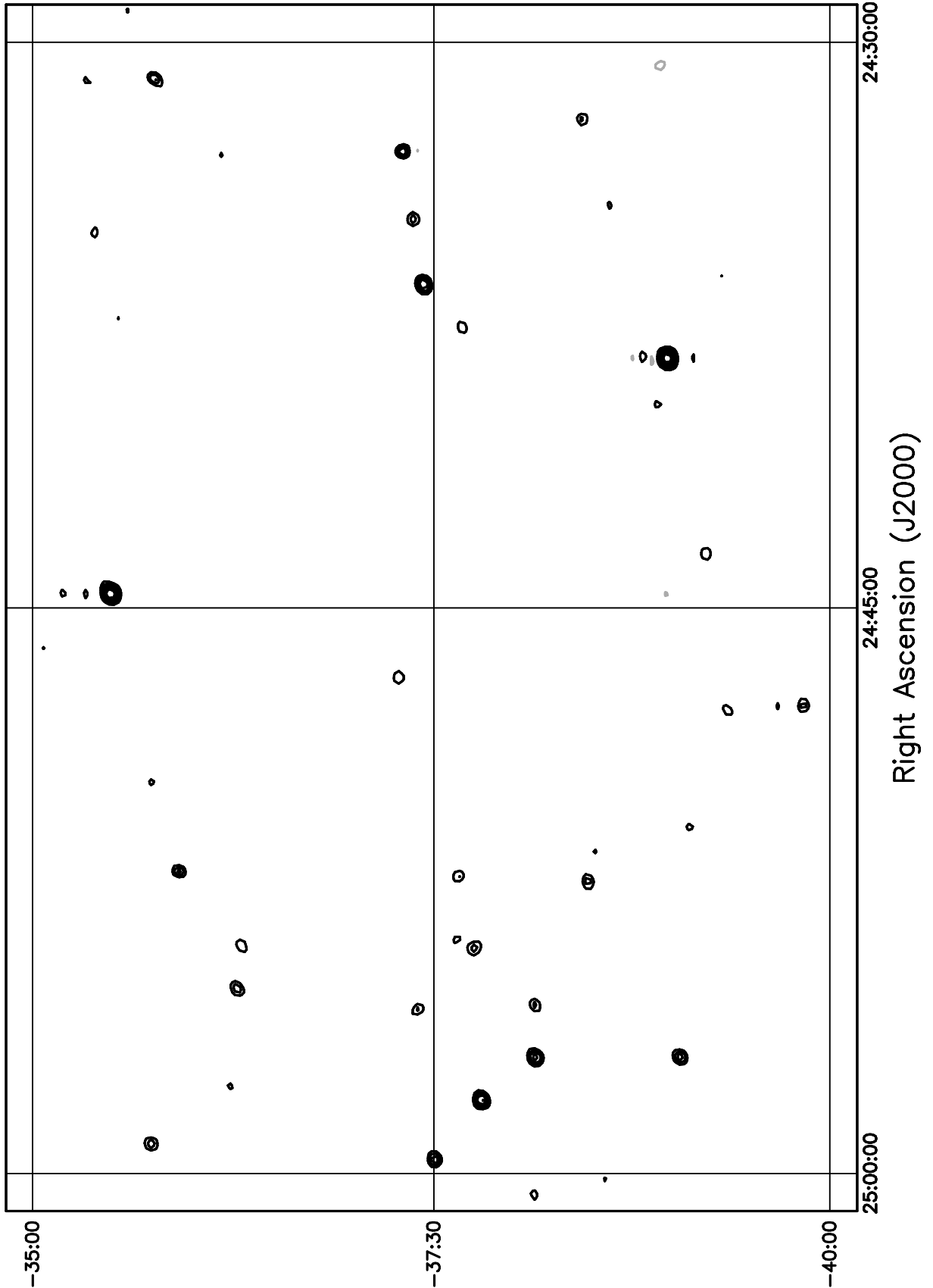
Figure 5.69: Contour plot for the range $24^h30^m \leq RA \leq 25^h00^m$, $-35° \leq \delta \leq -30°$. Contour levels are -5.04, -3.6, -2.52, -1.8, -1.08, 1.08, 1.8, 2.52, 3.6, 5.04, 7.2, 10.08, 14.4, 20.16, 28.8, 39.6, 54, 72, 100.8, 136.8, 180, 216, 252, 288 Jy beam^{-1}.
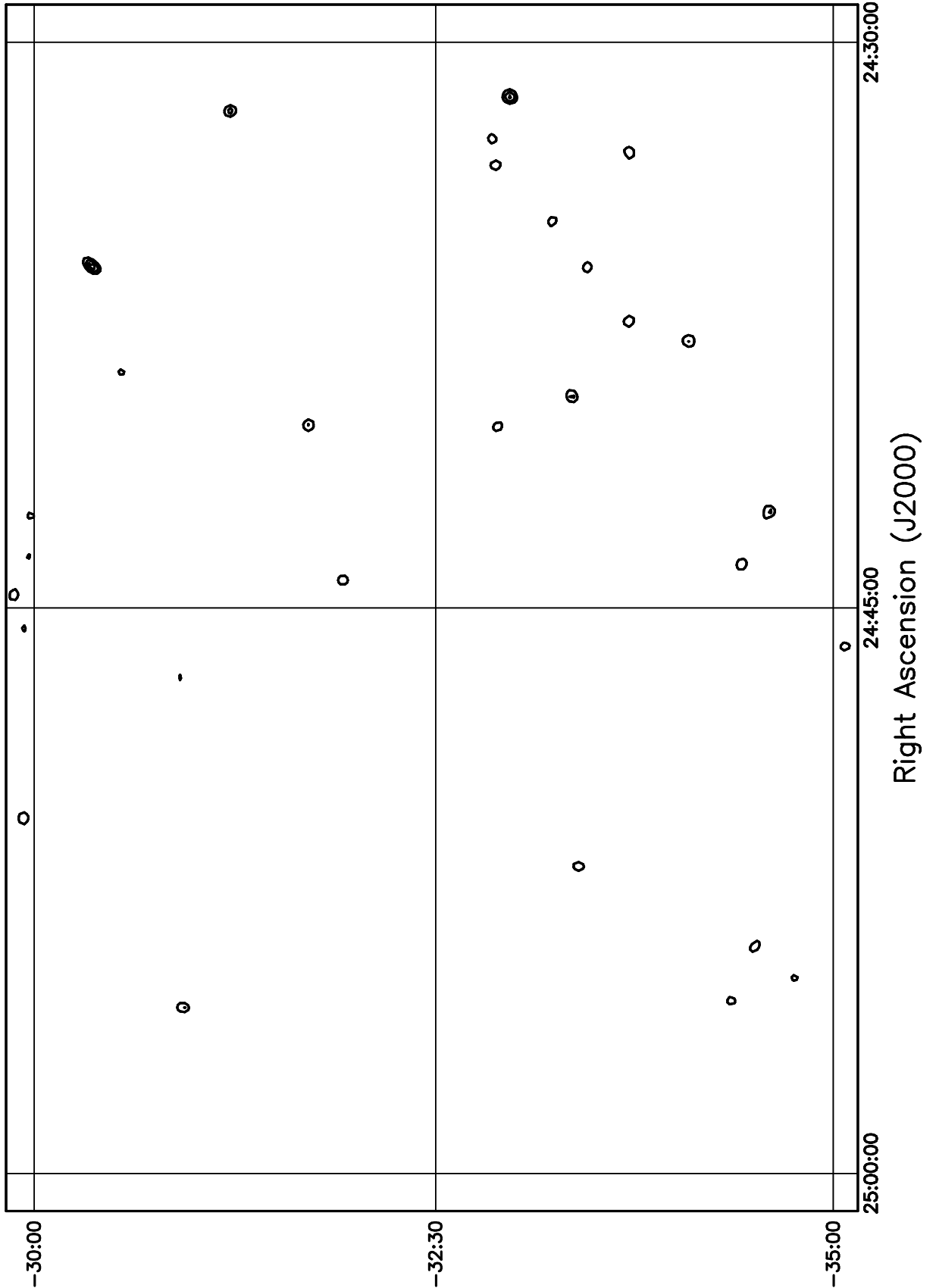
Figure 5.70: Contour plot for the range $24^h30^m \leq RA \leq 25^h00^m$, $-30° \leq \delta \leq -25°$. Contour levels are -5.04, -3.6, -2.52, -1.8, -1.08, 1.08, 1.8, 2.52, 3.6, 5.04, 7.2, 10.08, 14.4, 20.16, 28.8, 39.6, 54, 72, 100.8, 136.8, 180, 216, 252, 288 Jy beam^{-1}.
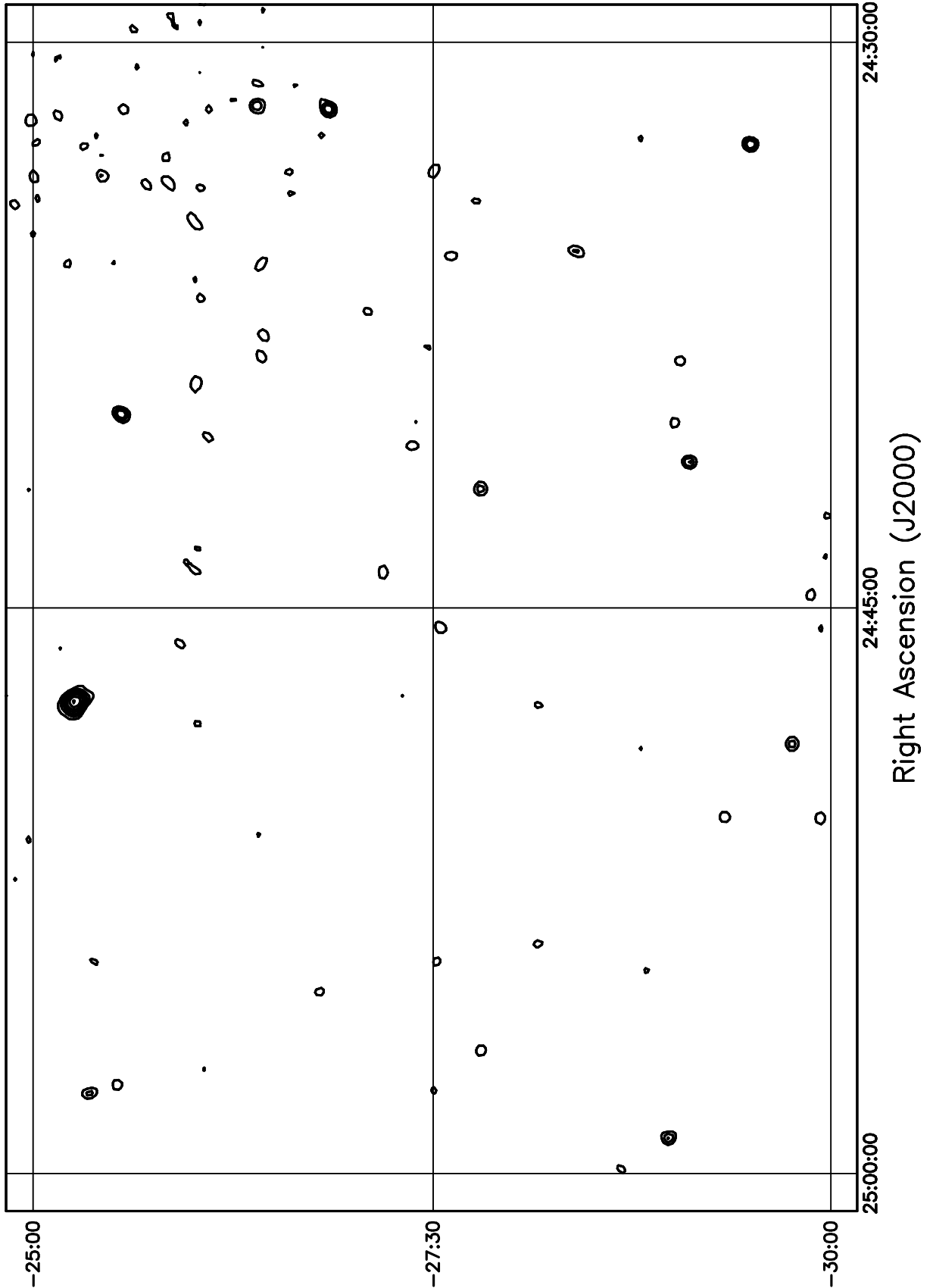
Figure 5.71: Contour plot for the range $24^h30^m \leq RA \leq 25^h00^m$, $-25° \leq \delta \leq -20°$. Contour levels are -5.04, -3.6, -2.52, -1.8, -1.08, 1.08, 1.8, 2.52, 3.6, 5.04, 7.2, 10.08, 14.4, 20.16, 28.8, 39.6, 54, 72, 100.8, 136.8, 180, 216, 252, 288 Jy beam^{-1}.
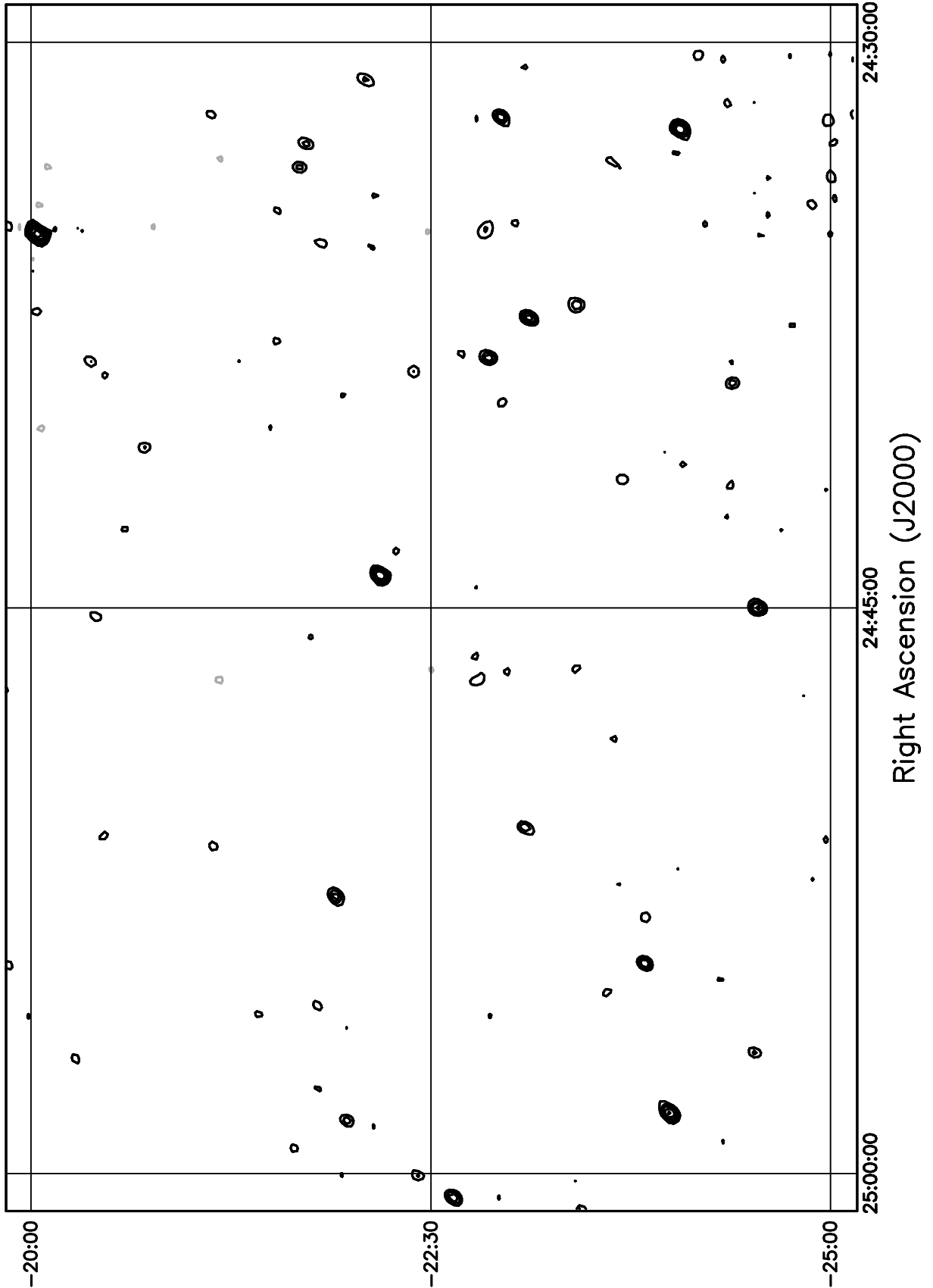
Figure 5.72: Contour plot for the range $24^h30^m \leq RA \leq 25^h00^m$, $-20° \leq \delta \leq -15°$. Contour levels are -5.04, -3.6, -2.52, -1.8, -1.08, 1.08, 1.8, 2.52, 3.6, 5.04, 7.2, 10.08, 14.4, 20.16, 28.8, 39.6, 54, 72, 100.8, 136.8, 180, 216, 252, 288 Jy beam^{-1}.
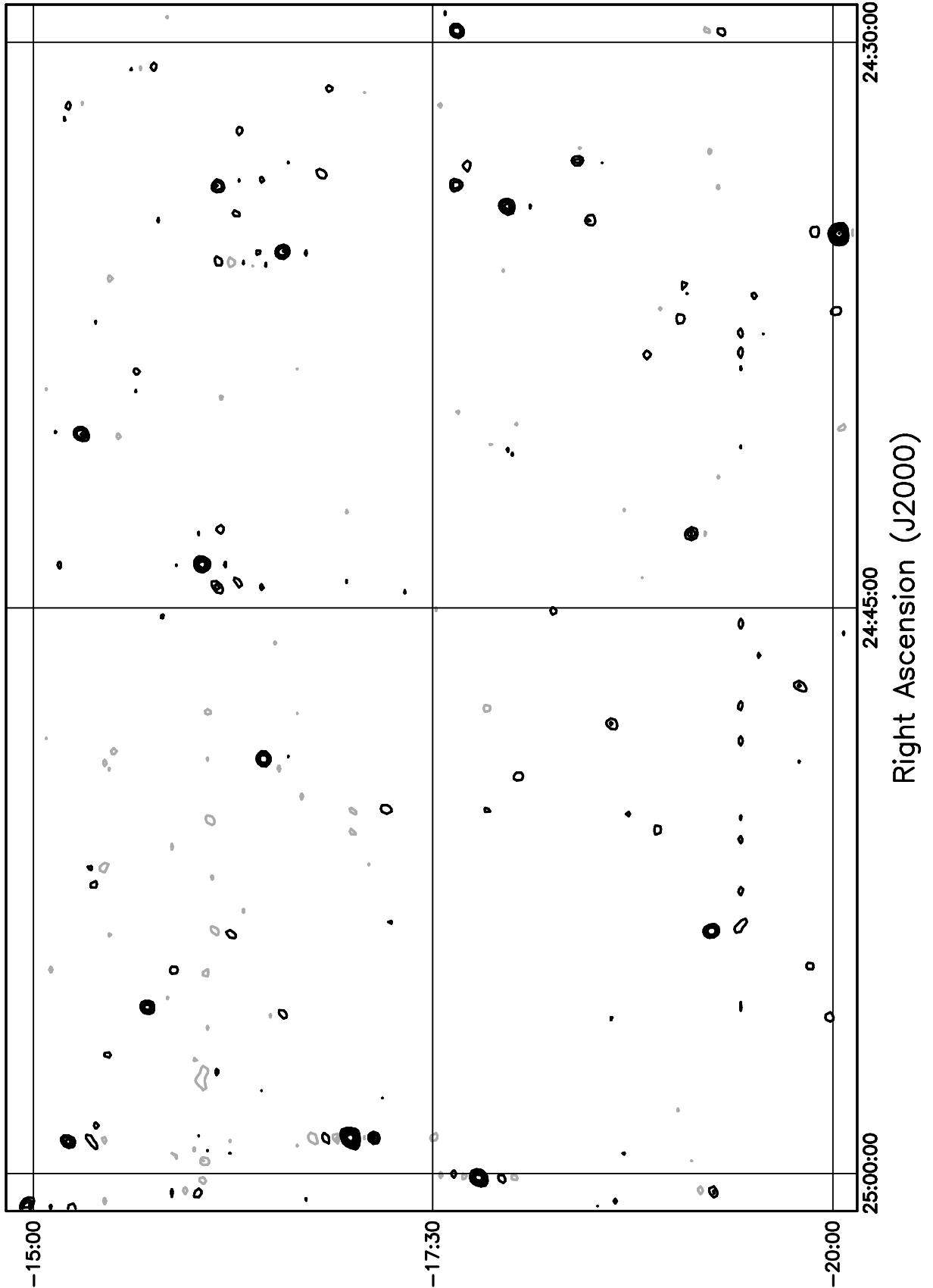
Figure 5.73: Contour plot for the range $24^h30^m \leq RA \leq 25^h00^m$, $-15° \leq \delta \leq -10°$. Contour levels are -5.04, -3.6, -2.52, -1.8, -1.08, 1.08, 1.8, 2.52, 3.6, 5.04, 7.2, 10.08, 14.4, 20.16, 28.8, 39.6, 54, 72, 100.8, 136.8, 180, 216, 252, 288 Jy beam^{-1}.
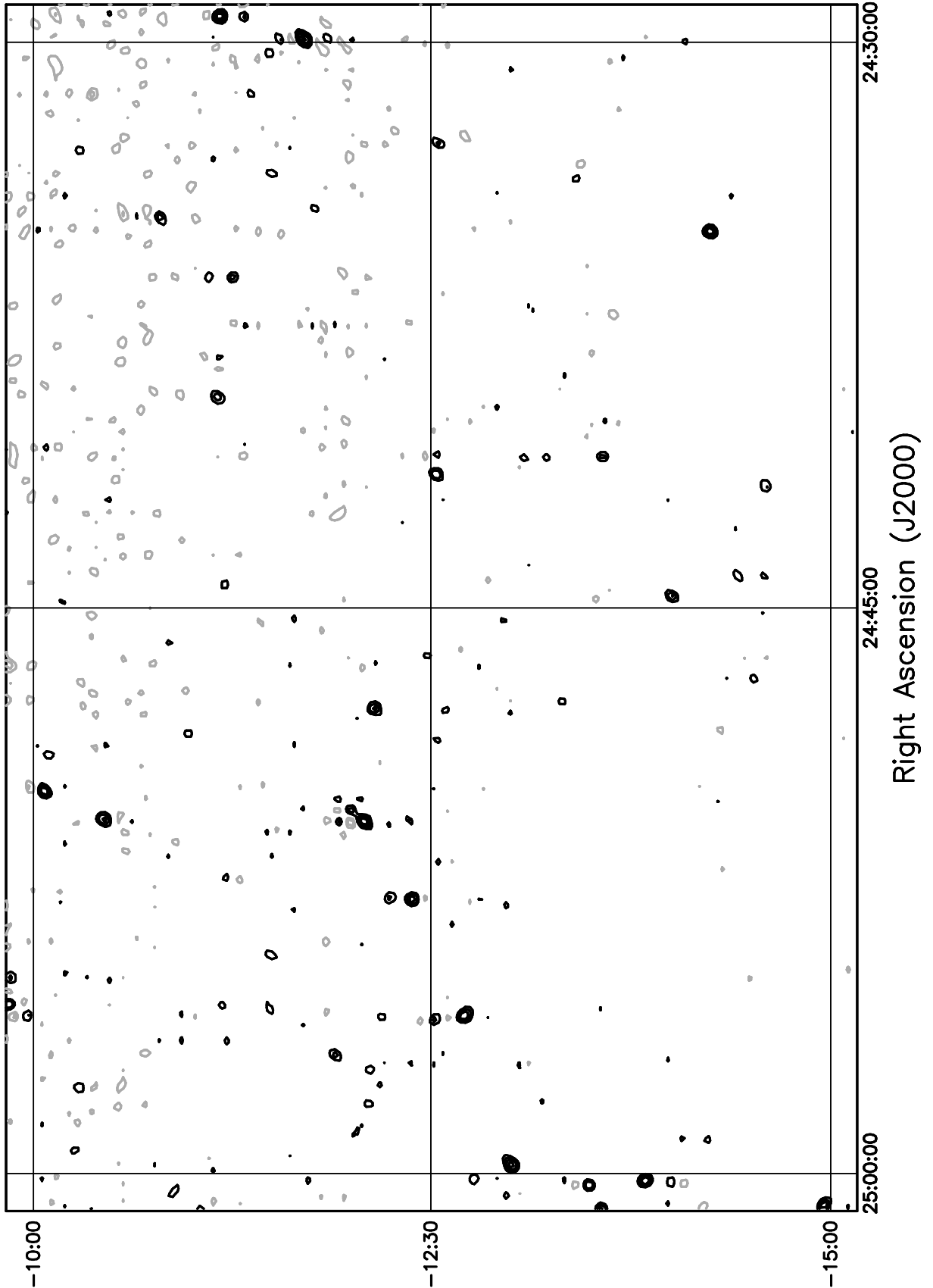
Figure 5.74: Contour plot for the range $01^h00^m \leq RA \leq 01^h30^m$, $-75° \leq \delta \leq -70°$. Contour levels are -5.04, -3.6, -2.52, -1.8, -1.08, 1.08, 1.8, 2.52, 3.6, 5.04, 7.2, 10.08, 14.4, 20.16, 28.8, 39.6, 54, 72, 100.8, 136.8, 180, 216, 252, 288 Jy beam^{-1}.
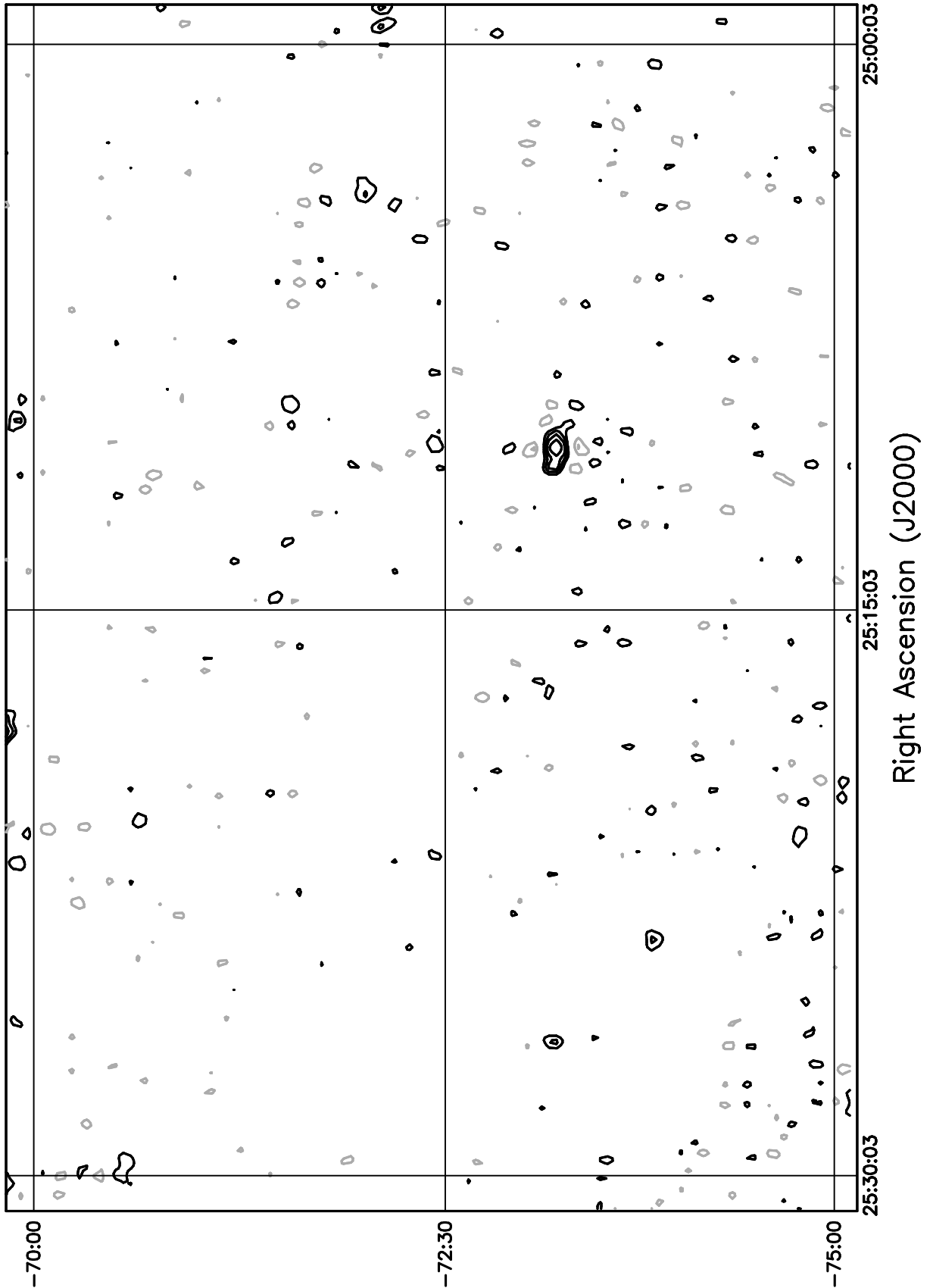
Figure 5.75: Contour plot for the range $01^h00^m \leq RA \leq 01^h30^m$, $-70° \leq \delta \leq -65°$. Contour levels are -5.04, -3.6, -2.52, -1.8, -1.08, 1.08, 1.8, 2.52, 3.6, 5.04, 7.2, 10.08, 14.4, 20.16, 28.8, 39.6, 54, 72, 100.8, 136.8, 180, 216, 252, 288 Jy beam^{-1}.
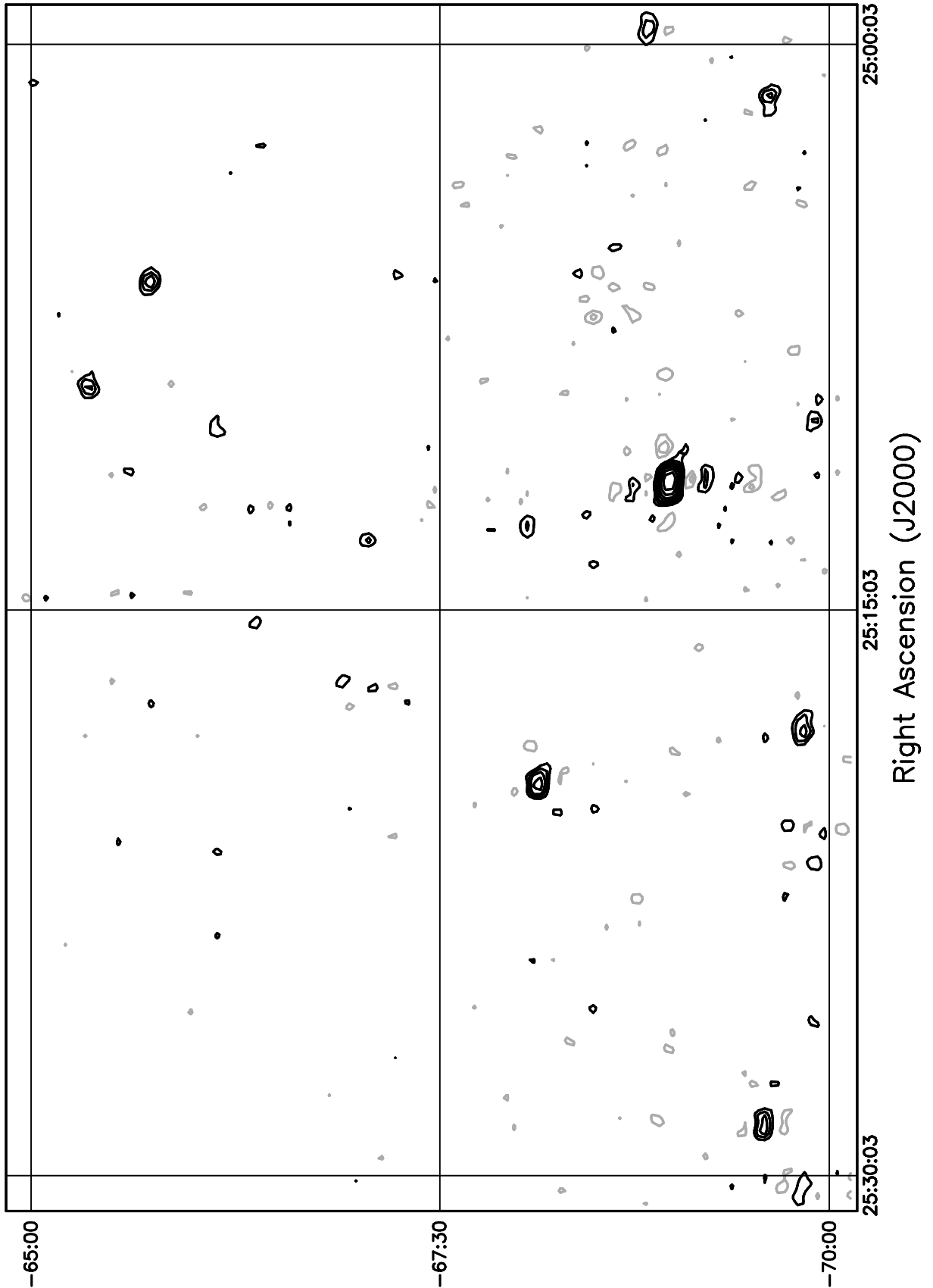
Figure 5.76: Contour plot for the range $01^h00^m \leq RA \leq 01^h30^m$, $-65° \leq \delta \leq -60°$. Contour levels are -5.04, -3.6, -2.52, -1.8, -1.08, 1.08, 1.8, 2.52, 3.6, 5.04, 7.2, 10.08, 14.4, 20.16, 28.8, 39.6, 54, 72, 100.8, 136.8, 180, 216, 252, 288 Jy beam^{-1}.
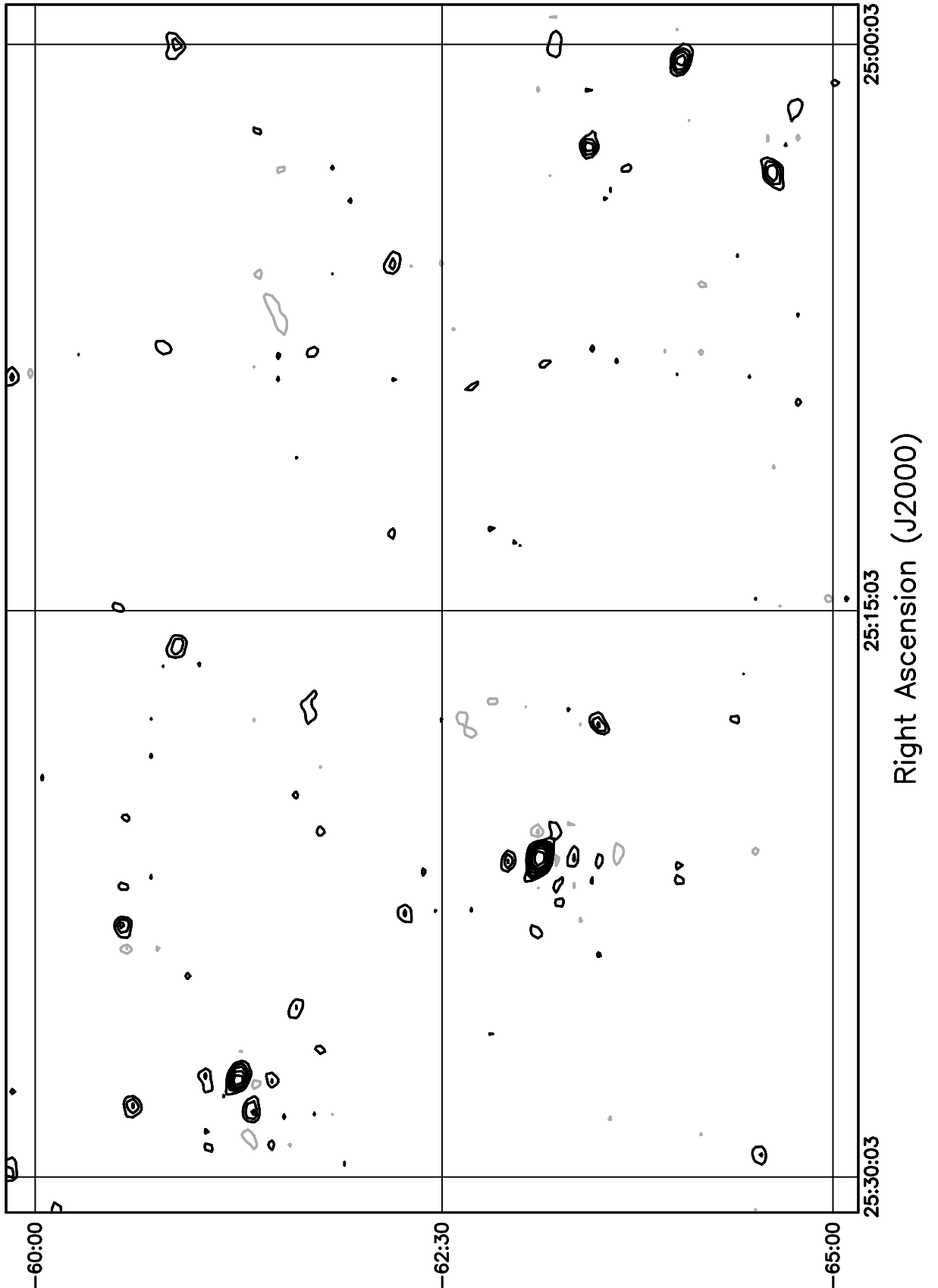
Figure 5.77: Contour plot for the range $01^h00^m \leq RA \leq 01^h30^m$, $-60° \leq \delta \leq -55°$. Contour levels are -5.04, -3.6, -2.52, -1.8, -1.08, 1.08, 1.8, 2.52, 3.6, 5.04, 7.2, 10.08, 14.4, 20.16, 28.8, 39.6, 54, 72, 100.8, 136.8, 180, 216, 252, 288 Jy beam^{-1}.
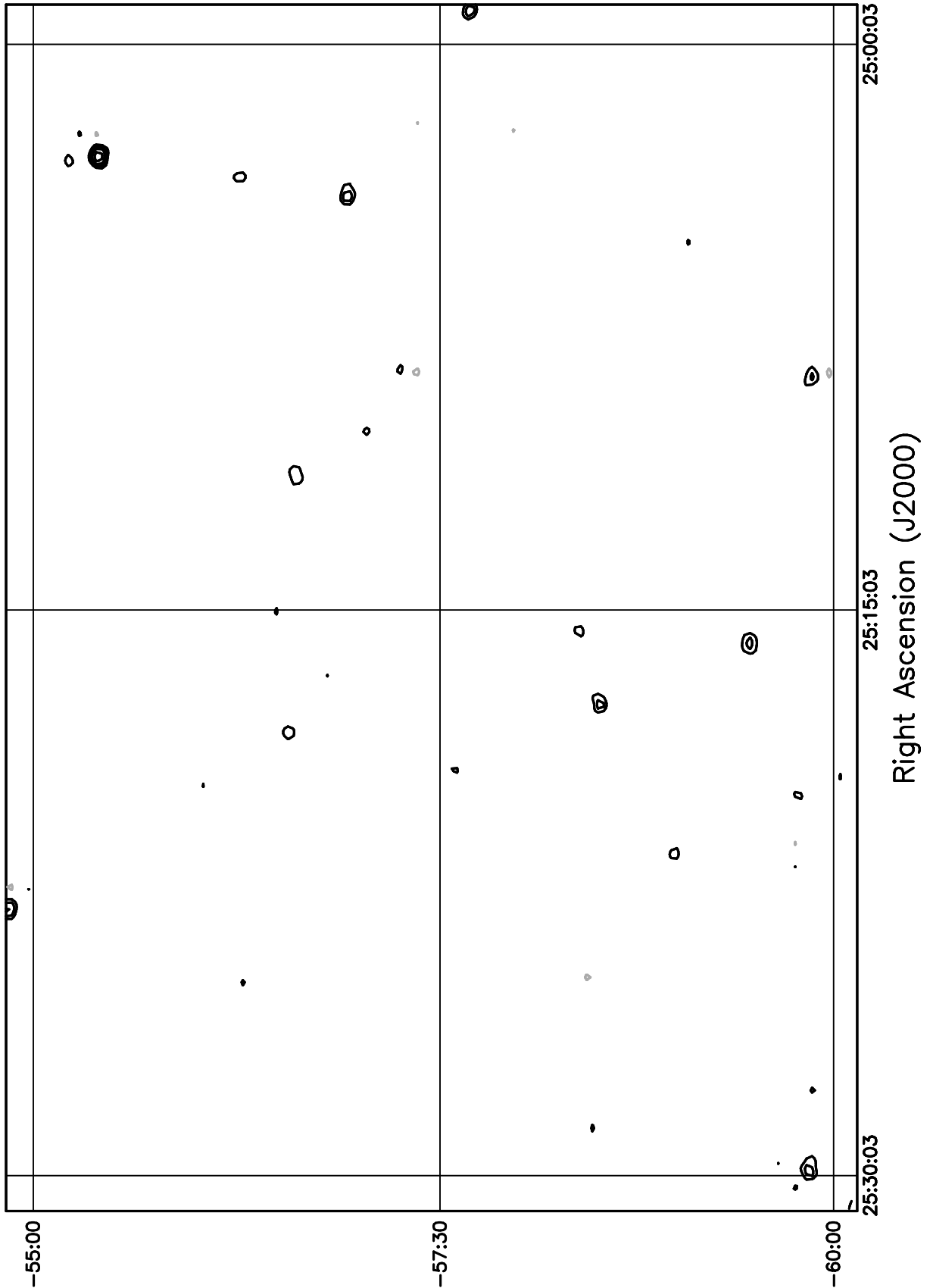
Figure 5.78: Contour plot for the range $01^h00^m \leq RA \leq 01^h30^m$, $-55° \leq \delta \leq -50°$. Contour levels are -5.04, -3.6, -2.52, -1.8, -1.08, 1.08, 1.8, 2.52, 3.6, 5.04, 7.2, 10.08, 14.4, 20.16, 28.8, 39.6, 54, 72, 100.8, 136.8, 180, 216, 252, 288 Jy beam^{-1}.
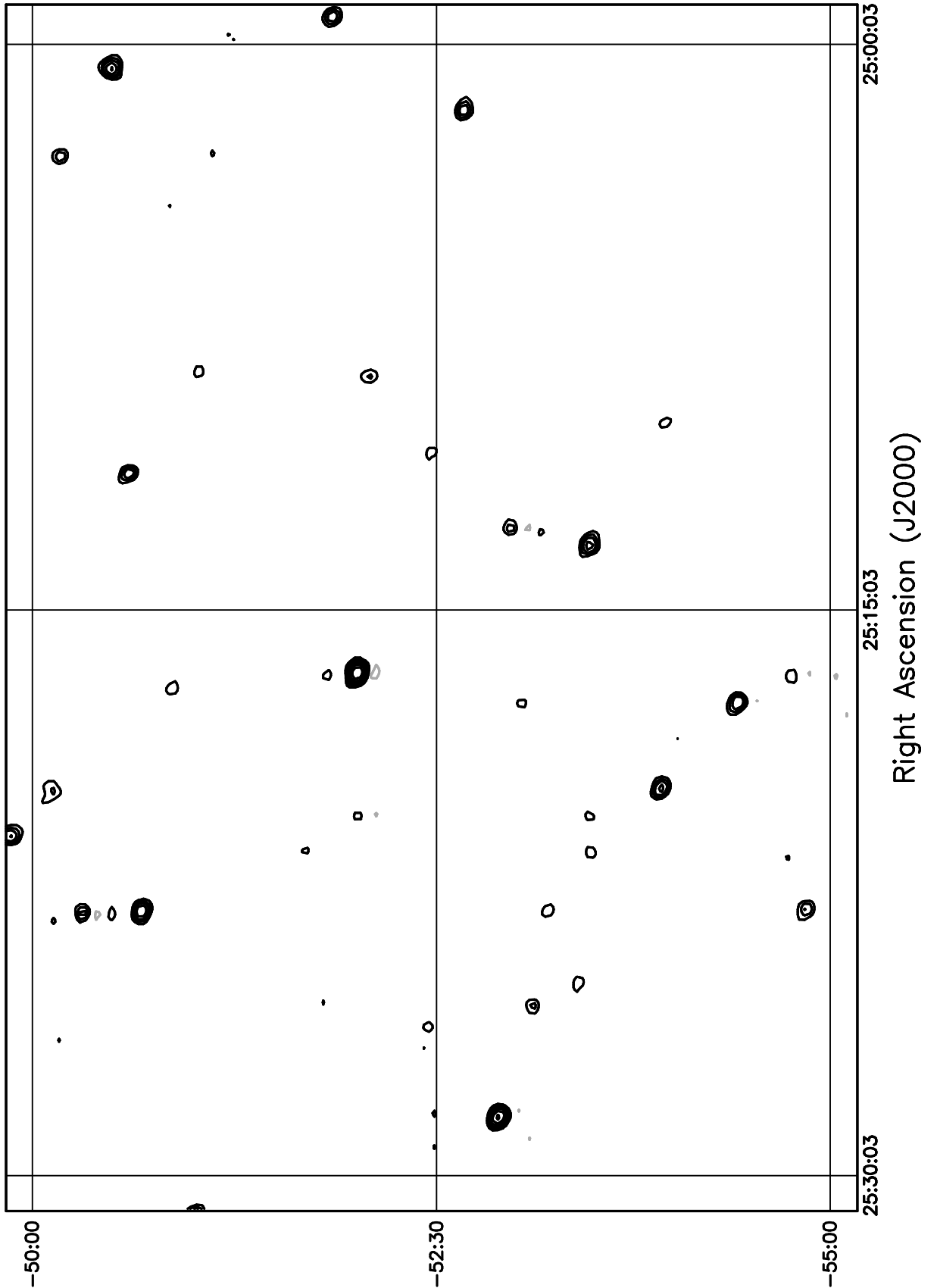
Figure 5.79: Contour plot for the range $01^h00^m \leq RA \leq 01^h30^m$, $-50° \leq \delta \leq -45°$. Contour levels are -5.04, -3.6, -2.52, -1.8, -1.08, 1.08, 1.8, 2.52, 3.6, 5.04, 7.2, 10.08, 14.4, 20.16, 28.8, 39.6, 54, 72, 100.8, 136.8, 180, 216, 252, 288 Jy beam^{-1}.
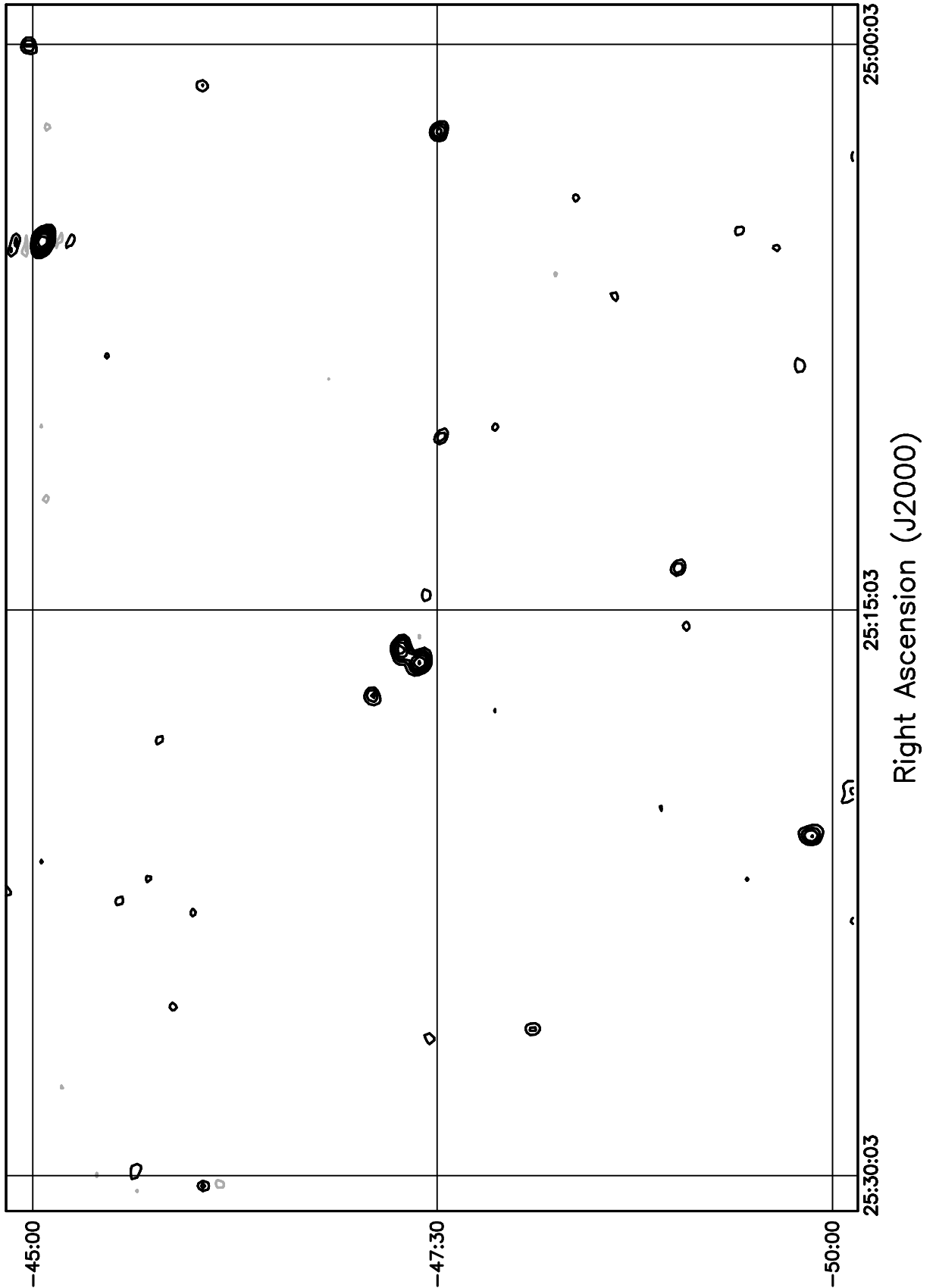
Figure 5.80: Contour plot for the range $01^h00^m \leq RA \leq 01^h30^m$, $-45° \leq \delta \leq -40°$. Contour levels are -5.04, -3.6, -2.52, -1.8, -1.08, 1.08, 1.8, 2.52, 3.6, 5.04, 7.2, 10.08, 14.4, 20.16, 28.8, 39.6, 54, 72, 100.8, 136.8, 180, 216, 252, 288 Jy beam^{-1}.
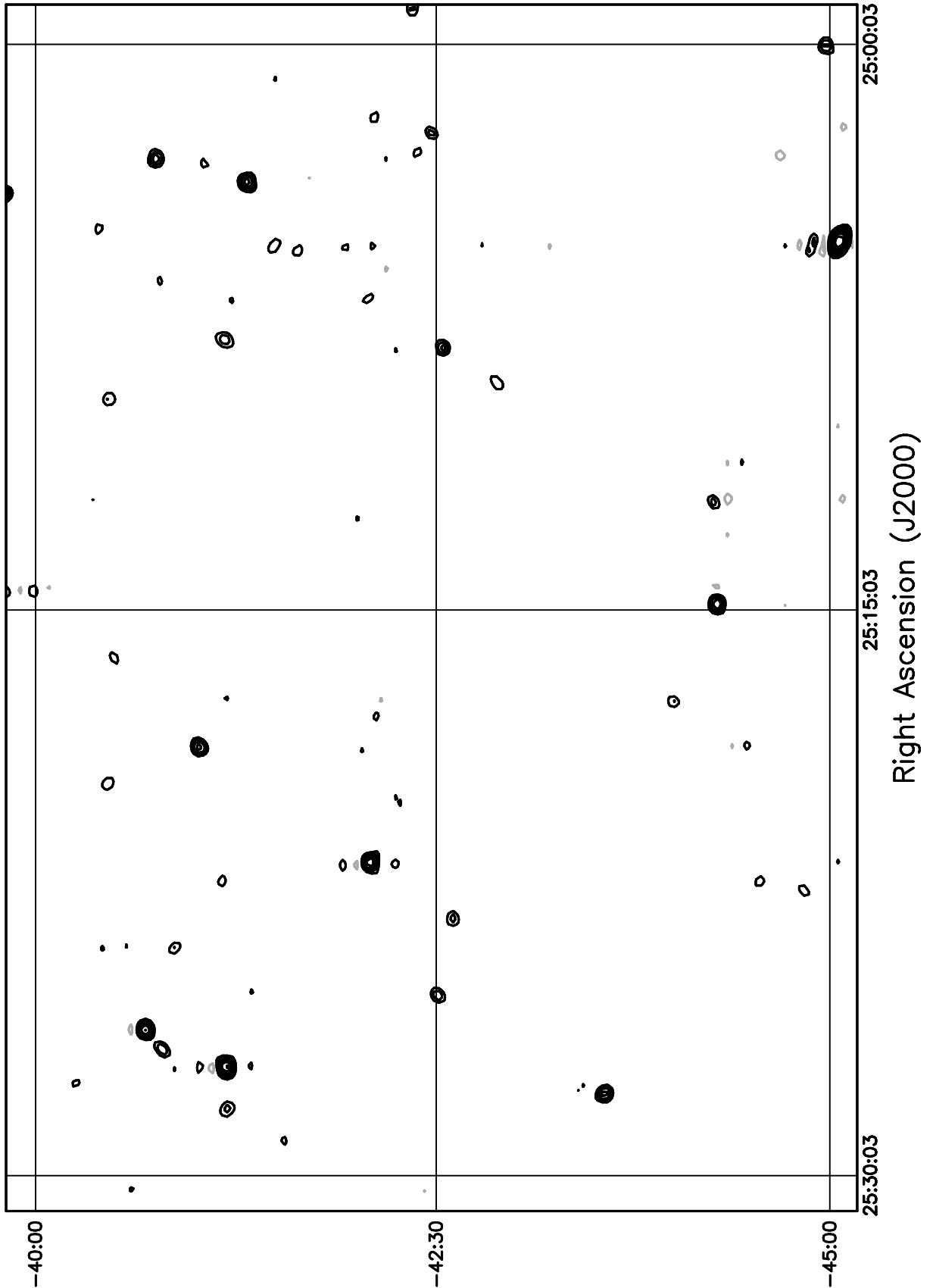
Figure 5.81: Contour plot for the range $01^h00^m \leq RA \leq 01^h30^m$, $-40° \leq \delta \leq -35°$. Contour levels are -5.04, -3.6, -2.52, -1.8, -1.08, 1.08, 1.8, 2.52, 3.6, 5.04, 7.2, 10.08, 14.4, 20.16, 28.8, 39.6, 54, 72, 100.8, 136.8, 180, 216, 252, 288 Jy beam^{-1}.
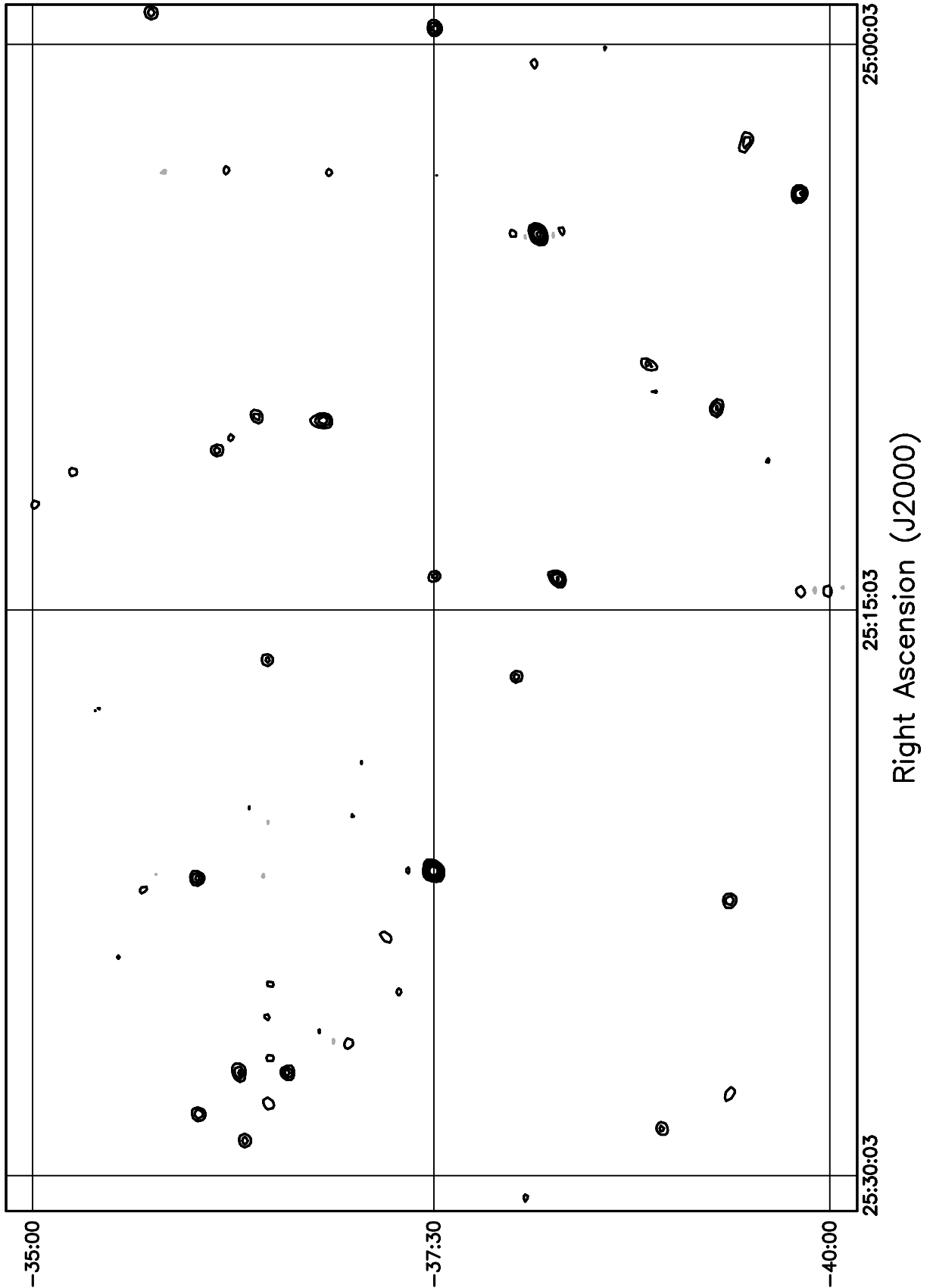
Figure 5.82: Contour plot for the range $01^h00^m \leq RA \leq 01^h30^m$, $-35° \leq \delta \leq -30°$. Contour levels are -5.04, -3.6, -2.52, -1.8, -1.08, 1.08, 1.8, 2.52, 3.6, 5.04, 7.2, 10.08, 14.4, 20.16, 28.8, 39.6, 54, 72, 100.8, 136.8, 180, 216, 252, 288 Jy beam^{-1}.
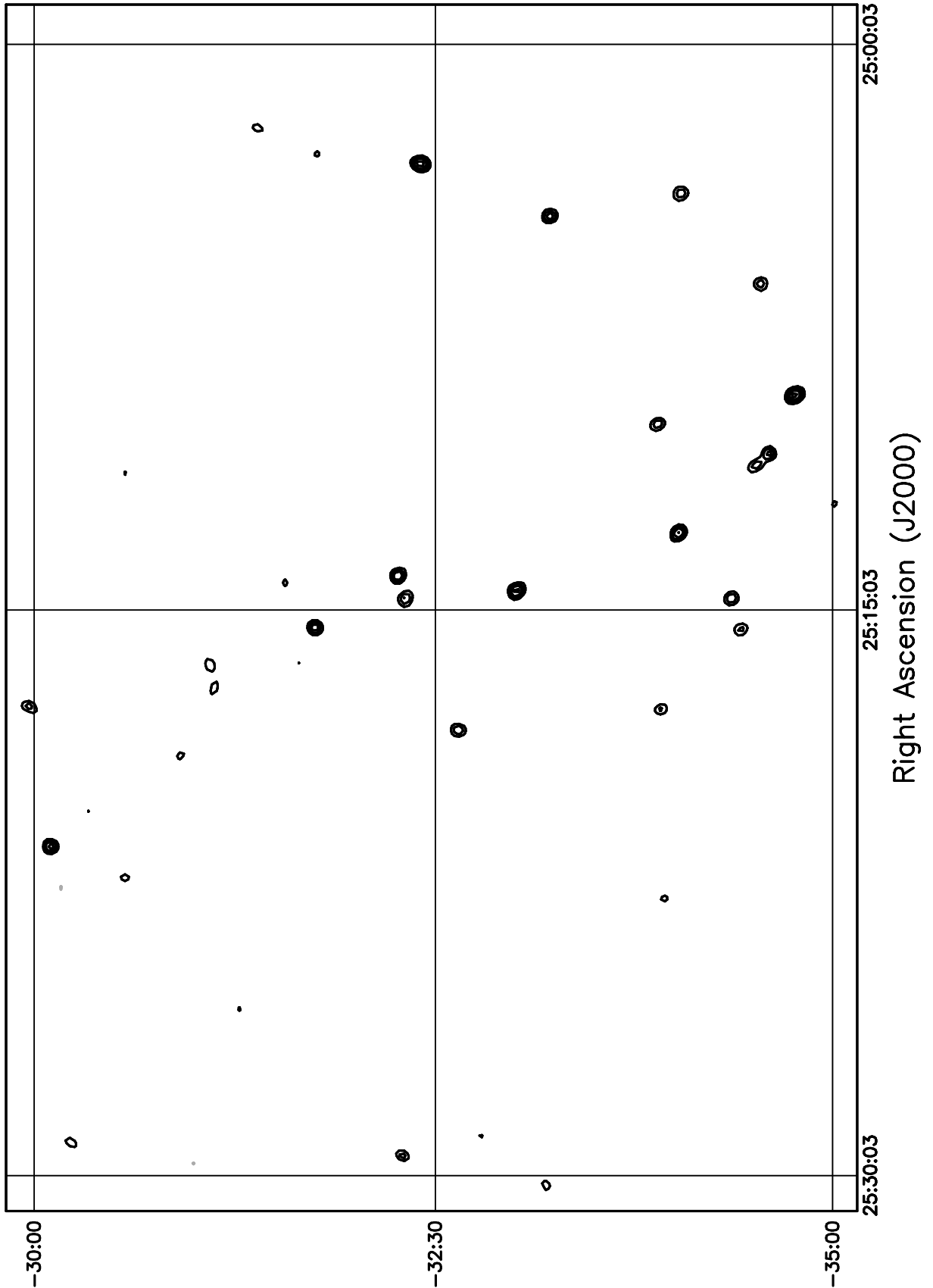
Figure 5.83: Contour plot for the range $01^h00^m \leq RA \leq 01^h30^m$, $-30° \leq \delta \leq -25°$. Contour levels are -5.04, -3.6, -2.52, -1.8, -1.08, 1.08, 1.8, 2.52, 3.6, 5.04, 7.2, 10.08, 14.4, 20.16, 28.8, 39.6, 54, 72, 100.8, 136.8, 180, 216, 252, 288 Jy beam^{-1}.
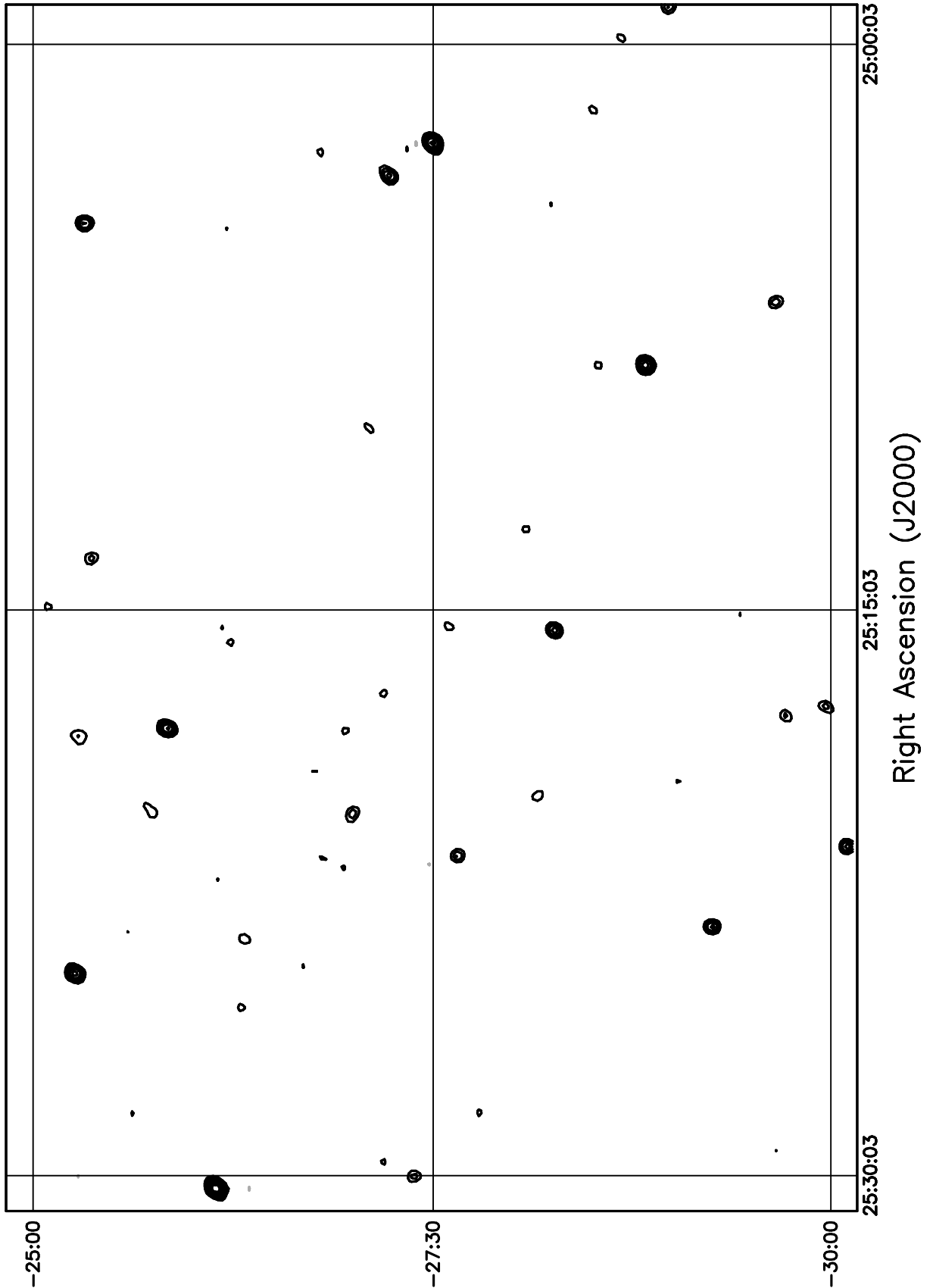
Figure 5.84: Contour plot for the range $01^h00^m \leq RA \leq 01^h30^m$, $-25° \leq \delta \leq -20°$. Contour levels are -5.04, -3.6, -2.52, -1.8, -1.08, 1.08, 1.8, 2.52, 3.6, 5.04, 7.2, 10.08, 14.4, 20.16, 28.8, 39.6, 54, 72, 100.8, 136.8, 180, 216, 252, 288 Jy beam^{-1}.
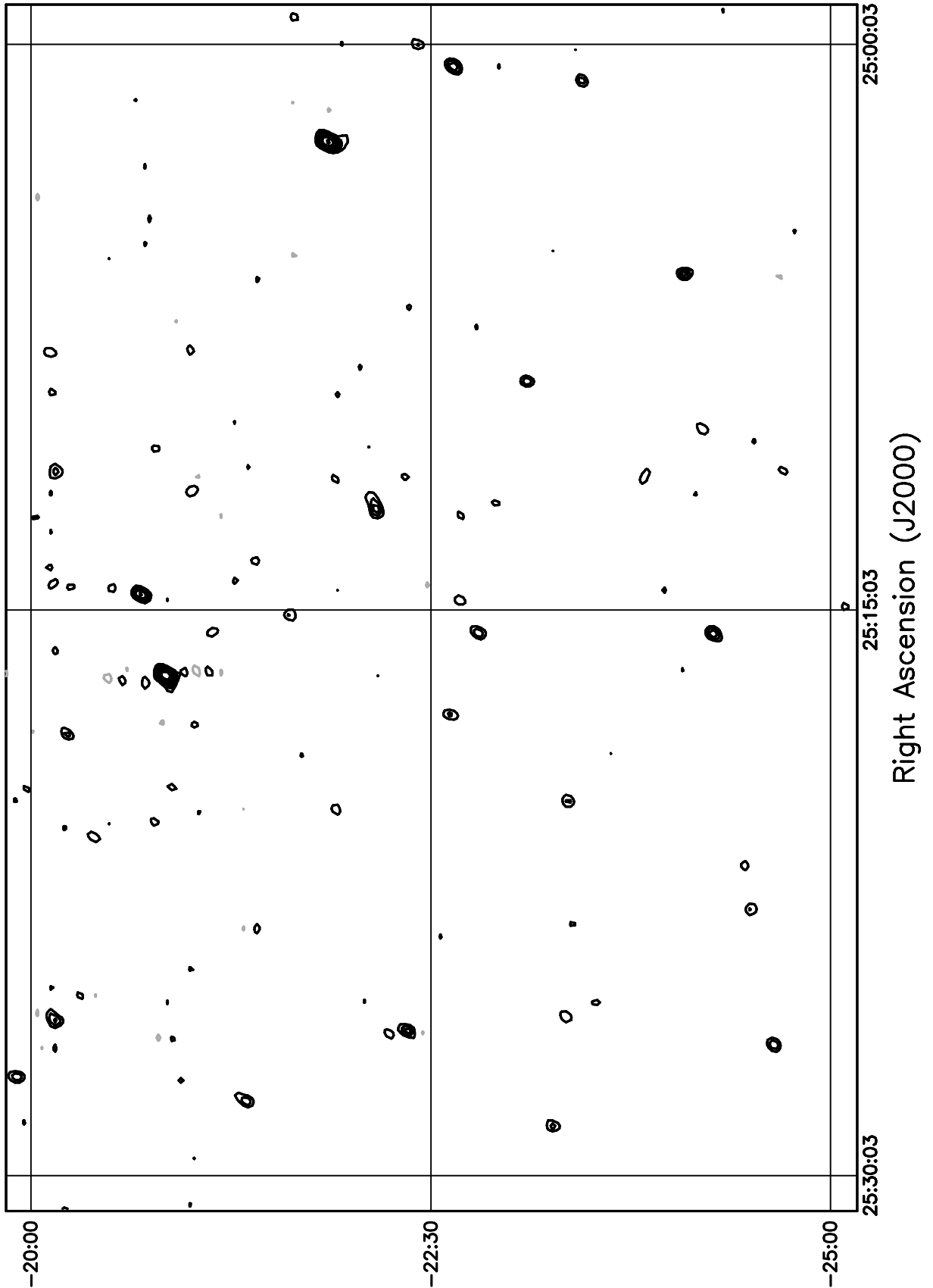
Figure 5.85: Contour plot for the range $01^h00^m \leq RA \leq 01^h30^m$, $-20° \leq \delta \leq -15°$. Contour levels are -5.04, -3.6, -2.52, -1.8, -1.08, 1.08, 1.8, 2.52, 3.6, 5.04, 7.2, 10.08, 14.4, 20.16, 28.8, 39.6, 54, 72, 100.8, 136.8, 180, 216, 252, 288 Jy beam^{-1}.
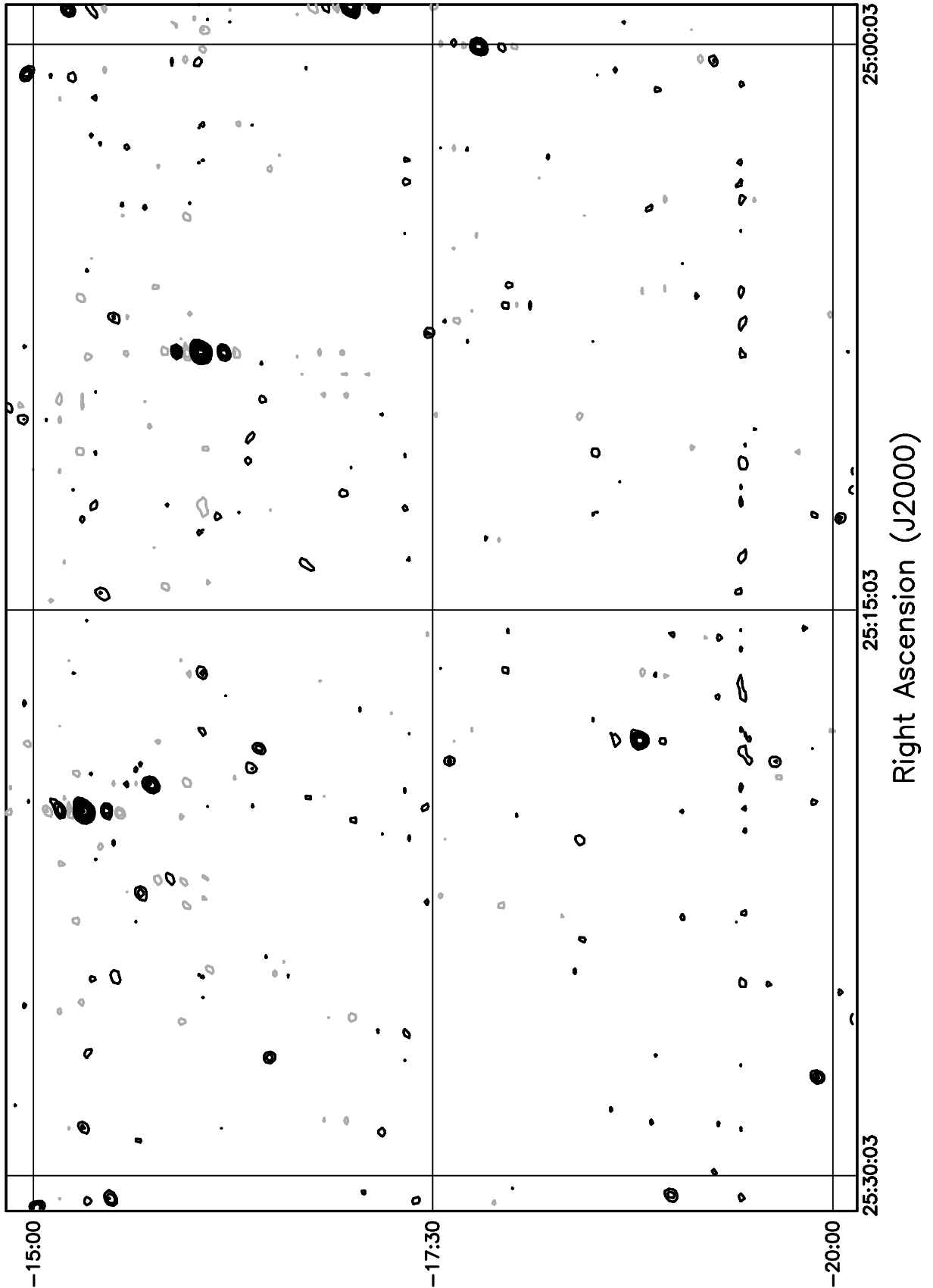
Figure 5.86: Contour plot for the range $01^h00^m \leq RA \leq 01^h30^m$, $-15° \leq \delta \leq -10°$. Contour levels are -5.04, -3.6, -2.52, -1.8, -1.08, 1.08, 1.8, 2.52, 3.6, 5.04, 7.2, 10.08, 14.4, 20.16, 28.8, 39.6, 54, 72, 100.8, 136.8, 180, 216, 252, 288 Jy beam^{-1}.
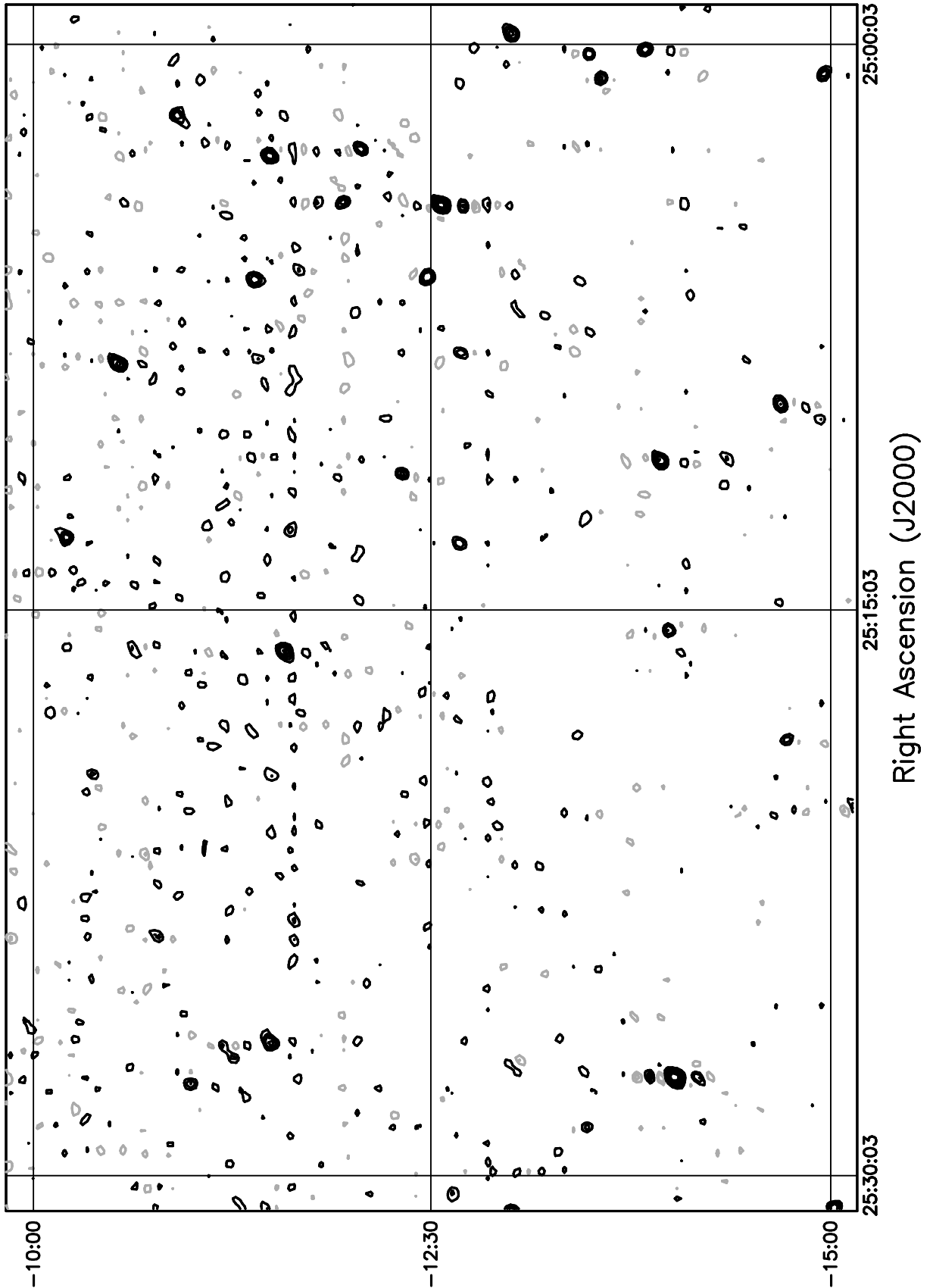
Figure 5.87: Contour plot for the range $01^h30^m \leq RA \leq 02^h00^m$, $-75° \leq \delta \leq -70°$. Contour levels are -5.04, -3.6, -2.52, -1.8, -1.08, 1.08, 1.8, 2.52, 3.6, 5.04, 7.2, 10.08, 14.4, 20.16, 28.8, 39.6, 54, 72, 100.8, 136.8, 180, 216, 252, 288 Jy beam^{-1}.


Right Ascension (J2000)
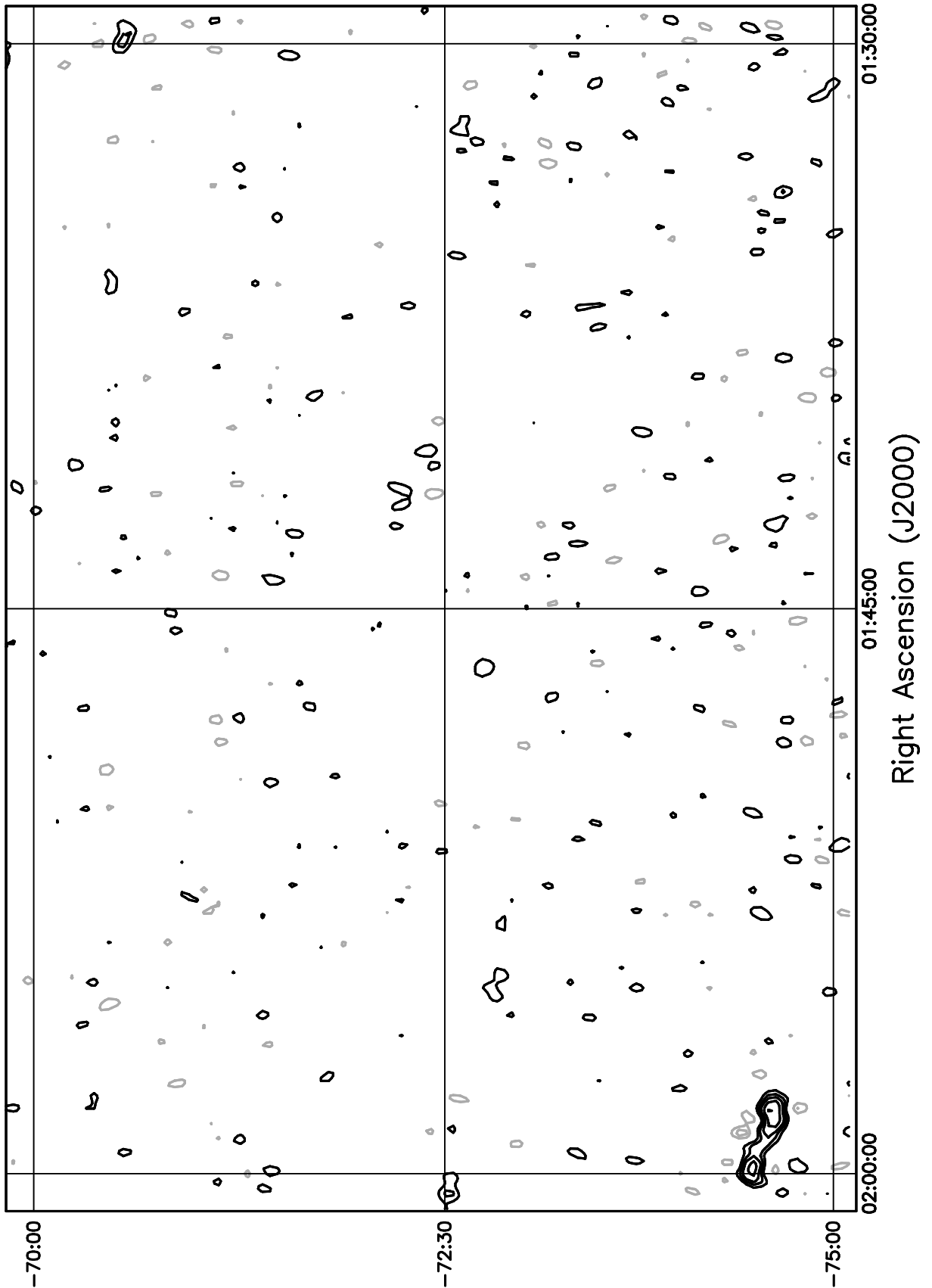
Figure 5.88: Contour plot for the range $01^h30^m \leq RA \leq 02^h00^m$, $-70° \leq \delta \leq -65°$. Contour levels are -5.04, -3.6, -2.52, -1.8, -1.08, 1.08, 1.8, 2.52, 3.6, 5.04, 7.2, 10.08, 14.4, 20.16, 28.8, 39.6, 54, 72, 100.8, 136.8, 180, 216, 252, 288 Jy beam^{-1}.
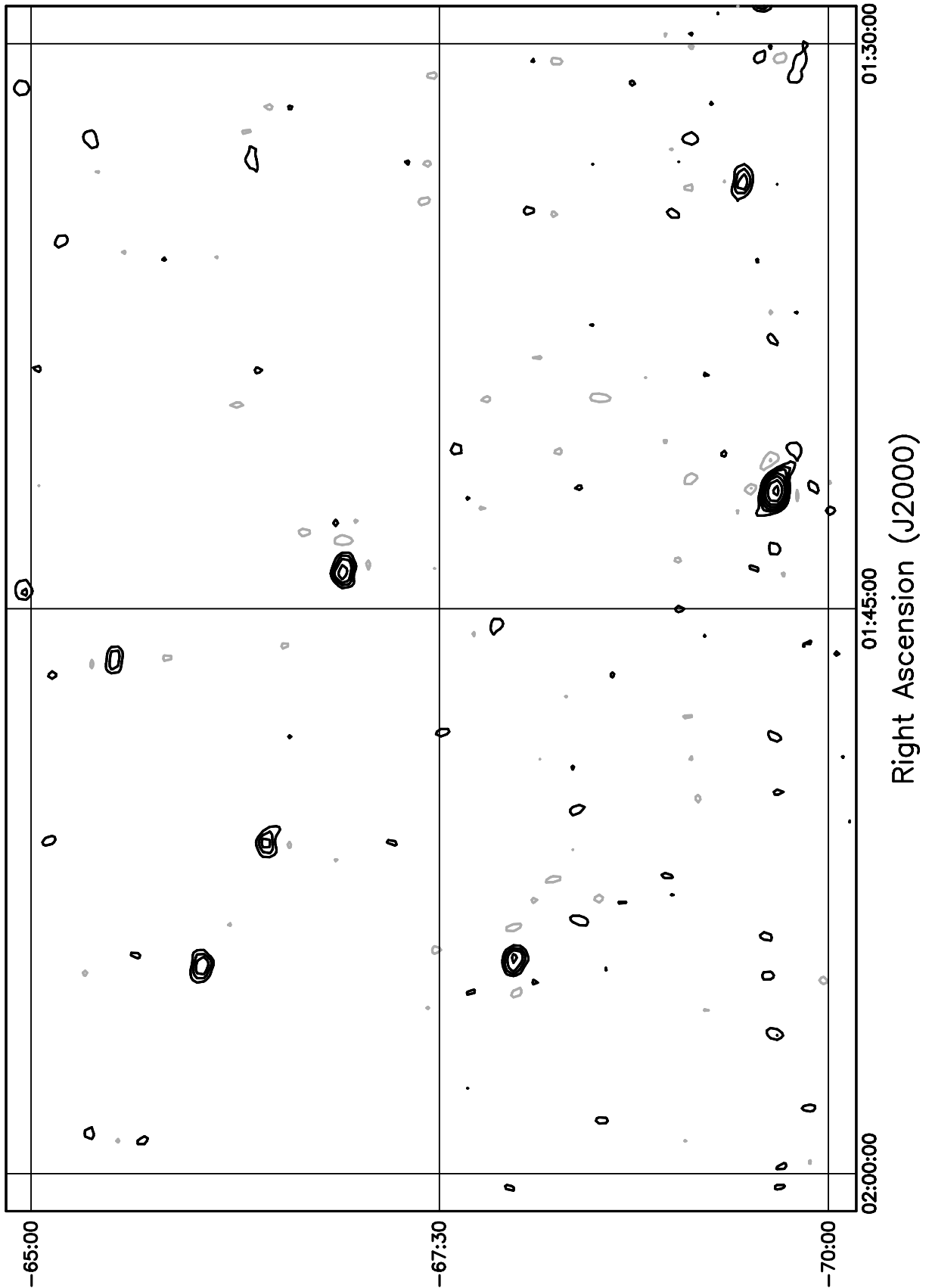
Figure 5.89: Contour plot for the range $01^h30^m \leq RA \leq 02^h00^m$, $-65° \leq \delta \leq -60°$. Contour levels are -5.04, -3.6, -2.52, -1.8, -1.08, 1.08, 1.8, 2.52, 3.6, 5.04, 7.2, 10.08, 14.4, 20.16, 28.8, 39.6, 54, 72, 100.8, 136.8, 180, 216, 252, 288 Jy beam^{-1}.
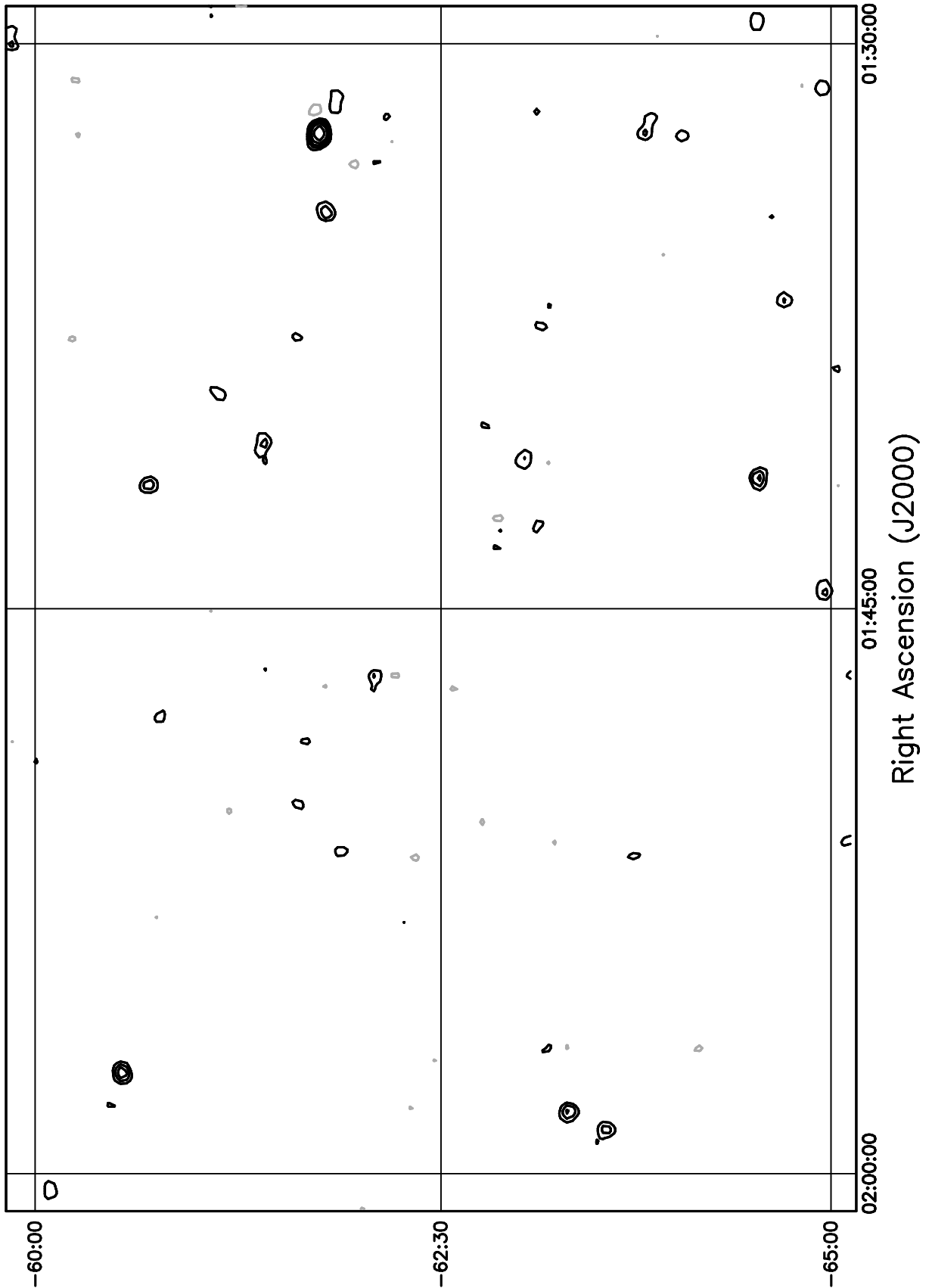
Figure 5.90: Contour plot for the range $01^h30^m \leq RA \leq 02^h00^m$, $-60° \leq \delta \leq -55°$. Contour levels are -5.04, -3.6, -2.52, -1.8, -1.08, 1.08, 1.8, 2.52, 3.6, 5.04, 7.2, 10.08, 14.4, 20.16, 28.8, 39.6, 54, 72, 100.8, 136.8, 180, 216, 252, 288 Jy beam^{-1}.
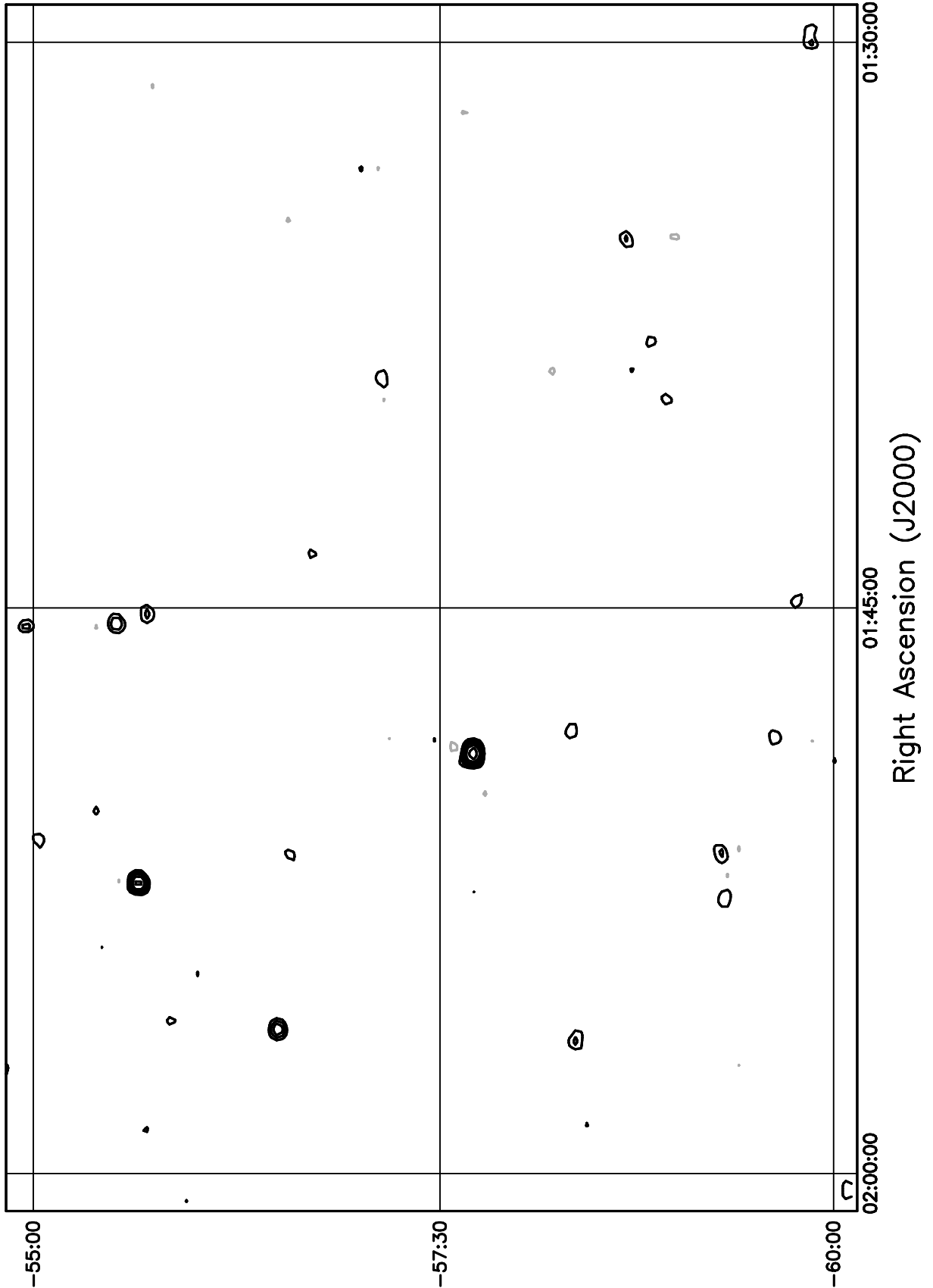
Figure 5.91: Contour plot for the range $01^h30^m \leq RA \leq 02^h00^m$, $-55° \leq \delta \leq -50°$. Contour levels are -5.04, -3.6, -2.52, -1.8, -1.08, 1.08, 1.8, 2.52, 3.6, 5.04, 7.2, 10.08, 14.4, 20.16, 28.8, 39.6, 54, 72, 100.8, 136.8, 180, 216, 252, 288 Jy beam^{-1}.
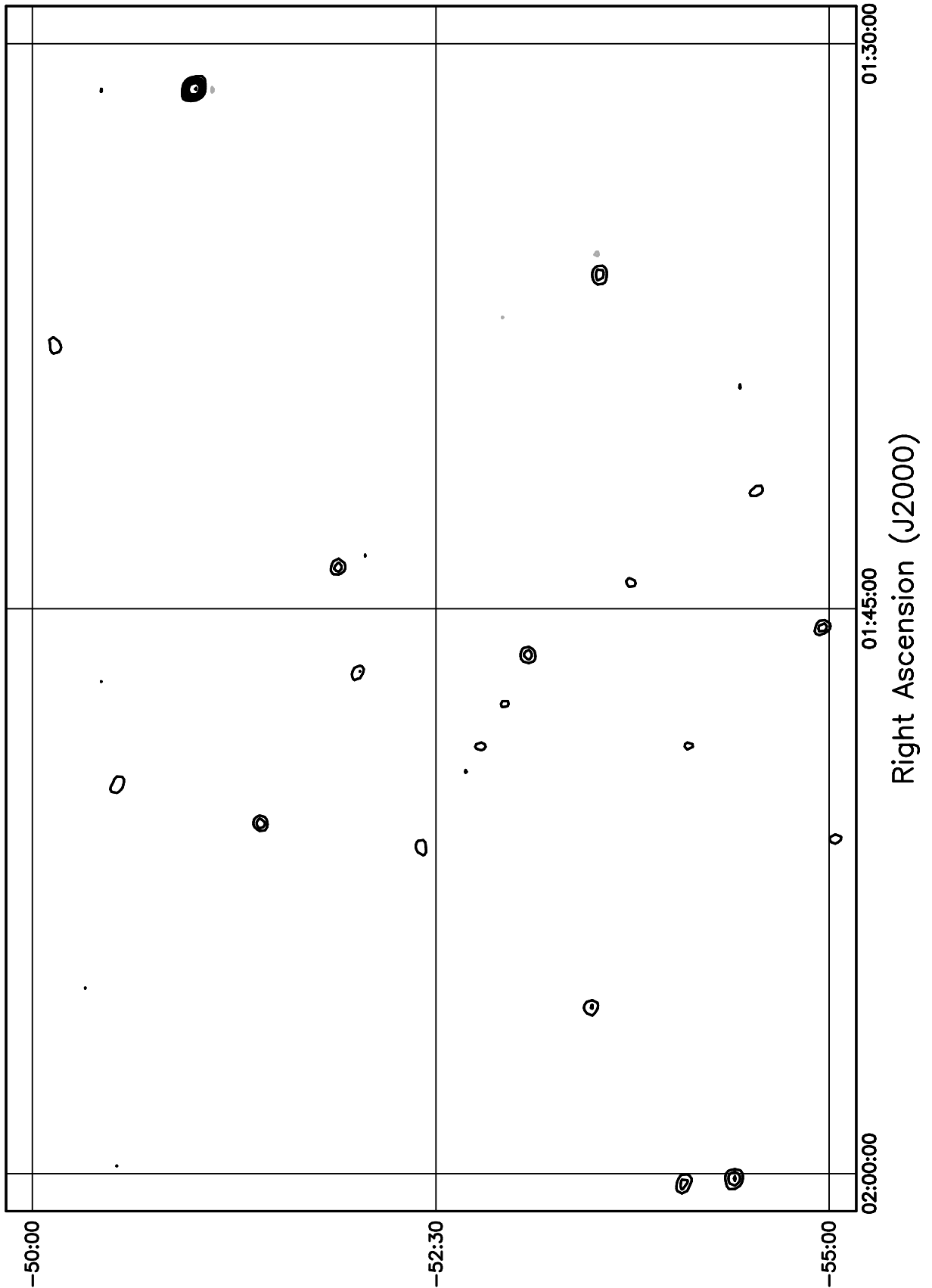
Figure 5.92: Contour plot for the range $01^h30^m \leq RA \leq 02^h00^m$, $-50° \leq \delta \leq -45°$. Contour levels are -5.04, -3.6, -2.52, -1.8, -1.08, 1.08, 1.8, 2.52, 3.6, 5.04, 7.2, 10.08, 14.4, 20.16, 28.8, 39.6, 54, 72, 100.8, 136.8, 180, 216, 252, 288 Jy beam^{-1}.

Right Ascension (J2000)
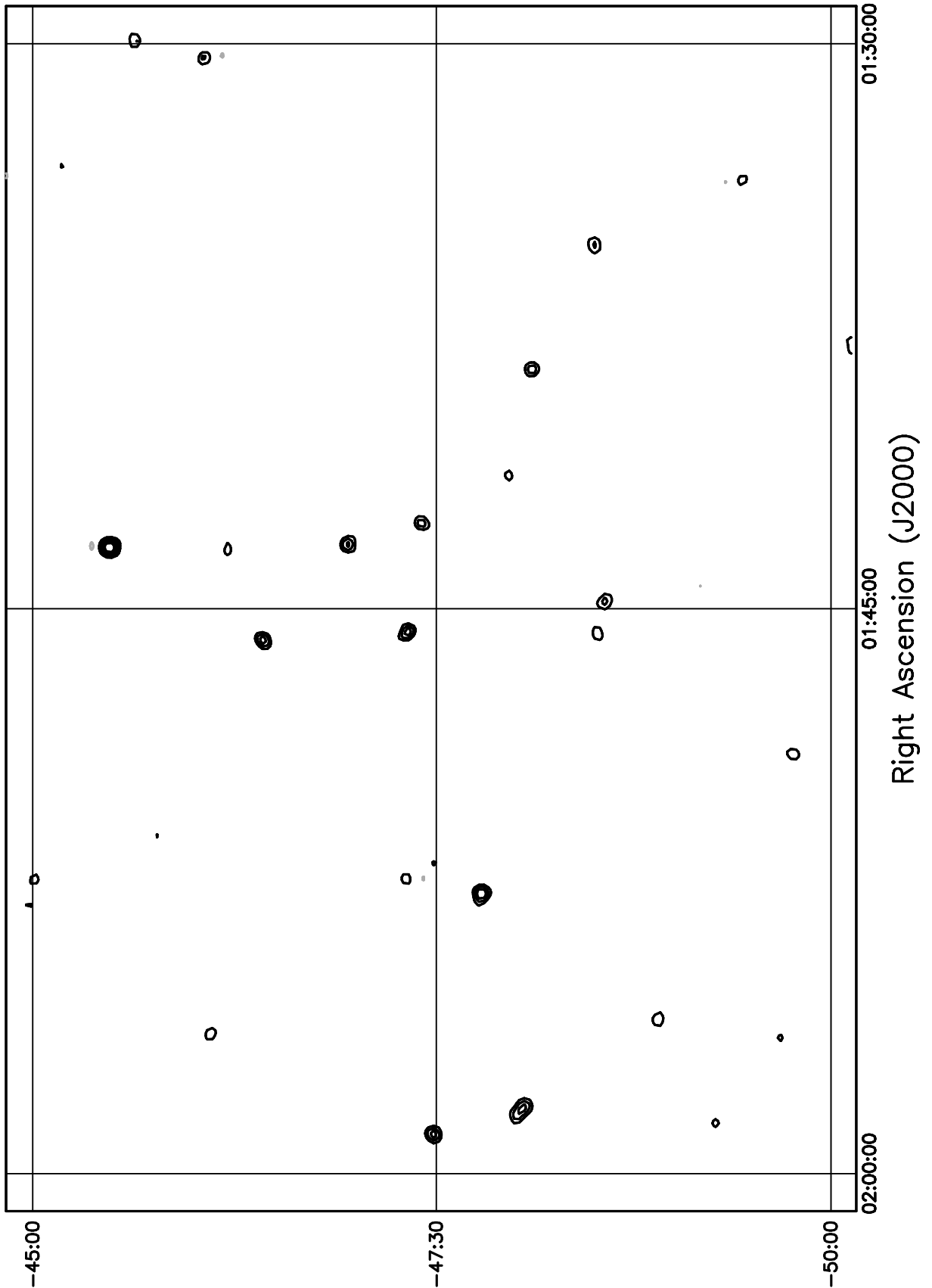
Figure 5.93: Contour plot for the range $01^h30^m \leq RA \leq 02^h00^m$, $-45° \leq \delta \leq -40°$. Contour levels are -5.04, -3.6, -2.52, -1.8, -1.08, 1.08, 1.8, 2.52, 3.6, 5.04, 7.2, 10.08, 14.4, 20.16, 28.8, 39.6, 54, 72, 100.8, 136.8, 180, 216, 252, 288 Jy beam^{-1}.
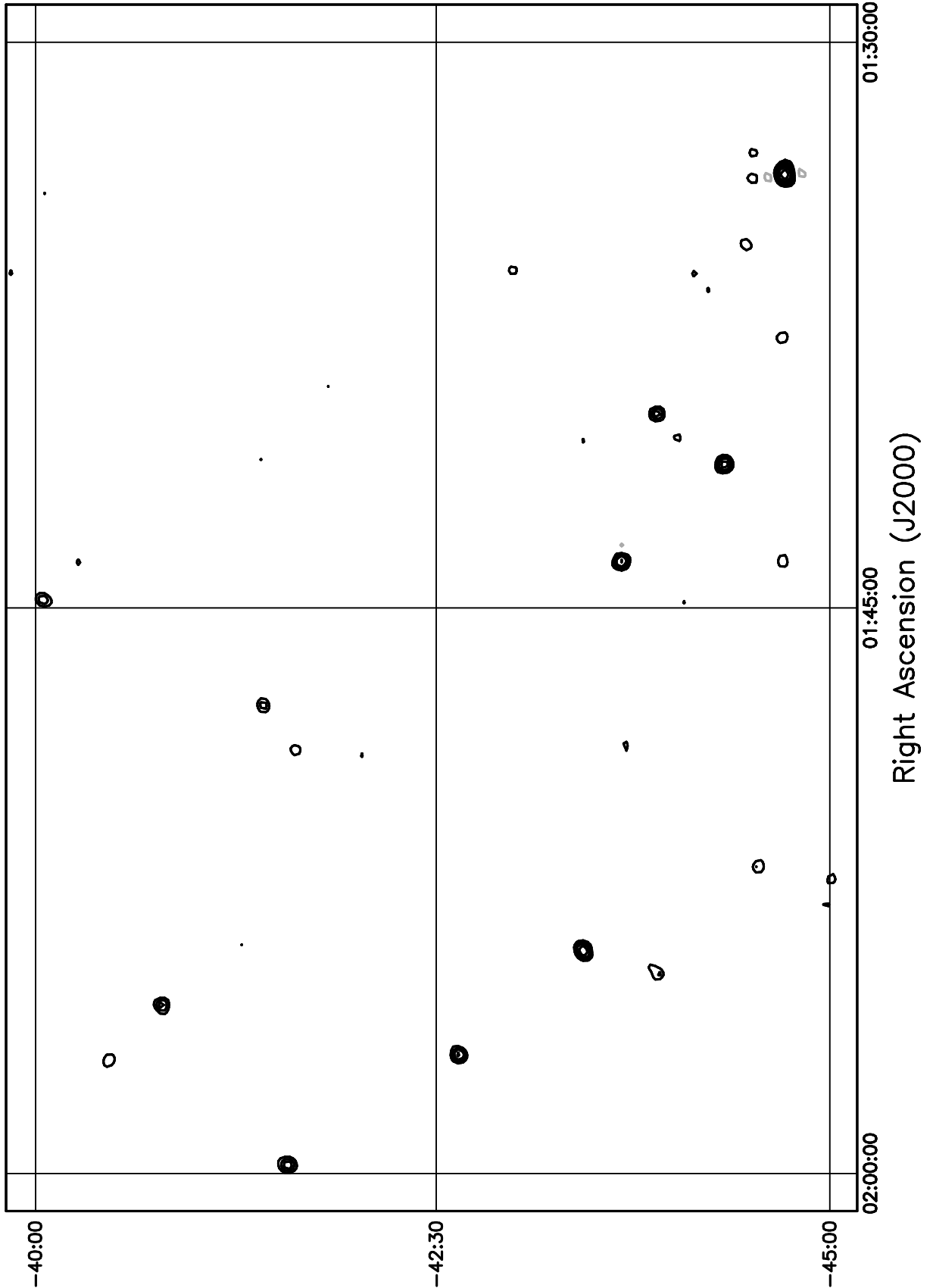
Figure 5.94: Contour plot for the range $01^h30^m \leq RA \leq 02^h00^m$, $-40° \leq \delta \leq -35°$. Contour levels are -5.04, -3.6, -2.52, -1.8, -1.08, 1.08, 1.8, 2.52, 3.6, 5.04, 7.2, 10.08, 14.4, 20.16, 28.8, 39.6, 54, 72, 100.8, 136.8, 180, 216, 252, 288 Jy beam^{-1}.
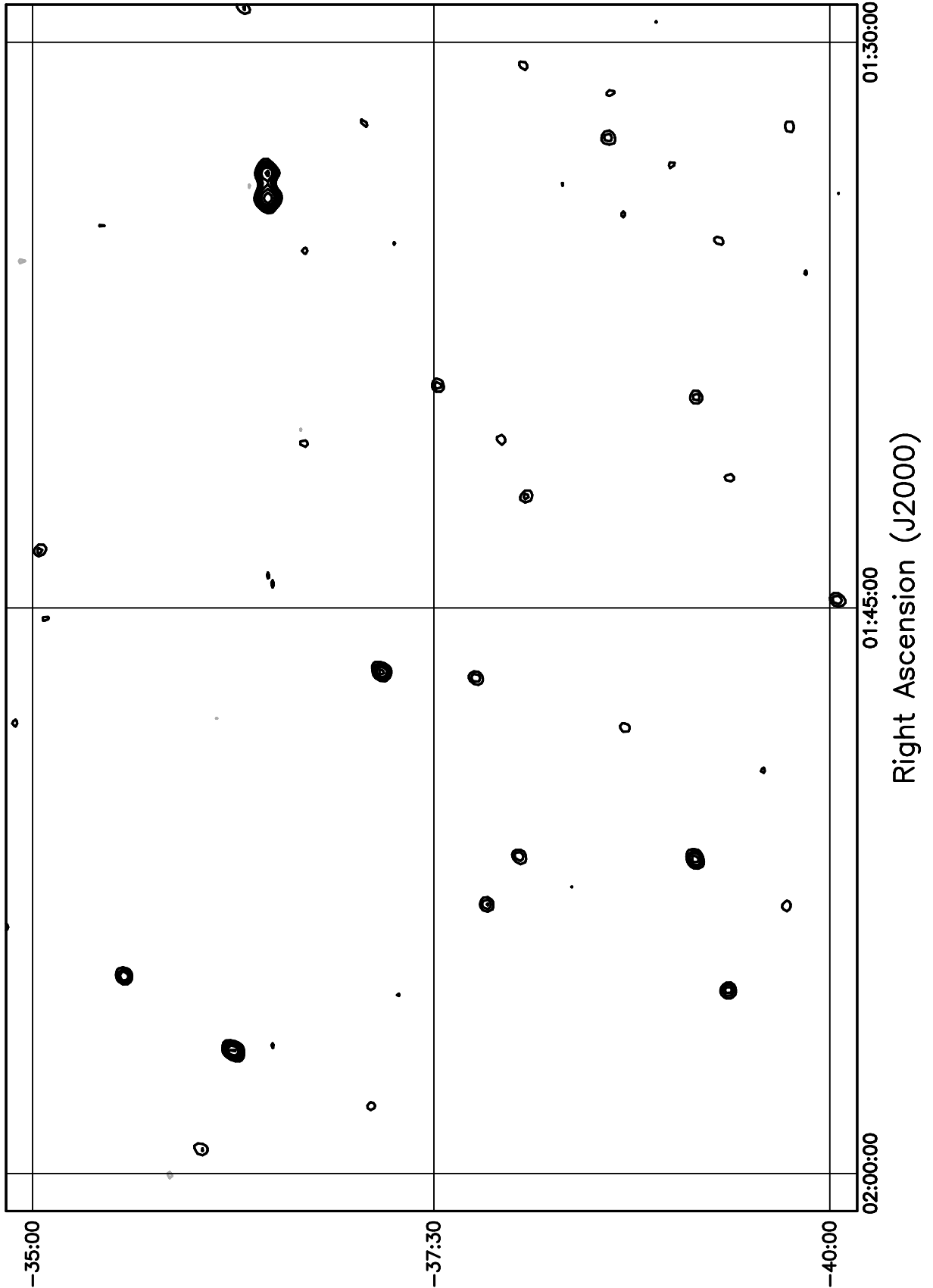
Figure 5.95: Contour plot for the range $01^h30^m \leq RA \leq 02^h00^m$, $-35° \leq \delta \leq -30°$. Contour levels are -5.04, -3.6, -2.52, -1.8, -1.08, 1.08, 1.8, 2.52, 3.6, 5.04, 7.2, 10.08, 14.4, 20.16, 28.8, 39.6, 54, 72, 100.8, 136.8, 180, 216, 252, 288 Jy beam^{-1}.

Right Ascension (J2000)
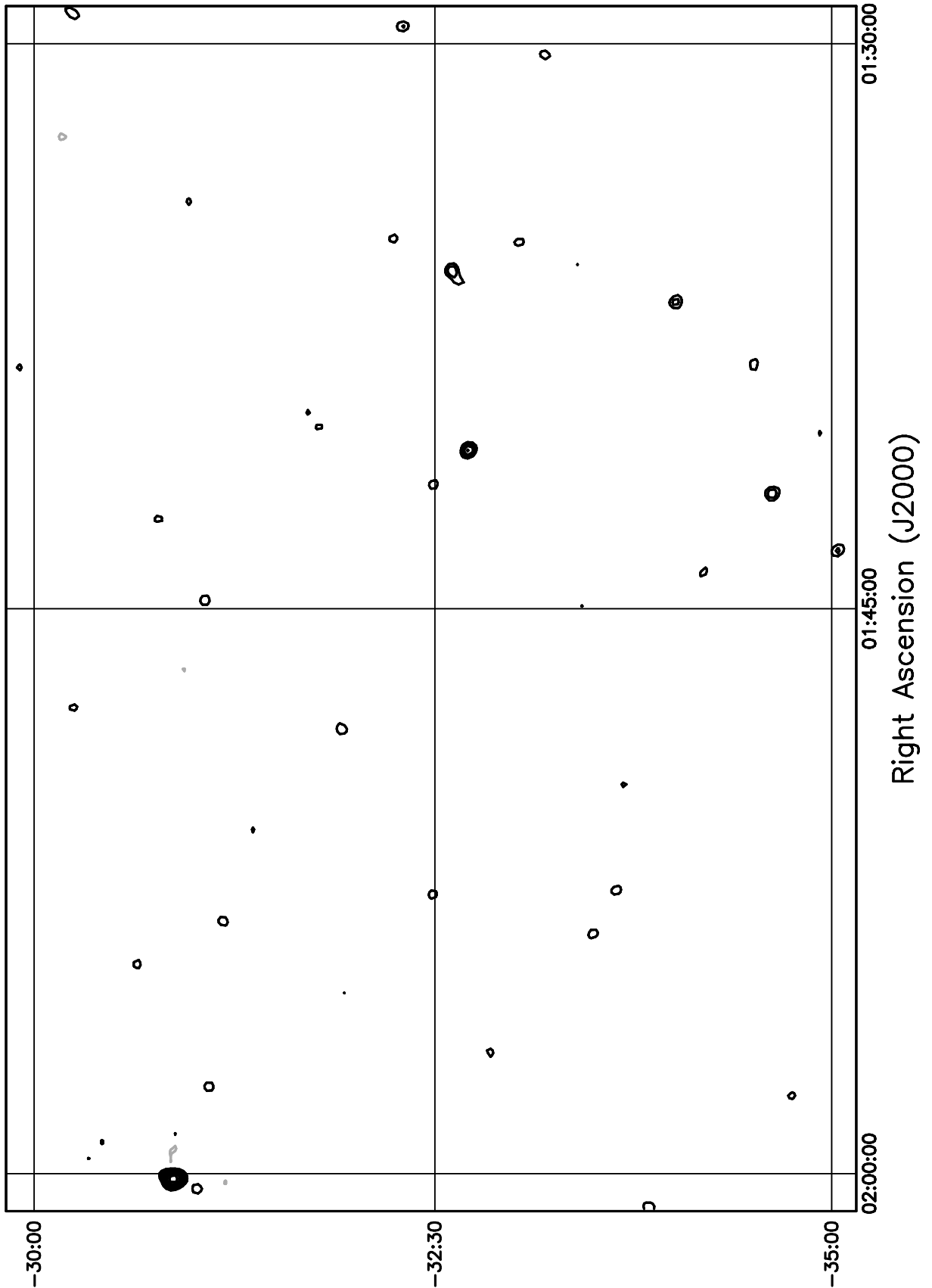
Figure 5.96: Contour plot for the range $01^h30^m \leq RA \leq 02^h00^m$, $-30° \leq \delta \leq -25°$. Contour levels are -5.04, -3.6, -2.52, -1.8, -1.08, 1.08, 1.8, 2.52, 3.6, 5.04, 7.2, 10.08, 14.4, 20.16, 28.8, 39.6, 54, 72, 100.8, 136.8, 180, 216, 252, 288 Jy beam^{-1}.
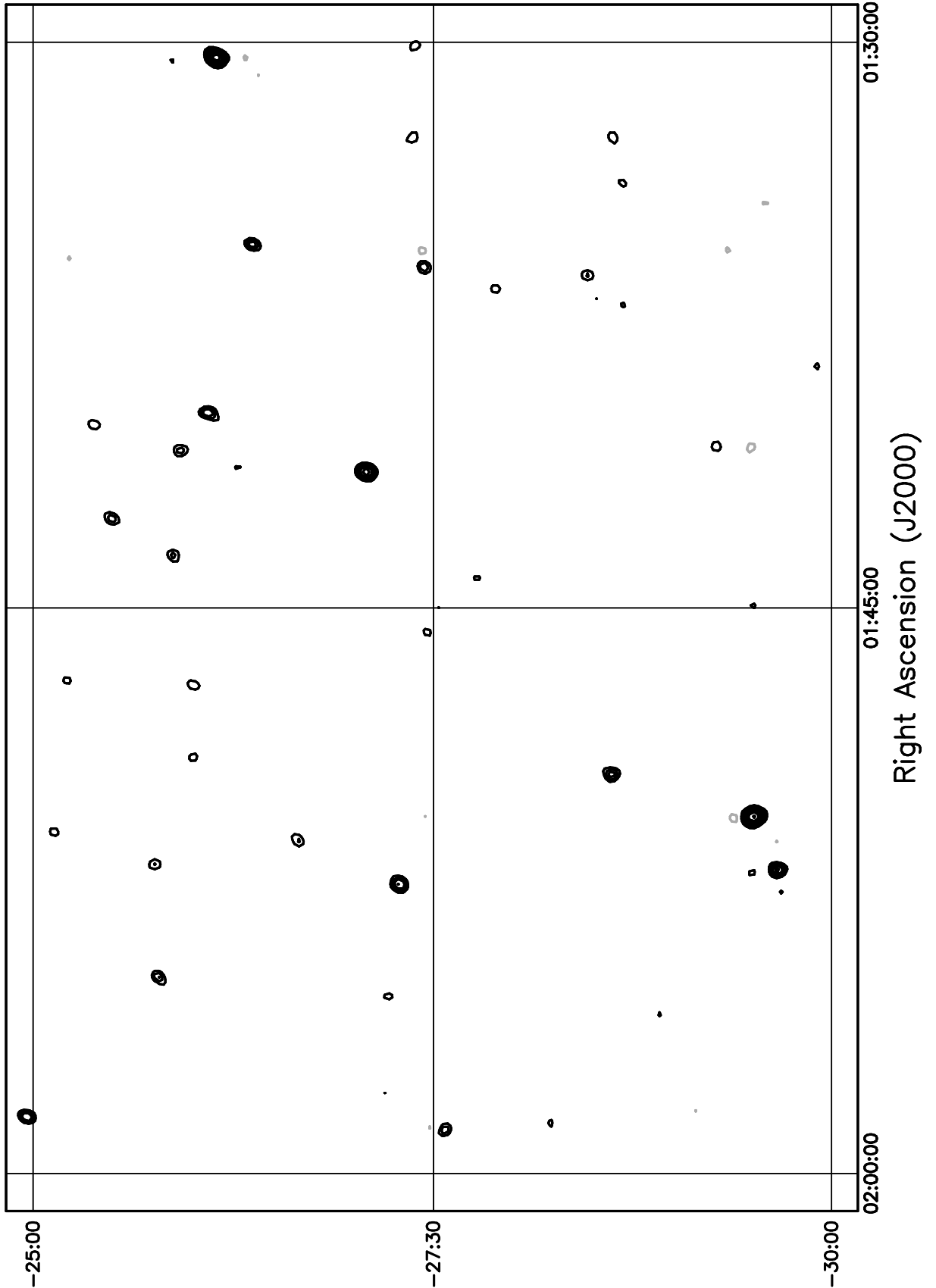
Figure 5.97: Contour plot for the range $01^h30^m \leq RA \leq 02^h00^m$, $-25° \leq \delta \leq -20°$. Contour levels are -5.04, -3.6, -2.52, -1.8, -1.08, 1.08, 1.8, 2.52, 3.6, 5.04, 7.2, 10.08, 14.4, 20.16, 28.8, 39.6, 54, 72, 100.8, 136.8, 180, 216, 252, 288 Jy beam^{-1}.
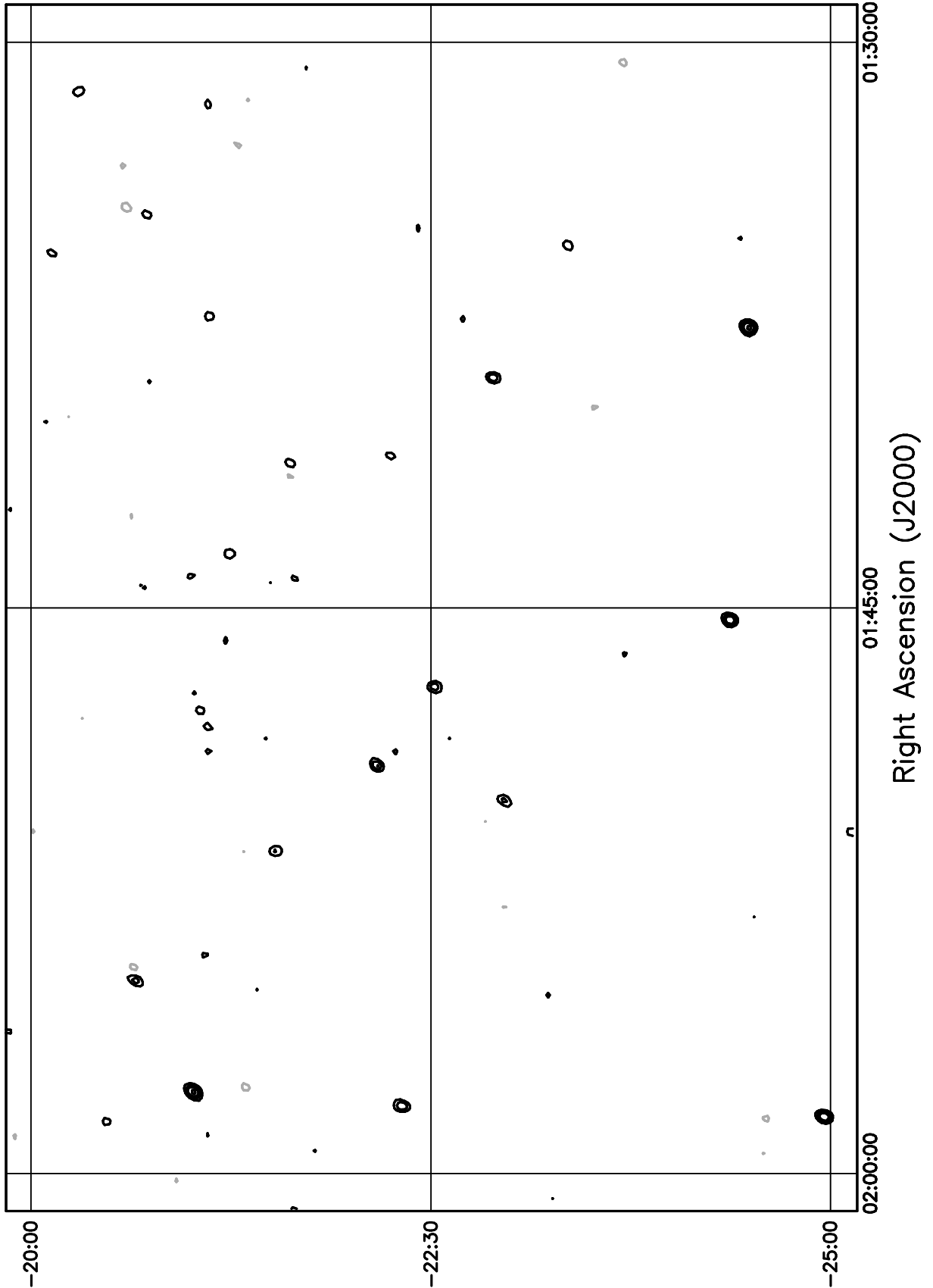
Figure 5.98: Contour plot for the range $01^h30^m \leq RA \leq 02^h00^m$, $-20° \leq \delta \leq -15°$. Contour levels are -5.04, -3.6, -2.52, -1.8, -1.08, 1.08, 1.8, 2.52, 3.6, 5.04, 7.2, 10.08, 14.4, 20.16, 28.8, 39.6, 54, 72, 100.8, 136.8, 180, 216, 252, 288 Jy beam^{-1}.
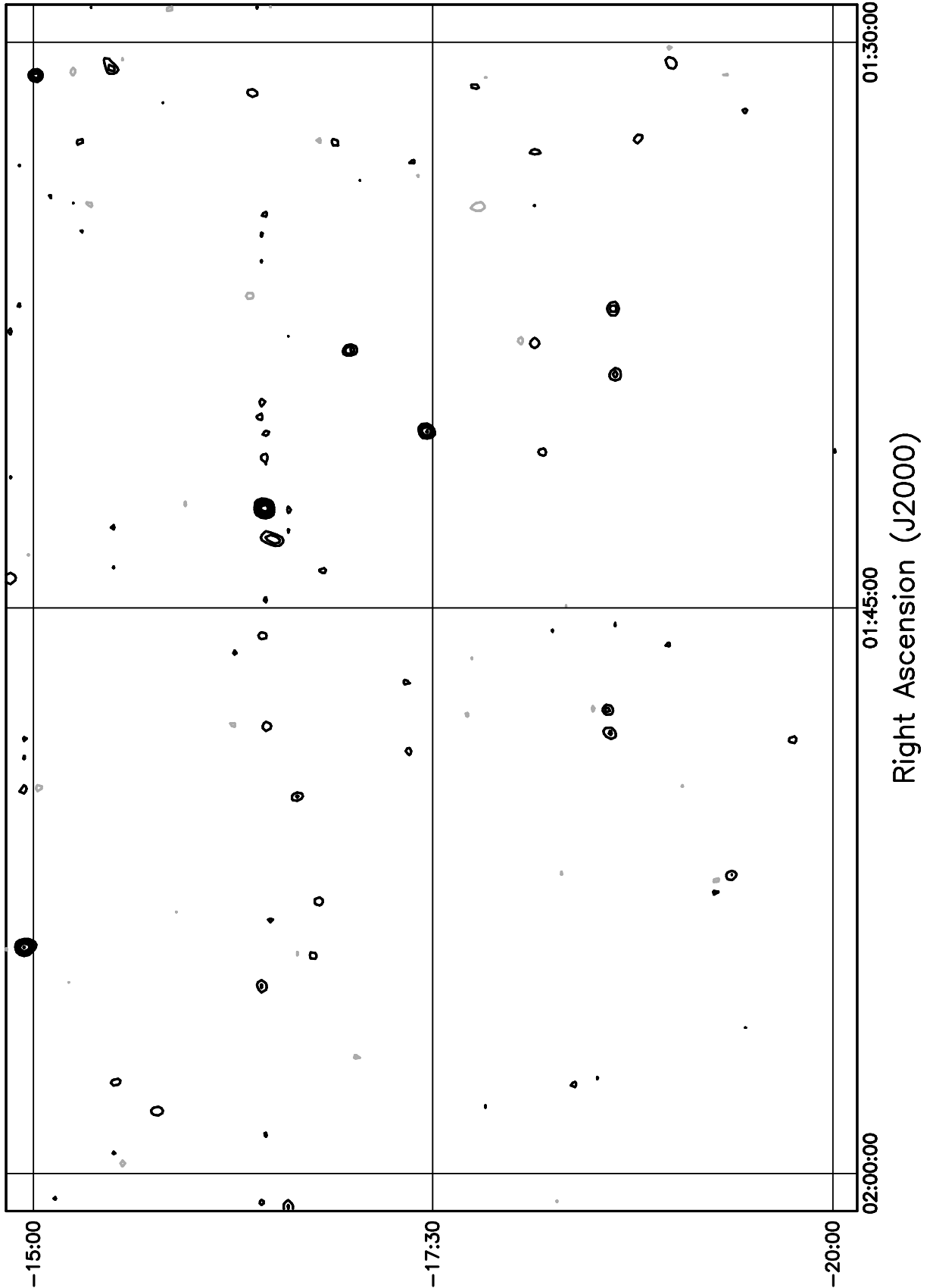
Figure 5.99: Contour plot for the range $01^h30^m \leq RA \leq 02^h00^m$, $-15° \leq \delta \leq -10°$. Contour levels are -5.04, -3.6, -2.52, -1.8, -1.08, 1.08, 1.8, 2.52, 3.6, 5.04, 7.2, 10.08, 14.4, 20.16, 28.8, 39.6, 54, 72, 100.8, 136.8, 180, 216, 252, 288 Jy beam^{-1}.


Right Ascension (J2000)
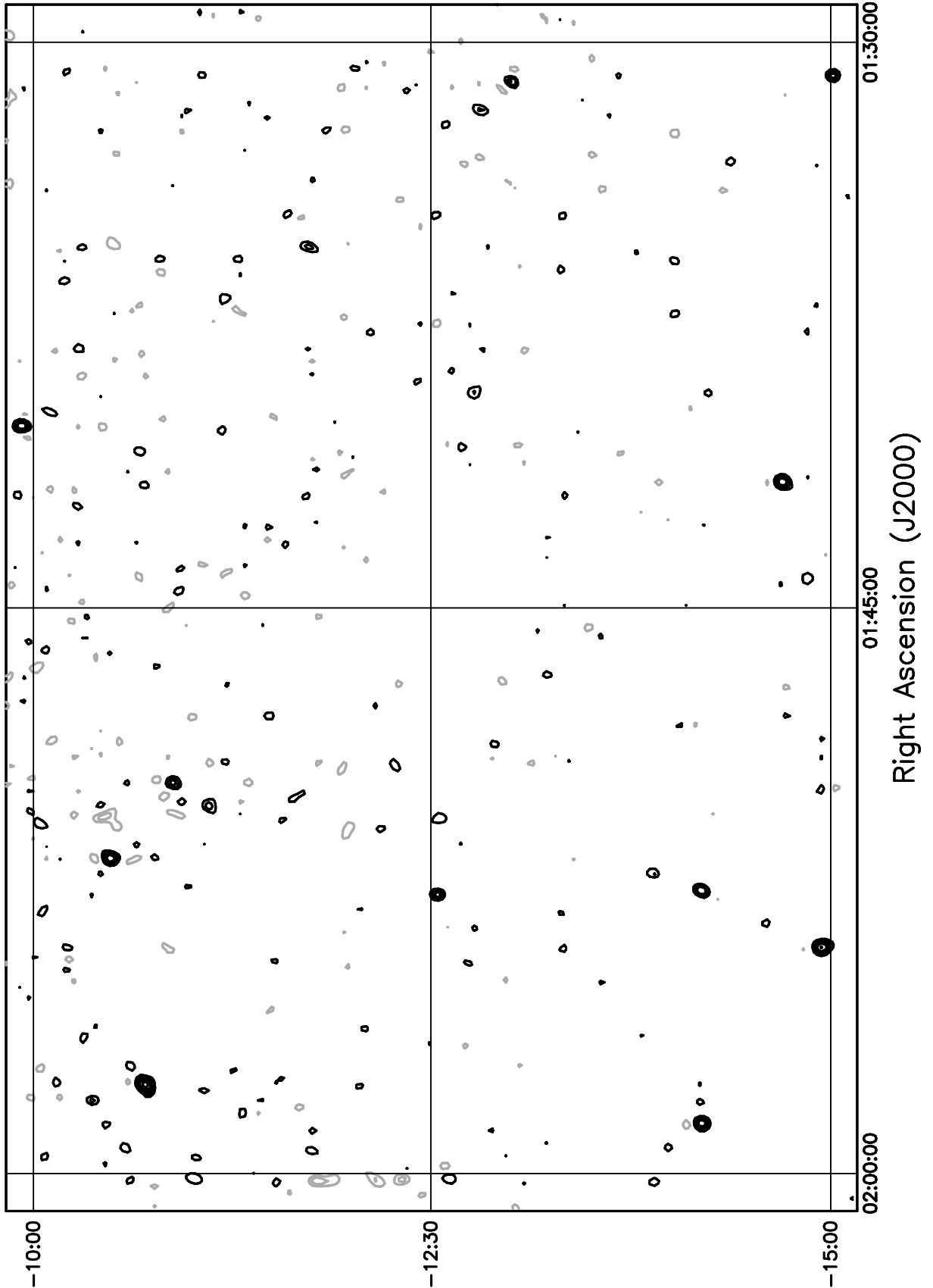
Figure 5.100: Contour plot for the range $02^h00^m \leq RA \leq 02^h30^m$, $-75° \leq \delta \leq -70°$. Contour levels are -5.04, -3.6, -2.52, -1.8, -1.08, 1.08, 1.8, 2.52, 3.6, 5.04, 7.2, 10.08, 14.4, 20.16, 28.8, 39.6, 54, 72, 100.8, 136.8, 180, 216, 252, 288 Jy beam^{-1}.
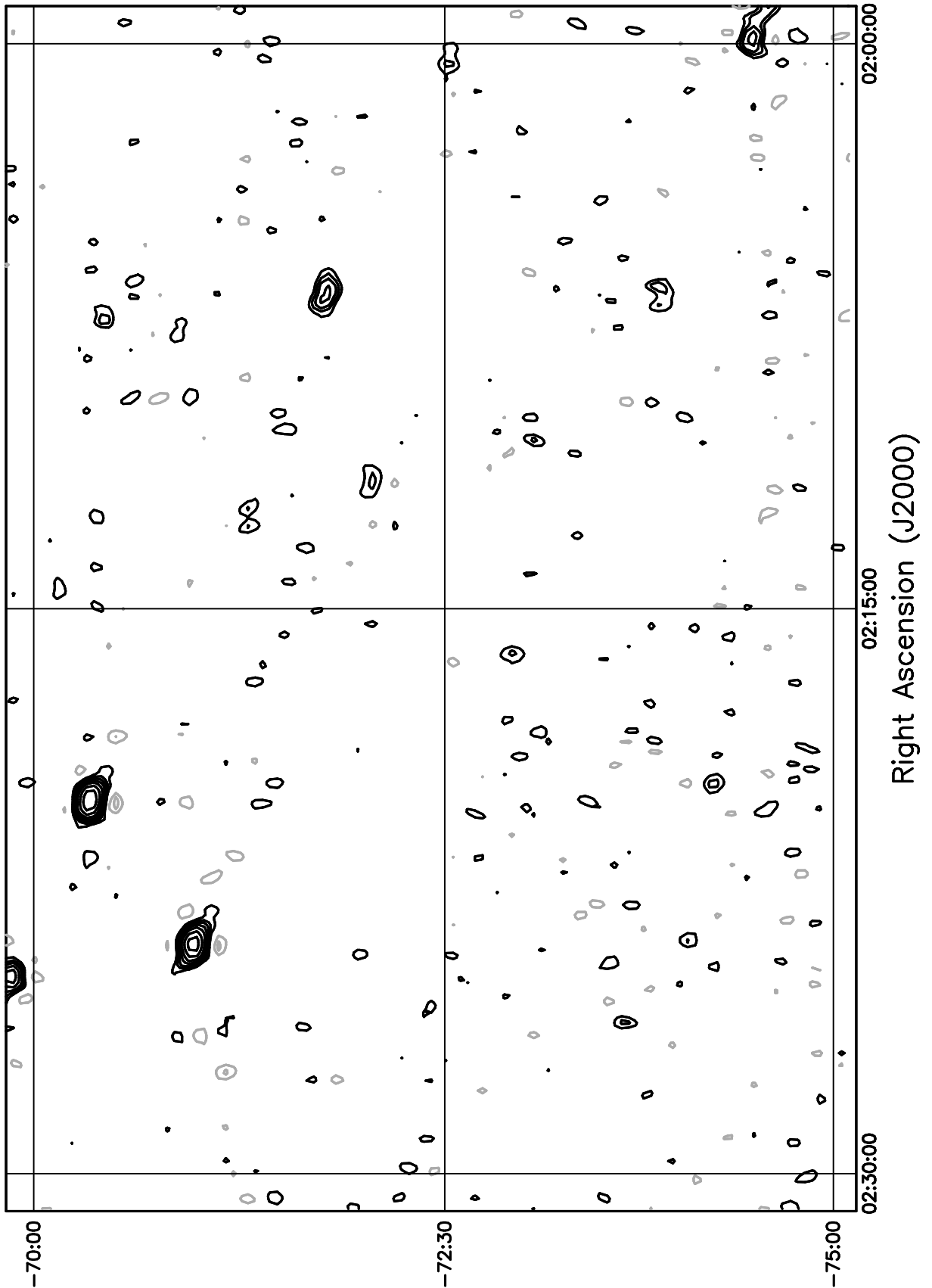
Figure 5.101: Contour plot for the range $02^h00^m \leq RA \leq 02^h30^m$, $-70° \leq \delta \leq -65°$. Contour levels are -5.04, -3.6, -2.52, -1.8, -1.08, 1.08, 1.8, 2.52, 3.6, 5.04, 7.2, 10.08, 14.4, 20.16, 28.8, 39.6, 54, 72, 100.8, 136.8, 180, 216, 252, 288 Jy beam^{-1}.
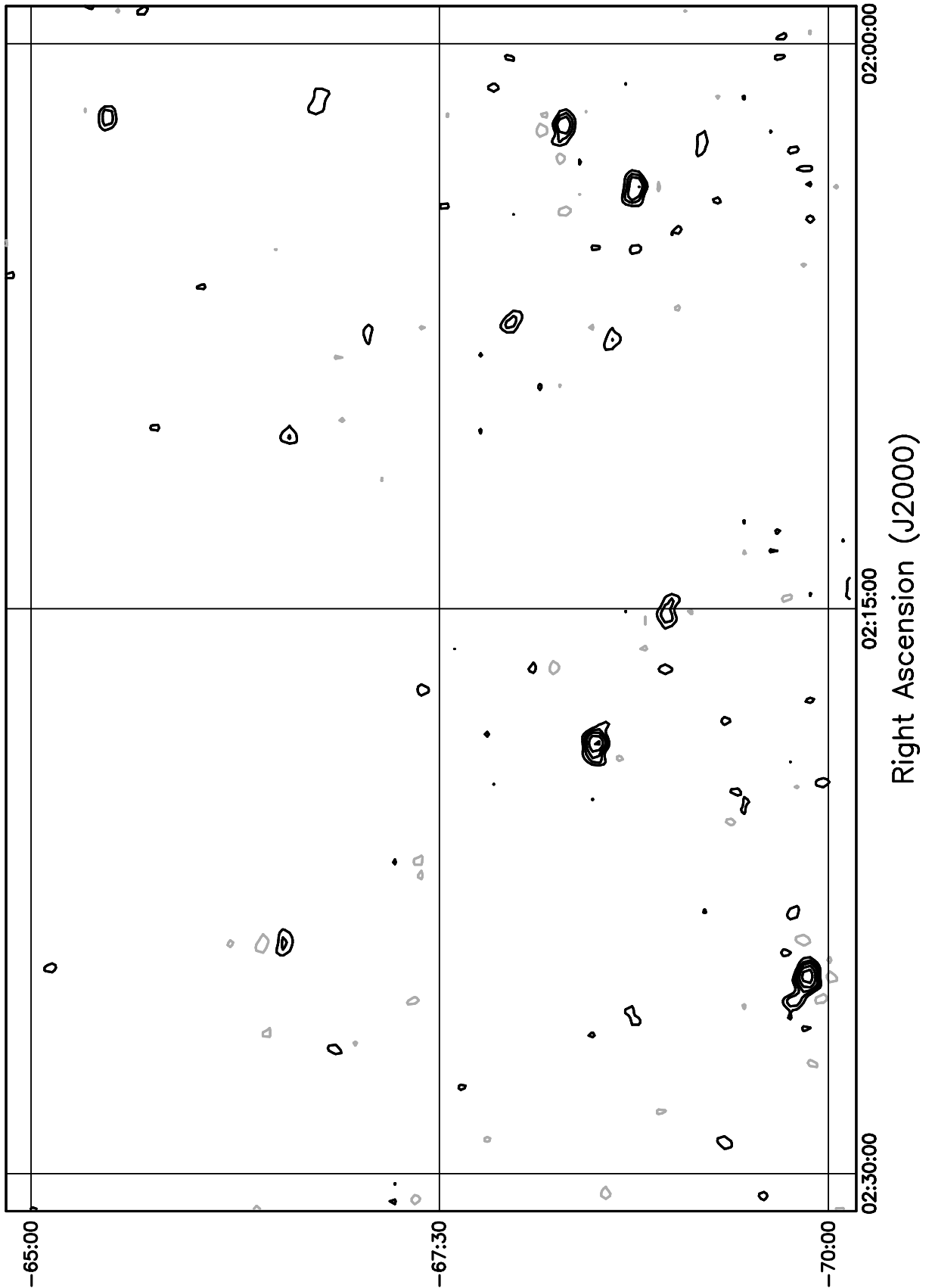
Figure 5.102: Contour plot for the range $02^h00^m \leq RA \leq 02^h30^m$, $-65° \leq \delta \leq -60°$. Contour levels are -5.04, -3.6, -2.52, -1.8, -1.08, 1.08, 1.8, 2.52, 3.6, 5.04, 7.2, 10.08, 14.4, 20.16, 28.8, 39.6, 54, 72, 100.8, 136.8, 180, 216, 252, 288 Jy beam^{-1}.
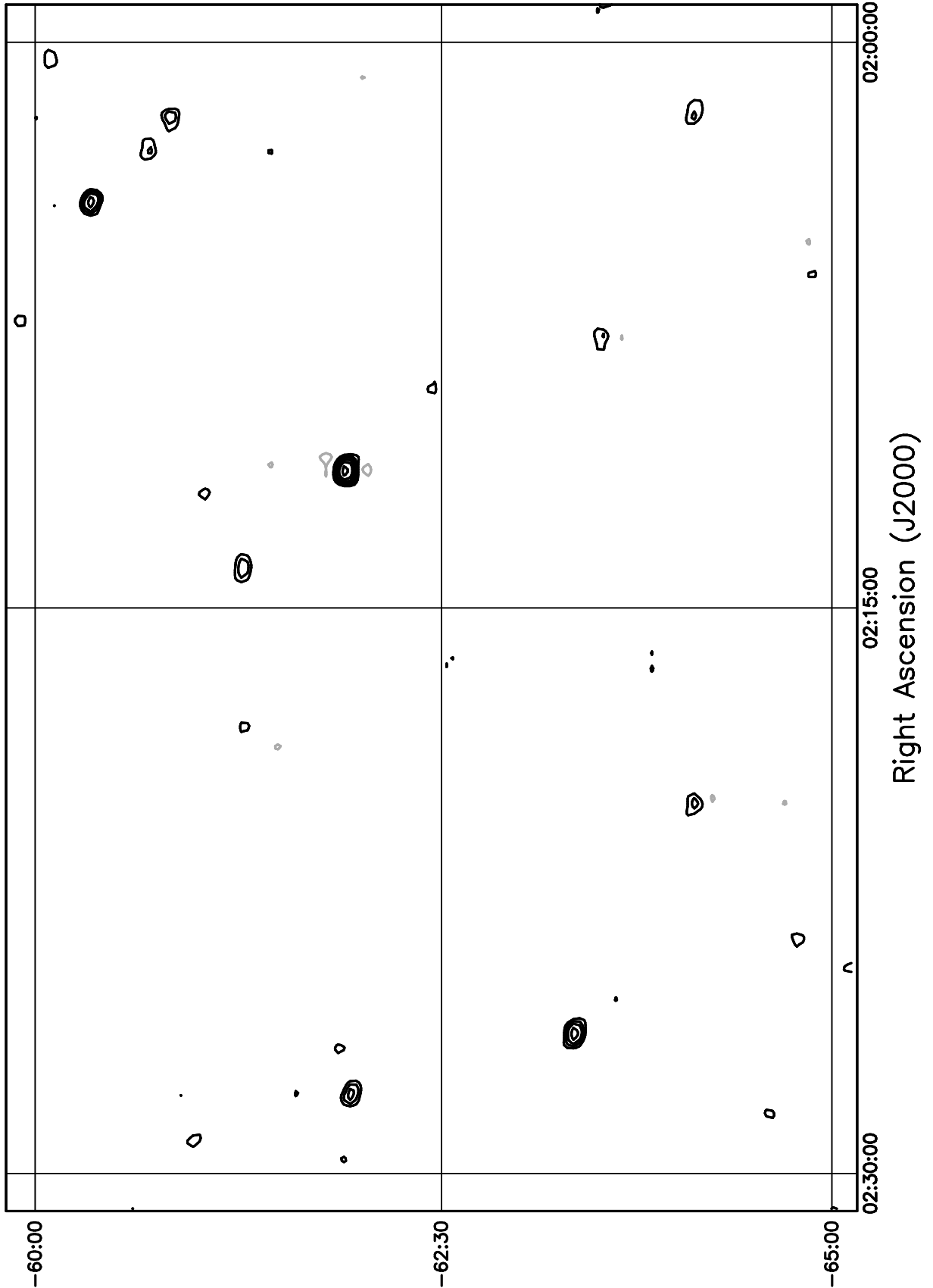
Figure 5.103: Contour plot for the range $02^h00^m \leq RA \leq 02^h30^m$, $-60° \leq \delta \leq -55°$. Contour levels are -5.04, -3.6, -2.52, -1.8, -1.08, 1.08, 1.8, 2.52, 3.6, 5.04, 7.2, 10.08, 14.4, 20.16, 28.8, 39.6, 54, 72, 100.8, 136.8, 180, 216, 252, 288 Jy beam^{-1}.
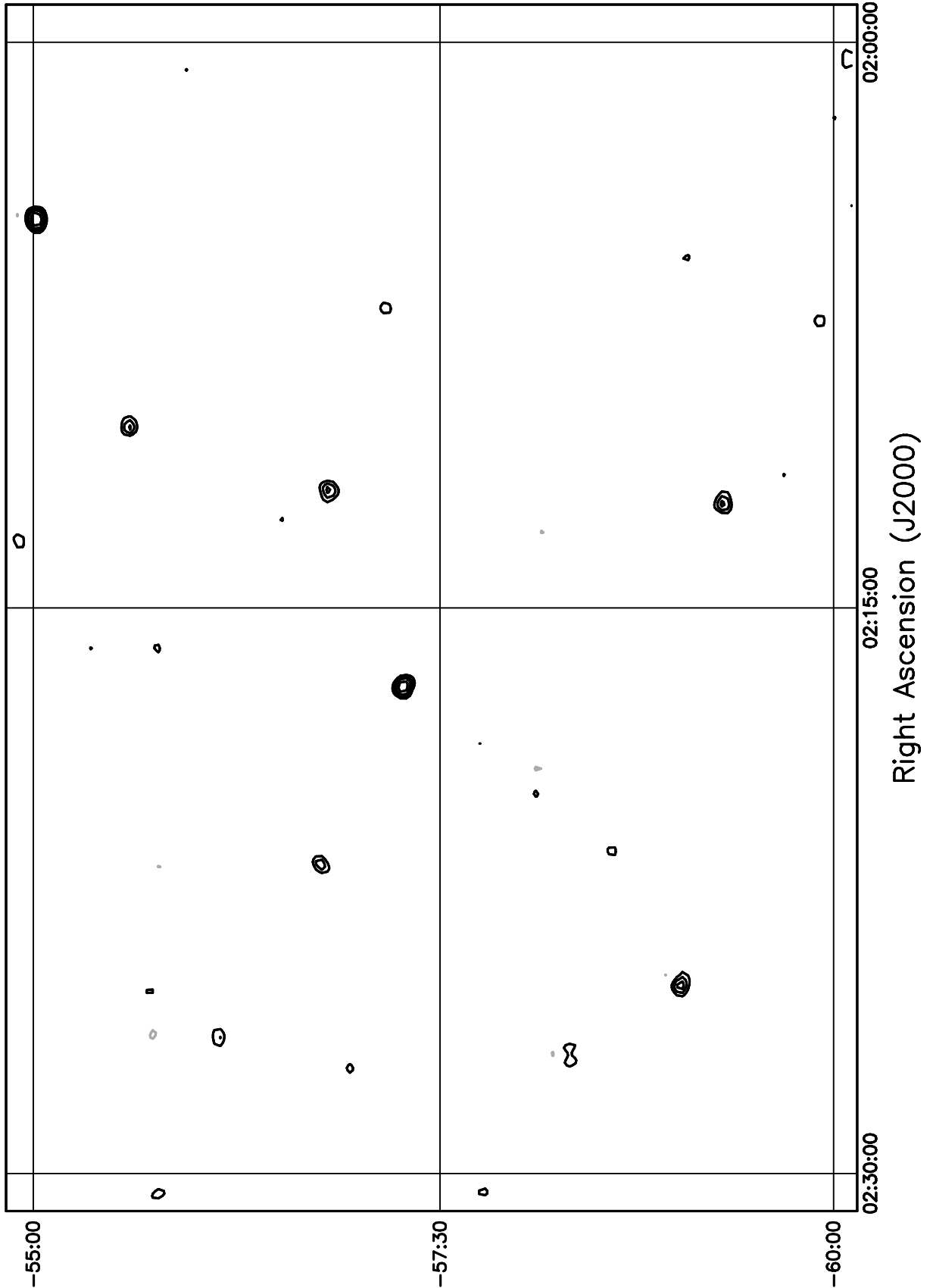
Figure 5.104: Contour plot for the range $02^h00^m \leq RA \leq 02^h30^m$, $-55° \leq \delta \leq -50°$. Contour levels are -5.04, -3.6, -2.52, -1.8, -1.08, 1.08, 1.8, 2.52, 3.6, 5.04, 7.2, 10.08, 14.4, 20.16, 28.8, 39.6, 54, 72, 100.8, 136.8, 180, 216, 252, 288 Jy beam^{-1}.
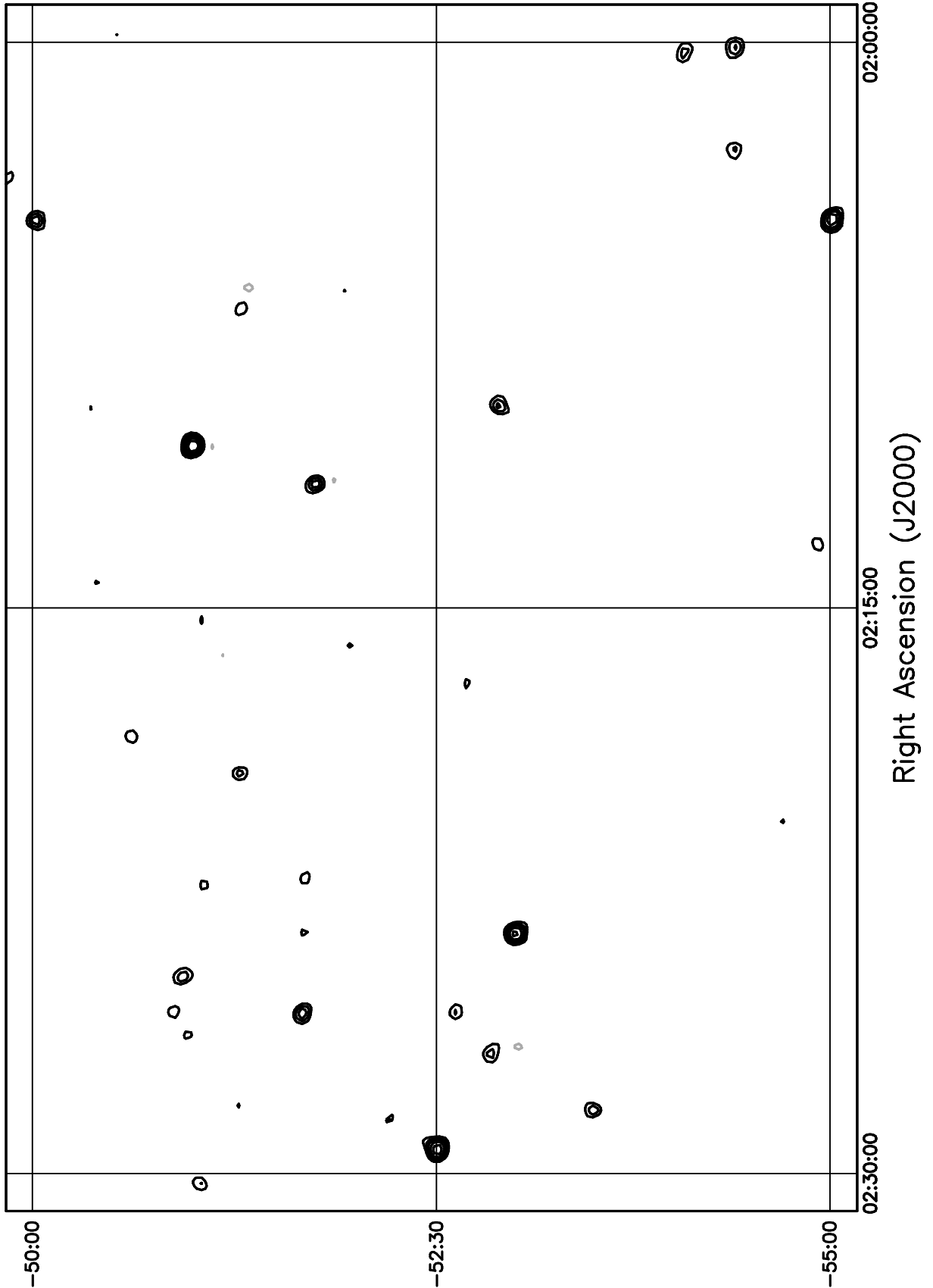
Figure 5.105: Contour plot for the range $02^h00^m \leq RA \leq 02^h30^m$, $-50° \leq \delta \leq -45°$. Contour levels are -5.04, -3.6, -2.52, -1.8, -1.08, 1.08, 1.8, 2.52, 3.6, 5.04, 7.2, 10.08, 14.4, 20.16, 28.8, 39.6, 54, 72, 100.8, 136.8, 180, 216, 252, 288 Jy beam^{-1}.
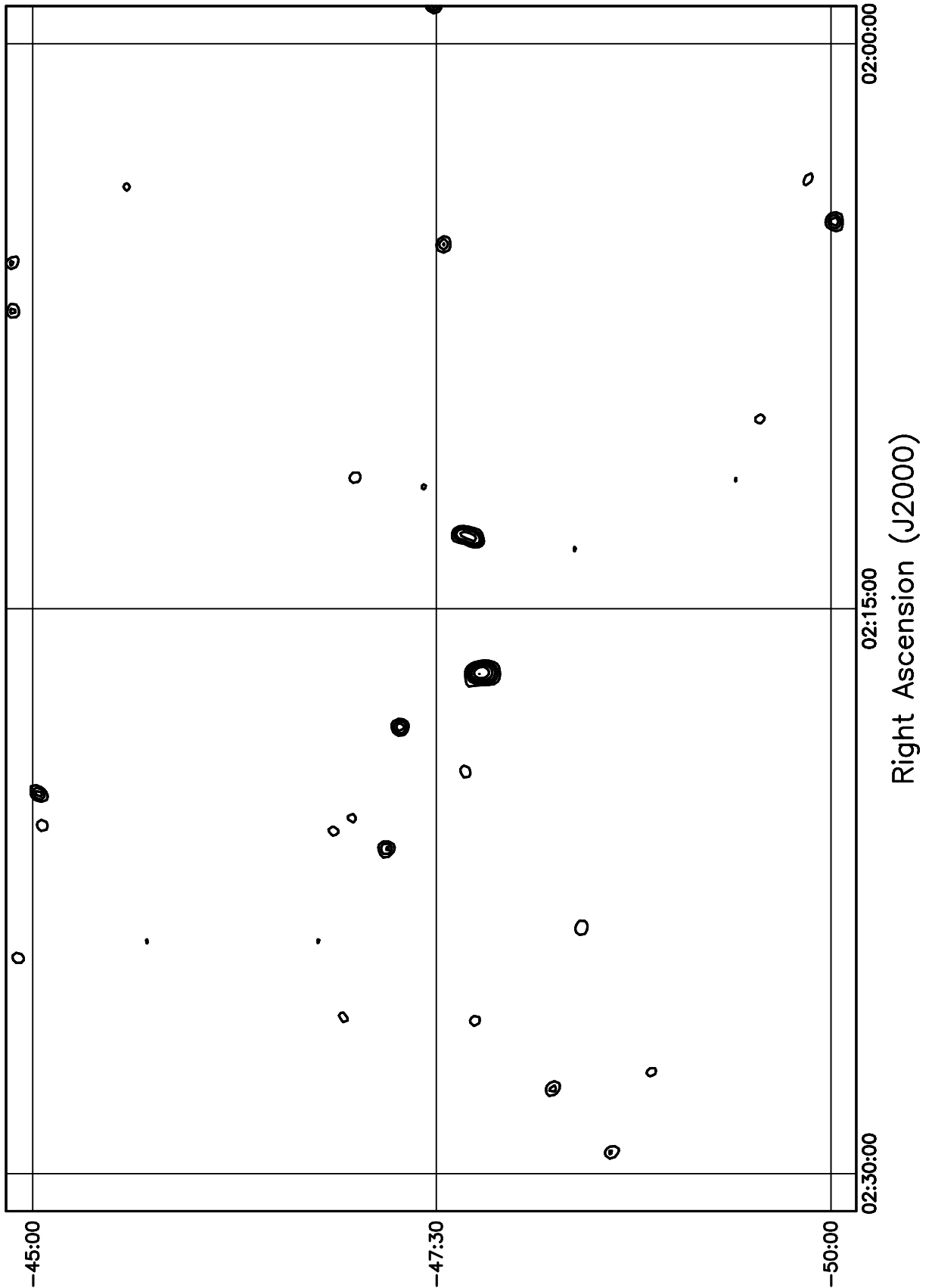
Figure 5.106: Contour plot for the range $02^h00^m \leq RA \leq 02^h30^m$, $-45° \leq \delta \leq -40°$. Contour levels are -5.04, -3.6, -2.52, -1.8, -1.08, 1.08, 1.8, 2.52, 3.6, 5.04, 7.2, 10.08, 14.4, 20.16, 28.8, 39.6, 54, 72, 100.8, 136.8, 180, 216, 252, 288 Jy beam^{-1}.
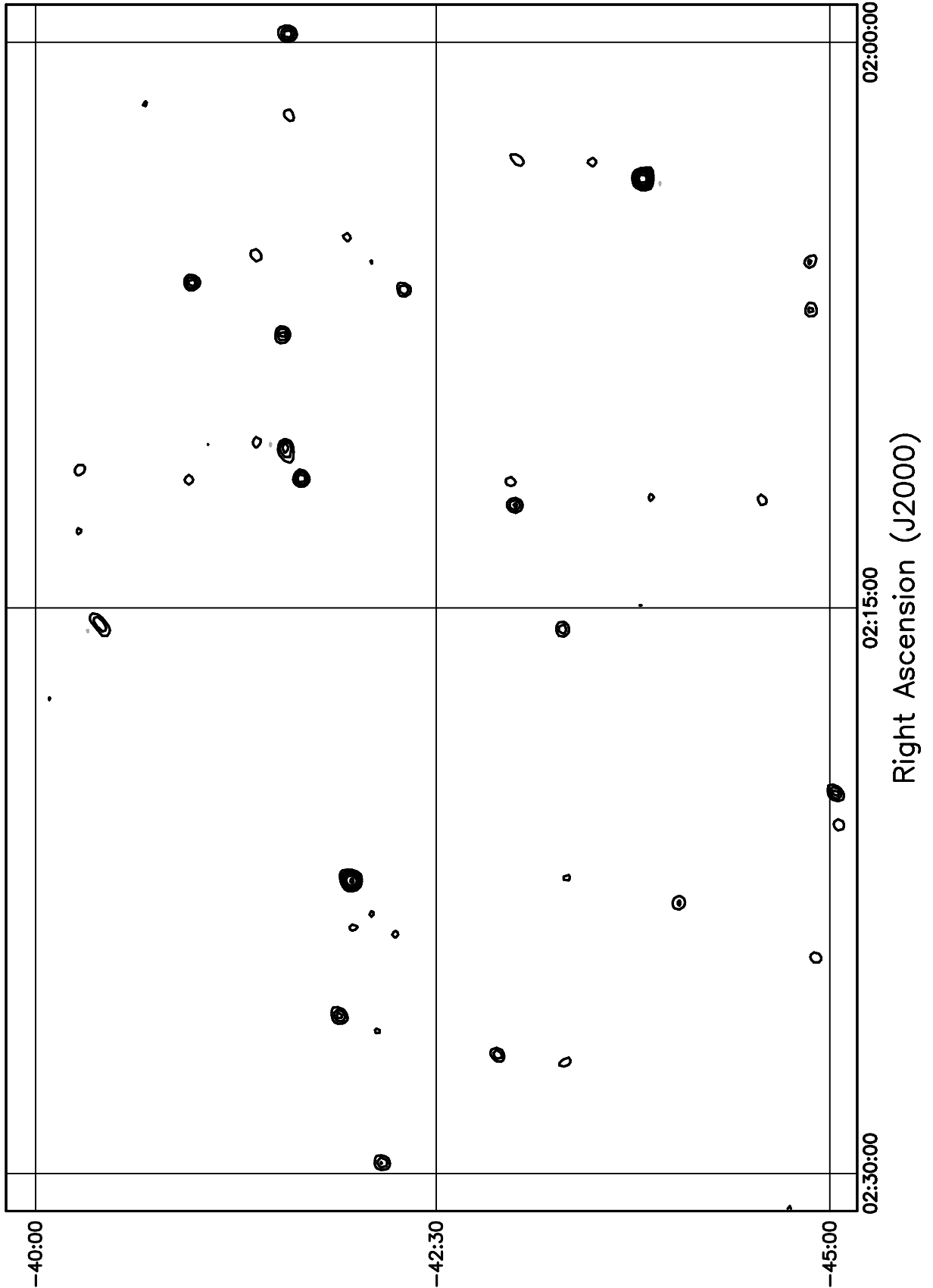
Figure 5.107: Contour plot for the range $02^h00^m \leq RA \leq 02^h30^m$, $-40° \leq \delta \leq -35°$. Contour levels are -5.04, -3.6, -2.52, -1.8, -1.08, 1.08, 1.8, 2.52, 3.6, 5.04, 7.2, 10.08, 14.4, 20.16, 28.8, 39.6, 54, 72, 100.8, 136.8, 180, 216, 252, 288 Jy beam^{-1}.
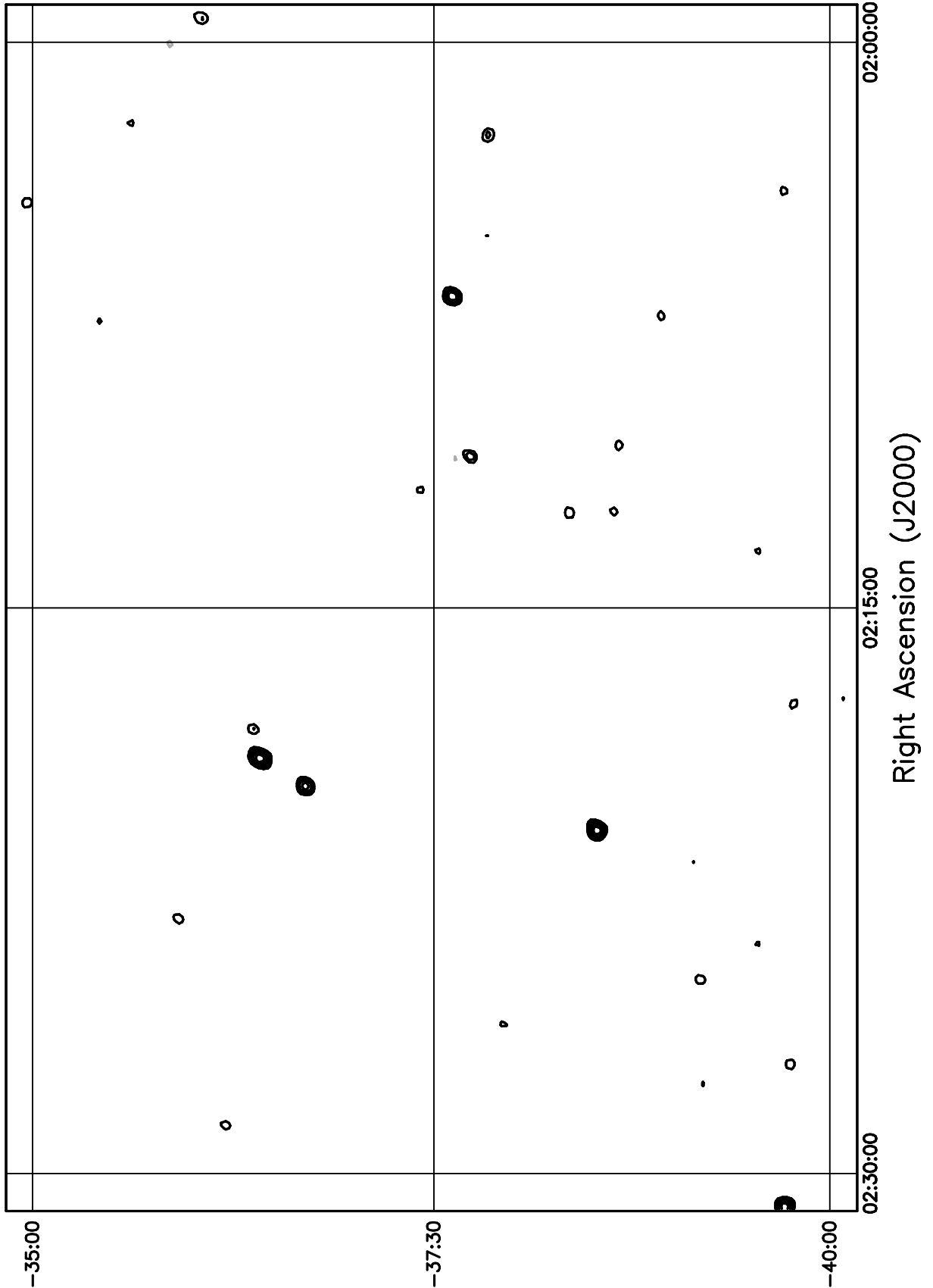
Figure 5.108: Contour plot for the range $02^h00^m \leq RA \leq 02^h30^m$, $-35° \leq \delta \leq -30°$. Contour levels are -5.04, -3.6, -2.52, -1.8, -1.08, 1.08, 1.8, 2.52, 3.6, 5.04, 7.2, 10.08, 14.4, 20.16, 28.8, 39.6, 54, 72, 100.8, 136.8, 180, 216, 252, 288 Jy beam^{-1}.

Figure 5.109: Contour plot for the range $02^h00^m \leq RA \leq 02^h30^m$, $-30° \leq \delta \leq -25°$. Contour levels are -5.04, -3.6, -2.52, -1.8, -1.08, 1.08, 1.8, 2.52, 3.6, 5.04, 7.2, 10.08, 14.4, 20.16, 28.8, 39.6, 54, 72, 100.8, 136.8, 180, 216, 252, 288 Jy beam^{-1}.
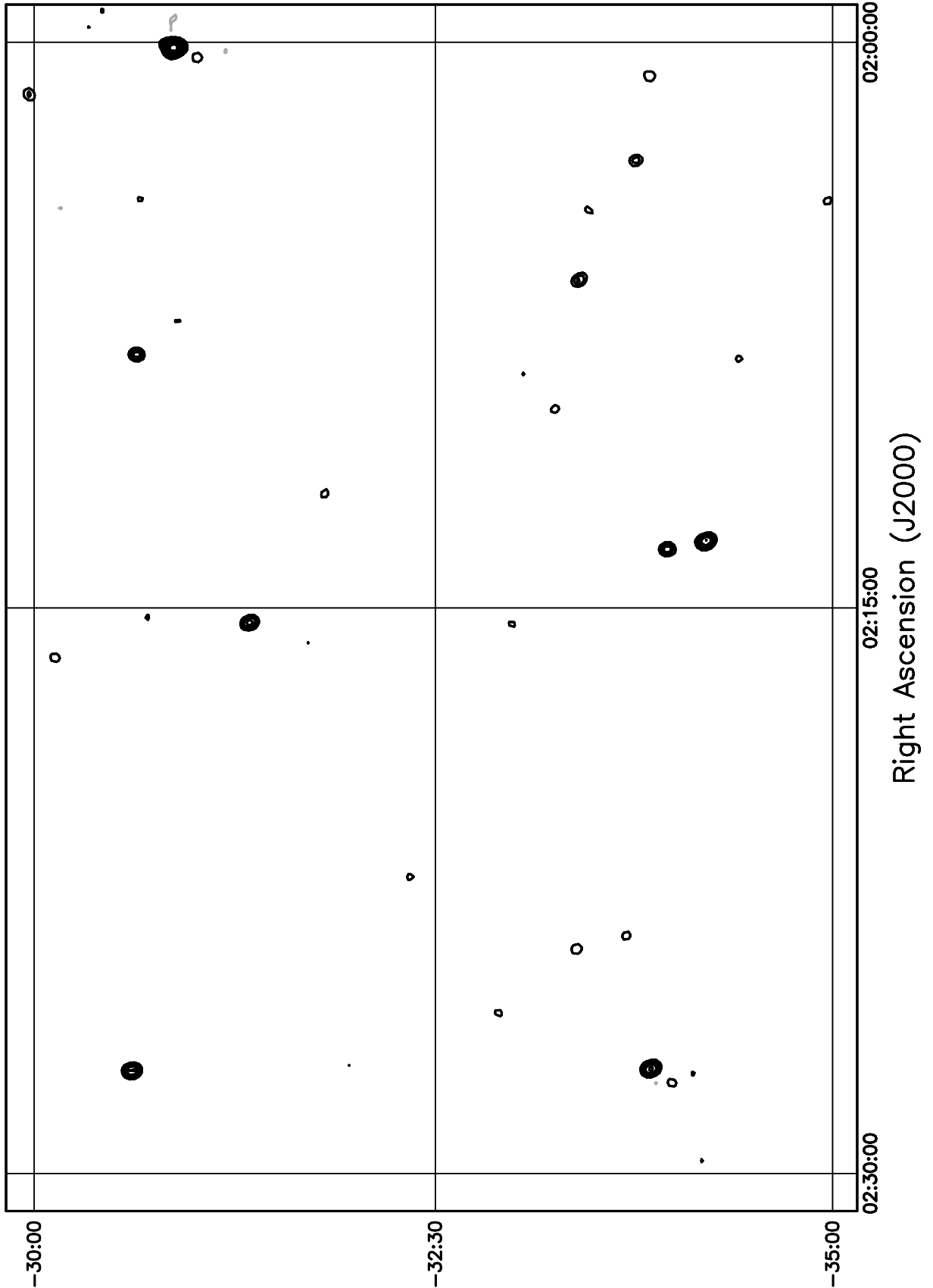
Figure 5.110: Contour plot for the range $02^h00^m \leq RA \leq 02^h30^m$, $-25° \leq \delta \leq -20°$. Contour levels are -5.04, -3.6, -2.52, -1.8, -1.08, 1.08, 1.8, 2.52, 3.6, 5.04, 7.2, 10.08, 14.4, 20.16, 28.8, 39.6, 54, 72, 100.8, 136.8, 180, 216, 252, 288 Jy beam^{-1}.
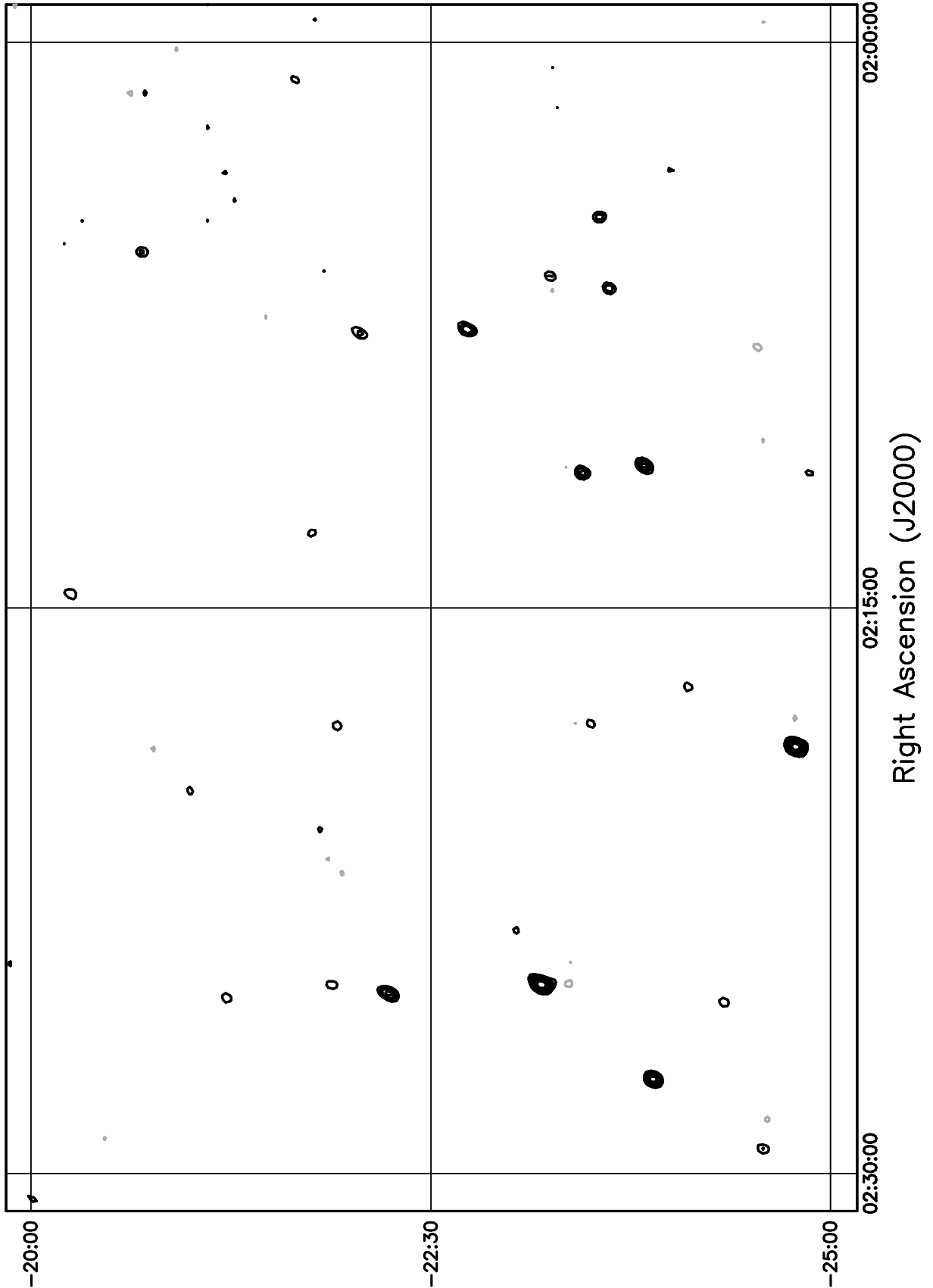
Figure 5.111: Contour plot for the range $02^h00^m \leq RA \leq 02^h30^m$, $-20° \leq \delta \leq -15°$. Contour levels are -5.04, -3.6, -2.52, -1.8, -1.08, 1.08, 1.8, 2.52, 3.6, 5.04, 7.2, 10.08, 14.4, 20.16, 28.8, 39.6, 54, 72, 100.8, 136.8, 180, 216, 252, 288 Jy beam^{-1}.
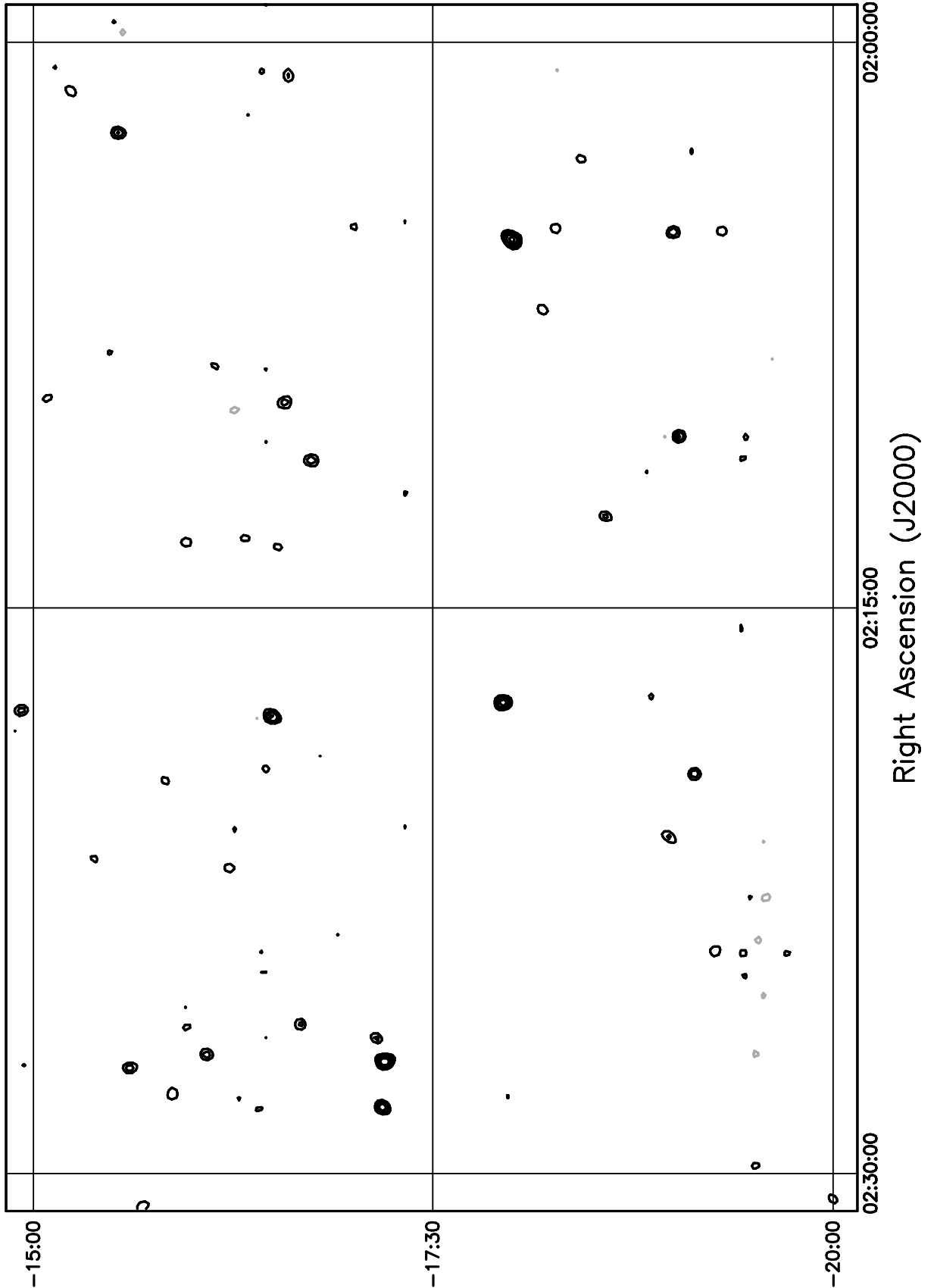
Figure 5.112: Contour plot for the range $02^h00^m \leq RA \leq 02^h30^m$, $-15° \leq \delta \leq -10°$. Contour levels are -5.04, -3.6, -2.52, -1.8, -1.08, 1.08, 1.8, 2.52, 3.6, 5.04, 7.2, 10.08, 14.4, 20.16, 28.8, 39.6, 54, 72, 100.8, 136.8, 180, 216, 252, 288 Jy beam^{-1}.
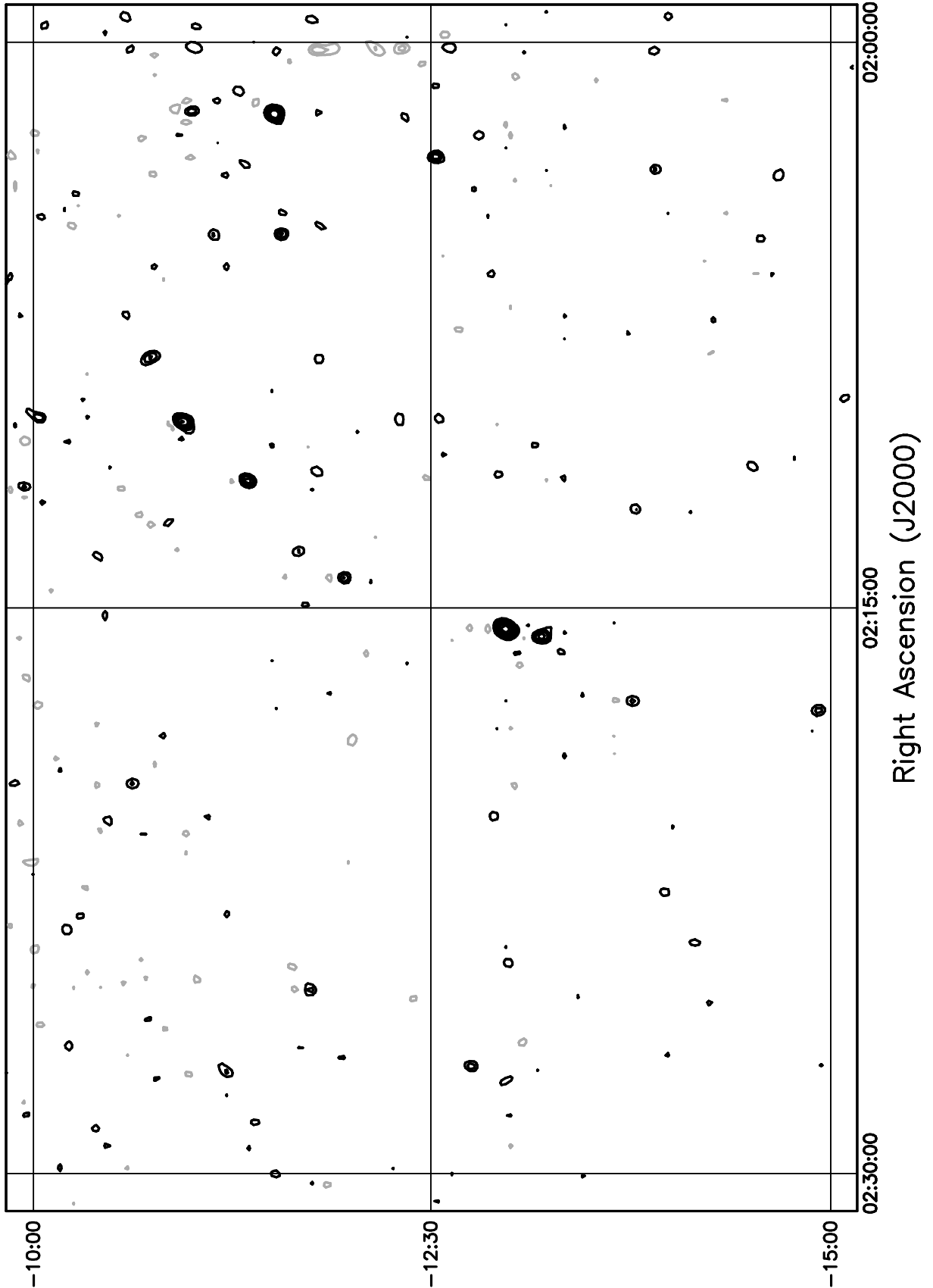
Figure 5.113: Contour plot for the range $02^h30^m \leq RA \leq 03^h00^m$, $-75° \leq \delta \leq -70°$. Contour levels are -5.04, -3.6, -2.52, -1.8, -1.08, 1.08, 1.8, 2.52, 3.6, 5.04, 7.2, 10.08, 14.4, 20.16, 28.8, 39.6, 54, 72, 100.8, 136.8, 180, 216, 252, 288 Jy beam^{-1}.
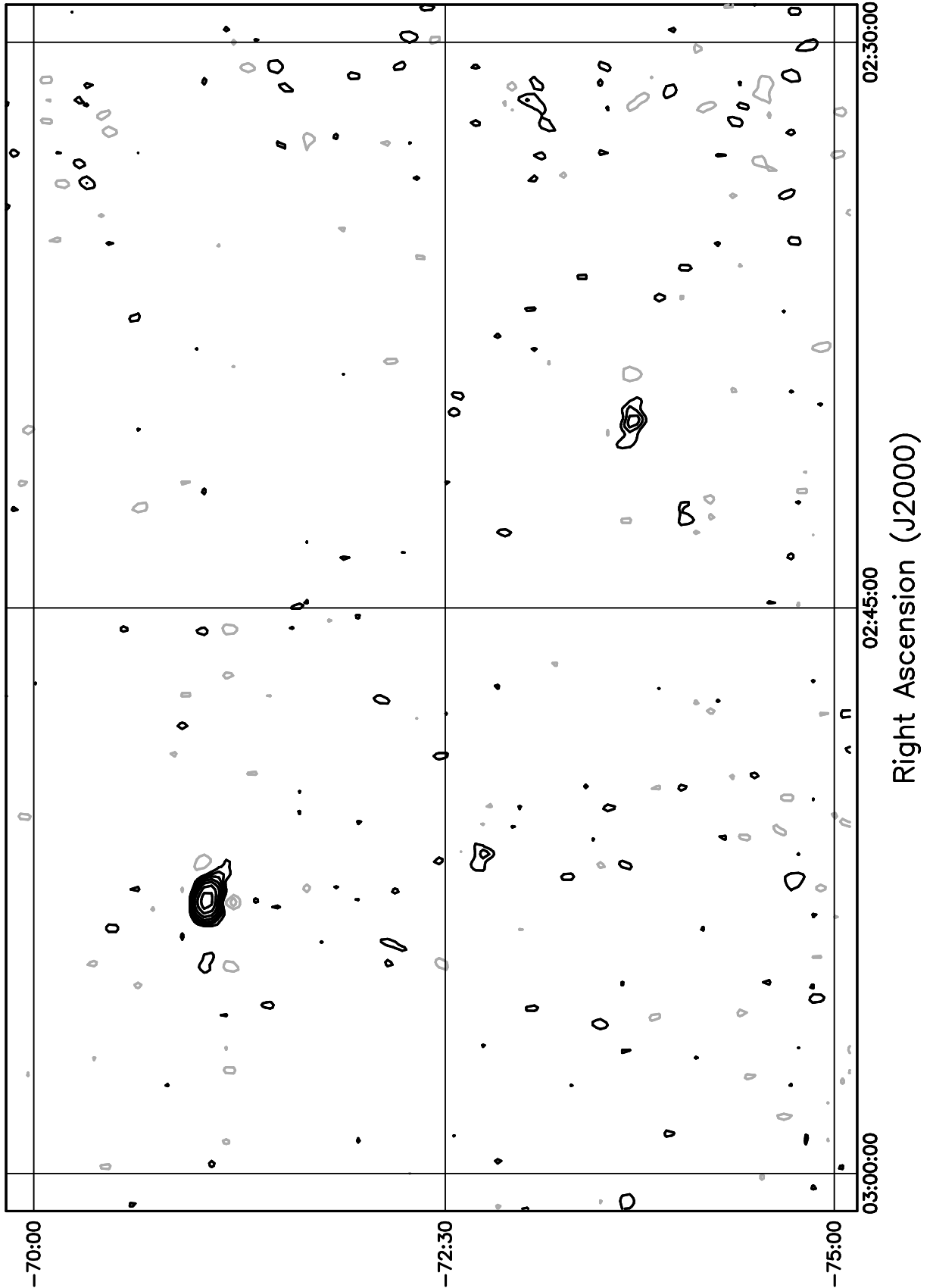
Figure 5.114: Contour plot for the range $02^h30^m \le RA \le 03^h00^m$, $-70° \le \delta \le -65°$. Contour levels are -5.04, -3.6, -2.52, -1.8, -1.08, 1.08, 1.8, 2.52, 3.6, 5.04, 7.2, 10.08, 14.4, 20.16, 28.8, 39.6, 54, 72, 100.8, 136.8, 180, 216, 252, 288 Jy beam^{-1}.
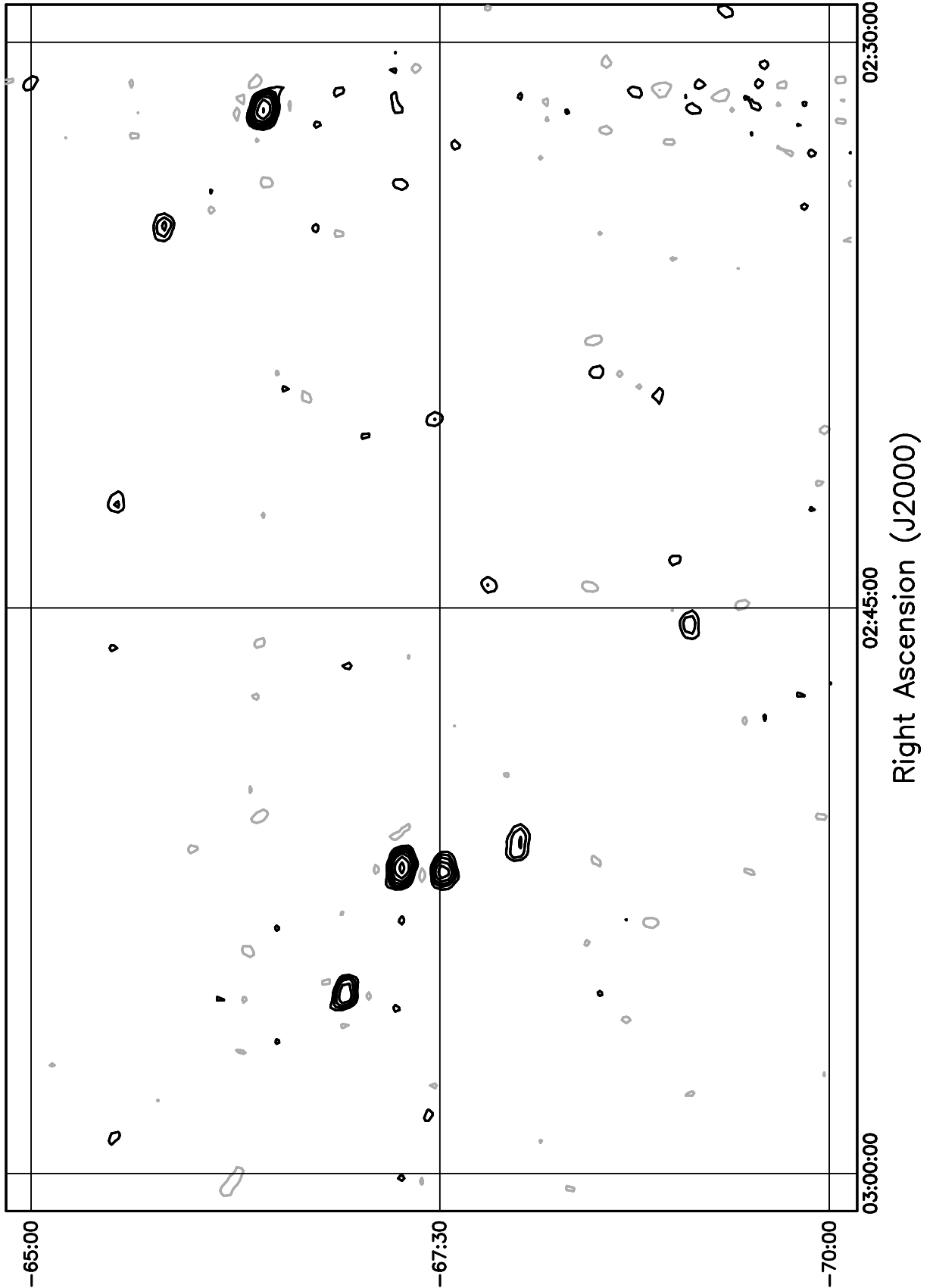
Figure 5.115: Contour plot for the range $02^h30^m \leq RA \leq 03^h00^m$, $-65° \leq \delta \leq -60°$. Contour levels are -5.04, -3.6, -2.52, -1.8, -1.08, 1.08, 1.8, 2.52, 3.6, 5.04, 7.2, 10.08, 14.4, 20.16, 28.8, 39.6, 54, 72, 100.8, 136.8, 180, 216, 252, 288 Jy beam^{-1}.
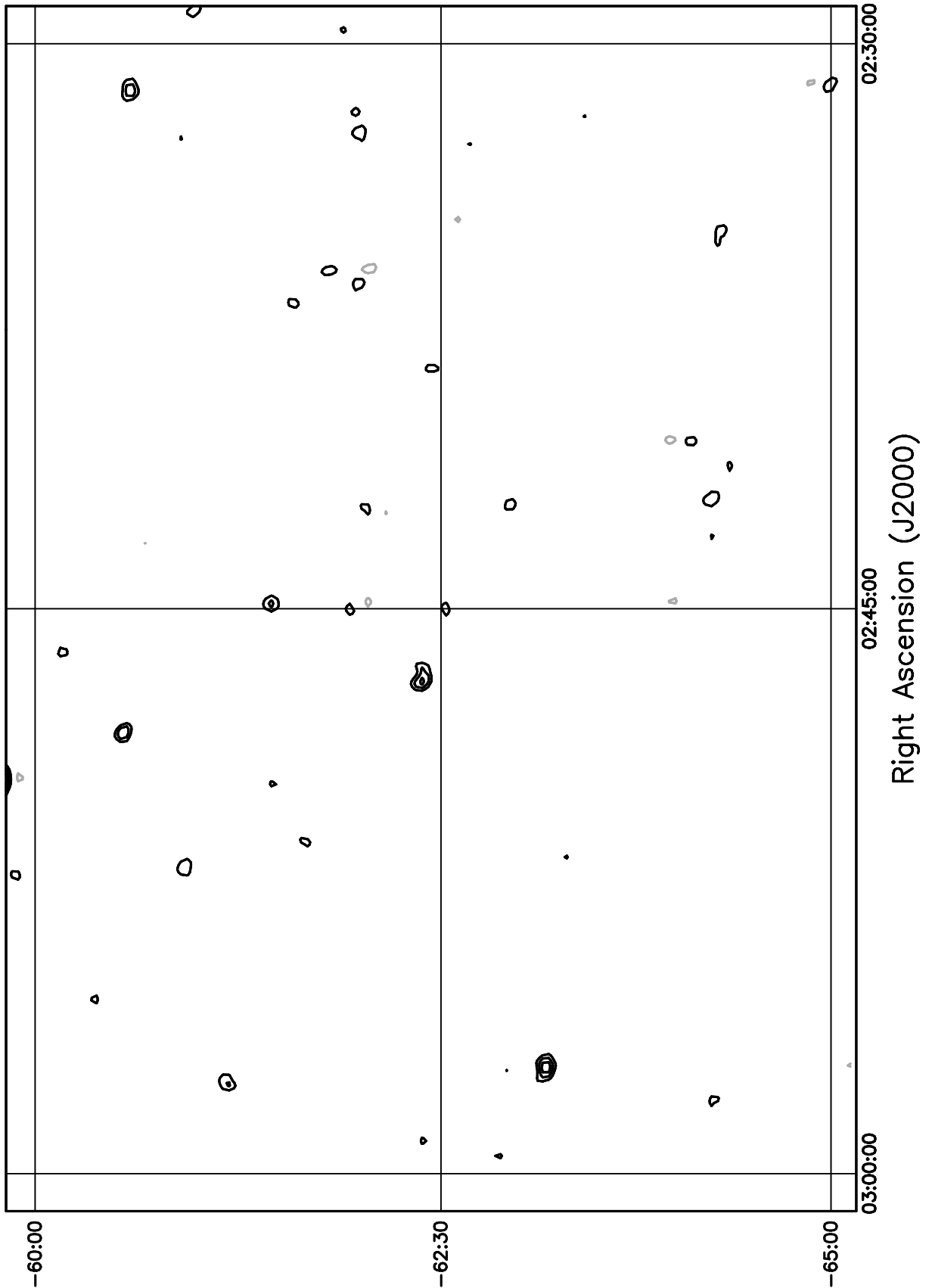
Figure 5.116: Contour plot for the range $02^h30^m \leq RA \leq 03^h00^m$, $-60° \leq \delta \leq -55°$. Contour levels are -5.04, -3.6, -2.52, -1.8, -1.08, 1.08, 1.8, 2.52, 3.6, 5.04, 7.2, 10.08, 14.4, 20.16, 28.8, 39.6, 54, 72, 100.8, 136.8, 180, 216, 252, 288 Jy beam^{-1}.
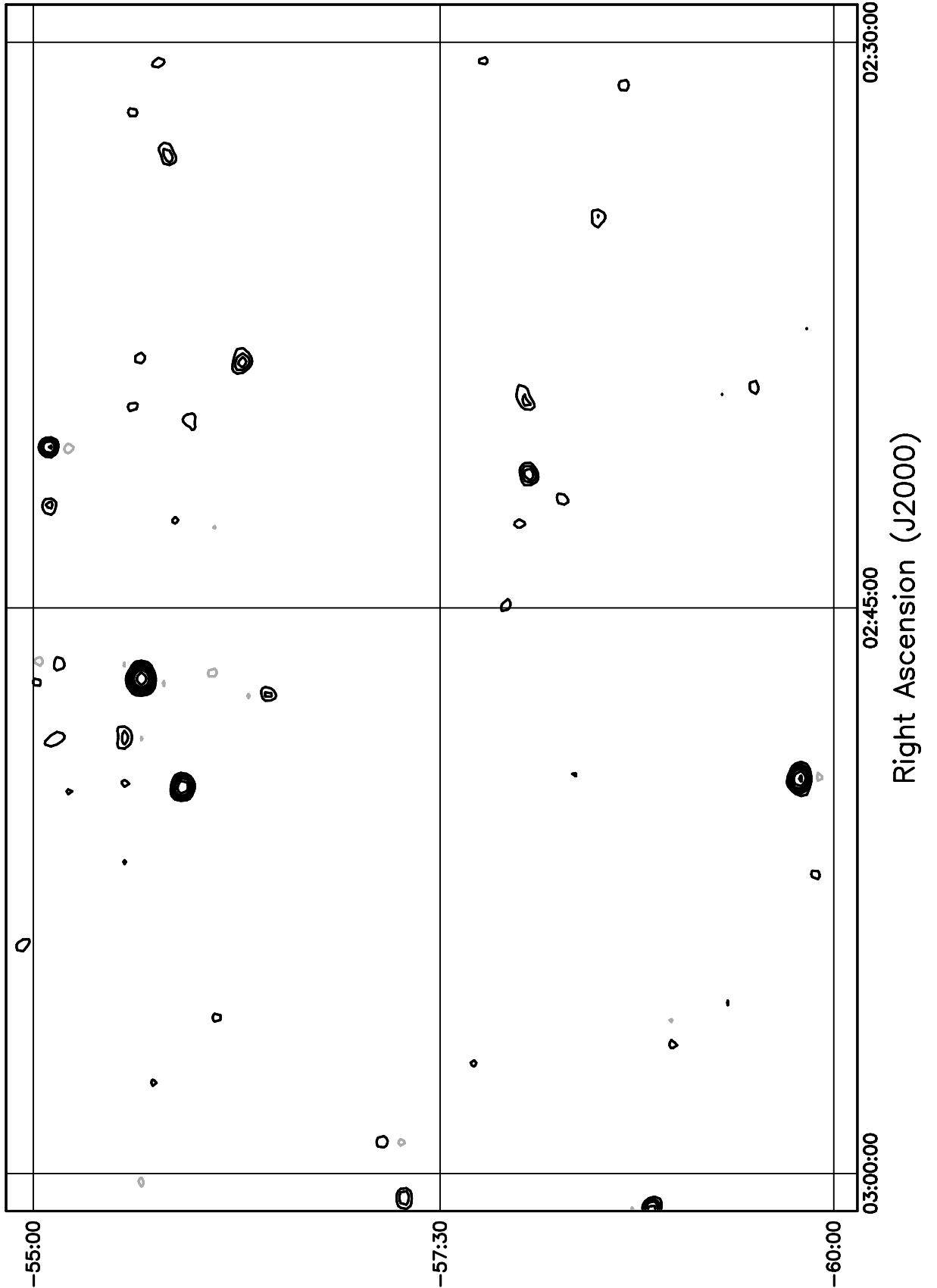
Figure 5.117: Contour plot for the range $02^h30^m \leq RA \leq 03^h00^m$, $-55° \leq \delta \leq -50°$. Contour levels are -5.04, -3.6, -2.52, -1.8, -1.08, 1.08, 1.8, 2.52, 3.6, 5.04, 7.2, 10.08, 14.4, 20.16, 28.8, 39.6, 54, 72, 100.8, 136.8, 180, 216, 252, 288 Jy beam^{-1}.
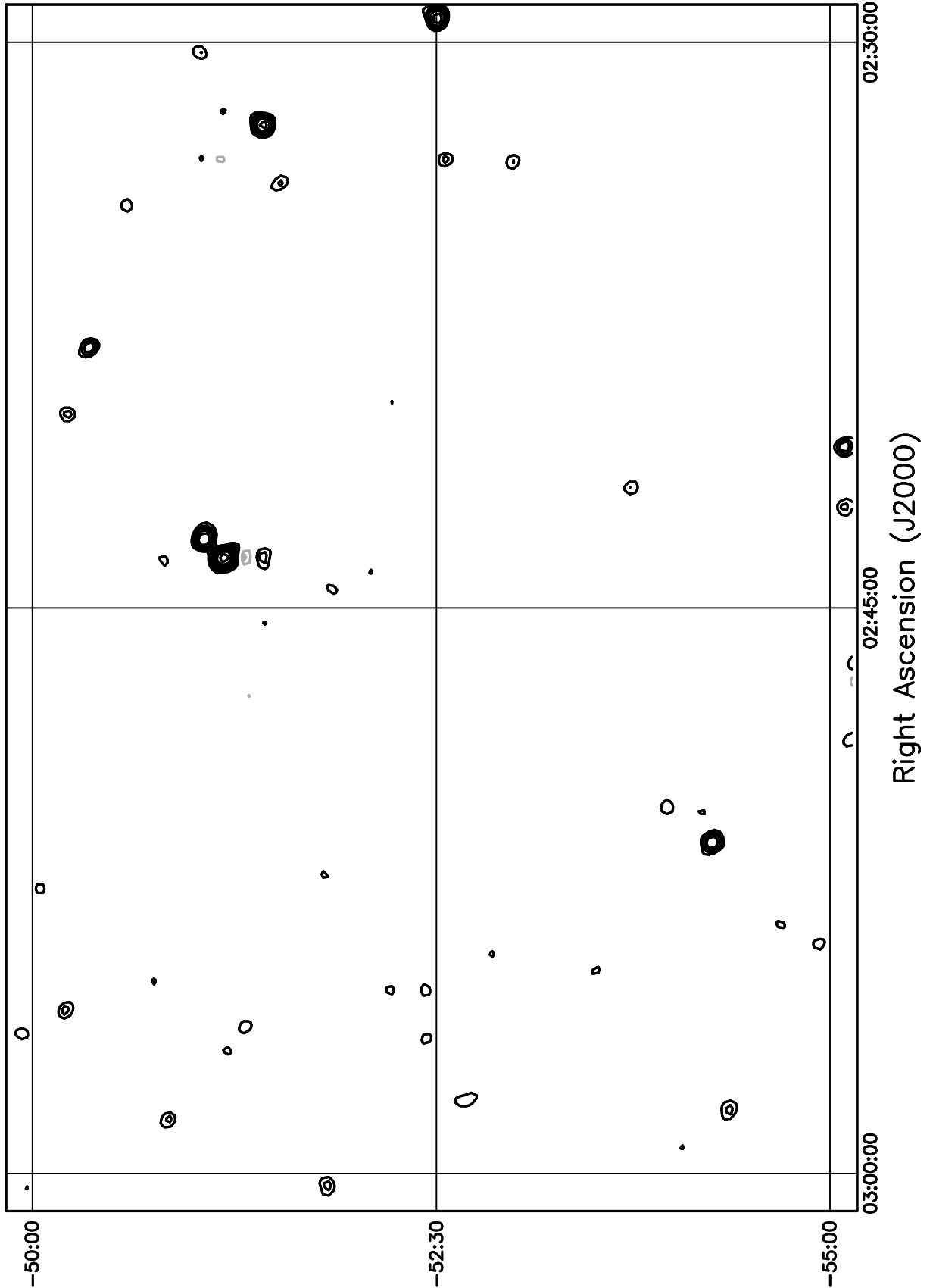
Figure 5.118: Contour plot for the range $02^h30^m \leq RA \leq 03^h00^m$, $-50° \leq \delta \leq -45°$. Contour levels are -5.04, -3.6, -2.52, -1.8, -1.08, 1.08, 1.8, 2.52, 3.6, 5.04, 7.2, 10.08, 14.4, 20.16, 28.8, 39.6, 54, 72, 100.8, 136.8, 180, 216, 252, 288 Jy beam^{-1}.
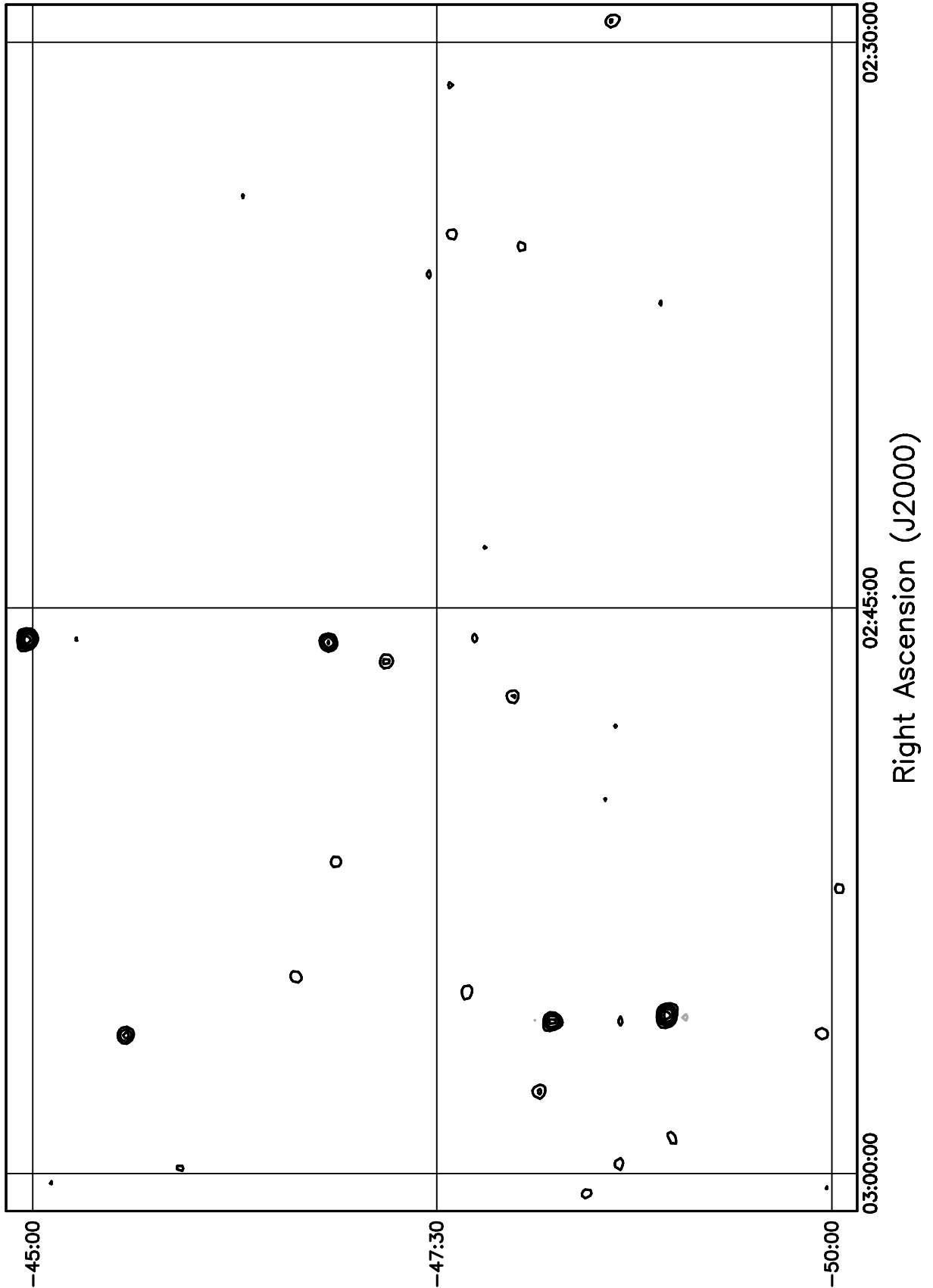
Figure 5.119: Contour plot for the range $02^h30^m \leq RA \leq 03^h00^m$, $-45° \leq \delta \leq -40°$. Contour levels are -5.04, -3.6, -2.52, -1.8, -1.08, 1.08, 1.8, 2.52, 3.6, 5.04, 7.2, 10.08, 14.4, 20.16, 28.8, 39.6, 54, 72, 100.8, 136.8, 180, 216, 252, 288 Jy beam^{-1}.
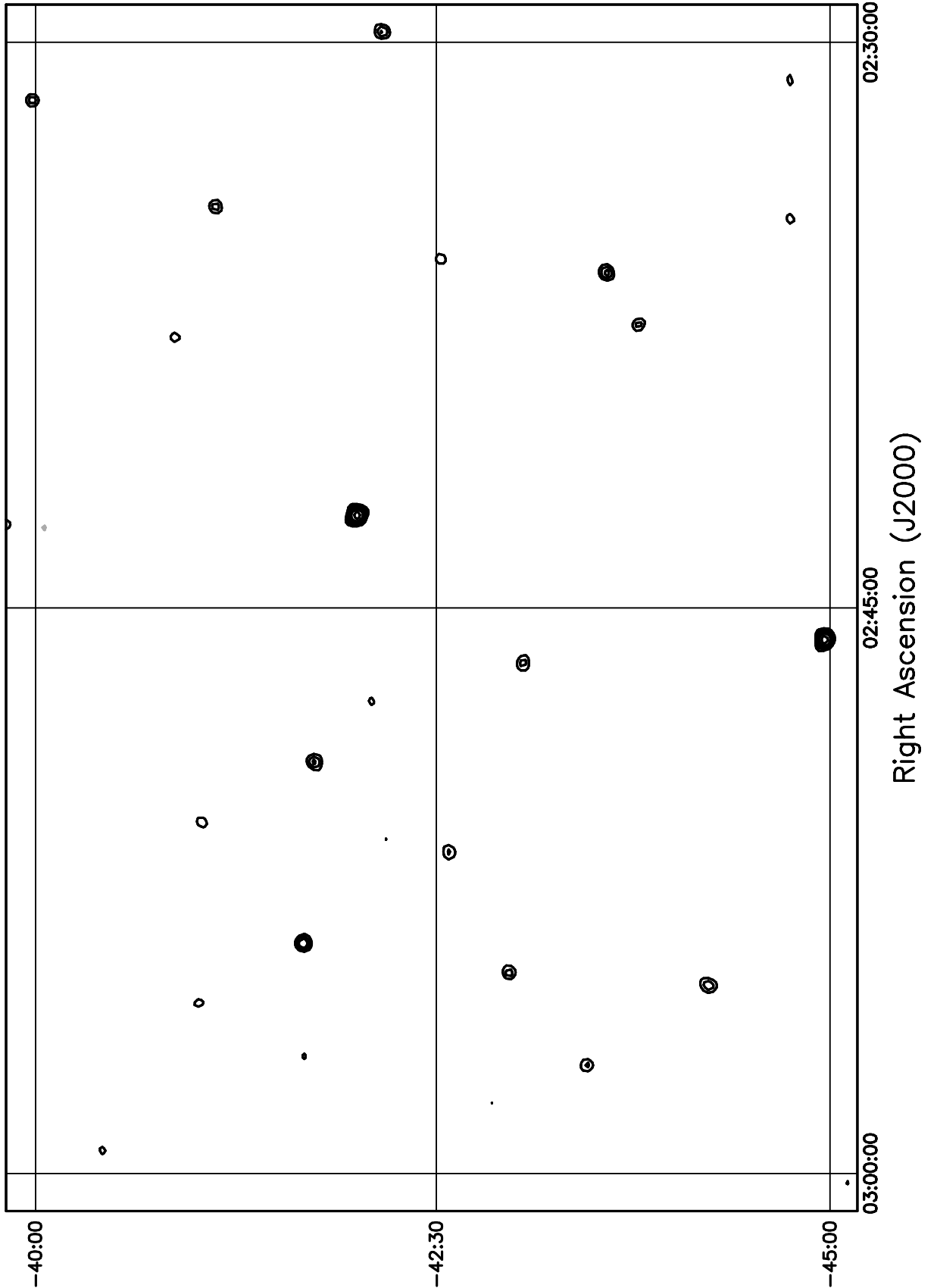
Figure 5.120: Contour plot for the range $02^h 30^m \leq RA \leq 03^h 00^m$, $-40° \leq \delta \leq -35°$. Contour levels are -5.04, -3.6, -2.52, -1.8, -1.08, 1.08, 1.8, 2.52, 3.6, 5.04, 7.2, 10.08, 14.4, 20.16, 28.8, 39.6, 54, 72, 100.8, 136.8, 180, 216, 252, 288 Jy beam^{-1}.
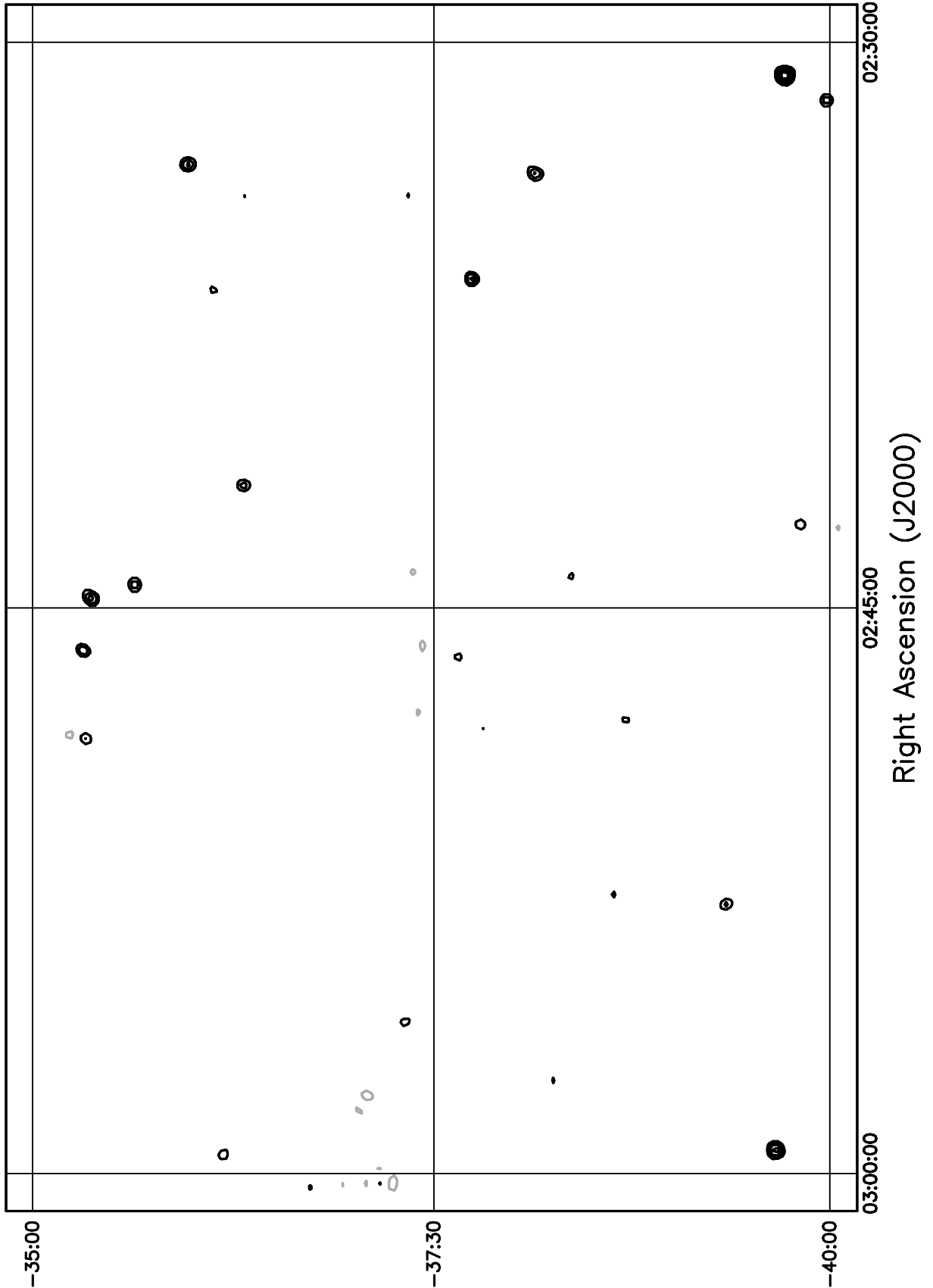
Figure 5.121: Contour plot for the range $02^h30^m \leq RA \leq 03^h00^m$, $-35° \leq \delta \leq -30°$. Contour levels are -5.04, -3.6, -2.52, -1.8, -1.08, 1.08, 1.8, 2.52, 3.6, 5.04, 7.2, 10.08, 14.4, 20.16, 28.8, 39.6, 54, 72, 100.8, 136.8, 180, 216, 252, 288 Jy beam^{-1}.
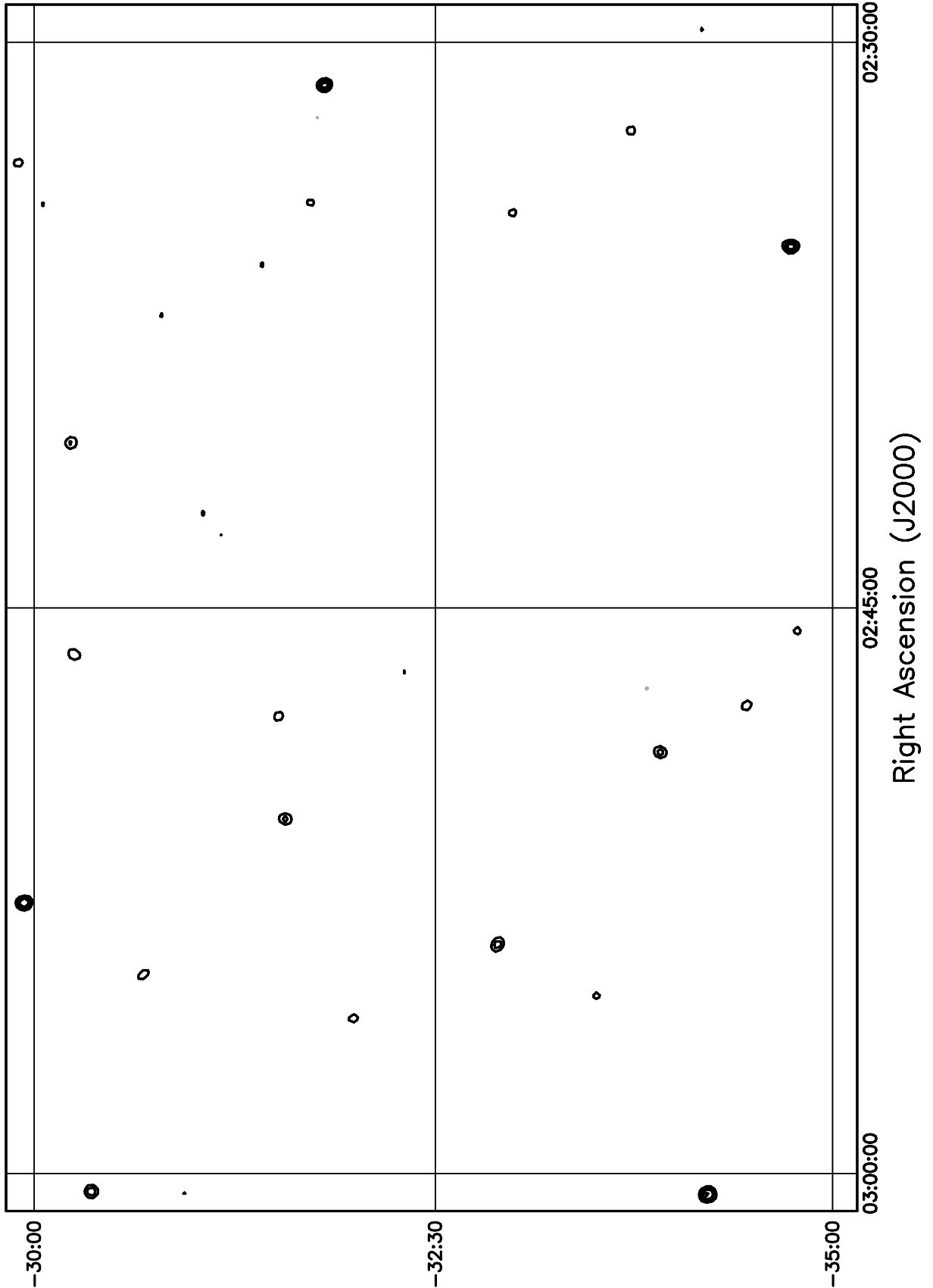
Figure 5.122: Contour plot for the range $02^h30^m \leq RA \leq 03^h00^m$, $-30° \leq \delta \leq -25°$. Contour levels are -5.04, -3.6, -2.52, -1.8, -1.08, 1.08, 1.8, 2.52, 3.6, 5.04, 7.2, 10.08, 14.4, 20.16, 28.8, 39.6, 54, 72, 100.8, 136.8, 180, 216, 252, 288 Jy beam^{-1}.


Right Ascension (J2000)
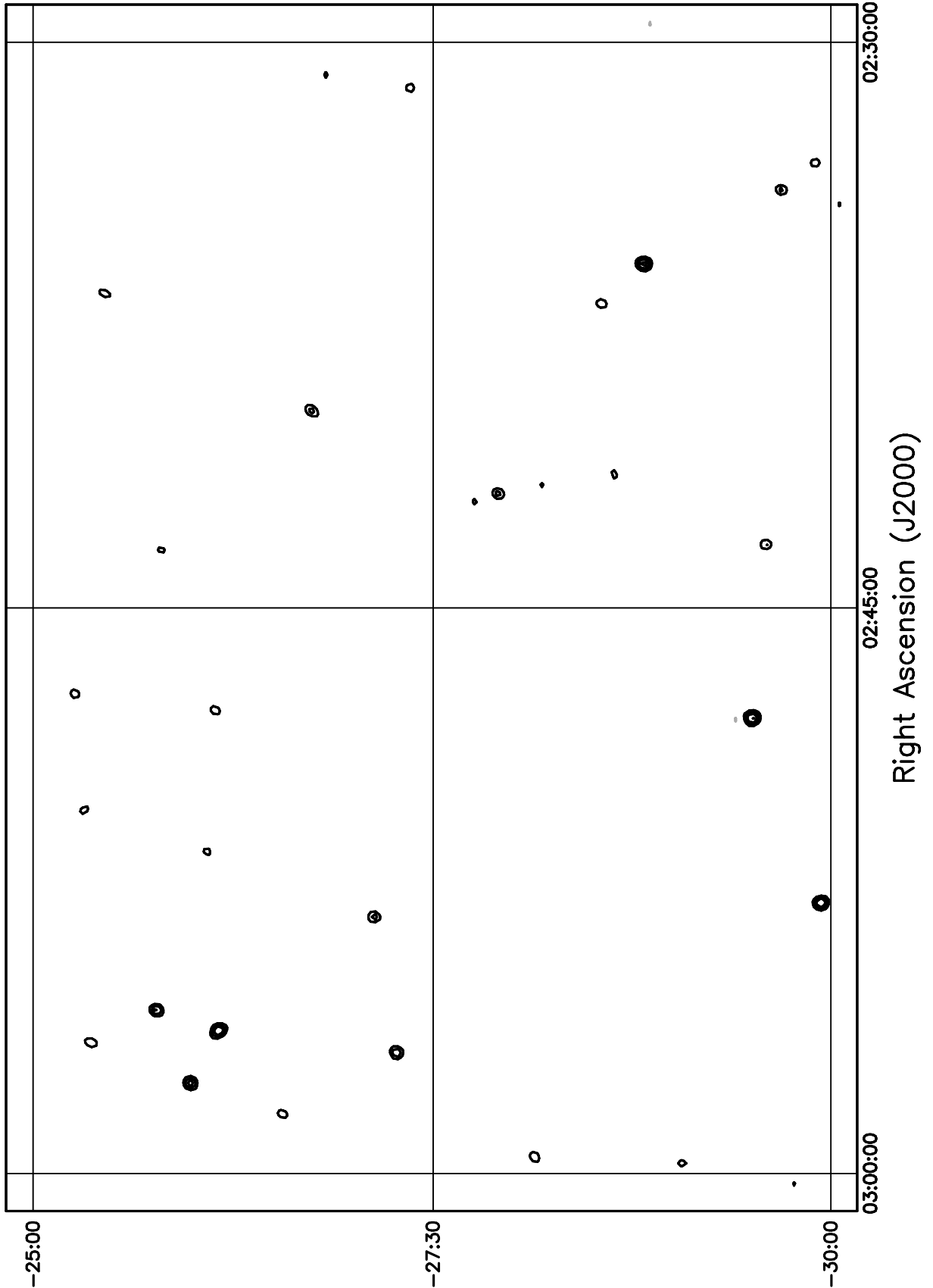
Figure 5.123: Contour plot for the range $02^h30^m \leq RA \leq 03^h00^m$, $-25° \leq \delta \leq -20°$. Contour levels are -5.04, -3.6, -2.52, -1.8, -1.08, 1.08, 1.8, 2.52, 3.6, 5.04, 7.2, 10.08, 14.4, 20.16, 28.8, 39.6, 54, 72, 100.8, 136.8, 180, 216, 252, 288 Jy beam^{-1}.
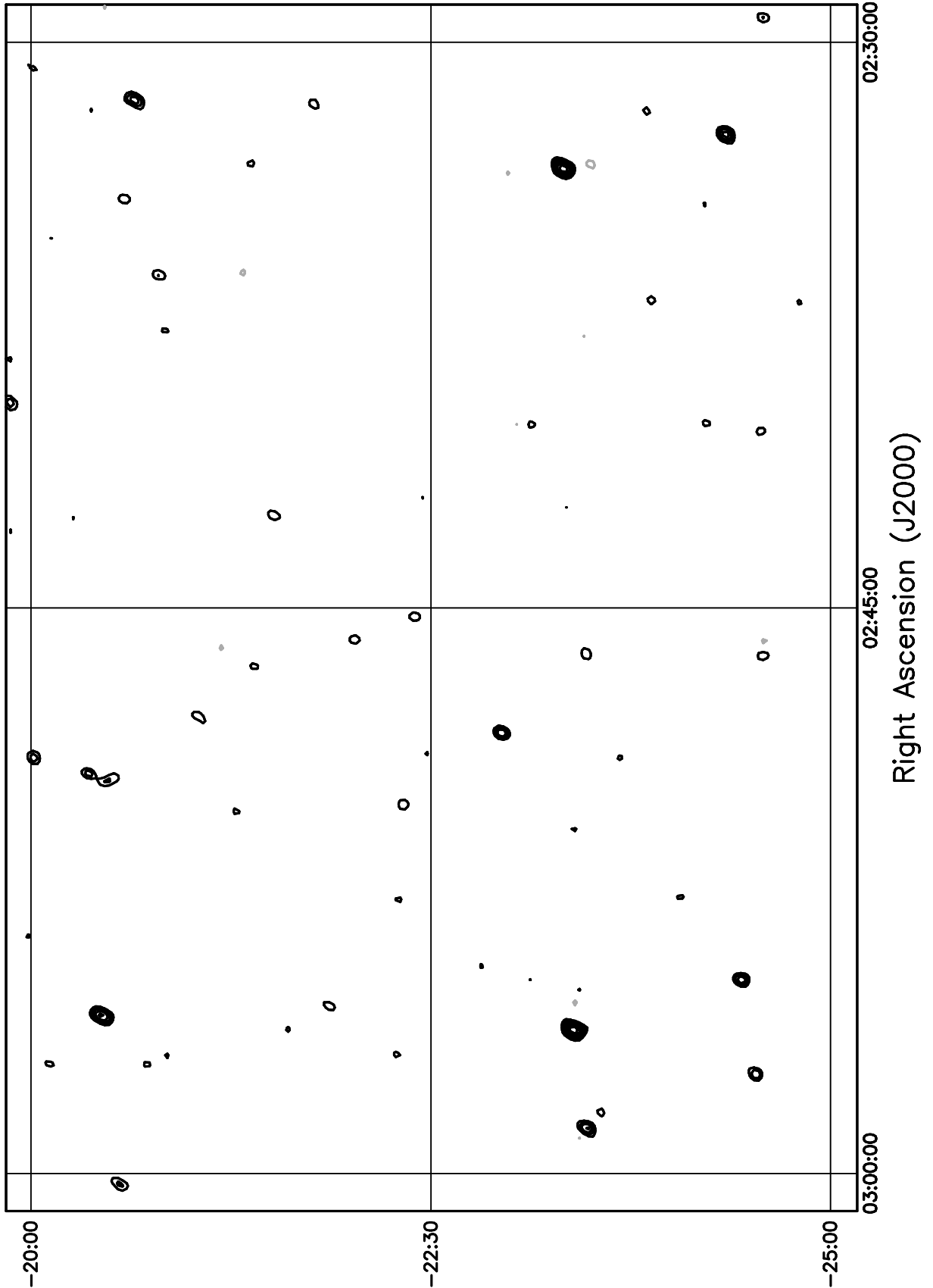
Figure 5.124: Contour plot for the range $02^h30^m \leq RA \leq 03^h00^m$, $-20° \leq \delta \leq -15°$. Contour levels are -5.04, -3.6, -2.52, -1.8, -1.08, 1.08, 1.8, 2.52, 3.6, 5.04, 7.2, 10.08, 14.4, 20.16, 28.8, 39.6, 54, 72, 100.8, 136.8, 180, 216, 252, 288 Jy beam^{-1}.
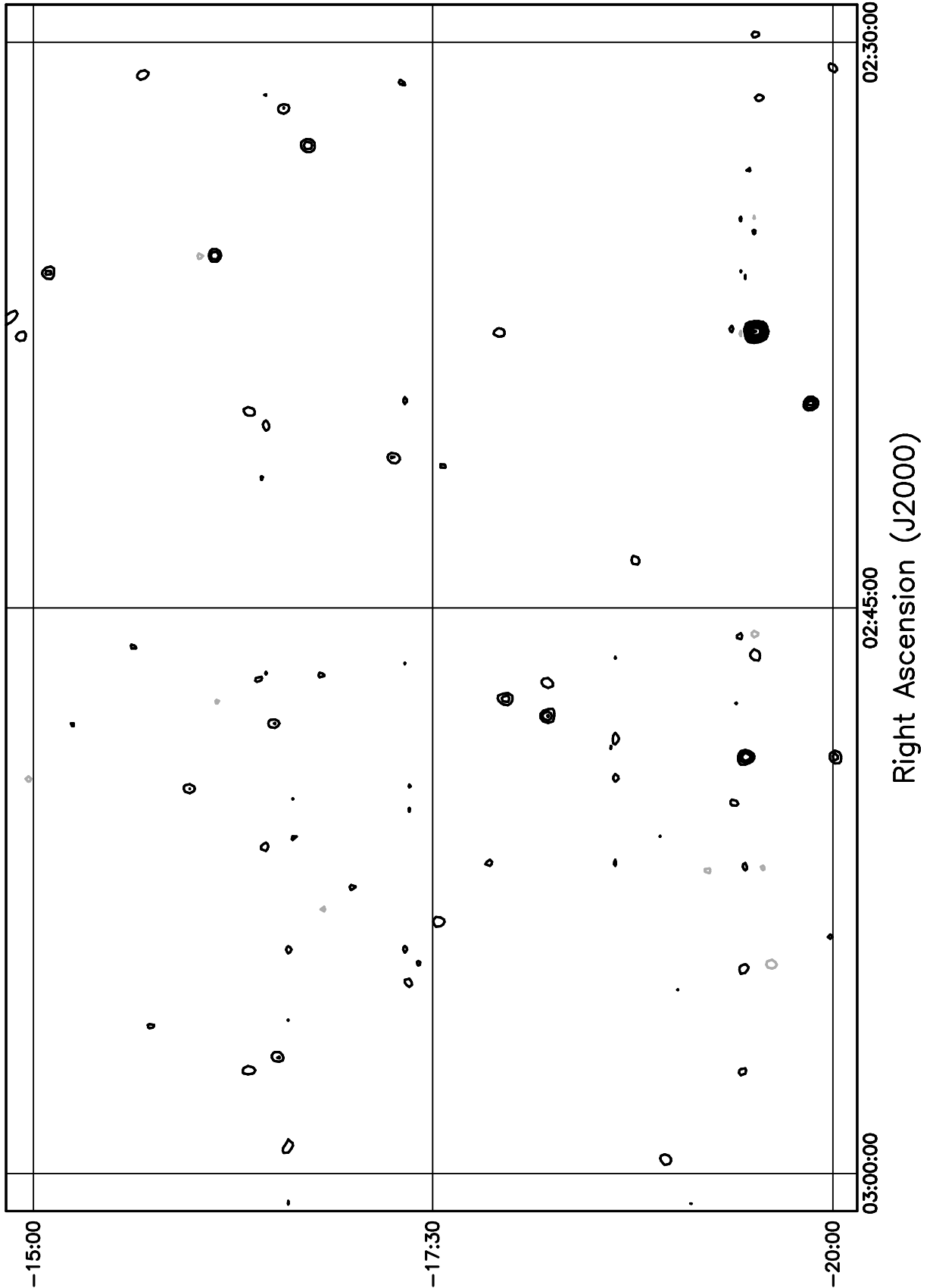
Figure 5.125: Contour plot for the range $02^h30^m \leq RA \leq 03^h00^m$, $-15° \leq \delta \leq -10°$. Contour levels are -5.04, -3.6, -2.52, -1.8, -1.08, 1.08, 1.8, 2.52, 3.6, 5.04, 7.2, 10.08, 14.4, 20.16, 28.8, 39.6, 54, 72, 100.8, 136.8, 180, 216, 252, 288 Jy beam^{-1}.
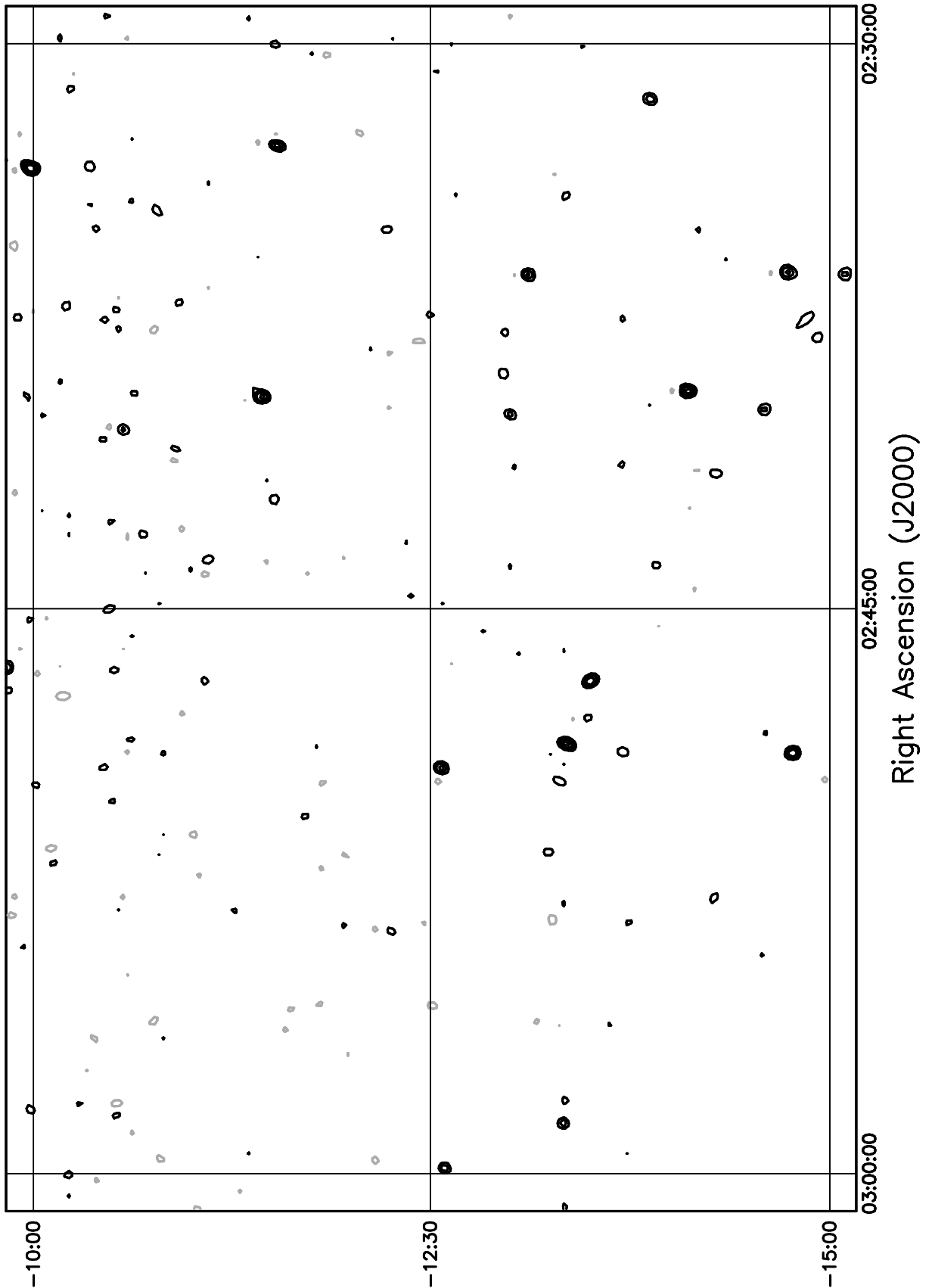
Figure 5.126: Contour plot for the range $03^h00^m \leq RA \leq 03^h30^m$ $-75° \leq \delta \leq -70°$. Contour levels are -5.04, -3.6, -2.52, -1.8, -1.08, 1.08, 1.8, 2.52, 3.6, 5.04, 7.2, 10.08, 14.4, 20.16, 28.8, 39.6, 54, 72, 100.8, 136.8, 180, 216, 252, 288 Jy beam^{-1}.
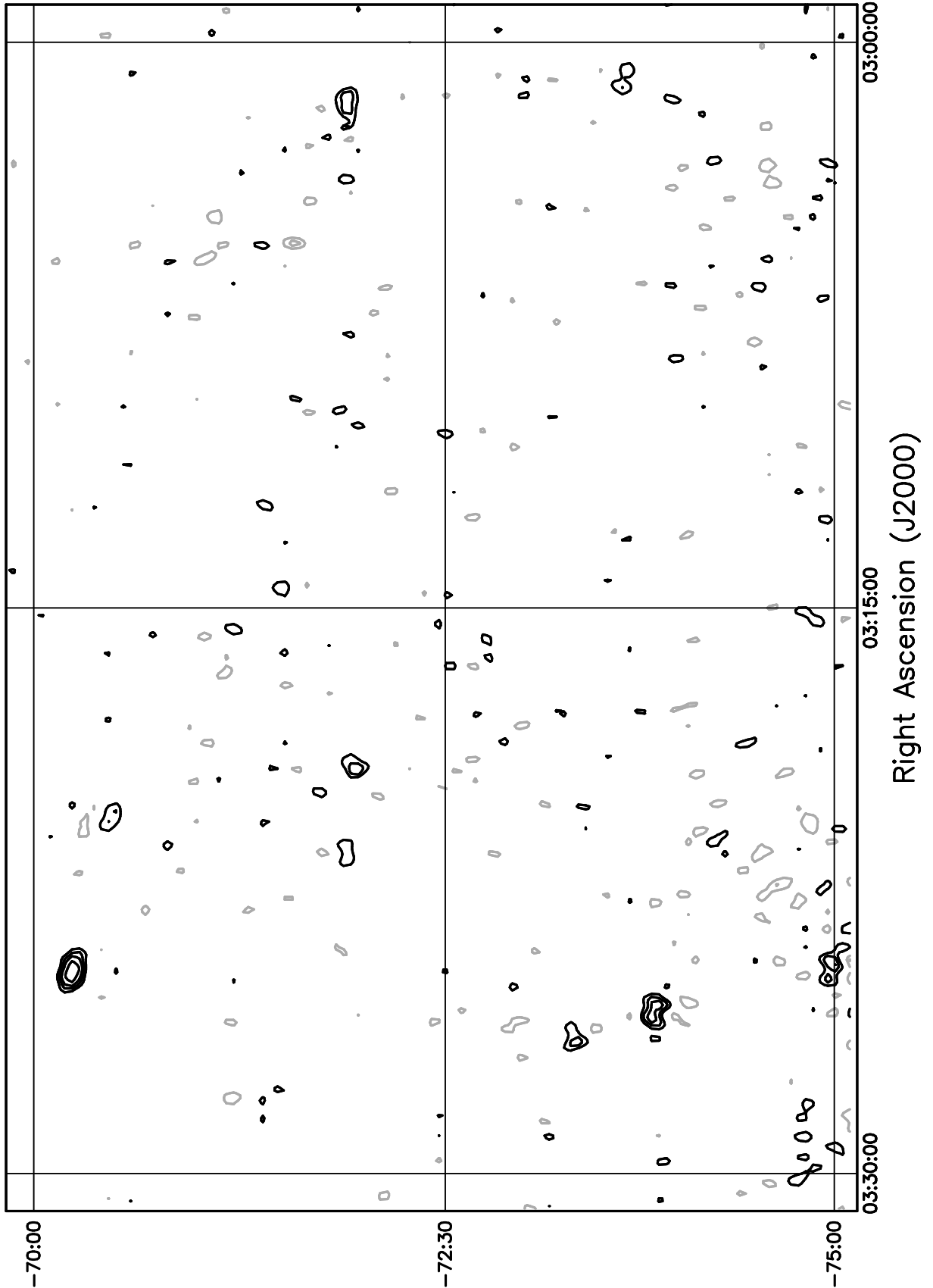
Figure 5.127: Contour plot for the range $03^h00^m \leq RA \leq 03^h30^m$ $-70° \leq \delta \leq -65°$. Contour levels are -5.04, -3.6, -2.52, -1.8, -1.08, 1.08, 1.8, 2.52, 3.6, 5.04, 7.2, 10.08, 14.4, 20.16, 28.8, 39.6, 54, 72, 100.8, 136.8, 180, 216, 252, 288 Jy beam^{-1}.
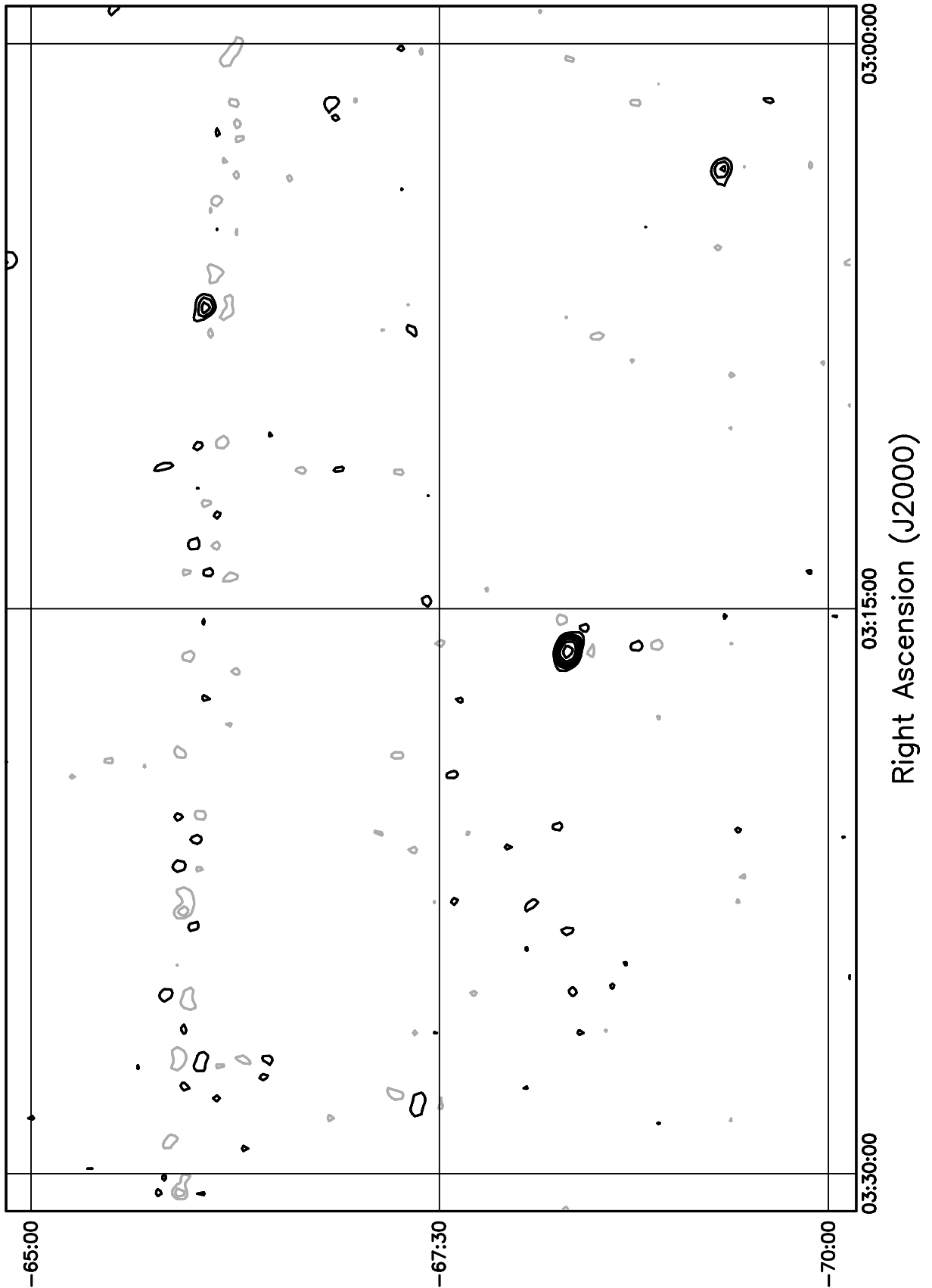
Figure 5.128: Contour plot for the range $03^h00^m \leq RA \leq 03^h30^m$ $-65° \leq \delta \leq -60°$. Contour levels are -5.04, -3.6, -2.52, -1.8, -1.08, 1.08, 1.8, 2.52, 3.6, 5.04, 7.2, 10.08, 14.4, 20.16, 28.8, 39.6, 54, 72, 100.8, 136.8, 180, 216, 252, 288 Jy beam^{-1}.
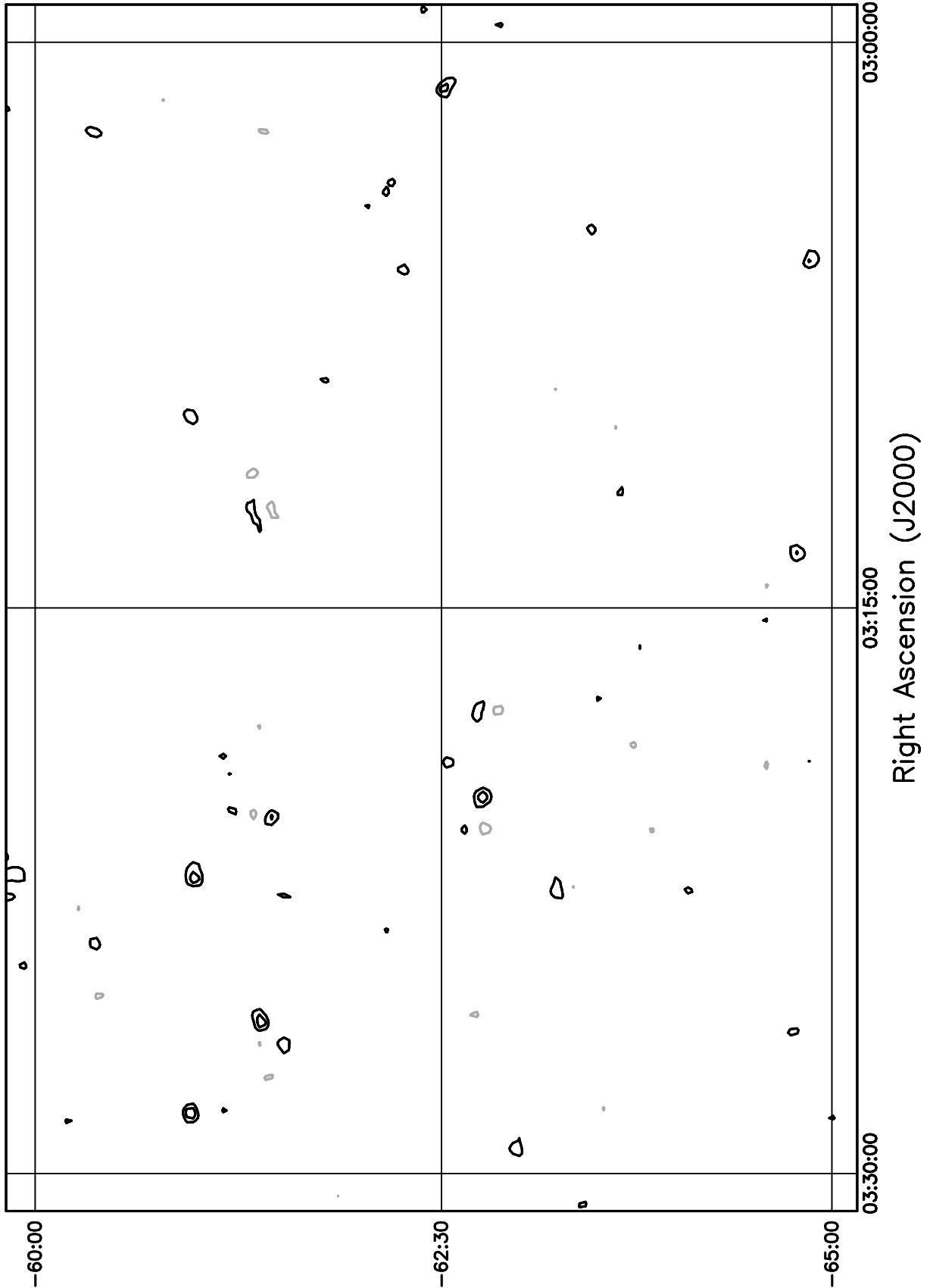
Figure 5.129: Contour plot for the range $03^h00^m \leq RA \leq 03^h30^m$ $-60° \leq \delta \leq -55°$. Contour levels are -5.04, -3.6, -2.52, -1.8, -1.08, 1.08, 1.8, 2.52, 3.6, 5.04, 7.2, 10.08, 14.4, 20.16, 28.8, 39.6, 54, 72, 100.8, 136.8, 180, 216, 252, 288 Jy beam^{-1}.
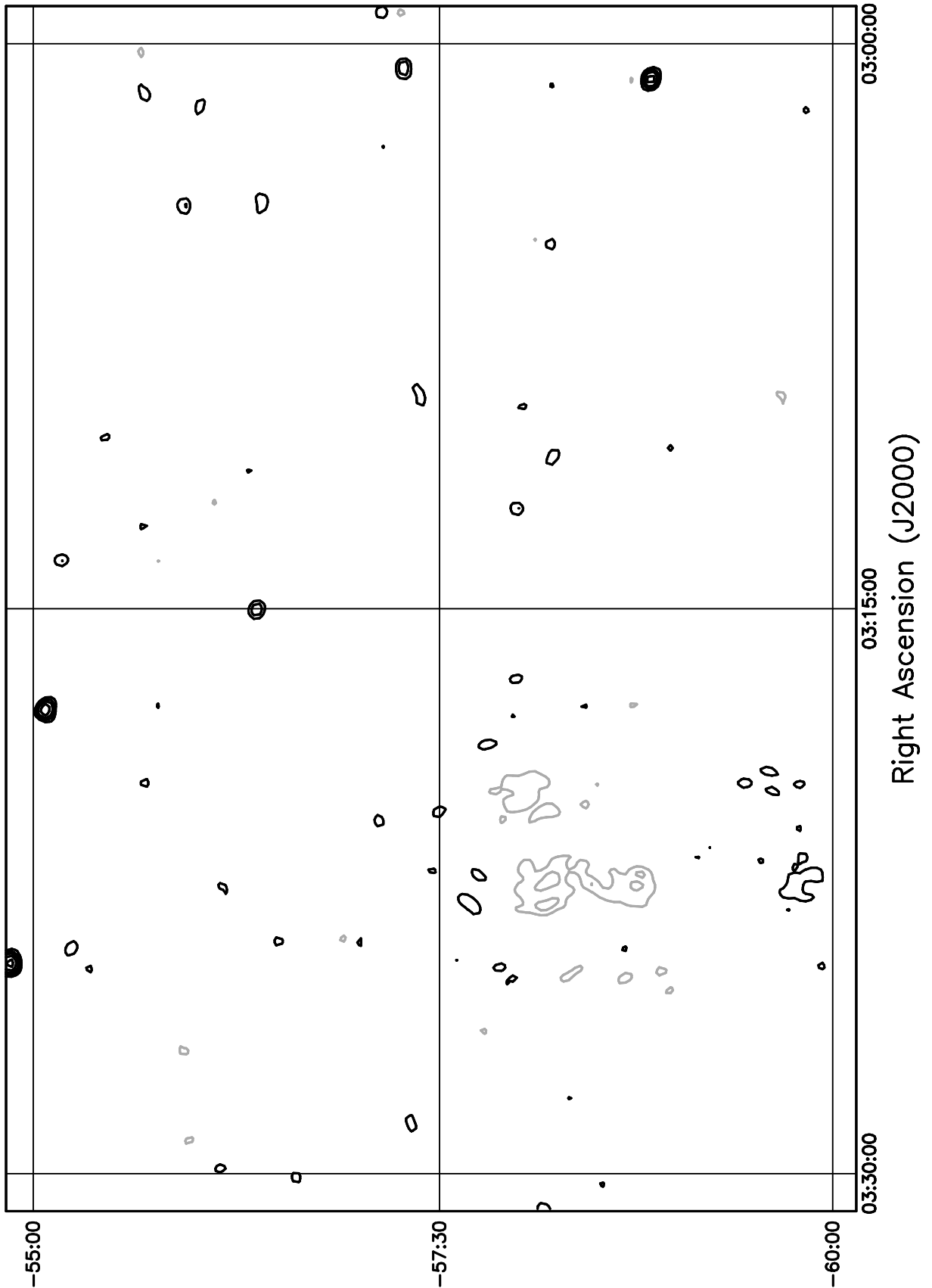
Figure 5.130: Contour plot for the range $03^h00^m \leq RA \leq 03^h30^m$ $-55° \leq \delta \leq -50°$. Contour levels are -5.04, -3.6, -2.52, -1.8, -1.08, 1.08, 1.8, 2.52, 3.6, 5.04, 7.2, 10.08, 14.4, 20.16, 28.8, 39.6, 54, 72, 100.8, 136.8, 180, 216, 252, 288 Jy beam^{-1}.
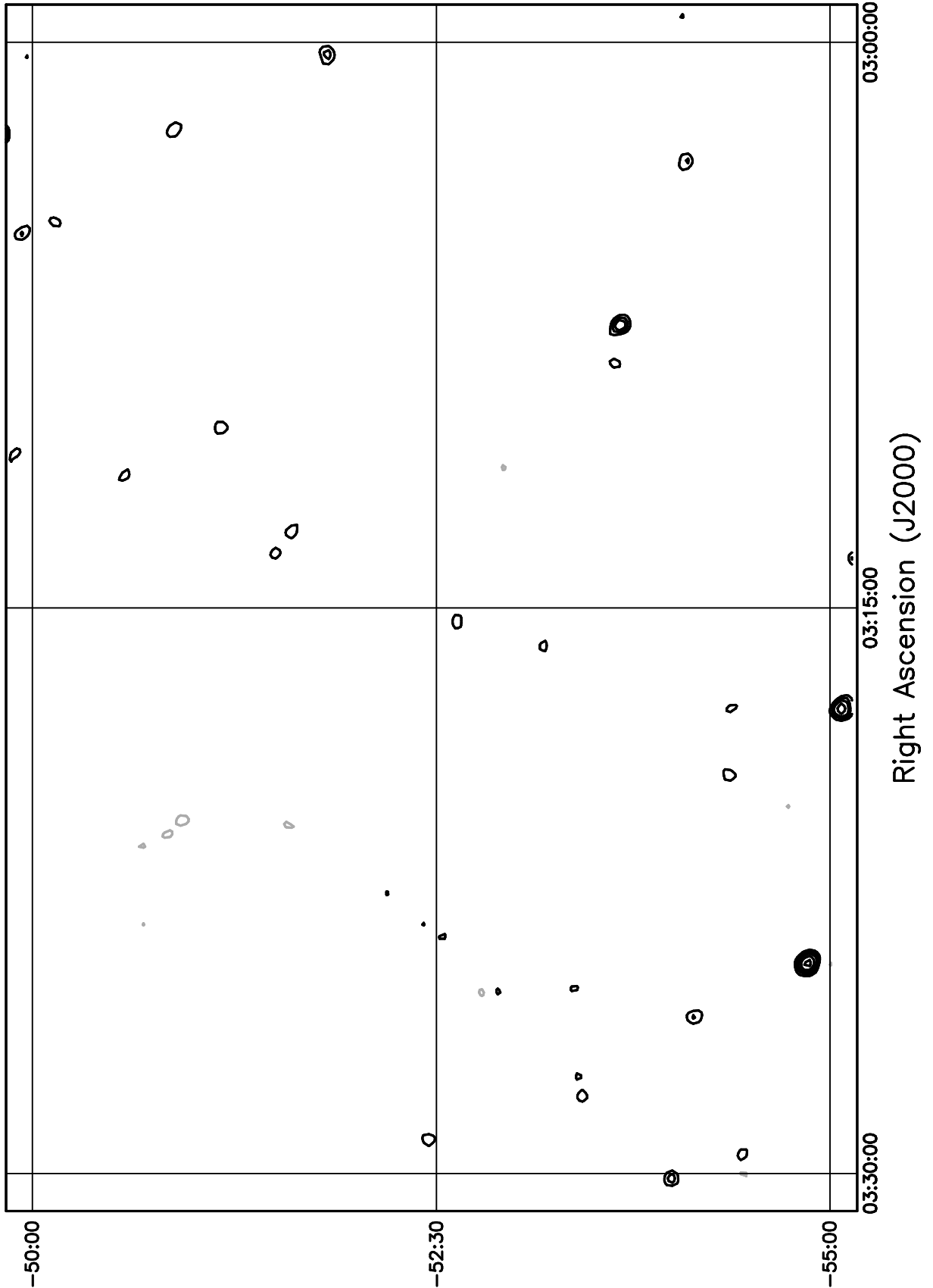
Figure 5.131: Contour plot for the range $03^h00^m \leq RA \leq 03^h30^m$ $-50° \leq \delta \leq -45°$. Contour levels are -5.04, -3.6, -2.52, -1.8, -1.08, 1.08, 1.8, 2.52, 3.6, 5.04, 7.2, 10.08, 14.4, 20.16, 28.8, 39.6, 54, 72, 100.8, 136.8, 180, 216, 252, 288 Jy beam^{-1}.
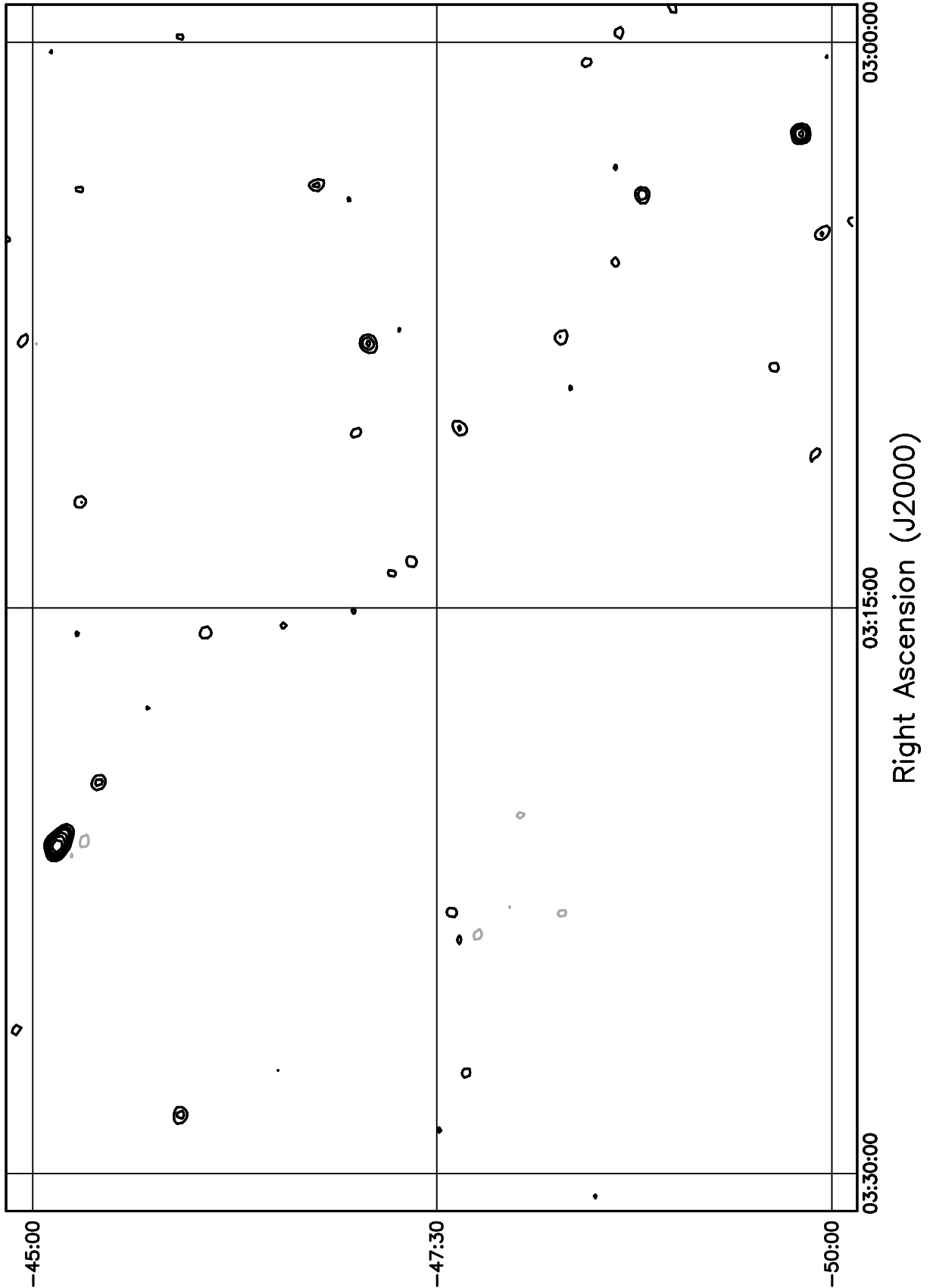
Figure 5.132: Contour plot for the range $03^h00^m \leq RA \leq 03^h30^m$ $-45° \leq \delta \leq -40°$. Contour levels are -5.04, -3.6, -2.52, -1.8, -1.08, 1.08, 1.8, 2.52, 3.6, 5.04, 7.2, 10.08, 14.4, 20.16, 28.8, 39.6, 54, 72, 100.8, 136.8, 180, 216, 252, 288 Jy beam^{-1}.
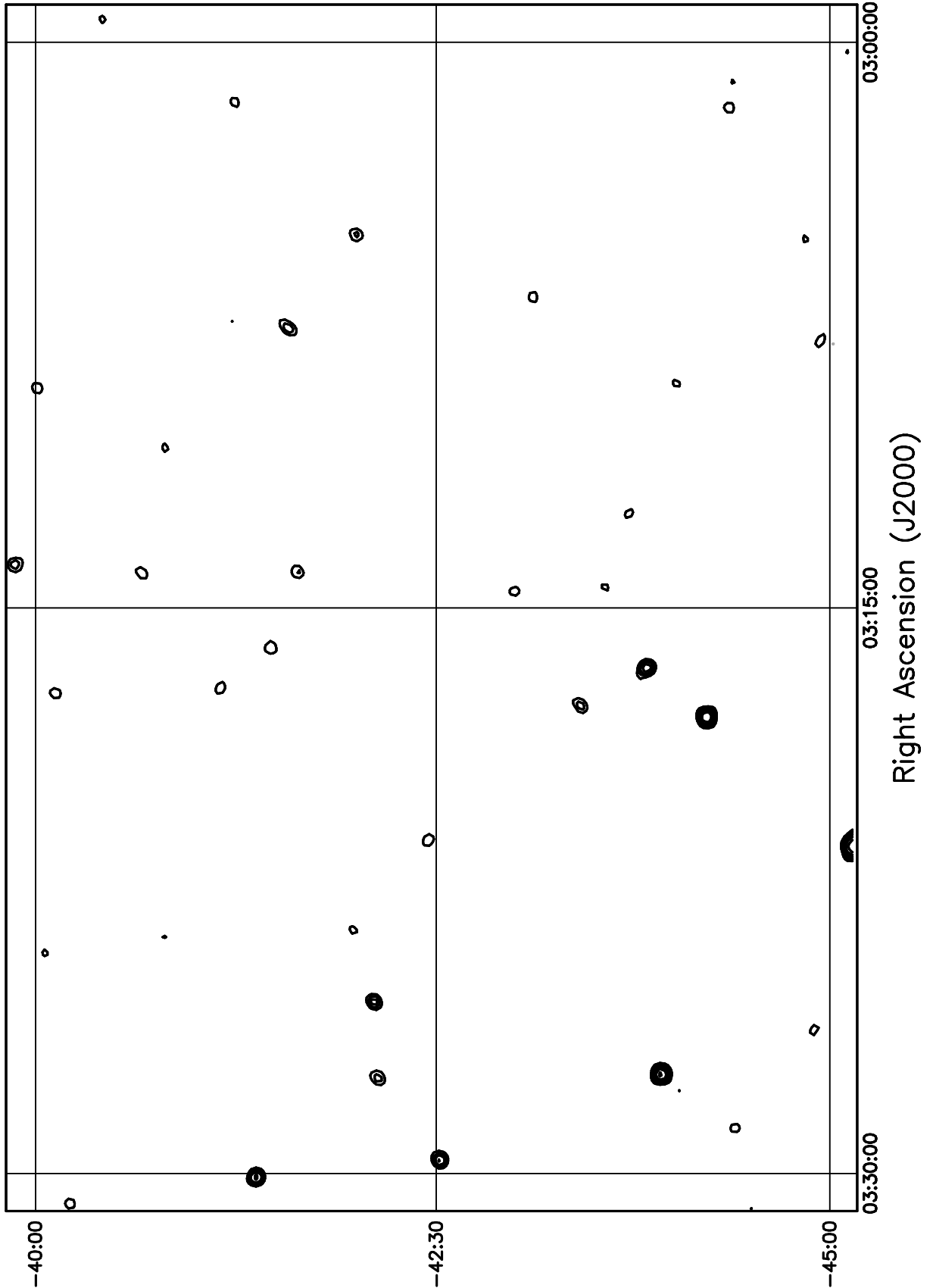
Figure 5.133: Contour plot for the range $03^h00^m \le RA \le 03^h30^m$ $-40° \le \delta \le -35°$. Contour levels are -5.04, -3.6, -2.52, -1.8, -1.08, 1.08, 1.8, 2.52, 3.6, 5.04, 7.2, 10.08, 14.4, 20.16, 28.8, 39.6, 54, 72, 100.8, 136.8, 180, 216, 252, 288 Jy beam^{-1}.
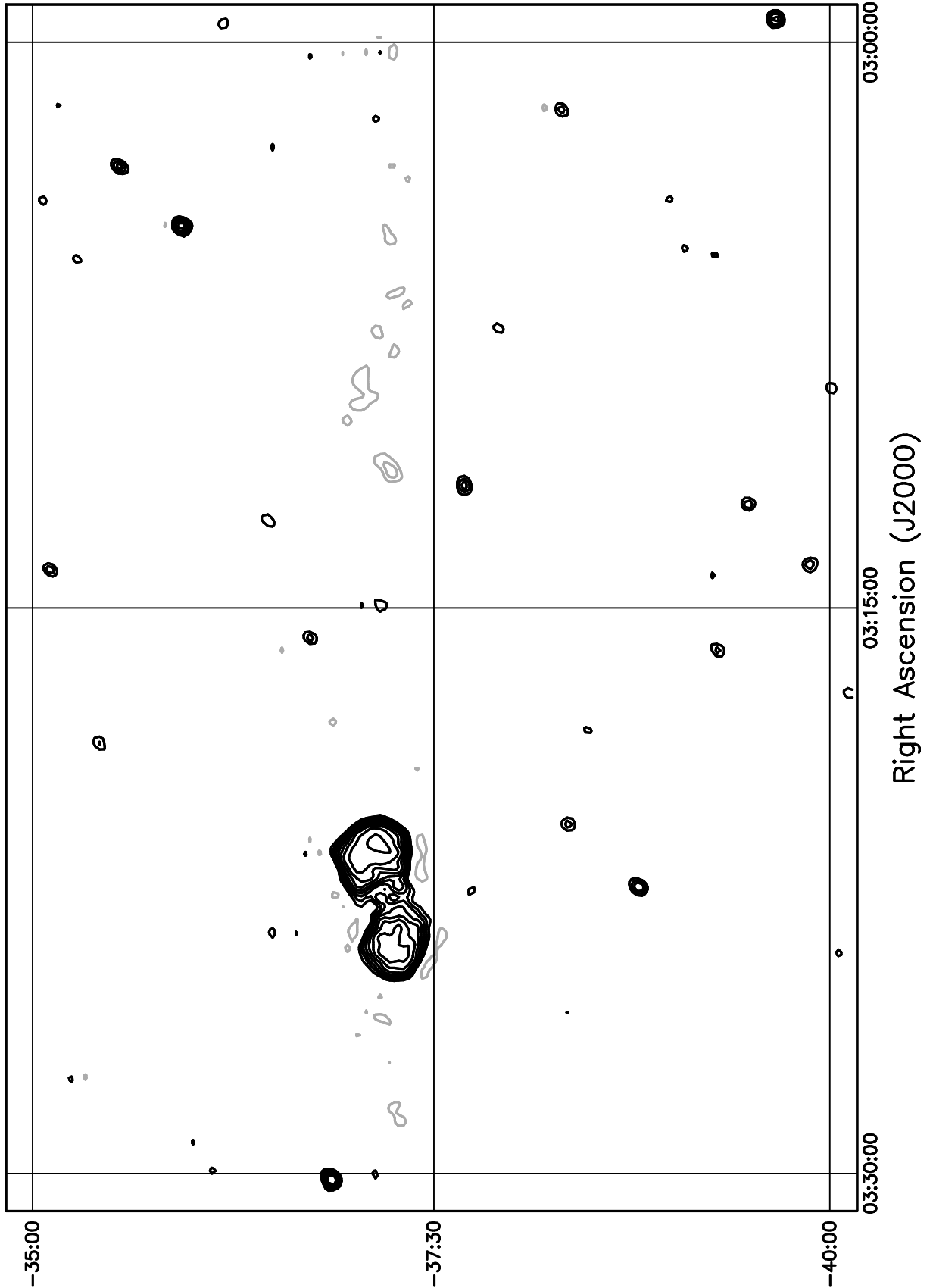
Figure 5.134: Contour plot for the range $03^h00^m \leq RA \leq 03^h30^m$ $-35° \leq \delta \leq -30°$. Contour levels are -5.04, -3.6, -2.52, -1.8, -1.08, 1.08, 1.8, 2.52, 3.6, 5.04, 7.2, 10.08, 14.4, 20.16, 28.8, 39.6, 54, 72, 100.8, 136.8, 180, 216, 252, 288 Jy beam^{-1}.
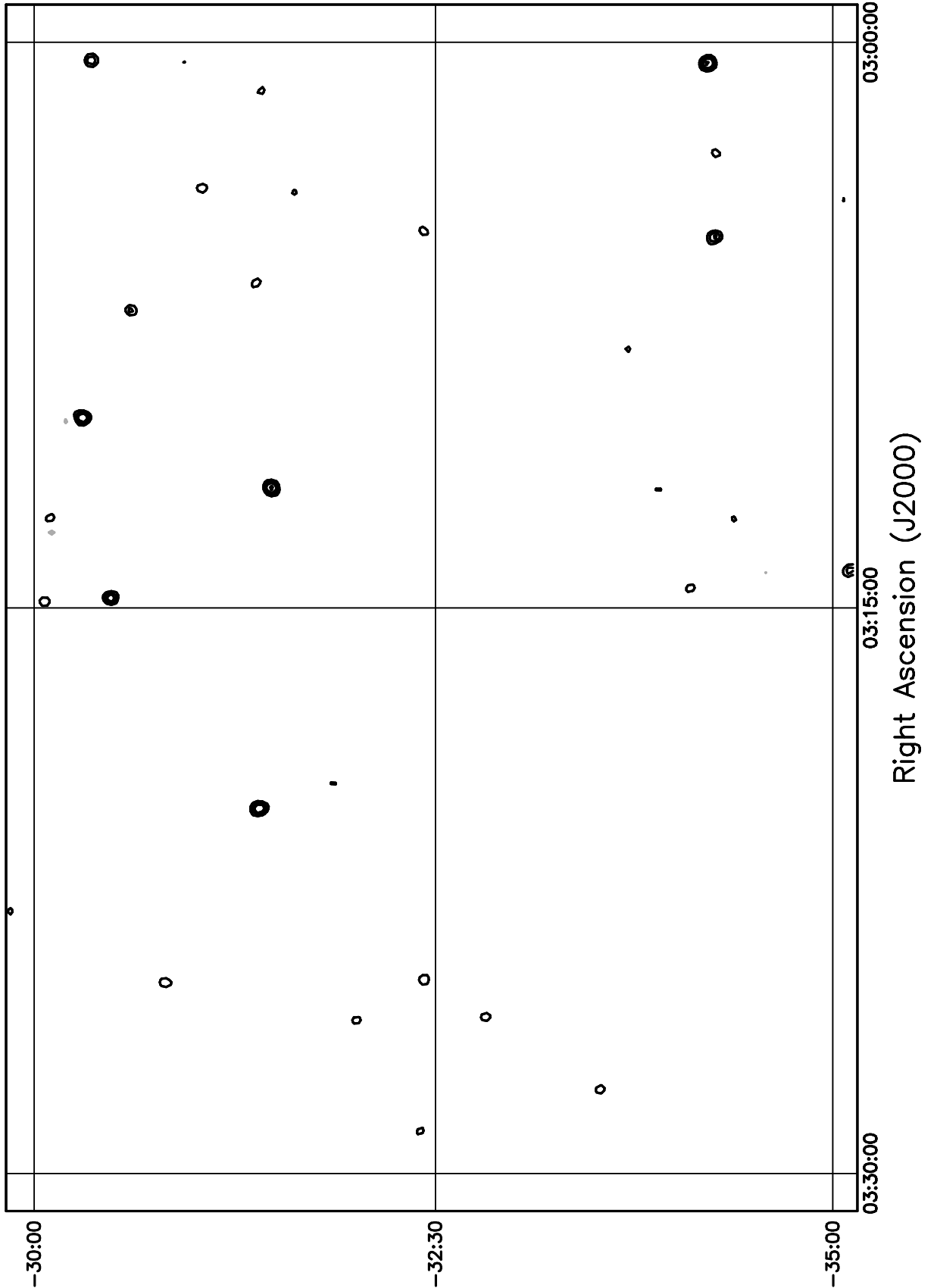
Figure 5.135: Contour plot for the range $03^h00^m \leq RA \leq 03^h30^m$ $-30° \leq \delta \leq -25°$. Contour levels are -5.04, -3.6, -2.52, -1.8, -1.08, 1.08, 1.8, 2.52, 3.6, 5.04, 7.2, 10.08, 14.4, 20.16, 28.8, 39.6, 54, 72, 100.8, 136.8, 180, 216, 252, 288 Jy beam^{-1}.
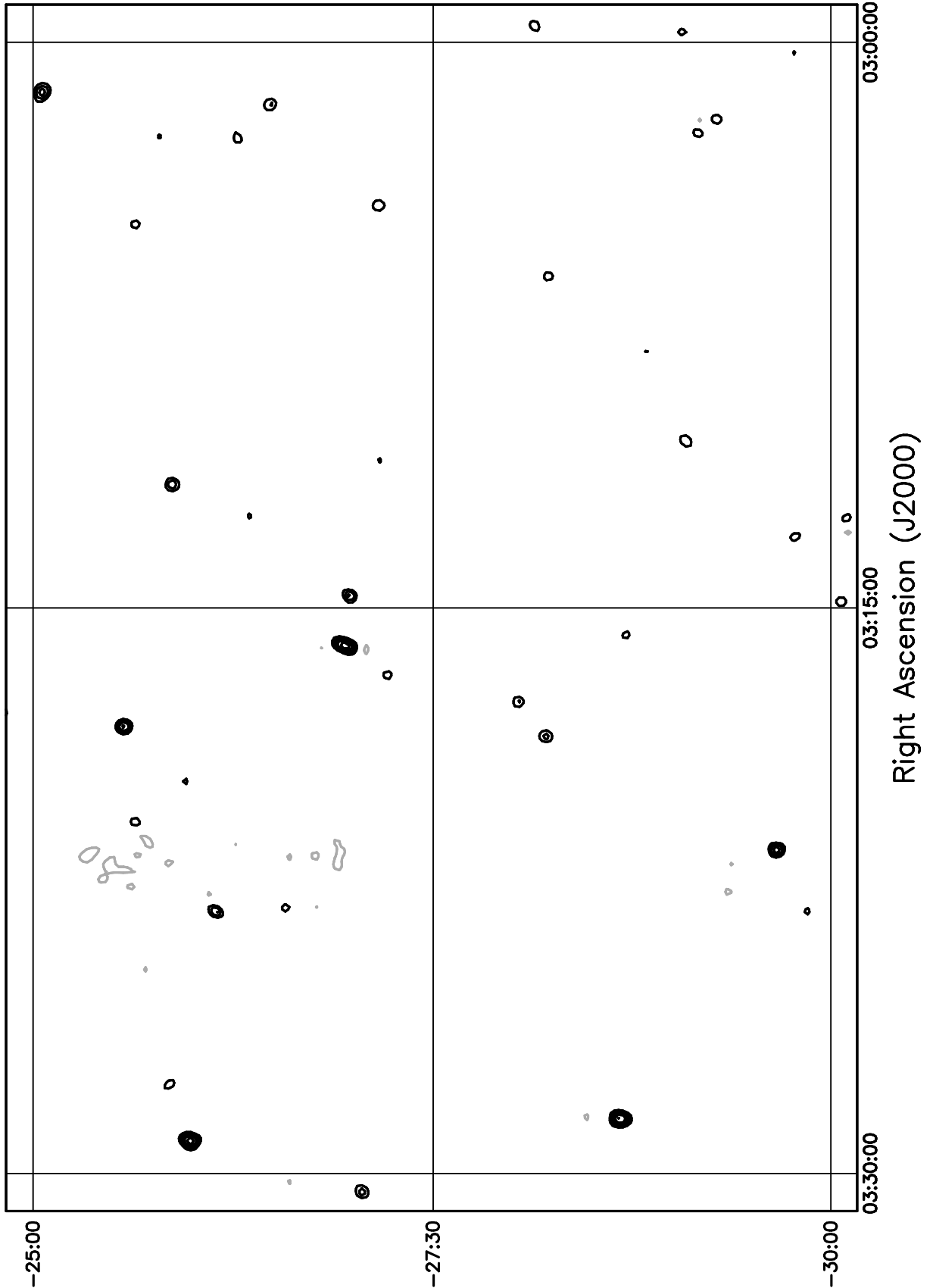
Figure 5.136: Contour plot for the range $03^h00^m \leq RA \leq 03^h30^m$ $-25° \leq \delta \leq -20°$. Contour levels are -5.04, -3.6, -2.52, -1.8, -1.08, 1.08, 1.8, 2.52, 3.6, 5.04, 7.2, 10.08, 14.4, 20.16, 28.8, 39.6, 54, 72, 100.8, 136.8, 180, 216, 252, 288 Jy beam^{-1}.
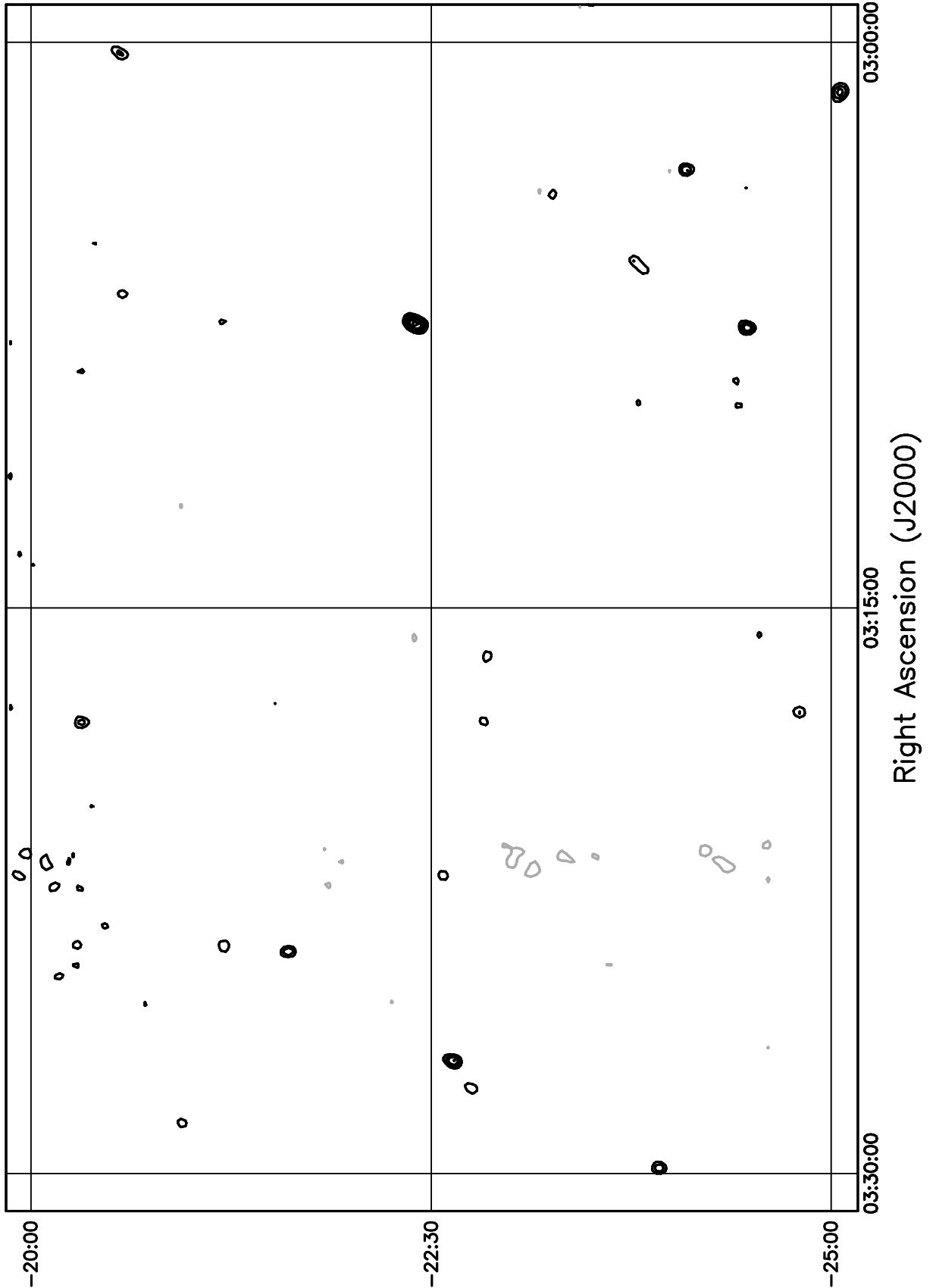
Figure 5.137: Contour plot for the range $03^h00^m \leq RA \leq 03^h30^m$ $-20° \leq \delta \leq -15°$. Contour levels are -5.04, -3.6, -2.52, -1.8, -1.08, 1.08, 1.8, 2.52, 3.6, 5.04, 7.2, 10.08, 14.4, 20.16, 28.8, 39.6, 54, 72, 100.8, 136.8, 180, 216, 252, 288 Jy beam^{-1}.

Right Ascension (J2000)
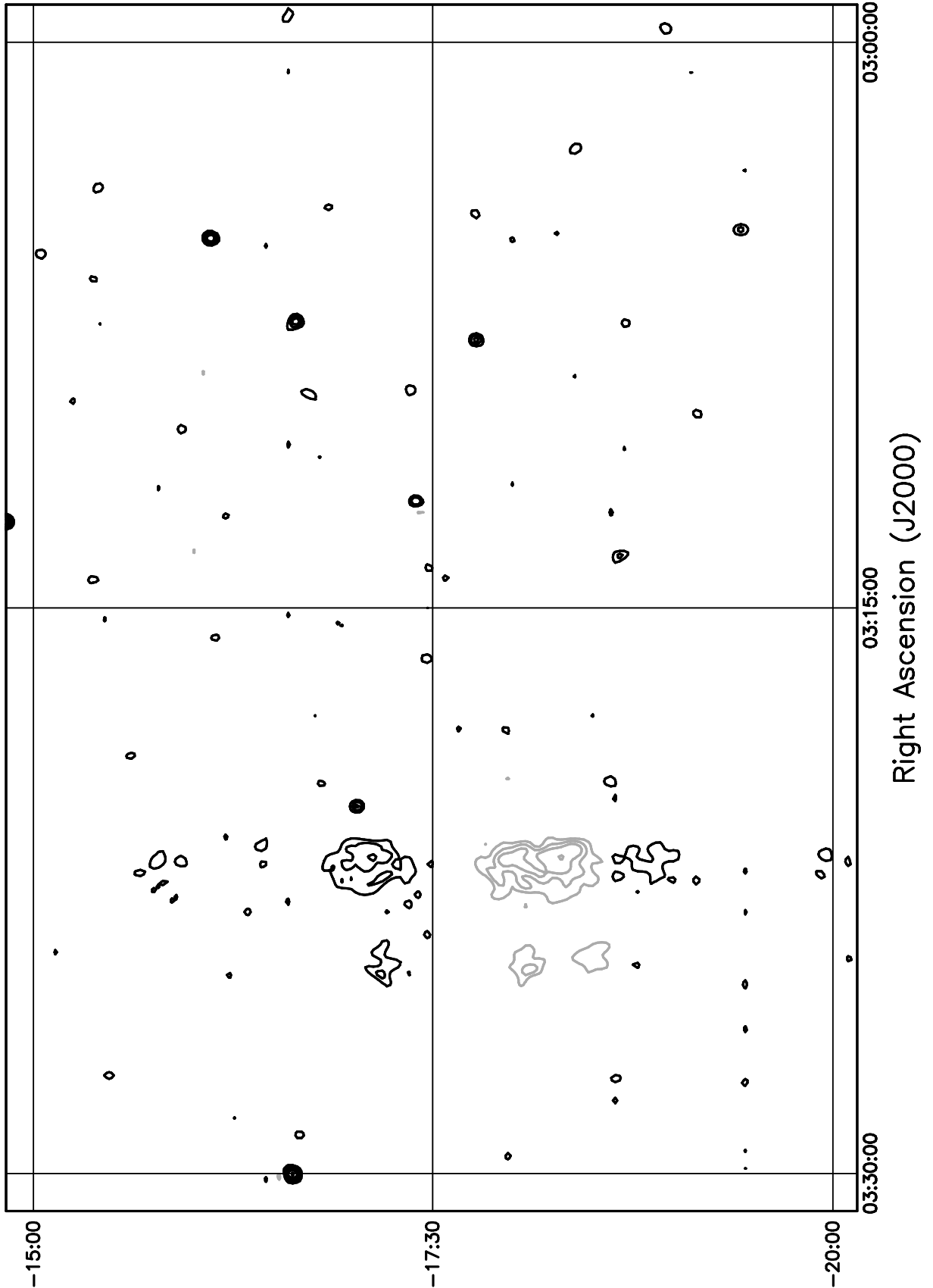
Figure 5.138: Contour plot for the range $03^h00^m \leq RA \leq 03^h30^m$ $-15° \leq \delta \leq -10°$. Contour levels are -5.04, -3.6, -2.52, -1.8, -1.08, 1.08, 1.8, 2.52, 3.6, 5.04, 7.2, 10.08, 14.4, 20.16, 28.8, 39.6, 54, 72, 100.8, 136.8, 180, 216, 252, 288 Jy beam^{-1}.
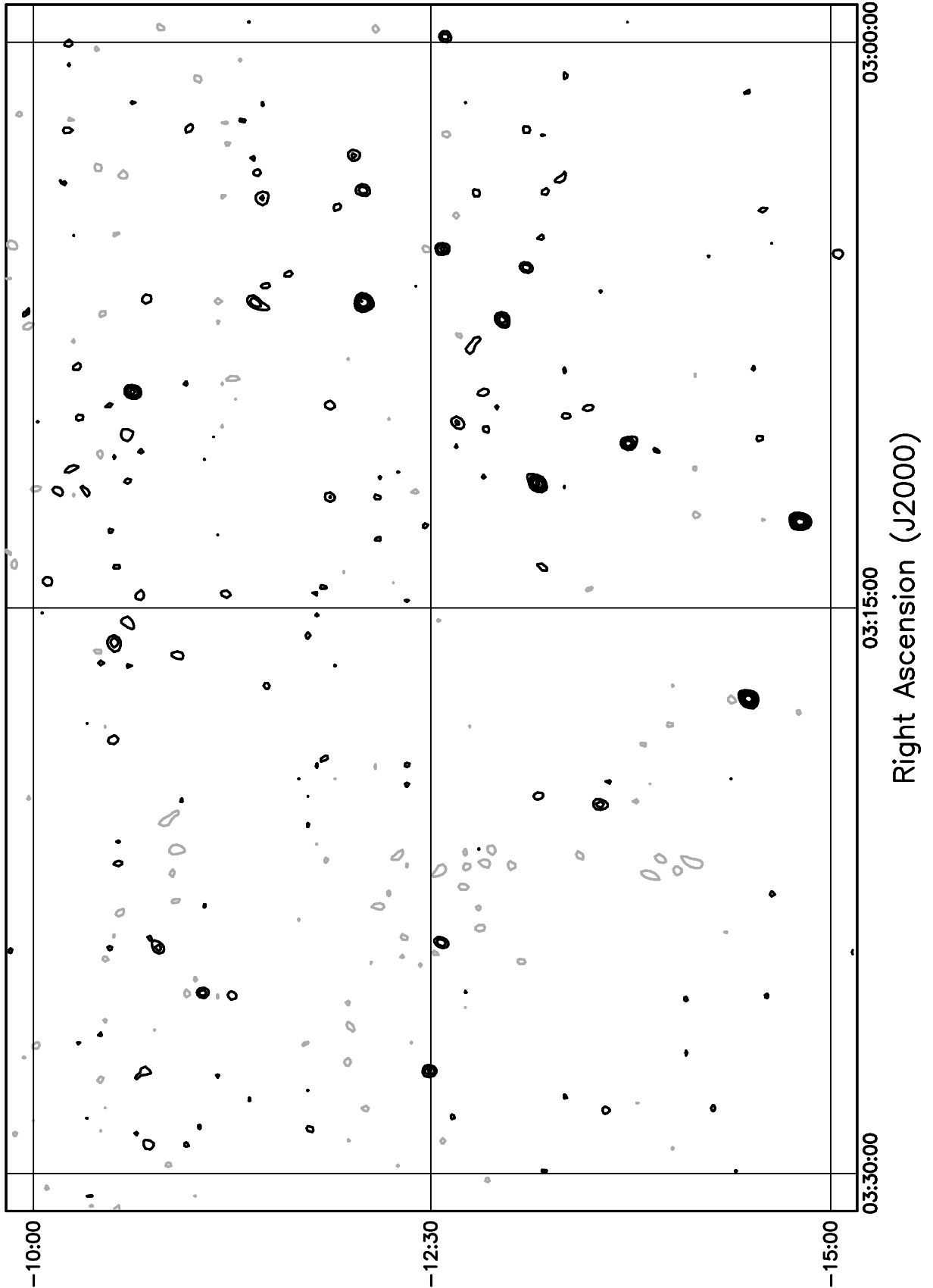
Figure 5.139: Contour plot for the range $03^h30^m \leq RA \leq 04^h00^m$, $-75° \leq \delta \leq -70°$. Contour levels are -7.56, -5.4, -3.78, -2.7, -1.62, 1.62, 2.7, 3.78, 5.4, 7.56, 10.8, 15.12, 21.6, 30.24, 43.2, 59.4, 81, 108, 151.2, 205.2, 270, 324, 378, 432 Jy beam^{-1}.
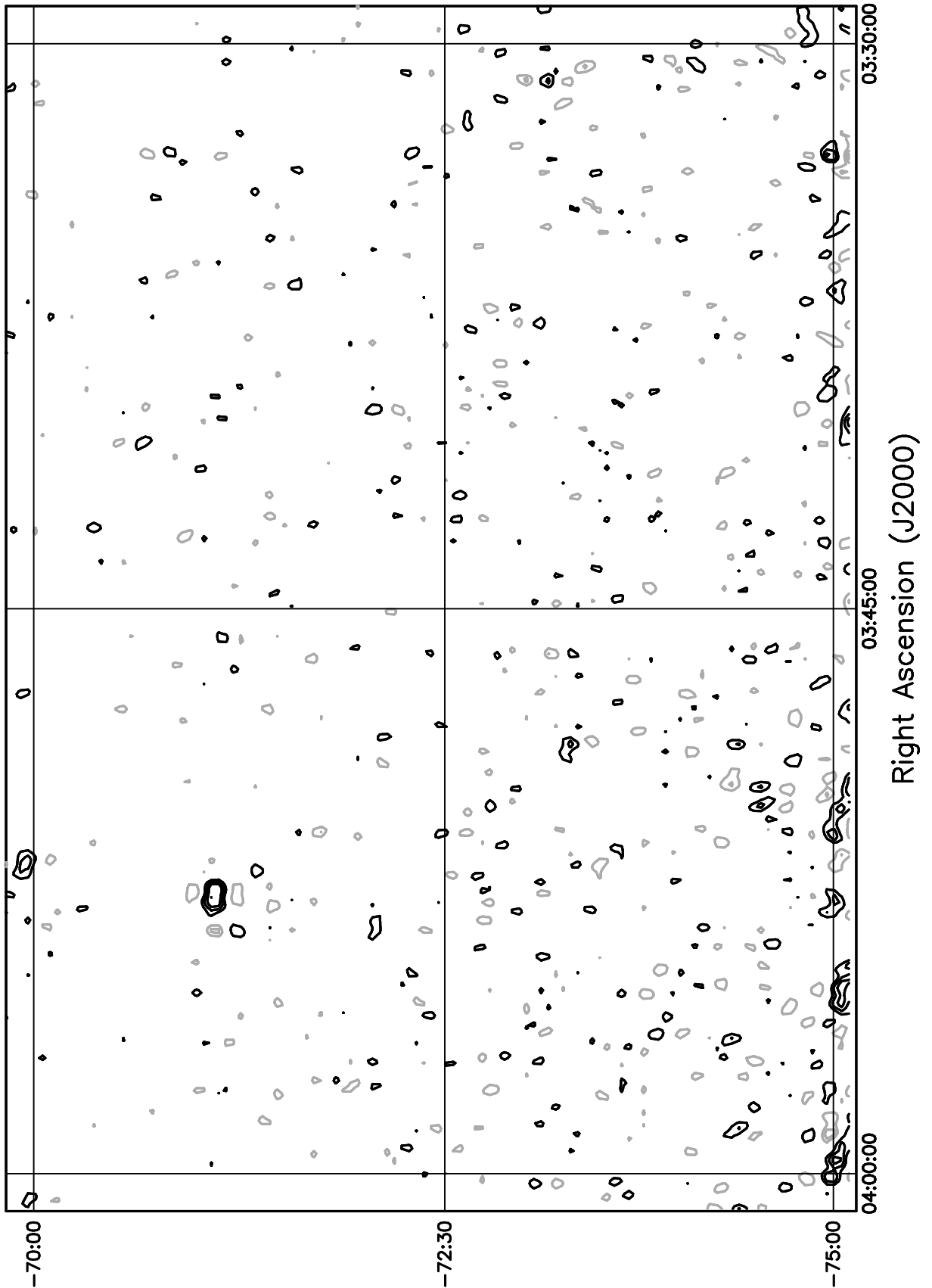
Figure 5.140: Contour plot for the range $03^h30^m \leq RA \leq 04^h00^m$, $-70° \leq \delta \leq -65°$. Contour levels are -7.56, -5.4, -3.78, -2.7, -1.62, 1.62, 2.7, 3.78, 5.4, 7.56, 10.8, 15.12, 21.6, 30.24, 43.2, 59.4, 81, 108, 151.2, 205.2, 270, 324, 378, 432 Jy beam^{-1}.
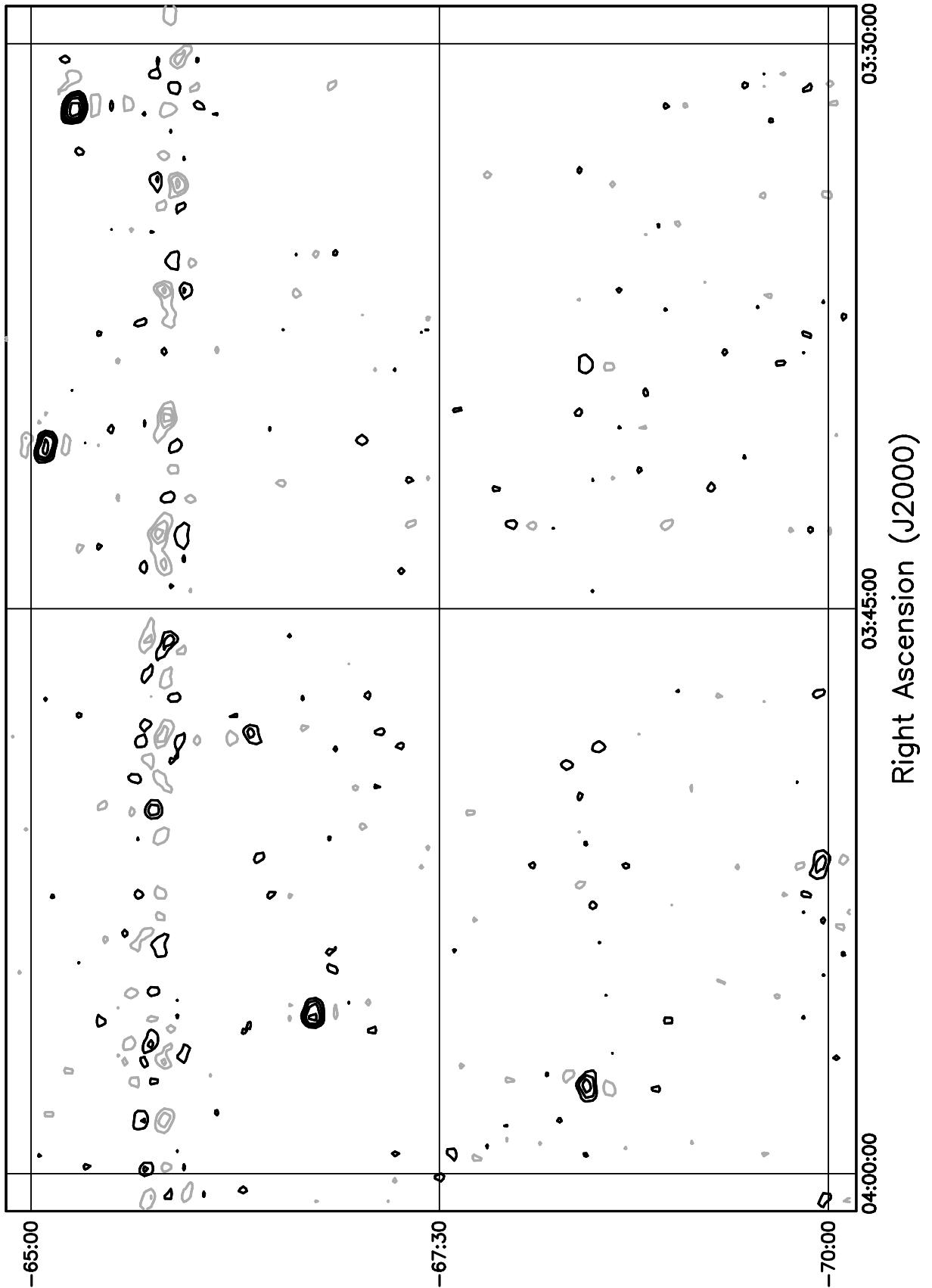
Figure 5.141: Contour plot for the range $03^h30^m \leq RA \leq 04^h00^m$, $-65° \leq \delta \leq -60°$. Contour levels are -7.56, -5.4, -3.78, -2.7, -1.62, 1.62, 2.7, 3.78, 5.4, 7.56, 10.8, 15.12, 21.6, 30.24, 43.2, 59.4, 81, 108, 151.2, 205.2, 270, 324, 378, 432 Jy beam^{-1}.
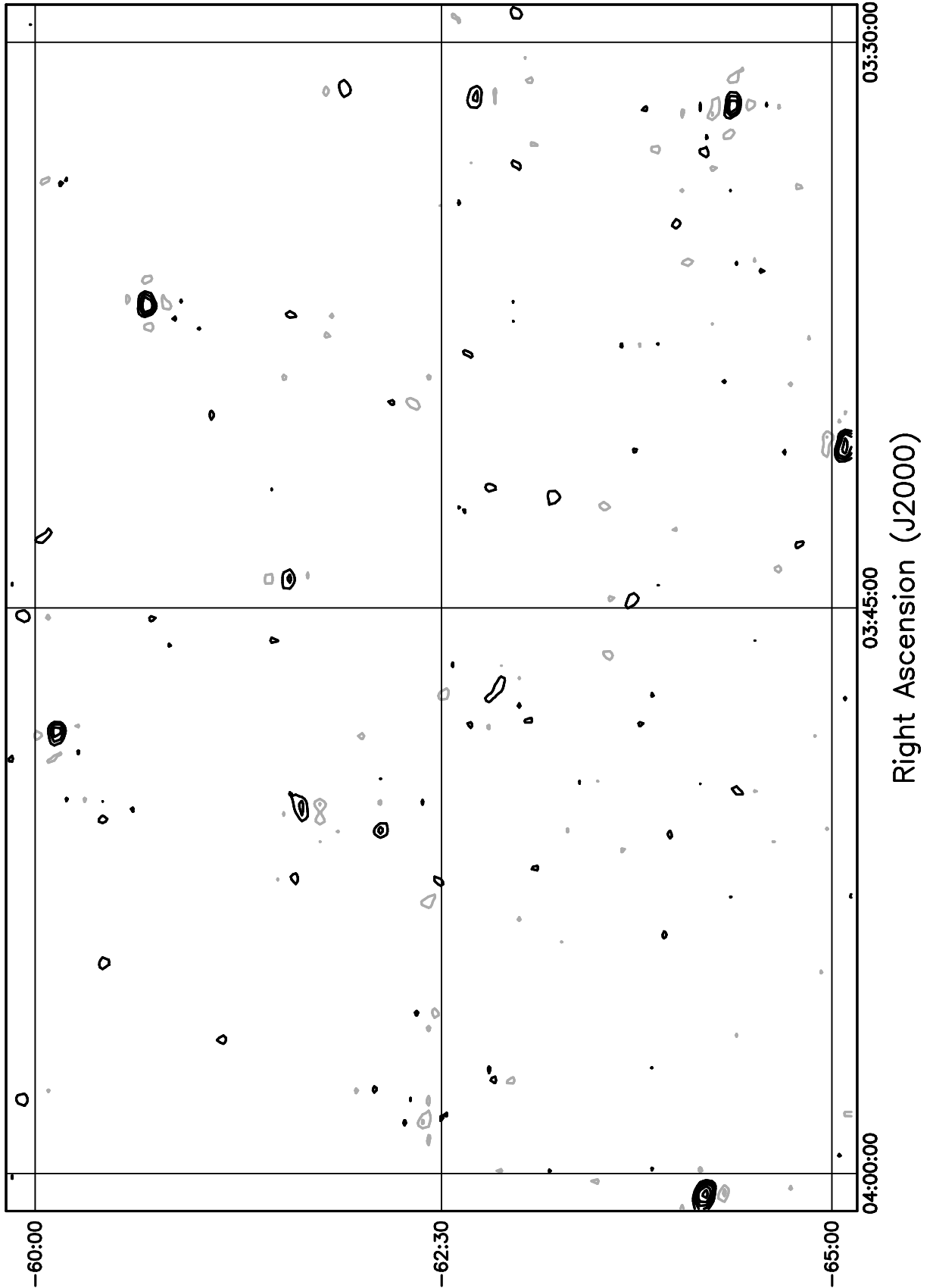
Figure 5.142: Contour plot for the range $03^h30^m \leq RA \leq 04^h00^m$, $-60° \leq \delta \leq -55°$. Contour levels are -7.56, -5.4, -3.78, -2.7, -1.62, 1.62, 2.7, 3.78, 5.4, 7.56, 10.8, 15.12, 21.6, 30.24, 43.2, 59.4, 81, 108, 151.2, 205.2, 270, 324, 378, 432, Jy beam^{-1}.
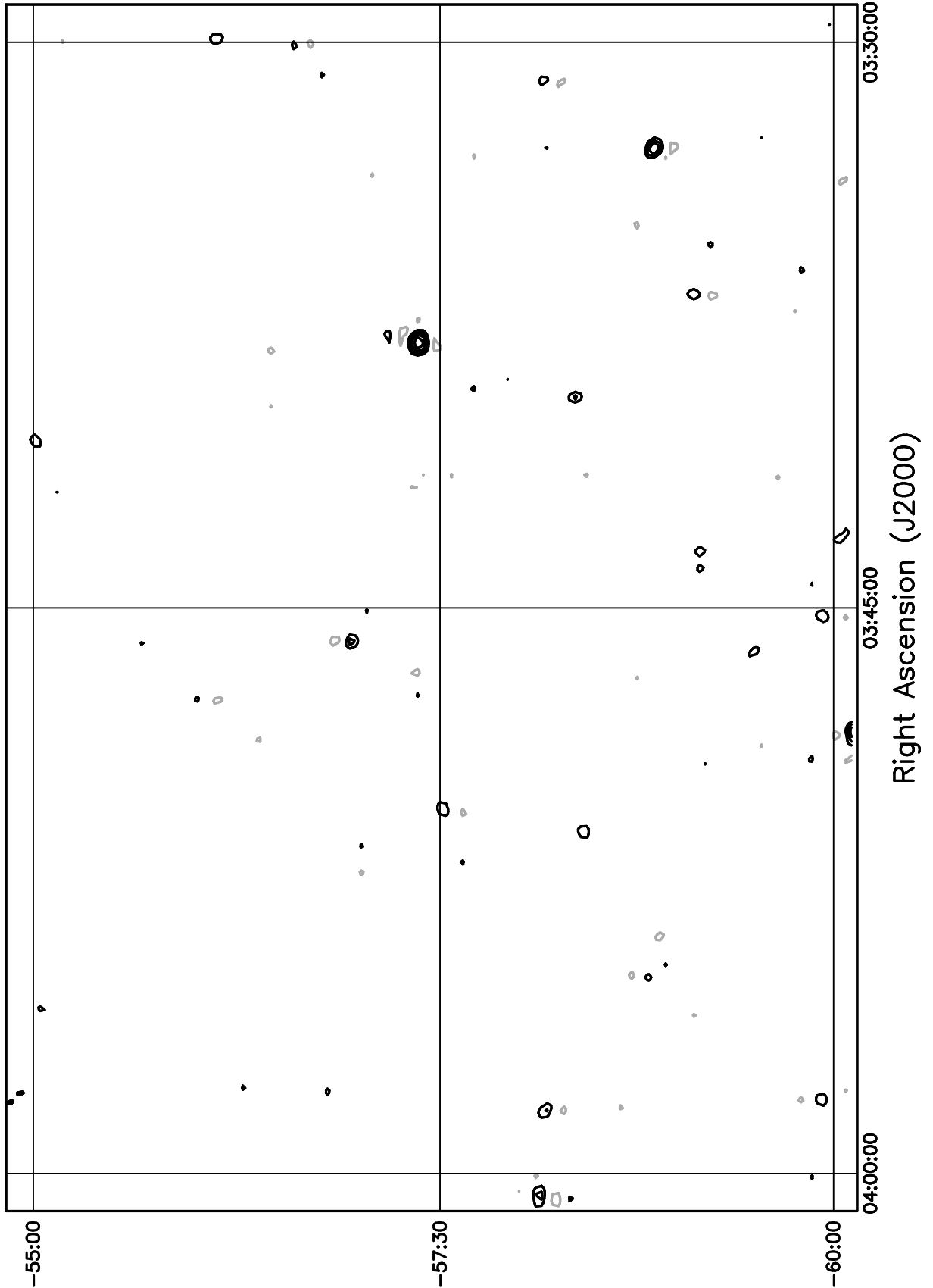
Figure 5.143: Contour plot for the range $03^h30^m \leq RA \leq 04^h00^m$, $-55° \leq \delta \leq -50°$. Contour levels are -7.56, -5.4, -3.78, -2.7, -1.62, 1.62, 2.7, 3.78, 5.4, 7.56, 10.8, 15.12, 21.6, 30.24, 43.2, 59.4, 81, 108, 151.2, 205.2, 270, 324, 378, 432 Jy beam^{-1}.
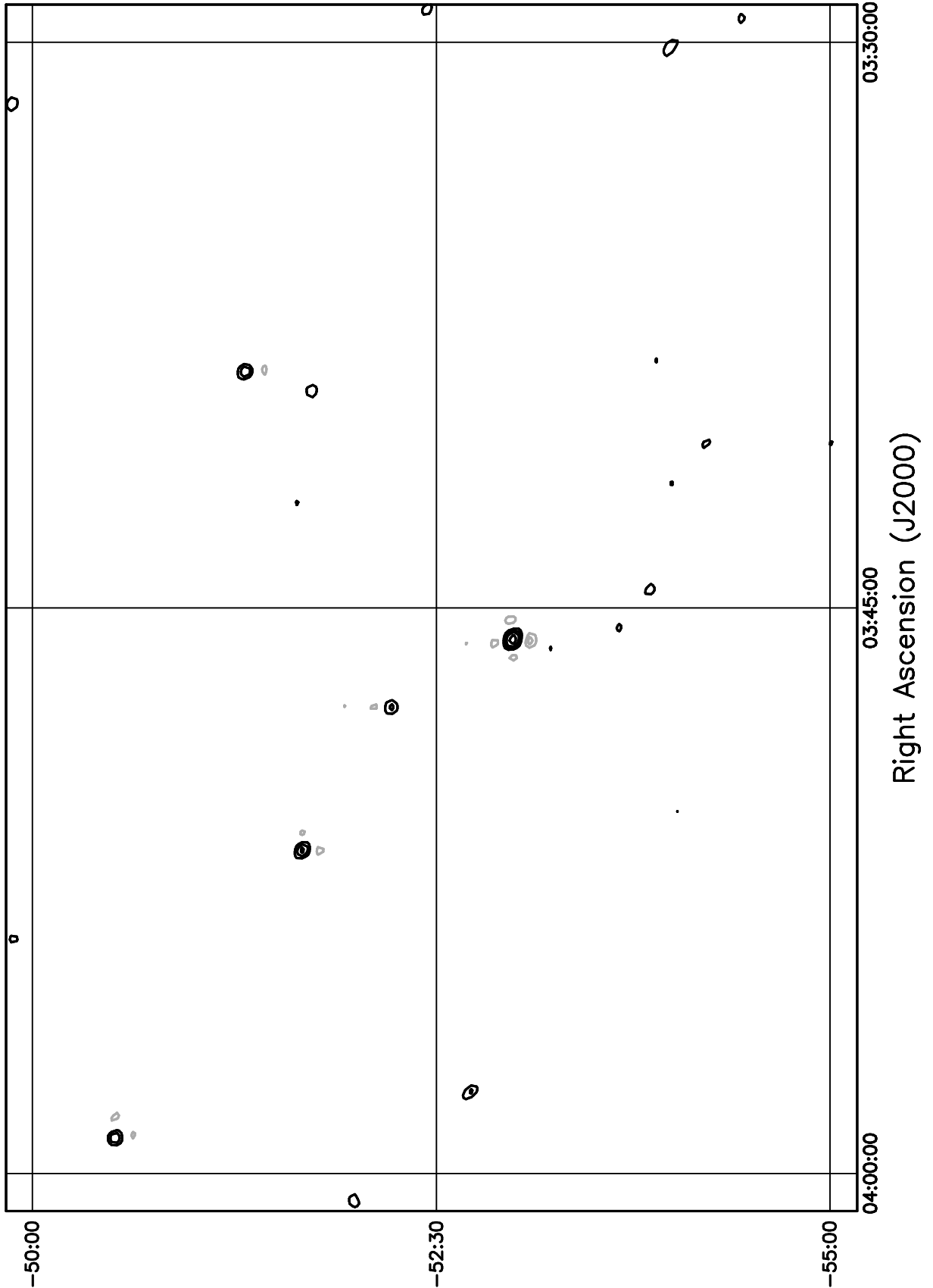
Figure 5.144: Contour plot for the range $03^h30^m \leq RA \leq 04^h00^m$, $-50° \leq \delta \leq -45°$. Contour levels are -7.56, -5.4, -3.78, -2.7, -1.62, 1.62, 2.7, 3.78, 5.4, 7.56, 10.8, 15.12, 21.6, 30.24, 43.2, 59.4, 81, 108, 151.2, 205.2, 270, 324, 378, 432 Jy beam^{-1}.
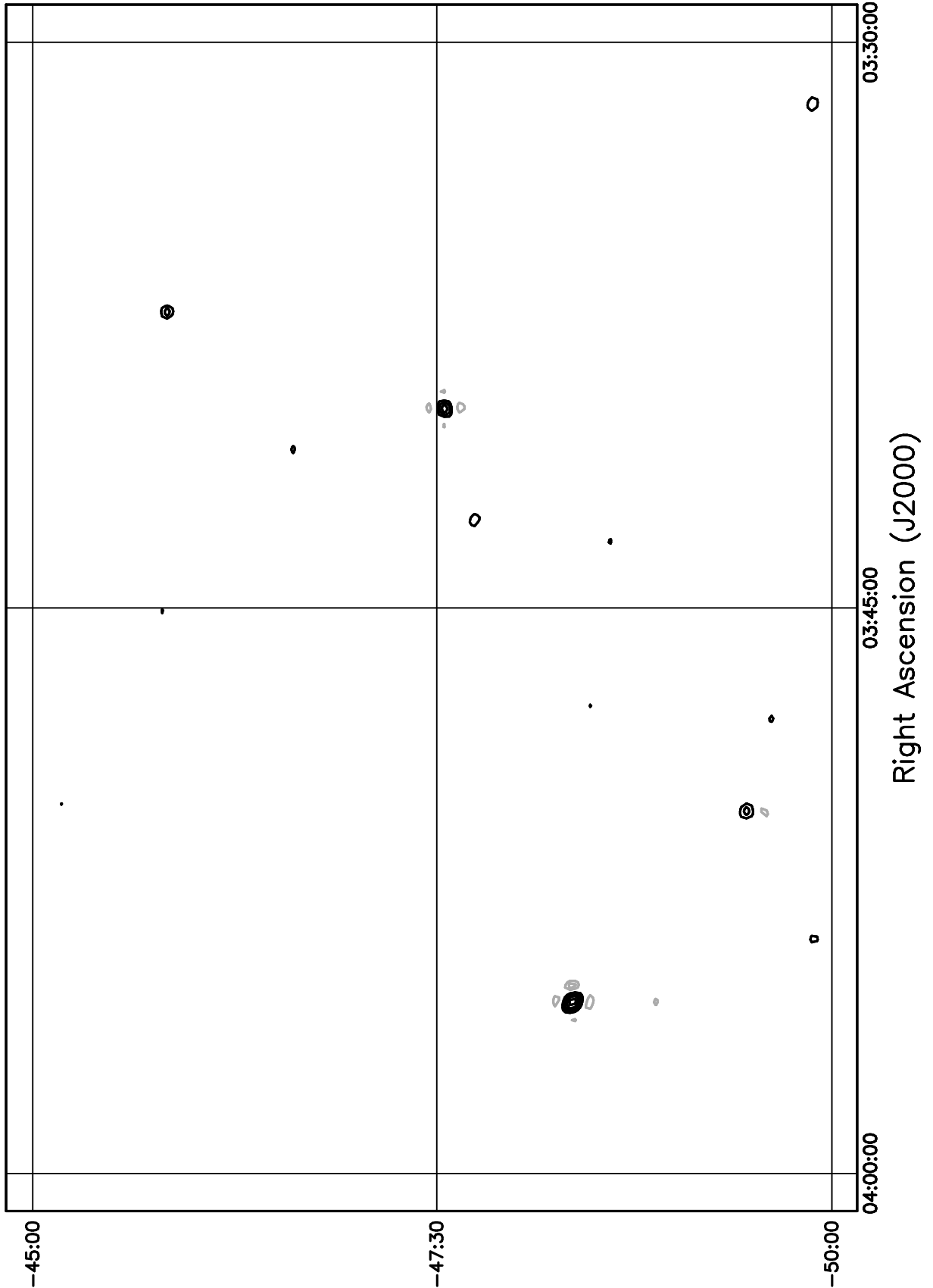
Figure 5.145: Contour plot for the range $03^h30^m \leq RA \leq 04^h00^m$, $-45° \leq \delta \leq -40°$. Contour levels are -7.56, -5.4, -3.78, -2.7, -1.62, 1.62, 2.7, 3.78, 5.4, 7.56, 10.8, 15.12, 21.6, 30.24, 43.2, 59.4, 81, 108, 151.2, 205.2, 270, 324, 378, 432 Jy beam^{-1}.
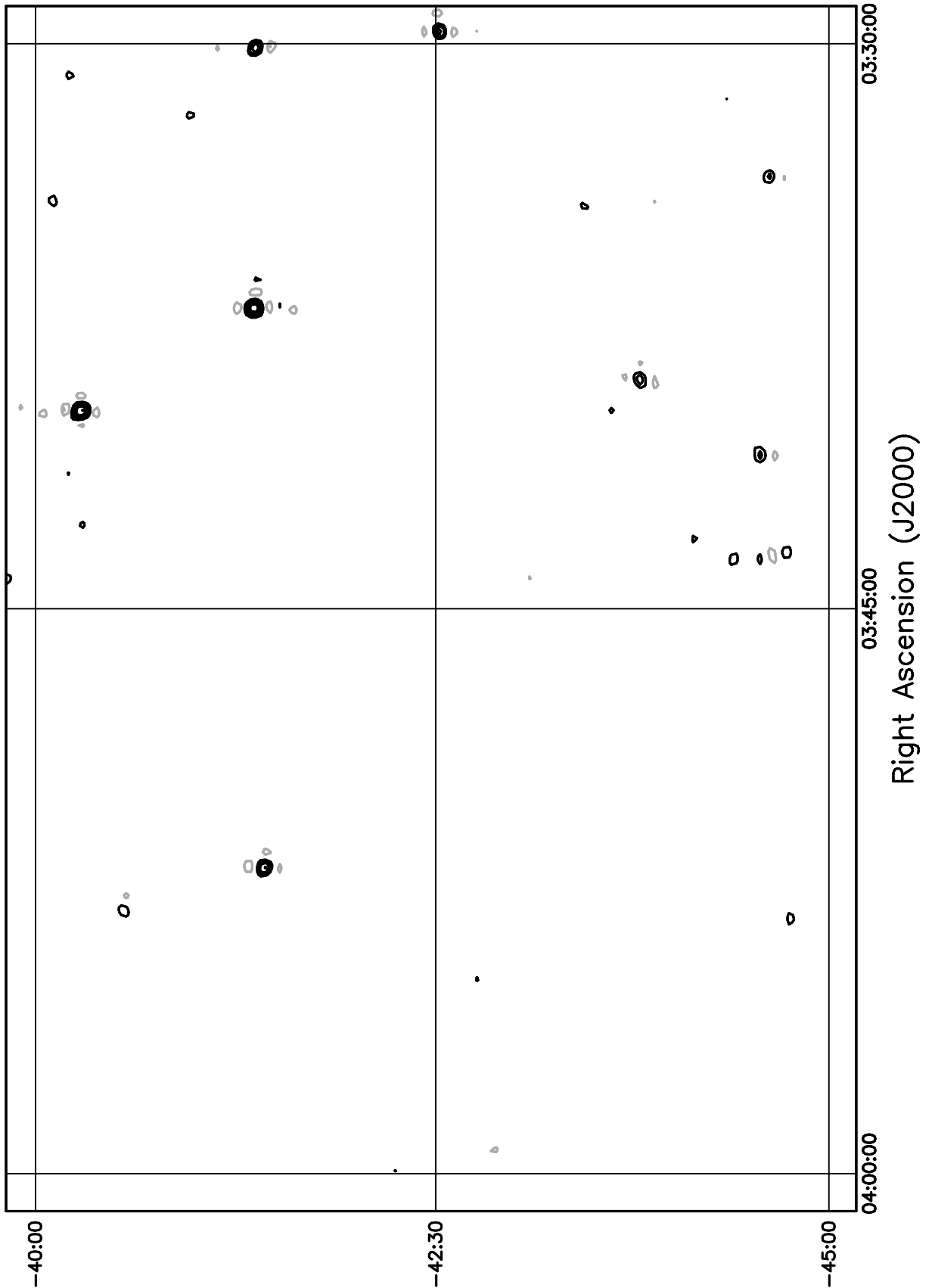
Figure 5.146: Contour plot for the range $03^h30^m \leq RA \leq 04^h00^m$, $-40° \leq \delta \leq -35°$. Contour levels are -7.56, -5.4, -3.78, -2.7, -1.62, 1.62, 2.7, 3.78, 5.4, 7.56, 10.8, 15.12, 21.6, 30.24, 43.2, 59.4, 81, 108, 151.2, 205.2, 270, 324, 378, 432 Jy beam^{-1}.
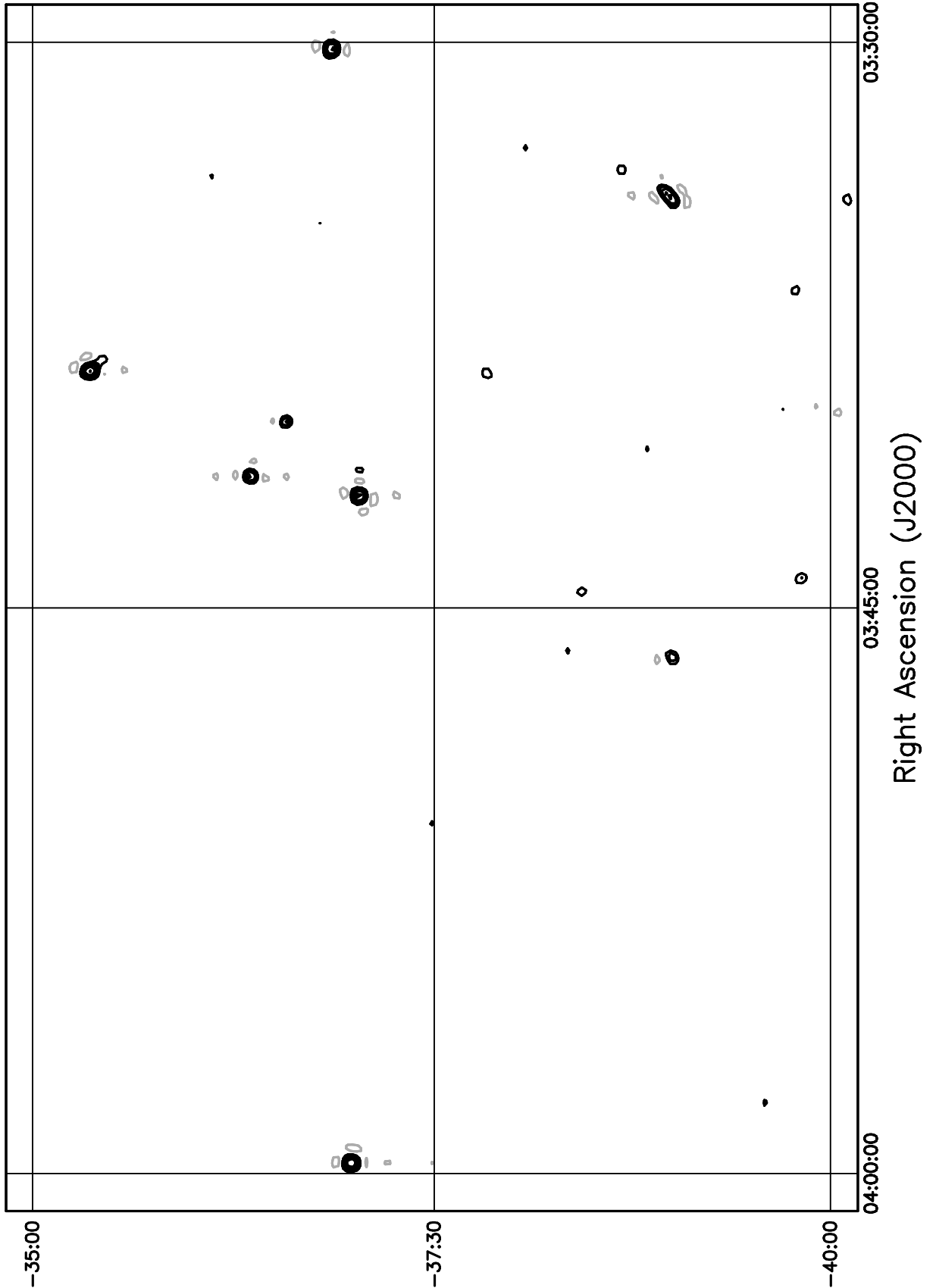
Figure 5.147: Contour plot for the range $03^h30^m \leq RA \leq 04^h00^m$, $-35° \leq \delta \leq -30°$. Contour levels are -7.56, -5.4, -3.78, -2.7, -1.62, 1.62, 2.7, 3.78, 5.4, 7.56, 10.8, 15.12, 21.6, 30.24, 43.2, 59.4, 81, 108, 151.2, 205.2, 270, 324, 378, 432 Jy beam^{-1}.
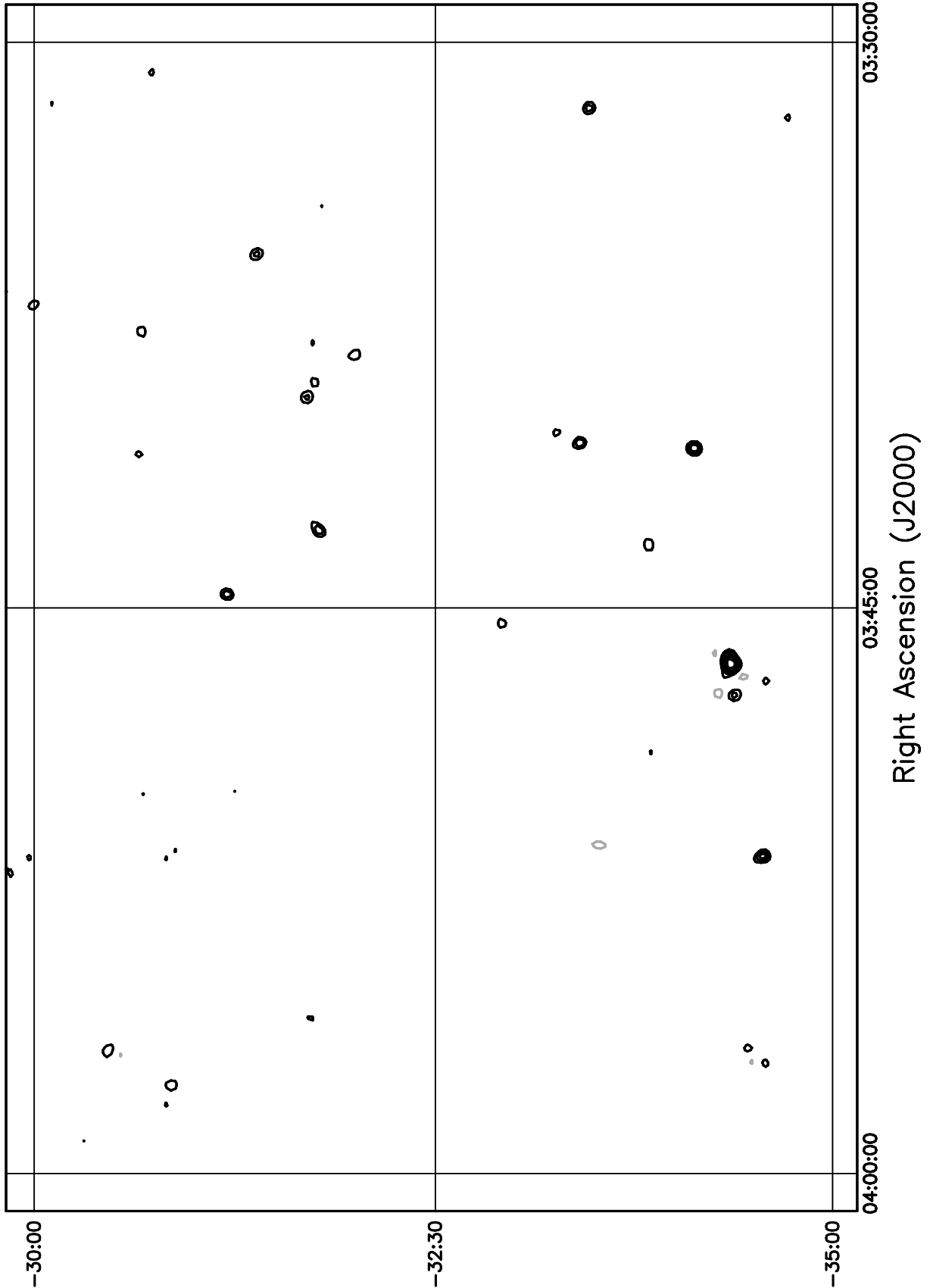
Figure 5.148: Contour plot for the range $03^h30^m \leq RA \leq 04^h00^m$, $-30° \leq \delta \leq -25°$. Contour levels are -7.56, -5.4, -3.78, -2.7, -1.62, 1.62, 2.7, 3.78, 5.4, 7.56, 10.8, 15.12, 21.6, 30.24, 43.2, 59.4, 81, 108, 151.2, 205.2, 270, 324, 378, 432 Jy beam^{-1}.
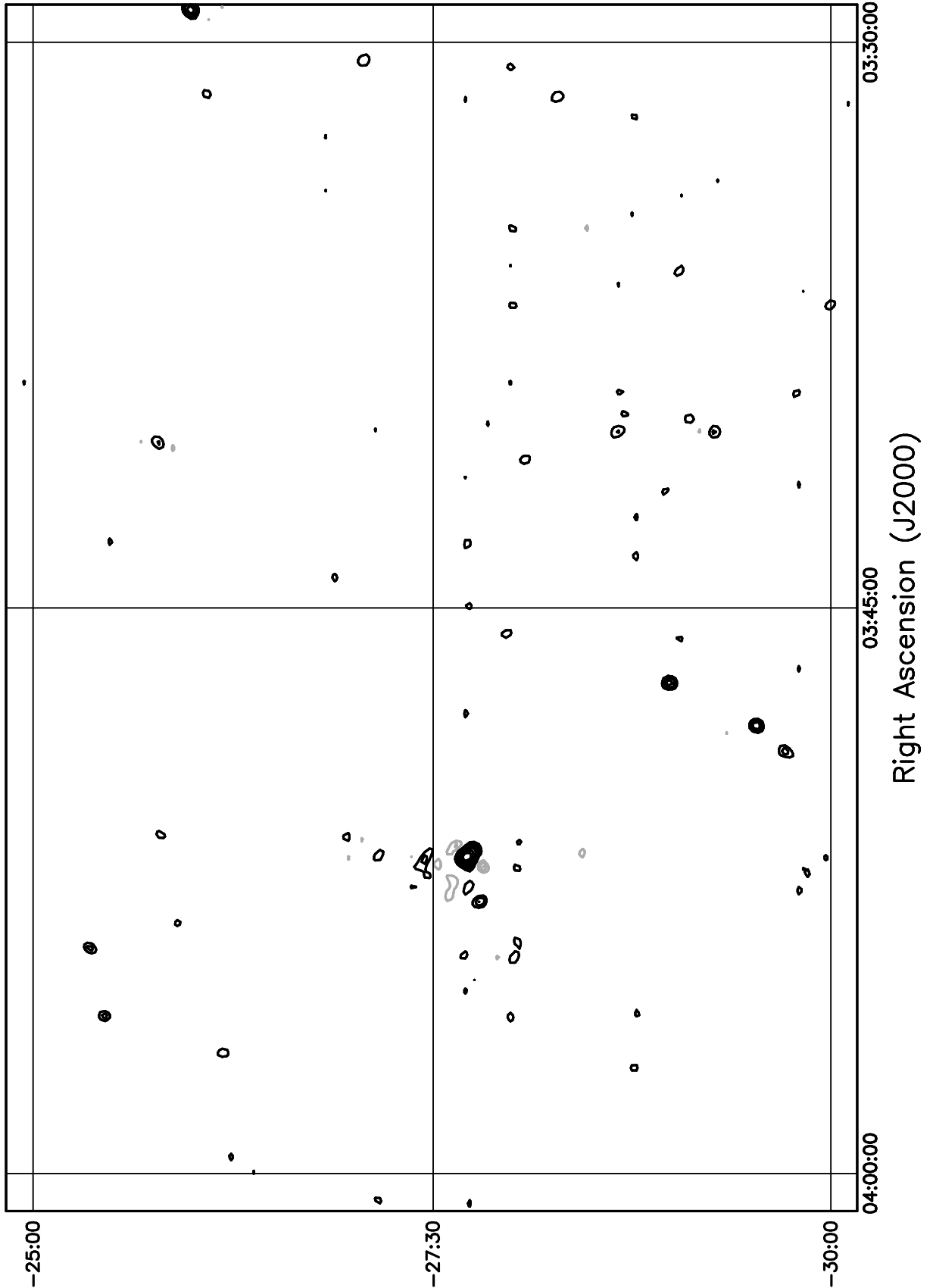
Figure 5.149: Contour plot for the range $03^h30^m \leq RA \leq 04^h00^m$, $-25° \leq \delta \leq -20°$. Contour levels are -7.56, -5.4, -3.78, -2.7, -1.62, 1.62, 2.7, 3.78, 5.4, 7.56, 10.8, 15.12, 21.6, 30.24, 43.2, 59.4, 81, 108, 151.2, 205.2, 270, 324, 378, 432 Jy beam^{-1}.
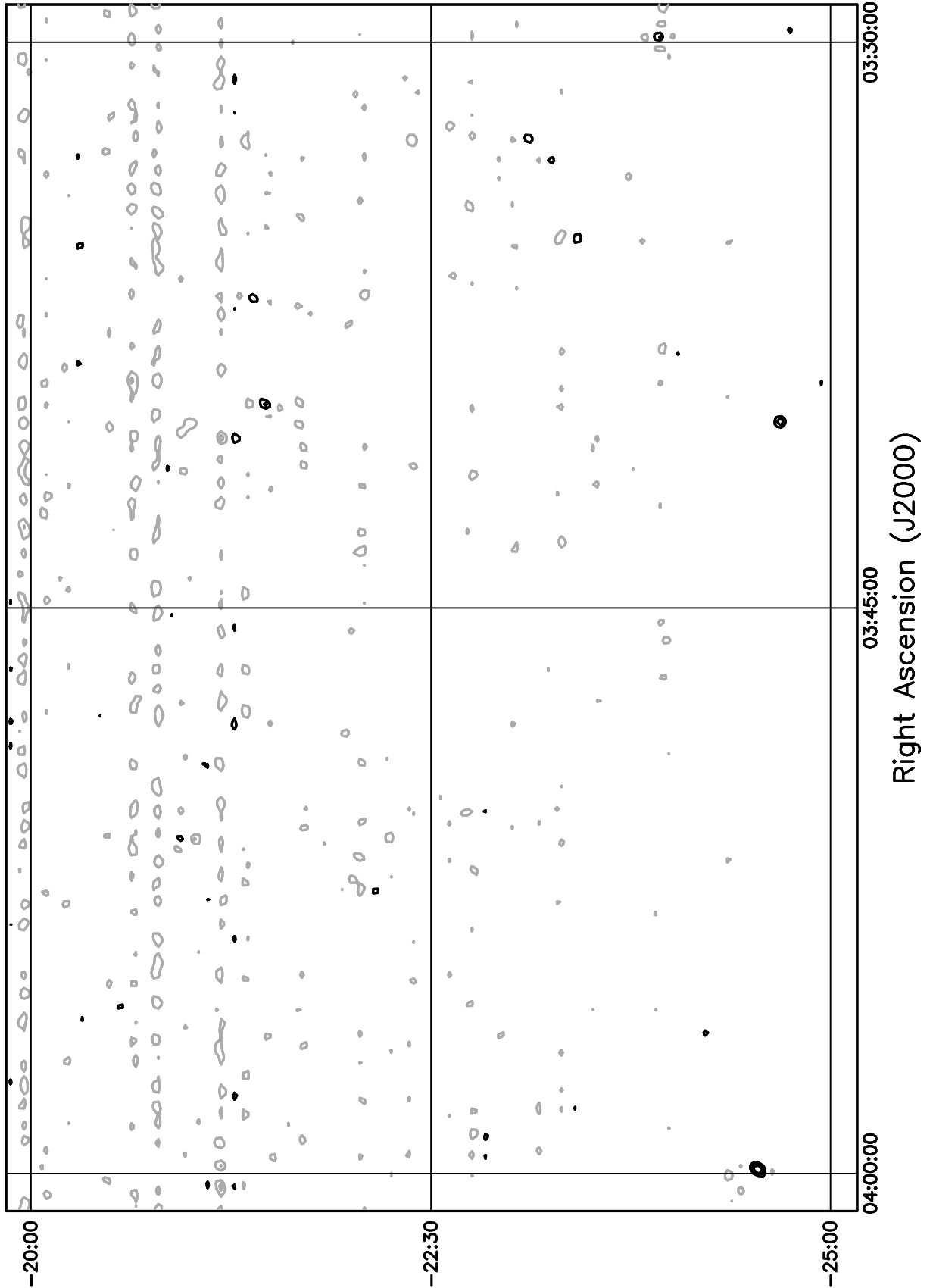
Figure 5.150: Contour plot for the range $03^h30^m \leq RA \leq 04^h00^m$, $-20° \leq \delta \leq -15°$. Contour levels are -7.56, -5.4, -3.78, -2.7, -1.62, 1.62, 2.7, 3.78, 5.4, 7.56, 10.8, 15.12, 21.6, 30.24, 43.2, 59.4, 81, 108, 151.2, 205.2, 270, 324, 378, 432 Jy beam^{-1}.
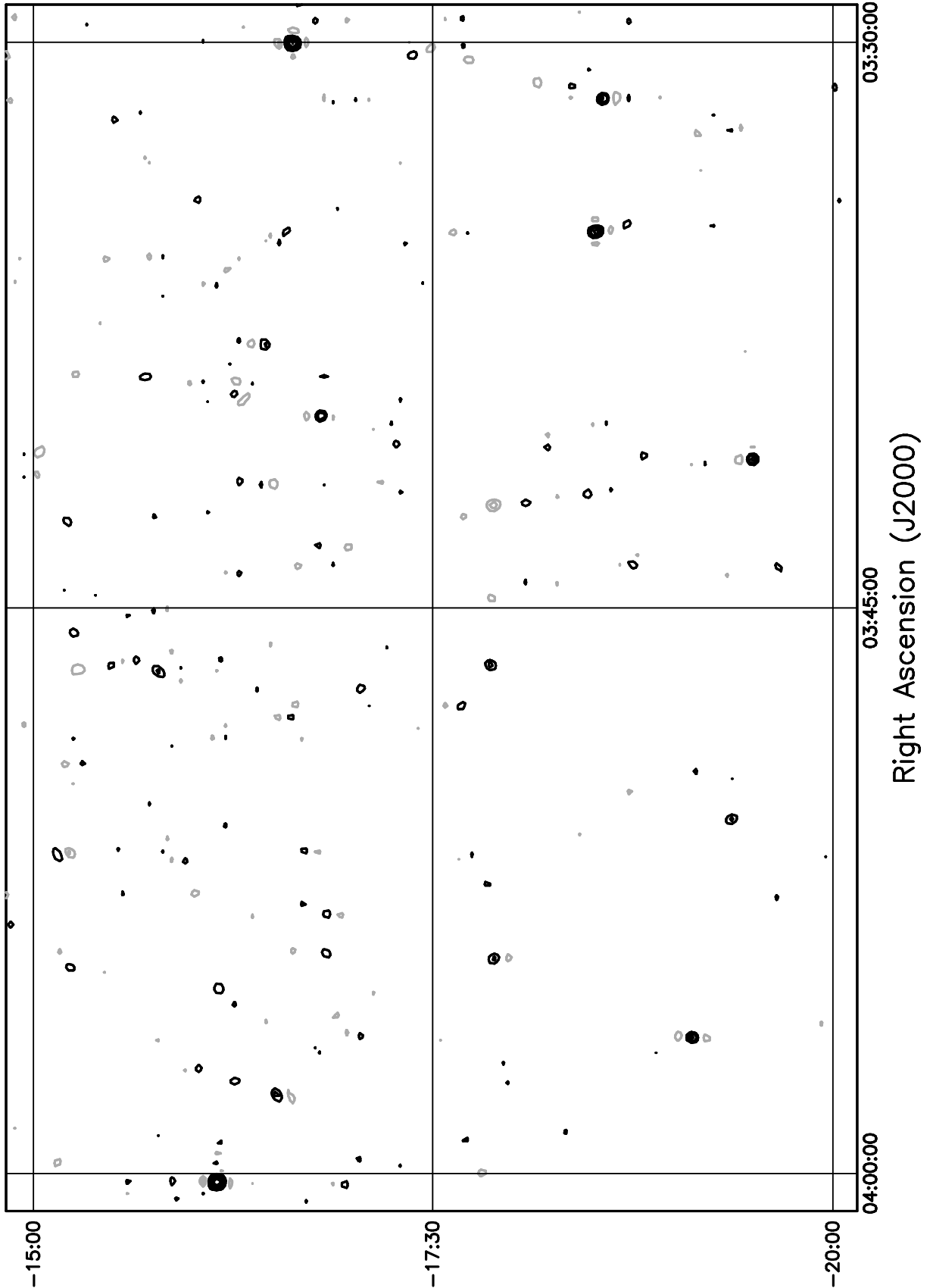
Figure 5.151: Contour plot for the range $03^h30^m \leq RA \leq 04^h00^m$, $-15° \leq \delta \leq -10°$. Contour levels are -7.56, -5.4, -3.78, -2.7, -1.62, 1.62, 2.7, 3.78, 5.4, 7.56, 10.8, 15.12, 21.6, 30.24, 43.2, 59.4, 81, 108, 151.2, 205.2, 270, 324, 378, 432 Jy beam^{-1}.
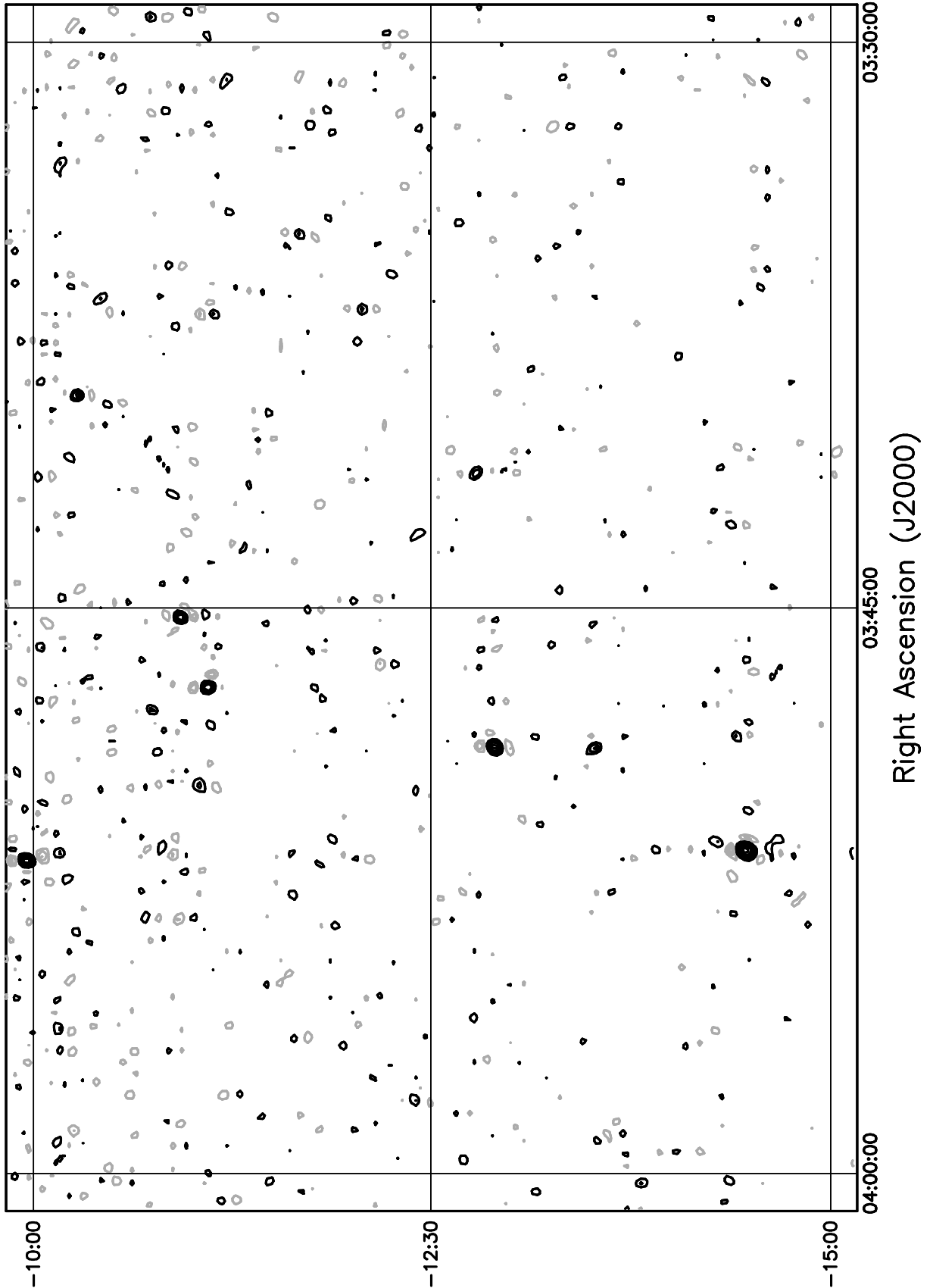
Figure 5.152: Contour plot for the range $04^h00^m \leq RA \leq 04^h30^m$, $-75° \leq \delta \leq -70°$. Contour levels are -7.56, -5.4, -3.78, -2.7, -1.62, 1.62, 2.7, 3.78, 5.4, 7.56, 10.8, 15.12, 21.6, 30.24, 43.2, 59.4, 81, 108, 151.2, 205.2, 270, 324, 378, 432 Jy beam^{-1}.
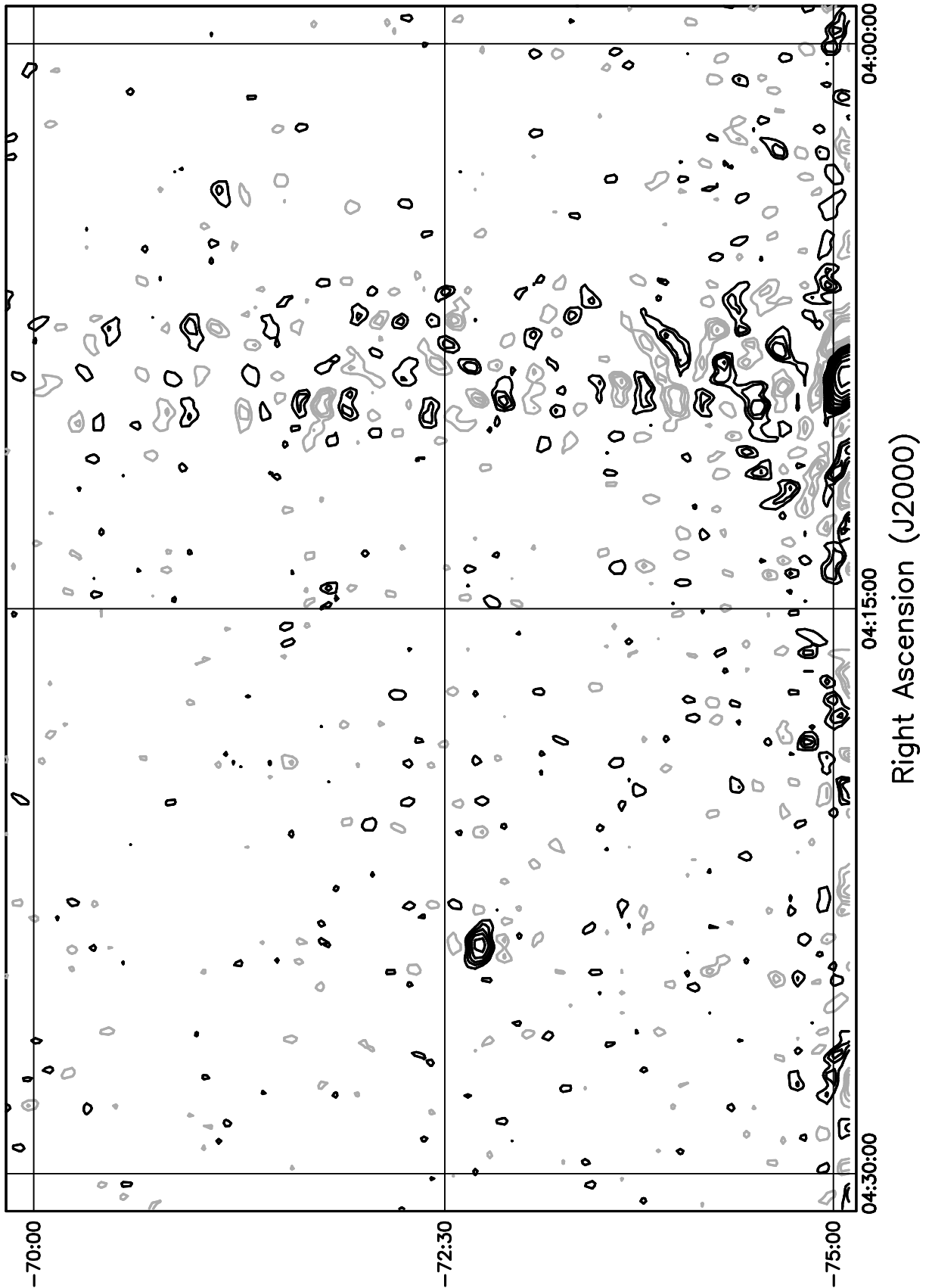
Figure 5.153: Contour plot for the range $04^h00^m \leq RA \leq 04^h30^m$, $-70° \leq \delta \leq -65°$. Contour levels are -7.56, -5.4, -3.78, -2.7, -1.62, 1.62, 2.7, 3.78, 5.4, 7.56, 10.8, 15.12, 21.6, 30.24, 43.2, 59.4, 81, 108, 151.2, 205.2, 270, 324, 378, 432 Jy beam^{-1}.
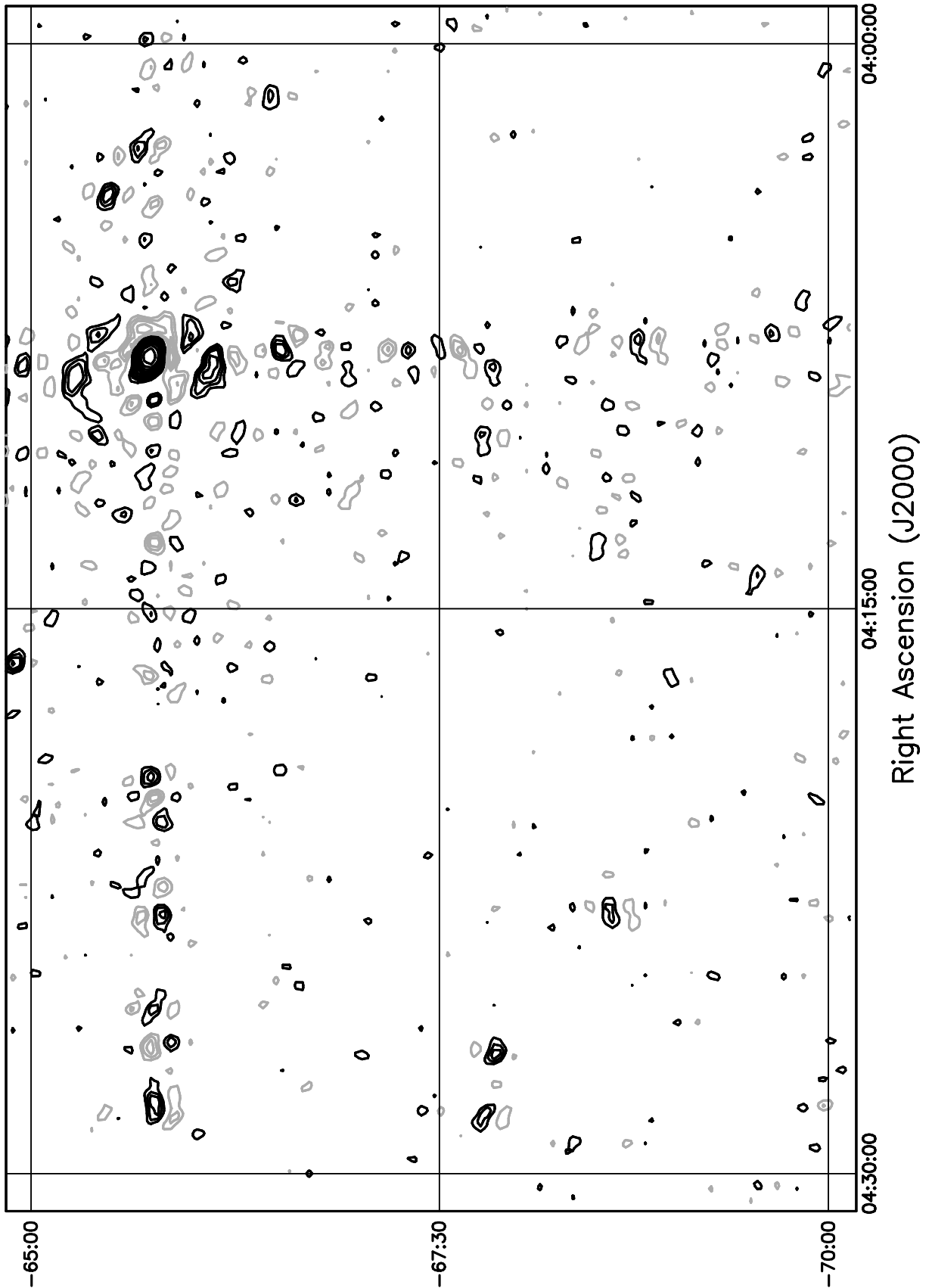
Figure 5.154: Contour plot for the range $04^h00^m \leq RA \leq 04^h30^m$, $-65° \leq \delta \leq -60°$. Contour levels are -7.56, -5.4, -3.78, -2.7, -1.62, 1.62, 2.7, 3.78, 5.4, 7.56, 10.8, 15.12, 21.6, 30.24, 43.2, 59.4, 81, 108, 151.2, 205.2, 270, 324, 378, 432 Jy beam^{-1}.
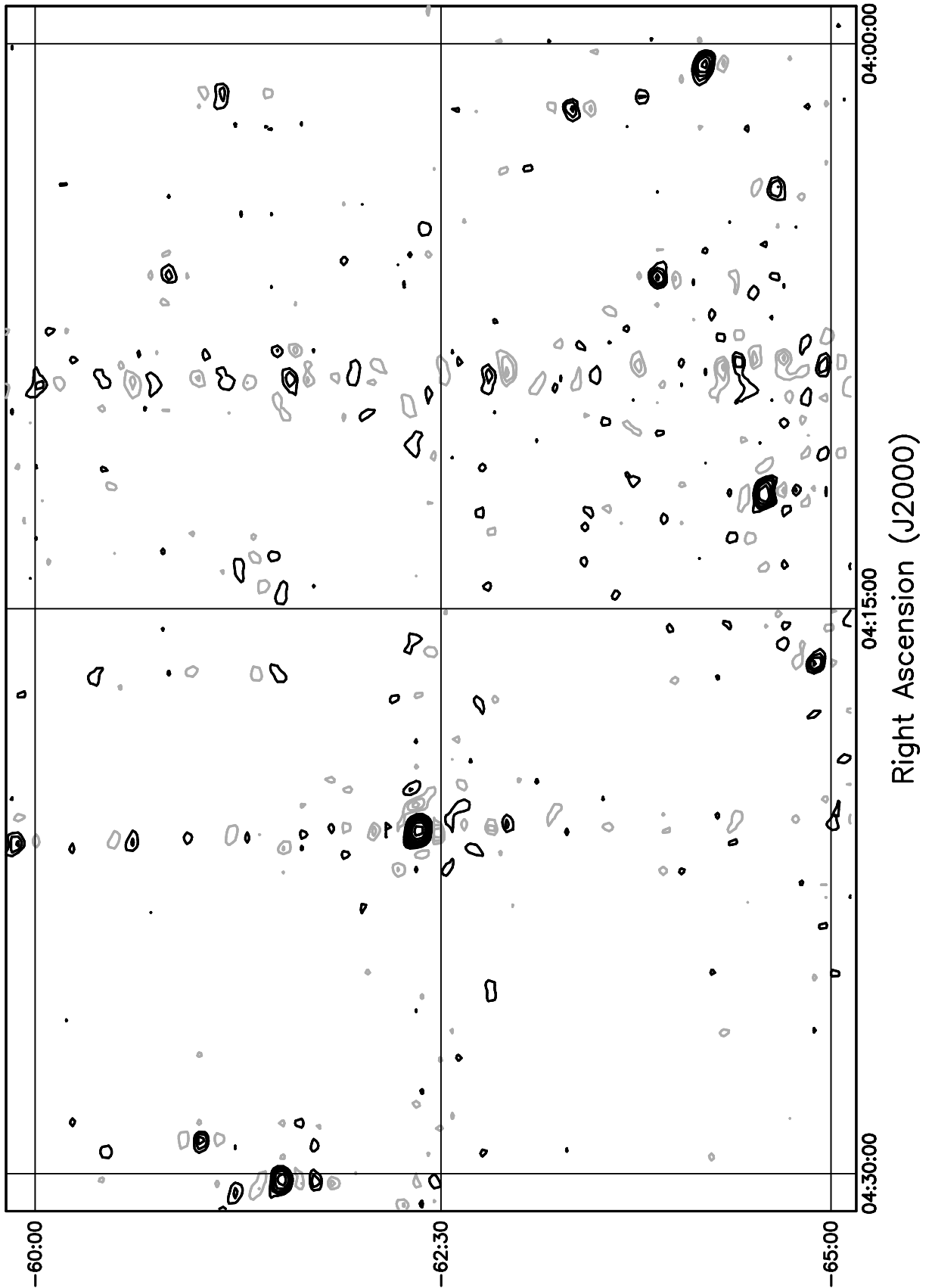
Figure 5.155: Contour plot for the range $04^h00^m \le RA \le 04^h30^m$, $-60° \le \delta \le -55°$. Contour levels are -7.56, -5.4, -3.78, -2.7, -1.62, 1.62, 2.7, 3.78, 5.4, 7.56, 10.8, 15.12, 21.6, 30.24, 43.2, 59.4, 81, 108, 151.2, 205.2, 270, 324, 378, 432 Jy beam^{-1}.
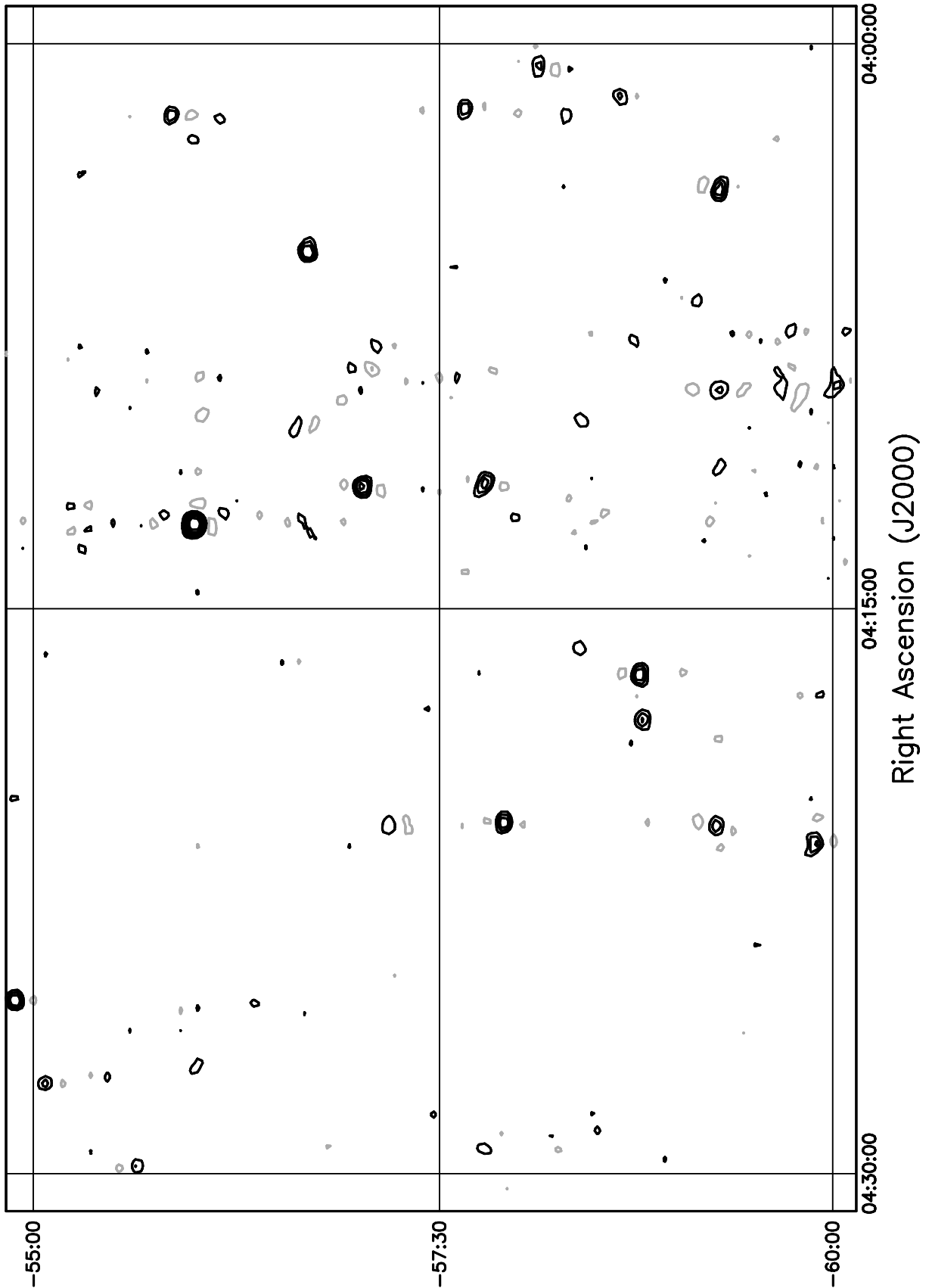
Figure 5.156: Contour plot for the range $04^h00^m \leq RA \leq 04^h30^m$, $-55° \leq \delta \leq -50°$. Contour levels are -7.56, -5.4, -3.78, -2.7, -1.62, 1.62, 2.7, 3.78, 5.4, 7.56, 10.8, 15.12, 21.6, 30.24, 43.2, 59.4, 81, 108, 151.2, 205.2, 270, 324, 378, 432 Jy beam^{-1}.
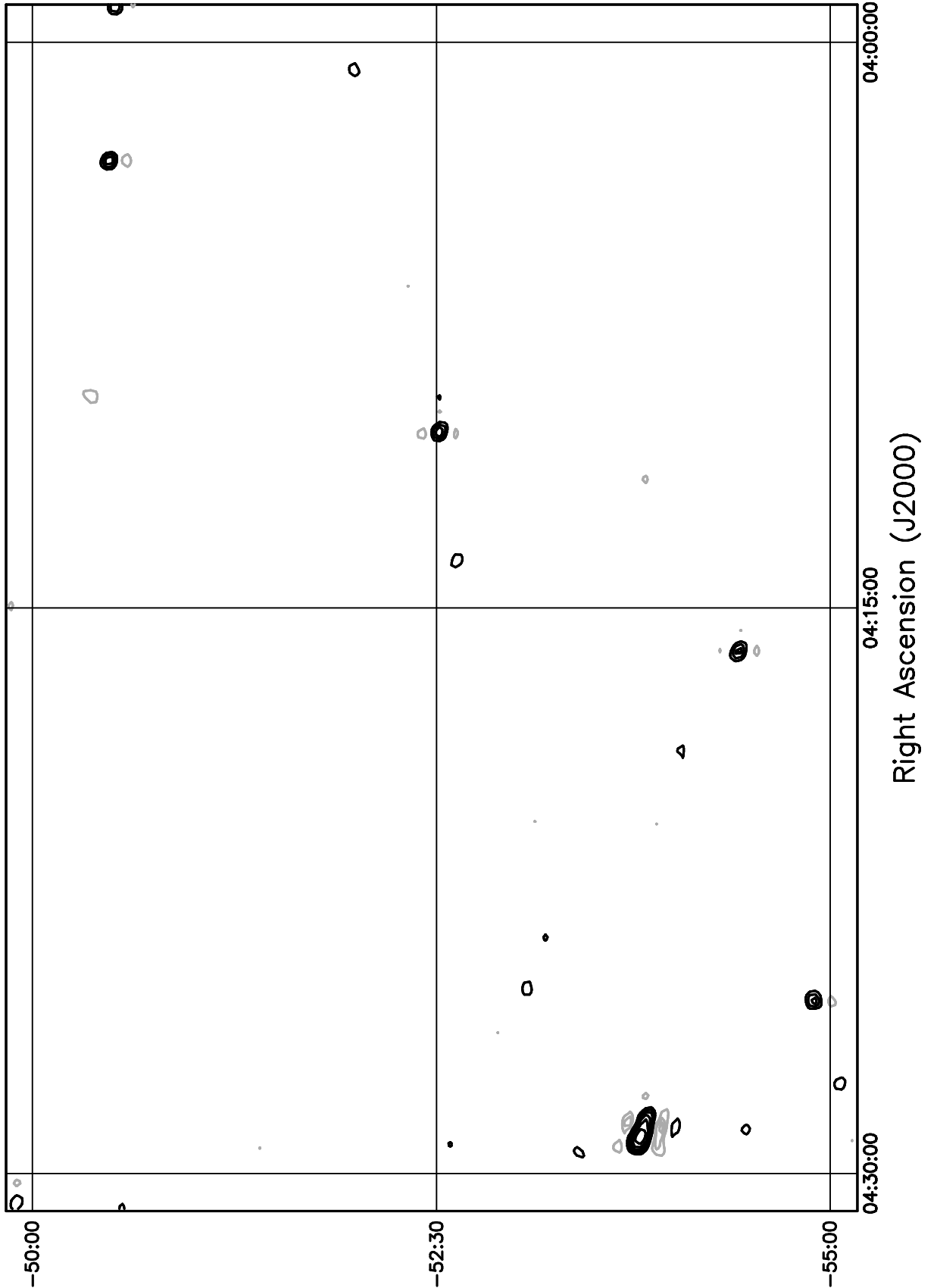
Figure 5.157: Contour plot for the range $04^h00^m \leq RA \leq 04^h30^m$, $-50° \leq \delta \leq -45°$. Contour levels are -7.56, -5.4, -3.78, -2.7, -1.62, 1.62, 2.7, 3.78, 5.4, 7.56, 10.8, 15.12, 21.6, 30.24, 43.2, 59.4, 81, 108, 151.2, 205.2, 270, 324, 378, 432 Jy beam^{-1}.
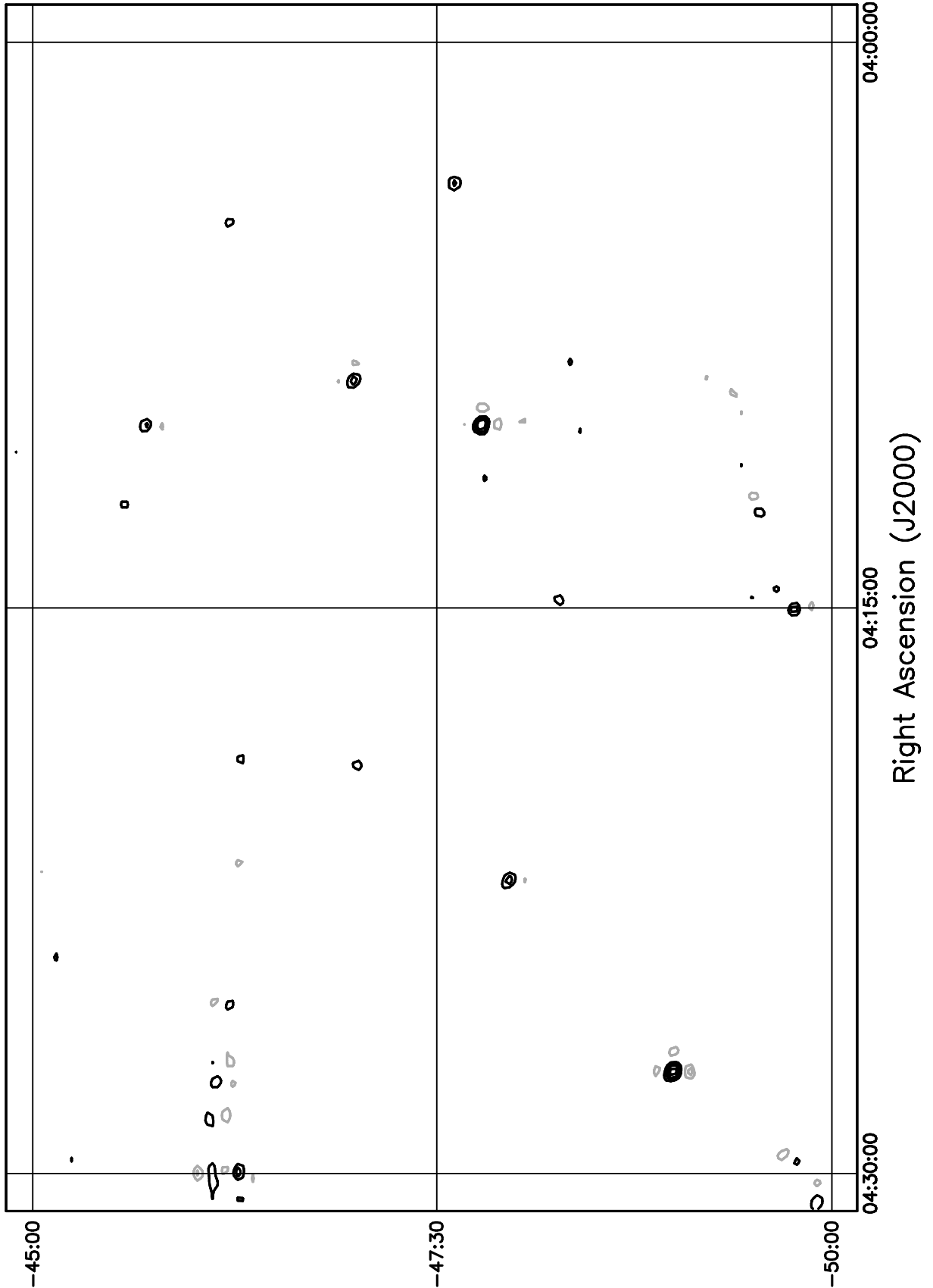
Figure 5.158: Contour plot for the range $04^h00^m \leq RA \leq 04^h30^m$, $-45° \leq \delta \leq -40°$. Contour levels are -7.56, -5.4, -3.78, -2.7, -1.62, 1.62, 2.7, 3.78, 5.4, 7.56, 10.8, 15.12, 21.6, 30.24, 43.2, 59.4, 81, 108, 151.2, 205.2, 270, 324, 378, 432 Jy beam^{-1}.
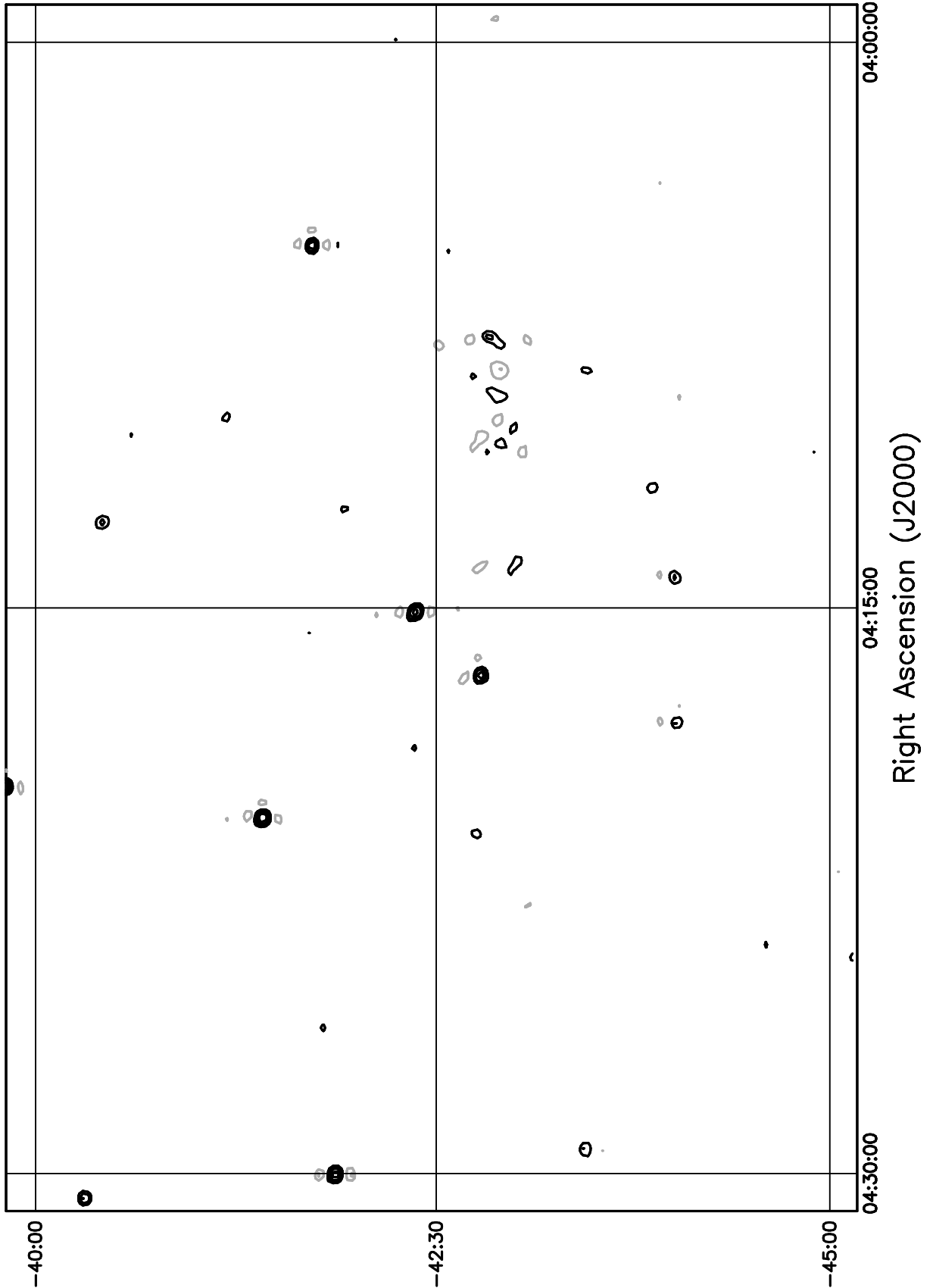
Figure 5.159: Contour plot for the range $04^h00^m \leq RA \leq 04^h30^m$, $-40° \leq \delta \leq -35°$. Contour levels are -7.56, -5.4, -3.78, -2.7, -1.62, 1.62, 2.7, 3.78, 5.4, 7.56, 10.8, 15.12, 21.6, 30.24, 43.2, 59.4, 81, 108, 151.2, 205.2, 270, 324, 378, 432 Jy beam^{-1}.
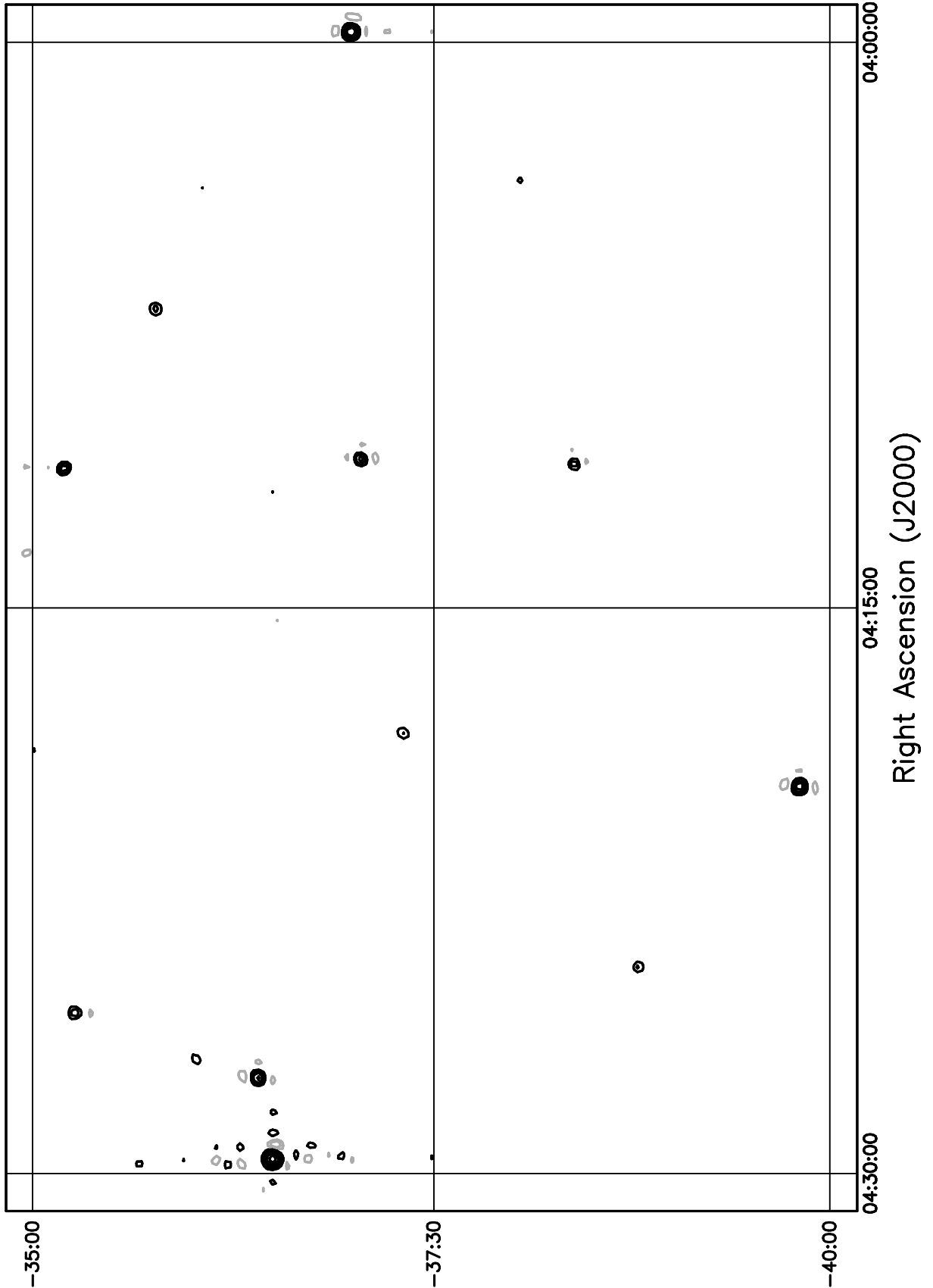
Figure 5.160: Contour plot for the range $04^h00^m \leq RA \leq 04^h30^m$, $-35° \leq \delta \leq -30°$. Contour levels are -7.56, -5.4, -3.78, -2.7, -1.62, 1.62, 2.7, 3.78, 5.4, 7.56, 10.8, 15.12, 21.6, 30.24, 43.2, 59.4, 81, 108, 151.2, 205.2, 270, 324, 378, 432 Jy beam^{-1}.
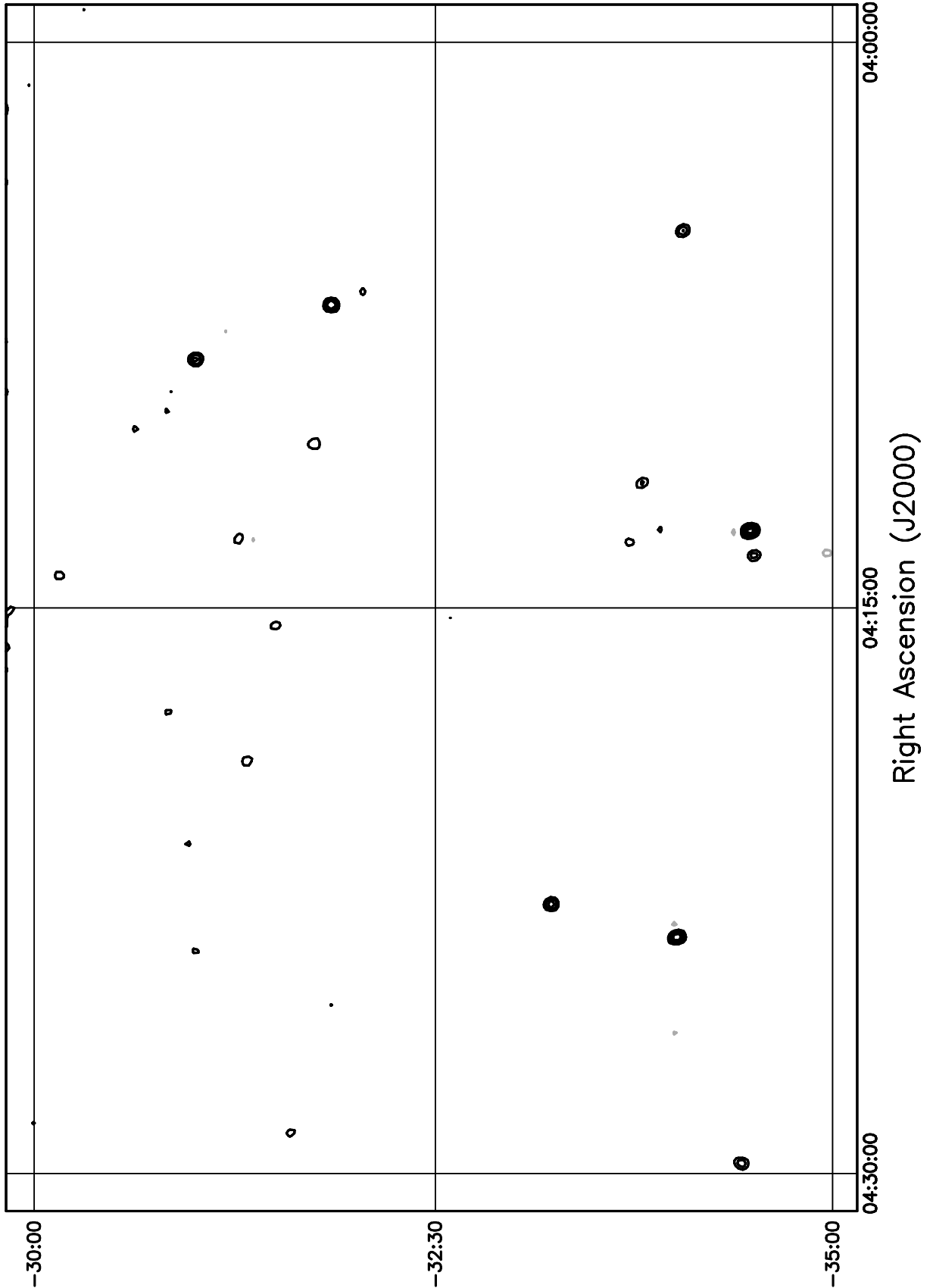
Figure 5.161: Contour plot for the range $04^h00^m \leq RA \leq 04^h30^m$, $-30° \leq \delta \leq -25°$. Contour levels are -7.56, -5.4, -3.78, -2.7, -1.62, 1.62, 2.7, 3.78, 5.4, 7.56, 10.8, 15.12, 21.6, 30.24, 43.2, 59.4, 81, 108, 151.2, 205.2, 270, 324, 378, 432 Jy beam^{-1}.
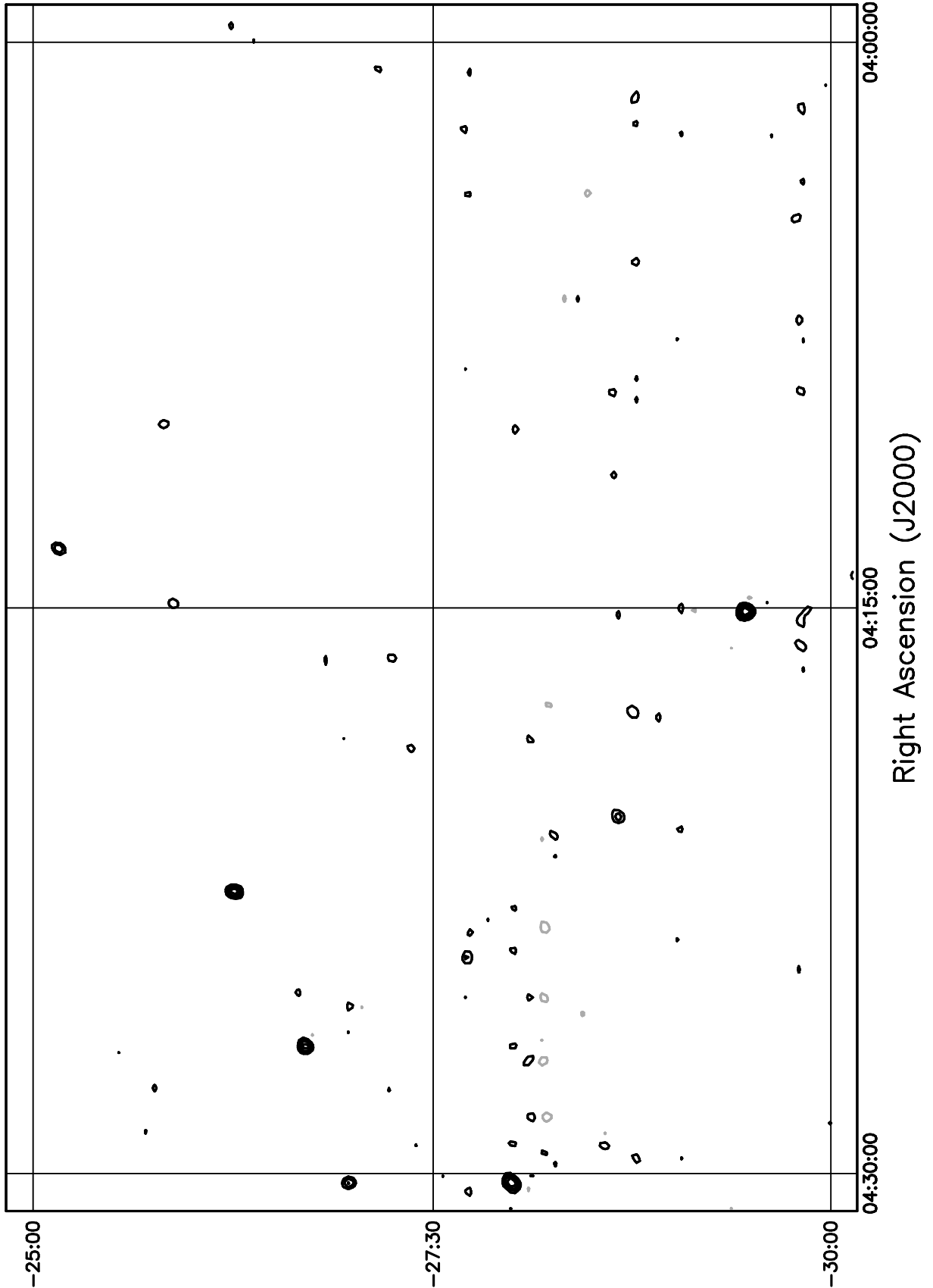
Figure 5.162: Contour plot for the range $04^h00^m \leq RA \leq 04^h30^m$, $-25° \leq \delta \leq -20°$. Contour levels are -7.56, -5.4, -3.78, -2.7, -1.62, 1.62, 2.7, 3.78, 5.4, 7.56, 10.8, 15.12, 21.6, 30.24, 43.2, 59.4, 81, 108, 151.2, 205.2, 270, 324, 378, 432 Jy beam^{-1}.
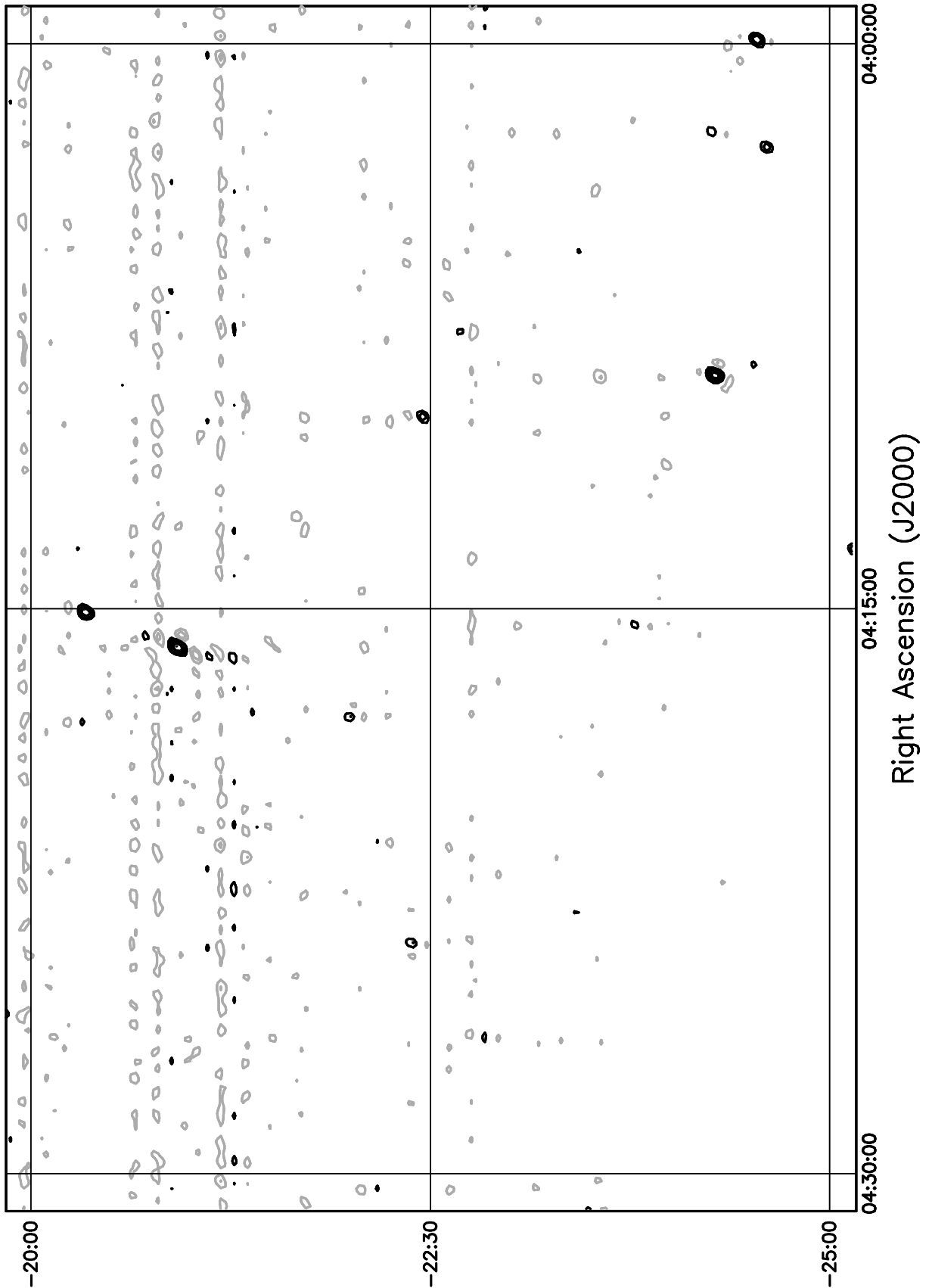
Figure 5.163: Contour plot for the range $04^h00^m \leq RA \leq 04^h30^m$, $-20° \leq \delta \leq -15°$. Contour levels are -7.56, -5.4, -3.78, -2.7, -1.62, 1.62, 2.7, 3.78, 5.4, 7.56, 10.8, 15.12, 21.6, 30.24, 43.2, 59.4, 81, 108, 151.2, 205.2, 270, 324, 378, 432 Jy beam^{-1}.
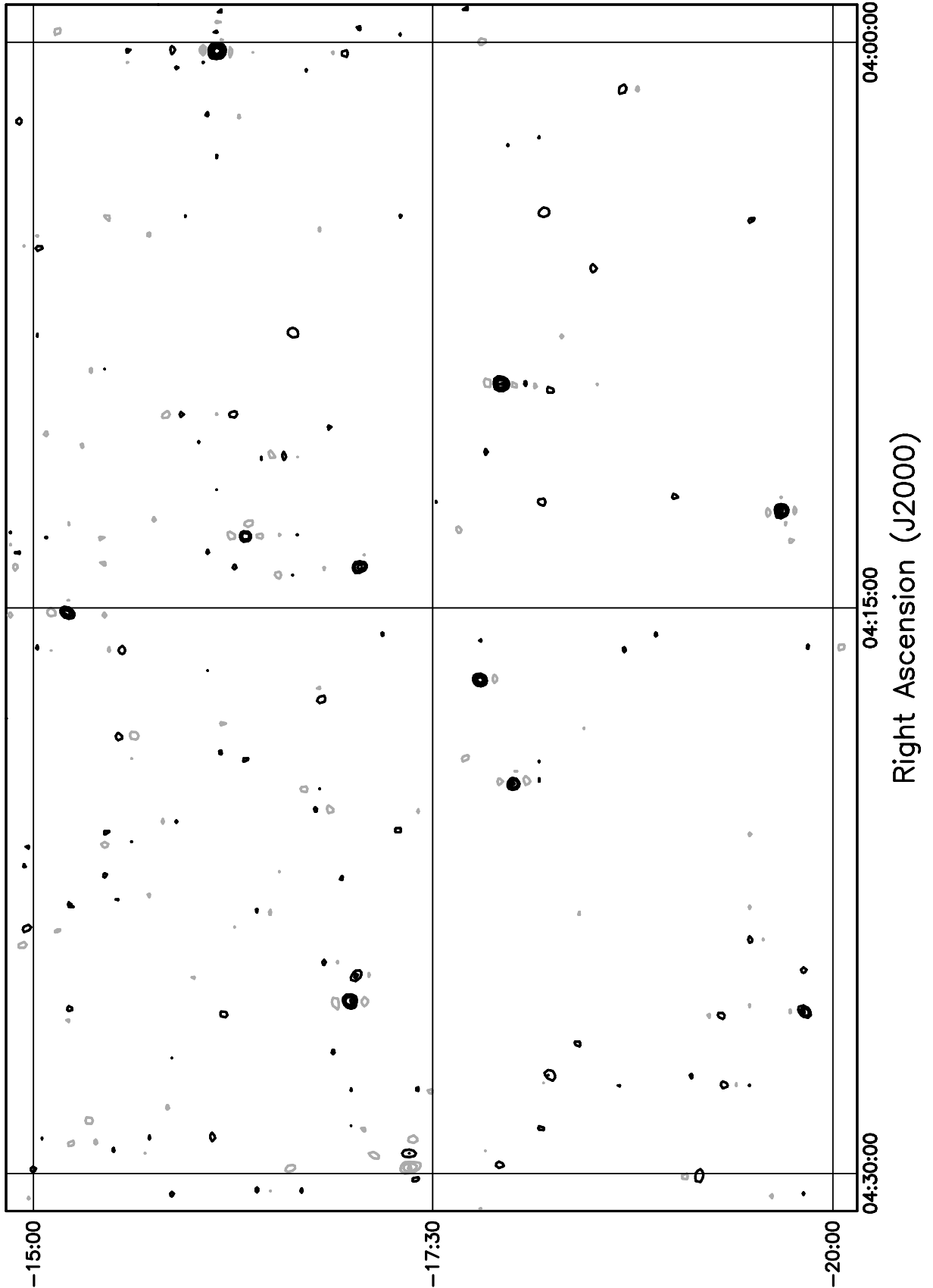
Figure 5.164: Contour plot for the range $04^h00^m \leq RA \leq 04^h30^m$, $-15° \leq \delta \leq -10°$. Contour levels are -7.56, -5.4, -3.78, -2.7, -1.62, 1.62, 2.7, 3.78, 5.4, 7.56, 10.8, 15.12, 21.6, 30.24, 43.2, 59.4, 81, 108, 151.2, 205.2, 270, 324, 378, 432 Jy beam^{-1}.
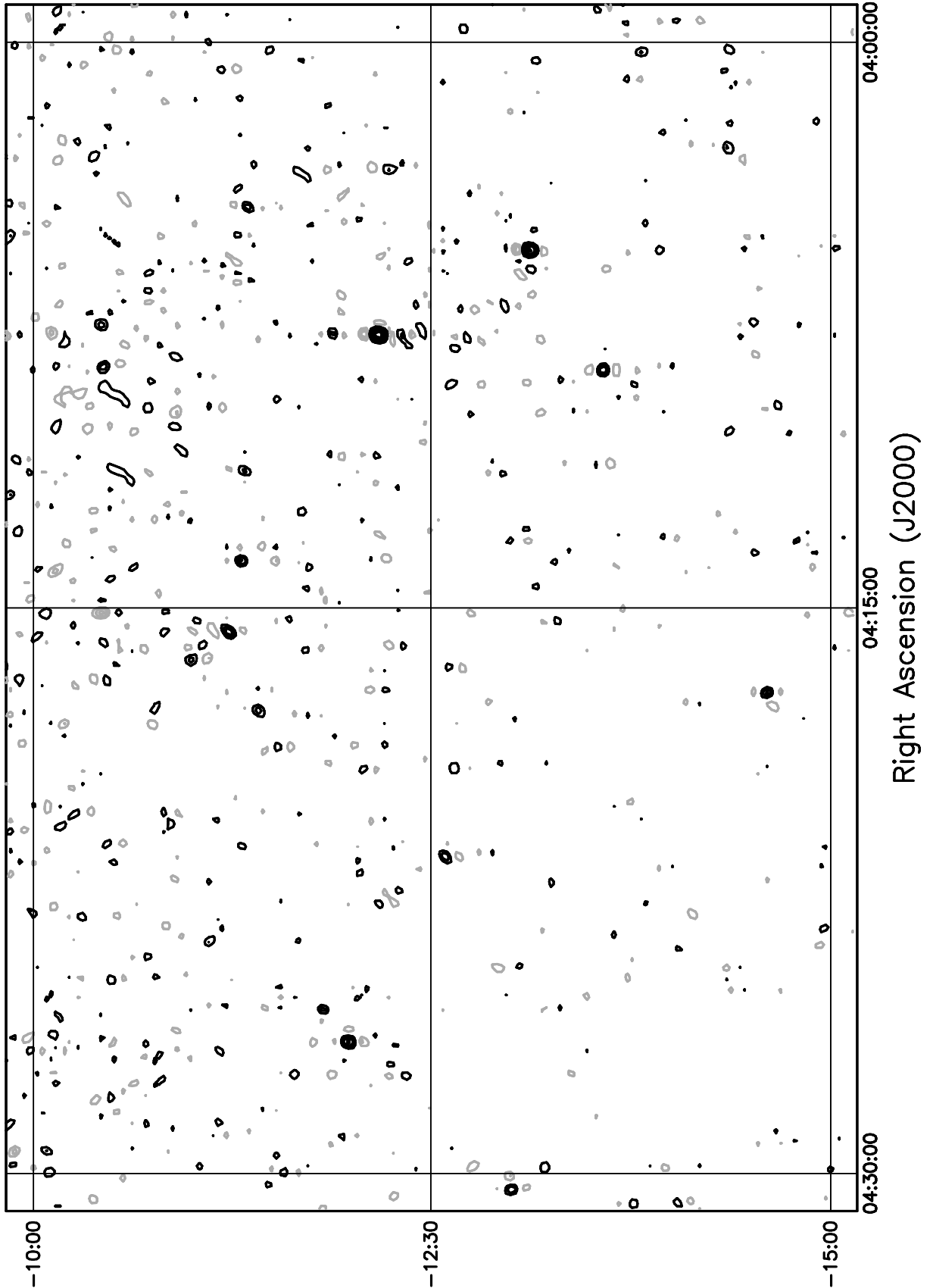
Figure 5.165: Contour plot for the range $04^h30^m \leq RA \leq 05^h00^m$, $-75° \leq \delta \leq -70°$. Contour levels are -7.56, -5.4, -3.78, -2.7, -1.62, 1.62, 2.7, 3.78, 5.4, 7.56, 10.8, 15.12, 21.6, 30.24, 43.2, 59.4, 81, 108, 151.2, 205.2, 270, 324, 378, 432 Jy beam^{-1}.
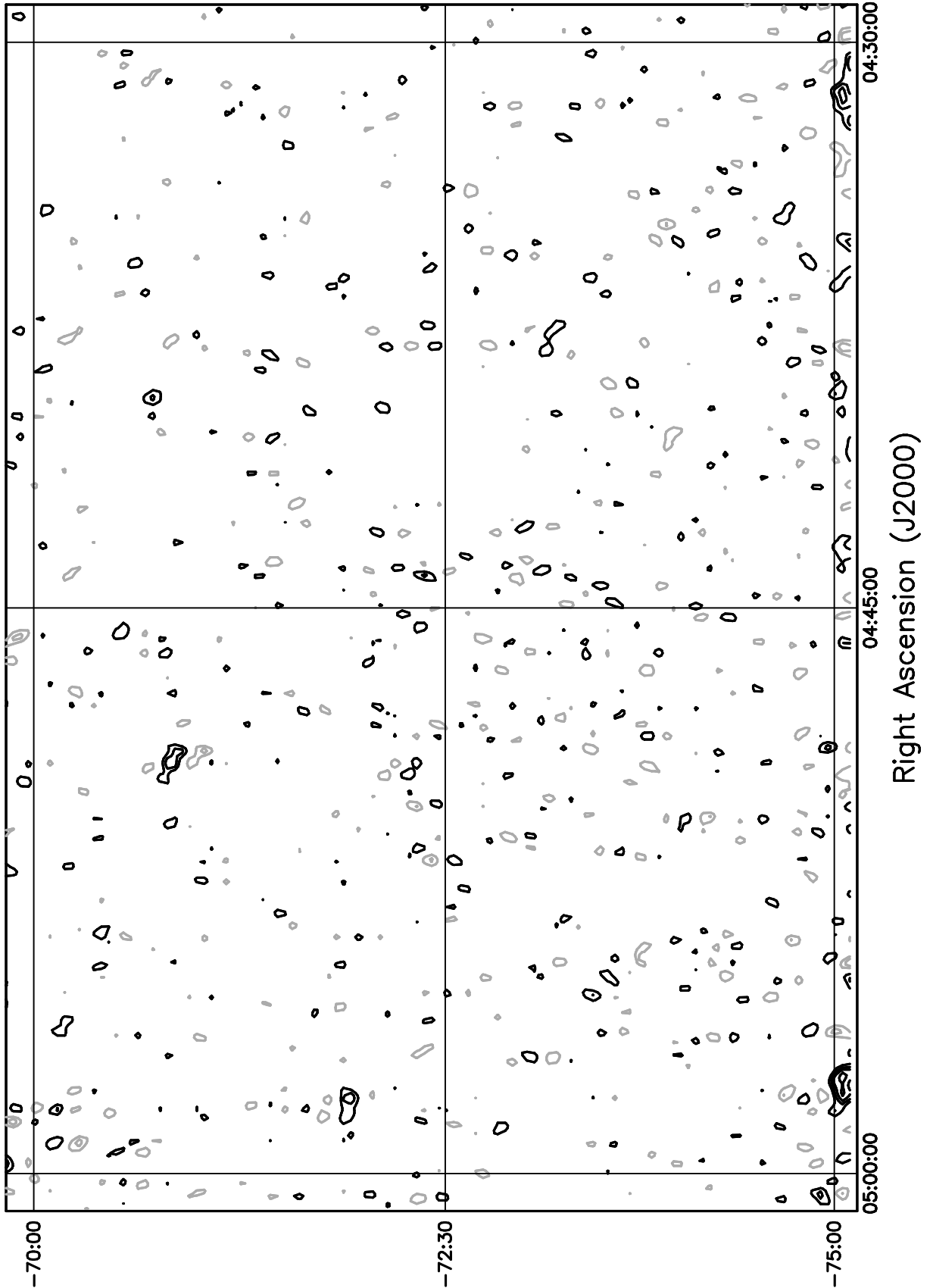
Figure 5.166: Contour plot for the range $04^h30^m \leq RA \leq 05^h00^m$, $-70° \leq \delta \leq -65°$. Contour levels are -7.56, -5.4, -3.78, -2.7, -1.62, 1.62, 2.7, 3.78, 5.4, 7.56, 10.8, 15.12, 21.6, 30.24, 43.2, 59.4, 81, 108, 151.2, 205.2, 270, 324, 378, 432 Jy beam^{-1}.
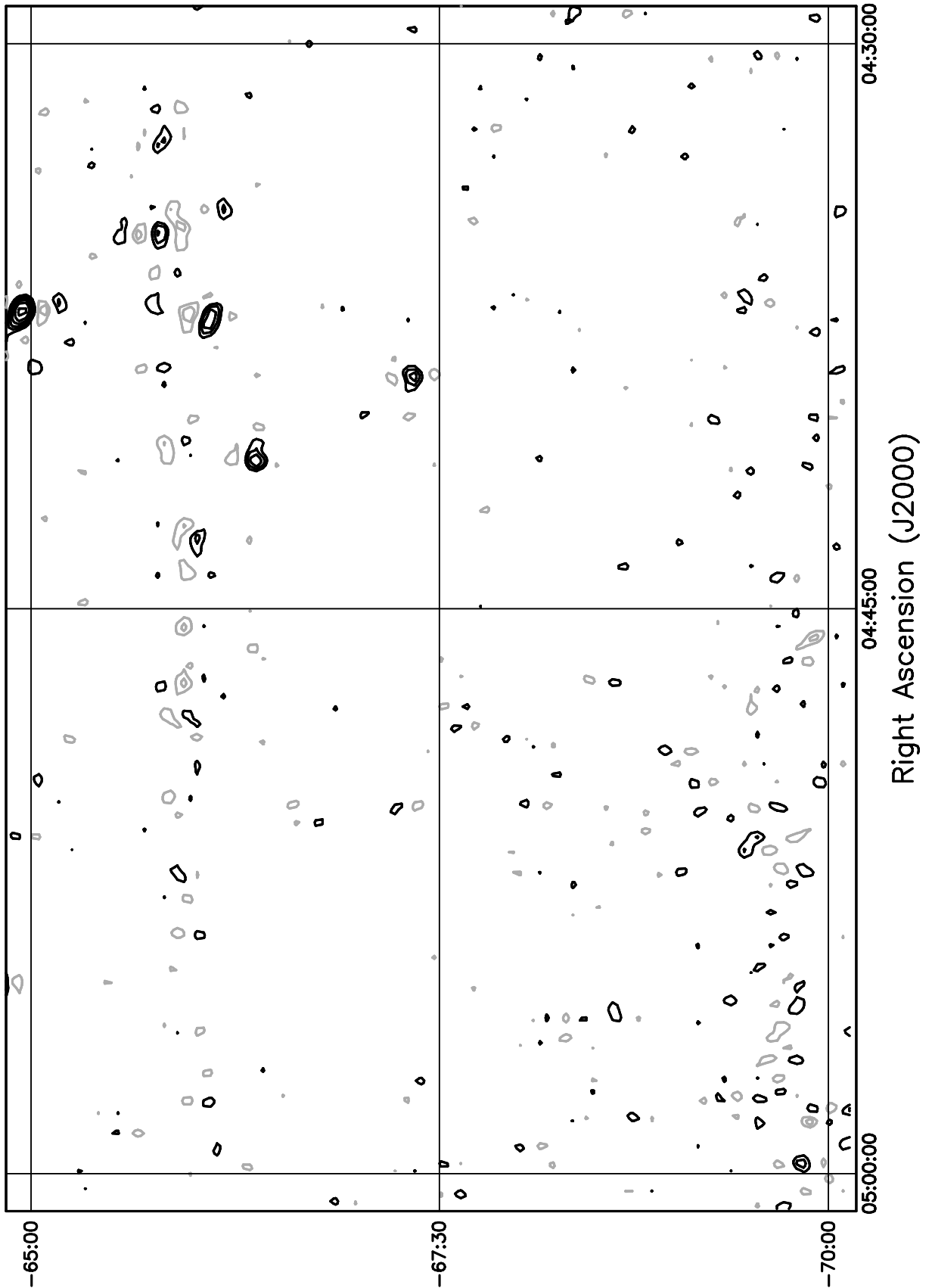
Figure 5.167: Contour plot for the range $04^h30^m \leq RA \leq 05^h00^m$, $-65° \leq \delta \leq -60°$. Contour levels are -7.56, -5.4, -3.78, -2.7, -1.62, 1.62, 2.7, 3.78, 5.4, 7.56, 10.8, 15.12, 21.6, 30.24, 43.2, 59.4, 81, 108, 151.2, 205.2, 270, 324, 378, 432 Jy beam^{-1}.
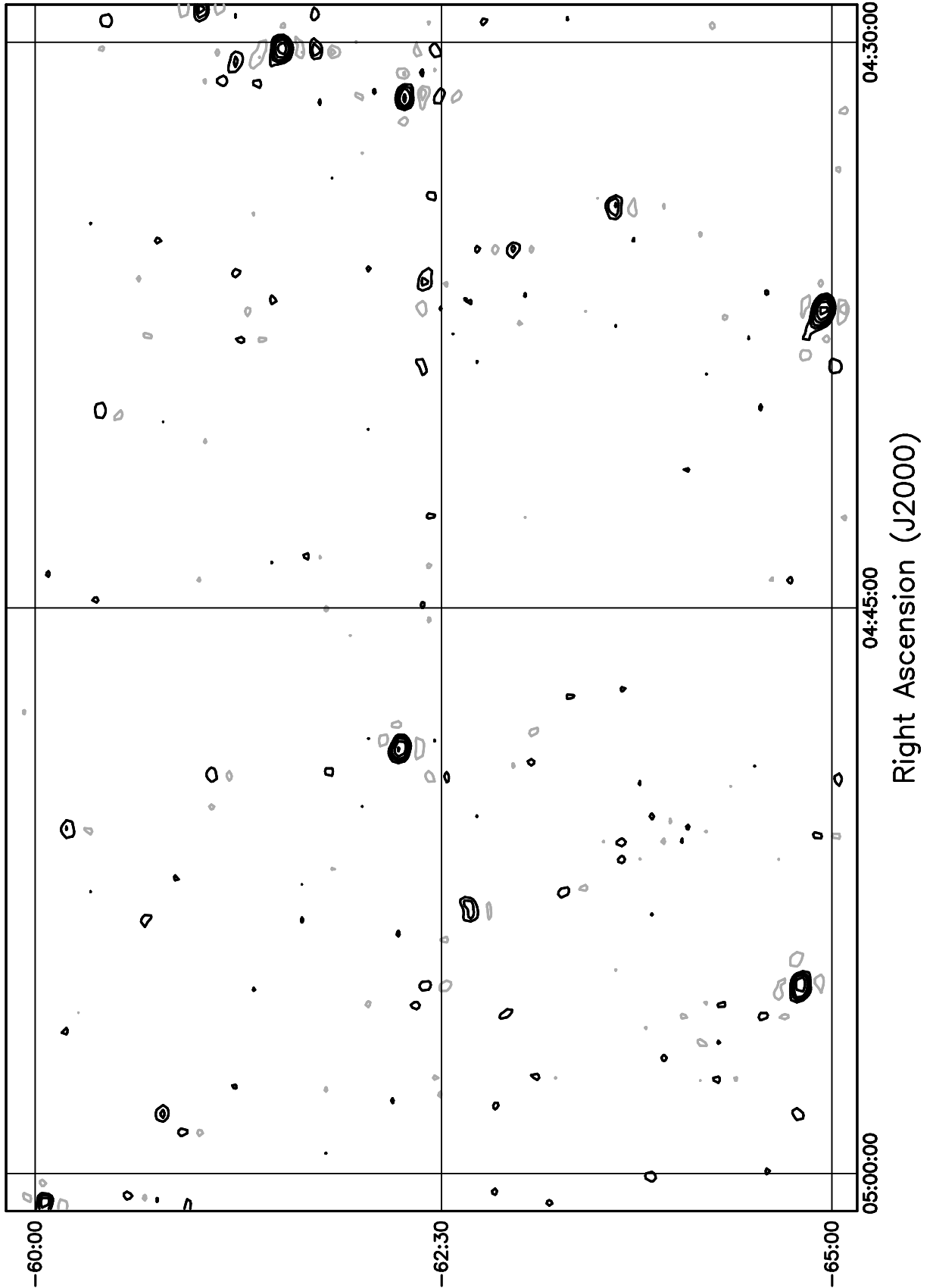
Figure 5.168: Contour plot for the range $04^h30^m \leq RA \leq 05^h00^m$, $-60° \leq \delta \leq -55°$. Contour levels are -7.56, -5.4, -3.78, -2.7, -1.62, 1.62, 2.7, 3.78, 5.4, 7.56, 10.8, 15.12, 21.6, 30.24, 43.2, 59.4, 81, 108, 151.2, 205.2, 270, 324, 378, 432 Jy beam^{-1}.
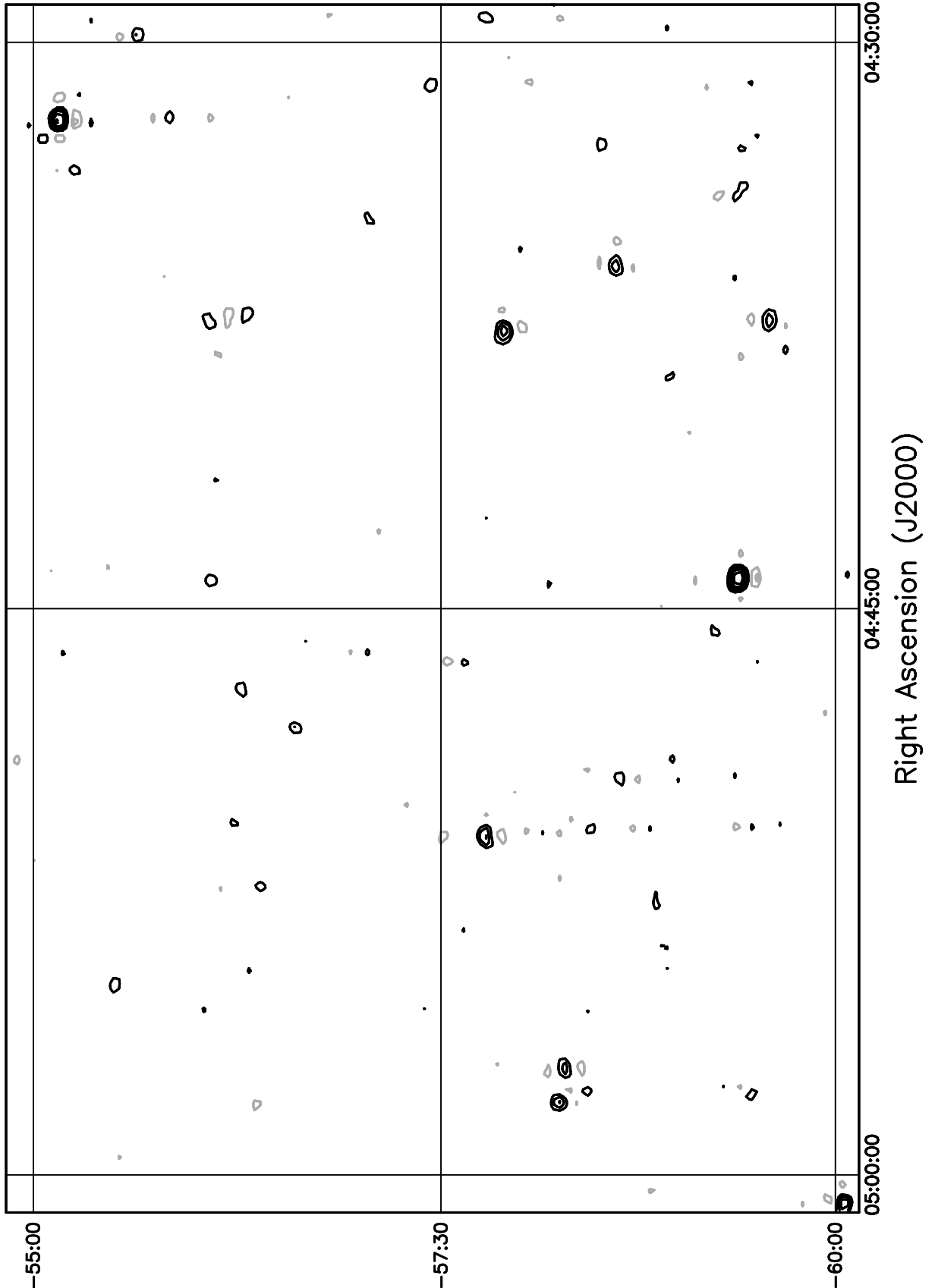
Figure 5.169: Contour plot for the range $04^h30^m \leq RA \leq 05^h00^m$, $-55° \leq \delta \leq -50°$. Contour levels are -7.56, -5.4, -3.78, -2.7, -1.62, 1.62, 2.7, 3.78, 5.4, 7.56, 10.8, 15.12, 21.6, 30.24, 43.2, 59.4, 81, 108, 151.2, 205.2, 270, 324, 378, 432 Jy beam^{-1}.
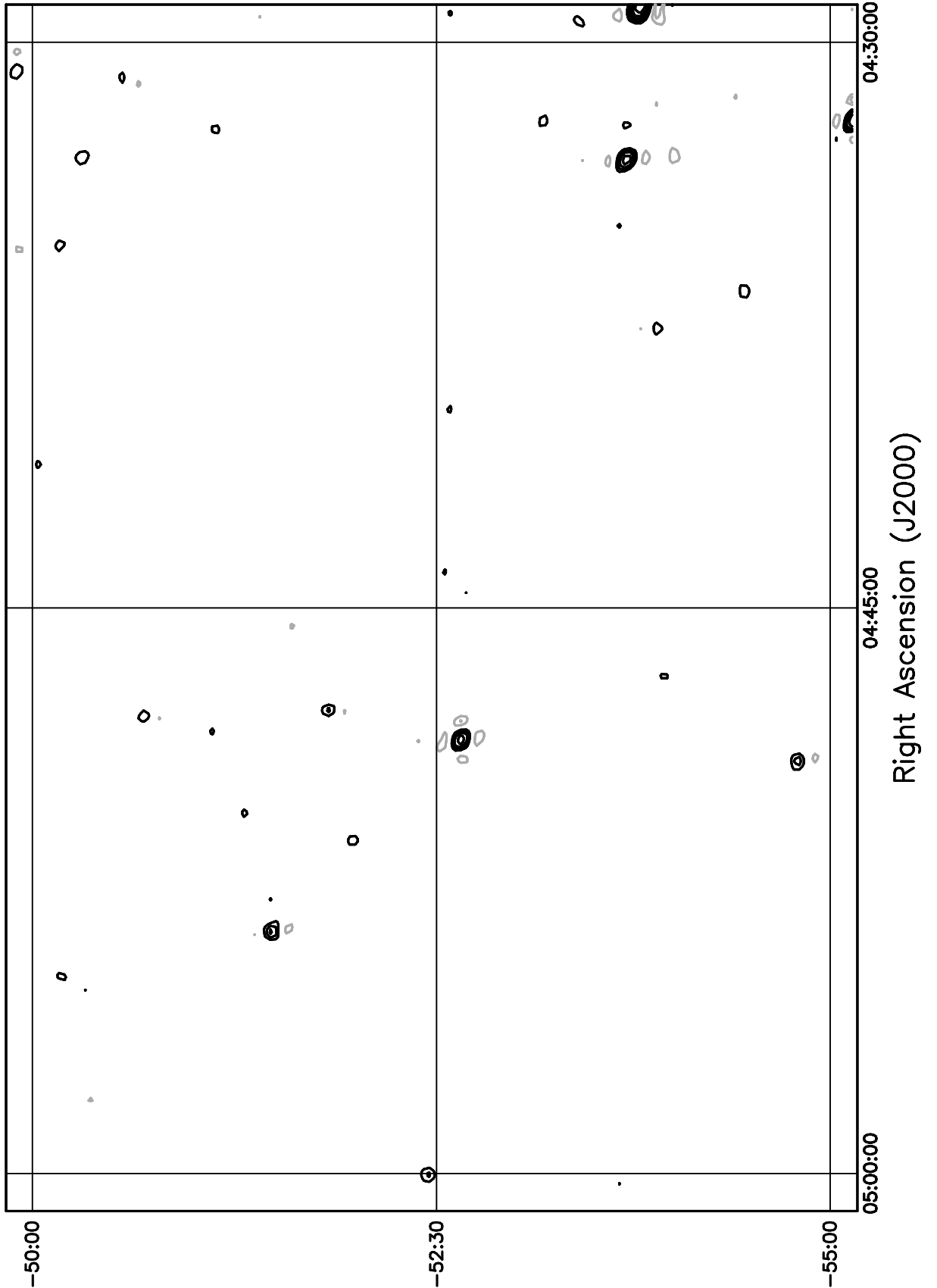
Figure 5.170: Contour plot for the range $04^h30^m \leq RA \leq 05^h00^m$, $-50° \leq \delta \leq -45°$. Contour levels are -7.56, -5.4, -3.78, -2.7, -1.62, 1.62, 2.7, 3.78, 5.4, 7.56, 10.8, 15.12, 21.6, 30.24, 43.2, 59.4, 81, 108, 151.2, 205.2, 270, 324, 378, 432 Jy beam^{-1}.
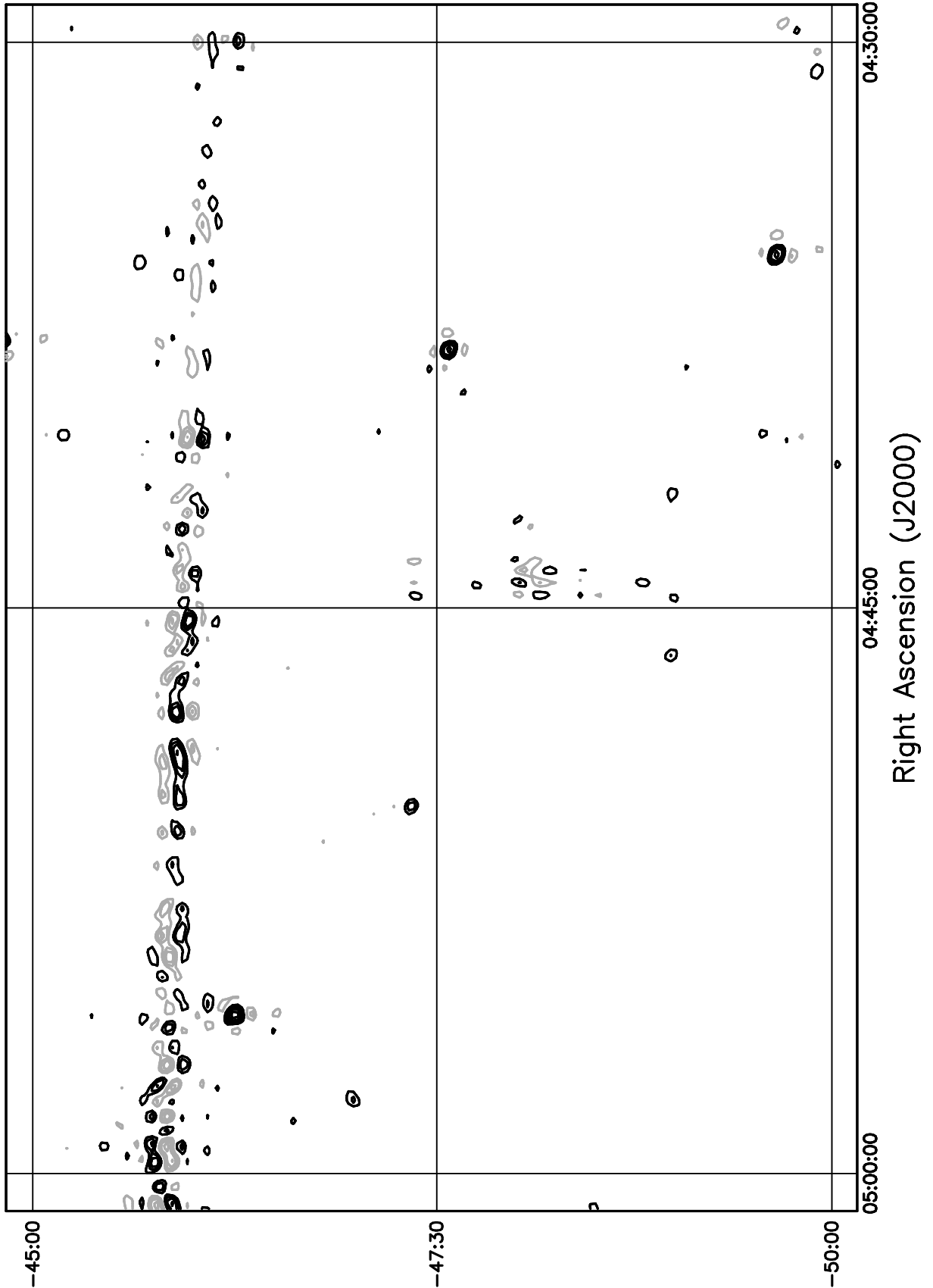
Figure 5.171: Contour plot for the range $04^h30^m \leq RA \leq 05^h00^m$, $-45° \leq \delta \leq -40°$. Contour levels are -7.56, -5.4, -3.78, -2.7, -1.62, 1.62, 2.7, 3.78, 5.4, 7.56, 10.8, 15.12, 21.6, 30.24, 43.2, 59.4, 81, 108, 151.2, 205.2, 270, 324, 378, 432 Jy beam^{-1}.
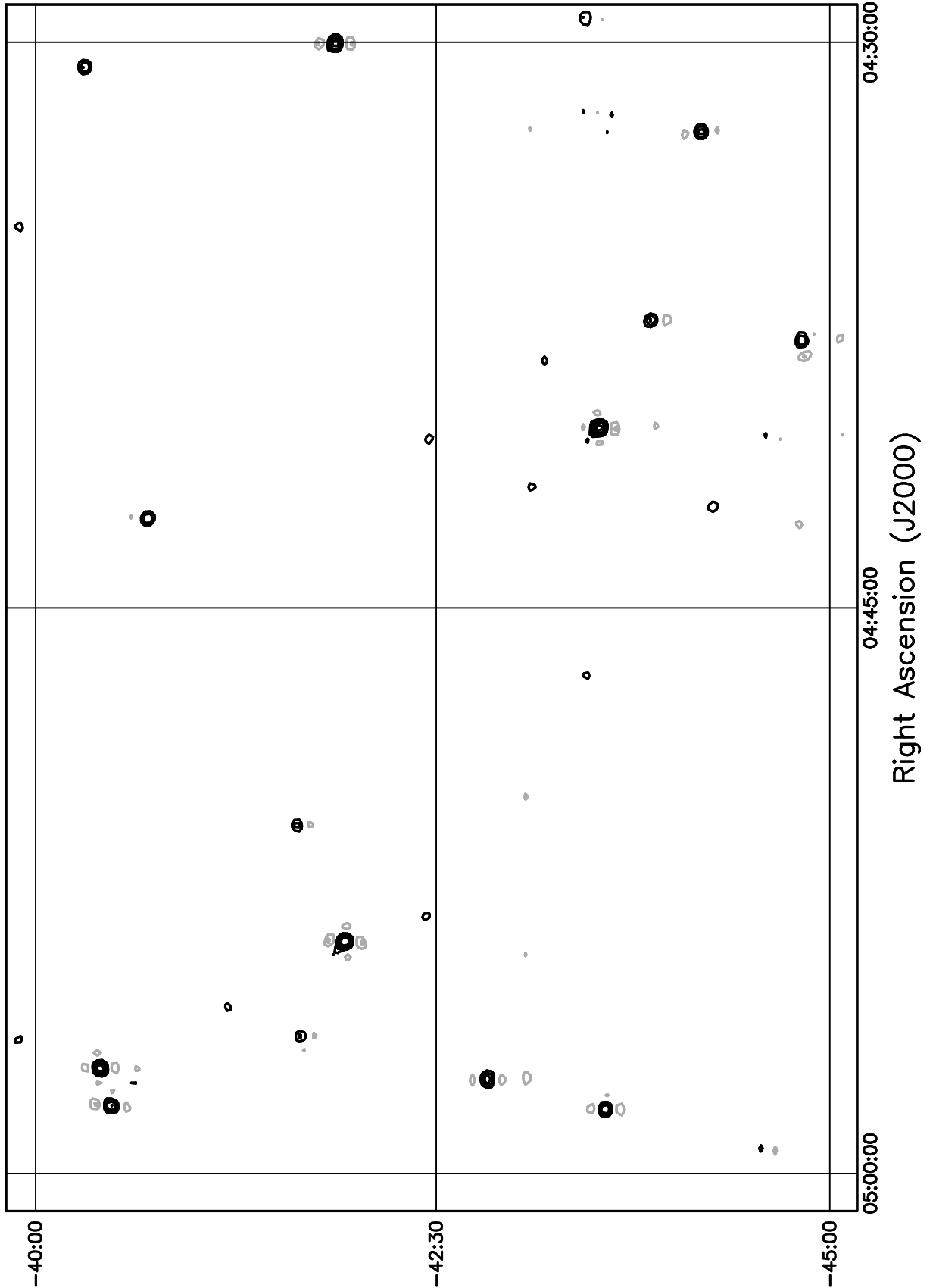
Figure 5.172: Contour plot for the range $04^h30^m \leq RA \leq 05^h00^m$, $-40° \leq \delta \leq -35°$. Contour levels are -7.56, -5.4, -3.78, -2.7, -1.62, 1.62, 2.7, 3.78, 5.4, 7.56, 10.8, 15.12, 21.6, 30.24, 43.2, 59.4, 81, 108, 151.2, 205.2, 270, 324, 378, 432 Jy beam^{-1}.
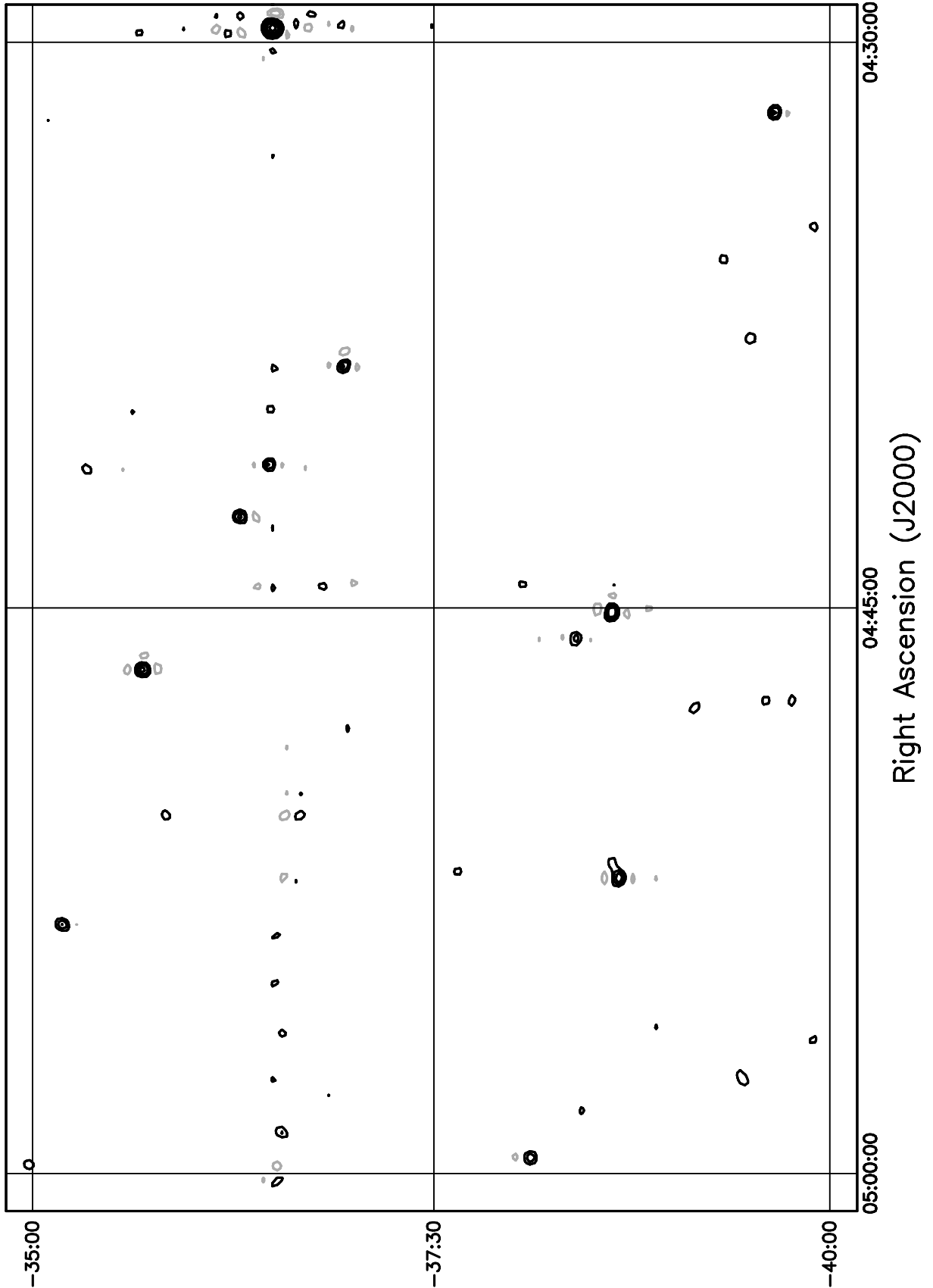
Figure 5.173: Contour plot for the range $04^h30^m \leq RA \leq 05^h00^m$, $-35° \leq \delta \leq -30°$. Contour levels are -7.56, -5.4, -3.78, -2.7, -1.62, 1.62, 2.7, 3.78, 5.4, 7.56, 10.8, 15.12, 21.6, 30.24, 43.2, 59.4, 81, 108, 151.2, 205.2, 270, 324, 378, 432 Jy beam^{-1}.
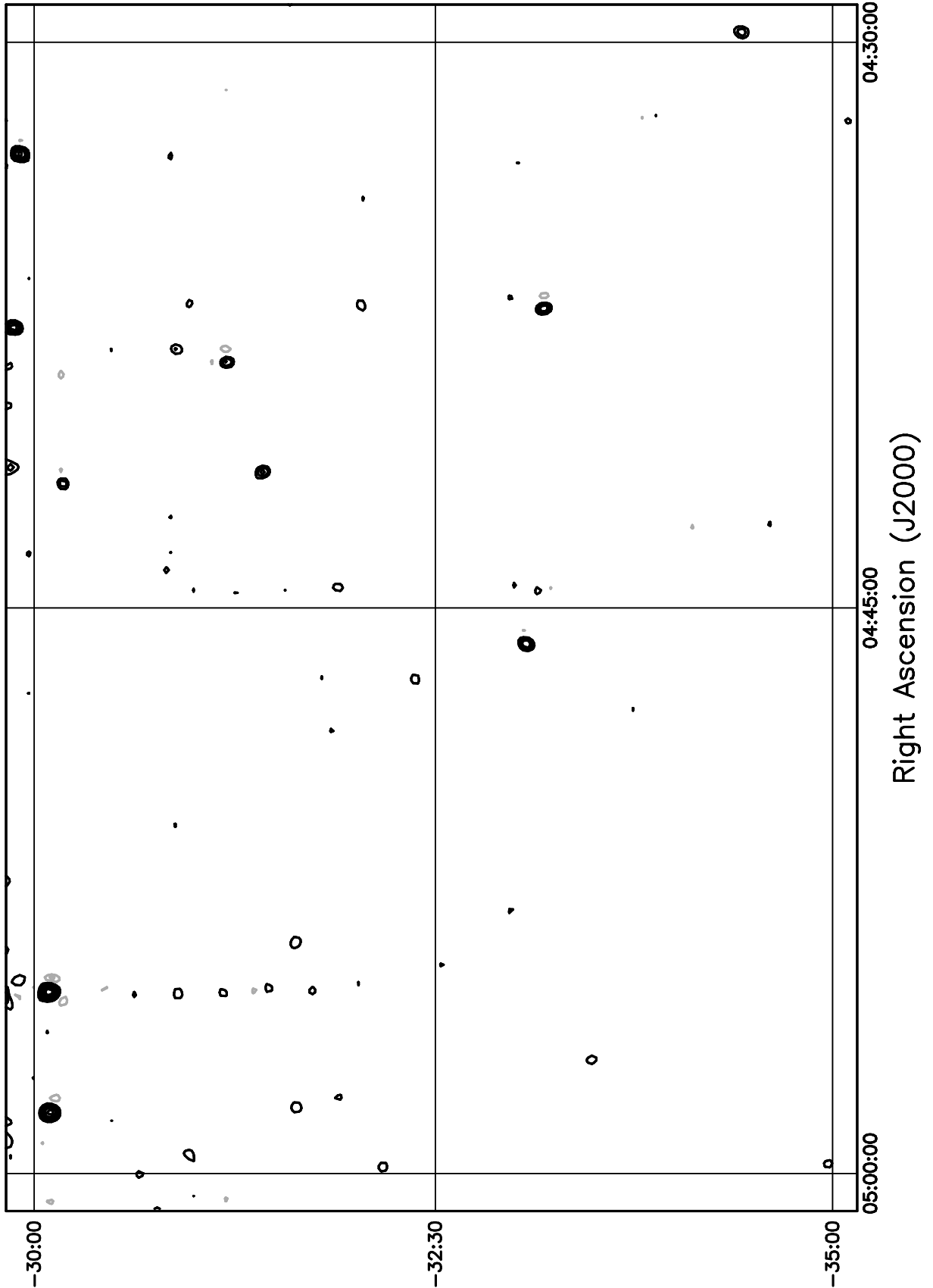
Figure 5.174: Contour plot for the range $04^h30^m \leq RA \leq 05^h00^m$, $-30° \leq \delta \leq -25°$. Contour levels are -7.56, -5.4, -3.78, -2.7, -1.62, 1.62, 2.7, 3.78, 5.4, 7.56, 10.8, 15.12, 21.6, 30.24, 43.2, 59.4, 81, 108, 151.2, 205.2, 270, 324, 378, 432 Jy beam^{-1}.
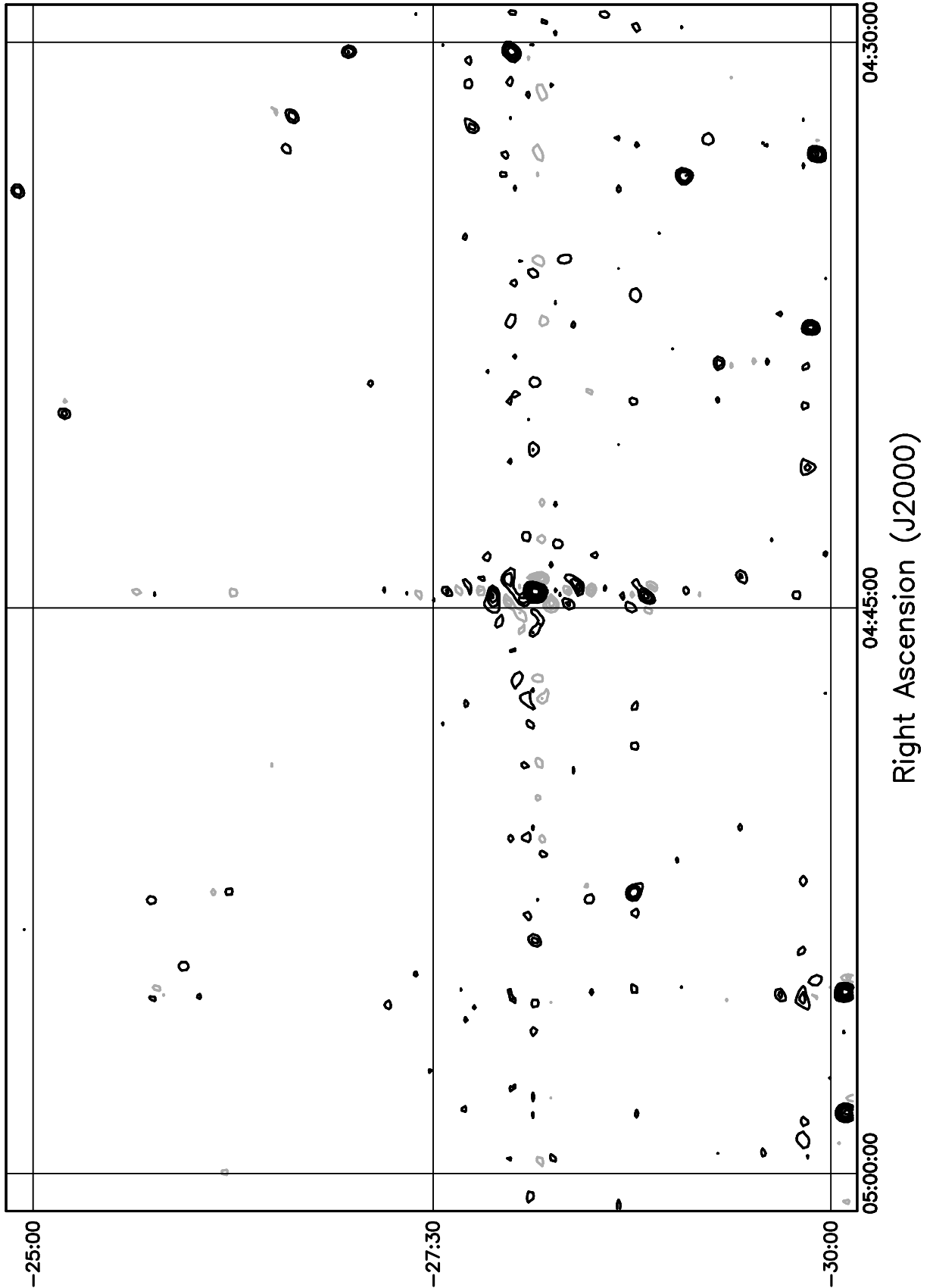
Figure 5.175: Contour plot for the range $04^h30^m \leq RA \leq 05^h00^m$, $-25° \leq \delta \leq -20°$. Contour levels are -7.56, -5.4, -3.78, -2.7, -1.62, 1.62, 2.7, 3.78, 5.4, 7.56, 10.8, 15.12, 21.6, 30.24, 43.2, 59.4, 81, 108, 151.2, 205.2, 270, 324, 378, 432 Jy beam^{-1}.
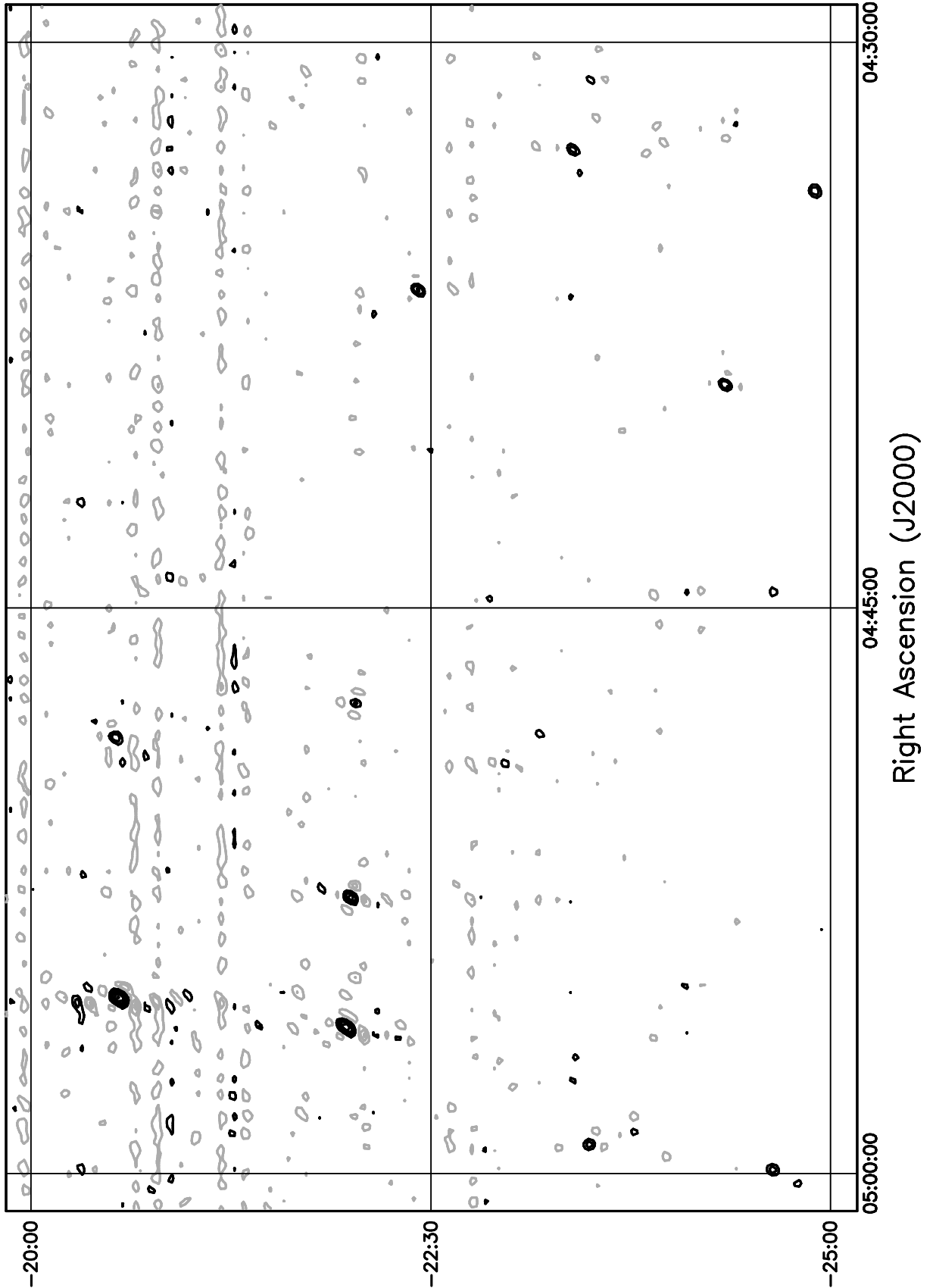
Figure 5.176: Contour plot for the range $04^h30^m \leq RA \leq 05^h00^m$, $-20° \leq \delta \leq -15°$. Contour levels are -7.56, -5.4, -3.78, -2.7, -1.62, 1.62, 2.7, 3.78, 5.4, 7.56, 10.8, 15.12, 21.6, 30.24, 43.2, 59.4, 81, 108, 151.2, 205.2, 270, 324, 378, 432 Jy beam^{-1}.
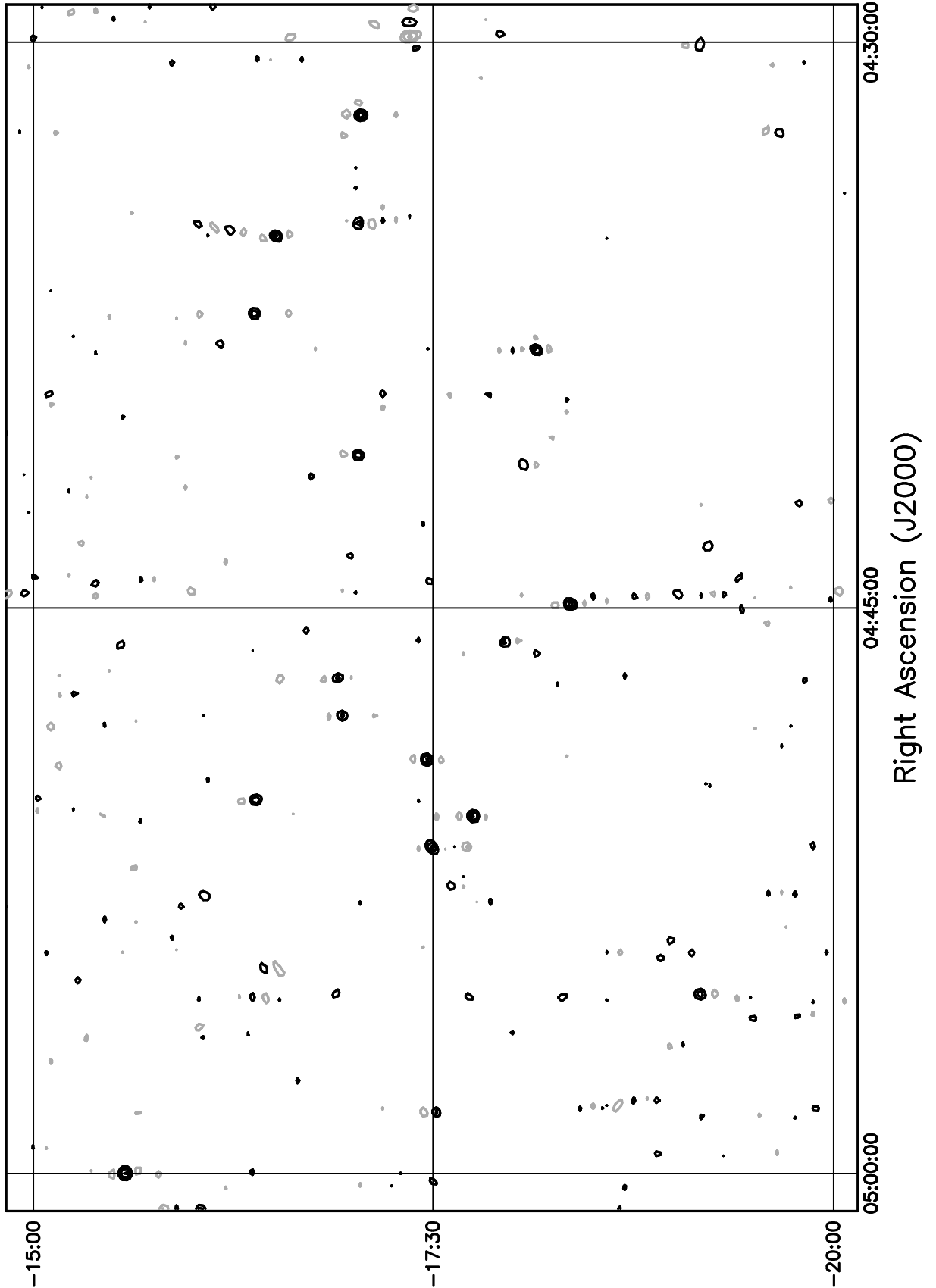
Figure 5.177: Contour plot for the range $04^h 30^m \leq RA \leq 05^h 00^m$, $-15° \leq \delta \leq -10°$. Contour levels are -7.56, -5.4, -3.78, -2.7, -1.62, 1.62, 2.7, 3.78, 5.4, 7.56, 10.8, 15.12, 21.6, 30.24, 43.2, 59.4, 81, 108, 151.2, 205.2, 270, 324, 378, 432 Jy beam^{-1}.
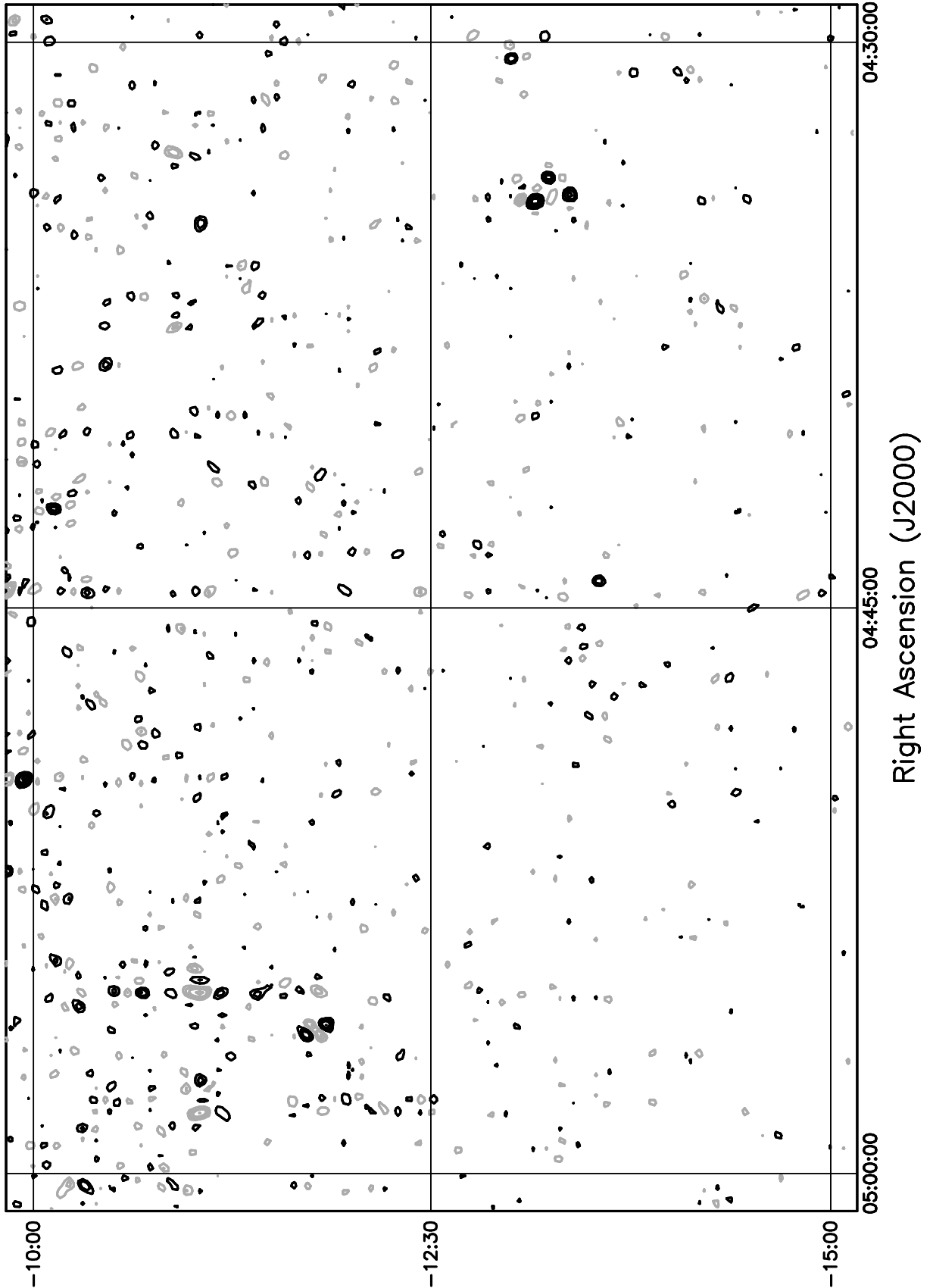
Figure 5.178: Contour plot for the range $05^h00^m \leq RA \leq 05^h30^m$, $-75° \leq \delta \leq -70°$. Contour levels are -7.56, -5.4, -3.78, -2.7, -1.62, 1.62, 2.7, 3.78, 5.4, 7.56, 10.8, 15.12, 21.6, 30.24, 43.2, 59.4, 81, 108, 151.2, 205.2, 270, 324, 378, 432 Jy beam^{-1}.
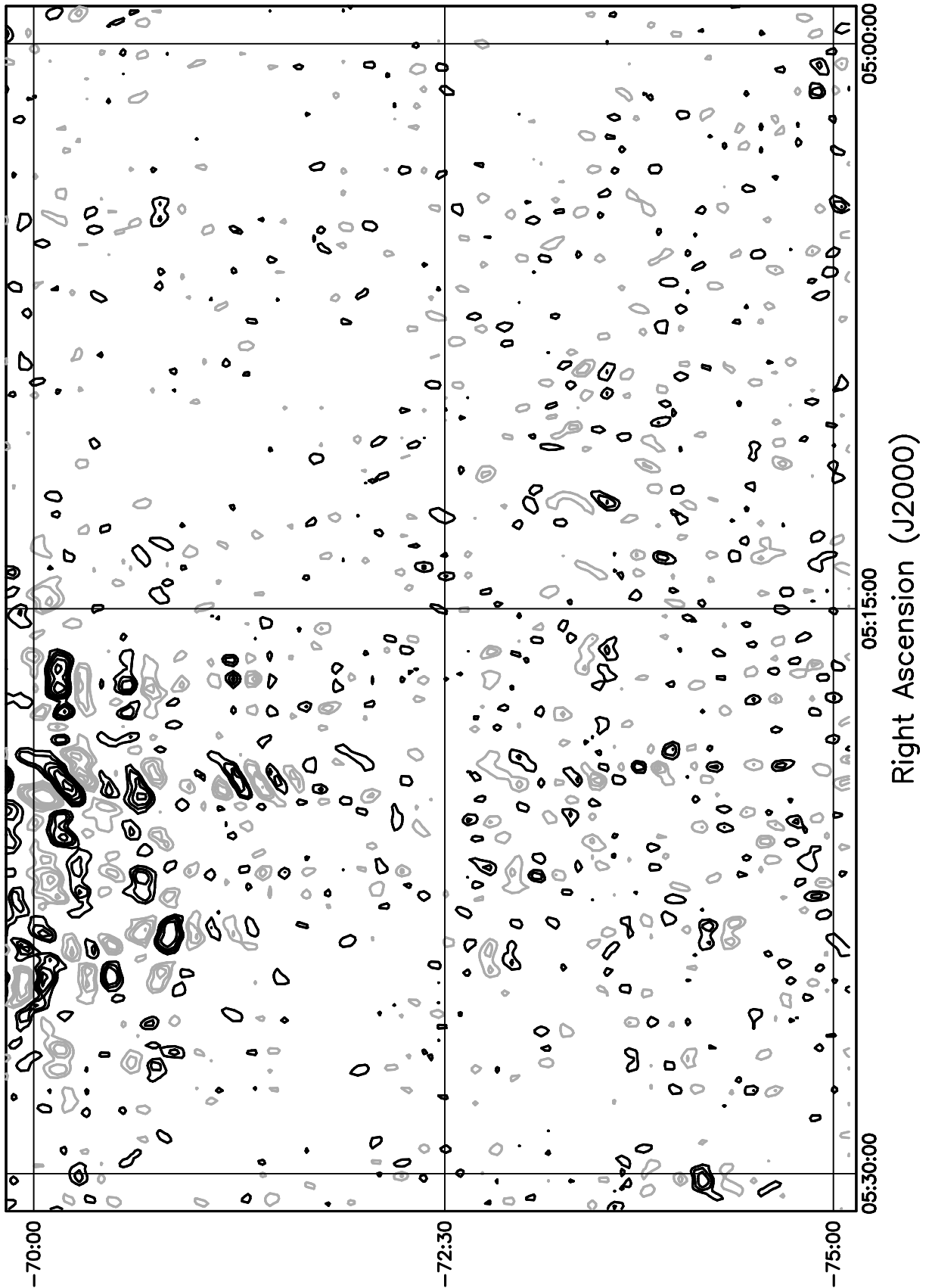
Figure 5.179: Contour plot for the range $05^h00^m \leq RA \leq 05^h30^m$, $-70° \leq \delta \leq -65°$. Contour levels are -7.56, -5.4, -3.78, -2.7, -1.62, 1.62, 2.7, 3.78, 5.4, 7.56, 10.8, 15.12, 21.6, 30.24, 43.2, 59.4, 81, 108, 151.2, 205.2, 270, 324, 378, 432 Jy beam^{-1}.
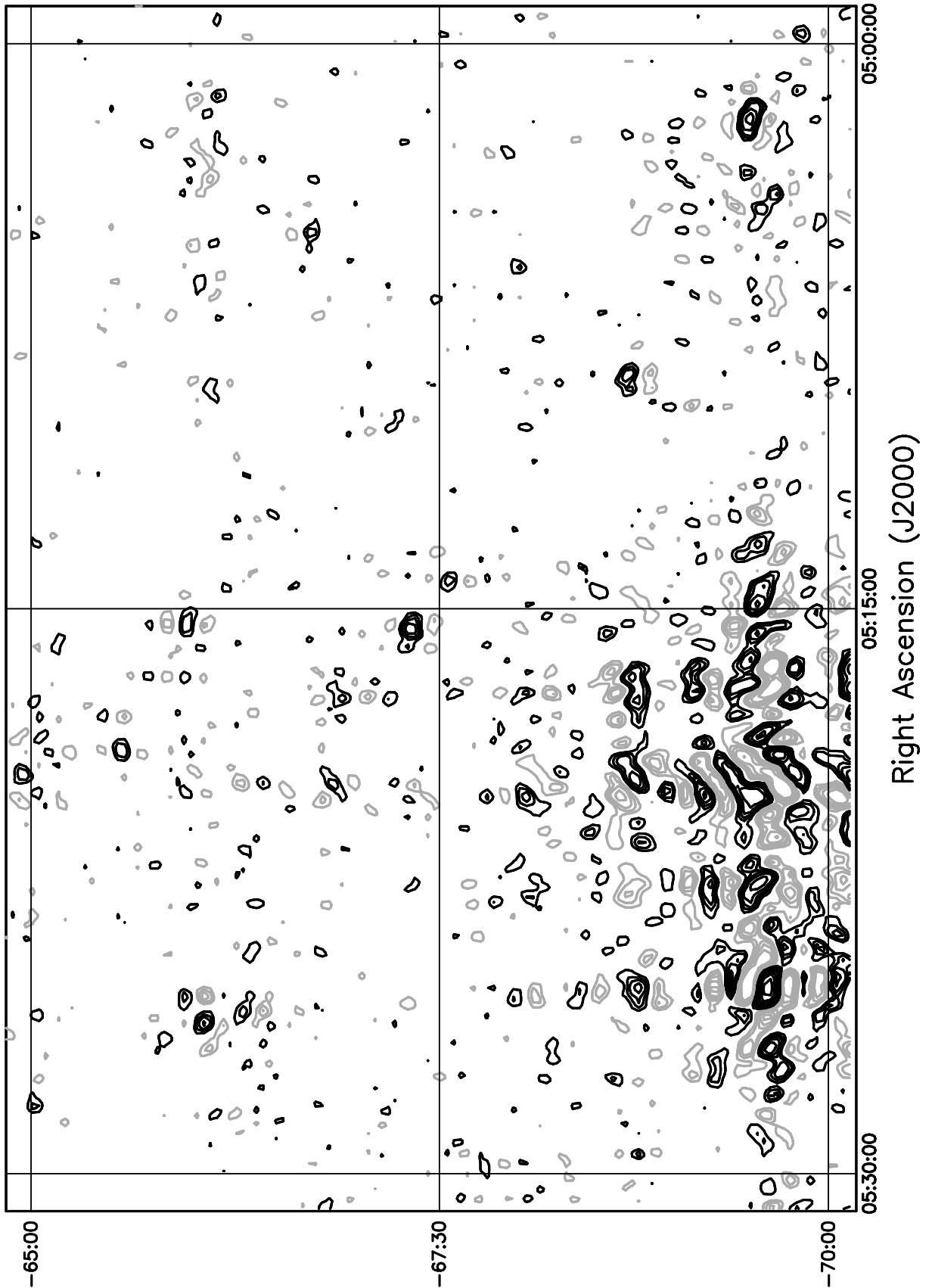
Figure 5.180: Contour plot for the range $05^h00^m \leq RA \leq 05^h30^m$, $-65° \leq \delta \leq -60°$. Contour levels are -7.56, -5.4, -3.78, -2.7, -1.62, 1.62, 2.7, 3.78, 5.4, 7.56, 10.8, 15.12, 21.6, 30.24, 43.2, 59.4, 81, 108, 151.2, 205.2, 270, 324, 378, 432 Jy beam^{-1}.
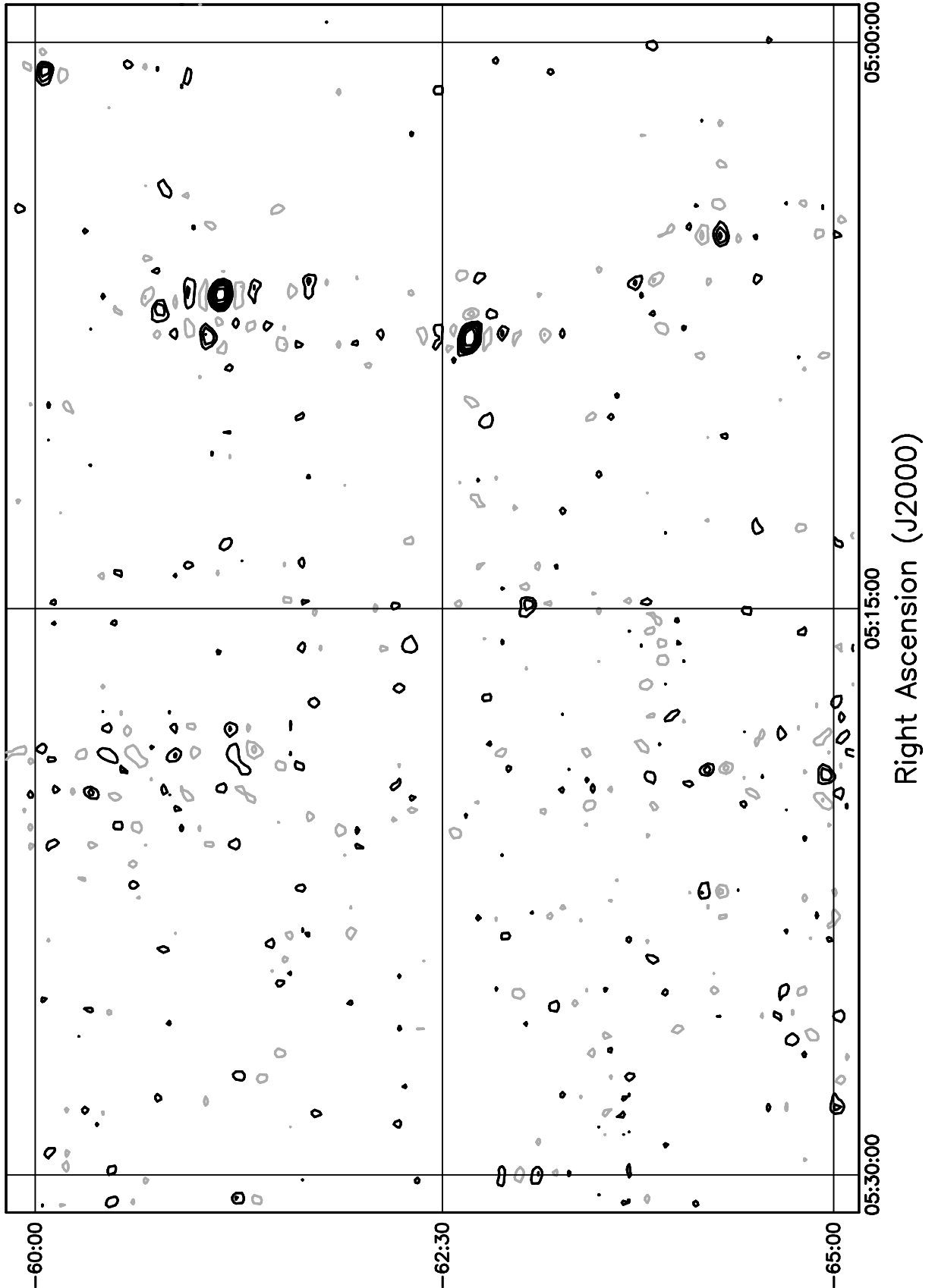
Figure 5.181: Contour plot for the range $05^h00^m \leq RA \leq 05^h30^m$, $-60° \leq \delta \leq -55°$. Contour levels are -7.56, -5.4, -3.78, -2.7, -1.62, 1.62, 2.7, 3.78, 5.4, 7.56, 10.8, 15.12, 21.6, 30.24, 43.2, 59.4, 81, 108, 151.2, 205.2, 270, 324, 378, 432 Jy beam^{-1}.
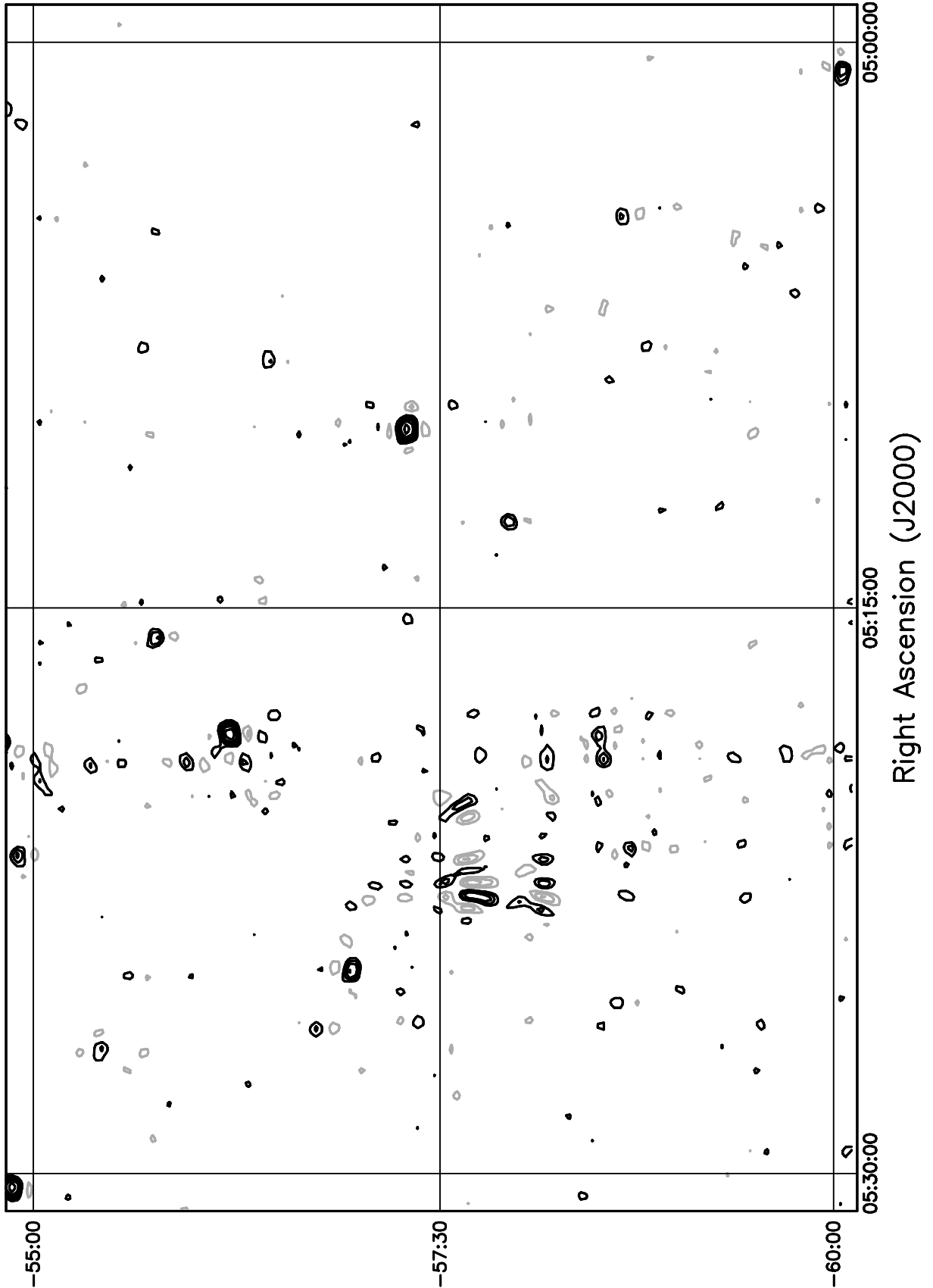
Figure 5.182: Contour plot for the range $05^h00^m \leq RA \leq 05^h30^m$, $-55° \leq \delta \leq -50°$. Contour levels are -7.56, -5.4, -3.78, -2.7, -1.62, 1.62, 2.7, 3.78, 5.4, 7.56, 10.8, 15.12, 21.6, 30.24, 43.2, 59.4, 81, 108, 151.2, 205.2, 270, 324, 378, 432 Jy beam^{-1}.
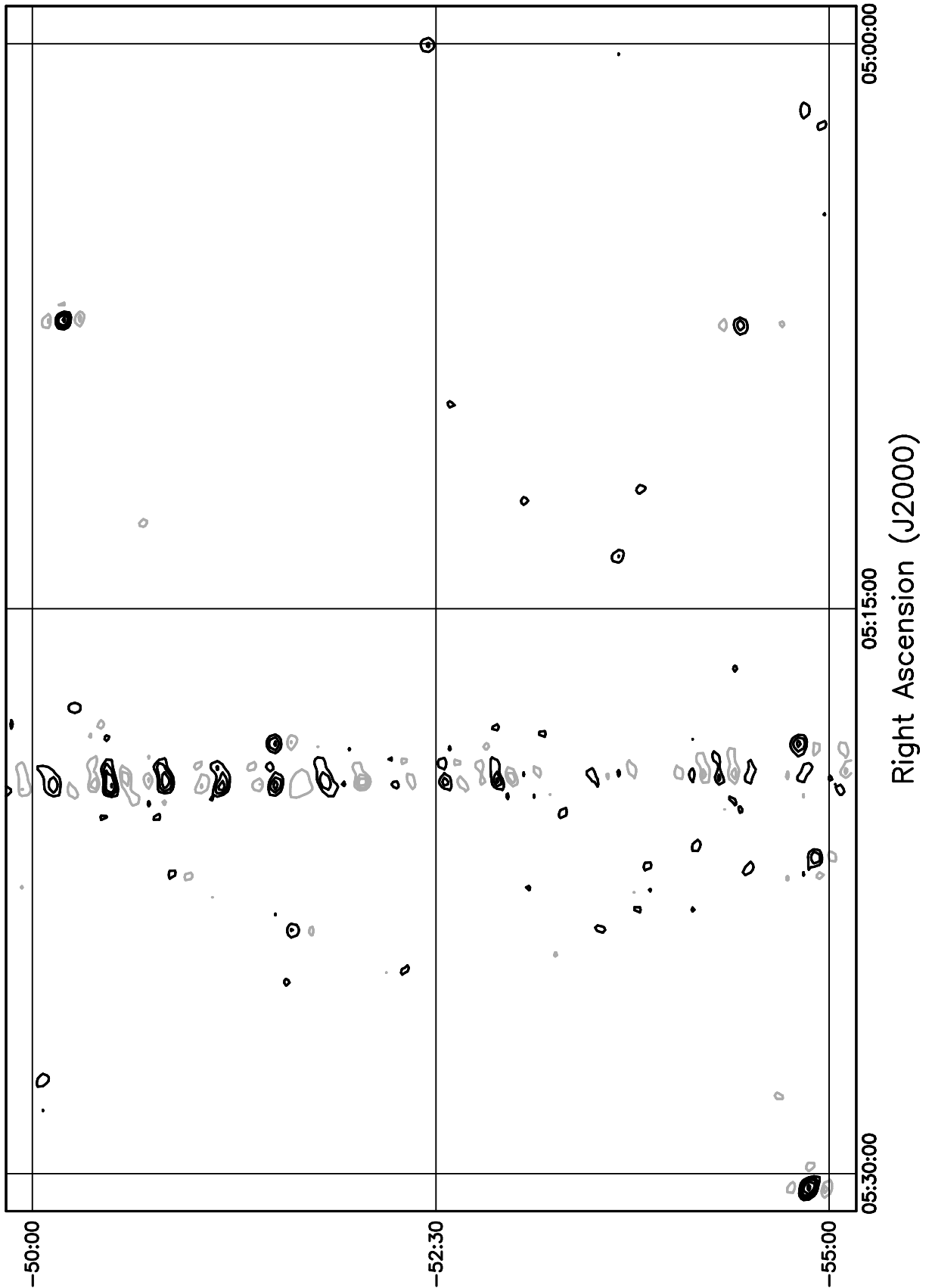
Figure 5.183: Contour plot for the range $05^h00^m \le RA \le 05^h30^m$, $-50° \le \delta \le -45°$. Contour levels are -7.56, -5.4, -3.78, -2.7, -1.62, 1.62, 2.7, 3.78, 5.4, 7.56, 10.8, 15.12, 21.6, 30.24, 43.2, 59.4, 81, 108, 151.2, 205.2, 270, 324, 378, 432 Jy beam^{-1}.
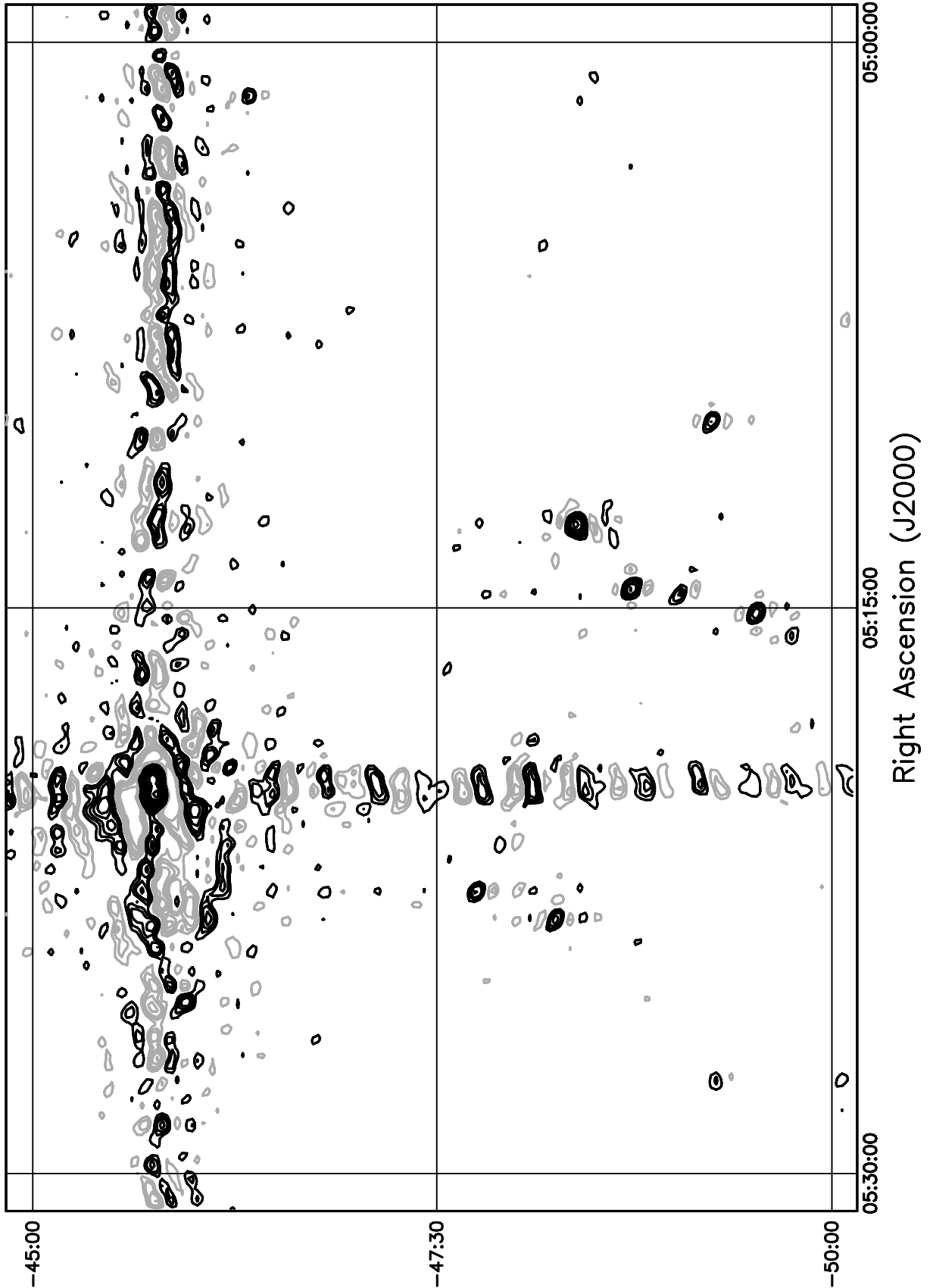
Figure 5.184: Contour plot for the range $05^h00^m \leq RA \leq 05^h30^m$, $-45° \leq \delta \leq -40°$. Contour levels are -7.56, -5.4, -3.78, -2.7, -1.62, 1.62, 2.7, 3.78, 5.4, 7.56, 10.8, 15.12, 21.6, 30.24, 43.2, 59.4, 81, 108, 151.2, 205.2, 270, 324, 378, 432 Jy beam^{-1}.
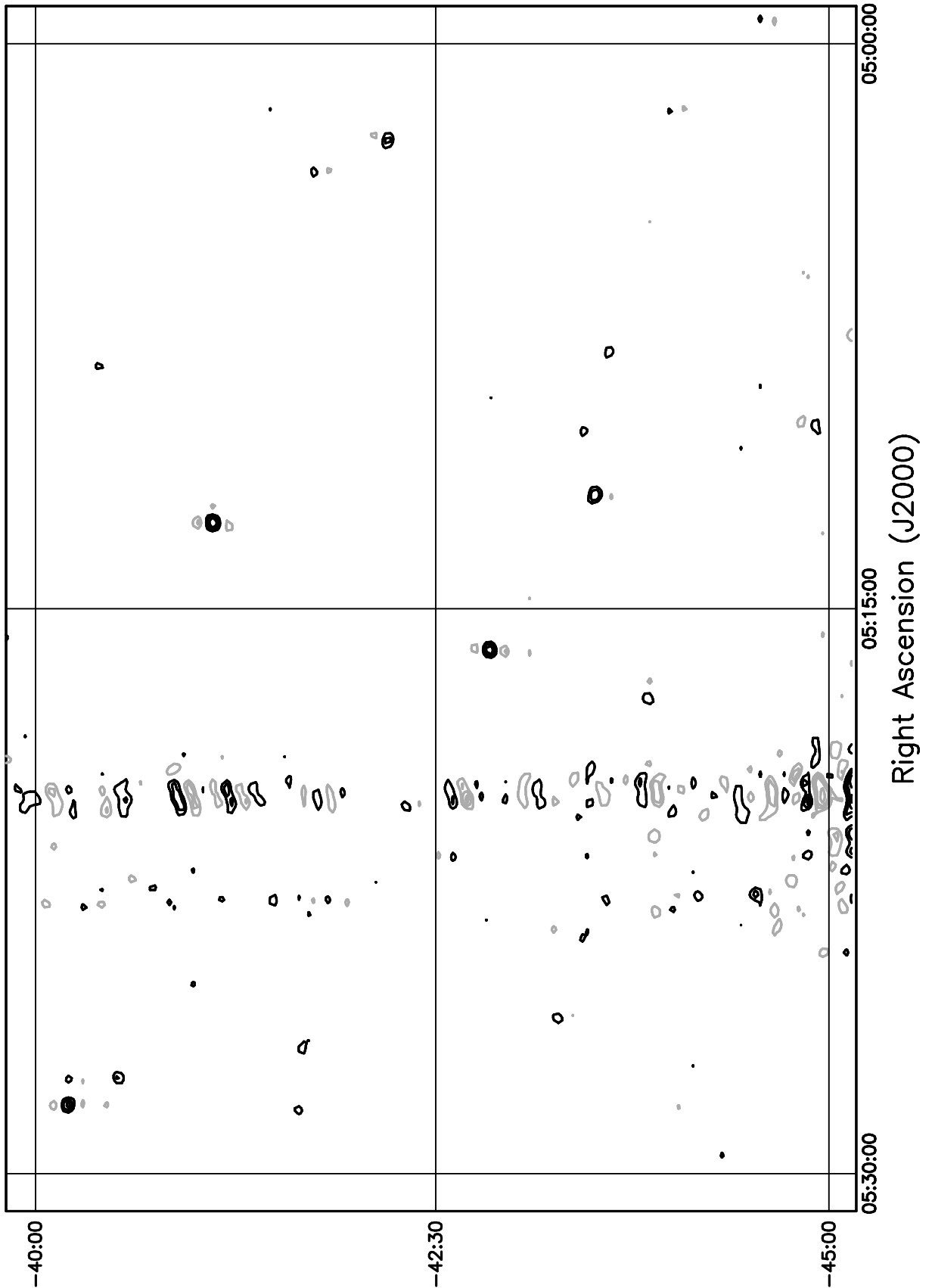
Figure 5.185: Contour plot for the range $05^h00^m \leq RA \leq 05^h30^m$, $-40° \leq \delta \leq -35°$. Contour levels are -7.56, -5.4, -3.78, -2.7, -1.62, 1.62, 2.7, 3.78, 5.4, 7.56, 10.8, 15.12, 21.6, 30.24, 43.2, 59.4, 81, 108, 151.2, 205.2, 270, 324, 378, 432 Jy beam^{-1}.
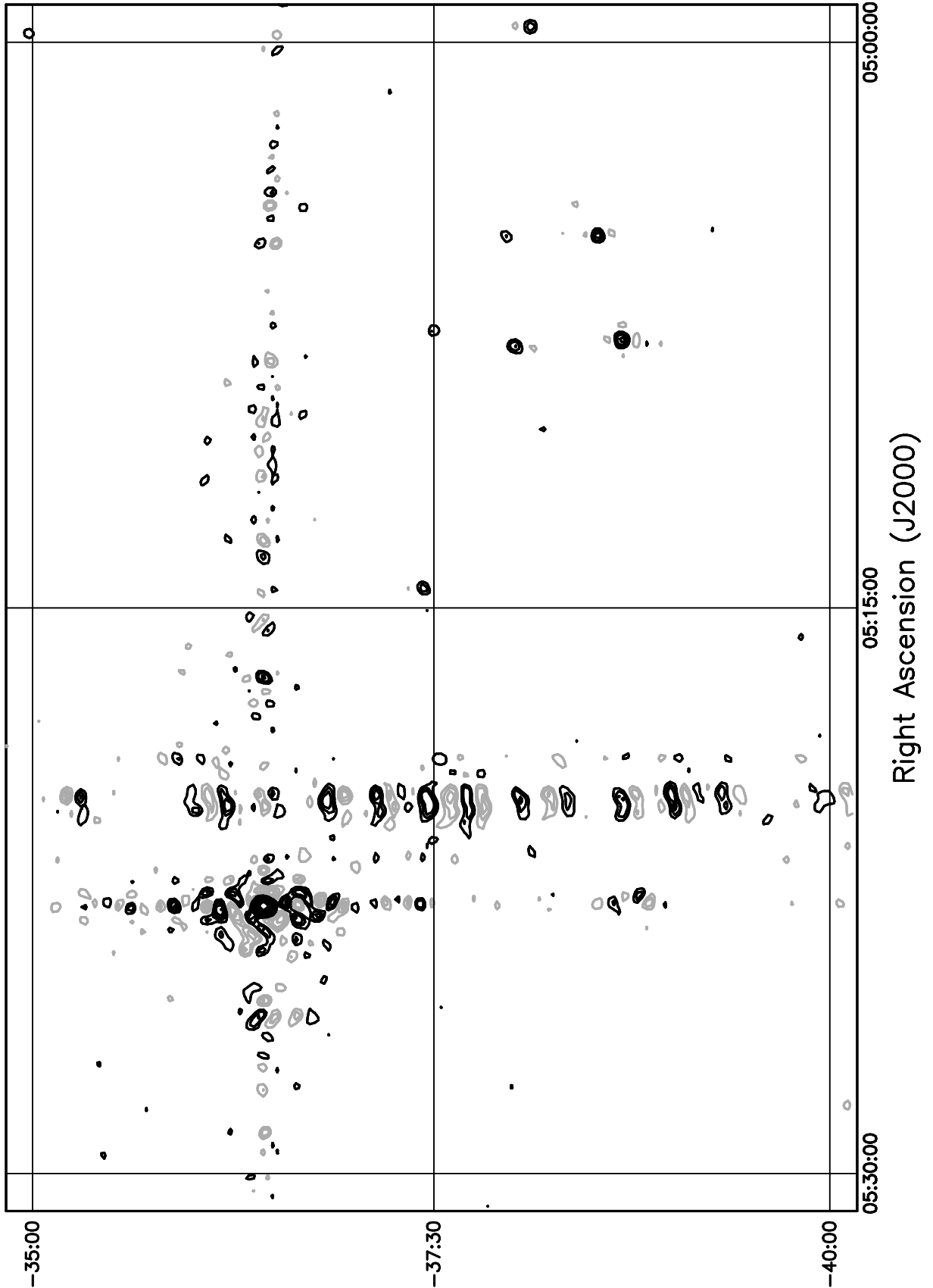
Figure 5.186: Contour plot for the range $05^h00^m \leq RA \leq 05^h30^m$, $-35° \leq \delta \leq -30°$. Contour levels are -7.56, -5.4, -3.78, -2.7, -1.62, 1.62, 2.7, 3.78, 5.4, 7.56, 10.8, 15.12, 21.6, 30.24, 43.2, 59.4, 81, 108, 151.2, 205.2, 270, 324, 378, 432 Jy beam^{-1}.
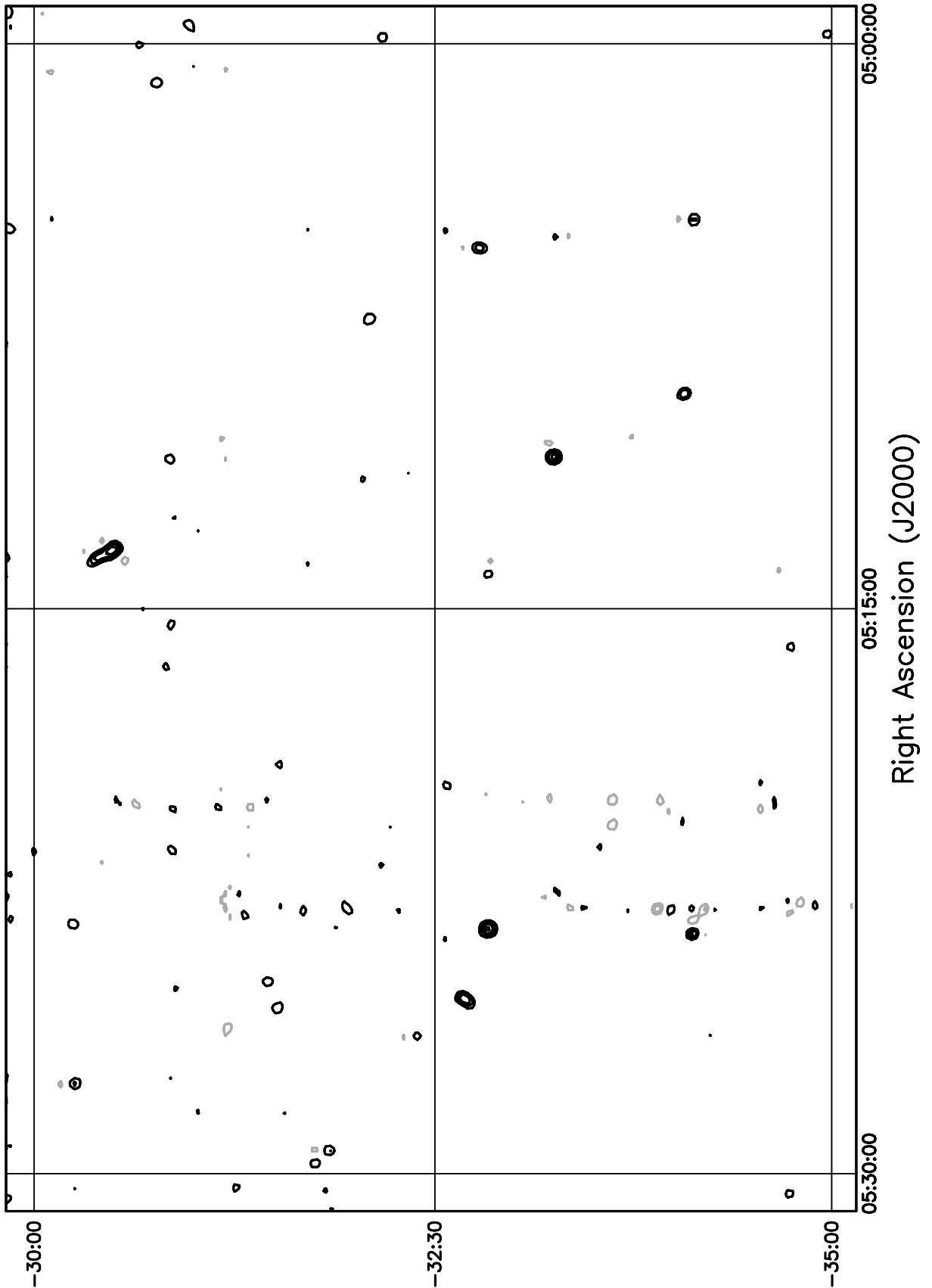
Figure 5.187: Contour plot for the range $05^h00^m \leq RA \leq 05^h30^m$, $-30° \leq \delta \leq -25°$. Contour levels are -7.56, -5.4, -3.78, -2.7, -1.62, 1.62, 2.7, 3.78, 5.4, 7.56, 10.8, 15.12, 21.6, 30.24, 43.2, 59.4, 81, 108, 151.2, 205.2, 270, 324, 378, 432 Jy beam^{-1}.
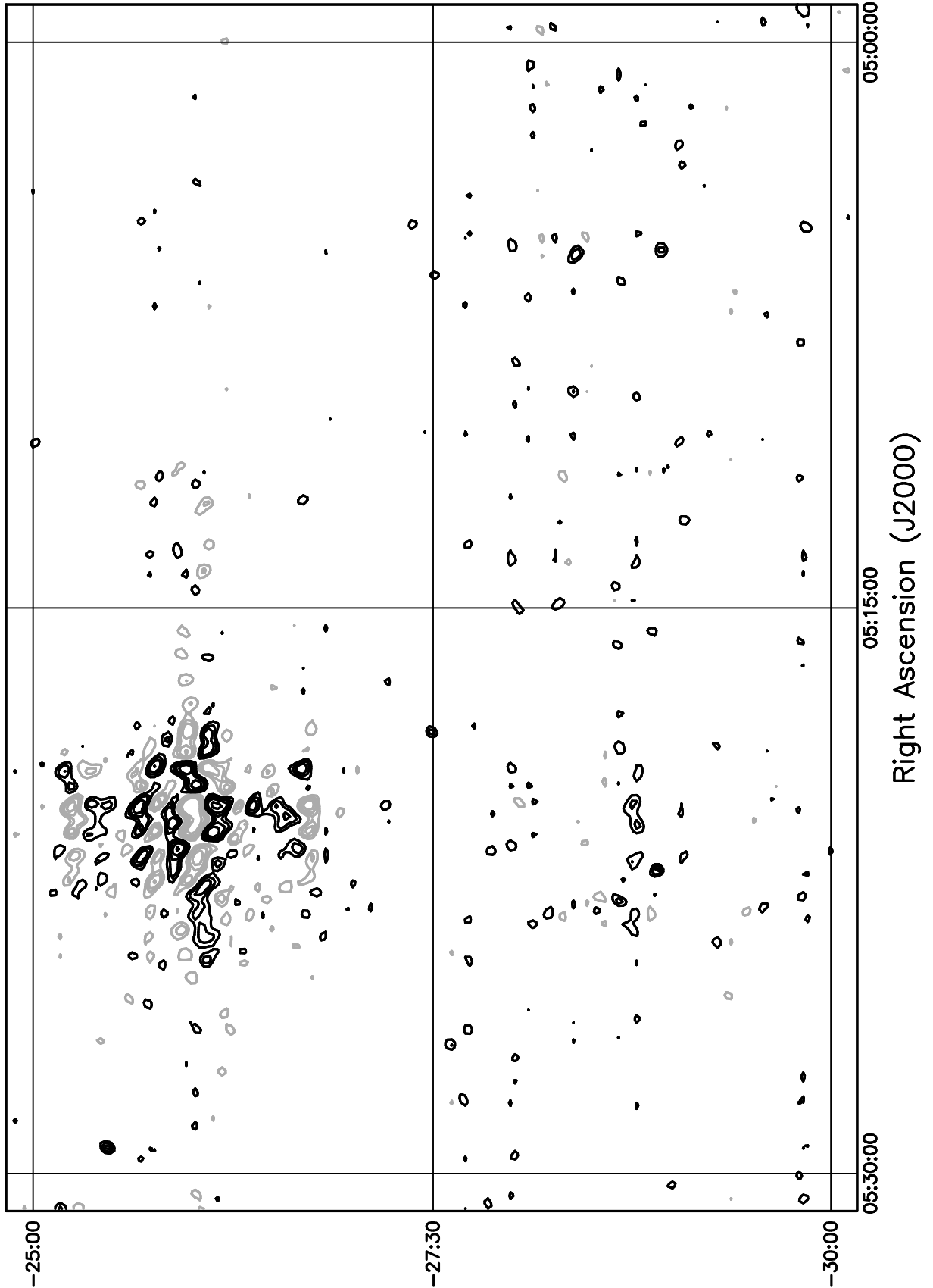
Figure 5.188: Contour plot for the range $05^h00^m \leq RA \leq 05^h30^m$, $-25° \leq \delta \leq -20°$. Contour levels are -7.56, -5.4, -3.78, -2.7, -1.62, 1.62, 2.7, 3.78, 5.4, 7.56, 10.8, 15.12, 21.6, 30.24, 43.2, 59.4, 81, 108, 151.2, 205.2, 270, 324, 378, 432 Jy beam^{-1}.
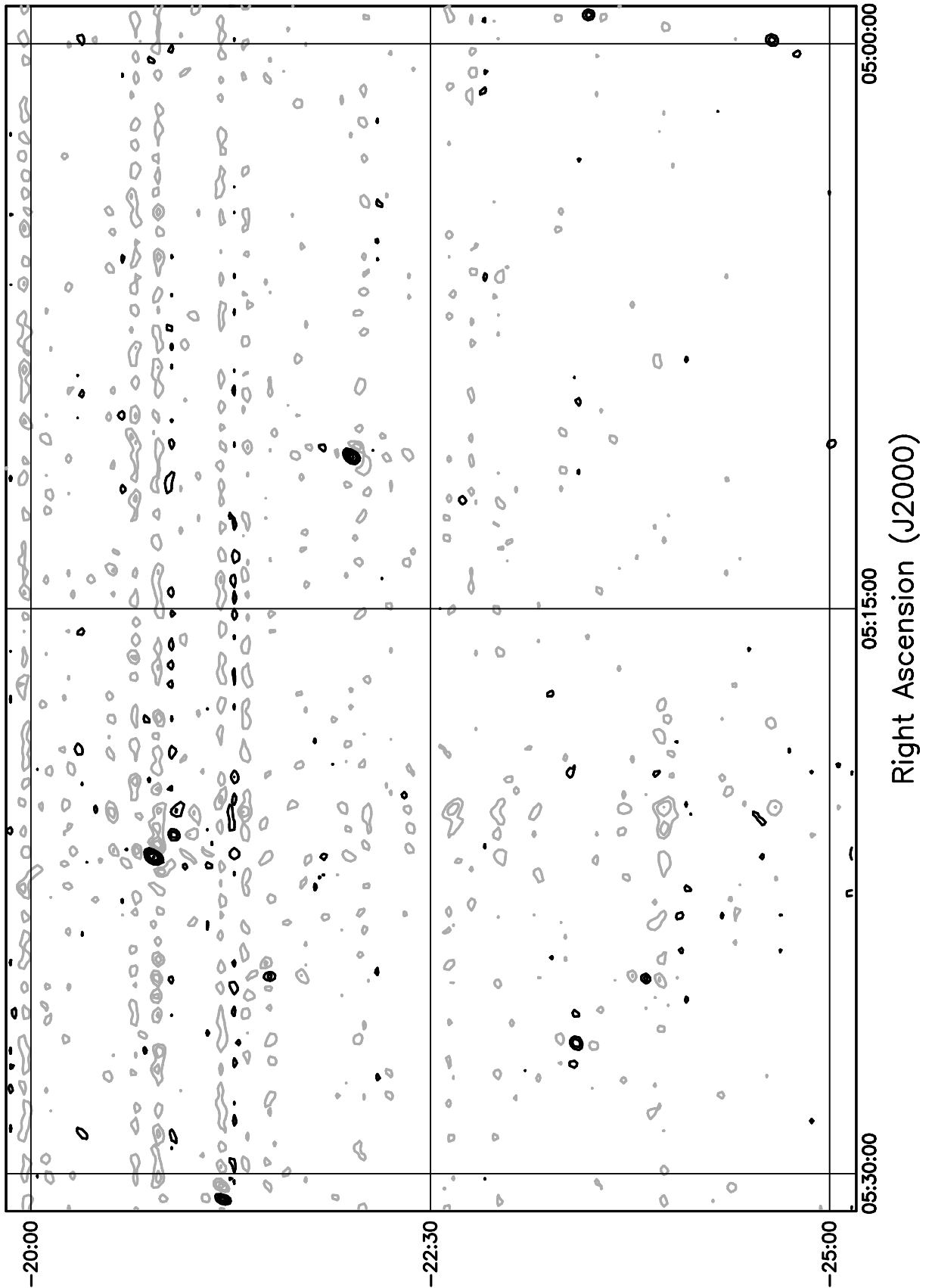
Figure 5.189: Contour plot for the range $05^h00^m \leq RA \leq 05^h30^m$, $-20° \leq \delta \leq -15°$. Contour levels are -7.56, -5.4, -3.78, -2.7, -1.62, 1.62, 2.7, 3.78, 5.4, 7.56, 10.8, 15.12, 21.6, 30.24, 43.2, 59.4, 81, 108, 151.2, 205.2, 270, 324, 378, 432 Jy beam^{-1}.
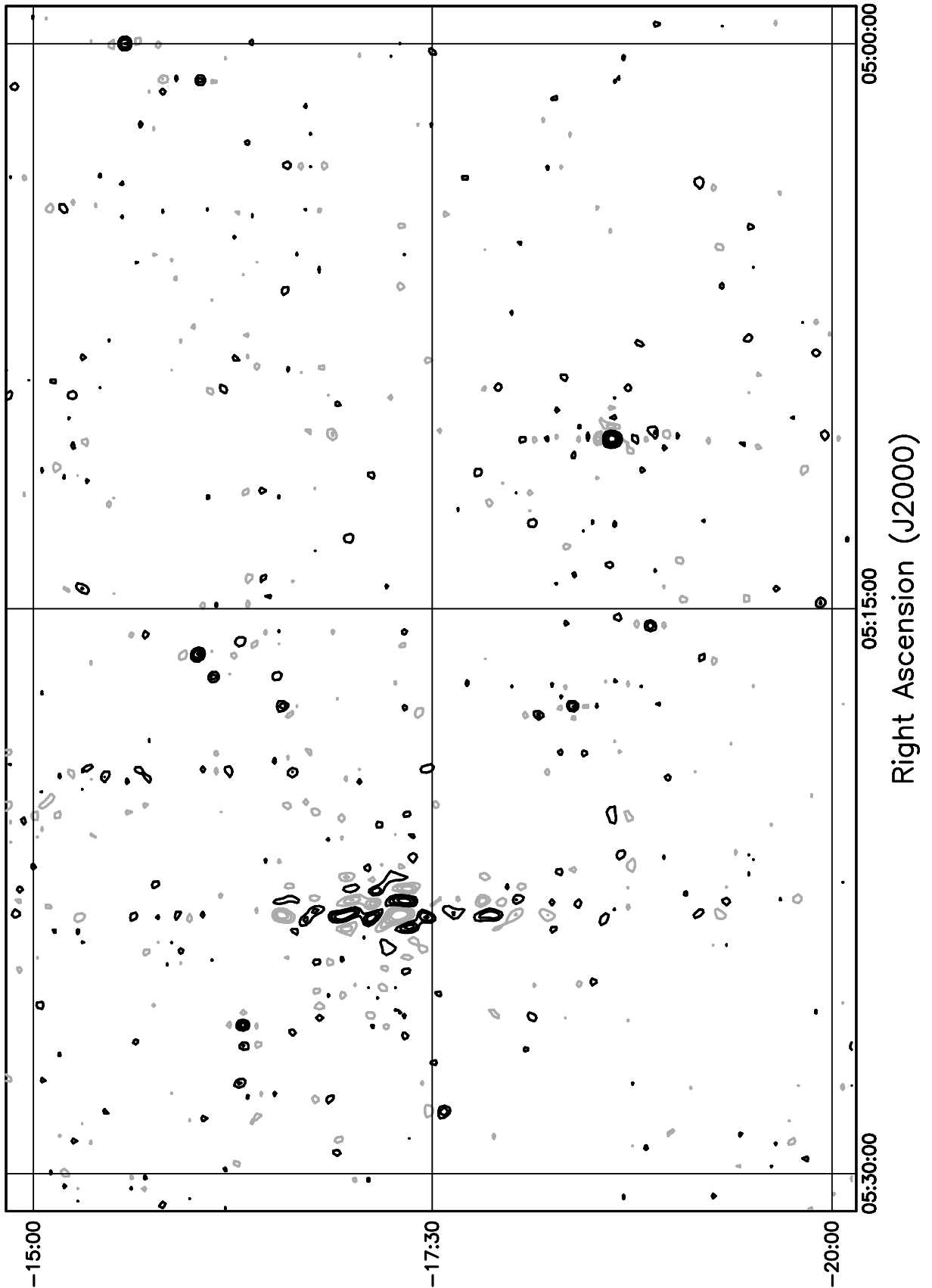
Figure 5.190: Contour plot for the range $05^h00^m \le RA \le 05^h30^m$, $-15° \le \delta \le -10°$. Contour levels are -7.56, -5.4, -3.78, -2.7, -1.62, 1.62, 2.7, 3.78, 5.4, 7.56, 10.8, 15.12, 21.6, 30.24, 43.2, 59.4, 81, 108, 151.2, 205.2, 270, 324, 378, 432 Jy beam^{-1}.
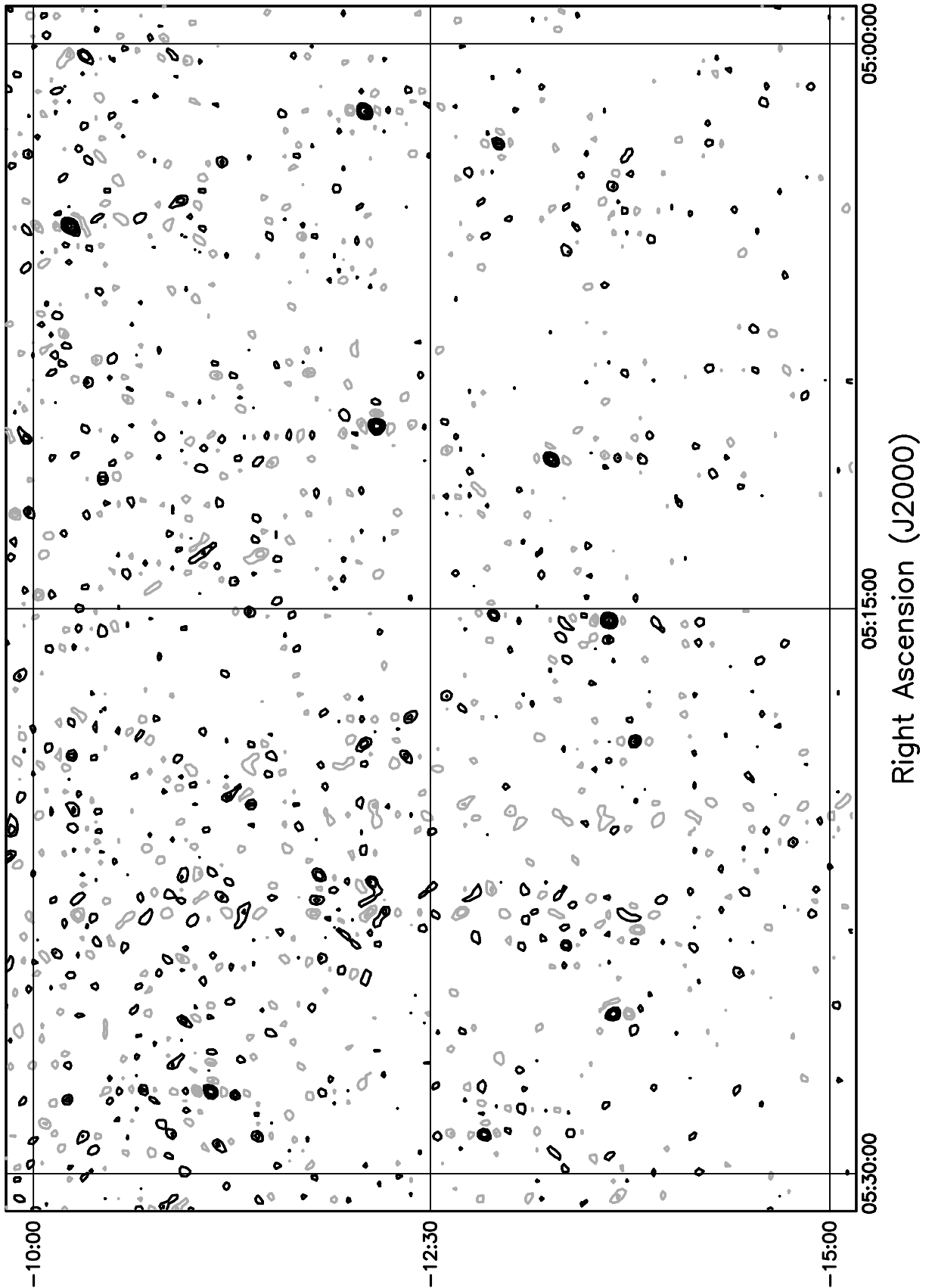
Figure 5.191: Contour plot for the range $05^h30^m \leq RA \leq 05^h54^m$, $-75° \leq \delta \leq -70°$. Contour levels are -7.56, -5.4, -3.78, -2.7, -1.62, 1.62, 2.7, 3.78, 5.4, 7.56, 10.8, 15.12, 21.6, 30.24, 43.2, 59.4, 81, 108, 151.2, 205.2, 270, 324, 378, 432 Jy beam^{-1}.
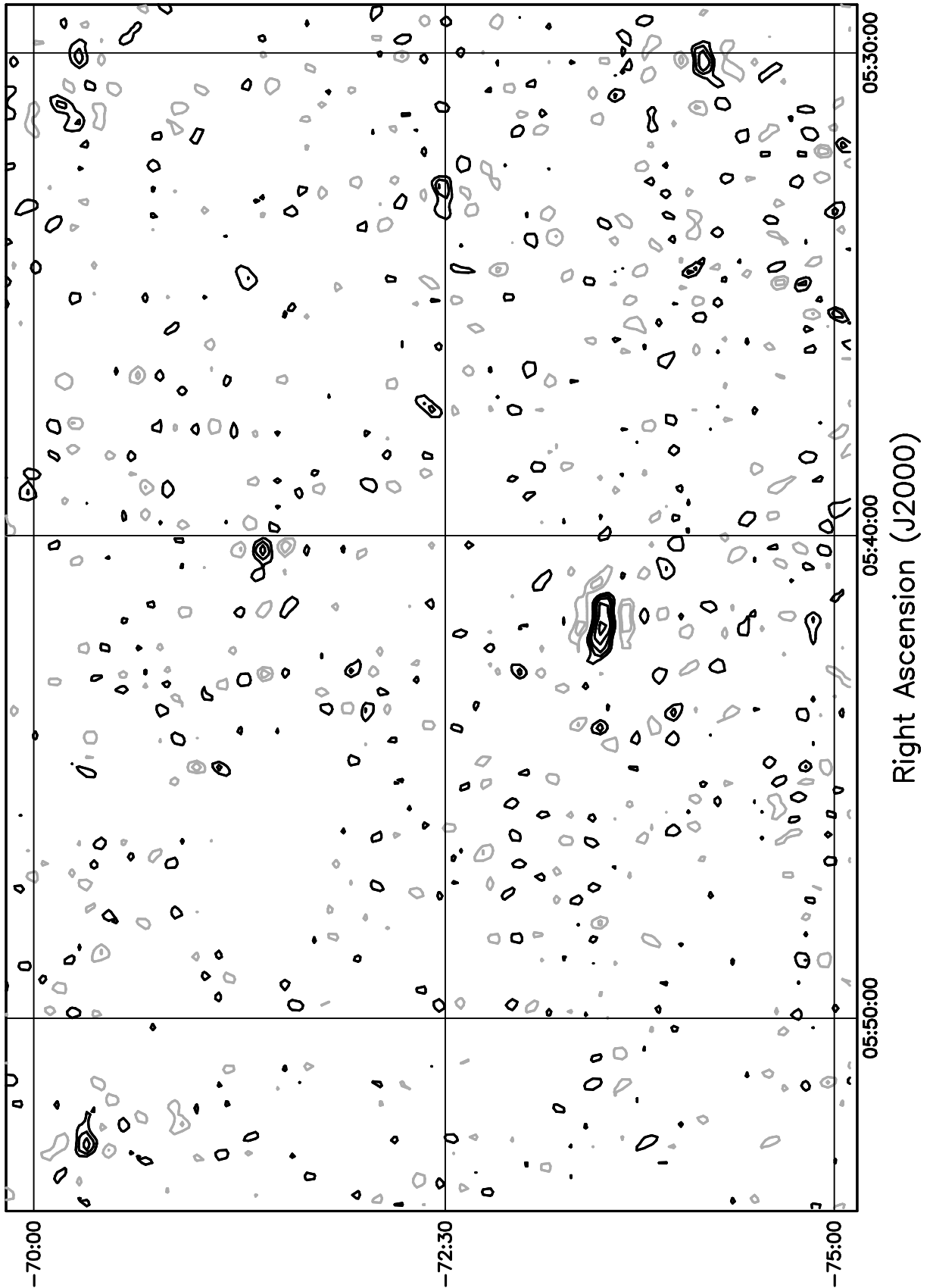
Figure 5.192: Contour plot for the range $05^h30^m \leq RA \leq 05^h54^m$, $-70° \leq \delta \leq -65°$. Contour levels are -7.56, -5.4, -3.78, -2.7, -1.62, 1.62, 2.7, 3.78, 5.4, 7.56, 10.8, 15.12, 21.6, 30.24, 43.2, 59.4, 81, 108, 151.2, 205.2, 270, 324, 378, 432 Jy beam^{-1}.
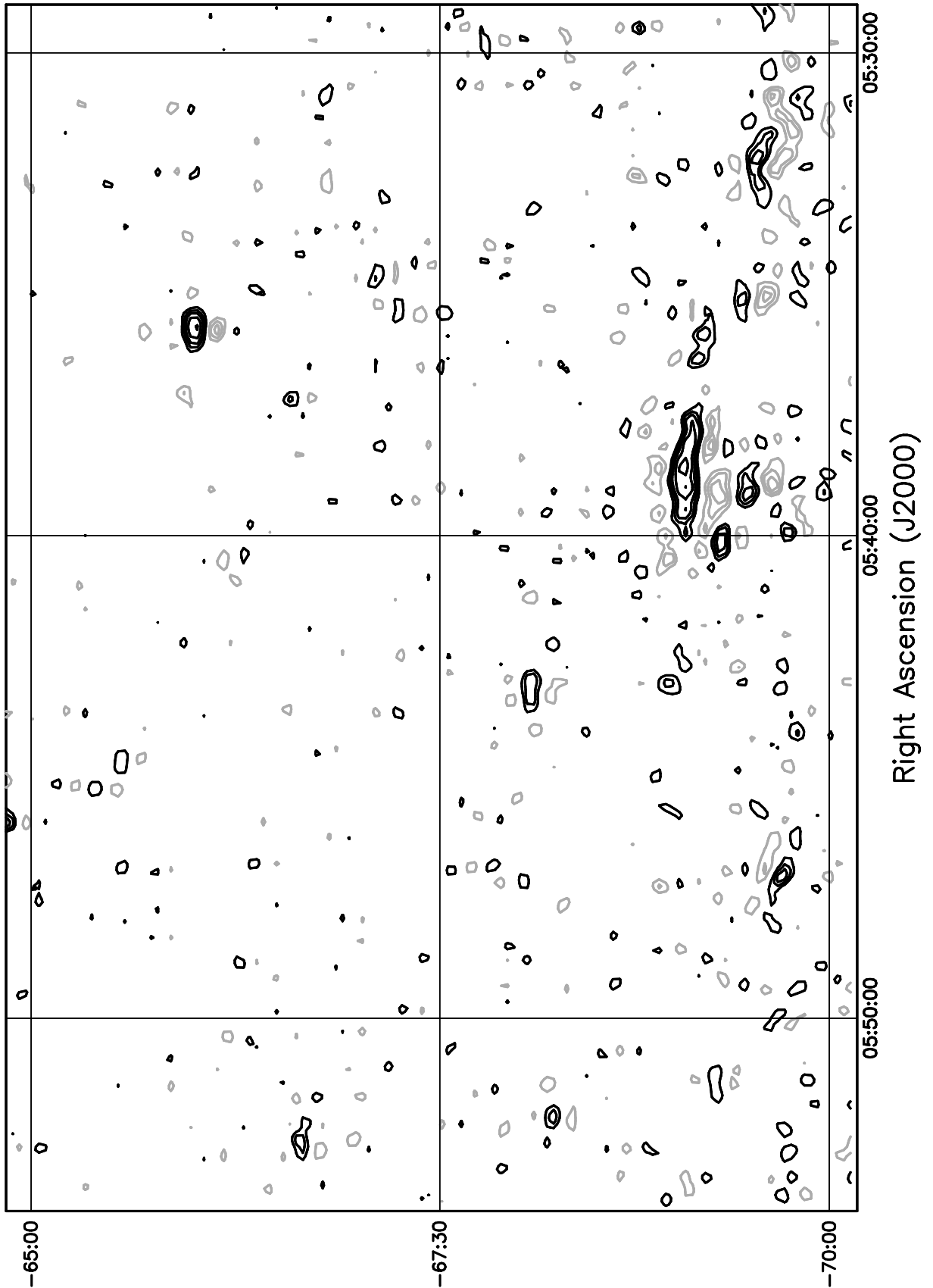
Figure 5.193: Contour plot for the range $05^h30^m \leq RA \leq 05^h54^m$, $-65° \leq \delta \leq -60°$. Contour levels are -7.56, -5.4, -3.78, -2.7, -1.62, 1.62, 2.7, 3.78, 5.4, 7.56, 10.8, 15.12, 21.6, 30.24, 43.2, 59.4, 81, 108, 151.2, 205.2, 270, 324, 378, 432 Jy beam^{-1}.
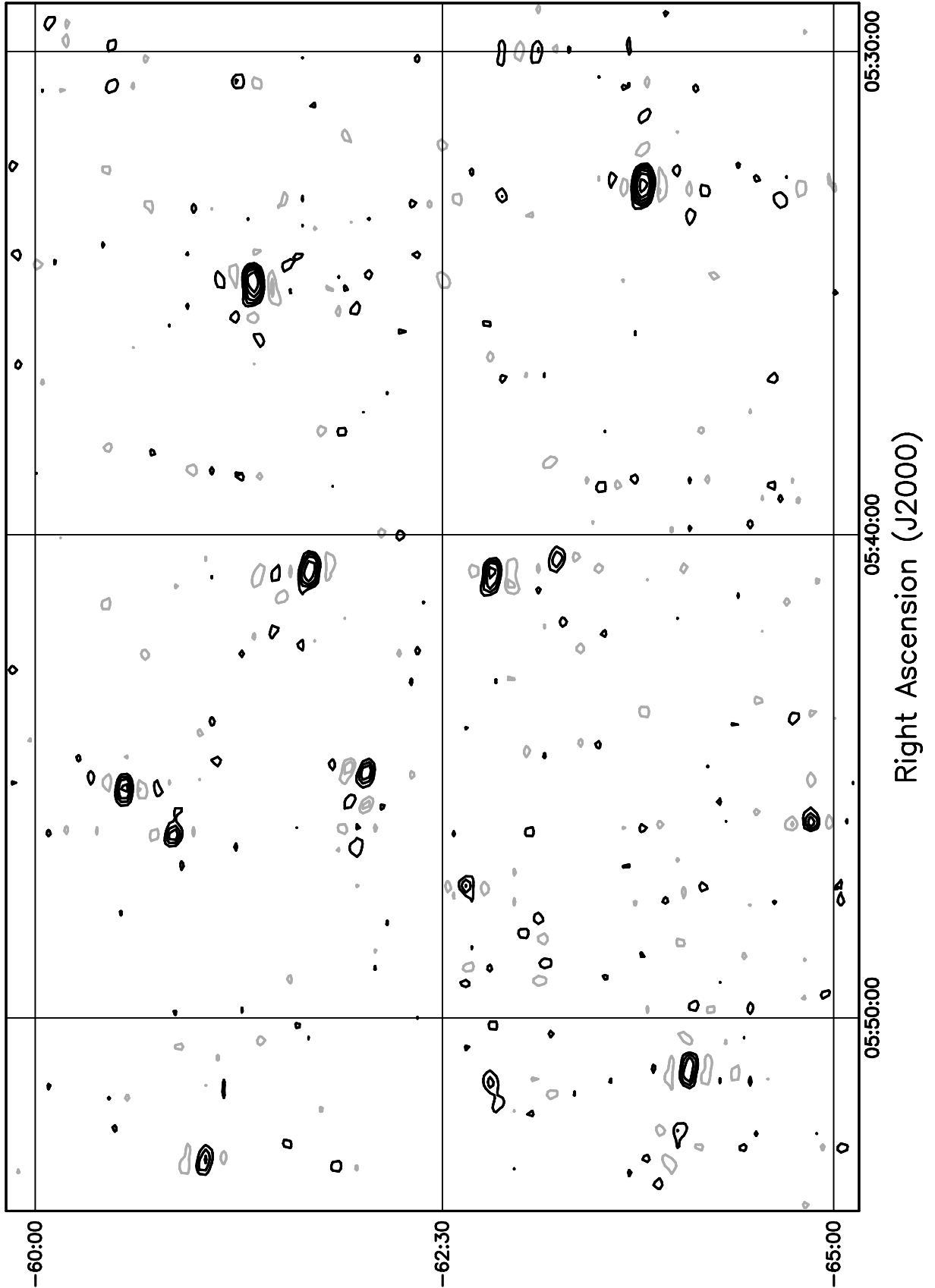
Figure 5.194: Contour plot for the range $05^h 30^m \leq RA \leq 05^h 54^m$, $-60° \leq \delta \leq -55°$. Contour levels are -7.56, -5.4, -3.78, -2.7, -1.62, 1.62, 2.7, 3.78, 5.4, 7.56, 10.8, 15.12, 21.6, 30.24, 43.2, 59.4, 81, 108, 151.2, 205.2, 270, 324, 378, 432 Jy beam^{-1}.
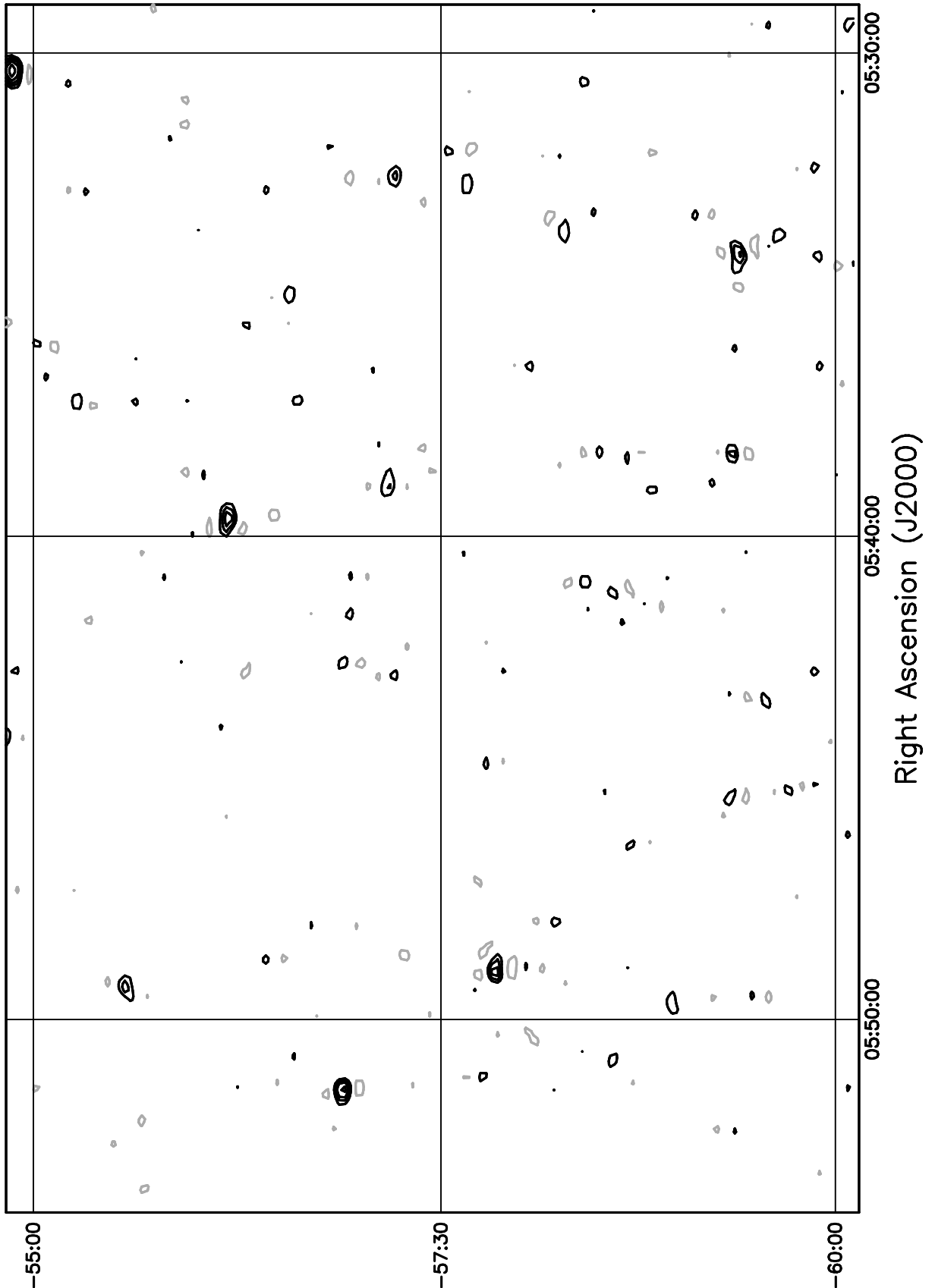
Figure 5.195: Contour plot for the range $05^h30^m \leq RA \leq 05^h54^m$, $-55° \leq \delta \leq -50°$. Contour levels are -7.56, -5.4, -3.78, -2.7, -1.62, 1.62, 2.7, 3.78, 5.4, 7.56, 10.8, 15.12, 21.6, 30.24, 43.2, 59.4, 81, 108, 151.2, 205.2, 270, 324, 378, 432 Jy beam^{-1}.
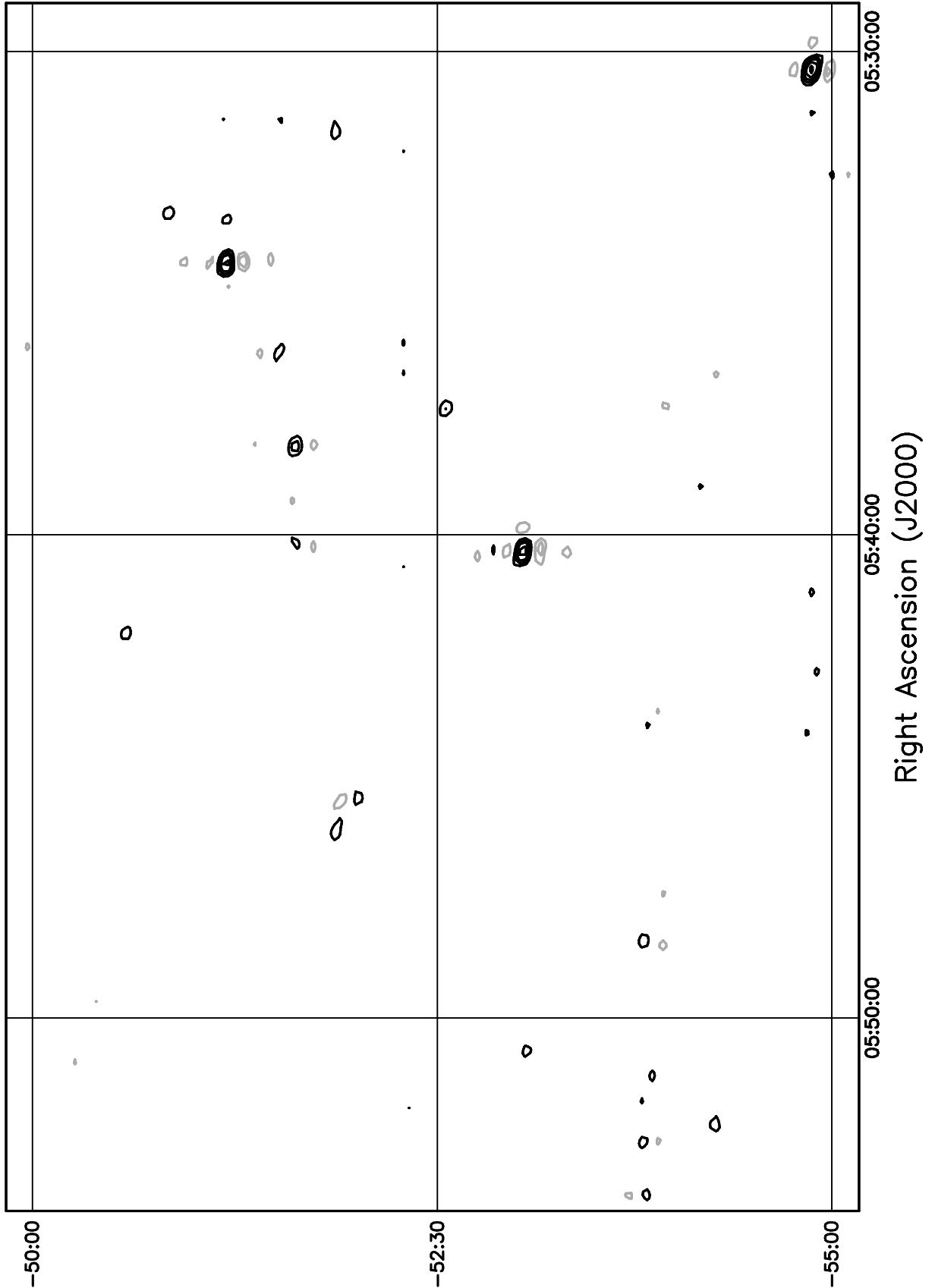
Figure 5.196: Contour plot for the range $05^h30^m \leq RA \leq 05^h54^m$, $-50° \leq \delta \leq -45°$. Contour levels are -7.56, -5.4, -3.78, -2.7, -1.62, 1.62, 2.7, 3.78, 5.4, 7.56, 10.8, 15.12, 21.6, 30.24, 43.2, 59.4, 81, 108, 151.2, 205.2, 270, 324, 378, 432 Jy beam^{-1}.

Right Ascension (J2000)
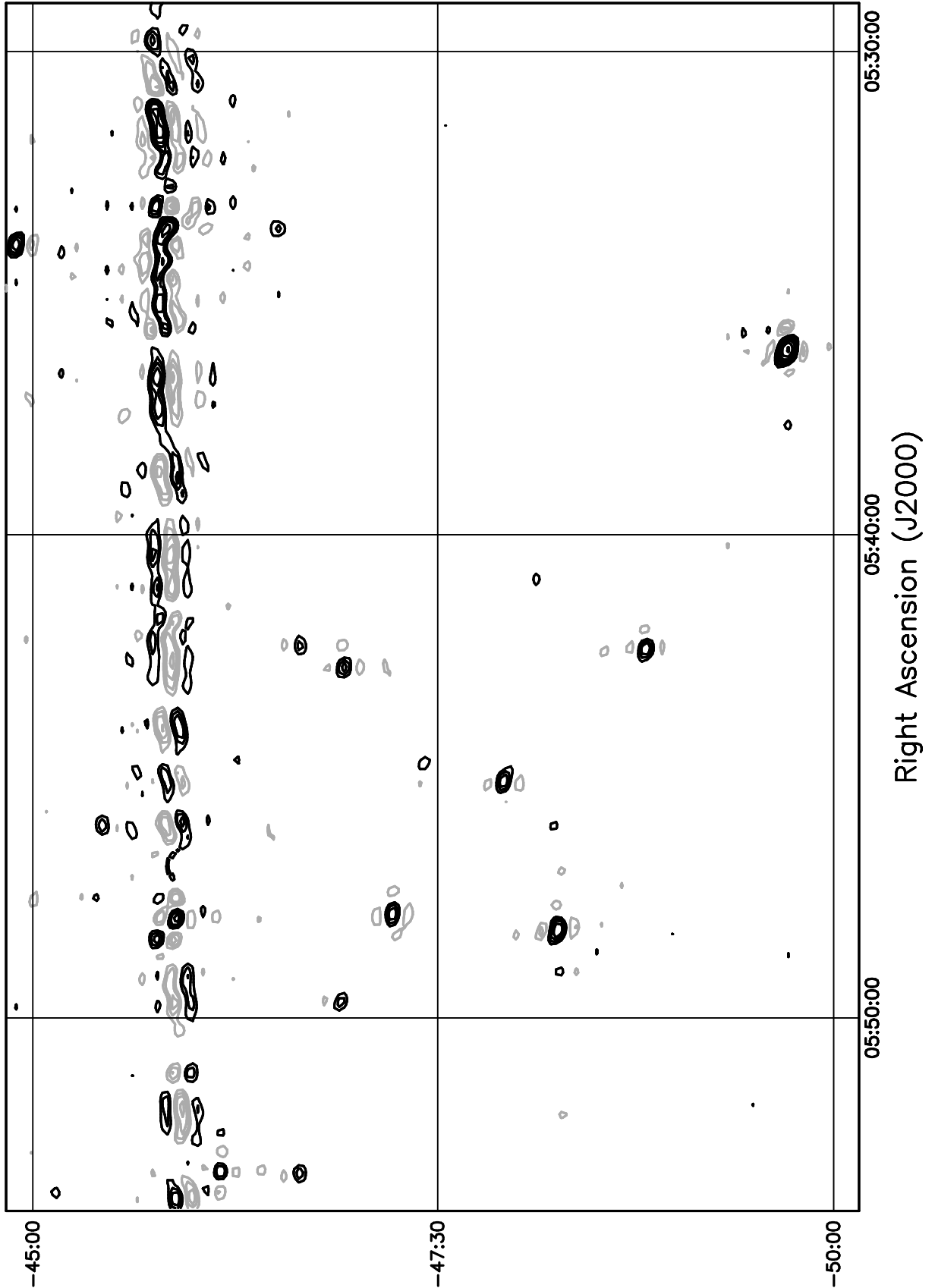
Figure 5.197: Contour plot for the range $05^h30^m \leq RA \leq 05^h54^m$, $-45° \leq \delta \leq -40°$. Contour levels are -7.56, -5.4, -3.78, -2.7, -1.62, 1.62, 2.7, 3.78, 5.4, 7.56, 10.8, 15.12, 21.6, 30.24, 43.2, 59.4, 81, 108, 151.2, 205.2, 270, 324, 378, 432 Jy beam^{-1}.
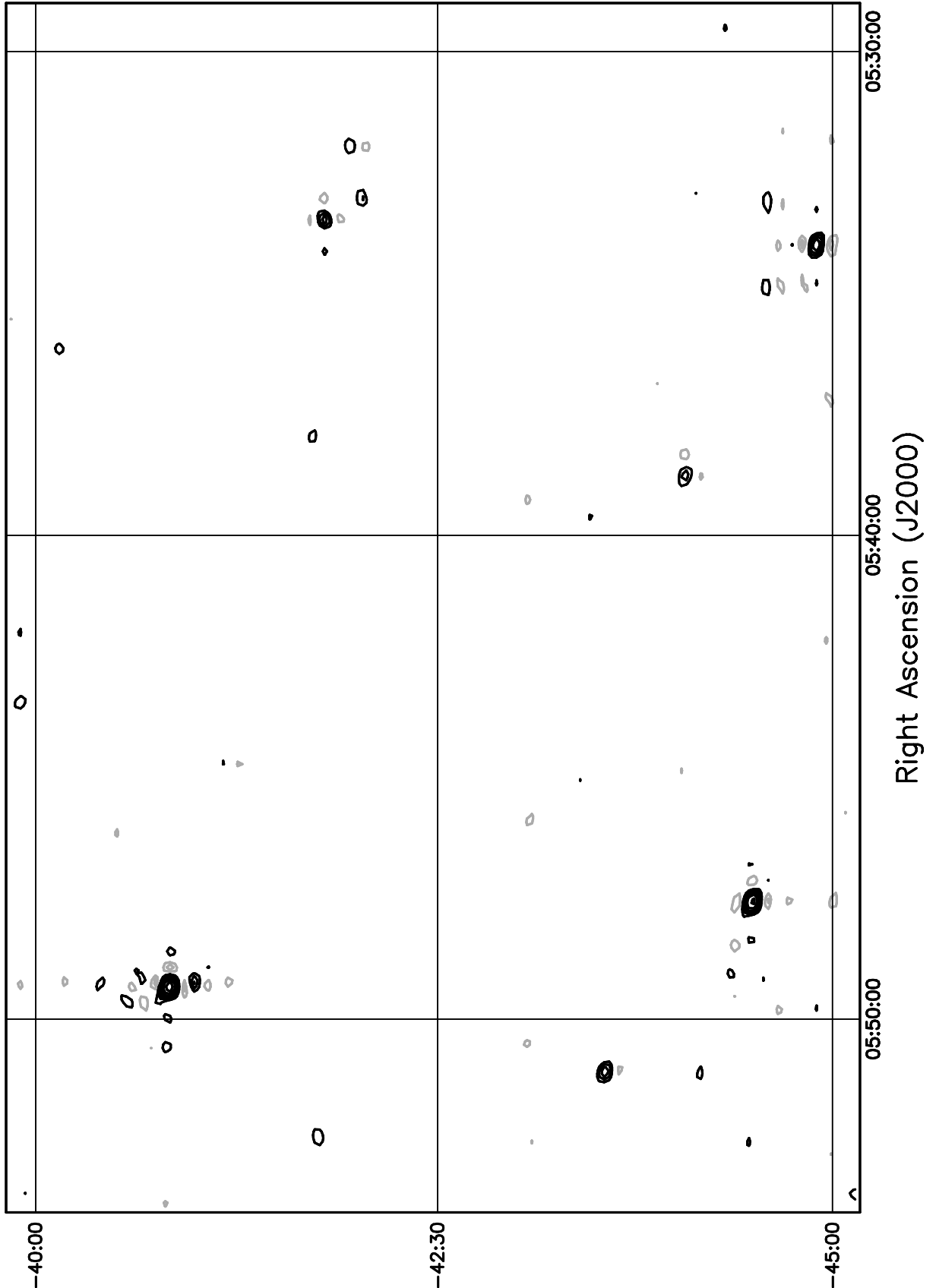
Figure 5.198: Contour plot for the range $05^h30^m \leq RA \leq 05^h54^m$, $-40° \leq \delta \leq -35°$. Contour levels are -7.56, -5.4, -3.78, -2.7, -1.62, 1.62, 2.7, 3.78, 5.4, 7.56, 10.8, 15.12, 21.6, 30.24, 43.2, 59.4, 81, 108, 151.2, 205.2, 270, 324, 378, 432 Jy beam^{-1}.
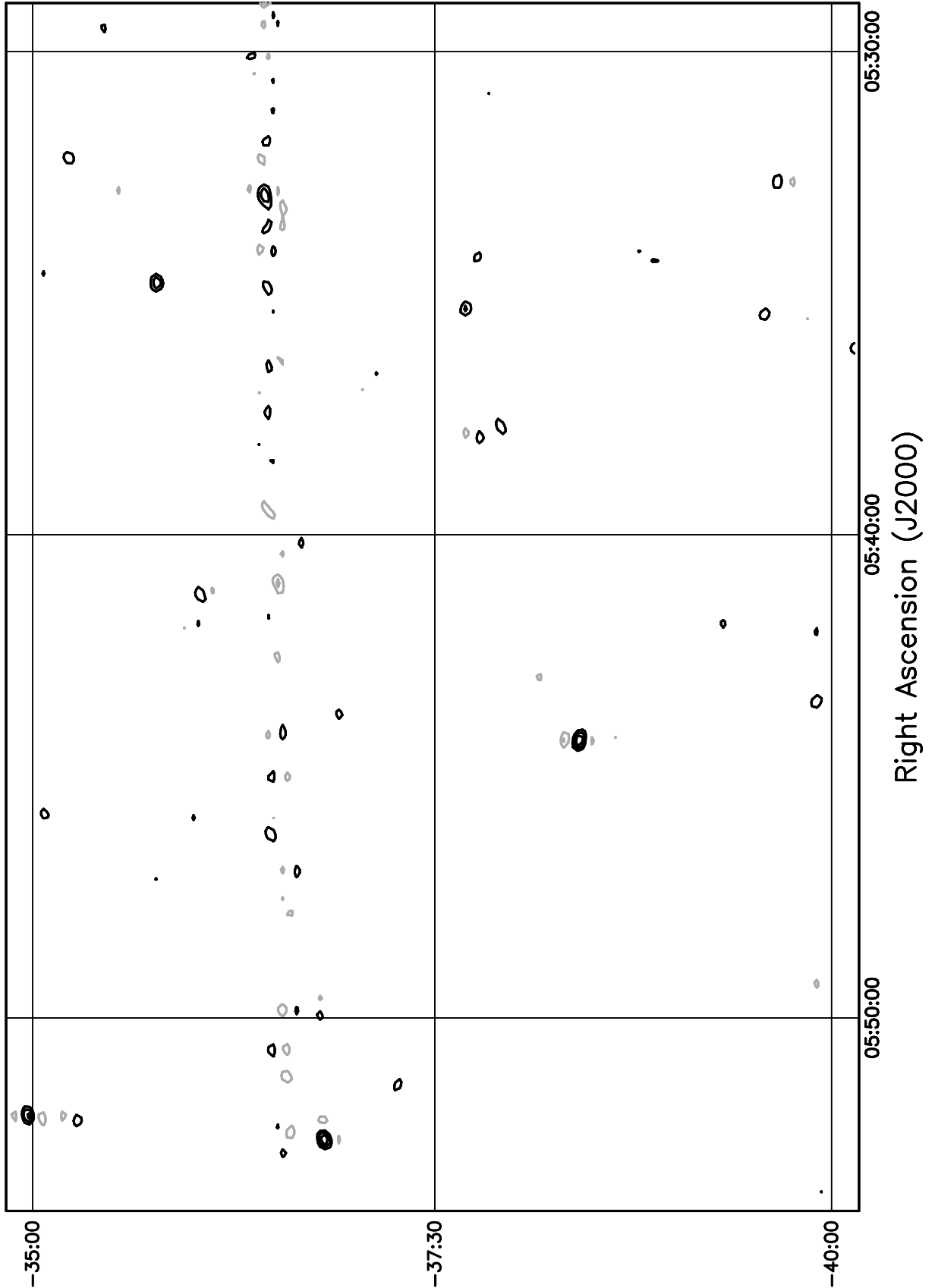
Figure 5.199: Contour plot for the range $05^h30^m \leq RA \leq 05^h54^m$, $-35° \leq \delta \leq -30°$. Contour levels are -7.56, -5.4, -3.78, -2.7, -1.62, 1.62, 2.7, 3.78, 5.4, 7.56, 10.8, 15.12, 21.6, 30.24, 43.2, 59.4, 81, 108, 151.2, 205.2, 270, 324, 378, 432 Jy beam^{-1}.
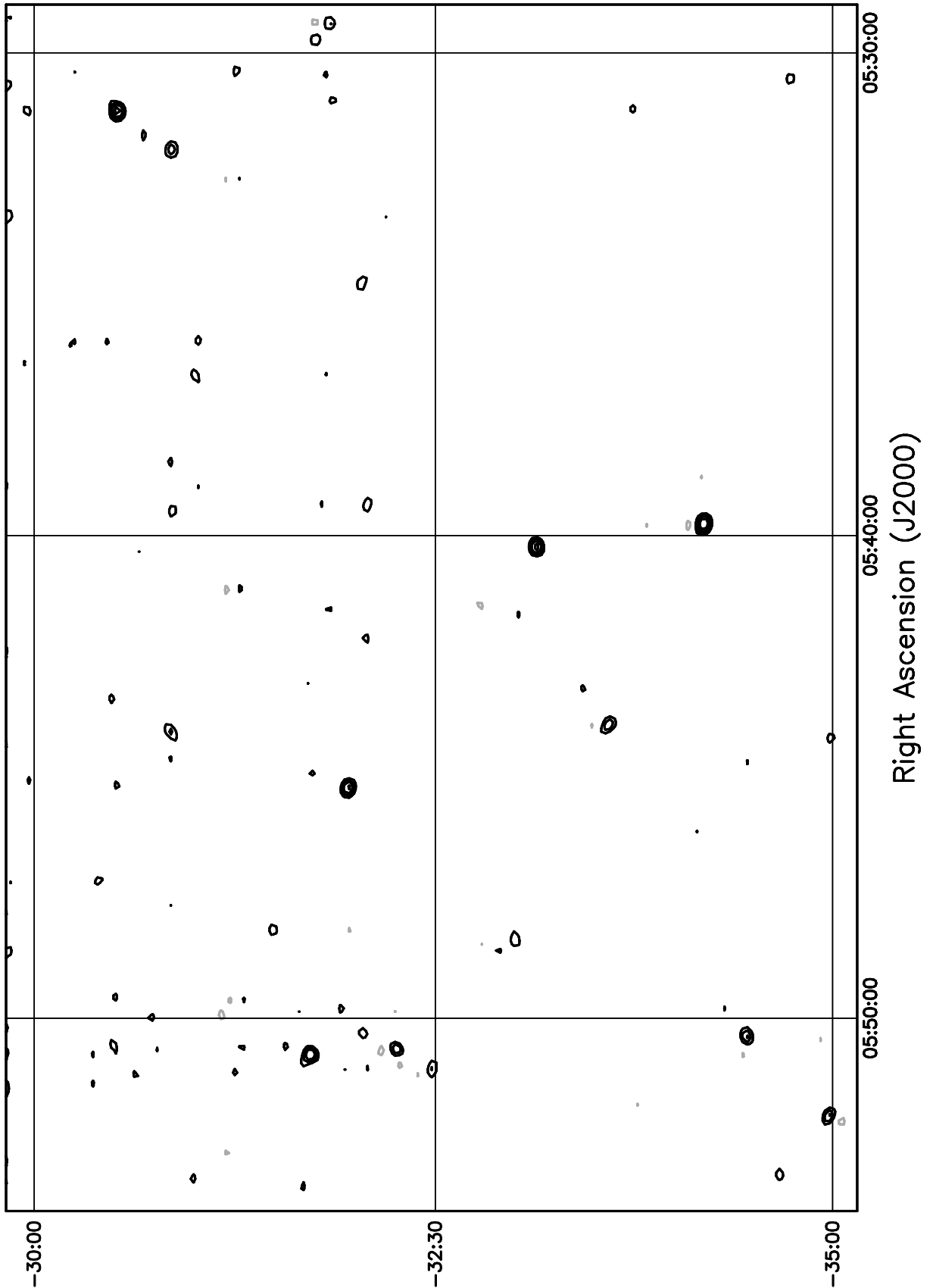
Figure 5.200: Contour plot for the range $05^h30^m \leq RA \leq 05^h54^m$, $-30° \leq \delta \leq -25°$. Contour levels are -7.56, -5.4, -3.78, -2.7, -1.62, 1.62, 2.7, 3.78, 5.4, 7.56, 10.8, 15.12, 21.6, 30.24, 43.2, 59.4, 81, 108, 151.2, 205.2, 270, 324, 378, 432 Jy beam^{-1}.
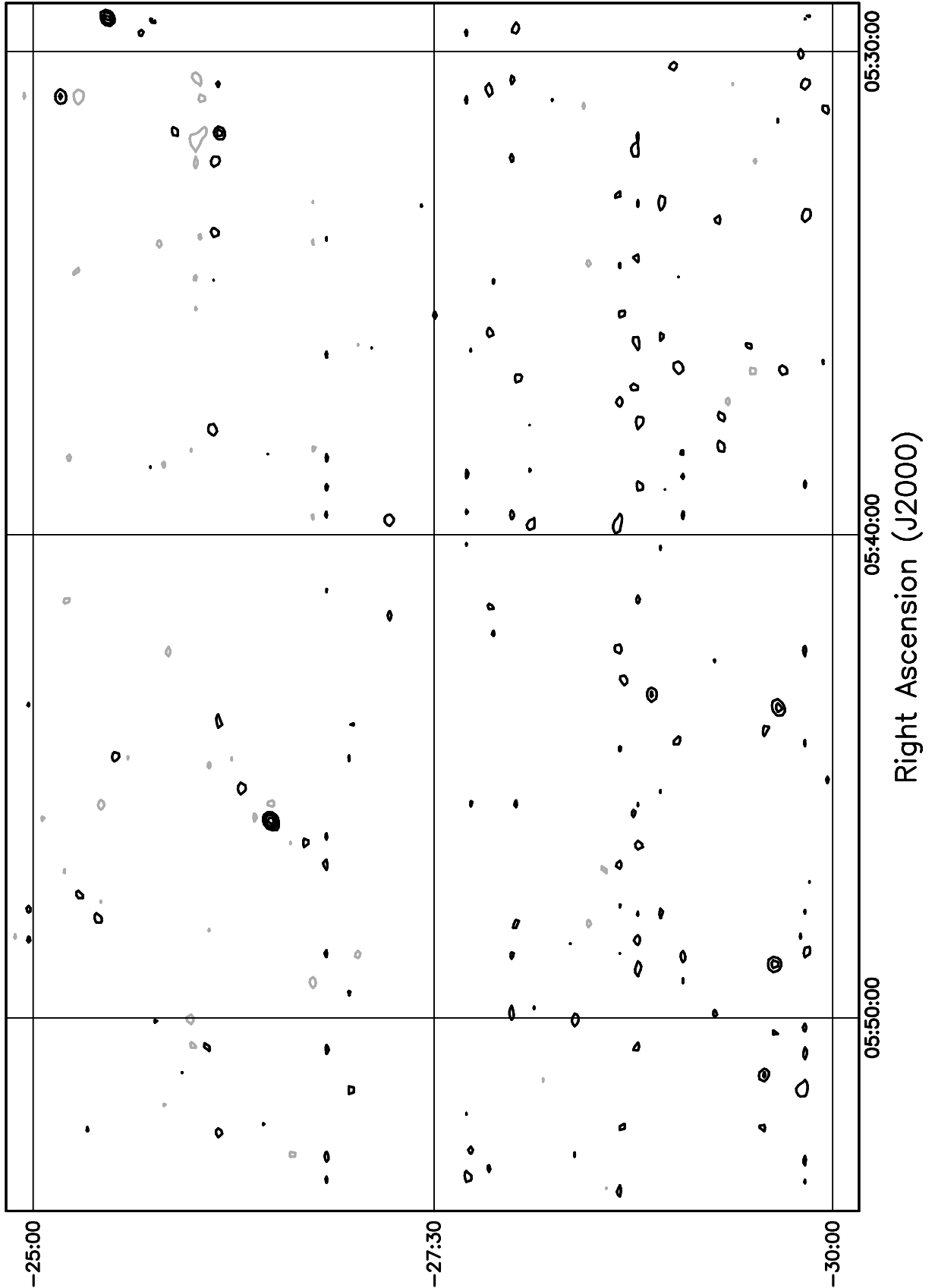
Figure 5.201: Contour plot for the range $05^h30^m \leq RA \leq 05^h54^m$, $-25° \leq \delta \leq -20°$. Contour levels are -7.56, -5.4, -3.78, -2.7, -1.62, 1.62, 2.7, 3.78, 5.4, 7.56, 10.8, 15.12, 21.6, 30.24, 43.2, 59.4, 81, 108, 151.2, 205.2, 270, 324, 378, 432 Jy beam^{-1}.
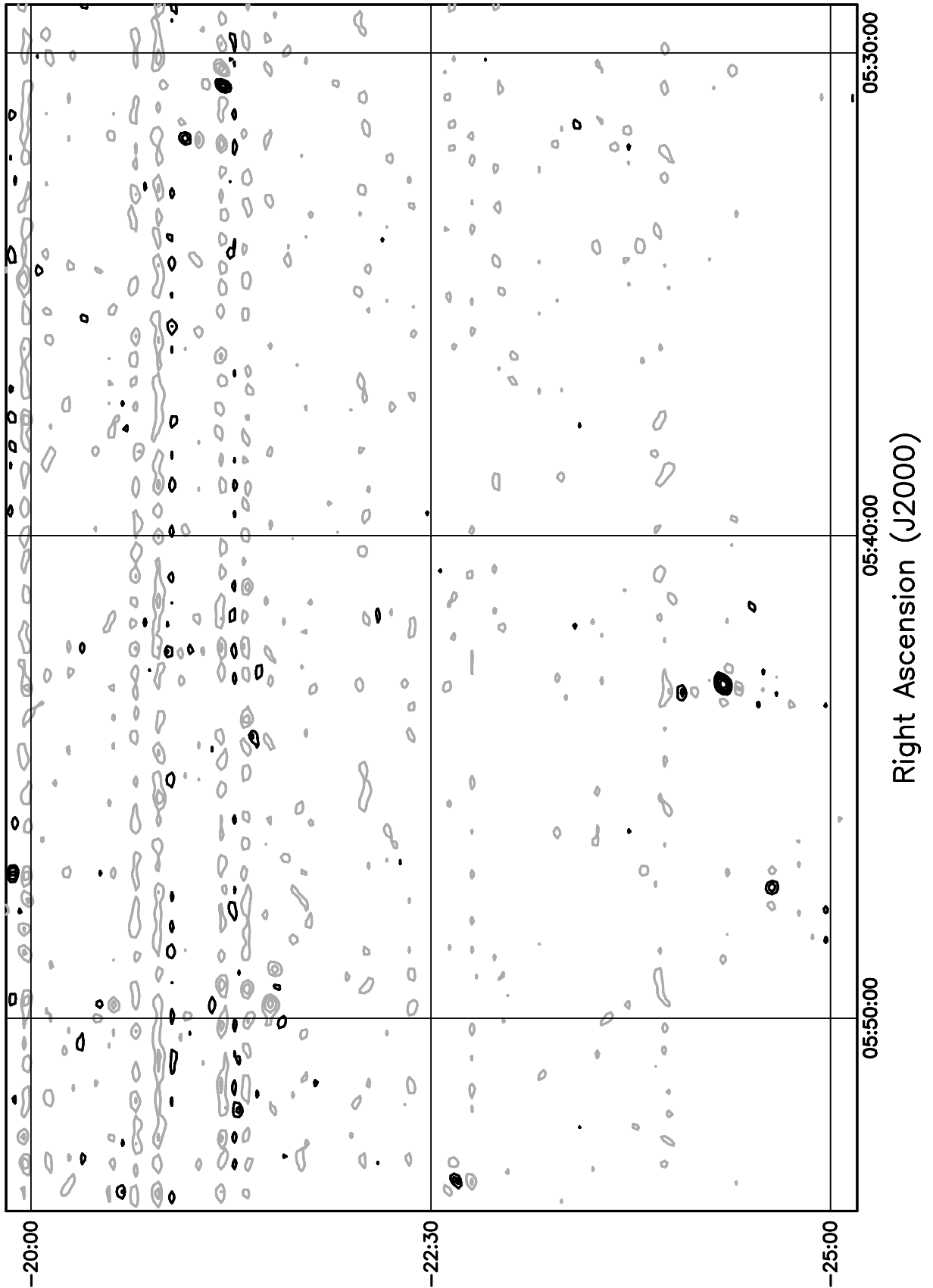
Figure 5.202: Contour plot for the range $05^h30^m \leq RA \leq 05^h54^m$, $-20° \leq \delta \leq -15°$. Contour levels are -7.56, -5.4, -3.78, -2.7, -1.62, 1.62, 2.7, 3.78, 5.4, 7.56, 10.8, 15.12, 21.6, 30.24, 43.2, 59.4, 81, 108, 151.2, 205.2, 270, 324, 378, 432 Jy beam^{-1}.
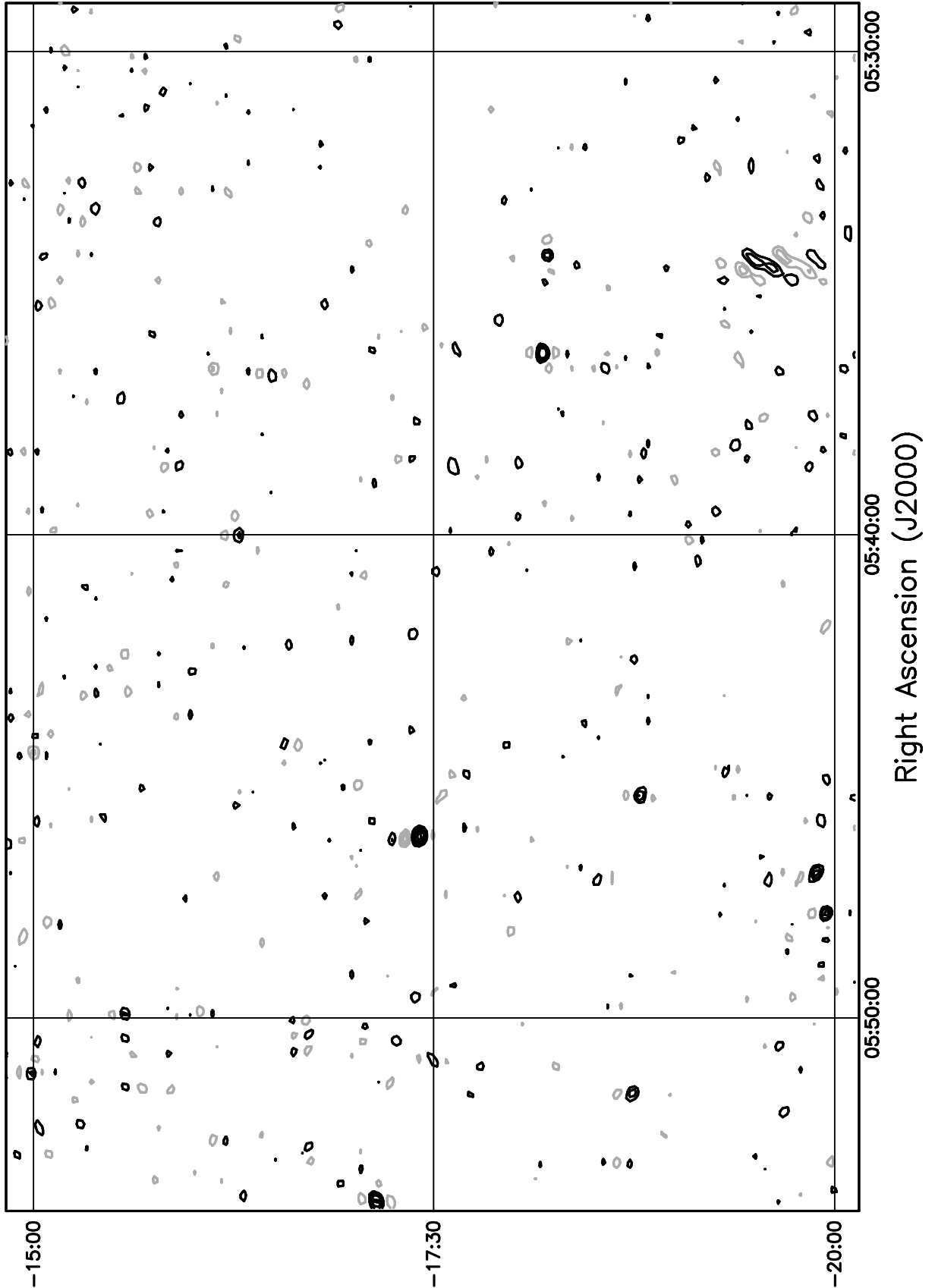
Figure 5.203: Contour plot for the range $05^h30^m \leq RA \leq 05^h54^m$, $-15° \leq \delta \leq -10°$. Contour levels are -7.56, -5.4, -3.78, -2.7, -1.62, 1.62, 2.7, 3.78, 5.4, 7.56, 10.8, 15.12, 21.6, 30.24, 43.2, 59.4, 81, 108, 151.2, 205.2, 270, 324, 378, 432 Jy beam^{-1}.
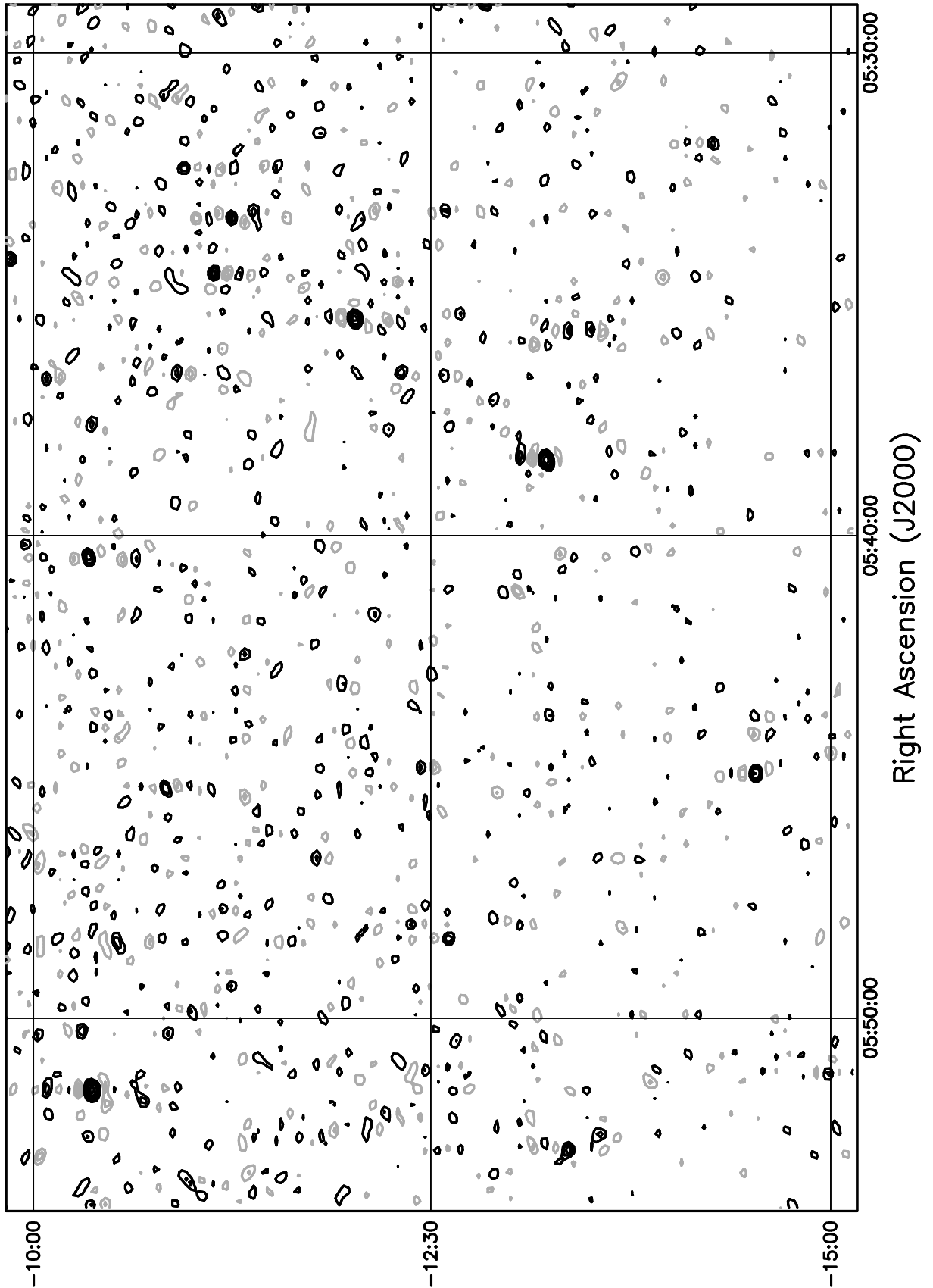
Table 5.4: 52 MS4 sources detected in the Set 1I MRT images

MRC name (B1950)	RA (J2000)	DEC (J2000)	$S_{151.5}$
0003-567	00 05 57	-56 28 29	12.44
0003-428	00 06 02	-42 34 42	7.68
0007-446	00 10 31	-44 22 58	12.66
0012-383	00 15 25	-38 05 09	7.13
0013-634	00 16 03	-63 10 10	17.86
0023-333	00 25 31	-33 03 46	10.25
0036-392	00 38 27	-39 00 06	7.67
0039-445	00 42 09	-44 14 08	14.97
0042-357	00 44 41	-35 30 36	9.98
0043-424	00 46 17	-42 07 53	21.67
0048-447	00 50 52	-44 28 36	8.61
0049-433	00 52 15	-43 06 43	11.13
0103-453	01 05 21	-45 05 31	14.23
0110-692	01 11 44	-69 00 02	11.68
0114-476	01 16 32	-47 25 35	6.2
0119-634	01 21 41	-63 09 10	12.84
0131-449	01 33 34	-44 44 29	10.1
0157-311	02 00 13	-30 53 41	21.15
0201-440	02 03 41	-43 50 08	10.52
0208-512	02 10 47	-51 01 08	7.62
0214-480	02 16 46	-47 48 53	8.11
0216-366	02 19 03	-36 26 25	9.71
0240-422	02 42 37	-42 01 55	9.94
0241-512	02 43 15	-51 05 16	7.86
0242-514	02 43 45	-51 12 36	19.11
0245-558	02 46 57	-55 41 29	20.53
0251-675	02 51 58	-67 18 18	10.3
0315-685	03 16 12	-68 21 16	8.2
0335-415	03 37 05	-41 23 35	10.46
0336-355	03 38 47	-35 23 08	10.95
0340-372	03 42 05	-37 03 35	8.42
0344-345	03 46 32	-34 22 58	11.65
0357-371	03 59 47	-37 00 40	12.87
0407-658	04 08 22	-65 45 18	40.13
0411-647	04 12 01	-64 36 17	7.31
0411-561	04 12 49	-56 01 00	12.11
0420-625	04 20 58	-62 23 53	18.36
0427-366	04 29 41	-36 31 11	13.31
0429-616	04 30 14	-61 32 43	6.75
0436-650	04 37 10	-64 59 08	8.09
0438-436	04 40 18	-43 33 32	7.16
0453-301	04 55 15	-30 07 09	15.26
0454-463	04 55 51	-46 16 28	7.03
0456-301	04 58 27	-30 07 39	9.94
0506-612	05 06 45	-61 09 50	9.93
0509-573	05 10 20	-57 19 42	8.72
0511-484	05 12 51	-48 24 24	12.96
0511-305	05 13 32	-30 30 17	4.95
0513-488	05 14 34	-48 45 24	8.2
0534-497	05 36 15	-49 44 15	11.58
0546-445	05 47 39	-44 31 09	8.81
0547-408	05 49 24	-40 51 24	14.1

Table 5.5: 62 MS4 sources detected in the Set I MRT images (Part 1)

MRC name (B1950)	RA (J2000)	DEC (J2000)	$S_{151.5}$
1756-663	18 1 21.5	-66 22 55	10.31
1814-519	18 18 7.1	-51 58 3	26.92
1814-637	18 19 35.1	-63 45 57	49.37
1817-391	18 20 36	-39 9 41	21.6
1817-640	18 22 17.3	-63 59 28	32.26
1818-557	18 22 20.7	-55 41 44	10.17
1819-673	18 24 38.1	-67 17 20	9.76
1827-360	18 30 59.1	-36 2 27	32.21
1829-344	18 32 32.7	-34 22 47	10.3
1831-668	18 36 58.5	-66 49 14	12.3
1839-487	18 43 16.4	-48 36 50	21.58
1840-404	18 44 28.6	-40 22 9	19.22
1853-303	18 57 10.7	-30 19 39	12.31
1854-663	19 0 0.2	-66 15 29	7.25
1917-546	19 21 52.6	-54 31 60	19.26
1922-627	19 27 26.6	-62 39 45	11.68
1923-328	19 26 28.4	-32 42 41	9.66
1929-397	19 33 24.4	-39 40 34	11.35
1932-464	19 35 56.8	-46 20 38	96.58
1933-587	19 37 32.3	-58 38 30	23.3
1940-406	19 43 52.1	-40 30 22	15.18
1953-425	19 57 14.7	-42 22 25	21.28
1954-552	19 58 16.8	-55 9 42	34.44
1955-357	19 59 3.3	-35 34 32	10
2006-566	20 10 22.5	-56 28 12	35.83
2009-524	20 13 21	-52 18 17	10.11
2013-557	20 18 1.3	-55 39 26	12.41
2020-575	20 24 20.3	-57 23 40	25.44
2031-359	20 34 44.4	-35 48 49	10.26
2032-350	20 35 47.5	-34 54 7	33.01
2041-604	20 45 20.3	-60 19 6	36.61
2049-368	20 52 17.7	-36 40 24	13.22
2052-474	20 56 15.7	-47 14 53	7.15
2059-641	21 3 26.9	-63 57 4	12.21

Table 5.6: 62 MS4 sources detected in the Set I MRT images (Part 2)

MRC name (B1950)	RA (J2000)	DEC (J2000)	$S_{151.5}$
2115-305	21 18 10.5	-30 19 21	16.01
2122-555	21 26 15.3	-55 21 17	11.85
2128-315	21 31 23.1	-31 21 14	10
2130-538	21 34 12.9	-53 36 39	8.42
2140-434	21 43 33.2	-43 12 53	20.84
2150-520	21 54 7.5	-51 50 2	21.54
2152-699	21 57 9.9	-69 41 23	178.19
2153-699	21 57 9.9	-69 41 23	178.19
2158-380	22 1 15.1	-37 46 54	10.02
2201-555	22 5 5.5	-55 17 39	14.13
2213-456	22 16 55.1	-45 21 32	5.72
2223-528	22 27 2.4	-52 33 16	21.3
2226-411	22 29 18.8	-40 51 38	14.27
2226-386	22 29 47.1	-38 24 13	14.82
2250-412	22 53 3.3	-40 57 60	31.42
2252-530	22 55 49.6	-52 45 31	20.33
2253-522	22 56 47.6	-51 58 30	14.67
2259-375	23 2 23.4	-37 18 12	13.71
2305-418	23 7 52.7	-41 32 44	9.03
2319-550	23 22 6.5	-54 45 32	14.15
2323-407	23 26 34.1	-40 27 28	16.72
2331-416	23 34 25.9	-41 25 36	33.23
2332-668	23 35 11	-66 36 58	14.34
2338-585	23 41 18.1	-58 16 11	19
2339-353	23 41 45.6	-35 6 20	11.26
2354-350	23 57 0.9	-34 45 32	26.3
2356-611	23 58 59.6	-60 54 41	108.62

Table 5.7: Sources detected in the Set II MRT images

MRT name (J2000)	RA (J2000)	DEC (J2000)	$S_{151.5}$	SNR
MRTJ0108-1604	01 08 17	-16 04 33	26.69	119.32
MRTJ0035-2004	00 35 09	-20 04 01	15.33	69.89
MRTJ0059-1700	00 59 07	-17 00 47	14.82	67.06
MRTJ0102-2152	01 02 41	-21 52 43	12.35	57.26
MRTJ0003-1727	00 03 23	-17 27 15	13.23	55.72
MRTJ0018-1242	00 18 52	-12 42 42	13.97	59.05
MRTJ0104-1235	01 04 23	-12 35 33	9.81	42.69
MRTJ0058-2401	00 58 28	-24 01 11	5.84	27.36
MRTJ0016-1430	00 16 20	-14 30 21	9.04	38.67
MRTJ0026-2004	00 26 14	-20 04 53	7.14	32.27
MRTJ0021-1910	00 21 13	-19 10 49	6.84	30.46
MRTJ0100-1748	01 00 11	-17 48 55	7.26	32.99
MRTJ0032-2405	00 32 22	-24 05 00	5.32	24.62
MRTJ0001-1659	00 01 06	-16 59 35	6.93	28.92
MRTJ0044-2212	00 44 12	-22 12 28	5.36	24.86
MRTJ0018-1022	00 18 60	-10 22 57	9.38	38.53
MRTJ0016-1929	00 16 01	-19 29 12	5.56	24.55
MRTJ0037-2308	00 37 23	-23 08 28	4.40	20.36
MRTJ0017-1256	00 17 08	-12 56 19	6.75	28.53
MRTJ0045-2434	00 45 03	-24 34 20	3.92	18.36
MRTJ0003-2329	00 03 49	-23 29 48	4.57	19.86
MRTJ0100-2240	01 00 42	-22 40 07	3.98	18.53
MRTJ0034-1759	00 34 25	-17 59 30	4.73	21.30
MRTJ0043-1605	00 43 55	-16 05 07	5.05	22.63
MRTJ0026-1248	00 26 11	-12 48 09	5.72	24.56
MRTJ0020-2015	00 20 29	-20 15 00	4.78	21.39
MRTJ0108-1613	01 08 18	-16 13 15	5.43	24.29
MRTJ0029-1143	00 29 59	-11 43 56	6.00	25.58
MRTJ0108-1033	01 08 35	-10 33 44	6.09	25.76
MRTJ0003-1740	00 03 43	-17 40 33	4.97	20.97
MRTJ0054-2351	00 54 30	-23 51 40	3.57	16.71
MRTJ0003-1440	00 03 11	-14 40 27	5.25	21.69
MRTJ0017-2237	00 17 59	-22 37 54	3.66	16.48
MRTJ0000-1055	00 00 59	-10 55 08	6.50	25.64
MRTJ0032-2257	00 32 03	-22 57 56	3.37	15.55
MRTJ0108-1555	01 08 16	-15 55 35	4.09	18.28
MRTJ0035-1635	00 35 37	-16 35 16	3.99	17.86
MRTJ0004-2306	00 04 02	-23 06 46	3.41	14.79
MRTJ0014-2338	00 14 04	-23 38 26	3.21	14.39

Chapter 6

Conclusions and possible directions for future work

In this chapter we summarise the important out comes of the present work, challenges faced and methodologies developed to meet those challenges. We would like to emphasise that this work has drawn substantially from the investigations carried out by researchers who worked earlier with MRT. We began this phase of work with the hope that we would complete the southern sky survey covering all the 24 hours of RA by adding images in the RA range $00^h \leq RA \leq 18^h$.However we have been able to complete imaging about a steradians of the sky in the RA range $00^h \leq RA \leq 06^h$. In view of this we have added a paragraph on possible future directions for data analysis

6.1 Conclusions

MRT was built with the main objective of surveying the southern sky at a low frequency (151.5 MHz). It is a non coplanar array using a fixed 2 km long E-W arm and a 1 km long NS arm, consisting of 16 trolleys mounted on a rail track for aperture synthesis. Imaging with MRT is really challenging. It takes 60 days of observing to cover up to 1 km NS baselines, sampling visibilities 1m apart. To obtain interference free data, our experience shows that at least 3 days of observations are required in each allocation. This stretches the time required to 180 days. In 180 days the Sun moves across the sky, spanning 12 hours of RA, playing a spoil sport in ones attempt to synthesise 24 hours of the sky. This further stretches the observation time required to 1 year.

Observations, with this background and adding time required for instrumental development testing and commissioning, took a span of 5 yeas to get 20,000 hours of observations (1 Terabyte of data) for the survey. Innovative methods of data base management (RFI mitigation, data quality assessment) were developed to facilitate data storage, data access and making the right choice of data for imaging. Innovation played a major role in developing imaging techniques for a non-coplanar array where tangent plane approximation

is taken to its extreme by imaging each pixel in the sky (This meant usage of Discrete Fourier transform for imaging). We also faced additional complexity deconvolving images made with such a non-coplanar array. The array responds differently to point sources in different directions. To minimize computations for imaging and deconvolution, we settled down for meridian transit imaging and storing several PSFs for deconvolution.

During the development phase of the project one found evolution of computing environment speeding our data processing but also burdening the software development with new tools to use. The efforts to meet these challenges culminated in imaging a steradian of the southern sky, in the range $18^h \leq RA \leq 24^h30^m$, $-75° \leq DEC \leq -10°$ (Set I images).

The present work began with the investigation of systematics in the positional errors of sources seen in the MRT source catalog. This is a by-product of Set I images. Systematics in positional errors were found when the positions of sources common to MRT and MRC (Large *et al.*, 1991) catalogues were compared. The positional errors in right ascension (RA) and declination (DEC) showed no systematics as a function of RA. However, errors showed a linear gradient as a function of DEC. The gradient in RA error is negligible whereas, DEC errors are significant and reach about 50% of the MRT beamwidth in declination. Pandey (2006) used one-dimensional (1-D) robust least-squares fit, to estimate the errors and corrected them in the source catalog. However, the errors remained in the images, which impede usefulness of MRT images for multi-wavelength analysis of sources.

At MRT, the visibility data is processed through several complex stages of data reduction specific to the array, especially, arising due to its non-coplanarity. It was therefore decided to correct for the errors in the image domain and avoid re-processing the visibility data.

We applied two-dimensional homography to correct for systematic positional errors in the image domain and thereby avoid re-processing the visibility data. Positions of bright (above 15 σ) point sources, common to MRT catalogue and MRC, were used to set up an over-determined system to solve for the homography matrix. After correction the errors were found to be within 10% of the beamwidth for these bright sources and the systematics are eliminated from the images. We are of the view that this technique will be of relevance to the new generation radio telescopes where, owing to huge data rates, only images after a certain integration would be recorded as opposed to raw visibilities. Our investigations cued to possible errors in the array geometry. We re-estimated the array geometry using the astrometry principle. The estimates show an error of 1 mm/m, which results in an error of about half a wavelength at 150 MHz for a 1 km north-south baseline. The estimates also indicate that the east-west arm is inclined by an angle of $\sim 40''$ to the true east-west direction.

We re-imaged regions of sky common to set I images using the re estimated array geometry and proved that the systematic positional errors disappear by incorporating the

new array geometry.

Having done this we set fourth about imaging the remaining 18 hours of RA range. The MRT database, its storage and access (1 Terabyte of data) for imaging and also imaging methods, are indeed complex. So we assembled a set of 8 computers inter-connected using a 100 Mbps ethernet link to store the intermediate products of analysis and also meet the demands of computing 18 hours of images. This is not possible by manually running the X-marmosat suite of programs. Having realised this we developed a set of software pipelines to run X-marmosat effectively on this MRT cluster.

The main focus of the new development was inter-process communication and homogenisation of the database which had kept changing in structure along with online system development and commissioning. We also paid attention to the fact that one required the final products in FITS image format to be able to distribute the images to the astronomical community.

Armed with good hardware and software environments, we examined the quality of data for the RA range 0 to 18 hours. We found that the data quality decreased as one moved away from the calibrators used for phase/amplitude calibration of the array. In view of this we designed and developed a field based calibration procedure to facilitate calibration. This helpled us to get calibration very close to the proximity of the sky area being analysed.

With feed back from data quality assessment we set fourth analysing 0 to 6 hours RA range. We used the 23 to 24 hour images from the set I to calibrate a 3 hours stretch of the data from 23 to 26 hours (X, A and B hours) This gave excellent results and the rms noise ($\sim$ 200 mJy) is among the best noise achieved at MRT. We used the images obtained for 3 hour to calibrate the subsequent hours and so on. The quality of images are within acceptable limits for 0 to 6 hours RA range. Unfortunately due to the propagation of calibration errors and the decrease in the quality of data, we were not able to image beyond 6 hours of RA range in the time available for this work.

This thesis presents images generated for $00^h \leq RA \leq 06^h$, $-75° \leq DEC \leq -10°$ range, covering approximately one steradian of the sky. The images are divided into half hour RA ranges and 5 degree in declinations.We find slightly higher level of noise in D, E, and F hours compared to B, C and D hours. We have been able to detect 3837 sources in Set II images. 1500 of these sources have matching MRC sources, When compared to MRC sources the positions of MRT sources did show offsets in RA and DEC (3% and 4%). After correcting for these, the positional errors as a function of RA and Dec show very low levels of systematic and the errors are randomly distributed around a cloud centered around zero with a radii $\sim$ 10% of the beamwidths in RA and DEC.

A comparison of flux density of sources common to MRT and MRC showed several interesting features (problems !!). Since the images were not brought to the same flux level after deconvolution we did find certain systematics in the ratio of MRT to MRC flux

densities as a function RA. We noticed a steady decrease of 5% of the median flux ratio in the RA range 00 to 04 hrs. The sources in images for the RA hours 04 to 05 (E hr) and 05 to 06 (F hr) hr showed a 15% to 20% percent offset in flux ratio. Pivoting around the flux density ratio for the source MRC2354-350 which used as a primary flux calibrator for MRT, we corrected for these systematics.

The ratio of these corrected flux densities as a function of DEC showed residual systematics. The southern most sources seem to be under corrected by 13% percent and northern sources over corrected by 10% by the primary beam used. To remove these systematics we recalibrated our primary beam. This showed that the primary beam peaks around DEC $\sim 47°$ and falls off slowly at higher southern declinations than the sky towards the northern hemisphere. After applying these corrections, we found the ratio of flux densities of MRT to MRC sources does not show any visible systematics as a function of either RA and/or DEC. The revised flux density scale required no adjustments with respect to the flux density of the primary flux calibrator MRC2354-350 (within 3%). It's flux density is 26.65 at 151.5 MHz. The revised flux density scale shows a median spectral index of 0.87. This numbers is along the expected lines.

In this thesis we have presented a source catalog of $\sim$3500 sources. From this we extracted a subset of sources which match with MS4 sources. In this phase of preliminary analysis of images and source catalog we have not been able to derive a satisfactory value for completeness. It is important to weed out sources picked up from artefacts in images and sidelobes of sources left unCleaned after deconvolution. However, of the sources available we have noted a list of sources which have steep spectral indices ($RA < -1.3$). We hope to pursue a study of them using GMRT,ATCA etc.

The MRT has a very good UV coverage with baselines going down to 2m both along EW and S. With this we were indeed expecting to detect extended sources in the images. As a first step we started with Jones & McAdam (1992) paper on the structure of southern extragalactic radio sources and looked for extended sources in MRT images at the position of the sources given in the paper. We were able to detect all the 71 sources listed in the paper in the range RA 0 to 6 hrs. 33 of these sources show extended emission at 151.5 MHz. In addition we find 16 extended sources in MRT not listed in Jones & McAdam (1992) paper. The median spectral index of the 33 extended sources common to MRT and SUMSS is 0.74. We have prepared a source list including the integrated flux densities and spectral indices of these sources. We envisage a follow-up study of these sources in our future work.

6.2   Possible directions for future work

Imaging 6 to 18 hrs of RA range remains to be carried out with improvisation of the methods used for data quality assessment. This is essential to chose good quality data

to image the 12 hour RA range. It is profitable to consider incorporating the following 3 important steps in imaging at MRT:

1. Self calibration after analysing a given RA range (3 hr RA range). It is profitable to re-run imaging routines using the sources detected in the first round. This was not done with the amount of time required to re-run the process. Investigations to optimise re-running time also deserves attention.

2. Presently imaging is carried out only on meridian. One has to develop a 2-D imaging algorithm which would take into account the changing sidelobe pattern as a function of hour angle imaged.

3. At an appropriate stage in self-calibration it is useful to incorporate "peeling" which is a modified version of uv clean or uv subtract. All these steps are bound to have an impact on the dynamic range of images and will also contribute to improve the sensitivity of the MRT images.

4. It is also useful to consider porting the measured MRT visibilities to FITS format. This will enable usage of methods under development at MWA and LOFAR for widefield imaging

References

BAARS, J.W.M., GENZEL, R., PAULINY-TOTH, I.I.K. & WITZEL, A. (1977). The absolute spectrum of CAS A - an accurate flux density scale and a set of secondary calibrators. *Astronomy and Astrophysics*, **61**, 99–106. 58

BALDWIN, J.E., BOYSEN, R.C., HALES, S.E.G., JENNINGS, J.E., WAGGETT, P.C., WARNER, P.J. & WILSON, D.M.A. (1985). The 6C survey of radio sources. I - Declination zone delta greater than +80 deg. *MNRAS*, **217**, 717–730. 5

BLUNDELL, K.M., RAWLINGS, S., EALES, S.A., TAYLOR, G.B. & BRADLEY, A.D. (1998). A sample of 6C radio sources designed to find objects at redshift z > 4 - I. the radio data. *MNRAS*, **295**, 265–279. 5

BOWERS, F.K. & KLINGLER, R. (1974). Quantization Noise of Correlation Spectrometers. *Astronomy and Astrophysics Supplement*, **15**, 373–+. 14, 82

BURGESS, A.M. & HUNSTEAD, R.W. (2006). The Molonglo Southern 4 Jy sample (ms4). i. Definition. *Astronomical Journal*, **131**, 100–113. 7, 8, 25, 60

CALABRETTA, M.R. & GREISEN, E.W. (2002). Representations of celestial coordinates in FITS. *Astronomy and Astrophysics*, **395**, 1077–1122. 54

CHRISTIANSEN, W.N. & HOGBOM, J.A. (1969). *Radiotelescopes, by W. N. Christiansen and J. A. Hogbom*. Cambridge U.P., London,. 39

CONDON, J.J., COTTON, W.D., GREISEN, E.W., YIN, Q.F., PERLEY, R.A., TAYLOR, G.B. & BRODERICK, J.J. (1998). The NRAO VLA Sky Survey. *Astronomical Journal*, **115**, 1693–1716. 2

DE BREUCK, C., VAN BREUGEL, W., RÖTTGERING, H.J.A. & MILEY, G. (2000). A sample of 669 ultra steep spectrum radio sources to find high redshift radio galaxies. *Astronomy and Astrophysics Supplement Series*, **143**, 303–333. 101

DE BRUYN, G.A. (2009). LOFAR and Wide Field Imaging. In *Proceedings of Wide Field Astronomy Technology for the Square Kilometre Array (SKADS 2009). 4-6 November 2009. Chateau de Limelette, Belgium. Published online at ¡A*

href="http://pos.sissa.it/cgi-bin/reader/conf.cgi?confid=132"¿http://pos.sissa.it/cgi-bin/reader/conf.cgi?confid=132¡/A¿, id.69. 5

DODSON, R. (1997). *The Mauritius Radio Telescope and a study of Selected Super Nova Remnants Associated with Pulsars*. Ph.D. thesis, University of Durham, Department of Physics. 17, 18, 25, 49

DOUGLAS, J.N., BASH, F.N., BOZYAN, F.A., TORRENCE, G.W. & WOLFE, C. (1996). The Texas Survey of radio sources covering -35.5 degrees < declination < 71.5 degrees at 365 mhz. *Astronomical Journal*, **111**, 1945–+. 4

EALES, S.A. (1985). A sample of 6C sources selected at the peak of the source counts - part three - an investigation of the variation of the sizes of radio sources with cosmic epoch. *MNRAS*, **217**, 179–. 5

ERICKSON, W., J., M.M. & ERB, K. (1982). The Clark Lake Teepee-Tee Telescope. *ApJS*, **50**, 403. 14

GOLAP, K. (1998). *Synthesis Imaging at 151.5 MHz using the The Mauritius Radio Telescope*. Ph.D. thesis, University of Mauritius, Physics Department. 3, 86

GOLAP, K. & UDAYA SHANKAR, N. (2001). Deconvolution of Wide-field Images from a Non-Coplanar T-Array. *Journal of Astrophysics and Astronomy*, **22**, 251–262. 17

GOLAP, K., DODSON, R. & UDAYA SHANKAR, N. (1995). A calibration scheme for the Mauritius Radio Telescope. *Bulletin of the Astronomical Society of India*, **23**, 574–+. 21

GOLAP, K., UDAYA SHANKAR, N., SACHDEV, S., DODSON, R. & SASTRY, V., CH. (1998). A low frequency radio telescope at Mauritius for a southern sky survey. *J. Astrophys. Astr.*, **19**, 35–53. 7, 11, 13, 14, 15, 16, 21, 55

GREEN, D.A. (2009). A Catalogue of Galactic Supernova Remnants (Green, 2009). *VizieR Online Data Catalog*, **7253**, 0–+. 8, 105

HARTLEY, R. (1997). In defense of the eight-point algorithm. *IEEE Transactions on Pattern Analysis and Machine Intelligence*, **19**, 580–593. 35

HARTLEY, R.I. & ZISSERMAN, A. (2004). *Multiple View Geometry in Computer Vision*. Cambridge University Press, ISBN: 0521540518, 2nd edn. 33, 35

HASLAM, C.G.T., KLEIN, U., SALTER, C.J., STOFFEL, H., WILSON, W.E., CLEARY, M.N., COOKE, D.J. & THOMASSON, P. (1981). A 408 MHz all-sky continuum survey. I - Observations at southern declinations and for the North Polar region. *Astronomy and Astrophysics*, **100**, 209–219. 61

Jarvis, M.J., Rawlings, S., Eales, S., Blundell, K.M., Bunker, A.J., Croft, S., McLure, R.J. & Willott, C.J. (2001). A sample of 6C radio sources designed to find objects at redshift z > 4 - III. imaging and the radio galaxy K-z relation. *MNRAS*, **326**, 1585–1600. 5

Jones, P.A. & McAdam, W.B. (1992). The structure of southern extragalactic radio sources. *The Astrophysical Journal Supplement Series*, **80**, 137–203. 8, 38, 64, 106, 107, 289

Kassim, N.E., Lazio, T.J.W., Ray, P.S., Crane, P.C., Hicks, B.C., Stewart, K.P., Cohen, A.S. & Lane, W.M. (2004). The low-frequency array (LOFAR): opening a new window on the universe. *Planetary and Space Science*, **52**, 1343–1349. 2

Klamer, I.J., Ekers, R.D., Bryant, J.J., Hunstead, R.W., Sadler, E.M. & De Breuck, C. (2006). A search for distant radio galaxies from SUMSS and NVSS - III. Radio spectral energy distributions and the z-α correlation. *Monthly Notices of the Royal Astronomical Society*, **371**, 852–866. 102

Lane, W.M., Cohen, A.S., Lazio, T.J.W., Kassim, N.E., Cotton, W.D., Perley, R.A., Condon, J.J. & Erickson, W.C. (2005). The VLA Low-frequency Sky Survey (VLSS). In *Bulletin of the American Astronomical Society*, vol. 37 of *Bulletin of the American Astronomical Society*, 1201–+. 5

Large, M.I., Cram, L.E. & Burgess, A.M. (1991). A machine-readable release of the Molonglo Reference Catalogue of radio sources. *The Observatory*, **111**, 72–75. 4, 30, 287

Mauch, T., Murphy, T., Buttery, H.J., Curran, J., Hunstead, R.W., Piestrzynski, B., Robertson, J.G. & Sadler, E.M. (2003). SUMSS: a wide-field radio imaging survey of the southern sky - II. the source catalogue. *MNRAS*, **342**, 1117–1130. 4, 37

Mauch, T., Murphy, T., Buttery, H.J., Curran, J., Hunstead, R.W., Piestrzynski, B., Ropbertson, J.G. & Sadler, E.M. (2008). Sydney University Molonglo Sky Survey (SUMSS V2.1) (Mauch+ 2008). *VizieR Online Data Catalog*, **8081**, 0–+. 3

Morales, M.F., Bowman, J.D., Cappallo, R., Hewitt, J.N. & Lonsdale, C.J. (2006). Statistical EOR detection and the Mileura Widefield Array. *New Astronomy Review*, **50**, 173–178. 2, 6

Nayak, A., Daiboo, S. & Udaya Shankar, N. (2010). Two-dimensional homography-based correction of positional errors in widefield mrt images. *MNRAS*, **408**, 1061–1069. 29

PANDEY, V. & UDAYA SHANKAR, N. (2006). A steradian of the southern sky at 151.5 MHz using the Mauritius Radio Telescope. *Long Wavelength Astrophysics, 26th meeting of the IAU, Joint Discussion 12, 21 August 2006, Prague, Czech Republic*, **12**. iv, 19, 26, 79, 80

PANDEY, V.N. (2006). *A Southern Sky Survey at 151.5 MHz using the Mauritius Radio Telescope*. Ph.D. thesis, Raman Research Institute. 3, 8, 16, 17, 18, 21, 22, 23, 24, 25, 26, 29, 30, 44, 49, 50, 55, 58, 60, 64, 66, 71, 72, 81, 84, 86, 87, 96, 102, 105, 287

RENGELINK, R.B., TANG, Y., DE BRUYN, A.G., MILEY, G.K., BREMER, M.N., ROETTGERING, H.J.A. & BREMER, M.A.R. (1997). The Westerbork Northern Sky Survey (WENSS), i. a 570 square degree mini-survey around the north ecliptic pole. *A & A Supplement series*, **124**, 259–280. 4

ROGER, R.S., COSTAIN, C.H. & BRIDLE, A.H. (1973). The low-frequency spectra of nonthermal radio sources. *Astrophysical Journal*, **78**, 1030–+. 58

SACHDEV, S. (1999). *Wide Field Imaging With The Mauritius Radio Telescope*. Ph.D. thesis, University of Mauritius, Physics Department. 64, 85, 86

SACHDEV, S. & UDAYA SHANKAR, N. (2001a). Detection, Excision and Statistics of Interference at the Mauritius Radio Telescope. *Journal of Astrophysics and Astronomy*, **22**, 213–228. 17

SACHDEV, S. & UDAYA SHANKAR, N. (2001b). Wide-field imaging with the Mauritius Radio Telescope. *Journal of Astrophysics and Astronomy*, **22**, 229–250. 15, 17, 21, 49

SAUNDERS, R., BALDWIN, J.E. & WARNER, P.J. (1987). A totally incomplete sample of extended 6C radio sources. *MNRAS*, **225**, 713–721. 5

SCHOENMAKERS, A.P., DE BRUYN, A.G., RÖTTGERING, H.J.A. & VAN DER LAAN, H. (2000). Radio galaxies with a 'double-double' morphology - III. the case of B1834+620. *MNRAS*, **315**, 395–406. 4

SLEE, O.B. & SIEGMAN, B.C. (1988). A survey for metrewave variability in extragalactic radio sources. *MNRAS*, **235**, 1313–1341. 25, 60, 64, 70

SOMANAH, R. (2007). *A low Resolution Survey of the Southern Sky Survey at 151.5 MHz using the Mauritius Radio Telescope*. Ph.D. thesis, University of Mauritius, Physics Department. 17

THOMPSON, A.R., MORAN, J.M. & SWENSON, G.W.J. (2001). *Interferometry and Synthesis in Radio Astronomy, 2nd Edition*. John Wiley and Sons, London. 39, 42, 81

Udaya Shankar, N. & Pandey, V.N. (2006). Hierarchical RFI mitigation system at the Mauritius Radio Telescope. *Astronomical Data Management, 26th meeting of the IAU, Special Session 6, 22 August, 2006 in Prague, Czech Republic, SPS6, #22*, **6**. 17, 20

Udaya Shankar, N., Golap, K., Sachdev, S., Dodson, R., Katwaroo, M. & Sastry, C. (2002). Imaging with the Mauritius Radio Telescope challenges and results. *Astrophysics and Space Science*, **282**, 15–28. 7, 11, 30

van Weeren, R.J., Röttgering, H.J.A. & Brüggen, M. (2011). Diffuse steep-spectrum sources from the 74 MHz VLSS survey. *Astronomy & Astrophysics*, **527**, A114+. 101

Wall, L., Christiansen, T. & Orwant, J. (2000). *Programming Perl, Third edition*. O'Reilly, Sebastopol, CA, USA. 51

White, R.L., Becker, R.H., Helfand, D.J. & Gregg, M.D. (1997). A Catalog of 1.4 GHz Radio Sources from the FIRST Survey. *Astrophysical Journal*, **475**, 479–+. 88

Zhang, X.Z., Reich, W., Reich, P. & Wielebinski, R. (2003). On the Spectral Index-Flux Density Relation for Large Samples of Radio Sources. *Chinese Journal of Astronomy and Astrophysics*, **3**, 347–358. 101, 102